université PARIS-SACLAY

Catalytic properties at the nanoscale probed by surface x-ray diffraction and coherent diffraction imaging

Propriétés catalytiques à l'échelle nanométrique sondées par diffraction des rayons X de surface et imagerie de diffraction cohérente

Thèse de doctorat de l'université Paris-Saclay

École doctorale n° 564, Physique en Île-de-France (PIF)
Spécialité de doctorat: Physique
Graduate School: Physique. Référent: Faculté des sciences d'Orsay

Thèse préparée dans les unités de recherche **Synchrotron Soleil (Université Paris-Saclay)** et **Modélisation et Exploration des Matériaux (Université Grenoble Alpes, CEA)**, sous la direction d'**Alessandro COATI**, Docteur, la co-direction de **Marie-Ingrid RICHARD**, Directrice de recherche, et le co-encadrement de **Andrea RESTA**, Docteur

Thèse soutenue à Paris-Saclay, le 12 janvier 2024, par

David SIMONNE

Composition du jury

Membres du jury avec voix délibérative

Sylvain RAVY Directeur de recherche, LPS, Université Paris-Saclay	Président du jury
Andreas STIERLE Professeur, University of Hamburg / DESY	Rapporteur & Examinateur
Thomas CORNELIUS Directeur de recherche, IM2NP, Aix-Marseille Université	Rapporteur & Examinateur
Gerardina CARBONE Dr., Lund University	Examinatrice
Virginie CHAMARD Directrice de recherche, Institut Fresnel, Aix-Marseille Université	Examinatrice

THÈSE DE DOCTORAT

NNT : 2024UPASP001

université PARIS-SACLAY

ÉCOLE DOCTORALE
Physique en Île-de-France (PIF)

Titre: Propriétés catalytiques à l'échelle nanométrique sondées par diffraction des rayons X de surface et imagerie de diffraction cohérente

Mots clés: Diffraction de rayons X, Catalyse hétérogène, Surface, Structure cristalline, Déformation, Oxydation de l'ammoniac

Résumé:

Le principal objectif de ce travail est d'étudier des catalyseurs hétérogènes *in situ* et *operando* pendant l'oxydation de l'ammoniac en se rapprochant des valeurs de température et pression industrielles. Actuellement, ce processus catalytique et les changements structurels associés sont mal compris. Nous proposons d'utiliser différents échantillons en platine - nanoparticules et monocristaux - afin de réduire l'écart entre les études scientifiques sur échantillons modèles et les catalyseurs utilisés en industrie. L'activité catalytique des différents échantillons est mesurée pour lier structure et sélectivité durant la réaction, qui peut être focalisée vers la production d'azote (N_2), d'oxyde nitrique (NO), ou de protoxyde d'azote (N_2O). Le développement d'une catalyse hétérogène avec une sélectivité ciblant les 100 % est un défi constant, ainsi que la compréhension de la durabilité, du vieillissement, et de la désactivation du catalyseur. Trois techniques ont été principalement utilisées, l'imagerie par diffraction cohérente de Bragg, la diffraction des rayons X de surface et la spectroscopie photoélectronique des rayons X, combinées à des mesures par spectrométrie de masse. Ces techniques sont compatibles avec des conditions de pression ambiantes, permettant de réduire l'écart de pression entre expérience et industrie en catalyse hétérogène. Mesurer la structure de nanoparticules à l'échelle nanométrique permet de révéler les effets de volume, de tension et de compression de surface et d'interface, ainsi que l'existence de différents types de défauts. En complément des études d'imagerie par diffraction cohérente de rayons X en condition de Bragg sur des nanoparticules individuelles, l'étude d'un ensemble de nanoparticules est effectuée *via* la diffraction des rayons X à incidence rasante. La diffraction cohérente de rayons X en condition de Bragg étant une technique récente, une organisation typique de la réduction et de l'analyse des données est proposée. L'importance d'étudier plusieurs particules a été mise en perspective par l'étude comparative de deux particules durant l'oxydation de l'ammoniac à 300 °C et 400 °C, en fonction du rapport entre O_2 et NH_3. Différents comportements ont été révélés sur les deux nanoparticules, qui présentent une taille, une forme, des facettes et un état de déformation initial différents, alors qu'aucun important changement n'a été mesuré en dessous de 600 °C par diffraction de surface. Une particule a montré une diminution/augmentation réversible de la déformation homogène lorsque l'ammoniac a été introduit/retiré du réacteur. L'apparition d'un défaut à 400 °C est liée à une augmentation non réversible et importante de la déformation homogène lors de l'oxydation de l'ammoniac pour la seconde particule, qui continue d'augmenter en fonction du rapport entre ammoniac et oxygène. Cette évolution structurelle est clairement visible en 3D, avec des volumes de densité électronique de Bragg manquants. De plus, deux type de surfaces présente sur les nanoparticules ({111} et {100}) ont été étudiées à l'aide de monocristaux par diffraction des rayons X en surface, et spectroscopie photoélectronique par rayons X. De ce fait, la structure de surface ainsi que la présence d'espèces adsorbées peuvent être reliées à l'activité catalytique mesurée, permettant une meilleure compréhension du mécanisme de réaction. Différentes reconstructions de surfaces ont été mesurées sur le Pt(100) pendant la réaction, ce qui n'est pas le cas pour le Pt(111). La présence d'oxygène est liée à une importante rugosité de surface, alors que la présence d'ammoniac à une baisse de celle-ci. De plus, différentes oxydes, ainsi que des structures transitoires ont été identifiés sur les deux monocristaux. La mesure de différents niveaux par spectroscopie photoélectronique à rayons X a permis de lier une sélectivité accrue du Pt(100) vers NO par rapport au Pt(111) avec une plus importante présence d'oxygène adsorbée sur la surface.

université PARIS-SACLAY

ÉCOLE DOCTORALE
Physique en Île-de-France (PIF)

Title: Catalytic properties at the nanoscale probed by surface X-ray diffraction and coherent diffraction imaging

Keywords: X-ray diffraction, Heterogeneous catalysis, Surface, Crystal structure, Strain, Ammonia oxidation

Abstract: The main objective of this work is to study heterogeneous catalysts *in situ* and *operando* during the oxidation of ammonia by approaching industrial temperature and pressure values. Currently, this catalytic process and the associated structural changes are poorly understood, and we propose to use different samples in platinum, nanoparticles and single crystals in order to reduce the gap between scientific studies on model samples and catalysts used in industry. The catalytic activity of the different samples is measured to link structure and selectivity during the reaction, which can be focused towards the production of nitrogen (N_2), nitric oxide (NO), or nitrous oxide (N_2O). Developing heterogeneous catalysis with selectivity targeting 100 % is an ongoing challenge, as is understanding the durability, ageing, and deactivation of the catalyst itself. Three techniques were mainly used, Bragg coherent diffraction imaging, surface X-ray diffraction and X-ray photoelectron spectroscopy, combined with mass spectrometry measurements. These techniques are compatible with ambient pressure, making it possible to reduce the difference in pressure between surface science studies and industrial conditions for heterogeneous catalysis. Measuring the structure of nanoparticles at the nanoscale makes it possible to reveal the effects of volume, surface and interface tension and compression, as well as the existence of different types of defects. In addition to imaging studies by coherent X-ray diffraction in Bragg conditions on individual nanoparticles, the study of a set of nanoparticles is carried out *via* grazing incidence X-ray diffraction. Coherent X-ray diffraction in Bragg conditions being a recent technique, a typical organisation of data reduction and analysis is proposed. The importance of studying several particles was put into perspective by the comparative study of two particles during the oxidation of ammonia at 300 °C and 400 °C as a function of the pressure ratio between O_2 and NH_3. Different behaviours were revealed on the two nanoparticles, which present a different size, shape, facet coverage and initial deformation state, while no significant changes were measured below 600 °C by diffraction of surface. One particle showed a reversible decrease/increase in homogeneous strain when ammonia was introduced/removed from the reactor. The appearance of a defect at 400 °C is linked to a non-reversible and significant increase in the homogeneous deformation during the oxidation of ammonia for a second particle, which continues to increase as a function of the ratio between ammonia and oxygen. This structural evolution is clearly visible in 3D, with missing Bragg electron density volumes. In addition, two types of surfaces present on the nanoparticles ({111} and {100}) were also studied using single crystals by surface X-ray diffraction and X-ray photoelectron spectroscopy. Therefore, the surface structure as well as the presence of adsorbed species can be linked to the measured catalytic activity, allowing a better understanding of the reaction mechanism. Different surface reconstructions were measured on Pt(100) during the reaction, which is not the case for Pt(111). The presence of oxygen is linked to significant surface roughness, while the presence of ammonia is linked to a reduction in roughness. Furthermore, different oxides, as well as transient structures, were identified on the two single crystals. The measurement of different levels by X-ray photoelectron spectroscopy made it possible to link an increased selectivity of Pt(100) towards NO compared to Pt(111) to a greater presence of oxygen adsorbed on the surface.

Dedication

I would like to dedicate this thesis to Brittany who has pushed and supported me every day since we've met in a crystallography course.

Declaration

I hereby declare that this thesis is my original work and has not been presented and will not be presented to any other university or institution for a similar or any other degree or professional qualification. I have acknowledged all sources of information that have been used in the thesis, including any assistance that has been received during the research and writing process. Any contribution by individuals or sources other than my own has been cited and acknowledged. I understand that any act of plagiarism or academic dishonesty is a violation of the academic integrity policy of the University Paris-Saclay, and I am aware of the potential consequences.

David Simonne

Acknowledgements

I extend my deepest gratitude to Andrea for his unwavering support throughout the duration of this thesis. You have contaminated me with your love of Linux and open source technology, and set a strong example in terms of commuting to work by bicycle, which I failed to follow in rainy and cold days. Thank you very much for all the feedback that you gave me about this thesis, down to the details in the figure placement, font size, line width, and sentence length. Pursuing your interest in the study of the ammonia oxidation has allowed me to explore a large subject. This work has given me a missing sense of purpose, as it feels like my contribution is ever so slightly adding to the global endeavour in combating global warming and climate change.

I am immensely grateful for the shared beamtimes, the camaraderie during strenuous long shifts in summer or winter, skipping breakfast or dinner, compiling data while monitoring the sample heater.

Thank you Alessandro for being engaged in everything you do, at work and outside, for taking care of all the tedious work so that I could have the best possible experience, for inviting me to have meals, for the nice chats during commute, and for providing the SixS beamline with good Italian coffee. I am most importantly grateful for all the crucial scientific feedback you have provided during this thesis, for accompanying me during beamtime, and for your attention to detail down to the many index of the many equations illustrating this thesis.

Thank you Marie-Ingrid for being so driven by your love of science that everybody around wants to participate, for arranging my stay in Grenoble and bringing all of the padawans to conferences, for always being in a good mood and ready to discuss new challenging experiments. Thank you for the support regarding especially BCDI, a technique with a data analysis process quite difficult to decipher in the first months, and that always brings new questions and new experiment ideas.

Thank you to my three advisors for being good mentors, allowing me to teach, to participate in schools and numerous beamtimes, for having my best interest in mind at all times and for trusting me. I have learned an incredible amount from each of you and particularly appreciated the beamtime at Diamond, during which the four of us collected many electrons, but also shared meaningful conversations around a pint of beer and delicious stew.

I am very grateful to the research staff of SixS, to Alina and Yves for helping me when I was lost in the reciprocal space, to Benjamin without which none of the experiments could be possible, and to Michèle for her numerous advice. Thank you also Frédéric for spending a lot of time in helping us regarding BCDI and SXRD code development. Thank you to all the young researchers at SOLEIL for creating a group so that Saclay did not feel too remote and secluded. Thank you for the direction of SOLEIL who has supported my going to different conferences, abroad and in France, as well as for providing a superb working environment.

I of course have a specific thought for the Grenoble legions, half of whom I don't know half as well as I should like, and half of whom I know from half my stay spent in beamtime. Maxime, for introducing me to the world of political satire videos during ammonia oxidation cycles at SixS; Corentin, for the delightful culinary explorations in Grenoble, and for lending me the ID01 bicycle; Clément, for your constant positivity and our conversations about

the promising future of PhD students; Nikita and Mattia, for the shared moments over a refreshing beer and the intense MSSBB games during Hercules; Ewen, for representing Bretagne alongside me; Edoardo, for the initiative of LAN parties, and the unforgettable Quake games; and Noor, for being an exceptional office (and coffee) mate in Grenoble.

I would also like to thank Steven for his great advice and for kind conversations, as well as Tobias and Joël for facilitating my stay in Grenoble for a few months during this thesis. Thank you Vincent for letting me participate in the engaging ESRF tutorials, and Jérôme for starting the large work of bringing our BCDI community together in code development. My heartfelt appreciation to Sarah and Stéphane for their warm hospitality in Marseille and their engaging discussions.

I feel very grateful towards Virginie and Christian who have followed me during the thesis by participating in the CSI, even available on weekends so that I would not miss registrations deadlines.

Thank you Andrea, Davide, Elisa and all the others from the university of Torino for making me want to pursue an academic path. Thank you Davide again for hosting me in Grenoble after the ESRF user meeting because my train got cancelled, thank you Alessia and Giorgio for welcoming me.

Thank you to all the MaMaSELF members without which I would never have kept studying physics and material science, and thus missed on studying in many countries, discovering new cultures, and mindsets. Thank you Michael for bringing me to the world of neutron diffraction at Munich, and for letting me participate in my first beamtime at the ILL with Ulrike, a master and PhD student that had to learn a lot fast, but sadly not fast enough to handle the beam polarisation well.

Thank you to all the professors from Rennes that transmitted me their love of physics, especially Pr. Guérin that permitted me to study one year in Japan, thank you to Pr. Iwai for accepting me as part of his group in Sendaï.

Finally, to my family, whose unwavering support has bolstered my every endeavour, to Lucas, whose shared passion for science has been a source of motivation, and to my parents, for their trust and encouragement in my global pursuits. Thank you to all my friends that have seen me being projected in numerous states during those three years, and without which I would probably not have kept the same level of sanity.

I extend my thanks to the esteemed members of the jury for their invaluable feedback and constructive critique, shaping the course of this work.

Furthermore, I acknowledge the invaluable support and resources provided by synchrotron SOLEIL, the CEA Grenoble, and the ERC Carine, without which this research endeavour would not have been feasible.

Lastly, I express my gratitude to all those who have, in various capacities, contributed to the completion of this thesis.

Résumé étendu en français

Dans le premier chapitre de cette thèse, l'oxydation de l'ammoniac (NH_3) ainsi que son importance est présentée. La réaction peut être décrite par trois équations qui, en fonction du rapport stoechiométrique entre NH_3 et O_2, ont des produits différents.

$$4NH_3 + 3O_2 \rightarrow 6H_2O + 2N_2 \quad (1)$$
$$4NH_3 + 4O_2 \rightarrow 6H_2O + 2N_2O \quad (2)$$
$$4NH_3 + 5O_2 \rightarrow 6H_2O + 4NO \quad (3)$$

Cette réaction et ses produits associés ont exercé une profonde influence au cours des $20^{ème}$ et $21^{ème}$ siècles, jouant un rôle central par exemple dans l'industrie des engrais (procédé d'Ostwald, *via* la synthèse acide nitrique) et les changements démographiques associés. Malgré son importance industrielle cruciale, les diverses applications industrielles liées au procédé d'Ostwald ont contribué de manière significative à la fois au changement climatique et à la pollution toujours croissante de nos écosystèmes.

Bien qu'il s'agisse d'une réaction catalytique majeure, les mécanismes d'action exacts de l'oxydation de l'ammoniac ne sont pas encore entièrement compris. Notamment, l'origine d'importants changements morphologiques durant l'utilisation des catalyseurs en industrie (fig. 1), liés à une *activation* de l'échantillon permettant une meilleure sélectivité vers NO, est encore inconnue.

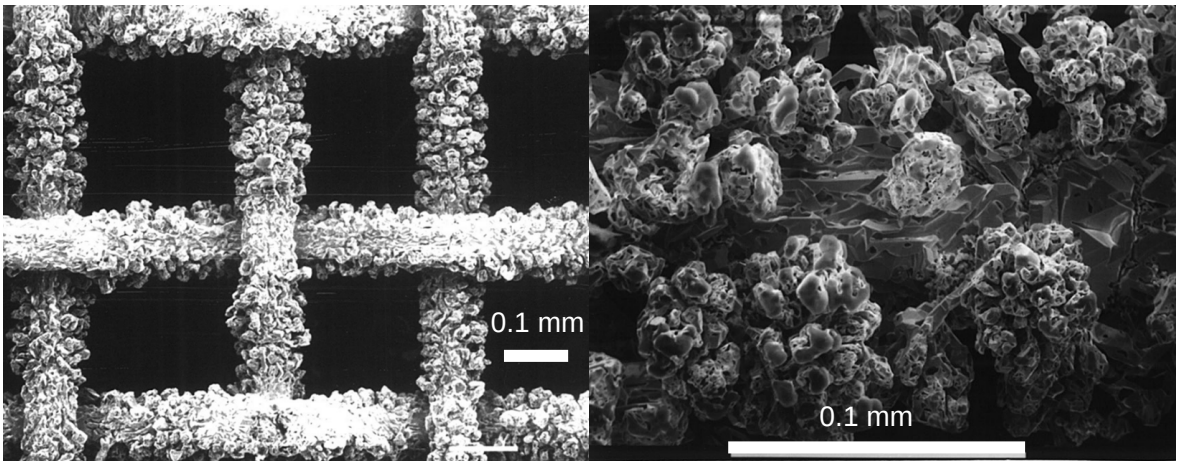

Figure 1: Images obtenues par microscope électronique à balayage, gazes reconstruits (Pt-Rh) montrant l'existence de motifs en forme de chou-fleur après utilisation en industrie (droite). Adapté depuis Bergene et al. (1996). La barre horizontale mesure 0.1 mm.

Obtenir une compréhension complète de ces mécanismes est essentiel pour contrôler la sélectivité des réactions. De plus, une compréhension plus approfondie du mécanisme de réaction est prometteuse pour le développement de nouveaux catalyseurs capables de s'affranchir de la dépendance aux métaux précieux coûteux, ou de fonctionner à plus basse température.

Cette thèse vise à étudier l'oxydation catalytique de l'ammoniac à pression ambiante en couplant plusieurs techniques de diffraction et de spectroscopie. Pour ce faire, trois techniques principales ont été utilisées, l'imagerie par diffraction cohérente de Bragg, la diffraction des rayons X de surface et la spectroscopie photoélectronique des rayons X, combinées à des mesures par spectrométrie de masse (tab. 1). Ces techniques sont compatibles avec des conditions de pression proches de l'ambiante, permettant de réduire l'écart de pression en catalyse hétérogène. Le réacteur utilisé pour étudier la réaction catalytique hétérogène sur la ligne SixS (SOLEIL) est déjà compatible avec les environnements hautement oxydants (Rijn et al. 2010; Resta et al. 2020), et permet des expériences de diffraction des rayons X en surface à haute pression et d'imagerie par diffraction cohérente de Bragg.

Pour combler le fossé matériel, des nanoparticules et monocristaux de platine ont été utilisés. Tout au long de ce travail, de faibles rapports de pression partielle O_2/NH_3 et des basses températures ont été liés à la sélectivité vers N_2, alors que des rapports O_2/NH_3 et températures élevés ont été liés à une sélectivité accrue vers NO et N_2O. Ceci est cohérent avec la sélectivité rapportée pour les catalyseurs industriels, ce qui soutient l'utilisation de nanoparticules et de monocristaux comme catalyseurs modèles pour améliorer la compréhension du système.

Les éléments optiques nécessaires à l'utilisation d'un faisceau cohérent focalisé ont été implémentés et caractérisés. L'extension du panel de techniques disponibles contribuera à combler le fossé entre les matériaux et pressions utilisés en industrie par rapport à ceux utilisés en sciences de surfaces. Dans le futur, les utilisateurs du synchrotron auront la possibilité d'étudier les réactions catalytiques dans des conditions et environnements équivalents, mais avec des techniques différentes.

L'expérience de spectroscopie photoélectronique à rayons X a été réalisée sur la ligne de lumière B07 (Diamond), également compatible avec les hautes pressions (Held et al. 2020). L'écart entre le matériau et la pression est partiellement comblé en fonctionnant à des températures supérieures à l'amorçage du catalyseur, à une pression presque industrielle.

Technique	Diffraction des rayons X en surface	Diffraction cohérente des rayons X en condition de Bragg	Spectroscopie photoélectronique par rayons X
Échantillons	Monocristaux de Pt(111) et Pt(100), particules de platine	Particules de platine isolées	Monocristaux de Pt(111) et Pt(100),
Information	Structure de surface, rugosité, relaxation & phases crystallographiques	Forme, champs de déformation et de déplacement de l'objet unique	Présence d'espèces de surfaces, quantité & état d'oxydation
Ligne de lumière	SixS (SOLEIL)	SixS (SOLEIL)	B-07 (Diamond Light Source)

Tableau 1: Techniques utilisées dans le cadre de cette thèse employant les rayons X.

Le deuxième chapitre fourni un aperçu concis de la catalyse hétérogène et des principes fondamentaux régissant l'interaction entre les rayons X et la matière. Cette section met l'accent sur les origines, les avantages et les contraintes de chaque technique utilisée dans l'étude, en soulignant comment les rayons X peuvent observer indirectement les réactions catalytiques en détectant des marqueurs uniques laissés sur les matériaux. Le concept de sites actifs est introduit ainsi que le lien entre adsorption et déformation de surface, crucial pour l'étude de la réaction catalytique avec les techniques de diffraction des rayons X, intrinsèquement sensible à la déformation du réseau dans les cristaux.

La ligne de lumière SixS du synchrotron SOLEIL, principal outil pour la plupart des expériences, est présentée, mettant l'accent sur les dernières avancées en matière de techniques expérimentales et de matériel spécifique à la ligne de lumière.

De plus, la thèse présente les différents logiciels utilisés pour la réduction et l'analyse des données développés au cours de ce travail, en se concentrant sur l'analyse complète pour

l'imagerie par diffraction cohérente de Bragg, une technique qui n'a pas encore atteint son plein potentiel grâce au développement de synchrotrons de 4ème-génération et de clusters de calcul puissants. Une description du logiciel *Gwaihir* (Simonne, Carnis et al. 2022), qui vise à faciliter la réduction et l'analyse des données dans le langage de programmation *Python*, tout en encourageant une adoption plus large de la technique à travers une interface graphique, est fournie.

Les troisième et quatrième chapitres présentent les résultats de la thèse durant l'étude de différents échantillons pendant l'oxydation de l'ammoniac. L'étude de la réaction est réalisée *operando*, en explorant l'espace de paramètres multidimensionnel défini par la température de fonctionnement, la pression totale et le rapport O_2 / NH_3. Pour explorer la corrélation entre la structure de surface et l'activité catalytique, des données de spectrométrie de masse sont collectées simultanément avec toutes les mesures.

Dans le chapitre 3, des nanoparticules de platine sont utilisées pour explorer la relation entre morphologie/structure et sélectivité à pression ambiante et à haute température, au moyen d'une vaste gamme de rapports de pression partielle O_2/NH_3, favorisant soit la production de N_2 ou NO. Ces nanoparticules présentes une distribution de taille entre 350 nm et 800 nm.

La possibilité que différents phénomènes se produisent dans les mêmes conditions de réaction a été révélée. D'importantes différences ont en effet été mesurées entre les informations moyennes obtenues par diffraction de surface sur un échantillon exhibant des milliers de particules, et les informations obtenues par diffraction cohérente sur des particules uniques.

Les nanoparticules de platine épitaxiées sur saphir ont d'abord été mesurées à 300 °C, 500 °C et 600 °C par diffraction de surface lors de l'oxydation de l'ammoniac, en commençant par l'introduction de l'ammoniac dans le réacteur, et suivie d'une augmentation progressive de la pression d'oxygène ($O_2/NH_3 = \{0, 0{,}5, 1, 2, 8\}$). La forme moyenne des nanoparticules de Pt est principalement constituée de facettes de types {111}, {110}, {100} et {113}.

Un re-facetage des particules est notamment révélé à 600 °C lors des conditions de réaction. Une fois que $O_2/NH_3 = 1$, et en augmentant les rapports oxygène/ammoniac, le taux de couverture des facettes {110} et {113} diminue, remplacée par des facettes de type {111}, et {100} qui sont favorisées (fig. 2).

Une particule a ensuite été imagée par imagerie cohérente en condition de Bragg sous atmosphère inerte, à des températures comprises entre 25 °C et 600 °C. Une dislocation présente à l'interface depuis la température ambiante jusqu'à 125 °C a été éliminée avec succès par recuit au-dessus de 800 °C. Il a été démontré que cette dislocation a un impact sur la relaxation thermique de la particule. De plus, les facettes {111} proches de l'interface évoluent entre des facettes de type {211}, {221} et {110} en fonction de la température de l'échantillon et de la déformation interfaciale. L'introduction d'ammoniac dans le réacteur à 600 °C a entraîné une inversion de la déformation des facettes, probablement à l'origine de la création d'un réseau de dislocations interfaciales, mettant en évidence le lien entre facette et déformation interfaciale dans les nanoparticules.

L'importance de la forme des particules, de la taille des facettes, de leur taux de couverture ainsi que de l'état de déformation initial a été mise en perspective par l'étude comparative de deux particules durant l'oxydation de l'ammoniac à 300 °C et 400 °C, en fonction du rapport entre O_2 et NH_3. Différents comportements ont été révélés sur les deux nanoparticules, qui présentent une taille, une forme, une couverture de facettes et un état de déformation initial différents, alors qu'aucun important changement n'a été mesuré en dessous de 600 °C par diffraction de surface. La surface de la plus grande nanoparticule (particule *C*, 800 nm de largeur) est constituée de facettes de type {111}, {110} et {100}.

La particule *C* a montré une diminution/augmentation réversible de la déformation homogène lorsque l'ammoniac a été introduit/retiré du réacteur, et n'a pas pu être reconstruite sans la présence d'ammoniac. Une augmentation non réversible de la déformation hétérogène

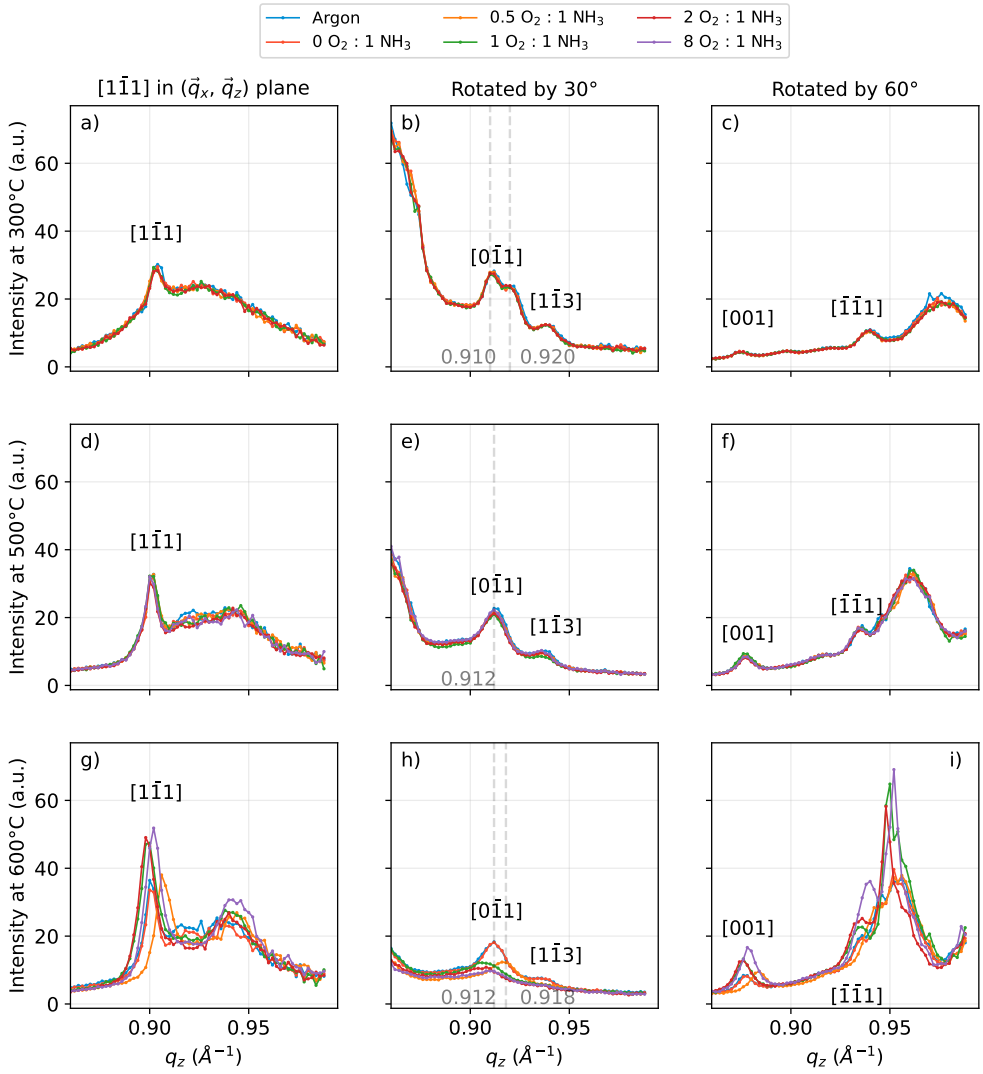

Figure 2: Évolution de l'intensité diffusée prise le long d'une zone carrée perpendiculaire à la direction [111], à trois positions différentes dans le plan ($\vec{q}_x, \vec{q}_z$) pour sonder l'évolution de l'intensité des tiges de troncature cristalline sur une assemblée de particules en diffraction de surface.

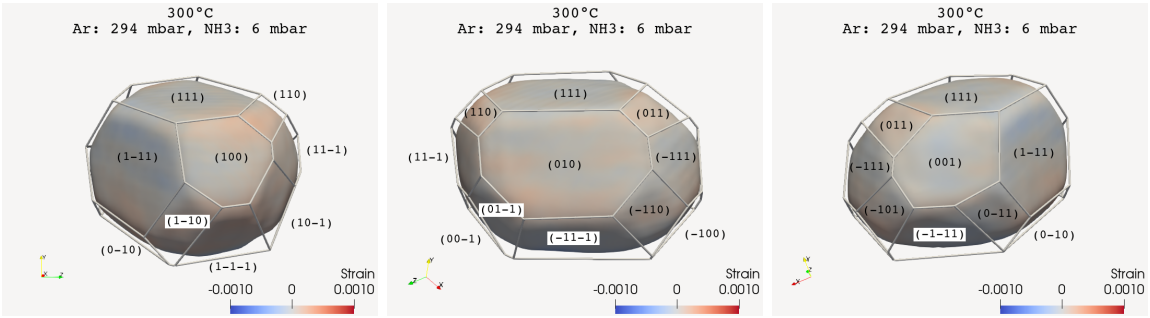

Figure 3: Surface de la particule C reconstruite à 300 °C sous atmosphère d'argon (inerte). La surface est colorée par les valeurs de la déformation hétérogène hors plan pour chaque voxel de surface, la limite de chaque facette est délimitée par d'épaisses lignes blanches. Mesures effectuées en diffraction cohérente des rayons X.

a été mesurée à 300 °C lors de la première exposition de l'échantillon à des conditions de réaction (O_2/NH_3 = 0,5), aucune augmentation de ce type n'a été reproduite aux mêmes conditions à 400 °C.

L'augmentation de déformation homogène liée à la présence/absence d'ammoniac n'a pas été reproduite sur la deuxième nanoparticule (particule *B*, 300 nm de large). Contrairement à la particule précédente (*C*), la particule *B* à des facettes de type {113} également présentes à sa surface.

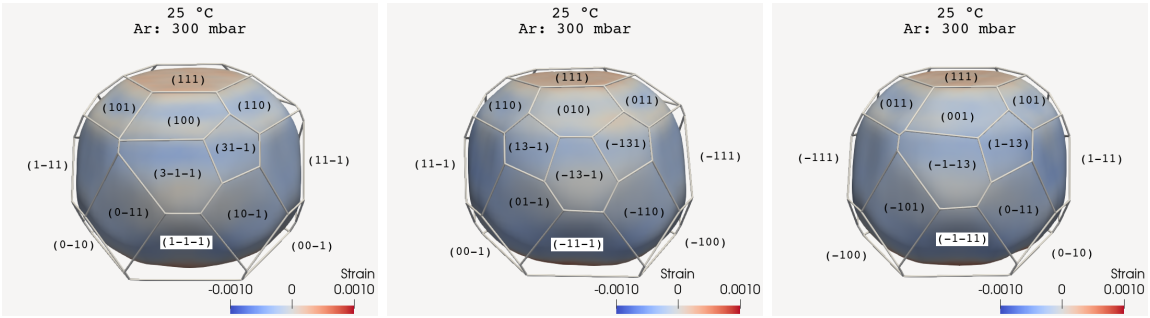

Figure 4: Surface de la particule B reconstruite à 25 °C sous atmosphère d'argon (inerte). La surface est colorée par les valeurs de la déformation hétérogène hors plan pour chaque voxel de surface, la limite de chaque facette est délimitée par d'épaisses lignes blanches.

Une augmentation non réversible de la déformation hétérogène a également été mesurée à 300 °C, mais induite par la présence d'ammoniac, sans oxygène. La possibilité d'avoir un échantillon oxydé peut expliquer cette évolution sous atmosphère réductrice, mais n'est pas observée pour la particule *C*. L'apparition d'un défaut à 400 °C est liée à une augmentation non réversible et importante de la déformation homogène lors de l'oxydation de l'ammoniac, qui continue d'augmenter en fonction du rapport entre ammoniac et oxygène. Cette évolution structurelle est clairement visible en 3D, avec des volumes de densité électronique de Bragg manquants (ann. A). La présence de défauts pourrait jouer un rôle important dans le champ de déformation du catalyseur et donc dans ses propriétés catalytiques. Il est possible que cette transformation correspond à l'origine de la transformation observée dans les catalyseurs industriels. Une activation globale du catalyseur à 300 °C et 400 °C a été rapportée tandis que le rapport O_2/NH_3 était maintenu égal à 2, avec une production accrue de NO, et dans une moindre mesure N_2O, au détriment de N_2.

En conclusion, il est primordial de sonder différentes nanoparticules avant de tirer une conclusion sur leur comportement global lors d'une réaction catalytique hétérogène.

Pour mieux comprendre le rôle de chaque facette dans le comportement des nanoparticules de Pt, des expériences de diffraction de surface et de spectroscopie photoélectronique à rayons X ont été réalisées à 450 °C sur des monocristaux de Pt(111) et Pt(100). Les échantillons ont d'abord été exposés à une atmosphère riche en oxygène (80 mbar) pour oxyder les surfaces de Pt (pression totale toujours maintenue à 500 mbar grâce à l'utilisation d'argon). Deux rapports oxygène/ammoniac différents sont utilisés après l'oxydation de surface, en introduisant d'abord 10 mbar d'ammoniac ($O_2/NH_3 = 8$), puis en réduisant la pression d'oxygène à 5 mbar ($O_2/NH_3 = 0.5$). L'expérience de spectroscopie photoélectronique à rayons X a été réalisée avec les mêmes rapports ammoniac/oxygène, mais à des pressions partielles plus faibles (environ 10 %), et sans garder la pression totale constante.

La présence d'oxydes de platine est surveillée afin de comprendre son importance dans le mécanisme réactionnel, ainsi que dans d'éventuelles reconstructions du catalyseurs. Les différents résultats sont résumés dans le tableau 2.

L'oxydation des deux surfaces est d'abord discutée. Une couche épaisse de Pt_3O_4 a été identifiée sur Pt(100), dans un arrangement Pt(100)-(2 × 2) et d'épaisseur moyenne égale à 16 Å (*i.e.* 3 cellules unitaires). Des signaux décalés dans l'espace réciproque par rapport aux

O_2 (mbar)	NH_3 (mbar)	Pt(111)	Pt(100)
0	0	Pas de couche d'oxyde / pas de reconstruction	Pas de couche d'oxyde / pas de reconstruction
80	0	Deux superstructures hexagonales tournés Pt(111)-(6 × 6)-R±8.8° (mono-couche) Après 9 h30 min: superstructure Pt(111)-(8 × 8) (multicouche)	Couche épaisse épitaxiée de Pt_3O_4, Pt(100)-(2 × 2) et signaux décalés en H ou K (mono-couche)
80	10	Pas de couche d'oxyde / pas de reconstruction Signaux faibles au niveau O 1s	Pt(100)-(10 × 10) reconstruction (multicouche) et signaux décalés en H ou K (mono-couche) Sélectivité vers NO supérieure Signal important au niveau O 1s en comparaison avec Pt(111)
10	10	Pas de couche d'oxyde / pas de reconstruction Aucun signal au niveau O 1s N_a et $NH_{3,a}$ au niveau N 1s	Structure Pt(100)-Hex (mono-couche) Aucun signal au niveau O 1s Seulement N_a au niveau N 1s
0	10	Pas de couche d'oxyde / pas de reconstruction	Suppression progressive de la structure Pt(001)-Hex
0	0	Pas de couche d'oxyde / pas de reconstruction	Pas de couche d'oxyde / pas de reconstruction
5	0	Retour aux mêmes structures qu'à 80 mbar de O_2, mais avec une cinétique diminuée	Structures transitoires, différentes des signaux observée à 80 mbar de O_2

Tableau 2: Résumé des structures de surface identifiées par diffraction de surface et des changements pertinents dans les niveaux mesurés par spectroscopie photoélectronique des rayons X, combinées à des mesures par spectrométrie de masse.

pics Pt_3O_4 sont également mesurés. Les signaux liés au Pt_3O_4 et décalés ont été mesurés 1 h après l'introduction de l'oxygène, mais n'ont pas pu être détectés sous une atmosphère réduite en oxygène (5 mbar), même après plusieurs heures. Des signaux transitoires sont en effet mesurés, soulignant l'importance de la pression partielle d'oxygène dans l'oxydation de surface.

Le Pt_3O_4 n'a pas été observé sur Pt(111). Néanmoins, une superstructure commensurable Pt(111)-(8×8) a été clairement identifiée après 9 h30 min de temps écoulé sous une atmosphère à forte teneur en oxygène, et après 23 h30 min sous une atmosphère réduite en oxygène. À partir de la distribution d'intensité des signaux hors plan associés, il a été déterminé que cette structure avait quelques couches d'épaisseur. Des signaux supplémentaires dans le plan sont également détectés dès que de l'oxygène est introduit dans le réacteur, à basse et haute pression d'oxygène, liés à une structure Pt(111)-(6 × 6)-R±8.8°. L'intensité de ces signaux diminue une fois que la structure Pt(111)-(8 × 8) est présente, ce qui soutient un lien précurseur entre les deux structures. Les signaux mesurés dans le niveau O 1s dans une atmosphère réduite en oxygène et attribués aux espèces d'oxygène de surface sont plus élevés pour le Pt (100) que pour le Pt (111), montrant que la surface du Pt (100) est plus facilement oxydée que le Pt (111). L'oxydation des surface Pt(111) et du Pt(100) est aussi liée à une rugosité de surface accrue et à une déformation compressive hors plan par rapport à l'atmosphère inerte pour le Pt(111).

Différents comportements ont été mesurés sur les deux surfaces lors de conditions de réaction. Sous un rapport O_2/NH_3 élevé, qui favorise la production de NO, les oxydes de surface sont directement éliminés du Pt(111), mais reconstruits avec un arrangement (10x10) sur Pt(100) . Les signaux des espèces oxygénées au niveau de O 1s sont faibles pour le Pt(111), difficiles à dissocier du fond, alors que les pics sont clairement détectés pour le Pt(100). La différence de présence d'oxygène en surface est déjà observée lors de la précédente oxydation de surface. La reconstruction de la surface du Pt(100) est liée à la présence persistante d'espèces oxygénées de surface lors de l'oxydation de l'ammoniac, différant ainsi de la surface du Pt(111). De plus, la sélectivité envers NO est augmentée pour le Pt(100), également liée à la présence plus importante d'oxygène en surface, qui est prédite comme cruciale dans la production de NO lors du mécanisme réactionnel (Novell-Leruth, Valcárcel et al. 2005; Offermans, Jansen and van Santen 2006; Offermans, Jansen, Van Santen et al. 2007; Imbihl et

al. 2007; Novell-Leruth, Ricart et al. 2008). Une rugosité de surface importante est également observée dans ces conditions pour les deux surfaces.

Le Pt(111) et Pt(100) montrent tout deux une sélectivité similaire vers N_2 en abaissant le rapport O_2/NH_3 à 0.5. L'ampleur de la déformation hors plan (relaxation de surface) et la rugosité de la surface sont déjà réduites dans ces conditions pour le Pt(111), mais restent à des valeurs similaires pour Pt (100). Sur les deux surfaces, les espèces d'oxygène sont absentes du niveau O 1 et l'azote atomique adsorbé est mesuré. L'ammoniac adsorbé est également observé sur le Pt(111).

La différence de déformation hors plan (relaxation de surface) lors de la diminution du rapport O_2/NH_3 de 8 à 0.5 est du même ordre de grandeur, mais de nature différente, environ 0.06 % de déformation en tension / compression sur le Pt(100) / Pt(111). Plus important encore, il est clair que la contrainte est contenue dans les couches supérieures des catalyseurs au platine. Si l'on considère un voxel de surface Pt(100) de 10 nm d'épaisseur, la déformation moyenne correspondante du voxel serait égale à 0.002 % par rapport au réseau global. Par conséquent, le changement de déformation entre les conditions de réaction devient difficile à résoudre, ce qui peut expliquer pourquoi aucune différence n'est observée sur les particules *C* lors de l'oxydation de l'ammoniac. Un autre facteur à prendre en compte est l'augmentation de la rugosité de surface liée à la forte pression d'oxygène, qui a pour effet de diminuer l'intensité des photons diffusés loin du pic de Bragg, et va ainsi réduire la résolution expérimentale. Des études supplémentaires à haute résolution pourraient contribuer à comprendre l'effet des adsorbats sur la relaxation de surface.

La thèse démontre l'importance de combiner les mesures de particules individuelles et des assemblages de particules. Par imagerie de diffraction cohérente de Bragg, nous avons démontré qu'en fonction de la morphologie (forme, taille, type de facette et couverture, *etc.*) et de l'état de déformation initial des particules de Pt, différentes évolutions structurelles sont observées (en termes de déformation, de morphologie et de défauts) lors de l'oxydation de l'ammoniac. Une meilleure représentation des différents comportements suivis par les particules de platine au cours de la réaction, en mesurant plusieurs particules individuelles, semble indispensable pour une compréhension globale de la relation structure-activité. Il est à noter que la déformation à l'interface particule/support semble exercer une influence prononcée sur le comportement des particules. Les nanoparticules servent de plate-forme pour explorer simultanément l'évolution structurelle de diverses facettes crystallographiques, alors que les monocristaux permettent de mieux isoler les comportements des facettes uniques sur les nanoparticules.

En conclusion, l'utilisation de trois techniques de rayons X différentes a permis de mieux appréhender les mécanismes à l'oeuvre lors de l'oxydation de l'ammoniac.

Contents

Chapter 1

Introduction

The use of catalysts has several advantages such as faster, selective, and more energy-efficient chemical reactions, directed towards producing higher amounts of the desired product while reducing undesired byproducts. Reactions impossible without catalysts can also be enabled. Over the years, scientists have developed specialised catalysts for various applications, today 90 % of chemical processes involve catalysts in at least one of their steps (Weiner 1998; Vries et al. 2012). Notable advancements in catalysis have led to the production of plastics, pharmaceuticals, fuels and fertilisers (Fechete et al. 2012).

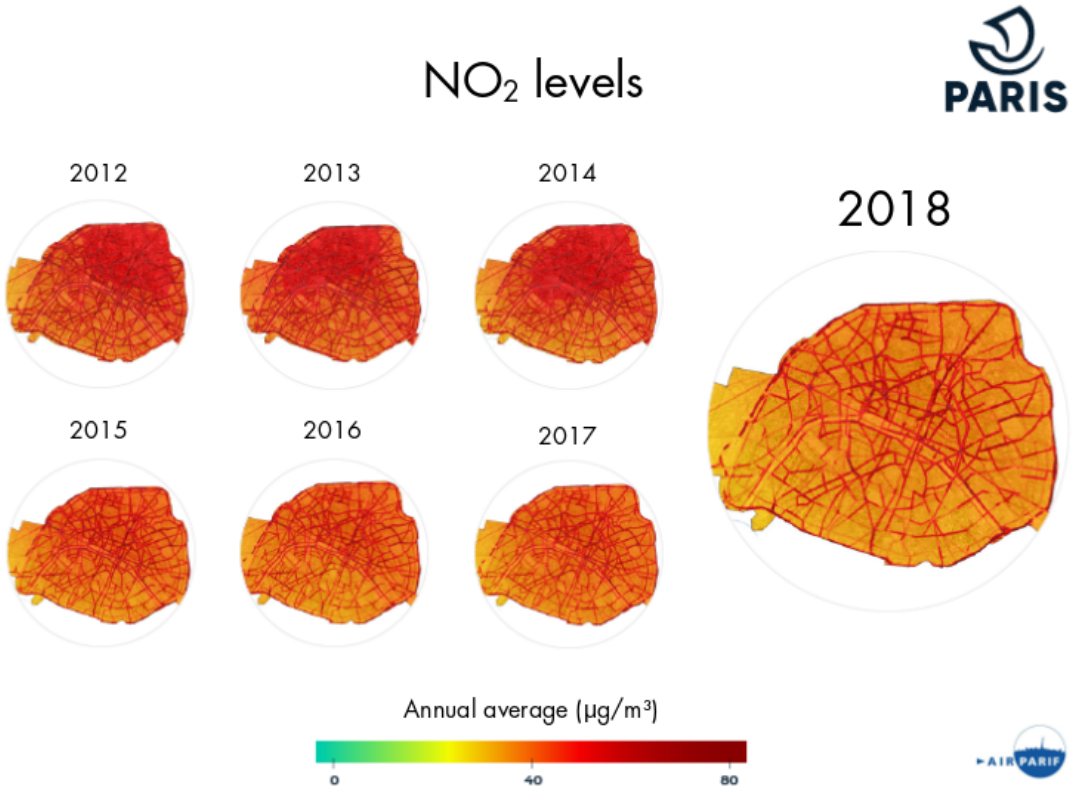

Figure 1.1: NO_2 levels in Paris near the main traffic roads remained on average twice superior to the annual limit of 40 µg/m^3 *(AirParif 2023) between 2012 and 2018, despite a global decrease since 2012.*

Several new challenges have emerged in the field of catalysis related to reducing environmental impact, and developing sustainable processes. First, environmental challenges concern minimising and/or managing by-products, reducing contamination in effluents/wastewaters,

using sustainable sources of raw materials, and energy supplies (Ludwig et al. 2017; Lange 2021). Secondly, economical challenges imply using cheaper, readily available raw materials, increased productivity, and decreased lag-time between discovery to commercialisation (Suzuki et al. 2019; Günay et al. 2021). For example, recent studies suggest that alternative, more economical catalysts, such as non-noble metals, and other derived metal-based compounds, must be tested as possible substitutes for the most frequently used noble metals, very efficient but expensive (Zhong et al. 2021; Ruan et al. 2022). For green catalysis, the best material it not only the cheapest but most importantly the least impactful on the environment, e.g. in terms of material extraction, life span, and selectivity towards reducing pollutants and greenhouses gases (Lange 2021).

Catalysis also has a role to play to combat pollution and create cleaner energy with for example the development of efficient water-splitting technologies (Ahmad et al. 2015), and enhancing the use of biomass and other energy vectors such as ammonia (Fang et al. 2022). Challenges also arise in automotive exhaust where catalysts participate in the reduction of the emissions of toxic gases and nanoparticles (WHO 2023; Heck and Farrauto 2001; Gandhi et al. 2003). Some of the major air pollutants such as nitrogen oxides, (NO_x), and particulate matter (PM) are emitted by road traffic (65 % of NO_x, ≈35 % of PM), mainly by diesel vehicles, and directly inhaled by nearby major city inhabitants. To set a striking example, in Paris in 2018, 700 000 inhabitants were exposed to NO_2 concentrations exceeding the regulations (fig. 1.1), 60 000 inhabitants for PM_{10}, and all Parisians were concerned by exceeding the World Health Organisation (WHO) recommendations for $PM_{2.5}$ (AirParif 2023). Air quality is the main environmental concern of Île-de-France residents (65 % of total mentions) ahead of climate change (63 %) and food (38 % - AirParif 2023). Diesel engines are also used in the heavy industry impacting the surrounding areas in terms of atmosphere quality.

1.1 The oxidation of ammonia

1.1.1 The Haber-Bosch and Ostwald processes

Today, about 50 % of the world population relies on nitrogen-based fertilisers to produce the food necessary to their alimentation.

The story of ammonia begins in the early 20^{th} century with the discovery in 1902 of the Ostwald process that permitted the synthesis of nitric acid from the oxidation of ammonia (Ostwald 1902a; Ostwald 1902b). Wilhelm Ostwald later received the Nobel price in 1909 *"in recognition of his work on catalysis and for his investigations into the fundamental principles governing chemical equilibria and rates of reaction"*.

Seven years after the discovery, in 1909, Fritz Haber designed a process for the synthesis of ammonia which was later improved by Carl Bosch. It is today known as the Haber-Bosch process, and is at the origin of the mass production of ammonia using metallic catalysts (Hosmer 1917; Parsons 1919). Fritz Haber received the Nobel prize in 1918 *"for the synthesis of ammonia from its elements"* (Jerome 1920) and Carl Bosch in 1931 *"in recognition of his contributions to the invention and development of chemical high pressure methods"*.

Since the discovery of the Ostwald and Haber-Bosch processes that allowed the mass production of nitrogen-based fertilisers, the world population increase has been relying on their production and use for agriculture (J. W. Erisman et al. 2008). Today, about 50 % of the world population relies on nitrogen-based fertilisers to produce the food necessary to

their alimentation (fig. 1.2).

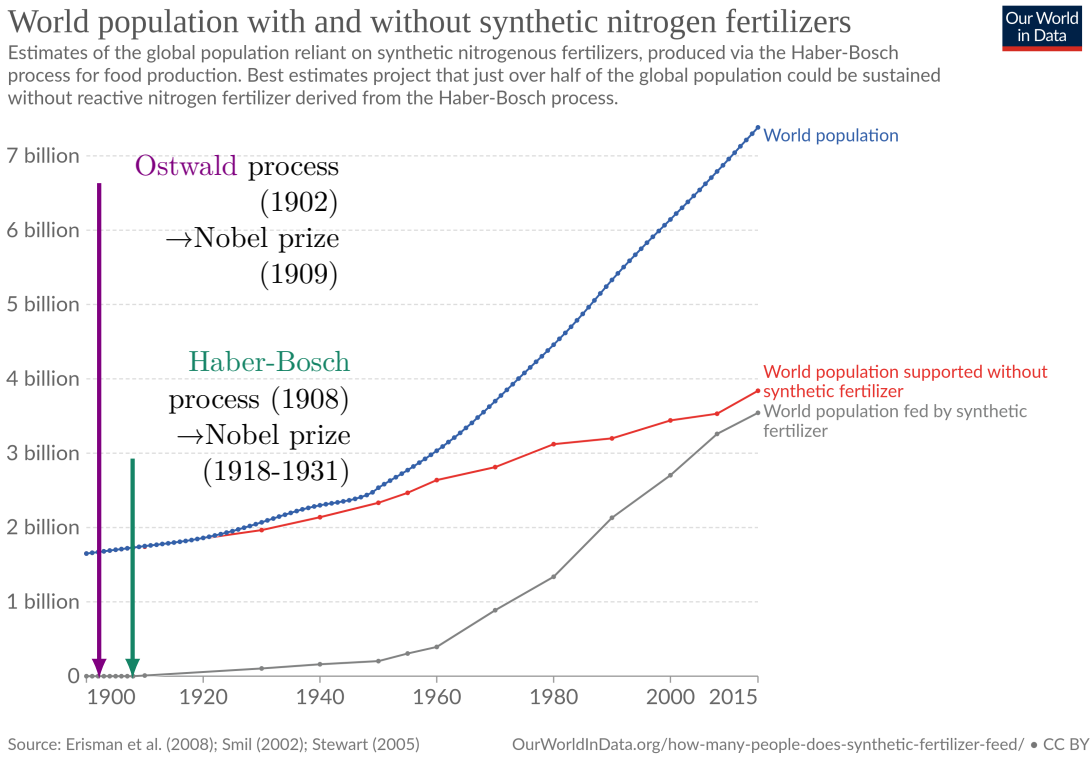

Figure 1.2: Figure adapted from Our World In Data (OWID 2023).

The oxidation of ammonia (NH_3) can be described by three equations that, depending on the stoechiometric ratio between NH_3 and O_2, have different products.

$$4NH_3 + 3O_2 \rightarrow 6H_2O + 2N_2 \tag{1.1}$$
$$4NH_3 + 4O_2 \rightarrow 6H_2O + 2N_2O \tag{1.2}$$
$$4NH_3 + 5O_2 \rightarrow 6H_2O + 4NO \tag{1.3}$$

The first equation (eq. 1.1) yields nitrogen (N_2), a naturally occurring gas that does not pollute the environment nor shows any toxic behaviour towards humans. The second equation (eq. 1.2) yields nitrous oxide (N_2O), a powerful greenhouse effect gas, and thus an often unwanted by-product. The third equation (eq. 1.3) yields nitric oxide, also called nitrogen monoxide (NO), which is the main desired product for the subsequent production of nitric acid (HNO_3) with the Ostwald process. The characteristics of the many different gases linked to the oxidation of ammonia are recapitulated in tab. 1.1.

$$2NH_3 + 8NO \rightarrow 5N_2O + 3H_2O \tag{1.4}$$
$$4NH_3 + 6NO \rightarrow 5N_2 + 6H_2O \tag{1.5}$$
$$2NO \rightarrow N_2 + O_2 \tag{1.6}$$
$$2NH_3 + 3N_2O \rightarrow 4N_2 + 3H_2O \tag{1.7}$$
$$2NH_3 \rightarrow N_2 + 3H_2 \tag{1.8}$$

Known side reactions to the oxidation of ammonia are the recombination of nitric oxide (NO) with unreacted ammonia that leads to the production of water, nitrogen, or nitrous oxide (eq. 1.4 - 1.5). The thermal decomposition of nitric oxide (eq. 1.6), also lowers the total yield of the reaction when aiming at the production of nitric oxide.

Formula	NH_3	N_2	N_2O	NO	NO_2	HNO_3	NH_4NO_3	$CO(NH_2)_2$
Name	Ammonia	Nitrogen	Nitrous oxide, Laughing gas	Nitrogen oxide, Nitric oxide Nitrogen monoxide	Nitrogen dioxide	Nitric acid	Ammonium nitrate	Urea
Origin	Haber-Bosch process	Naturally present in the atmosphere, Ammonia oxidation, Selective catalytic reaction (SCR)	Ammonia oxidation, Emissions from nitrogen-based fertilisers	Ammonia oxidation, Anthropogenic sources (combustion process, industry, agriculture, ...) Naturally produced from lightning or volcanoes	Ostwald process (step 1) Anthropogenic sources (combustion process, industry, agriculture, ...) Naturally produced from lightning or volcanoes	Ostwald process (step 2)	Nitric acid neutralisation with ammonia	Ammonia
Major use	Ostwald process (fertilisers), Direct use in soil, Fuel, Hydrogen carrier, Cooling, SCR	Ammonia production	Medicine, Propellant	Production of nitric acid	Production of nitric acid	Fertiliser production, Nitration (explosives, dyes, ...), Propellant, Etching	Fertilising agent, Explosives	Fertilising agent, SCR to reduce NO_x into N_2
Toxicity	Dangerous for the environment Toxic, Corrosive	Asphyxiation by displacing O_2	Anaesthetic, euphoric	Oxidising, Corrosive, Toxic	Oxidising, Corrosive, Toxic, Health hazard	Oxidising, Corrosive		
Pollution	PM formation		Ozone depletion	Smog, acid rains, ozone depletion, Precursor to NO_2 in the atmosphere	Smog, acid rains, ozone formation	Decomposes towards NO_2	Decomposes into NO_2 when used as fertiliser, Eutrophication	Decomposes into NH_3 when used as fertiliser, Eutrophication
Greenhouse effect			Very important (298 CO_2 eq.)				Nitrogen-based fertiliser release N_2O in the atmosphere	Nitrogen-based fertiliser release N_2O in the atmosphere

Table 1.1: Nitrogen based species involved in the oxidation of ammonia, the Haber-Bosch process, the Ostwald process or nitrogen-based fertilisers. Information compiled from various sources: Thiemann et al. 2000; Harrison et al. 2001; Baerns et al. 2005; Imbihl et al. 2007; Hatscher et al. 2008; Davidson 2009; Resta et al. 2020; Borodin et al. 2021; Pottbacker et al. 2022.

N_2O may also react with ammonia to produce nitrogen and water (eq. 1.7). It is also possible to observe the dissociation of ammonia resulting in the production of N_2 and H_2 (eq. 1.8) when outside industrial reacting conditions.

Reactions 1.1, 1.2, 1.3 and 1.4 are strongly exothermic, leading to a significant increase of the catalyst temperature during the reaction (Hatscher et al. 2008).

$$2NO + O_2 \rightarrow NO_2 \tag{1.9}$$

$$3NO_2 + H_2O \rightarrow 2HNO_3 + NO \tag{1.10}$$

The second (eq. 1.9) and third (eq. 1.10) stages of the Ostwald process stem from the production of NO *via* the first stage, *i.e.* the oxidation of ammonia (eq. 1.3). Nitrogen dioxide (NO_2) is produced from NO which then reacts with water in liquid phase to form nitric acid, an important actor in multiple industrial processes (tab. 1.1). Nitric acid is for example used to produce fertilisers such as ammonium nitrate (eq. 1.11).

$$HNO_3 + NH_3 \rightarrow NH_4NO_3 \tag{1.11}$$

Today, the ammonia oxidation is an essential catalytic reaction, 80 % of the world production of nitric acid is used in the production of nitrogen-based fertilisers, a production expected to continuously grow in the future years (J. Lim et al. 2021). Nitric acid is also extremely important for nitration, *i.e.* the introduction of a nitro group into a chemical compound (Hughes et al. 1950), crucial for the production of inks, dyes, explosives, and pharmaceuticals (F. Lee 2005; Ouellette et al. 2014). Nitric acid can also be used as a rocket propellant (Mason 1956; Oommen et al. 1999).

Ammonia has also been investigated as a potential energy vector for hydrogen fuel cells, which has reignited the interest in understanding the complex system drawn by the many simultaneous reactions (Afif et al. 2016; Jeerh et al. 2021). Moreover, ammonia can also be used for the reduction of nitrogen oxides (eqs. 1.4 - 1.7), aiming at the production of nitrogen. In all cases, particular focus is on two products of the reaction, namely, NO and N_2, which is where heterogeneous catalysis plays an important role.

1.2 The importance of heterogeneous catalysis

1.2.1 Industry conditions and catalysts

When aiming at the production of nitric acid, selectivity towards the production of NO must be achieved during the ammonia oxidation (eq. 1.3), *i.e.* during the first stage of the Ostwald process. The production of nitrogen oxide is possible *via* direct methods, *i.e.* by reacting nitrogen and oxygen above 2000 °C. However, such processes are not used due to their low energy efficiency and product selectivity. This is at the origin of the selective, heterogeneous catalytic oxidation of ammonia towards the production of nitrogen oxide (Hatscher et al. 2008). Only at high temperature, high O_2/NH_3 ratios, and by the use of catalysers, is the production of NO favoured over N_2 and N_2O (eq. 1.1 - fig. 1.3).

Since the 1930s, the presence of rhodium (≈10 % Rh) in knitted Pt-Rh gauzes catalysts at favourable reaction conditions (e.g. 900 °C - 12 bar - excess O_2) allowed a 98 % NO yield to be achieved, 4 % higher than for pure platinum, while also increasing the catalyst lifetime, and decreasing the material loss (Kaiser 1909; Handforth et al. 1934; Heck, Bonacci et al. 1982; Hatscher et al. 2008).

In order to understand the reaction mechanism occurring on the catalyst surface, and the role of Pt and Rh in the catalyst stability and selectivity, scientists have been studying the

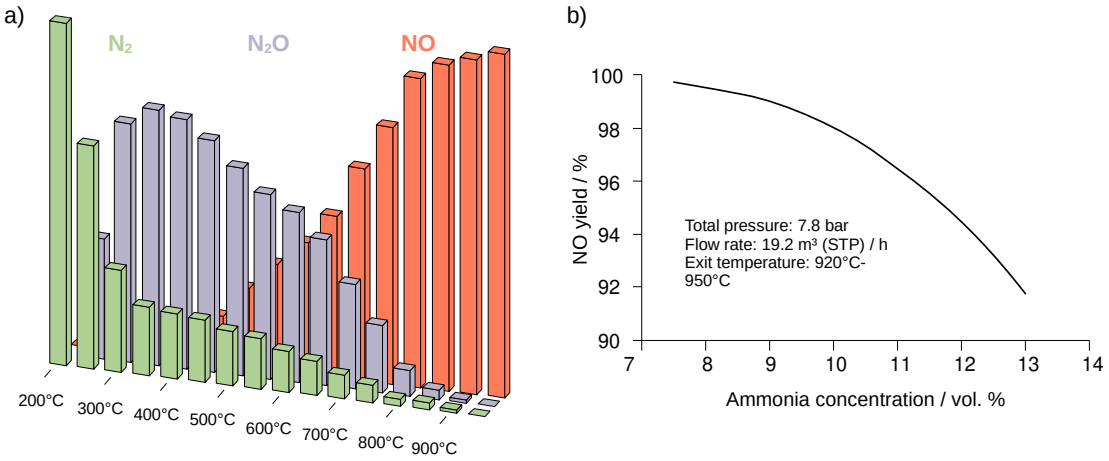

*Figure 1.3: a) Temperature dependence product distribution during ammonia oxidation at industrial conditions (*12 bar - *excess O_2). b) Dependence of NO yield on initial ammonia concentration. Figures adapted from literature (Heck, Bonacci et al. 1982; Hatscher et al. 2008).*

reaction by different methods since the beginning of last century. A comprehensive review of the ammonia oxidation is given by Hatscher et al. (2008). Relevant findings of the past 100 years will be resumed below.

The importance of high temperature for the selective production of NO was demonstrated early by temperature dependant studies (Nutt et al. 1968; Pignet et al. 1974; Y. Li and Armor 1997), while a restructuring of the catalyst, also called catalytic *etching*, was put into evidence by the means of *ex-situ* SEM (scanning electron microscopy) imaging of industrial samples (R. McCabe et al. 1974; Flytzani-Stephanopoulos et al. 1979; A. R. McCabe et al. 1986). This *activation process* leads to an increase selectivity towards NO while the gauzes undergo a transformation towards a roughened surface, composed of pits, facets, and large *cauliflower* patterns (fig. 1.4). The roughening of the catalyst surface can double the active surface area (Hatscher et al. 2008).

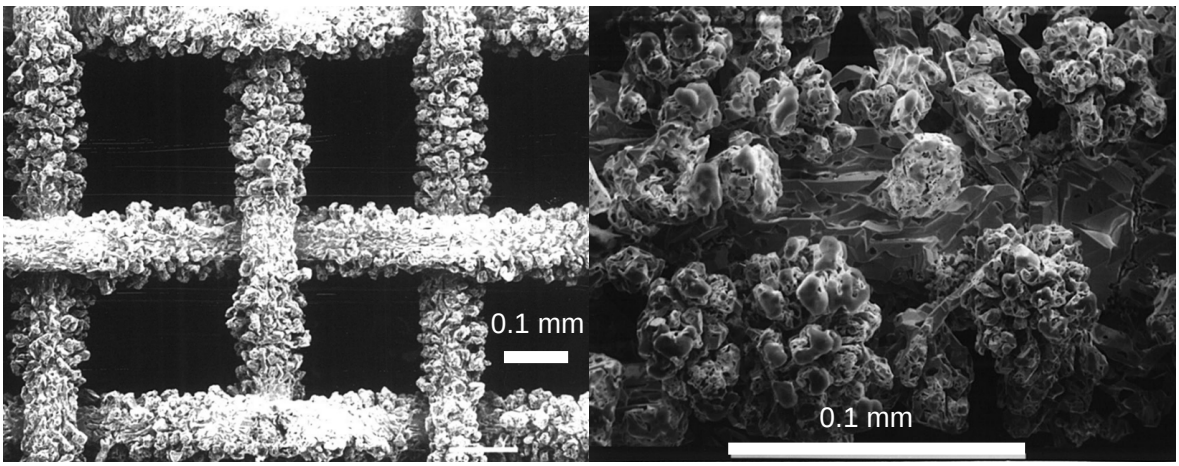

Figure 1.4: SEM images of Pt-Rh reconstructed gauzes with cauliflower patterns after use in industry, taken from Bergene et al. (1996). The horizontal bar is 0.1 mm *wide.*

The deactivation of Pt-Rh industrial catalysts after long exposure times have been explained by rhodium enrichment, and the presence of rhodium oxides (Fierro et al. 1990; Fierro et al. 1992; Bergene et al. 1996). However, a deactivation process was also reported on pure Pt catalyst (Ostermaier et al. 1974), linked to the presence of platinum oxides (Ostermaier et al. 1976).

The role of volatile surface oxides in the roughening and etching of the catalyst surface

was theorised by Wei et al. (1996), and confirmed experimentally by Nilsen et al. (2001). The transport of Pt and Rh was found to be permitted by the simultaneous presence of surface oxides and high temperature gradient areas, *i.e.* 800 °C to 1400 °C over 100 mm, decreasing with increasing Rh content and decreasing oxygen pressure (Hannevold et al. 2005a).

Ex-situ characterisation of Pt and Pt-Rh industrial gauzes by x-ray powder diffraction and electron microscopy allowed the identification of defect sites at the origin of high temperature gradient areas during reaction. The existence of such areas allows the restructuring process to occur nearby initial defects by the formation of PtO_2 and RhO_2 oxides, depositing metallic atoms on colder regions, and also leading to the loss of some of the precious metals constituting the catalyst (Hannevold et al. 2005b).

The progressive deactivation of the catalyst due to the ever increasing presence of Rh_2O_3 (A. R. McCabe et al. 1986) was refuted by Hannevold et al. (2005b), explaining that such oxide could only form during the cooling of the catalyst, which is a good example of the limitation of *ex-situ* works. A Pt_3O_4 catalyst used for the oxidation of ammonia was proven to be unstable at working temperature above 690 °C, decomposing into a pure Pt phase after 7 h of operation (Zakharchenko 2001). Overall, the role of platinum and rhodium oxides in the catalyst activation/deactivation process is not fully understood.

Nevertheless, the presence of rhodium in the catalysts limits the loss of platinum during operation, thus reducing the cost of industrial scale ammonia oxidation. The replacement of the material loss constitutes the second biggest expense in the production of fertilisers after the production/purchase of ammonia (Hatscher et al. 2008).

1.2.2 Reaction mechanism

First studies performed at low pressure and different temperatures have supported a Langmuir-Hinshelwood mechanism during ammonia oxidation (Nutt et al. 1969; Pignet et al. 1974; Ostermaier et al. 1974; Pignet et al. 1975; Gland and Korchak 1978b). Both reactants are adsorbed and decomposed on top of the catalyst surface, the final pathway towards the production of nitrogen or nitric oxide depending on the ratio between the O_2 and NH_3 partial pressures.

The importance of adsorbed atomic oxygen (O_a), and adsorbed hydroxyl groups (OH_a) in the de-hydrogenation of ammonia on both Pt(111) (Mieher et al. 1995) and Pt(100) surface was put into evidence by molecular beam studies under various oxygen coverage (J. M. Bradley et al. 1995; J. Bradley et al. 1997; van den Broek et al. 1999; M. Kim et al. 2000). High oxygen coverage on Pt(100) has shown to reduce the production of nitrogen, mainly produced by the dissociation of nitric oxide (NO), favoured at lower temperatures over NO desorption (J. M. Bradley et al. 1995).

Asscher et al. (1984) have reported the existence of a mechanism involving oxygen in the gas phase reacting with adsorbed NH_x species on Pt(111) for the production of NO, evidence of which was not observed in recent studies.

At ultra-high vacuum (UHV), the rotated hexagonal reconstruction of clean Pt(100) (R. Hammer et al. 2016) was found to impinge on NH_3 de-hydrogenation at low temperature (−123 °C) (J. Bradley et al. 1997). Between 125 °C and 350 °C, the ammonia oxidation stabilises the (1x1) phase by the formation of NH_x intermediates (Rafti et al. 2007).

The importance of atomic steps in the catalytic activity was first revealed by Gland et al. (1978a; 1980). A more recent study of the oxidation of ammonia on several model catalysts (Pt(533), Pt(443), Pt(865), Pt(100), Pt foil) to investigate the structure selectivity by Yingfeng (2008) linked the presence of steps and kinks with higher catalytic activity in the 1×10^{-9} bar to 1×10^{-5} bar range. Similar results have revealed that the Pt(533) is 2 to 4 times more active than Pt(443) below 1×10^{-5} bar (Scheibe et al. 2005). Moreover, the production of N_2 was confirmed to be promoted by lower temperatures, and a reduced O_2/NH_3 ratio in the incoming gas flow, while higher temperatures and an elevated O_2/NH_3

ratio tend to result in a higher selectivity towards the formation of NO (Zeng and Imbihl 2009). The importance of steps at ambient pressure was revealed to be most important when aiming at producing N_2 at low temperature, but could not be correlated to an increase in NO production at high temperature in a comparative study of the Pt(111) and Pt(211) surfaces (Ma et al. 2019). Moreover, it was shown that the adsorbed NH_3 hopping rate (that describes the mobility or diffusion of NH_3) is close to its desorption rate on Pt(111) terrace sites, making it unlikely to reach the steps where it may react rather than desorb from the catalyst surface (Borodin et al. 2021).

Rebrov et al. (2002) detailed the reaction kinetics and mechanism with a 13 step, temperature dependent model, the parameters of which have been refined with data collected from the reactants and products partial pressures evolution in a micro-reactor. A wide range of conditions was explored, including ambient pressures of NH_3 (0.01 bar to 0.12 bar) and O_2 (0.10 bar to 0.88 bar), in a large temperature range (250 °C to 400 °C). A dual adsorption site mechanism was proposed, with a preference for hollow site for oxygen species, and for top or bridge sites for nitrogen species, while NO species have been reported to exist on both top and bridge sites.

Pérez-Ramirez et al. (2004) have also attempted to study the kinetics of the reaction by directly analysing the selectivity of catalysts used in industry (*i.e.* Pt-Rh and Pt gauzes), above 700 °C, by the means of reactant gas pulses. The heterogeneous catalysis reaction mechanism was found to be similar on both sample. A pre-exposition of the catalysts to oxygen facilitated the de-hydrogenation of NH_3, the decomposition towards N_2 was not detected without oxygen. A high oxygen coverage of the catalyst was linked to the formation of NO, strongly bound oxygen favours the production of N_2, whereas weakly bound oxygen was associated to NO selectivity. The importance of adsorbed oxygen species to prevent spontaneous NO dissociation was confirmed, confirming previous works (J. M. Bradley et al. 1995). In a second study, increasing the O_2/NH_3 ratio to 10 pushed NO selectivity to almost 100 %, N_2 and N_2O production being both suppressed by favouring NO desorption (Pérez-Ramírez, E. V. Kondratenko et al. 2009).

The advent of density functional theory (DFT) brought forward theoretical explanations of the reaction mechanism for the first time. For example, a study combining DFT calculations and temporal analysis of products (TAP) by Baerns et al. (2005) confirmed the importance of adsorbed surface oxygen (O_a) and hydroxyl groups (OH_a) for the de-hydrogenation of NH_3 on the catalyst surface. N_2O could only be detected at ambient pressures, N_2 is favoured at lower temperature, whereas NO is favoured at higher temperatures. Importantly for the use of model catalysts, no difference in the temperature dependant production of N_2 and NO between a Pt(533) single crystal, Pt foil, and knitted Pt gauzes could be observed. Surface roughening of the catalyst at ambient pressure was linked to activation and selectivity change for a Pt foil. Interestingly, the deactivation of Pt catalysts due to the adsorption of nitrogen species below 115 °C was put into evidence, but with a reactivation above that temperature (Sobczyk et al. 2004).

The first studies performed under industrially relevant conditions brought forward two recurrent problems when carrying out low pressure studies. (i) the production of N_2O was rarely discussed because undetected. Van den Broek et al. (1999) first hypothesised that NO was a precursor in the production of nitrous oxide, produced *via* an additional reaction with adsorbed oxygen. N_2O was then detected also by Pérez-Ramirez et al. (2004), Baerns et al. (2005) and Kondratenko et al. (2007), which confirmed the precursor role of NO in its production. N_2 was hypothesised to be produced from the association of two adsorbed nitrogen atoms, after the de-hydrogenation process. Previous works mentioning oxidation of adsorbed ammonia by gas phase atoms was contradicted. (ii) the known roughening process of the catalyst at working conditions could not be reproduced without long working times, and high pressures. Kinetic studies on poly-crystalline Pt up to 10 bar but at temperatures below

385 °C observed the roughening transition (Kraehnert et al. 2008), which proved difficult to fit with developed kinetic models, attributed to local increase in temperature and surface area.

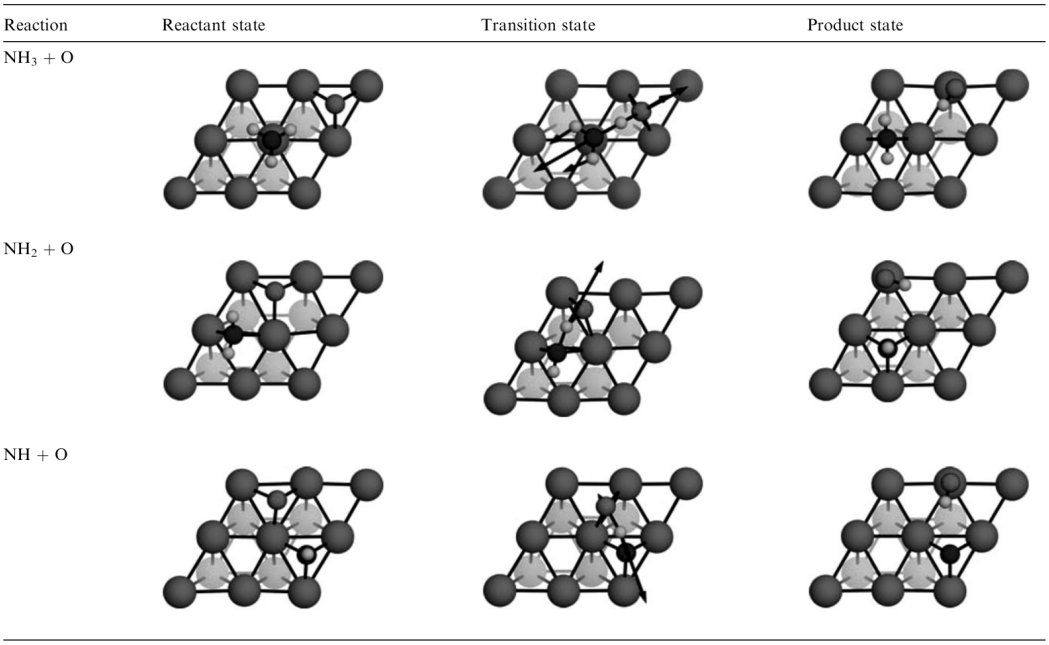

Figure 1.5: Example of NH_3 stripping process by adsorbed O, taken from Imbihl et al. (2007). From grey to black colours are lower layer of Pt(111), hydrogen atoms, upper layer of Pt(111), oxygen atoms, and nitrogen atoms.

Novell-Leruth et al. (2005) confirmed the adsorption of NH_3 and NH_2 to occur respectively on top and bridge sites for both Pt(100) and Pt(111), but with a more favourable adsorption process on Pt(100). Similar adsorption energies have been reported for NH and N that both adsorb on hollow sites Additional DFT studies of the reaction pathways and kinetics confirmed a mechanism following a step-by-step decomposition of ammonia on the catalyst surface. The stripping of the hydrogen atoms from adsorbed ammonia was reported to be facilitated by the presence of oxygen species, confirming the key role of oxygen in the production of not only nitric oxide, but also nitrogen (Offermans, Jansen and van Santen 2006). A comparative study between the Pt(100), Pt(111) and Pt(211) surfaces did not reveal a strong structure sensitivity of the NH_3 stripping process (Offermans, Jansen, Van Santen et al. 2007).

Imbihl et al. (2007) have further improved the understanding of the production of N_2O, which happens not only by the recombination of two adsorbed NO species but also *via* the reaction between adsorbed NO and NH_x species. The first de-hydrogenation step was found to be the slowest, while the desorption of NO is the rate limiting-step when aiming at the selective production of nitric oxide (Novell-Leruth, Ricart et al. 2008). Interestingly, for the first time different oxygen species were reported to be responsible for the de-hydrogenation process depending on the surface structure, respectively O for Pt(111) (fig. 1.5) and OH for Pt(100). A high energy barrier for NO desorption and N_2O formation explain the high temperature needed for their production in comparison with N_2.

Despite the large amount of work in the previous and current century, the mechanism of the oxidation of ammonia is still unclear. Studies performed at ultra high vacuum have paved the way for the understanding of model catalyst systems, followed by works at progressively higher pressures, but without reaching industrial conditions during *operando* studies on model systems. Moreover, many characterisation of used catalysts have been performed *ex-situ*.

This shows that the complete understanding of the mechanisms ruling heterogeneous

catalysis comes from developing novel methods, compatible with very high pressures and temperatures, especially when aiming at the study of a complex system with many competing reactions. For example, Pottbacker et al. (2022) have presented a new characterisation method to facilitate the study of the reaction kinetics at industrial conditions, by precisely measuring the temperature and compositional gradients present on the catalyst surface. Cross checking such information with results gathered on model systems at industrious conditions, e.g. active sites and structure, will aid the comprehension of the reaction mechanism.

Replacing precious metals in industrial reactor can be thought as the natural step that will follow the comprehension of the reaction mechanism. For example, the performance of new material has already been explored with V_2O_5 catalyst, reaching promising NO yields at atmospheric pressure between 300 °C to 650 °C (Ruan et al. 2022). Enabling selective mechanisms to function at lower working temperature can also result in a large economy of energy.

1.3 Environmental impact

1.3.1 Greenhouse effect

As illustrated earlier in fig. 1.2, nitrogen-based fertilisers have permitted an industrial development of agriculture. Fertilisers can be either ammonium- or nitrate-based. When plants do not fully absorb all the nutrients, a series of microbe-mediated transformations occur which leads to the release of nitrogen back into the atmosphere, primarily as nitrogen gas (N_2) and, to a lesser extent, as N_2O.

For an equal amount of N_2O and CO_2, nitric oxide will trap 298 times more heat than the carbon dioxide over the next 100 years (MIT 2023), responsible for 6.2 % of the total U.S.A. greenhouse gases emissions in 2021 (fig. 1.6). Moreover, the production of the necessary ammonia which is in turn used for fertilisers often relies on natural gas to provide hydrogen, meaning that each ton of NH_3 produced is equivalent to the emission of 1.9 t of CO_2 (Rafiqul et al. 2005; J. G. Chen et al. 2018).

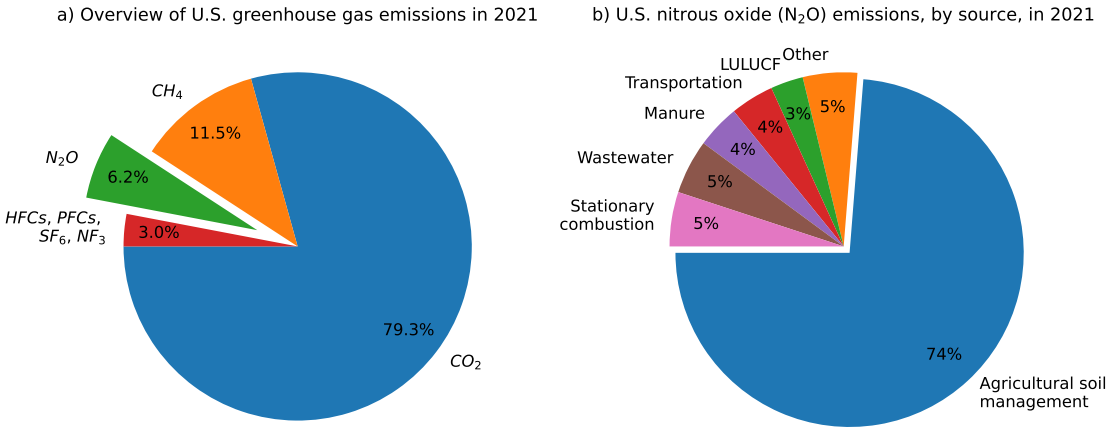

Figure 1.6: Pie charts underlining the importance of different gas in the total US greenhouse gas emissions in 2021 (a) and the specific contribution of nitrogen-based fertilisers to the total N_2O emissions in 2021. LULUCF means Land Use, Land-Use Change, and Forestry. Adapted from EPA 2023.

The presence of N_2O in the atmosphere can be linked to the development of agriculture towards a productivity model, helped by the means of nitrogen-based fertilisers. Thus, the amount of nitric oxide, which has an atmospheric lifetime of 114 years, is expected to decrease

in the future years in the northern hemisphere, but increase in the southern hemisphere following such transitions (Solomon 2007; Davidson 2009).

In a review of the presence of N_2O in the atmosphere linked to human activities, Pérez-Ramirez et al. (2003) have shown that the most important contribution to nitrous oxide in the atmosphere is not only from unused volumes of nutrients, but also from nitric acid manufacture. Understanding and limiting the origin of N_2O by controlling the process selectivity is thus capital to limit the amount of nitric oxide released in the atmosphere.

1.3.2 Pollution

Nevertheless, it can also be interesting to be able to remove NH_3 from the atmosphere, a colourless gas with a pungent odour, that irritates the eyes, nose, throat, and respiratory tract if inhaled in small amounts due to its corrosive nature; and poisonous in large quantities. Ammonia also pollutes and contributes to the eutrophication (excessive growth of algae) and acidification of terrestrial and aquatic ecosystems, and forms secondary particulate matter (PM2.5) when combined with other pollutants in the atmosphere (tab. 1.1). Nitric acid can also be linked to acid rains (Galloway et al. 1981). Moreover, nitrogen-based fertilisers and other human activities can lead to nitrogen runoff into water bodies, contributing to eutrophication and causing harm to aquatic ecosystems (tab. 1.1). Approximately half of the production of ammonia is lost to the environment (J. Erisman et al. 2007).

Finally, the important effect of nitrogen oxides (NO_x, *i.e.* NO, NO_2, and N_2O) on the environment has brought forward the necessity to control their emissions, especially from the exhaust of diesel engines that are responsible for 65 % of their emissions. The selective catalytic reaction (SCR) using urea or ammonia as reductant (tab. 1.1) has proven to be effective and to reach 95 % efficiency (Mitsubishi 2023). However, there can be a subsequent problem of unreacted ammonia *slipping* from the reaction, which is also an important subject of study (Thermofischer 2023).

To efficiently remove ammonia, the selectivity of the ammonia oxidation reaction must be tuned towards the production of N_2, which is the only non pollutant and toxic gas.

Lim et al. (2021) have underlined that if the current methodologies for producing ammonia and nitric acid remain unchanged, carbon emissions originating from the manufacturing of fixed fertiliser feedstocks could exceed 1300 MtCO2eq/yr, highlighting the pressing necessity for sustainable alternatives.

Therefore, depending on the application of the ammonia oxidation, the catalytic reaction must be tuned towards a specific product, this *selectivity* is controlled by the reaction temperature, pressure, the reactant ratio, and the type of catalyst. To be able to drive the reaction, the impact of each parameter *at relevant industrial conditions* on the product pressure must be studied.

1.4 From industry to model catalysis

> "A long standing conundrum in the catalysis community emerged at the interface between surface science and heterogeneous catalysis, better known as the pressure and materials gap."
>
> *Nature Catalysis editorial, 2018.*

Pressure and material gap are limiting the understanding of catalyst operation (tab. 1.2). X-rays are intrinsically well suited when working at high pressures thanks to their high

penetration in gases, which made them a promising probe to access sample environments approaching industrial condition.

	Pressure	Material	Temperature
Industry	1 bar to 12 bar	Knitted gauzes wires (diameter ≈80 µm)	750 °C to 900 °C
Literature	UHV, mbar	Single crystals	25 °C to 900 °C
This study	Near ambient pressure (0.5 bar)	Single crystals and nanoparticles	25 °C to 600 °C

Table 1.2: Ammonia oxidation conditions: comparison between industry and model catalysts. Reproducing the same exact industrial reaction conditions and sample can be difficult in a laboratory due to the nature of the probe, the sensitivity of the technique, and the design of reactor cells for synchrotrons (Hatscher et al. 2008). This is the so-called material and pressure gap in heterogeneous catalysis.

Bridging the pressure and material gap by the development of new x-ray techniques has been the subject of several dissertations in recent years. Ackermann (2007) has for example pushed forward the use of *operando* surface x-ray diffraction (SXRD) for the study of heterogeneous catalysis. This effort has also been focused towards spectroscopy techniques such as x-ray photoelectron spectroscopy (XPS) or x-ray absorption spectroscopy (XAS) (Dann 2019). Progress in bridging the pressure gap and material gap has been preceded by the development of catalysis reactors compatible with synchrotrons beamlines. Such reactors are closed environments penetrable by x-rays, and accommodating a wide range of temperature, total pressure and gas compositions (Rijn et al. 2010; M.-I. Richard et al. 2017; Castán-Guerrero et al. 2018).

The samples often used during SXRD and XPS experiments are single crystals, much larger than industrial samples. For example, the industrial gauzes used during the oxidation of ammonia have a diameter of about 80 µm, whereas single crystals are typically cm large (fig. 1.7). These kind of samples only exhibit a single type of structure on their surface (e.g. (111), (100)), reducing the complexity of the catalyst surface. The reason behind their use is a large surface area exposed to the reacting gases, and thus an increased surface signal, most important to understand heterogeneous catalysis which is a surface process (Goodman 1994). Nevertheless, they can show some limitations, for example large Pt(111) single-crystals exhibit a significant amount of steps on their surface also contributing to the catalytic activity (Calle-Vallejo, Pohl et al. 2017).

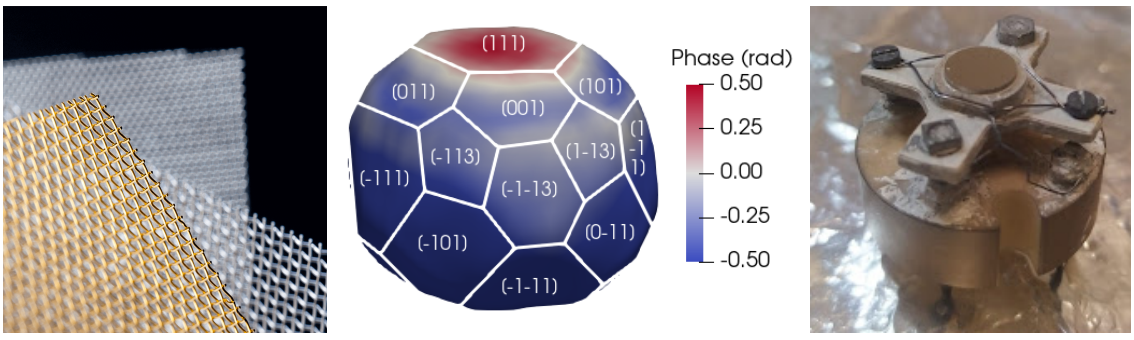

Figure 1.7: Left: platinum gauzes used in industry, diameter ≈80 µm, image taken from industry website (Platinum / Rhodium Catalyst Gauzes 2023). Middle: reconstructed Pt particle, surface coloured by the displacement of surface layers from their equilibrium positions, diameter of about 300 nm. The orientation of each facet on the particle surface is indicated. Right: Pt(111) single crystal used in SXRD and XPS experiments, diameter ≈8 mm, thickness ≈2 mm.

Only recently have supported platinum nanoparticles (≈1 nm large) been used during the oxidation of ammonia, showing a remarkable selectivity towards NO at high temperature and atmospheric pressure (Schäffer et al. 2013). Reducing Pt supported nanoparticles by H_2 showed to improve their catalytic activity below 200 °C in a study aiming at the production of N_2 (Svintsitskiy et al. 2020). Similarly, supported palladium nanoparticles have shown high selectivity towards production of N_2 in the selective catalytic oxidation of NH_3 below 200 °C (Dann 2019). Nanoparticles allow to better understand heterogeneous catalysis since they exhibit a various amount of active sites such as different facets (e.g. (111), (110), (100), ...), edges, corners and defects (fig. 1.7). They are thus considered a good approximation of real catalysts (Somorjai et al. 2007; Molenbroek et al. 2009; Roldan Cuenya 2010; An et al. 2012; Schauermann et al. 2013). Studies have shown that nanoparticle surface strain can be controlled, opening up a new path to tune and optimise nanoparticle catalysts (S. Zhang et al. 2014; Sneed et al. 2015; H. Wang et al. 2016).

Bragg coherent diffraction imaging (BCDI) is a young technique (I. K. Robinson, Vartanyants et al. 2001), only recently applied to catalysis (Ulvestad, Sasikumar et al. 2016), that can only be applied to sub-micron samples due to instrumental limitations (Marchesini, Chapman et al. 2003). Indeed, the sample can not be larger than the coherence lengths of the beam, about 1 µm at 3^{rd} generation synchrotrons. The x-ray beam, focused by some optical elements to micrometer size to respect this requirement, must fully illuminate the sample during the experimental process. Therefore, BCDI can contribute to reducing the material gap in heterogeneous catalysis.

However, samples below a certain size are not easily measured experimentally with other diffraction techniques because the outcoming photon flux is proportional to the sampled volume (Willmott 2009). This limitation also exists in BCDI, despite the highly focused beam, which draws a limit between experimental samples (so far, the smallest imaged nanoparticle is 20 nm large - Björling et al. 2019; Carnis, Kirner et al. 2021) and the few nm large nanoparticles typically used in density-functional theory (DFT) or molecular dynamics (MD). DFT and MD are theoretical approaches to molecular adsorption and particle relaxation only limited by the current computational power. Moreover, the ability to resolve the surface signal with BCDI is still limited in comparison with SXRD, which is why both techniques are here used together to obtain a better understanding of the dynamics at play during the catalytic reaction.

1.5 Aim and Scope

The catalytic oxidation of ammonia has exerted a profound influence in the 20^{th} and 21^{st} century, playing a pivotal role in the fertiliser industry and associated demographic shifts. Despite its critical industrial significance, the various industrial applications linked to the Ostwald process have significantly contributed to both climate change, and to the ever growing pollution of our ecosystems.

In this first chapter, the importance of the oxidation of ammonia has been underlined. It was shown that despite being a major catalytic process in a multi-billion industry, the exact mechanisms of action are not yet understood. Obtaining a comprehensive understanding of these mechanisms is essential for controlling reaction selectivity, thereby mitigating pollution arising from NH_3 and NO_x, as well as reducing the greenhouse effect induced by NO_2. Moreover, a deeper understanding of the reaction mechanism holds promise for the development of novel catalysts that can move away from the reliance on expensive precious metals.

This thesis aims at studying the catalytic reaction at near ambient pressure by the means of diffraction and spectroscopy synchrotron techniques. The reactor used to study heterogeneous catalytic reaction at the SixS beamline (SOLEIL) is already compatible with highly

oxidative environments (Rijn et al. 2010; Resta et al. 2020), and will permit high pressure surface x-ray diffraction and Bragg coherent diffraction imaging experiments. Optical elements necessary for the use of a focused coherent beam have been implemented and characterised. Extending the panel of available techniques will help bridging the material and pressure gap by bringing forth the possibility for synchrotron users to study catalytic reactions at the same exact conditions and environment, but with different techniques.

X-ray photoelectron spectroscopy has been carried out at the B07 beamline (Diamond), also compatible with high pressures (Held et al. 2020). Both the material and pressure gap have been partly bridged by operating at temperatures above the catalyst light-off, at almost industrial pressure.

The study of the reaction is performed *operando*, by exploring the large parameter space defined by the operating temperature, total pressure, and O_2/NH_3 ratio. The utilisation of diverse samples will contribute to a comprehensive understanding of the underlying structural dynamics. Integrating the evolution of the catalyst surface structure with the nature of adsorbed species during the reaction will help validate the reaction mechanism.

1.6 Thesis outline

The first chapter has briefly presented the history of the oxidation of ammonia, and its societal impacts, setting the stage of this thesis.

The second chapter will provide a concise overview of heterogeneous catalysis, and the fundamental principles governing the interaction between x-rays and matter. This section emphasises the origins, advantages, and constraints of each technique used in the study, highlighting how x-rays can indirectly observe catalytic reactions by detecting unique markers left on the materials. The SixS beamline at synchrotron SOLEIL, the primary tool for most experiments, is introduced, emphasising the latest advancements in experimental techniques and beamline-specific hardware. Additionally, the thesis presents the software used for data reduction and analysis developed during this work, focusing on a comprehensive workflow for Bragg coherent diffraction imaging, a technique that has yet to reach its full potential through the development of 4^{th}-generation synchrotrons and powerful computing clusters. A description of the software *Gwaihir* (Simonne, Carnis et al. 2022), which aims to facilitate the reduction and analysis of data in the *Python* programming language, while encouraging broader adoption of the technique through a user-friendly graphical interface, is provided.

The third and fourth chapters present results from the *operando*, near-ambient pressure study of catalytic reactions using synchrotron techniques. Pt nanoparticles and single crystals are employed to explore the structure-selectivity relationship at ambient pressure and high temperature, by the means of a vast array of O_2/NH_3 partial pressure ratios, favouring either the production of N_2 or NO. The presence of platinum oxides is monitored in order to understand its importance in the reaction mechanism, as well as in potential catalyst reconstructions. Thus, the difference in activity between different crystalline facets is studied with different samples that, together, offer a good compromise between industrial catalysts and compatibility with the experimental setup of synchrotron beamlines. Complementary studies with x-ray photoelectron spectroscopy are performed at the same O_2/NH_3 ratio and temperature. Information about the presence or not of nitrogen and oxygen species on the catalyst surface will improve the understanding of the reaction mechanism. Finally, to explore the correlation between surface structure and catalytic activity, mass spectrometry data is collected simultaneously to all measurements.

The last chapter will serve as a general conclusion, resuming the results obtained from each technique, and detailing the perspectives enabled by this thesis.

Chapter 2

Theory and methods

2.1 Introduction

Understanding the different mechanisms at play when photons interact with matter is of crucial importance to decide how to use x-rays as a probe in material science. Different phenomena are at the source of different techniques (tab. 2.1 - fig. 2.1), e.g. scattering brings surface x-ray diffraction (SXRD) and Bragg coherent diffraction imaging (BCDI). Both techniques are used during this thesis, yielding complementary information about the sample atomic structure.

X-ray absorption together with the photoelectric effect explained by Einstein in 1905 are at the origin of the third technique used during this work, x-ray photoelectron spectroscopy, sensitive to the chemical environment of the adsorbates present on the sample's surface.

Technique	Surface x-ray Diffraction (SXRD)	Bragg Coherent Diffraction Imaging (BCDI)	X-ray Photoelectron Spectroscopy (XPS)
Sample	Pt(111) and Pt(100) single crystals and Pt particles	Isolated Pt particles	Pt(111) and Pt(100) single crystals
Information	Surface structure, roughness, relaxation & crystallographic phases	Shape, 3D displacement and strain arrays of unique object	Surface species presence, quantity & oxidation state
Beamline	SixS (SOLEIL)	SixS (SOLEIL)	B-07 (Diamond Light Source)

Table 2.1: X-ray techniques carried out in the frame of this thesis.

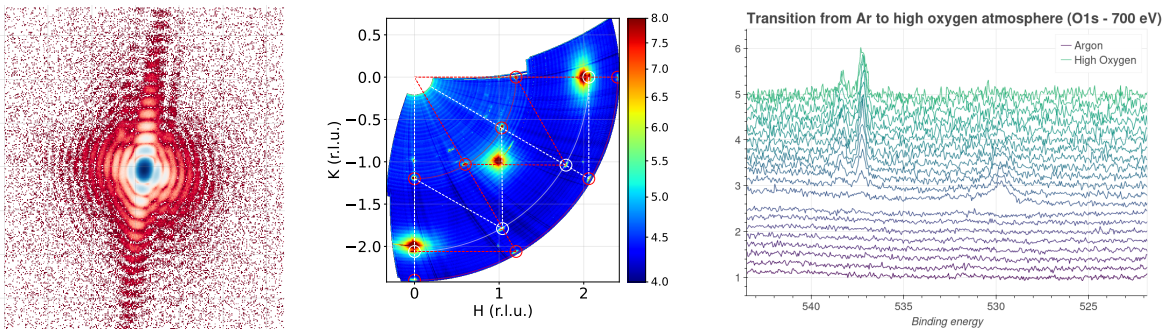

Figure 2.1: Left: 2D diffraction pattern collected using BCDI at the SixS beamline (SOLEIL synchrotron) Middle: reciprocal space in-plane map collected using SXRD at the SixS beamline. Right: near ambient pressure XPS spectra measured during a transition between two atmospheres (Ar and O_2), collected using XPS at the B07 beamline (Diamond synchrotron).

This chapter will discuss heterogeneous catalysis, focusing on its key principles and the associated primary reaction mechanisms. The concept of active sites will be introduced together with the link between adsorption and surface strain, crucial for the study of catalytic reaction with x-ray diffraction techniques, intrinsically sensitive to lattice strain in crystals. The origin of each technique from fundamentals that not only tailor their experimental design but also the information one can gain from their use will be detailed (tab 2.1).

Finally, the importance of open-source, user-friendly, comprehensive, and detailed computer programs will be addressed with the example of Gwaihir, a *Python* software developed during this thesis not only to bring new users to BCDI, but also to facilitate the data analysis workflow. A brief description of the other softwares used during this thesis will also be given.

2.2 Heterogeneous Catalysis

A catalyst is a substance that speeds up a chemical reaction, or lowers the temperature or pressure needed to start one, without itself being consumed during the reaction. Catalysis is the process of adding a catalyst to facilitate a reaction.

Chemical reactions involve the breaking, rearranging, and rebuilding of bonds between atoms in molecules, resulting in the formation of new molecules. Catalysts play a crucial role in enhancing the efficiency of these reactions by providing an alternative route for the reaction with a lower *activation energy* E_a, the minimum energy that must be attained for the reaction to take place. This process facilitates the breaking and formation of chemical bonds, increasing the reaction rate (Schlögl 2015; Hagen 2016), described by the rate equation (eq. 2.1).

$$\text{rate} = k[A]^a[B]^b \tag{2.1}$$

k is the rate constant, $[A]$ and $[B]$ are the reactants concentrations, a, b are the order of reaction referring to how the concentration of the reactants affects the rate of the reaction.

The impact of changing the temperature T of the reaction and the activation energy is directly set in the rate constant defined by the Arrhenius equation (eq. 2.2), R is the gas constant.

$$k \propto e^{\frac{-E_a}{RT}} \tag{2.2}$$

2.2.1 Mechanisms

Heterogeneous catalysis is a type of catalytic process where the catalyst exists in a different phase (solid, liquid, or gas) from the reactants. Most commonly, the catalyst is in the solid phase, while the reactants are in either the gas or liquid phase. This distinction sets heterogeneous catalysis apart from homogeneous catalysis, where the catalyst and reactants are in the same phase. One of the key advantages of heterogeneous catalysis is the ease of catalyst separation and reuse. Since the catalyst is in a different phase, it can be easily separated from the reaction mixture once the reaction is complete. This makes the catalyst recyclable and economically attractive for industrial processes (Fechete et al. 2012).

There are a few key parameters to take into account when comparing the efficiency and performance between different catalysts (Boudart 1995; M. Zhang et al. 2019; Wachs 2022).

The *turnover frequency* (TOF) refers to the number of reactant molecules catalysed into product molecules by a single catalyst site per unit of time, expressed in units of moles of product formed per second per mole of active catalyst site, it is an indicator of the catalyst activity. The *turnover number* (TON) refers to the total number of reactant molecules that are converted into product molecules by a single catalyst site over the entire course of a reaction, and provides a measure of the catalyst's overall *activity* and *stability* before deactivation. Finally, the *selectivity* of the catalyst refers to its ability to favour the formation of a specific product or products over undesired products.

Developing a catalyst that simultaneously fulfils all the desired requirements of high stability, selectivity, and activity for every chemical reaction remains an ongoing scientific pursuit (Hagen 2016).

The Sabatier principle, at the origin of the Nobel price of chemistry of 1912 (Che 2013), states that when a heterogeneous catalyst is used, there exists an optimum catalyst binding energy for the reactant on the catalyst surface. On one hand, if the catalyst binding energy is too weak, the reactant molecules do not adsorb strongly enough on the catalyst, leading to low reaction rates. On the other hand, if the catalyst binding energy is too strong, the reactant molecules bind too tightly and do not easily react with the other reactant, resulting in low selectivity and efficiency. Moreover, if the adsorption is too strong, the product of the reaction is not able to desorb from the active site.

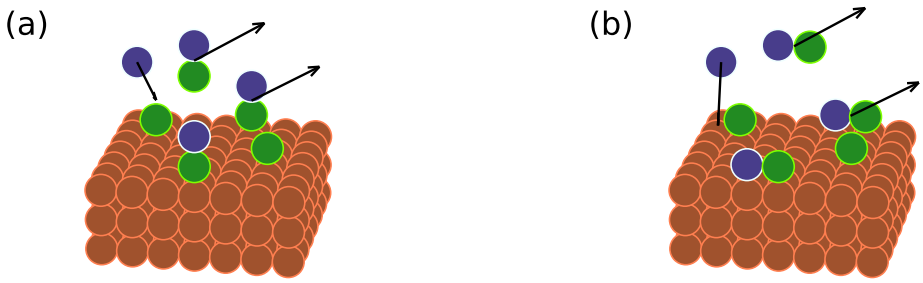

Figure 2.2: In the Eley Rideal mechanism (a) one of the reactants interacts directly from the gas phase with an adsorbed molecule of the other reactant, whereas for the Langmuir Hinshelwood mechanism (b) both of the reactants are adsorbed on nearby sites of the catalyst's surface.

In a founding study in 1922, Langmuir detailed the possible mechanisms of actions for heterogeneous catalysis. When studying bi-molecular reactions, the Langmuir–Hinshelwood and Eley-Rideal mechanisms are two main mechanisms of interest (Bratan et al. 2022). In the Langmuir–Hinshelwood mechanism, both reactants are adsorbed in nearby sites at the surface of the catalyst, and react on the surface to form the product which is subsequently desorbed from the surface (Prins 2018; Ross 2019). In the Eley–Rideal mechanism, a reactant in the gas phase comes and interacts with the adsorbed reactant without being itself adsorbed, followed by the desorption of the product (Rideal 1939; Weinberg 1996) (fig. 2.2).

In a third mechanism, an atom from the surface layer of the catalyst reacts with an adsorbed reactant, which creates a vacancy in his original position on the surface when the products is desorbed. This vacancy is then replaced by an atom that can either come from the bulk of the catalyst, or from the dissociation of the catalyst atoms from the product molecule in the gas phase (Mars et al. 1954; Doornkamp et al. 2000). This is called the Mars-Van Krevelen mechanism.

The Langmuir–Hinshelwood mechanism seems to be generally preferred, the bonding of the reactant molecules to the atoms weakening its bonds and preparing the molecule for reaction by reducing the activation energy required for the reaction to occur (Baxter et al.

2002).

The complete heterogeneous catalytic reaction consists in a series of elementary steps such as reactant dissociation, adsorption, surface diffusion, surface chemical reactions, and desorption that are nowadays extensively studied *via* different theoretical computing methods such as density functional theory (DFT - Reuter et al. 2004; Molenbroek et al. 2009; Y. Li, S. H. Chan et al. 2015; Gaggioli et al. 2019; Chatelier 2020) or more recently machine learning (Kitchin 2018; Schlexer Lamoureux et al. 2019; Anstine et al. 2023) as a function of the reaction parameters.

Due to the increase of interest in the field of catalysis, synchrotron techniques have been developed to study reactions *operando*, meaning that the reaction happens while being observed (Meirer et al. 2018). The first step towards the use of these experimental methods is to understand what specific signatures on the working catalyst can be identified using an x-ray probe.

2.2.2 Active sites in heterogeneous catalysis

Heterogeneous catalysis being a surface process, the tendency is to use small catalysts which maximise the surface area to volume ratio, increasing the number and variety of available active sites for catalysis, while favouring the emergence of edges and corners (Zambelli et al. 1996; Hendriksen et al. 2010; Vogt et al. 2022). This statement is at the origin of the push towards ever smaller samples for heterogeneous catalysis, by controlling and investigating their shape (H. Lee et al. 2006; Tian et al. 2007; Bratlie et al. 2007; I. Lee et al. 2009), bringing forward nanoparticle catalysis (Che and Bennett 1989; Raimondi et al. 2005; Aricò et al. 2005; Molenbroek et al. 2009; Santen et al. 2010; Schauermann et al. 2013). As an example, platinum (Pt) nanoparticles are of great interest for the petrochemical industry (Astruc et al. 2005; Astruc 2020), fuel cell technology and for automobile exhaust gas purification (Heck and Farrauto 2001).

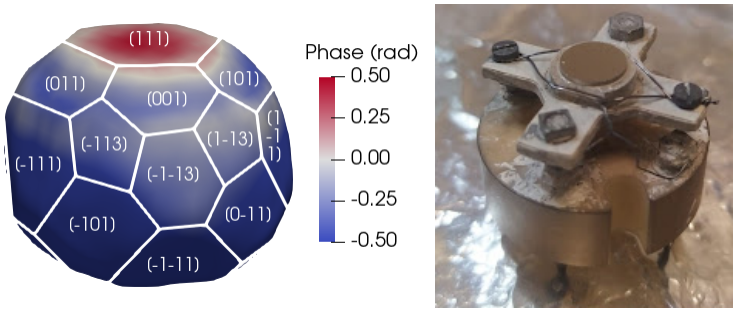

Figure 2.3: Catalytically active samples studied with x-ray operando techniques. Left: reconstructed Pt particle (diameter 300 nm*) measured at SixS, with its surface coloured by the phase values linked to the displacement of surface layers from their equilibrium positions. The orientation of each facet on the particle surface is indicated. Right: Pt* (111) *single crystal used in SXRD and XPS experiments, diameter of about* 8 mm*.* {111} *facets are present on both samples, occupying* ≈36 % *of the particle surface.*

The surface of nanoparticles can be understood as constituted of facets (fig. 2.3) whose crystallographic orientation depends on the nanoparticle material, size, synthesis route, and on the absence (Wulff construction) or not (Winterbottom construction) of substrate (Wulff 1901; Winterbottom 1967; Boukouvala et al. 2021). This can be linked to the minimisation of the particle surface energy (e.g. depending on the material and facet type), and of interfacial energy. Between facets are the nanoparticle edges and corners, notorious for being very favourable adsorption sites due to a low local coordination geometry (W. J. Huang et al. 2008; Jiang et al. 2009).

The orientation and structure of each facet on the nanoparticle surface, described by its

Miller (hkl) indices, has a key role in the surface strain, and in the adsorption properties of the catalysts (Zhou et al. 2012; C.-Y. Wu et al. 2017; Altantzis et al. 2019; T. Wu et al. 2021). Surface atoms of different facets have for example different coordination numbers. In the case of supported nanoparticles, the initial strain in the particle can be linked not only to surface stress, but also to hetero-epitaxial stress from the relationship with the substrate. The morphology and shape of supported nanoparticles was shown to be linked to the type of facets present on the nano-catalyst surface (Ndolomingo et al. 2020). Re-faceting can also occur induced by heterogeneous catalytic reactions, as highlighted by Vendelbo et al. (2014) with the example of CO oxidation.

Moreover, surface roughness can also strongly affect the electronic structure of the surface atoms, and therefore its adsorption properties (Dicke et al. 2000; Hendriksen et al. 2010; Resta et al. 2020). The formation of surface oxides on specific facets of Pt-Rh nanoparticles has also been correlated with an increased activity during the oxidation of CO (Hejral, Franz et al. 2018).

Calle-Valejo et al. (2014; 2015; 2018; 2023) have used DFT calculations to show an approximate linear trend between the *generalised* coordination number $\overline{CN}(i)$ of a nanoparticle surface atom i with n_i neighbours (eq. 2.3) and its adsorption properties. Their work highlights the importance of taking into account not only the number of first-nearest neighbours, but also the number of second nearest neighbours, which also underlines the importance of surface roughness. The *Taylor ratio* translates this effect by defining the fraction between active sites and the total exposed surface (Taylor et al. 1925).

$$\overline{CN}(i) = \sum_{j=1}^{n_i} \frac{cn(j)}{cn_{max}} \tag{2.3}$$

where $cn(j)$ is the coordination number of the surface site for atom j, and cn_{max} the maximum number of first nearest neighbour in the bulk.

However, strong adsorption sites are not always the most active sites, following the Sabatier principle, it is possible that if the adsorption is too strong, there is no subsequent desorption of the reaction product (Nilsson et al. 2005; Jiang et al. 2009).

The activity of single facets can also be studied with *single crystals*, larger samples synthesised so that their macroscopic surface can be considered as a single crystallographic plane (fig. 2.3).

2.2.3 Linking strain and reactivity

A modern theoretical approach to the interaction between surface and adsorbates in heterogeneous catalysis has been proposed by Hammer, Norskov and Mavrikakis (1995; 1998; 2000; 2009) for transition metals, which is at the origin of the strain-reactivity studies in the frame of this thesis.

In a crystalline lattice, the energy levels of electrons are so close that they form bands (Ashcroft et al. 1976). The study considers that the energy levels of the d-bands in transition metals is responsible for bonding and adsorption in catalytic reactions. The main conclusion being a direct relation between lattice strain, adsorption energy and surface reactivity, confirmed by later studies (Jakob et al. 2001; Kitchin et al. 2004; Kibler et al. 2005; Gsell et al. 1998; Ontaneda et al. 2015; Weissmüller 2019). Moreover, d-bands narrowing effects also justify the difference between bulk, surfaces steps and kinks in terms of reactivity (Haydock et al. 1972; Desjonquères et al. 1975; Egelhoff 1987; B. Hammer 2006; Khorshidi et al. 2018). In Mavrikakis et al. (1998), the application of tensile or compressive lattice strain is shown to cause the d-band centre to shift upward or downward, leading to a strengthening or weakening of the bonding of adsorbed oxygen on a Ru (0001) surface, respectively. The

magnitude of this effect was also shown to depend on the nature of the adsorbed specie, the dissociation of CO facilitated by an increase of tensile strain.

The type of facets, edges and corners exhibited on the surface are of key importance when investigating the role of the nanoparticle structure on its catalytic activity and selectivity. (Abuin et al. 2019).

The application of this approach has been demonstrated by Wang et al. in 2016, which pioneered scientific studies for strain engineering in catalysis (Nilsson Pingel et al. 2018). Techniques sensitive to the catalyst structure, *i.e* to the lattice strain, are employed (Somorjai 1991). For example, strain has been proven to impact the catalytic properties of the catalyst with surface x-ray diffraction (Resta et al. 2020), and Bragg coherent diffraction imaging (Ulvestad, Sasikumar et al. 2016; D. Kim, Chung, S. Kim et al. 2019; Björling et al. 2019; Passos et al. 2020; Carnis, Kshirsagar et al. 2021; Carnis, L. Gao, Fernández et al. 2021; Dupraz, N. Li et al. 2022).

2.3 X-ray interaction with matter

2.3.1 Scattering from electrons and atoms

The duality between wave and particles was first mentioned by Max Planck and Albert Einstein in the early 20^{th} century and generalised to all matter by Louis-Victor de Broglie in 1924 with the famous formula:

$$\lambda = \frac{h}{p} \tag{2.4}$$

Electromagnetic waves, *i.e.* light or photons can be characterised by their energy E in eV and wavelength λ in m. p corresponds to the momentum transfer. The conversion between is realised thanks to Planck's constant $h = 6.626 \times 10^{-34}$ J s and the speed of light in vacuum $c = 2.9979 \times 10^{8}$ m /s:

$$E = \frac{hc}{\lambda} \tag{2.5}$$

The properties of the photon and its use in our society depends on its energy and wavelength. For example, visible light is situated between 1.65 eV and 3.26 eV, micro-waves used in our everyday life are situated between 10^{-6} eV and 10^{-3} eV. On the other side of the electromagnetic spectrum are higher energy photons such as x-rays (10^{2} eV to 10^{5} eV) and γ-rays ($>10^{5}$ eV).

Hard x-rays have a wavelength of a few Å (10^{-10} m) making them the perfect probe to study the structures of materials at the atomic scale thanks to different interactions with matter.

Cross-sections

When electromagnetic wave interacts with matter it will be attenuated by absorption, reflection or scattering. Each process can be quantified depending on the atoms (and thus on its electronic cloud and nucleus) the beam interacts with, and the energy on the incident photon (fig. 2.4). The cross-section for a particular process p is defined as follows (Willmott 2009):

$$\sigma_p = (\Lambda_p N_i)^{-1} \tag{2.6}$$

Λ_p is the attenuation length in m, *i.e.* the length after which the beam's intensity is reduced to $1/e$, N_i is the atomic number-density in atoms/unit volume.

Compton scattering, also named inelastic scattering, is a process during which some of the incident electromagnetic wave energy is transferred to the atoms' electrons. This results

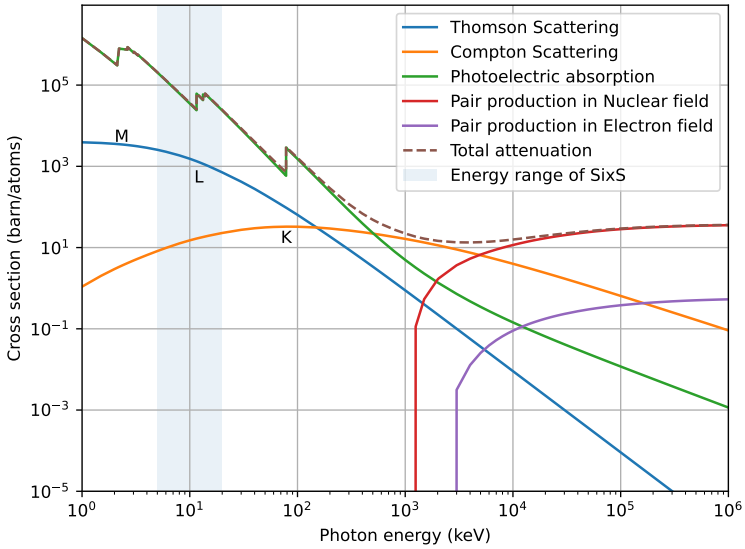

Figure 2.4: Cross-sections for platinum (Z=78) corresponding to different processes occurring when photons interact with matter. Data taken from the NIST (National Institute of Standards and Technology) (Berger et al. 2010) website. The energy range of the SixS beamline at SOLEIL is highlighted in blue.

in a lower energy for the scattered photon (and therefore a higher wavelength) compared to the incident photon.

In the frame of this thesis, the (elastic) Thomson scattering cross-section is the most important, at the origin of x-ray diffraction. This process is dominant for energies below 200 keV, in the x-ray regime, together with photoelectric absorption.

Scattering from an electron

This discussion of x-ray scattering begins by considering scattering from a single free electron using classical electromagnetic theory. During elastic scattering, the oscillating electric field of the incident x-ray wave exerts an electromagnetic force on the electron, causing it to accelerate and oscillate in the same direction as the incident electronic field.

During an elastic scattering event, the oscillating electron emits a spherical electromagnetic wave with the same wavelength as the incident beam (Thomson scattering). The scattered field $\vec{E}_{scatt}$ is then proportional to the incident electromagnetic field $\vec{E}_{in}$ as follows (Jens Als-Nielsen 2011):

$$\frac{|\vec{E}_{scatt}(R,\, t)|}{|\vec{E}_{in}|} = -r_0 \frac{e^{\vec{k}.\vec{R}}}{|\vec{R}|} |\hat{\epsilon}.\hat{\epsilon}'| \tag{2.7}$$

$|\vec{R}|$ is the distance at which the scattering is detected at the time t, $\hat{\epsilon}$ and $\hat{\epsilon}'$ are respectively the polarisation vectors of the incident and scattered electromagnetic fields. The minus sign illustrates a phase shift of π between the incident and scattered wave, r_0 is the Thomson scattering length or the classical radius of the electron defined as:

$$r_0 = \frac{e^2}{4\pi\epsilon_0 m_e c^2} \tag{2.8}$$

with m_e the mass of the electron and ϵ_0 the permittivity of free space.

The differential cross-section for Thomson scattering measures the efficiency of the scattering in the volume occupied by a solid angle $d\Omega$ in the direction $\vec{R}$ (Jens Als-Nielsen 2011).

It is defined as follows:

$$\frac{d\sigma_{ts}}{d\Omega} = \frac{|\vec{E}_{scatt}(R,t)|^2 R^2}{|\vec{E}_{in}|^2} \tag{2.9}$$

By substituting eq. 2.7 into eq. 2.9, it becomes clear that the scattering is proportional to the Thomson scattering length, and that the intensity is attenuated depending on the dot product between the two polarisation. The polarisation factor P for scattered beams is defined as $P = |\hat{\epsilon}.\hat{\epsilon}'|^2$, the differential cross-section can be written as:

$$\frac{d\sigma_{ts}}{d\Omega} = r_0^2 |\hat{\epsilon}.\hat{\epsilon}'|^2 = r_0^2 P \tag{2.10}$$

The effect of the polarisation of the incident beam is illustrated in figure 2.5. At synchrotrons, where the incident beam has a horizontal polarisation, working in the vertical plane $(\vec{x}, \vec{z})$ is preferable to maximise the intensity of the scattered field.

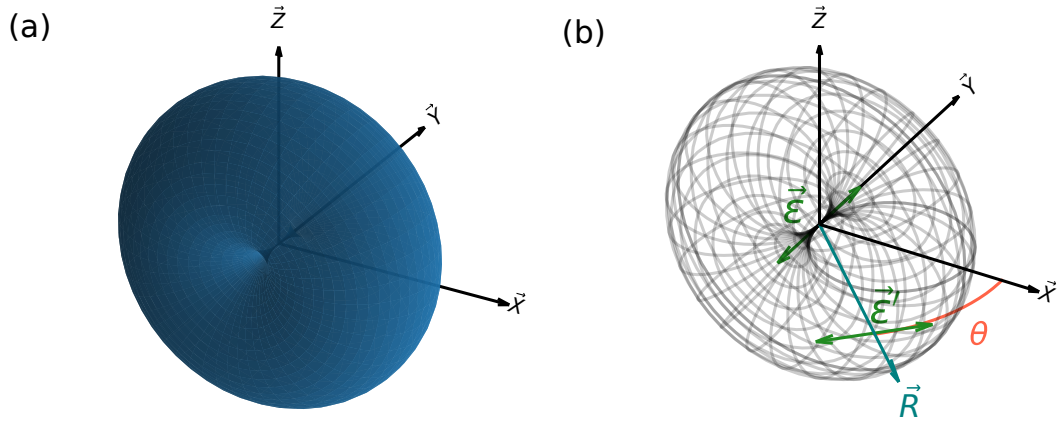

Figure 2.5: Effect of relation between synchrotron x-ray polarisation $\hat{\epsilon}$ and scattered x-ray polarisation $\hat{\epsilon}'$ on the scattered field. The scattered field intensity is attenuated by a $\cos(\theta)$ factor, where θ is the angle between the plane perpendicular to the electric field and the direction of observation $\vec{R}$. $\vec{x}$ is parallel to the beam.

The total cross-section for the scattering event by a single free electron can be computed by integrating the differential cross-section over all the possible scattering angles, *i.e.* by averaging all possible polarisation directions (Willmott 2009). This yields $\sigma_{ts} = 8\pi r_0^2/3 = 0.665\,\text{b}$, ($1\,\text{barn}$ is equal to $10^{-28}\,\text{m}^2$). The total Thomson scattering cross-section is constant, independent of the incoming photon energy. This result holds for x-rays for which the scatterer *i.e.* the electron can be considered as free (Willmott 2009).

Scattering from a single atom

As discussed above, the main scatterer for Thomson scattering is the electron. An atom can be described as a small volume $d^3\vec{r}$ in which the electrons are localised. The electromagnetic field scattered from an atom is therefore proportional to the atomic electronic density $\rho_{atom}(\vec{r})$. For a single atom of atomic number Z:

$$\int \rho_{atom}(\vec{r}) d^3\vec{r} = Z \tag{2.11}$$

To describe the phase of the scattered field, which depends on the phase of each incident wave at each point in the scattering volume (fig. 2.6), the scattering vector, $\vec{q}$, is introduced (eq. 2.12), to derive the amplitude of a scattering event in the direction defined by the scattering angle 2θ.

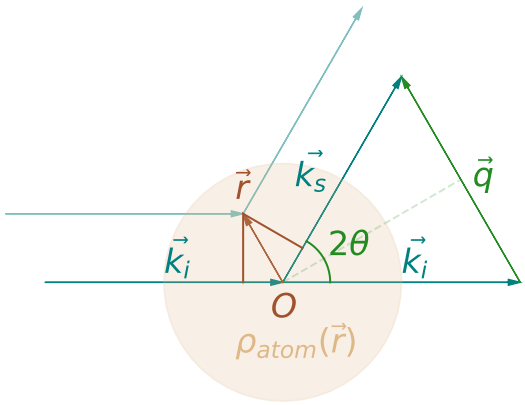

Figure 2.6: Geometry of the scattering vector $\vec{q}$ in reciprocal space, 2θ is the scattering angle. The magnitude of the scattering vector can be derived from the scattering angle θ that draws a line cutting $\vec{q}$ at $|\vec{q}|/2$.

$$\vec{q} = \vec{k}_s - \vec{k}_i. \tag{2.12}$$

The phase difference between a wave scattered at a position O and a wave scattered at a distance $\vec{r}$ from O is equal to $(\vec{k}_s - \vec{k}_i).\vec{r} = \vec{q}.\vec{r}$ (fig. 2.6 - Jens Als-Nielsen 2011).

From fig. 2.6, and the relation between wavevector and wavelength ($k = 2\pi/\lambda$), the scattering vector modulus can be written as a function of the wavelength of the incident beam λ, and of the direction of detection defined by the scattering angle 2θ (eq. 2.13). Is it assumed here that the scattering event is elastic ($|\vec{k}_i| = |\vec{k}_s|$), and that the waves are plane waves parallel to each other when in the small scattering volume $d^3\vec{r}$.

$$|\vec{q}| = \frac{4\pi}{\lambda} \sin\theta \tag{2.13}$$

Each electron in the small volume $d^3\vec{r}$ will have a contribution proportional to the Thomson scattering length r_0 to the scattered field, with a phase factor $e^{i\vec{q}.\vec{r}}$. The total contribution of one atom to the scattered field in the direction of the scattering vector $\vec{q}$ is computed by integrating over the volume occupied by the atom.

$$-r_0 \int \rho_{atom}(\vec{r}) e^{i\vec{q}.\vec{r}} d\vec{r} = -r_0 f^0(\vec{q}) = -r_0 FT[\rho_{atom}(\vec{r})] \tag{2.14}$$

The scattering amplitude as a function of $\vec{q}$ is described by the atomic from factor $f^0(\vec{q})$, which is defined as the Fourier transform of the atomic electronic density $\rho_{atom}(\vec{r})$ (Paganin 2006). The values for the atomic from factor can be approximated by a sum of Gaussians using tabulated coefficients (a_i, b_i and c, eq. 2.15) available online (Brown et al. 2006). It decreases with $\vec{q}$ (or $\sin(\theta)/\lambda$) as illustrated in figure 2.7.

$$f^0(\vec{q}) = \sum_{i=1}^{4} a_i \exp(-b_i(\frac{q}{4\pi})^2) + c \tag{2.15}$$

The scattering intensity is equal to the square of the scattering amplitude. For example, the scattering intensity of palladium atoms (Z=46) at $|\vec{q}| \approx 2.75\,\text{Å}^{-1}$ is only $\approx 31\,\%$ of that of platinum atoms (Z=78). In the case of oxygen (Z=8), the intensity falls down to $\approx 6.7\,\%$. This difference in scattering intensity between elements becomes crucial when working with small objects that have a small scattering volume such as nanoparticles.

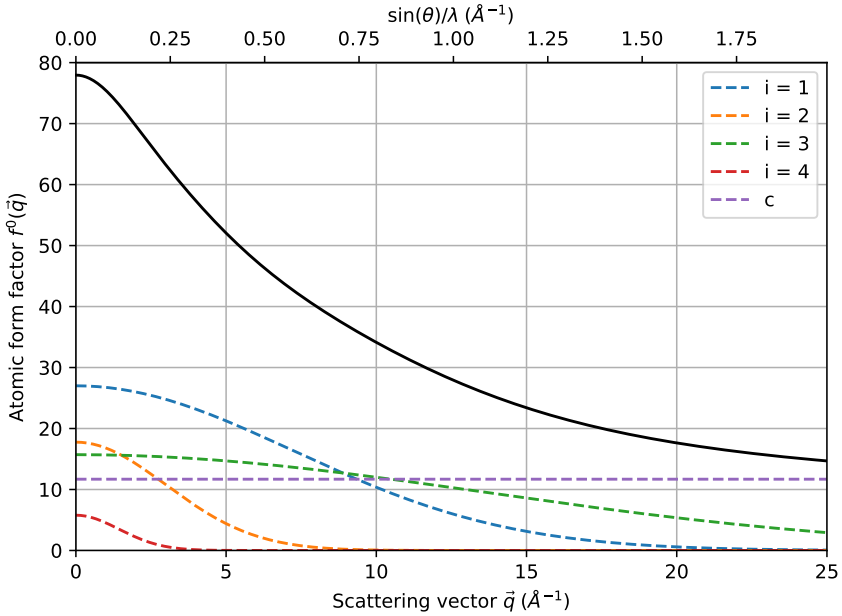

Figure 2.7: Atomic form factor calculated for platinum (Z=78) using tabulated values (Brown et al. 2006) for equation 2.14. See http://lampx.tugraz.at/~hadley/ss1/crystaldiffraction/atomicformfactors/formfactors.php. The scattering intensity decreases with the scattering angle θ but increases with the incident wavelength λ. i and c respectively designate the Gaussian contribution and constant in eq. 2.15.

2.3.2 Refraction, reflection and absorption effects

For now, the electron has been considered as free. However, electrons in atoms or molecules exist in discrete bound states (characterised by a binding energy E_b), and their response to the incoming electromagnetic field becomes dependent on the incoming energy. In a classical point of view, the bound electron can be reconsidered as a damped harmonic oscillator with associated resonant frequencies ω_b corresponding to the electron's binding energy. First, when approaching the binding energy, the amplitude of the electron's oscillation is reduced and so is the atomic form factor by a real energy-dependant factor $f'(\hbar\omega)$. Secondly, the oscillation of the scattering electron experiences a phase lag. This is taken into account by introducing an imaginary energy-dependent factor $f''(\hbar\omega)$. The atomic form factor $f^0(\vec{q})$ must therefore be corrected by these two correction factors, the total atomic form factor $f(\vec{q},\hbar\omega)$ is defined as follows (Jens Als-Nielsen 2011):

$$f(\vec{q},\hbar\omega) = f^0(\vec{q}) + f'(\hbar\omega) + if''(\hbar\omega) = f_1(\vec{q},\hbar\omega) + if_2(\hbar\omega) \tag{2.16}$$

The values of the correction factors f' and f'', also known as the dispersion corrections to f^0, depend on the electronic structure of the atom and are maximum when approaching the binding energies of the electrons in the atom. To understand the impact of the correction factors on the electromagnetic wave inside a material, the complex refraction index n is introduced, which for x-rays can be written as (Jens Als-Nielsen 2011):

$$n = 1 - \delta + i\beta = 1 - \frac{r_0\lambda^2}{2\pi}\sum_i N_i f_i(\vec{q}=0) \tag{2.17}$$

$$\delta = \frac{r_0\lambda^2}{2\pi}\sum_i N_i f_{i,1}(\vec{q}=0) \tag{2.18}$$

$$\beta = \frac{r_0\lambda^2}{2\pi}\sum_i N_i f_{i,2} \tag{2.19}$$

with $f_i(\vec{q}=0)$ the total atomic form factor of the atom i in the forward direction ($\vec{q}=0$), and N_i the number of atoms corresponding to the element i per unit volume. δ is the refractive index and β the absorption index.

When x-rays impinge on a plane surface between air (n=1) and another medium of refractive index n, x-rays are refracted. The wavelength changes to λ/n, and the direction of propagation becomes closer to the surface between both mediums. Below a certain incident angle known as the *critical angle* α_c, the x-rays will be totally reflected. This effect is used in focusing mirrors for optics, but also in techniques used to probe the surface of materials to obtain information about the surface density. The critical angle is approximately equal to $\sqrt{2\rho}$ (when $\beta = 0$) (Willmott 2009). During surface x-ray diffraction, the incoming angle perpendicular to the surface is kept to very low values approaching the critical angle. This limits the volume probed by the x-rays, increasing the contrast between the amplitude of the x-rays scattered from the latest surface layers in regard to the x-rays scattered from the bulk.

Far from the binding energies of the electron in the system, the correction factors f' in the expression of the scattering factor can be ignored. Finally, to highlight the impact of the complex part of the absorption index β, the electric field of a plane electromagnetic wave propagating in the $\vec{z}$ direction inside a material of refractive index n is expressed as follows:

$$E(\vec{z},t) = E_0 e^{i(n\vec{k}.\vec{z}-wt)} = E_0 e^{-\beta\vec{k}.\vec{z}} e^{i(\delta\vec{k}.\vec{z}-wt)} \tag{2.20}$$

The imaginary part of the form factor translates into an exponential decay of the intensity of the incoming wave as a function of the absorption index β, the intensity of the electromagnetic field decreases; *i.e.* the wave is absorbed by the material. The absorption of the photons by the material is at the origin of many different phenomena such as the promotion of electrons to either higher energetic bound states or directly to vacuum. The kinetic energy of the electrons released from the material in the latter scenario is equal to the incident photon energy $\hbar\omega$, minus the energy required to release the electron from its bound state E_b, minus the energy required for the electron to escape from the electronic cloud W (also known as the work function).

$$E_{kin} = \hbar\omega - W - E_b \tag{2.21}$$

Measuring the kinetic energy of the photoelectron that escaped the material yields direct information about the different binding energies present in the material, *i.e.* about its electronic structure. The study of these binding/kinetic energies is at the origin of x-ray photoelectron spectroscopy (XPS), a technique used in this thesis to study the electronic structure of the atoms within the topmost atomic layers of the catalyst. Electrons released from atoms in deep layers are ultimately absorbed by the surrounding atoms. The cross-section for XPS is directly proportional to the absorption cross-section σ_a (eq. 2.22, fig. 2.4) which can be derived from the imaginary atomic form factor:

$$\sigma_a(\hbar\omega) = 2r_0\lambda f_2(\hbar\omega) \tag{2.22}$$

2.4 Scattering from crystals

A crystal is a solid material composed of a regular, repeating arrangement of atoms, ions, or molecules (*i.e.* a pattern), exhibiting a highly ordered structure with long-range periodicity in three dimensions.

A Bravais lattice refers to an infinite array of points (nodes) that represents the basic repeating unit of a crystal lattice, defining the translational symmetry of the crystal structure. It is characterised by a set of three basis vectors and their linear combinations, which generate the entire lattice when translated in space. The *primitive* unit cell is the smallest cell with which you can describe the crystal.

The structure of the Bravais lattice (cubic, hexagonal, ...) combined with the position of the patterns in the lattice and the symmetry relations between them defines the crystal *space group*. In total there exist 230 space group in crystallography. In the simplest case the pattern consists of a single atom, for example pure platinum ($Z = 78$) crystallises at room temperature in a facet centred cubic Bravais lattice (fig. 2.8).

The scattering factor $F_{crystal}$ of the crystal, that describes the amplitude of the scattered waves, is defined by the sum of the atomic scattering factor $f_j(\vec{q})$ of each atom present in the crystal. The phases between the scattered waves depend on the positions of the atoms $\vec{R}_j$ in the direction parallel to the scattering vector $\vec{q}$ (eq. 2.23). In other words, each atom can be described as a small volume $d^3\vec{r}$ in the electronic density $\rho(\vec{r})$, and the scattered field by the superposition of the contribution from the electronic cloud surrounding the atoms. The atomic scattering factor is equal to the Fourier transform of the electronic density of a single atom, the structure factor of a crystal can be written as the Fourier transform of the crystal electronic density (Paganin 2006).

$$F_{crystal}(\vec{q}) = \sum_{j}^{N_{atoms}} f_j(\vec{q}) e^{i\vec{q}.\vec{R}_j} = FT[\rho(\vec{r})] \tag{2.23}$$

$f_j(\vec{q})$ is the atomic scattering factor of the j^{th} atom at position $\vec{R}_j$ in a crystal made of N_{atoms} atoms. The Thomson scattering length is left apart for simplicity.

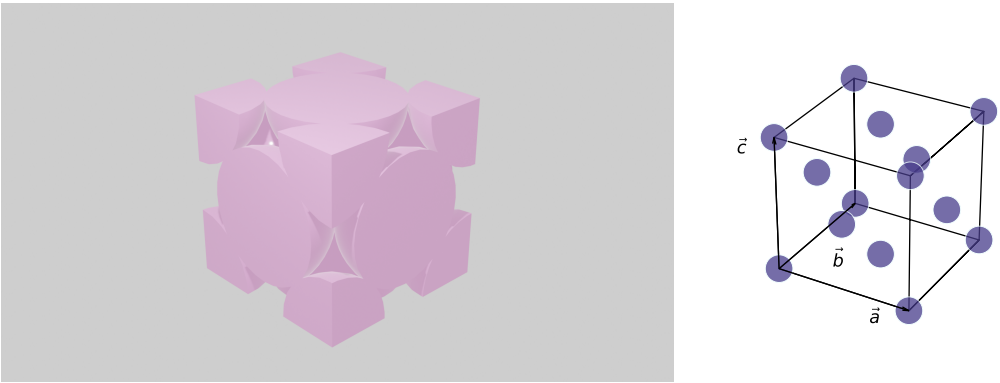

Figure 2.8: Face centred cubic (FCC) lattice of Pt (space group 225). Atoms are represented as solid spheres and situated on the corners and at the middle of the faces of the cube. A schematic representation of the unit cell is shown on the right to be able to visualise the positions of each atom. The lattice parameter at room temperature is $a = 3.92$ Å. Close packed direction is achieved along the diagonal of the lateral faces, the distance between the atoms then becomes 2.77 Å.

The position of any atom in the crystal $\vec{R}_j$ is equal to the sum of the position of the unit cell containing the atom $\vec{R}_{uc}$, plus its position within the unit cell $\vec{r}_j$. For a crystals made of N_{uc} unit cells, each composed of $N_{atoms,uc}$:

$$F_{crystal}(\vec{q}) = \sum_{j}^{N_{atoms,uc}} f_j(\vec{q}) e^{i\vec{q}.\vec{r}_j} \sum_{k}^{N_{uc}} e^{i\vec{q}.\vec{R}_k} \tag{2.24}$$

The Bravais lattice is defined by three basis vectors $\vec{a}$, $\vec{b}$, $\vec{c}$ and three angles α $[\angle(\vec{b},\vec{c})]$, β $[\angle(\vec{c},\vec{a})]$ and γ $[\angle(\vec{a},\vec{b})]$. Any vector $\vec{R}_k$ describing the position of a node in the real space can be created by a linear combination of these three vectors:

$$\vec{R}_k = n_1\vec{a} + n_2\vec{b} + n_3\vec{c}, \qquad (n_1, n_2, n_3) \in \mathbb{Z}^3 \tag{2.25}$$

To understand the contribution of the second sum in eq. 2.24 to the scattering amplitude, it is convenient to introduce the *reciprocal space* which is the Fourier transform of the real space. It is defined by three basis vectors $\vec{a}^*$, $\vec{b}^*$, $\vec{c}^*$. Similarly, the nodes of the reciprocal space can be accessed from its origin by a linear combination $\vec{G}_{hkl}$ of these three vectors.

$$\vec{a}^* = \frac{2\pi}{V}(\vec{b}\times\vec{c}), \qquad \vec{b}^* = \frac{2\pi}{V}(\vec{c}\times\vec{a}), \qquad \vec{c}^* = \frac{2\pi}{V}(\vec{a}\times\vec{b}), \qquad \vec{a}_i.\vec{a}_j^* = \delta_{i,j} \tag{2.26}$$

$$\vec{G}_{hkl} = h\vec{a}^* + k\vec{b}^* + l\vec{c}^*, \qquad (hkl) \in \mathbb{Z}^3 \tag{2.27}$$

By combining eq. 2.25 and eq. 2.27, the solution to the second sum in eq. 2.24, *i.e.* to the equation $\vec{q}.\vec{R}_k = n \times 2\pi$ ($n \in \mathbb{Z}$) is to write $\vec{q}$ as a linear combination of the reciprocal space vectors, *i.e.* as $\vec{G}_{hkl}$.

$$\vec{G}_{hkl}.\vec{R}_k = hn_1 + kn_2 + ln_3 = n \quad with\ n \in \mathbb{Z} \tag{2.28}$$

This is also known as the Laue condition, that ensures that only certain scattering vectors, corresponding to the reciprocal lattice points, fulfil the condition for constructive interference between the scattered waves. These specific scattering vectors $\vec{G}_{hkl}$ determine the scattering angles of the peaks observed in a diffraction pattern, also known as Bragg peaks.

2.4.1 Bragg's law

The intensity scattered from a crystal as a function of the scattering vector $\vec{q}$ provides information about the arrangement and spacing of crystalline planes perpendicular to $\vec{q}$. The Miller indices are a set of integers used to represent the planes' orientation and spacing. A plane denoted by the (h,k,l) indices intercepts the axes $\vec{a}$, $\vec{b}$, $\vec{c}$ on the points $|\vec{a}|/h, |\vec{b}|/k, |\vec{c}|/l$. The direction perpendicular to the (hkl) plane is written as $[hkl]$, the distance between each plane is d_{hkl}.

A Bragg peak results from the constructive interference between waves scattered on a specific set of crystalline planes, at discrete values of the incident angle θ. From fig. 2.9, the condition to have constructive interference is retrieved, also known as Bragg's law and given by eq. 2.29.

$$\lambda = 2d_{hkl}\sin\theta \tag{2.29}$$

In the case of a cubic Bravais lattice, the distance between Miller planes can be written as:

$$d_{hkl} = \frac{2\pi}{|\vec{a}^*|\sqrt{h^2+k^2+l^2}} = \frac{|\vec{a}|}{\sqrt{h^2+k^2+l^2}} \tag{2.30}$$

For a hexagonal Bravais lattice:

$$\frac{1}{{d_{hkl}}^2} = \frac{4}{3a^2}(h^2+hk+k^2) + \frac{l^2}{c^2} \tag{2.31}$$

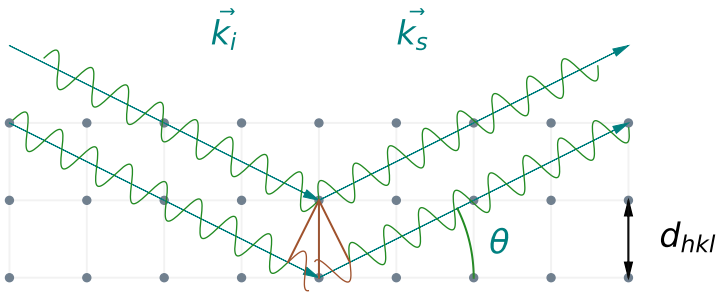

Figure 2.9: The difference in the path length (in red) between plane waves scattered at an angle θ is equal to $2d_{hkl}\sin\theta$. This distance must be an integer multiple of the wavelength for constructive interference to occur.

From eqs. 2.13 and 2.29, one falls back on the Laue condition which is a generalisation of Bragg's law. The diffraction order (n) in the Bragg's law equation can be omitted since it is implicitly determined by the Miller indices (hkl) representing the crystalline planes involved in the diffraction. Since the Laue condition is here verified, $|\vec{G}_{hkl}|$ is used rather than $|\vec{q}|$ in eq. 2.34.

$$|\vec{q}| = \frac{4\pi\sin(\theta)}{\lambda}, \tag{2.32}$$

$$\sin(\theta)/\lambda = \frac{1}{2d_{hkl}}, \tag{2.33}$$

$$|\vec{G}_{hkl}| = \frac{2\pi}{d_{hkl}} \tag{2.34}$$

When fulfilling the Laue (or Bragg) condition, the direction of the scattering vector is perpendicular to the crystalline planes represented by the (h,k,l) Miller indices, and its magnitude is inversely proportional to the distance between consecutive crystalline planes.

2.4.2 Structure factor

On one hand, in real space, the crystal electronic density can be formed by repeating the unit cell at each lattice point, *i.e.* it can be represented as a convolution of the lattice and unit cell functions. This representation captures the periodicity and arrangement of the crystal.

On the other hand, in reciprocal space (Fourier space), the crystal scattering factor $F_{crystal}$ is the Fourier transform of the electronic density. According to the convolution theorem, the Fourier transform of a convolution is equal to the product of the Fourier transforms of the individual functions (McAlister 2003). The scattering factor can therefore be expressed as the product of the Fourier transforms of the lattice and unit cell functions. These Fourier transforms are known as the lattice factor F_{lat} and the unit cell structure factor F_{uc}.

$$F_{crystal} = FT[\rho(\vec{r})] = F_{uc} \times F_{lat} \tag{2.35}$$

The lattice factor F_{lat} represents the periodic arrangement of the crystal lattice in Fourier space, corresponding to the reciprocal lattice. It determines the positions and intensities of the diffraction peaks in the scattering pattern. The unit cell structure factor F_{uc} describes the distribution of electron density within the unit cell of the crystal, and modulates the scattered beam amplitude depending on what atoms are in the unit cell (amplitude) and their positions (phase). By comparing eq. 2.24 and eq. 2.35, the unit cell structure factor is first identified and discussed.

$$F_{uc} = \sum_{j}^{N_{atoms}} f_j(\vec{q}) e^{i\vec{q}.\vec{r}_j} \tag{2.36}$$

Each diffraction peak in the scattering pattern corresponds to a specific Fourier component, representing a sinusoidal wave of electron density with a particular frequency and direction determined by its scattering vector $\vec{q}$, *i.e.* by its position in Fourier space. By knowing the phase relationships between these Fourier components, which can be obtained from the measured diffraction pattern, the electron density within the unit cell can be reconstructed. The superposition of these sinusoidal waves, representing the diffraction peaks or Fourier components, recreates the original electron density distribution of the crystal.

To summarise, the diffraction peaks in the scattering pattern represent the Fourier components of the crystal's electron density distribution. Their spatial frequencies and phase relationships carry information about the crystal structure. The structure factor F_{uc} is the summation of the contribution of each atom j at the position $\vec{r}_j$ in the unit cell, of atomic form factor $f_j(\vec{q})$, and for a given scattering vector $\vec{q}$. The position of each atom is defined in the unit cell by eq. 2.37, an example with the platinum atoms is given in tab. 2.2.

$$\vec{r}_j = x_j\vec{a} + y_j\vec{b} + z_j\vec{c} \tag{2.37}$$

Atom	Pt	Pt	Pt	Pt	Pt	Pt	Pt	Pt	Pt	Pt	Pt	Pt	Pt	Pt
x	0	0.5	0.5	0	1	0	1	0.5	1	0	1	0	1	0.5
y	0	0.5	0	0.5	0	1	1	1	0.5	0	0	1	1	0.5
z	0	0	0.5	0.5	0	0	0	0.5	0.5	1	1	1	1	1

Table 2.2: Position of platinum atoms in the face-centred cubic (FCC) unit cell. Illustrated in fig. 2.8. The first four atomic positions lead to the other positions by symmetry (space group 225).

Systematic extinctions ($F_{uc} = 0$) occur when certain diffraction peaks are forbidden due to the crystal's symmetry elements, such as the atomic positions. For example in the FCC lattice of platinum, systematic extinctions occur when the value of Miller indices are not all even or all odds. Otherwise, the amplitude of a Bragg peak detected at the scattering vector $\vec{q}$ is equal to $4 \times f_{Pt}(\vec{q})$ where $f_{Pt}(\vec{q})$ is the atomic scattering factor of platinum.

2.4.3 Lattice factor

If the scattering factor considers the composition of the unit cell, the lattice factor represents the contribution of the crystal lattice to the overall scattering amplitude. It takes into account the arrangement of atoms or scatterers within the crystal lattice, and their interaction with the incident wave.

By considering the different parts of eq. 2.24 and eq. 2.35, the lattice factor is now identified and discussed (eq 2.38). In the case of a simple cubic arrangement of unit cells in three directions perpendicular to each other, the sum over all unit cells N_{uc} in the crystal is simplified into three sums, each in one of the directions of the crystal lattice ($\vec{a}_x$, $\vec{a}_y$, $\vec{a}_z$), verifying $N_{uc} = N_{uc,x} \times N_{uc,y} \times N_{uc,z}$.

$$F_{lat} = \sum_{k}^{N_{uc}} e^{i\vec{q}.\vec{R}_k} = \sum_{n_x}^{N_{uc,x}} e^{in_x\vec{q}.\vec{a}_x} \times \sum_{n_y}^{N_{uc,y}} e^{in_y\vec{q}.\vec{a}_y} \times \sum_{n_z}^{N_{uc,z}} e^{in_z\vec{q}.\vec{a}_z} \tag{2.38}$$

$$F_{lat} = \prod_{j=\{x,y,z\}} \left(\sum_{n_j}^{N_{uc,j}} e^{in_j\vec{q}.\vec{a}_j} \right) \tag{2.39}$$

$$F_{lat} = \prod_{j=\{x,y,z\}} S_{N_{uc,j}}(\vec{q}.\vec{a}_j) \tag{2.40}$$

$$S_{N_{uc,j}}(\vec{q}.\vec{a}_j) = \sum_{n_j}^{N_{uc,j}} e^{in_j\vec{q}.\vec{a}_j} = \sum_{n_j}^{N_{uc,j}} e^{(i\vec{q}.\vec{a}_j)^{n_j}} = \frac{1 - e^{(iN_{uc,j}\vec{q}.\vec{a}_j)}}{1 - e^{(i\vec{q}.\vec{a}_j)}} \tag{2.41}$$

$$|S_{N_{uc,j}}(\vec{q}.\vec{a}_j)| = \frac{\sin(N_{uc,j}\vec{q}.\vec{a}_j/2)}{\sin(\vec{q}.\vec{a}_j/2)} \tag{2.42}$$

$$|S_{N_{uc,j}}(\vec{q}.\vec{a}_j)| \underset{N_{uc,j}\to\infty}{\longrightarrow} \approx \delta(\vec{q}) \tag{2.43}$$

Where $S_{N_{uc,j}}(\vec{q}.\vec{a}_j)$ is a function whose modulus tends towards a Dirac function when $N_{uc,j} \longrightarrow \infty$. The condition to observe maxima in eq. 2.42 is for the denominator to be equal to zero: $\frac{\vec{q}.\vec{a}_j}{2} = \pi$ which brings us back to the Laue condition: $\vec{q} = \vec{G}$ where $\vec{G}$ is a reciprocal space lattice vector (eq. 2.28). Minor peaks appear when the numerator is equal to one: $N_{uc,j}\frac{\vec{q}.\vec{a}_j}{2} \equiv \frac{\pi}{2}$. The distance between each minor peak in q-space is given by $\Delta q = \frac{2\pi}{N_{uc,j}\times a_j} = \frac{2\pi}{t_j}$, where t_j is the thickness of the crystal in the direction $\vec{a_j}$.

To resume, the lattice factor $F_{lat}(\vec{q})$ defines the shape of Bragg peaks. For a large crystal (*i.e.* a large number of unit cells in three directions), ideal Bragg peaks will look like Dirac functions (in reality they are widened due to different experimental factors). For small crystals such as nanoparticles, the fringes of the lattice factor will be further apart and their intensity more visible in contrast to the intensity of the main peak (fig. 2.18). In a more general sense, the lattice factor is the Fourier transform of the crystal's lattice, the effect of the Fourier transform is that fringes will be visible in the reciprocal space in directions perpendicular to the crystal's surface. The ability to effectively sample these fringes during experiments is at the root of the BCDI technique, to effectively retrieve the crystal shape (sec. 2.6). Moreover, the lattice factor also explains the existence of intensity rods in reciprocal space, used to probe the structure of the related surfaces with surface x-ray diffraction (sec. 2.5).

2.4.4 Coherence

Every x-ray source can be described by several parameters. The brilliance $\mathcal{B}$ is a measure of the distribution of flux in both space and angular range, it indicates how the flux is spread over the source area and solid angle.

$$\mathcal{B} = \frac{\text{photons}\,\text{s}^{-1}}{(\text{mm}^2\text{source area})(\text{mrad})^2(0.1\,\%\text{ bandwidth})} \tag{2.44}$$

The spectral flux, on the other hand, quantifies the number of photons passing through a defined area per second. Synchrotron facilities aim to optimise both the photon flux and brilliance, a higher flux meaning faster experiments, whereas a high brilliance can for example be important for those that need a coherent beam. In the last evolution from 3^{rd} to 4^{th} generation synchrotrons, the source size (convolution of the size of the photon source and the transverse size of the electron beam) has been reduced by an order of magnitude in the horizontal direction (Willmott 2009).

$$\epsilon = D \times \Delta\theta \tag{2.45}$$

The emittance ϵ is defined as the product of the source size D and the beam divergence $\Delta\theta$ (eq. 2.45), a low emittance is characteristic of a small source size and almost parallel emitted beams.

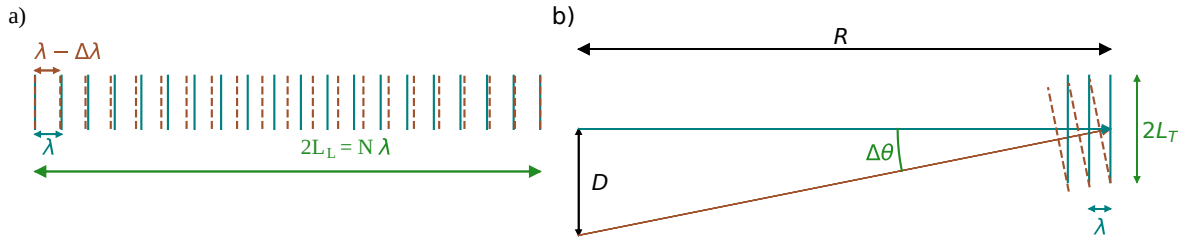

Figure 2.10: (a) Two waves become out of phase in the direction of the beam at a distance L_L from being in phase after $N/2$ wavelengths for λ and $(N+1)/2$ wavelengths for $\lambda - \Delta\lambda$. Since $N >> 1$, $N \approx \lambda/\Delta\lambda$, which yields eq. 2.46. (b) A plane wave emitted from one extremity of the source is out of phase with another plane wave emitted from the other extremity with maximum angular divergence $\Delta\theta$, at a distance L_T in the plane perpendicular to the direction of the beam, situated at a distance R from the source.

The longitudinal coherence length L_L describes the distance in the direction of the beam after which two waves of slightly different wavelength become out of phase due to the small extent of the beam bandwidth $\Delta\lambda$ (fig. 2.10 - a). The bandwidth is linked to the quality of the monochromator used to obtain a monochromatic beam through the relation $\lambda/\Delta\lambda$ (eq. 2.46).

$$L_L = \frac{\lambda^2}{2\Delta\lambda} \tag{2.46}$$

The transverse coherence length L_T describes the distance in the plane perpendicular to the beam after which two waves become out of phase due to the finite source size D and to the angular divergence of the beam $\Delta\theta$ (fig. 2.10 - b). By assuming that the source has a Gaussian profile, the standard deviation of the beam $\sigma_{H,V}$ in the horizontal and vertical directions perpendicular to the beam is linked to D (Willmott 2009, eq. 2.47).

$$L_{T,(H,V)} = \frac{\lambda}{2\Delta\theta_{(H,V)}} = \frac{\lambda R}{2D_{(H,V)}} = \frac{\lambda R}{2\sqrt{\pi}\sigma_{H,V}} \tag{2.47}$$

At synchrotrons, the vertical and horizontal source sizes are significantly different due to the shape of the electron beam, much more extended in the horizontal plane. The horizontal transverse coherence length is usually smaller and the limiting factor. The coherent volume is obtained by multiplying the two transverse coherence lengths $L_{T,H}$, $L_{T,V}$, and the longitudinal coherence length L_L. An example is given in sec. 2.7 for the SixS beamline of the synchrotron SOLEIL.

To perform Bragg coherent diffraction imaging experiments, the coherent volume must be larger than the sample. The beamlines must have low vertical and horizontal emittances, high monochromaticity, and a sample environment situated as far as possible from the source. Therefore, the coherent flux F_{coh} as a function of the wavelength is directly related to the brilliance and bandwidth of the source (Willmott 2009):

$$F_{coh} = \mathcal{B}\lambda^2\frac{\Delta\lambda}{\lambda} \tag{2.48}$$

Indeed, to be able to resolve the interference fringes resulting from the lattice factor, a high brilliance is crucial since the intensity of the total scattered field, proportional to the scattering volume, is weak.

This introduction is limited to the kinematical approach of diffraction, which means that the scattering is weak, so that multiple scattering can be ignored. This is explained by the finite size of the samples, e.g. surfaces and nanoparticles. This allows us to assume that the sample is only a perturbation to the incident field, and that the structure factor can be written as the Fourier transform of the electronic density (Born approximation). It is also assumed that the incident wave is plane within the scattering volume, and that the distance between the scatterer and the detector is large enough for the scattered waves to be considered planes (far-field or Fraunhofer regime).

2.5 Surface x-ray diffraction

Surface x-ray diffraction is a technique used to study the atomic structure and surface morphology of materials by analysing the diffraction pattern formed when x-rays interact with the surface of the material. In surface x-ray diffraction, the incident photon beam is directed towards the sample surface at a grazing angle of incidence to lower the penetration depth of the x-rays in the material, typically probing the top few atomic layers. The x-rays interact with the atoms in the topmost layer of the material and undergo scattering. The intensity of the scattered x-rays is then measured as a function of the scattering angle. The incident angle can be chosen to coincide with the critical angle of the material (sec. 2.3.2) to increase the intensity of the scattered beam due to total reflection, and to lower the bulk contribution to the intensity in comparison with the surface contribution (Feidenhans'l 1989; Moritz et al. 2022). However, since the intensity becomes so dependent on the incident angle, a misalignment of the incident beam can lead to relevant errors in the scattered beam intensity, the surface alignment is critical during surface x-ray diffraction experiments.

A typical experiment yields structure factors measured across the scattering space reachable with the instrument. The positions and intensities of the diffraction peaks provide insights into the arrangement of atoms near the surface, surface reconstruction, crystallographic orientation, lattice strain, and the presence of surface defects. The aim of the technique is to obtain geometrical information of the surface at the atomic level, from surface symmetry to singular atomic displacements within the unit cell.

2.5.1 Surface reconstructions

An example of surface reconstructions is given in fig. 2.11, where the latest atomic layer (green) does not have the same periodicity as the bulk layers (brown). This phenomenon gives rise to additional signals at positions defined by how the periodicity of the reconstruction relates to the periodicity of the bulk structure in the $\vec{a}$ and $\vec{b}$ directions (also named in-plane directions). The origin of this phenomenon can be linked to a different environment for surface atoms, in comparison with the bulk atoms (I. K. Robinson 1983; Feidenhans'l 1989).

In this example, the surface reconstructions can be described using the *Wood notation*, that quantifies the relation between the surface reconstruction unit vectors $(\vec{a}_r, \vec{b}_r)$ and the bulk unit vectors $(\vec{a}, \vec{b})$ (Wood 1964; Unertl 1996; Goncharova 2018). Let us take the example of fig. 2.11, for which the brown atoms correspond to the Pt(100) surface. The green reconstruction can be described as Pt(100)-p(2×4)-R0°. The p and -R0°can be omitted in a simpler notation, Pt(100)-(2×4). A possible rotation of the reconstruction arrangement with respect to the bulk layer would result in a specific angular value. If an atom was present in the center of the (2×4) arrangement, *i.e.* at (1, 2), the notation would change and become Pt(100)-c(2×4)-R0°.

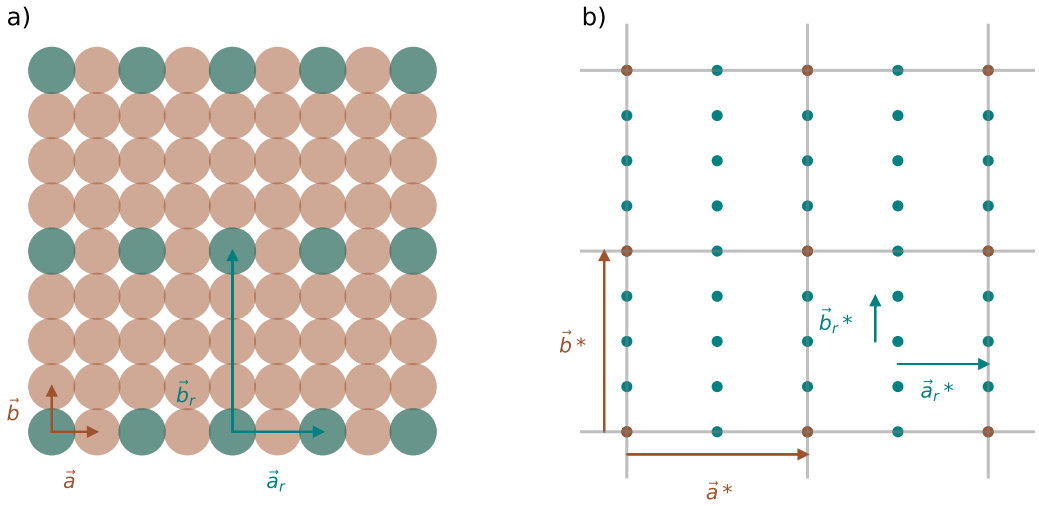

Figure 2.11: (a) Top view of the crystal surface, the last atomic layer (green) does not have the same periodicity as the bulk layers (brown), but a (2×4) periodicity. (b) HK plane in the reciprocal space, diffraction peaks are represented as small brown and green dots for the bulk and surface reconstruction, respectively. The bulk reciprocal lattice is represented in grey.

This surface reconstruction can also be described with a matrix, Pt(100)- $\begin{pmatrix} M_{ii} & M_{ij} \\ M_{ji} & M_{jj} \end{pmatrix}$-R0° , which gives $\vec{a}_r = M_{ii}\vec{a} + M_{ij}\vec{b}$, and $\vec{b}_r = M_{ji}\vec{a} + M_{jj}\vec{b}$. In this case $M_{ii}, M_{jj} = 2, 4$, and $M_{ij}, M_{ji} = 0, 0$.

2.5.2 Crystal truncation rods

It was shown in sec. 2.4.3 that the lattice factor is equivalent to the Fourier transform of the crystal shape. For infinitely large crystals, the lattice factor converges towards a three dimensional Dirac peak. When working with large single crystals for surface x-ray diffraction, the samples are considered to be infinitely large in the $\vec{a}, \vec{b}$ in the surface plane (in-plane) directions, and *semi-infinitely* large in the out-of-plane $\vec{c}$ direction, creating an infinitely large flat surface. In the real space, this can be mathematically described by the multiplication of the crystal lattice and a step-function, as illustrated in fig. 2.12. The convolution theorem states that the Fourier transform of the multiplication of two functions is the convolution of their Fourier transforms (McAlister 2003). The Fourier transform of the crystal lattice is the Lattice factor, when the Fourier transform of the step function is the inverse function $\frac{1}{q_z}$ (Andrews et al. 1985; I. K. Robinson 1986). This gives rise to a so called "rod" of intensity along the direction perpendicular to the truncated surface, a *crystal truncation rod* (CTR - fig. 2.12).

$A(\vec{q})$ is here defined as the scattering amplitude of an infinite 2D layer of atoms, the scattering amplitude for a semi infinite stack of those layers in the $\vec{c}$ direction can be written as (adapted from eq. 2.38):

$$F_{CTR} = A(\vec{q}) \sum_{n=-\infty}^{0} e^{in\vec{q}.\vec{c}} e^{-n\beta_{abs}} = \frac{A(\vec{q})}{1 - e^{in\vec{q}.\vec{c}} e^{-\beta_{abs}}} \tag{2.49}$$

β_{abs} is the absorption parameter. The intensity around a Bragg peak can then be written as a function of q_z, *i.e.* the deviation from the Laue condition in $\vec{c}^*$, $q = q_z + l|\vec{c}^*|$, l is the Miller index of the nearest Bragg peak.

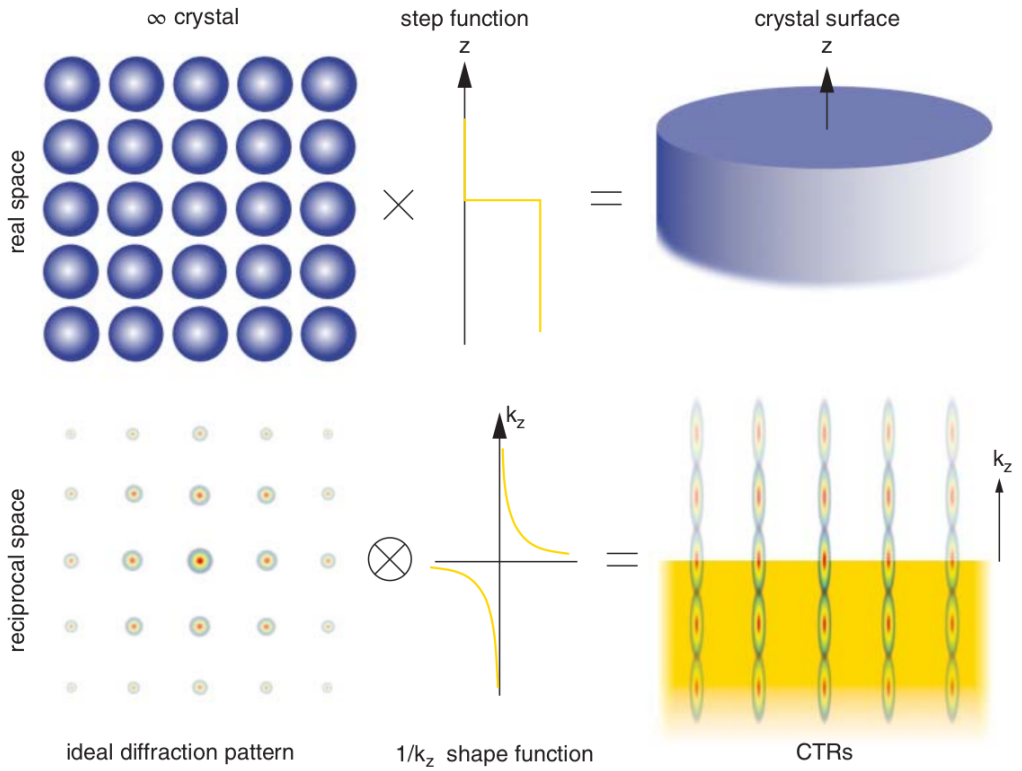

Figure 2.12: Describing a crystal surface by the multiplication of the crystal lattice by a step-function in real space explains the shape of crystal truncation rods in reciprocal space by the convolution theorem. Figure taken from Willmott 2009.

$$I_{CTR} = |F_{CTR}|^2 = \frac{|A(\vec{q})|^2}{(1 - e^{in\vec{q}.\vec{c}}e^{-\beta_{abs}})(1 - e^{in\vec{q}.\vec{c}}e^{-\beta_{abs}})} \approx \frac{|A(\vec{q})|^2}{q_z^2|\vec{c}|^2 + \beta_{abs}^2} \tag{2.50}$$

The amplitude of the signal between Bragg peaks in the reciprocal space becomes therefore proportional to $\frac{1}{q_z}$ in the $\vec{c}*$ direction and their intensity to $\frac{1}{q_z^2}$. This expression is only valid within the kinematical approach to diffraction.

The position in the reciprocal space that is exactly between Bragg peaks linked by the CTR can be called the *anti-Bragg* (I. K. Robinson and Tweet 1991), where the signal scattered from the surface is maximum compared to the signal scattered from the bulk which interferes destructively (Willmott 2009). This region, in which the surface structural information in contained, is accurately described using the kinematical diffraction theory and can therefore be described with eq. 2.50, in contrast with the Bragg peaks where multiple scattering cannot be ignored (Kaganer 2007). To be able to analyse CTRs, it is crucial to be able to obtain a good signal to noise ratio when measuring the anti-Bragg region, since the intensity difference with the Bragg peak can reach 8 orders of magnitude (Fadenberger et al. 2010). This can become difficult when the surface is roughened during the growth of surface layers (such as oxide growth), phase transitions, or due to the adsorption of molecules during catalysis (Zhdanov et al. 1997; Zhdanov et al. 1998). It can also be difficult to obtain a flat surface during polishing (Musket et al. 1982).

An effective way to represent roughness is *via* the β model, in which the n-surface layer (n increases towards the surface) is defined as occupying an area equivalent to $\beta^n \times A_{bulk}$ where A_{bulk} is the bulk surface area (I. K. Robinson 1986). The effect of roughness is illustrated in fig. 2.13. This model only serves to describe the roughness of the bulk structure and does not function to describe the roughness of additional surface structures.

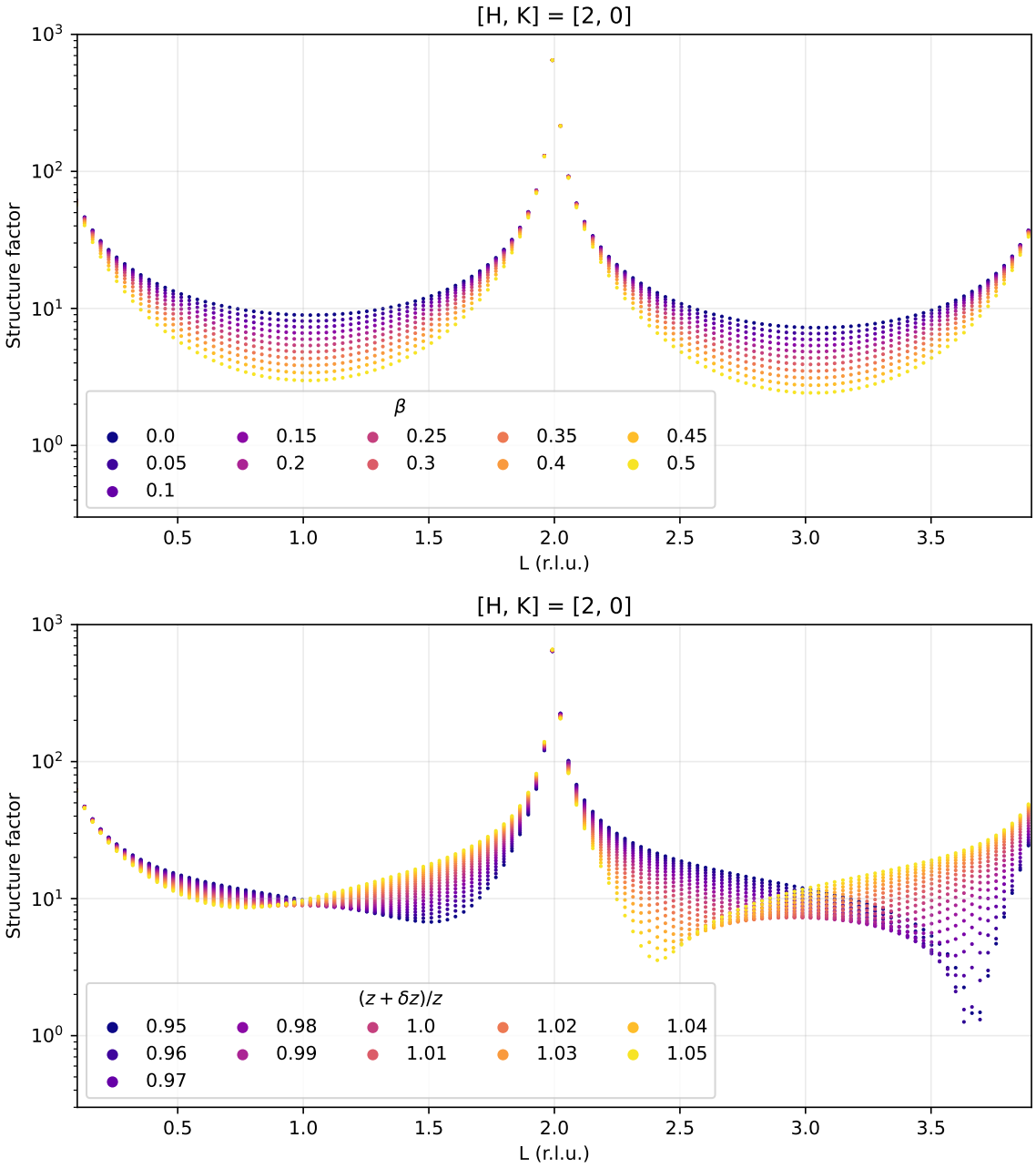

Figure 2.13: Simulated intensity of a [2, 0, L] crystal truncation rod perpendicular for a (100)-oriented Pt single crystal, computed with ROD (Vlieg 2000). (a) The intensity between the Bragg peaks decreases with increasing roughness. (b) δz corresponds to the displacement (or surface relaxation) of the last atomic layer perpendicular to the surface. Large surface relaxations induce an asymmetry in the CTR shape, and a shift in the position of the minimum between Bragg peaks.

Lattice strain is defined as the displacement of the surface atomic layers with respect to the bulk unit cell lattice parameters. Positive or negative strain, also called surface relaxation, has the effect of changing the position of the CTR minimum, and of skewing the shape of the CTR as illustrated in fig. 2.13.

Surface reconstructions also yield crystal truncation rods in the reciprocal space, perpendicular to the nodes of the reconstructed lattice, called super-structure rods (SSR). These rods are structured in L by the atomic positions. If the surface layer is flat, the scattered signal corresponds to a diffuse signal slowly decreasing as a function of L. To resume, the in-plane $[H, K]$ position give the periodicity of the surface structure. The intensity measured

along the corresponding SSR allows to extract the surface structure factors, and to identify the surface atomic positions.

2.5.3 Data collection

Visualising how the measurements of the scattered x-rays is performed with a diffractometer can quickly become complicated in three dimensions. The Ewald sphere is a representation of the diffraction process used in crystallography to visualise and interpret the diffraction of x-rays by a single crystal. It is a geometric construction that represents the reciprocal space constructed from the crystal lattice, centred at the origin of reciprocal space, and with a radius equal to the magnitude of the incident wavevector $\vec{k}_i$.

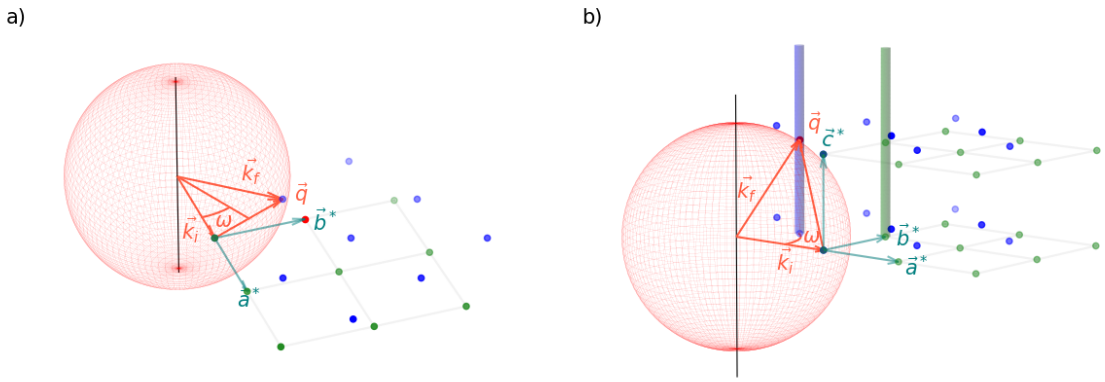

Figure 2.14: Ewald sphere represented together with the reciprocal lattice before (green) and after (blue) rotating the sample to satisfy the Laue condition. The node of the reciprocal lattice that satisfies the Laue condition is in red. For simplicity, only part of the reciprocal lattice is represented. (a) In-plane measurement ([H, K, L] = [0, 1, 0]), the sample is rotated in-plane by an angle ω equal to the Bragg angle. The detector must be at an in-plane angle $\gamma = 2\omega$ to detect the scattered x-rays. (b) Out-of-plane measurement for crystal truncation rods, the sample is rotated in-plane by an angle ω so that the [0, 1, L] CTR can be measured while keeping the incident angle at low values. Both detector angles must be rotated to keep the detector in the direction of the scattered x-rays, only the [0, 1, L] CTR is represented for simplicity.

The scattering vector $\vec{q}$ is determined by the incident and diffracted wavevectors, and represents the difference between them (eq. 2.12). The Laue condition for a particular reflection is satisfied when the scattering vector lies on the surface of the Ewald sphere (fig. 2.14), in other words, when the scattering vector corresponds to a point of intersection between the Ewald sphere and the reciprocal lattice points.

The Ewald sphere is represented in fig. 2.14 to highlight how the diffraction angles can be tuned to satisfy the Laue condition. Let us take the example of a diffractometer in a horizontal setup (fig. 2.15 - in red), μ and β are respectively the in-plane and out-of-plane rotation angles of the sample when γ and δ are the in-plane and out-of-plane rotation angles of the detector. The Laue condition is satisfied by rotating the reciprocal space, which is performed by rotating the sample (the reciprocal space rotates jointly with the atomic lattice). The detection of the scattered x-rays by the detector is then attained by placing the detector in the direction of the scattering wavevector $\vec{k}_s$.

For in-plane measurements, the Laue condition is fulfilled by rotating the in-plane sample angle μ to the Bragg angle. The detector in-plane angle γ must then be equal to $\gamma = 2\mu$ to measure the scattered x-rays in the direction of the scattering wavevector $\vec{k}_s$ (fig. 2.14 - a). The incident angle between $\vec{k}_i$ and the sample must be kept to low values, in the case of out-of-plane measurements, this brings some important constraints about the experiment geometry. For example, the $(0, 0, L)$ crystal truncation rod becomes impossible to measure,

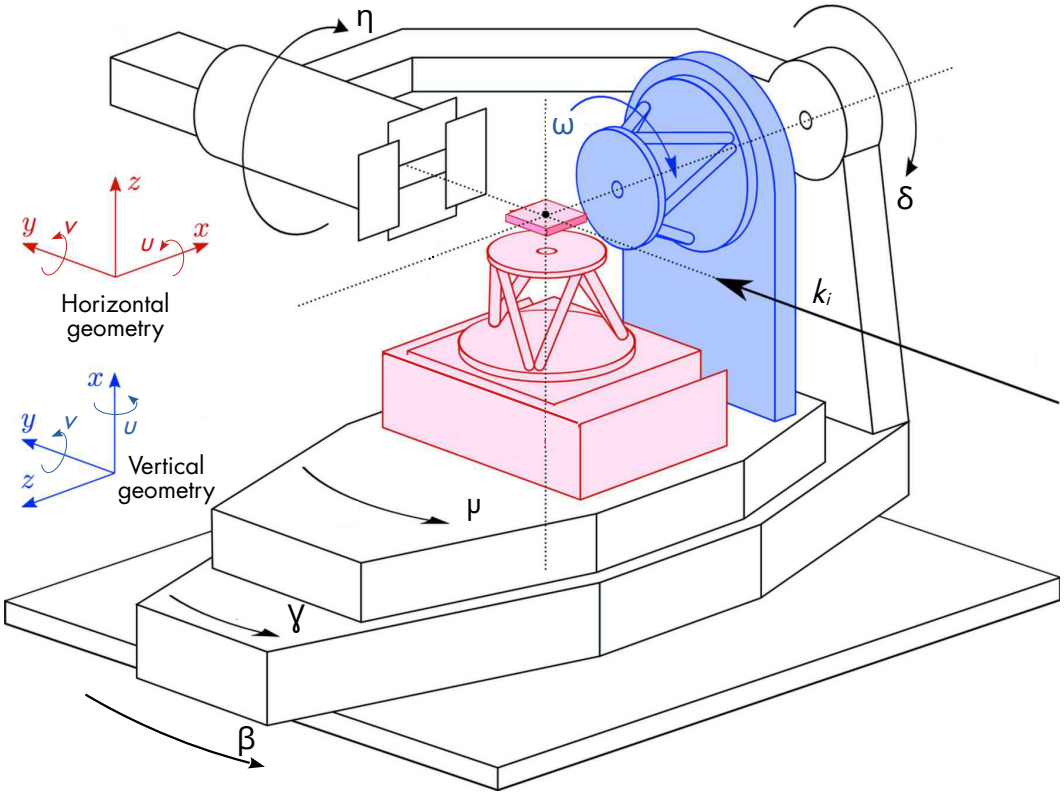

Figure 2.15: 2+3 multi-environment diffractometer (MED) used at SixS, figure adapted from Schlepütz, Mariager et al. 2011. The diffractometer has a horizontal (red) and vertical (blue) geometry, depending on the position of the sample.
The scattering plane is defined as parallel to the sample surface. The sample in-plane (out-of-plane) angular rotation is performed with μ (β) in the horizontal configuration, whereas ω (μ) is used in the vertical configuration.
γ and δ are respectively the in-plane (out-of-plane) and out-of-plane (in-plane) detector angles in the horizontal (vertical) configuration.
The u and v angles are pseudo-angles used to tilt the position of the sample with the goniometer. η is the rotation of the detector around its axis.

for other rods (e.g. $(0, 1, L)$, fig. 2.14 - b), the sample must be rotated in plane so that the top of the Ewald sphere intersects the rod in the reciprocal space (Vlieg 1997; Schlepütz, Herger et al. 2005).

As one can imagine from fig. 2.14 - b, there is a maximum value l_{max} that can be reached until the radius of the Ewald sphere becomes too low to ever intersects the rod in the reciprocal space, which depends on the incoming photon wavelength and on the crystal lattice. Furthermore, when for low L values the detector is in the vertical plane, for high L values the detector is almost parallel to the sample which limits the sampling of the reciprocal space. These experimental limitations are at the origin of how far in L the CTR can be measured, details about the experimental limitations and corrections factor for the measurement of crystal truncation rods can be found in Vlieg et al. (1997), Drnec et al. (2014). High-energy surface x-ray diffraction (Gustafson et al. 2014; Harlow et al. 2020; Hejral, Shipilin et al. 2021) has the potential to counter that limitation since the radius of the Ewald sphere increases, which simplifies the experimental setup to some extent.

The integrated intensity of a Bragg peak in photons/second, coming from a perfectly collimated monochromatic beam on a small crystal of N unit cells, neglecting absorption effects, can be expressed as follows (Jens Als-Nielsen 2011):

$$I_{sc}(\vec{q}) = \Phi r_0^2 P |F_{crystal}(\vec{q})|^2 \frac{V_s}{V_c} \times L(\lambda, \theta) \tag{2.51}$$

Φ is the incoming photon flux, P the polarisation factor, $F_{crystal}(\vec{q})$ the structure factor of the crystal, V_s is the scattering volume and V_c the volume of the unit cell.

The last term in eq. 2.51 is called the Lorentz factor, and is related to how the scattered intensity is integrated around the Bragg peak due to the distortion of the intensity distribution in the angular space. The Lorentz factor changes depending on how the data integration is performed (Robach et al. 2000; Drnec et al. 2014). Therefore, it is best to switch first from angular-space to q-space to avoid this correction, this is performed *via* the use of programs such as BINoculars (Roobol et al. 2015).

Understanding the dependence of the scattered intensity on the experimental parameters is extremely important when comparing experimental data with simulated structure factors. If the square-root of the integrated intensities is proportional to the structure factor modulus, the intensity must be corrected beforehand for the polarisation factor, especially when comparing different crystal truncation rods. Moreover, in the case of crystals that are larger than the beam-footprint, illumination effects must be considered since the scattering volume will depend on the incident angle between $\vec{k}_i$ and the surface plane.

2.5.4 X-ray reflectivity

To perform a measurement perpendicular to $[H, K] = [0, 0]$ in the horizontal geometry, β must be tuned together with the out-of-plane angle of the detector δ (fig. 2.16). This kind of measurement is called *specular* measurement, for which the direction of the scattering vector is only perpendicular to the surface, yielding information about the material electronic density only in the direction perpendicular to the surface.

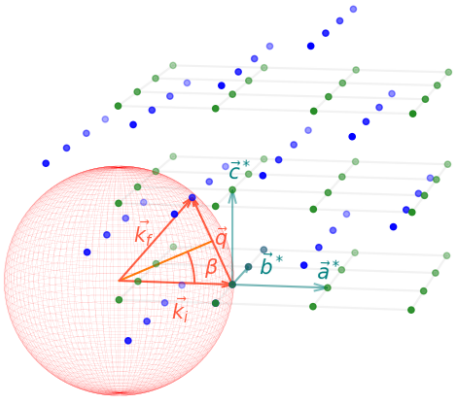

Figure 2.16: Ewald sphere represented together with the reciprocal lattice before (green) and after (blue) rotating the sample to satisfy the Laue condition. Measurements in the specular direction is performed by simultaneously rotating the out-of-plane sample angle β while the out-of-plane detector angle δ follows the relation $\delta = 2\beta$.

A description of the theory behind x-ray reflectivity which stems from the interaction between the incident, reflected, and transmitted plane waves at each interface can be found in several textbooks (Willmott 2009). To resume, the measured intensity R is equal to the square of the reflectivity amplitude $R = |r|^2$. After the critical angle α_c, the intensity decreases as a function of the inverse fourth power of the incident angle, and is proportional to the square of the electronic density. A rough surface will lead to an additional exponential decrease in the intensity after the critical angle. The formation of a new layer on top of the

substrate will lead to interferences between the waves reflected on both surfaces, resulting in the so called *Kiessig* fringes (Kiessig 1931), of width proportional to the thickness of the new layer.

Information about the formation of new surface layers as well as the roughness and thickness of each layer can be extracted by fitting a model to the scattered intensity. The technique can be used together with surface x-ray diffraction since it does not require a change of instrumental setup, and brings complementary information about the average roughness and thickness of surface layers.

2.6 Bragg coherent diffraction imaging

Bragg Coherent Diffraction Imaging (BCDI) (I. K. Robinson, Vartanyants et al. 2001; M. A. Pfeifer et al. 2006; I. Robinson et al. 2009) is a powerful technique for the non-destructive characterisation of material structure in three dimensions. It reaches unparalleled spatial and strain resolution for a scattering technique, few nanometres (Labat, M.-I. Richard et al. 2015; Cherukara, Cha et al. 2018) and 10^{-4} respectively (Newton, S. J. Leake et al. 2010; Lauraux, Cornelius et al. 2020).

The BCDI method is reliant on the coherence of the light available, thus only began to be exploited at third generation synchrotron sources (Miao, Charalambous et al. 1999; Miao, Kirz et al. 2000; I. K. Robinson, Vartanyants et al. 2001; Labat, Chamard et al. 2007; I. Robinson et al. 2009; Vaxelaire et al. 2010; Chamard et al. 2010; Clark, X. Huang et al. 2012; Clark, Beitra et al. 2013; W. Yang et al. 2013; Xiong et al. 2014), also the subject of reviews (Nugent 2010; Miao, Ishikawa et al. 2015). Since then it was developed into a characterisation tool for *in situ / operando* studies of materials structure, mostly applied to three fields: electrochemistry (Ulvestad, Singer et al. 2015), heterogeneous catalysis (Ulvestad, Sasikumar et al. 2016), and the structure and evolution of defects (Labat, M.-I. Richard et al. 2015). BCDI has gained from further source and beamline improvements as many synchrotrons have recently completed or are in the process of an upgrade from 3^{rd} to 4^{th} generation synchrotrons, which is predicted to allow the study of *in situ* dynamical phenomena (Lo et al. 2018). Focusing optics that allowed the development of coherent imaging techniques by increasing the coherent flux on the probed sample will be discussed in this section.

2.6.1 Scattering by strained crystals

In this thesis, the intensity scattered by a single crystal of dimensions below the coherent volume of the source is considered to introduce BCDI. The scattered waves interfere with each other, and maximum intensity is observed when the scattering vector satisfies the Laue condition.

Note that the following derivations only apply if the diffraction pattern is viewed at a distance far away from the diffracting object, in a region known as the far-field or Fraunhofer region (Willmott 2009), where the scattered waves can be considered as plane waves. Moreover, the scattering volume is assumed to be in the focal plane of the focusing optics and far from the source so that the waves in the scattering volume can also be described as plane waves. Finally, the scattering volume is assumed to be small with dimensions below the x-ray extinction length to ignore multiple scattering, and stay in the kinematical approach of diffraction. The incident field is assumed to be perfectly coherent in the longitudinal and transverse direction, with a homogeneous amplitude in the scattering volume. A discussion of the extent of these approximations is given in Godard et al . (2021).

The community has recently been investigating a dynamical approach to Bragg Coherent Diffraction Imaging (BCDI) (Yan et al. 2014; Shabalin et al. 2017; Hu et al. 2018; Y. Gao et al. 2022) using the Takagi-Taupin equations (Takagi 1962; Satio 1969). This method tends

to validate the kinematical approach when working with slightly strained sub-micron sized crystals (Karpov et al. 2019; Barringer et al. 2021). The phase of the incoming and scattered waves must however be corrected for refraction and absorption (Harder et al. 2007; Y. Gao et al. 2022) which does not contradict the main hypothesis of the kinematical approach which is that in the Born approximation, the structure factor of the crystal is equal to the Fourier transform of its electronic density (Paganin 2006).

Another approach is to write the structure factor as the sum of the atomic scattering factor multiplied by a phase component, over each atom present in the crystal (eq. 2.23). In general, the Fourier transform approach is preferred since one can use quick algorithms such as the Fast Fourier Transform (Cooley et al. 1965; Cochran et al. 1967) to compute the structure factor, whereas the atomistic approach relies on knowing the position of each atom in the crystal.

As seen in sec. 2.4.2, when considering the crystal to be made of repeating unit cells that organise themselves on the crystal lattice, the structure factor can also be written as the convolution between the Lattice factor F_{lat} and the unit cell structure factor F_{uc}. The shape of the scattering intensity around Bragg peaks is then given by F_{lat}, which is the Fourier transform of the crystal's lattice, whereas F_{uc} is the Fourier transform of the crystal's unit cell electronic density.

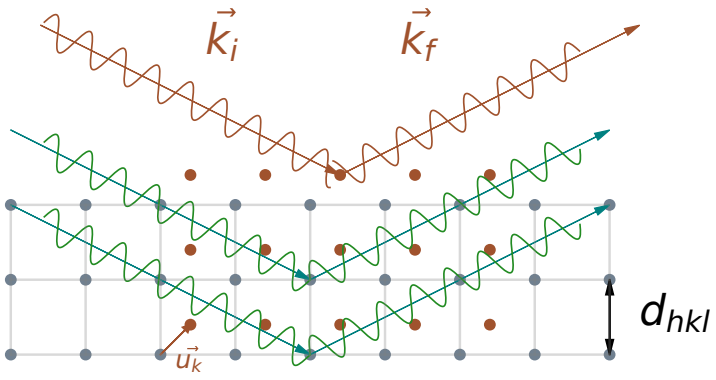

Figure 2.17: Simplified representation of a crystal in which each dot corresponds to a unit cell. The red dots represent displaced unit cells from their ideal position by a displacement vector $\vec{u}_k$, resulting in a shift in the phase of the scattered x-rays.

In the case of strained crystals (fig. 2.17), eq. 2.24 can be rewritten as follows:

$$F_{crystal}(\vec{q}) = \sum_{j}^{N_{atoms,uc}} f_j(\vec{q}) e^{i\vec{q}.(\vec{r}_{0,j}+\vec{u}_j)} \sum_{k}^{N_{uc}} e^{i\vec{q}.\vec{R}_k} \tag{2.52}$$

$$F_{crystal}(\vec{q}) = \sum_{j}^{N_{atoms,uc}} f_j(\vec{q}) e^{i\vec{q}.\vec{r}_{0,j}} \sum_{k}^{N_{uc}} e^{i\vec{q}.(\vec{R}_k+\vec{u}_k)} \tag{2.53}$$

where $\vec{r}_{0,j}$ is the ideal position of the atom j in the unit cell, and $\vec{u}_j$ the displacement from that position. In eq. 2.53, all atoms in the unit cell are considered to have the *same displacement* to be able to shift the displacement parameter from the atomic position to the unit cell position, $\vec{u}_k$ becomes the displacement of the unit cell k.

To reduce the complexity in the second part of eq. 2.53, only the intensity in a volume situated near the Bragg peak is considered so that $\vec{q} \approx \vec{G}$, $\vec{G}$ designates the reciprocal space vector that corresponds to the position of the Bragg peak in reciprocal space (M. A. Pfeifer et al. 2006; Minkevich et al. 2007; Harder et al. 2007).

$$F_{crystal}(\vec{q}) = \sum_{j}^{N_{atoms,uc}} f_j(\vec{q}) e^{i\vec{q}.\vec{r}_{0,j}} \sum_{k}^{N_{uc}} e^{i\vec{q}.\vec{R}_k} e^{i\vec{q}.\vec{u}_k} \tag{2.54}$$

$$F_{crystal}(\vec{q}) = \sum_{k}^{N_{uc}} F_{uc}(\vec{q}) e^{i\vec{q}.\vec{R}_k} e^{i(\vec{G}+\vec{q}-\vec{G}).\vec{u}_k} \tag{2.55}$$

$$F_{crystal}(\vec{q}) = \sum_{k}^{N_{uc}} F_{uc}(\vec{q}) e^{i\vec{q}.\vec{R}_k} e^{i\vec{G}.\vec{u}_k} \times e^{i(\vec{q}-\vec{G}).\vec{u}_k} \tag{2.56}$$

$$F_{crystal}(\vec{q} \approx \vec{G}) = \sum_{k}^{N_{uc}} F_{uc}(\vec{G}) e^{i\vec{q}.\vec{R}_k} e^{i\vec{G}.\vec{u}_k} \tag{2.57}$$

$$F_{crystal}(\vec{q} \approx \vec{G}) = DFT[F_{uc}(\vec{G}) e^{i\vec{G}.\vec{u}_k}]_{N_{uc}} \tag{2.58}$$

It is assumed that the variations of the unit cell structure factor $F_{uc}(\vec{q})$ are negligible when $\vec{q} \approx \vec{G}$, so that $F_{uc}(\vec{q})$ becomes $F_{uc}(\vec{G})$. One can recognise the expression of a discrete Fourier transform (DFT) of frequency $\vec{G}$, coefficient $F_{uc}(\vec{G})e^{i\vec{G}.\vec{u}_k}$, and N_{uc} samples (Cooley et al. 1965; Cochran et al. 1967; Favre-Nicolin 2011; Godard 2021). The approximation $\vec{q} \approx \vec{G}$ allows the use of a Fast Fourier Transform (FFT) algorithm to compute the DFT, with a linearithmic time complexity $O(n\,log(n))$. This approximation breaks down far away from the Laue condition, or if the strain is so important that the condition $(\vec{q}-\vec{G}).\vec{u}_k << 1$ is not anymore respected to move from eq. 2.56 to eq. 2.57 (Satio 1969).

In the case of highly strained crystal, or when the intensity must be computed far away from Bragg peaks, it is still possible to resort to so-called *atomistic* simulations, by computing the scattering intensity directly from the position of each atom in the crystal (eq. 2.23). However, the position of each atom must be known and, for a large crystal, the sum becomes too large to handle even with high-performance clusters due to a quadratic time complexity $O(n^2)$ (n is the number of operations). Atomistic simulations are usually used when studying crystals of dimensions below 100 nm (Dupraz, N. Li et al. 2022).

For a non-strained crystal, the Lattice factor is the same at each Bragg peak, equal to the Fourier transform of the crystal's lattice. In the case of a strained crystal, the additional phase factor introduced in eq. 2.58 breaks the centrosymmetry around each Bragg peak, due to the heterogeneous displacement field in the crystal. The effect of the displacement can be seen in the distortion of the scattering intensity around Bragg peaks. It is important to notice that the phase in eq. 2.58 is equal to the dot product between the displacement vector and the reciprocal space vector. This means that to possess the complete displacement field, one must collect the scattered intensity around three non-coplanar Bragg peaks (Newton, S. J. Leake et al. 2010) that will yield the displacement field over an orthogonal basis $(\vec{q}_x, \vec{q}_y, \vec{q}_z)$. The electronic density is also sometimes named Bragg electronic density to illustrate this sensitivity.

Data collection

The data collection during a BCDI measurement is performed by continuously rocking the sample around the incident angle, which will result in a tilt of the associated Ewald sphere, so that the detector probes a different slice of the reciprocal space at each step. This measurement is called a rocking curve (fig. 2.18 - left), the associated 3D scattering intensity is illustrated in fig. 2.18 (right).

The measurements are commonly collected in angular space, and can be converted into q-space to compare different Bragg peaks in the reciprocal space. However, this step is usually avoided since the intermediate interpolation process can be inaccurate, especially when the

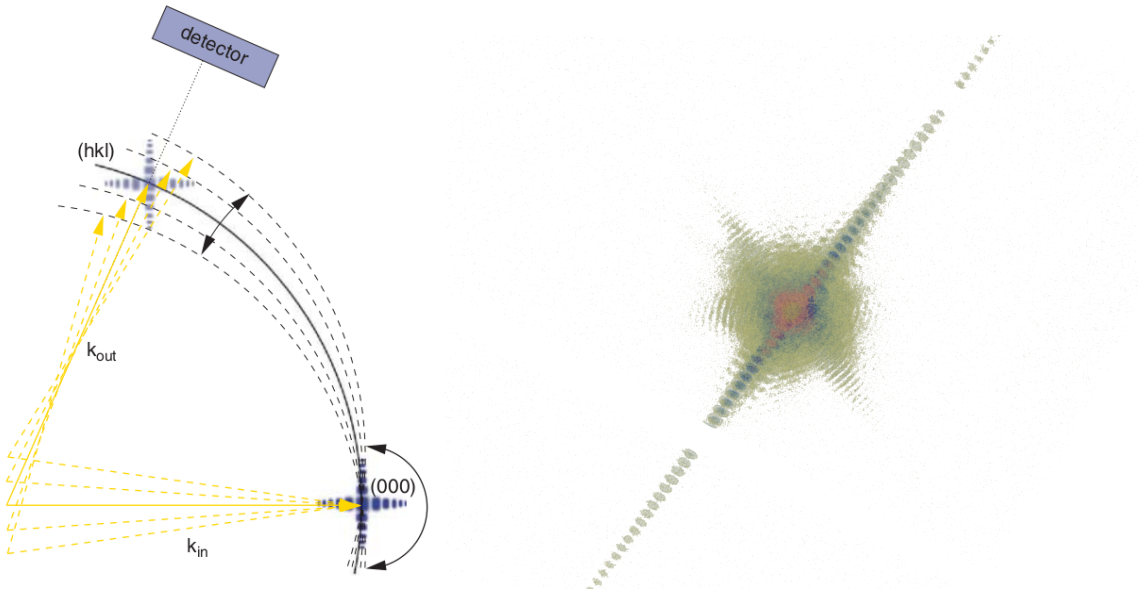

Figure 2.18: Left: rocking curve for the measurement of the 3D scattered intensity around a Bragg peak. Taken from Willmott 2009. Right: 3D diffraction pattern collected at SixS (SOLEIL). Different iso-surfaces from high (red) to low (yellow) intensity are plotted, highlighting the direction dependent drop of the scattered intensity as a function of $q_{hkl} + \delta q$ where δq is the distance from the centre of the Bragg peak.

scattering intensity is low. It is also possible to collect 3D measurements by tuning the energy of the incident beam (Cornelius et al. 2011).

2.6.2 Phase retrieval

As seen in sec. 2.5.3, the diffracted intensity collected by the detector is proportional to the squared modulus of the structure factor $F_{crystal}(\vec{q})$ (eq. 2.51), the phase of the scattered x-rays is lost during the measurement.

Without the phase information in reciprocal space, it is impossible to directly reconstruct the crystal electronic density with the help of an inverse discrete Fourier transform (IDFT, from eq. 2.23), and to obtain a detailed structural model of the crystal.

$$\rho(\vec{r}) = IDFT[F_{crystal}(\vec{q})] \tag{2.59}$$

It has been demonstrated that when fulfilling the *oversampling* condition, the phase lost during the measurement can be retrieved (Shannon 1949; Sayre 1952). The oversampling condition refers to the practice of sampling a signal at a higher sampling rate than the Nyquist rate (Miao, Kirz et al. 2000), which is twice the highest frequency present in the signal. Increasing the sampling rate in reciprocal space results in a denser set of data points in real space.

In the case of low-strained faceted crystals, the oversampling σ can be derived by computing the distance between the fringes (*i.e.* the interfringe) on rods in directions parallel to the normal of crystalline facets. It was shown that the interfringe δq observed on the rods is proportional to the size of the crystal in that direction, t, following the relation $\delta q = \frac{2\pi}{t}$ (sec. 2.4.3). For small crystals ($t <$ few um), the interfringe can be resolved depending on the experimental parameters. It thus becomes possible to oversample the fringes and to recover the phase information. The instrumental requirement for oversampling in the direction of a rod is that the detector must have at least two pixels between each fringe: $\sigma > 2$.

In three dimensions, the oversampling condition becomes $\sigma > 2^{1/3}$ (Miao, Sayre and Chapman 1998; Miao, Kirz et al. 2000; Miao and Sayre 2000). When it comes to Fourier

transforms, higher oversampling can offer several advantages such as reducing the possibility of aliasing (high-frequency components being mistakenly represented as lower frequencies due to insufficient sampling), spectral leakage (frequency components spread into neighbouring frequency bins in the Fourier transform, minimised if the frequency bins become narrower). Moreover, with more densely spaced samples, the interpolation process can more faithfully reconstruct the original signal without introducing artefacts. However, high oversampling rate take more measurement time, and can for example limit the number of rocking curves that can be recorded. An oversampling of three in each direction is in general sufficient to successfully reconstruct the probed samples (Dupraz 2015). The oversampling condition partly dictates the instrumental parameters which define the extent of the data voxels, the small volumes that constitute the 3D data array.

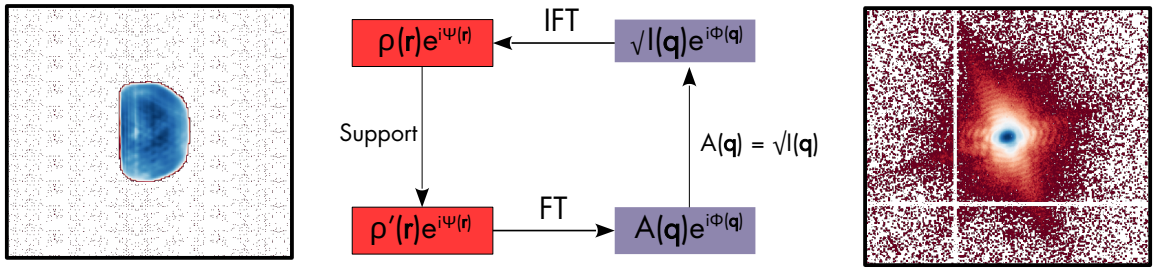

Figure 2.19: Iterative phase retrieval algorithms converge towards a solution by the means of real and reciprocal space constraints. $\rho'(\vec{r})$ is the updated Bragg electronic density after application of the support constraint.

Fienup et al. (1978; 1982; 1986) have laid the ground for computer methods permitting phase retrieval, once the oversampling condition has been satisfied. The error-reduction (ER) algorithm works by iterating between real and reciprocal space by the means of fast Fourier transforms (FFT) and inverse fast Fourier transforms (IFFT) methods. The process starts by assigning random phases to the square root of the measured scattered intensity ($I(\vec{q})$), to create a first guess of the scattered amplitude: $A(\vec{q}) = \sqrt{I(\vec{q})}e^{i\Phi(\vec{q})}$, proportional to the structure factor. The inverse Fourier transform yields a complex object $\rho(\vec{r})$ of amplitude proportional to the electronic density of the crystal (eq. 2.59), and with an additional phase factor linked to the displacement of the unit cells (eq. 2.58). A real space constraint is then applied by selecting a region above a certain threshold t of the modulus of the electronic density which is called the *support*. The electronic density outside the support is set to zero (eq. 2.60). The scattered amplitude is then computed with the Fourier transform of the electronic density, the following reciprocal space constraint consisting in replacing the amplitude of the computed amplitude by the square root of the measured intensity.

$$\rho(\vec{r}) = \begin{cases} 0 & \text{if } |\rho(\vec{r})| < t \\ \rho(\vec{r}) & \text{if } |\rho(\vec{r})| \geq t \end{cases} \tag{2.60}$$

By iterating between the real and reciprocal space, the algorithm converges towards a final solution for the electronic density (fig. 2.19).

A classical error-metric used to follow the convergence of the algorithm is the minimisation of the residuals between the square root of the measured intensity, and the amplitude computed from the Fourier transform of the electronic density. The main drawback of this error-metric is that each voxel is given the same weight, whereas the impact of the approximation detailed previously depend on the distance from the Bragg peak (Godard 2021). New metrics have been developed, such as the free log-likelihood (Favre-Nicolin, S. Leake et al. 2020), that have proven more robust.

More algorithms have since then been developed to help converge towards the final solution without being stuck in local minima such as the hybrid input-output (HIO) and relaxed

averaged alternating reflections (RAAR) algorithms, by introducing a new parameter, β, which relaxes the threshold condition in real space from the ER algorithm (Marchesini, He et al. 2003; Luke 2005; Marchesini 2007).

Finally, a major recent improvement of the phase retrieval algorithm is the possibility to take into account the partial coherence of the beam (Sinha et al. 1998; Vartanyants et al. 2001; Williams et al. 2007; Whitehead et al. 2009; Nugent 2010; B. Chen et al. 2012) together with the point-spread function of the detector by using the deconvolution Richardson-Lucy algorithm (Richardson 1972; Lucy 1974; Fish et al. 1995; Clark, X. Huang et al. 2012). The point-spread function (PSF) must first be approximated with a 3D Gaussian, Lorentzian or pseudo-voigt shape, depending on the expected coherence of the beam. It is refined during the last steps of the phase retrieval when the support is already well determined, to avoid any divergence from simultaneously having to refine both the support and the PSF.

Moreover, new methods such as convolution neural networks (CNN) are under study and have started to show some encouraging results, but are not yet sufficiently robust, particularly in the case of strained particles (Cherukara, Y. S. Nashed et al. 2018; Shen et al. 2019; H. Chan et al. 2021; J. W. Kim et al. 2021; L. Wu et al. 2021).

2.6.3 Resolution

The resolution of the reconstructed object, defined according to multiple parameters in the literature, is a prominent figure of merit for an imaging technique. The voxel size in real space $(2\pi/\delta q_x, 2\pi/\delta q_y, 2\pi/\delta q_z)$ depends on the extent of the collected volume in the reciprocal space $(\delta q_x, \delta q_y, \delta q_z)$. However, the voxel size would only be a good criteria to determine the resolution if the signal to noise ratio of the scattering intensity was important enough in all of the probed reciprocal space volume, so that all of the frequencies in the q-space could be effectively retrieved with the FFT algorithm. A high-intensity dynamic range detector is therefore needed to correctly probe intensities at the center, and extremities of the Bragg peaks (Latychevskaia 2018).

This is the case in simulated data, but not with experimental data, for which the noise starts to become important far away from the Bragg peak (Bikondoa et al. 2021), keeping in mind that the intensity decreases as a function of q^{-4} as a function of the distance from the Bragg peak (Marchesini, Chapman et al. 2003), depending also on the form factor (Croset 2017). The community has therefore relied so far on a few methods to estimate the spatial resolution of the reconstructed electronic density.

First, the Phase Retrieval Transfer Function (PRTF) (Chapman et al. 2006) is the *ratio* of the calculated amplitude $|A_k(\vec{q})|$ to the square-root of the measured intensity $\sqrt{I_k(\vec{q})}$ as a function of the resolution shell. The resolution shell k is defined as all voxels of position $q = \sqrt{q_x^2 + q_y^2 + q_z^2}$ that satisfy the condition $q \in [q_k, q_{k+1}]$. δq is the width of the resolution shell which divides the extent $[q_{min}, q_{max}]$ of the sampled reciprocal space in N shells so that $q_{max} = q_{min} + N \times \delta q$ and $q_{k+1} - q_k = \delta q$.

$$PRTF(q_k, q_{k+1}) = \frac{| < F_k(\vec{q}) > |}{< \sqrt{I_k(\vec{q})} >} \tag{2.61}$$

Secondly, the Fourier shell correlation (FSC) (Van Heel et al. 2005) measures the *normalised cross-correlation coefficient* between the amplitude of two independent reconstructions, also as a function of the resolution shell, but from two independent datasets collected with the same instrumental parameters:

$$FSC(q_k, q_{k+1}) = \frac{|\sum F_{1,k} F_{2,k}^*|}{\sqrt{\sum F_{1,k} F_{1,k}^* \times \sum F_{2,k} F_{2,k}^*}} \tag{2.62}$$

Both of these methods allow us to quantify the distance from the centre of the Bragg peak after which one of the criteria diverges, which yields a corresponding real space resolution. There are several limitations to these methods. First, the resolution curve as a function of $|\vec{q}|$ strongly depends on the width of the bins used to create the resolution shells. The number of voxels in each bin is dependent on the distance from the centre q_{min}, and the voxel size is usually not isotropic. Finally and most importantly, it supposes that the resolution is isotropic in reciprocal space, which is false since the signal to noise ratio will be much higher around the rods perpendicular to the crystal's facets (Cherukara, Cha et al. 2018). Indeed, the scattered intensity along the rods is proportional to the size (*i.e.* the number of unit cells) of the crystal in the direction perpendicular to the facet. Thus, for large facets, the rod intensity will be much more intense, increasing the resolution in that direction.

In real space, the spatial resolution can be quantified by differentiating line profiles of electron density amplitude across the object-air interface, and fitting these with a Gaussian profile. The average 3D spatial resolution is taken as 2σ of the fitted Gaussian (Hofmann et al. 2020). This method has the advantage of being straightforward, and direction sensitive.

One of the challenges encountered in Bragg coherent diffraction imaging is establishing a single, meaningful criterion for the spatial resolution. Its anisotropic nature further complicates this task, as commonly used criteria such as the phase retrieval transfer function (PRTF) or Fourier shell correlation (FSC) are isotropic. To address this, a new method for resolution assessment when aiming at the analysis of specific facets in real space could involve examining the extension of the corresponding crystal truncation rods in reciprocal space, before the signal becomes overwhelmed by counting noise from the lack of scattered photons. In this approach, the resolution of the measurement would not rely on the quality of the phase retrieval or the type of algorithms utilised, but solely on the quality of the measurement itself. Consequently, the significance of the sample's shape, as well as the measurement quality would be emphasised. For instance, a large planar particle featuring a sizeable (111) top facet would yield a more readily resolvable signal in the (111) direction compared to a smaller, spherical particle with a diminished (111) top facet.

Concerning the resolution of the retrieved atomic displacement, Labat et al. (2015) have demonstrated a displacement field accuracy of few pm along preferential directions, by comparing with simulated displacement fields. Another method is to work in a similar way to the Fourier shell correlation by replacing the shells of amplitude as a function of $\vec{q}$ by shells of strain as a function of the strain magnitude, and see if there exists a strain threshold below which the correlation drops. This method is then called the strain shell correlation (Girard 2020).

However, one must keep in mind that the upper threshold for the strain resolution exists based on the $(\vec{q}-\vec{G}).\vec{u}_k << 1$ condition, which mostly affects the quality of the phase retrieval. Highly strained crystals are very difficult to reconstruct and represent the next milestone in Bragg coherent diffraction imaging, recent methods have been proposed for specific cases such as phase transitions (Z. Wang et al. 2020). One could imagine a future in which the atomistic computation of the scattering factor has been so optimised that phase retrieval algorithms would only be needed to provide an initial guess to the electronic density, replaced in the final steps by a fitting of the computed amplitude to the square root of the measured intensity. A reverse Monte-Carlo method used already for the simulation of powder diffractograms could also be used (McGreevy 2001).

2.6.4 Facet analysis

After phase retrieval, it becomes possible to exploit the electronic density of the reconstructed crystal. Its surface corresponds to a layer of voxels in the three dimensional array. Carnis et al. (2019) have presented guidelines on how to correctly select the surface voxels, which are detailed below. The histogram in fig. 2.20 represents the number of voxels per bin of

normalised electronic density, the observed peak corresponds to the bulk voxels for which the amplitude of the electronic density is close to the maximum (fig. 2.20 - right). An empiric criterion to select the voxels that correspond to the crystal's surface is to take the lowest foot of that peak, here around 0.6, the surface being defined as the hull surrounding the bulk voxels.

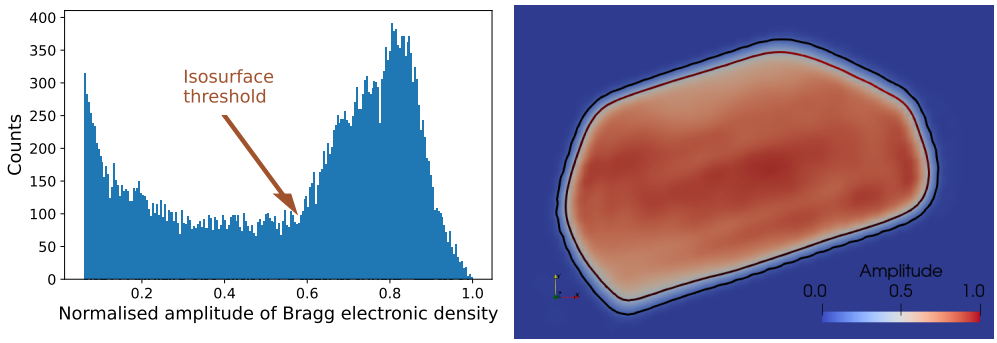

Figure 2.20: Histogram representing the distribution of the electronic density amplitude, normalised by its maximum (left). Values below 0.05 are ignored since they typically belong to voxels located far away from particle support. Amplitude of the electronic density in a slice of the reconstructed object (right). Two curves are drawn at the iso-surface values of 0.1 *(outer curve - black) and* 0.6 *(inner curve - red).*

Once the threshold for the iso-surface is selected, it is possible to visualise a contour of the object with specialised solutions such as *Paraview* (Ahrens et al. 2001 - fig. 2.22) or *Gwaihir* (Simonne, Carnis et al. 2022 - fig. 2.35).

The surface is usually created by using the Marching-Cubes algorithm (Lorensen et al. 1987), which works by assigning a scalar value to each voxel of the data (in our case the amplitude of the retrieved complex electronic density). An iso-value which acts as a threshold is selected by the user, separating the volume of the particle from the rest. Finally, by *marching* over the volume of the array, the algorithm derives a surface representation by assigning a configuration to each point in the array that depends on whether or not the 8 neighbouring cubes have values above or below the iso-value (fig. 2.21).

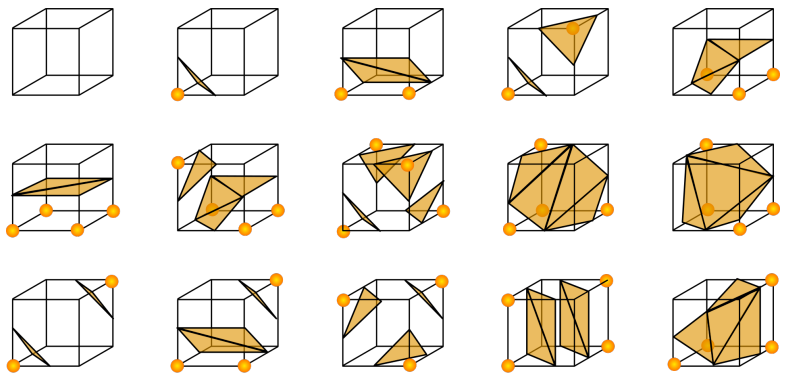

Figure 2.21: The Marching-cubes algorithm generates triangles connecting the vertices to form the mesh surface. Each selected configuration has a specific arrangement of vertices that dictate how to form triangles to create a smooth surface. Image taken from https://fr.wikipedia.org/wiki/Marching_cubes

Crystallographic facets can be identified on the surface of the reconstructed object when studying faceted objects with a highly coherent beam (M. I. Richard et al. 2018), allowing in-depth studies of facet dependent strain and displacements. Lattice strain and displacements are key information to retrieve during *in situ* and *operando* experiments in fields such as heterogeneous catalysis (Ulvestad, Sasikumar et al. 2016; Yau et al. 2017; D. Kim, Chung,

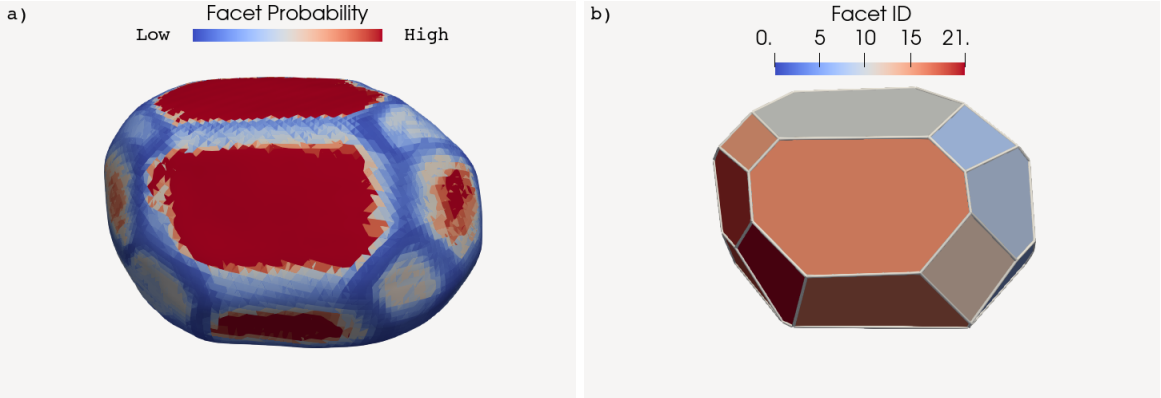

Figure 2.22: a) Surface of a reconstructed nanoparticle ($\varnothing \approx 800\,\mathrm{nm}$) with each surface voxel coloured by its probability to belong to a facet. The same surface is represented in b) with a hull in which each facet is drawn, delimited by thick white lines.

Facet id	Facet normal	Relative facet size	Average displacement (Å)	Average strain (10^{-4})
0	Edges and corner	NaN	−0.224(259)	0.20(86)
1	(111)	0.106	0.080(173)	−0.28(51)
2	$(\bar{1}\bar{1}\bar{1})$	0.223	0.052(260)	−1.17(64)
3	$(1\bar{1}0)$	0.106	0.080(173)	−0.28(51)
4	(100)	0.096	0.137(192)	0.27(49)

Table 2.3: The output of FacetAnalyser is a list of values for each facet. The accessible features are the facet size, the average strain and displacement (along the [111] direction, for the outermost voxel), and the coordinates of the normal to the facet surface. The uncertainty on the average displacement and strain corresponds to the standard deviation of the displacement and strain distribution, respectively.

Carnis et al. 2018; Fernàndez et al. 2019; Abuin et al. 2019; D. Kim, Chung, S. Kim et al. 2019; Kawaguchi, Keller et al. 2019; Suzana et al. 2019; Choi et al. 2020; Passos et al. 2020; Y. Y. Kim et al. 2021; Carnis, Kirner et al. 2021; Dupraz, N. Li et al. 2022) or electrochemistry (Ulvestad, Clark et al. 2015; Björling et al. 2019; Vicente et al. 2021; Kawaguchi, Komanicky et al. 2021; Carnis, L. Gao, Fernández et al. 2021; Atlan et al. 2023).

Retrieving the facets can be achieved by analysing the probability distributions of the orientations of triangle normals on a mesh representation of the object (Grothausmann, Fiechter et al. 2012). This method is used in the *Paraview* plugin *FacetAnalyser* (Grothausmann and Beare 2015), and yields a list of features detailed in tab. 2.3. The probability of each surface voxel to belong to a facet is illustrated in fig. 2.22. The orientation of each facet is retrieved by analysing the angles between the normal of each facet, also returned by the algorithm, and a reference direction.

In the case of highly resolved measurement, another approach could be inspired from image processing and convolutional neural networks, where 3D convolutions kernels are used to identify surfaces (Raschka et al. 2019). By tuning the kernel size and values, it is possible to be sensitive to boundaries in specific directions.

In this example, the FacetAnalyser plugin is used (fig. 2.22). Note that the edges and corners of the reconstructed particle are also retrieved together as the voxels not belonging to any facets. The contribution from atomic edges and corners to those voxels, sites of particular interest for heterogeneous catalysis (Taylor et al. 1925), depends on the spatial resolution of the experiment since averaged in the voxel size. The result depends on the algorithm input parameters, such as the minimum relative facet size, the angular acceptance for the facet normals, *etc.*

2.7 Synchrotron radiation for the study of materials

2.7.1 Synchrotron radiation

SOLEIL (Source Optimisée d'Énergie Intermédiaire du LURE (Laboratoire pour l'Utilisation du Rayonnement Électromagnétique)) is a 3^{rd} generation synchrotron source facility build in 2005, and localised near Paris (France). SOLEIL operates at an electron energy of 2.75 GeV, with a storage ring diameter of 100 m.

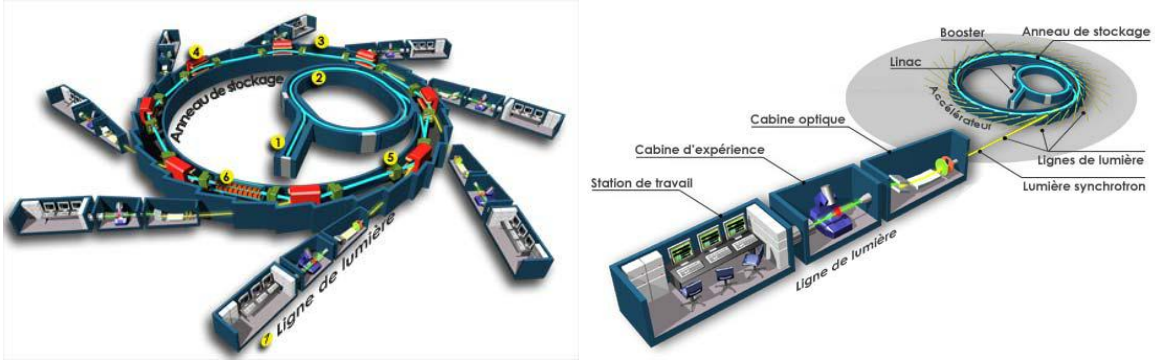

Figure 2.23: The storage ring of a synchrotron alternates between straight and curved sections (left). Insertion devices are situated along the straight sections, and deliver the synchrotron radiation to the beamline, separated in optical hutches, experimental end-stations and working stations (right). Copyright by SOLEIL (https://www.synchrotron-soleil.fr/en/research).

Synchrotron radiation is generated when electrons travelling at relativistic speeds are accelerated and forced to travel in curved trajectories by strong magnetic fields, supplied by *bending magnets*. The radiation spans a broad spectrum, from infrared to X-rays, depending on the electrons, the acceleration, and the strength of the magnetic fields.

First, electrons are produced by an electron gun, accelerated in a linear accelerator (LINAC), and by a booster ring. Secondly, electrons that reach the desired energy are injected into the *storage ring*, an almost circular vacuum chamber surrounded by strong magnets (fig. 2.23 - left). The magnetic fields in the ring act as a guiding force, bending the electrons' trajectories.

Due to their high energy, the electrons travel at speeds close to the speed of light, making them relativistic particles. As they move through the curved paths, they are accelerated and emit electromagnetic radiation tangentially to their trajectory as a result (Willmott 2009; Jens Als-Nielsen 2011).

By the use of insertion devices such as *wiggler* or *undulators*, synchrotron radiation is exceptionally bright and brilliant, with a high flux of photons and an excellent collimation. Wigglers are best used when in the need of a broad energy range, whereas undulators produce beams with extremely high brilliance, and narrow bandwidth. Each beamline at SOLEIL begins with one of those insertion devices or with a bending magnet (fig. 2.23 - right).

2.7.2 The SixS beamline

SixS (Surfaces Interfaces X-ray Scattering) is a wide-energy range beamline dedicated to the structural characterisation of surfaces and interfaces (solid/solid, solid/gas, solid/vacuum, solid/liquid), as well as nano-objects in controlled environments by the means of surface-sensitive x-ray scattering techniques.

The beamline operates with a U_{20} undulator situated before the front-end (shutter), which delivers a horizontally polarised beam. The beam is characterised by its horizontal and vertical full width at half maximum, respectively $FWHM_H = 913.7\,\mu m$ and $FWHM_V =$

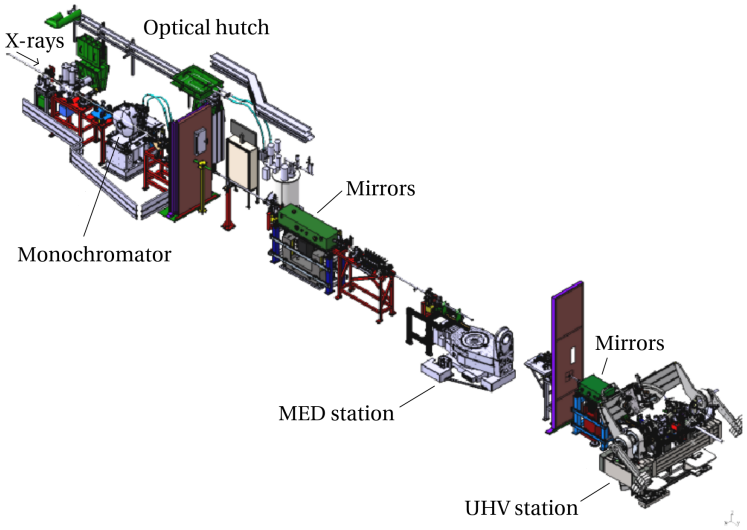

Figure 2.24: Schematic view of SixS, the monochromator is situated in the optical hutch, the focusing mirrors, the attenuators and the MED end-station are in the first experimental hutch. Additional mirrors and the UHV end-station are in the second experimental hutch. Only the MED end-station was used in the frame of this thesis. Taken from Chatelier (2020).

19.1 µm, and by its horizontal and vertical divergences, respectively $\Delta\theta_H = 14.5\,\mu\text{rad}$ and $\Delta\theta_V = 4.61\,\mu\text{rad}$.

A diaphragm is placed after the undulator to cut any parasitic signal from the source. A double crystal monochromator (DCM) of silicium (111) allows the selection of a monochromatic beam of thin bandwidth $\Delta\lambda$ in the range of 4 keV to 20 keV, after receiving the white beam. The crystals are cooled by liquid nitrogen due to the high intensity of the white beam, and produce harmonics depending on the incident angle of the beam through diffraction (Bragg's law, eq. 2.29). Primary slits are placed just before the DCM, to select a homogeneous portion of the beam, aiming to avoid fluctuations in the beam intensity. Secondary slits after the DCM are used to clean the signal after the monochromator. The vertical focus of the beam is then handled by a pair of mirrors, one of which can be slightly curved to focus the beam vertically anywhere between the MED and the UHV stations (fig. 2.24). Piezo-actuated and pneumatic attenuators are respectively situated before and after the mirrors, they limit the intensity of the incident beam (*e.g.* when working in the direct geometry). The first experimental end-station on the beam path is the multi-environment diffractometer, where the focused beam is approximately large by 60 µm vertically and 1500 µm horizontally. Additional focusing optics used for BCDI are present in the MED end-station and are detailed below. The distance between each element on the beamline is recapitulated in tab. 2.4, a sketch of the beamline is illustrated in fig. 2.24. The second experimental hutch, mainly used for ultra-high vacuum experiments, was not used during this thesis.

U_{20}	Diaphragm	Ring wall	Primary slits	DCM Si (111)	Secondary slits	Foc. mirror	Plan. mirror	Focusing optics (BCDI)	MED
0 m	11.7 m	15 m	16.7 m	18.8 m	≈19 m	24.5 m	25.5 m	≈30.5 m	31 m

Table 2.4: Distance between each main element that allows the focusing of a monochromatic beam on the multi environment diffractometer (MED) sample stage at SixS.

2.7.3 Multi environment diffractometer

The multi-environment diffractometer (MED) at SixS (fig. 2.25) can be used in either a vertical or horizontal configuration (fig. 2.15), and can accommodate a large variety of experimental chambers around the sample stage.

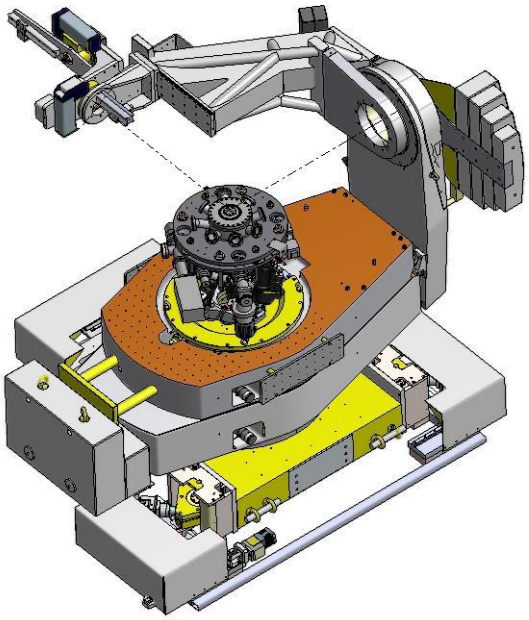

Figure 2.25: Multi-environment diffractometer (MED) (horizontal configuration), accommodating the XCAT reactor (Rijn et al. 2010) placed upon the hexapod. The hexapod allows the sample to move in three orthonormal directions, and three rotations.
Image copyright by Leiden Probe Microscopy (https://leidenprobemicroscopy.com).

Situated at a distance $R = 31\,\text{m}$ from the source, the transverse coherence length of the beam can be computed at the sample stage when working with an energy of 8.5 keV (working energy of the coherence optics) following eq. 2.47. For a Gaussian distribution, the FWHM is related to the standard deviation σ by the relation $FWHM = 2\sqrt{2ln(2)}\sigma$. The transverse coherent lengths are equal to $L_{T,H} = 3.3\,\mu\text{m}$, and $L_{T,V} = 157.3\,\mu\text{m}$.

The longitudinal coherence length can be computed from eq. 2.46, the ratio $\Delta\lambda/\lambda$ approximately equal to 10^{-4} at the energy of 8.5 keV gives $L_L = 729\,\text{nm}$. These values corresponds to perfect coherent lengths without taking into account any imperfection in the beamline elements (such as the monochromator) that can result in increasing the virtual source size and decreasing the transverse coherence lengths (Jacques 2010).

BCDI configuration

During this thesis, the horizontal configuration was used for SXRD experiments whereas the vertical configuration was used for BCDI experiments. Working in a vertical configuration is preferable for BCDI since it allows a larger range of incident angle (β, the incident angle in the horizontal configuration, is limited to 3°). The mirrors, that focus the beam in the horizontal configuration, are removed from the optical path. The focus of the beam is then handled by specific focusing optics detailed below.

The secondary slits are closed to 100 µm vertically and horizontally, acting as a secondary source during BCDI experiments, and reducing the effective size of the source seen by the focusing optics (Jacques 2010). So called *coherence* slits are placed just before the beam stop

to select a homogeneous portion of the beam that impinges on focusing refractive lenses called Fresnel zone plates (FZP), designed to work at an energy of 8.5 keV. The use of Fresnel zone plates (that preserve the coherent wavefront) together with coherence slits has been proven to increase the coherent flux impinging on the sample (Schroer et al. 2008; Diaz et al. 2009; Mastropietro et al. 2011).

An order-sorting aperture (OSA) and a beamstop block the direct beam and the higher diffraction orders from the FZP (fig. 2.26). Since the coherence slits also have the counter effect of decreasing the total photon flux on the sample, their width is subject to a compromise to increase the coherent flux on the sample.

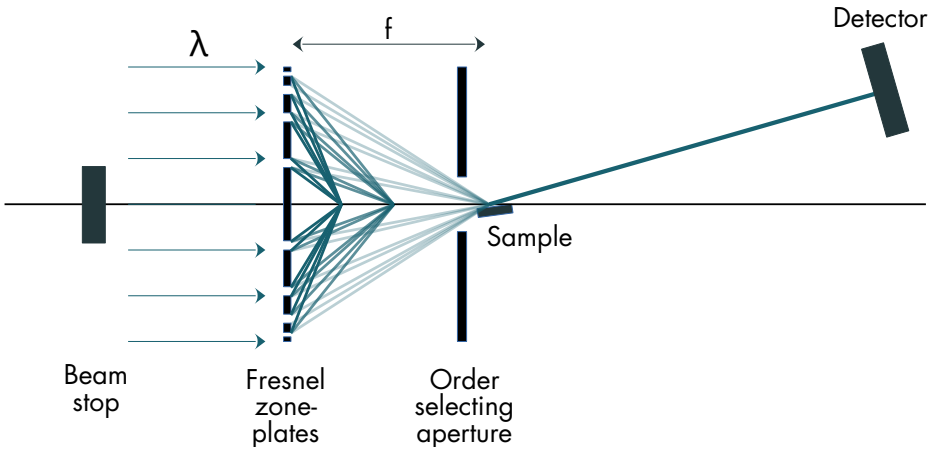

Figure 2.26: Focusing optics used for Bragg coherent diffraction imaging at the MED end-station, increasing the coherent flux on the sample. f stands for focal distance and λ for the wavelength of the incoming beam.

	Coherence slits	Beam stop	FZP	OSA	Beam
Diameter	60 µm × 20 µm	80 µm	300 µm	70 µm	≈1 µm
Sample distance	−400 mm	−220 mm	−200 mm	−50 mm	0 mm

Table 2.5: Diameter of the coherence focusing optics used to increase the coherent flux on the sample.

Improving Bragg coherent diffraction imaging at SixS

One of the bottlenecks of the BCDI technique is its slow data reduction and analysis process. On 3^{rd} generation synchrotrons that offer a lower coherent flux (eq. 2.48) than 4^{th} generation synchrotrons, the measurement time can also exceed several dozens of minutes. For example, at SixS, a rocking curve lasts between 20 min to 90 min depending on the particle size, the quality of the alignment, *etc.* Once the raw data is obtained, the particle must be *reconstructed*, so that the displacement and strain arrays can be retrieved. The analysis workflow can take up to an hour, totalling to a maximum of two hours from the start of the measurement to when the user has a first idea of the sample shape and structure.

SixS is a beamline that not only permits BCDI experiment but also SXRD experiment. When aiming at performing *operando* catalysis experiments, switching from one setup to another can take up to a few days. This leaves only a limited remaining amount of time to align the sample, find a suitable nanoparticle, and carry out the experimental plan.

Li et al. (2020), who have first shown that the SixS beamline could be used to carry out BCDI experiment, started to work on improving the BCDI measurement process. By comparing continuous and step-by-step measurements, they have shown that continuous scanning would result in the same data quality while decreasing the measurement dead-time by 30 %, thereby paving the way for quicker BCDI measurements.

During this thesis, the measurement process was further improved by taking advantage of the new possibility to perform continuous *on-the-fly* scans at SixS, while moving the sample plane with the hexapod. By working in specular geometry (fig. 2.16), and by simultaneously moving the sample with the hexapod and recording the Bragg scattered intensity with the detector, it is possible to map the sample surface with a sub-micron resolution (Chahine et al. 2014). An example of the mapping result is illustrated below in fig. 2.27. A nanoparticle with a width equal to 300 nm was identified with this technique (sec. 3.3), which is a good estimate of the resolution that can be attained, limited by the hexapod resolution (smallest step size equal to ≈300 nm) and the beam size.

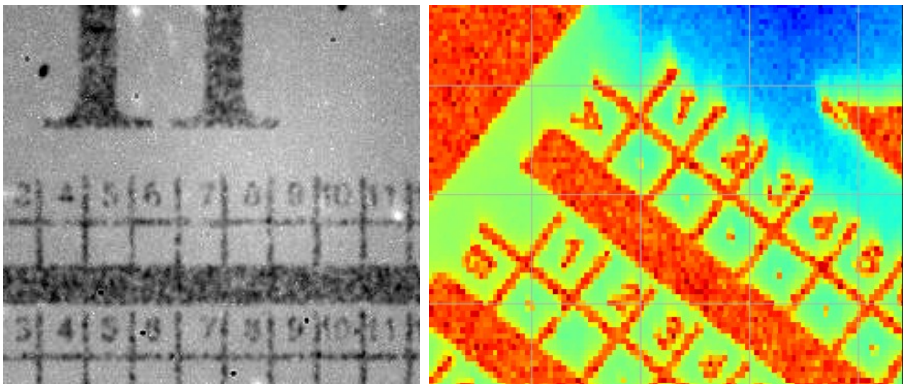

Figure 2.27: Microscope image of the sample seen through the sapphire window of the PEEK dome (left). Map of the sample performed in Bragg condition (right), the high intensity (red) areas correspond to platinum nanoparticles. The letters, numbers and isolated nanoparticles in the centre of squares can be recognised on the sample.

A data reduction software, *Gwaihir* (Simonne, Carnis et al. 2022), was developed primarily for the SixS beamline to counter the long analysis process, allowing a significant reduction in the analysis time from tens to few minutes. The following beamtimes profit from the new software by having a more *solution*-driven experimental process. Indeed, to be measured, a nanoparticle must be isolated, not too small (weak scattered intensity, e.g. > 100 nm at SixS), not too large (loss of coherence, fringes not visible, e.g. < 1000 nm at SixS), and not too initially strained (difficult to obtain a good guess of the support). These conditions are sometimes difficult to assert by simply looking at the diffraction pattern. Therefore, quick inversion using *Gwaihir* allows a faster decision process regarding the continuation or not of the nanoparticles measurement.

Successful first measurements have permitted the combined use of BCDI measurements from SixS with measurements from other imaging beamlines (ID01 - ESRF, P10 - DESY), designing a robust method to identify defects in the real space with convolutional neural networks (CNN) (B. Lim et al. 2021).

Catalysis reactor

A catalysis reactor is mounted on the sample stage of the MED for the study of catalytic reactions. A 3D view in the horizontal configuration with the high pressure surface diffraction reactor XCAT (X-ray CATalysis) set on the goniometer is illustrated in fig. 2.25.

This reactor is used for the study of heterogeneous catalysis (Rijn et al. 2010; Resta et al. 2020), and couples a UHV environment for classical surface science preparations (sputtering, annealing, evaporation) with an ambient pressure reactor. In the frame of this thesis, the metallic single crystals are purchased already cut and polished for SXRD experiments, introduced in the reactor and cleaned by sputtering (Taglauer 1990) before the experiment. It is also possible to heat the sample up to 900 °C for an extended period of time to anneal the sample after sputtering (Musket et al. 1982).

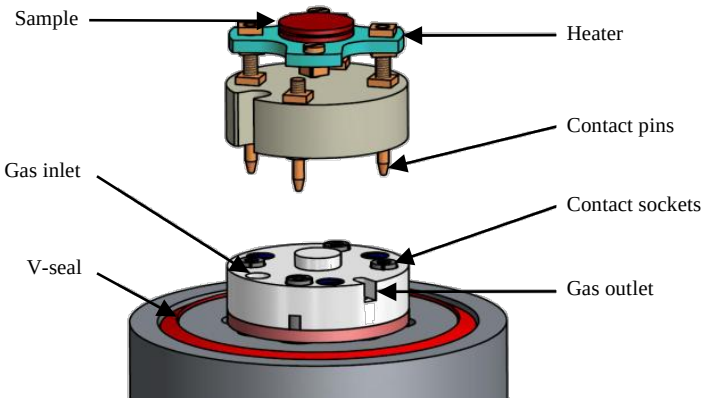

Figure 2.28: Sample holder used for the XCAT catalysis reactor.

The sample holder (fig. 2.28) consists of a cross-shaped graphite heater covered in boron nitride, held by two conductive screws in a thick (≈1 cm) and round ceramic slab. The protruding ends of the screws on the opposite side of the ceramic slab serve as contact pins used for the heater power circuit, and to securely fasten the sample holder to the reactor. A Beryllium or PEEK dome closes the reactor, two V-seals sealing the reactor atmosphere from the outside, two types of PEEK dome are available, with or without a sapphire window, allowing to observe the sample during the experiments with a microscope.

This design not only enables swift attachment and detachment of the sample holder but also ensures a robust setup in both horizontal and vertical orientations. The sample is then placed on top of the sample holder and set in place by a wire. All the materials used in the reactor were carefully chosen as not catalytically active for specific reactions. For example, tantalum parts (screws and wire) are used in oxygen rich environment (more resilient to oxide formation), whereas molybdenum parts are used in hydrogen rich environment (more resilient to hydride formation). A boron nitride paint additionally covers and protects the screws and wires used to fix the sample holder, as well as sample from oxidation effects.

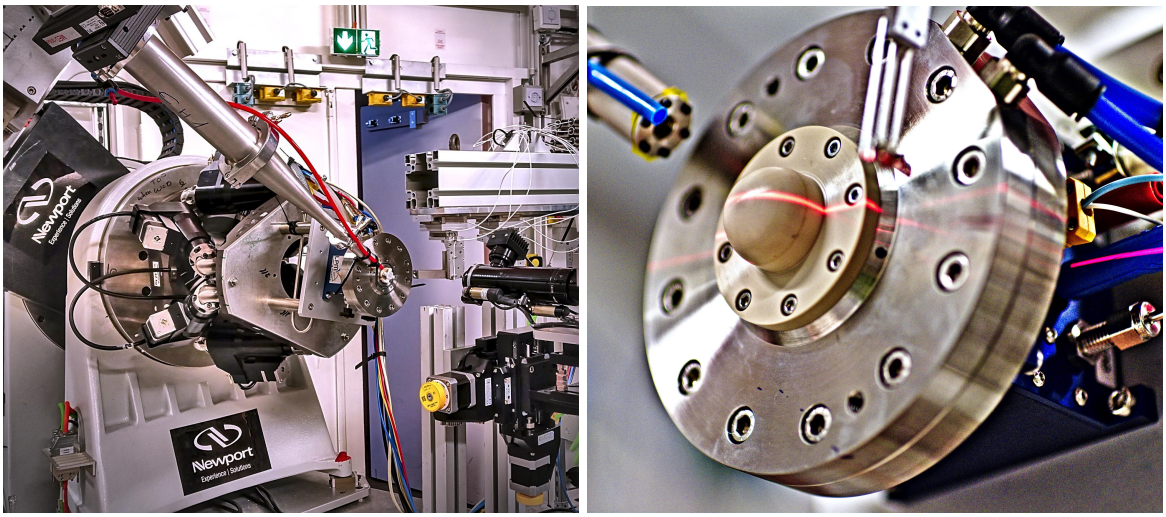

Figure 2.29: Left: MED end-station in vertical configuration for BCDI experiments. The OSA can be seen next to the reactor cell. The sample is visible in the absence of the reactor dome. The smaller version of the XCAT reactor cell seen in both images is completed with its PEEK dome on the right.

The gas composition inside the reactor is tuned by setting the flow for each gas in standard cubic centimetres per minute (SCCM). The inlet and outlet of the gases in the reactor volume are through holes in the ceramic slab that are set just below the sample holder (fig. 2.28).

The standard supported gases are argon (Ar), oxygen (O_2), nitrogen oxide (NO), carbon monoxide (CO) and hydrogen (H_2). It is possible to change the gases used by computing the correct conversion factor for a mass flow controller, each one originally set to work with a specific gas. For example, the bottle of H_2 was replaced by a bottle of ammonia (NH_3) during the experiments involving the catalytic oxidation of ammonia. Moreover, the pressure inside the volume of the reactor can be controlled by a pressure controller, from 100 mbar to 1200 mbar (fig. 2.30), in a small volume (≈10 mL), under batch or constant flow conditions.

Finally, the evolution of the product and reactant pressure during the catalytic reaction is probed by a residual gas analyser (RGA), connected to a leak from the reactor outlet (fig. 2.30).

Overall, this experimental setup allows the exploration of a large, multi-dimensional parameter space during heterogeneous catalysis experiments connecting reaction kinetics and surface structure.

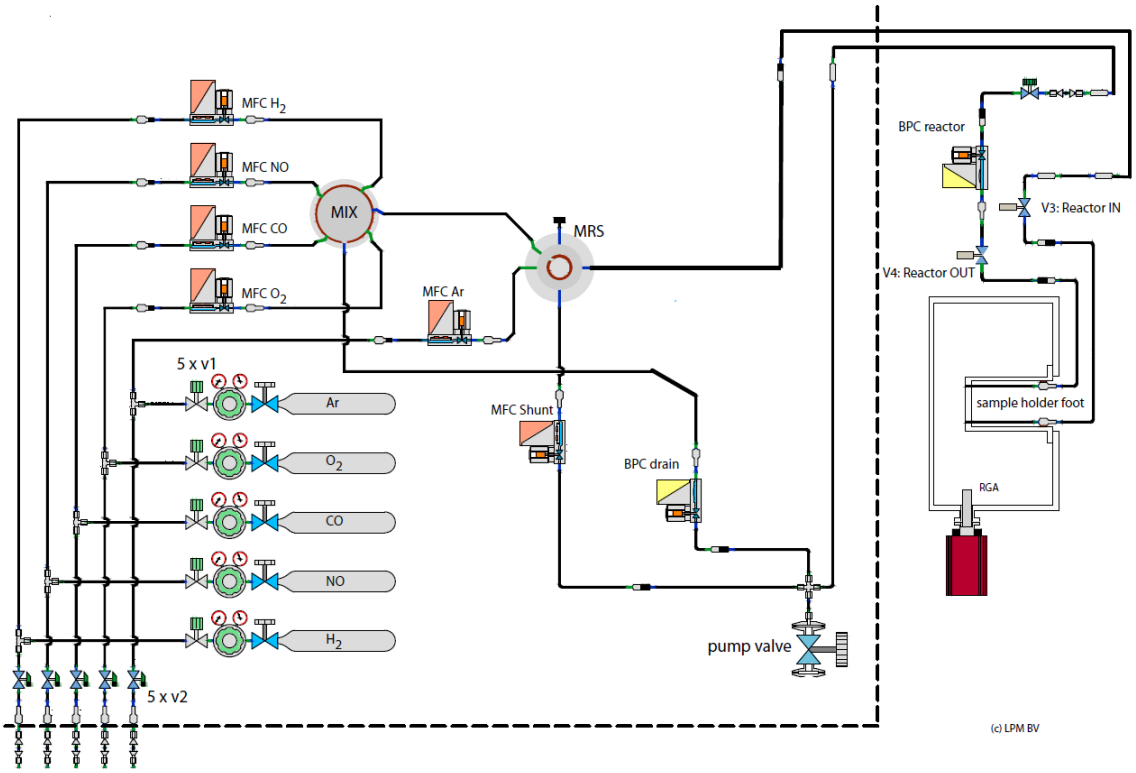

Figure 2.30: Gas supply system used at SixS together with the multi-environment diffractometer (MED) for the high pressure surface diffraction reactor. The mixing of reacting gases is performed before the reactor (MIX), argon is used as a carrier gas (MRS). The leak to the RGA is represented as a side circuit from the reactor outlet. Copyright by Leiden Probe Microscopy (https://leidenprobemicroscopy.com).

When performing BCDI measurements, a smaller version of the XCAT is used which is light enough to be supported vertically by the goniometer (fig 2.29). The two reactors have the same inner volume and host the same sample holder stage (fig 2.28). The main setbacks being the lack of sputtering gun and the impossibility to study catalytic reaction in batch mode (as opposite to flow mode) due to the design of the small reactor (the leak to the RGA is after the pressure controller in the small reactor).

The partial pressure of each gas detected after the leak in the main circuit (fig. 2.30) by the residual gas analyser can be converted back to partial pressures in the reactor by assuming

(i) ideal gas behaviour (ii) homogeneous temperatures in the reactor and RGA chamber (iii) no gas selectivity through the leak, *i.e.* the ratio between the partial pressures after the leak is the same that in the reactor (iv) all gases are detected by the RGA (v) the ratio between the incoming gases flow is the same as the ratio between the partial pressures in the reactor in the absence of reaction. The partial pressure of argon, which does not partake in the reaction, is then used to compute the partial pressure of each gas in the XCAT chamber.

For example, at a reactor pressure of 0.5 bar, a total gas flow of 50 mL/min, a partial gas flow of NH_3 equal to 1 mL/min, and a partial gas flow of argon equal to 49 mL/min, the partial pressure of argon in the reactor is estimated to be equal to 490 mbar. The goal of the use of the mass spectrometer in this thesis is not to perform a quantitative analysis of the catalyst activity but rather to compare the evolution of the product partial pressures for different atmospheres, which is compatible with the setup.

Since this reactor was designed for SXRD together with a 6-circle diffractometer, the entire surface of the sample is accessible during the experiment, which allows the full access to the reciprocal space to probe any particular symmetry, limited only by the extent of the Ewald sphere (*i.e.* a maximum extent in $\vec{q}$).

Detectors

Different detectors can be accommodated on the diffractometer arm. On one hand, the MERLIN (Bewley et al. 2006) combines a small pixel size (55 µm) with a large array (512×512 pixels), few gaps, and a large dynamic counting range, similar to the MAXIPIX detector (Ponchut et al. 2011) which was first used for coherence experiments on the beamline (Schavkan et al. 2013; N. Li et al. 2020). The pixel size is of main importance when computing the oversampling requirements (sec. 2.6.2).

On the other hand, the XPAD detector (Basolo et al. 2005; Dawiec et al. 2016) is used for surface x-ray diffraction experiments, its pixel size is equal to 130 µm. Different detectors can be used that change the array size, respectively (540×130) for the XPAD70 and (540×260) for the XPAD140. The area covered by the detector is larger than with the MERLIN. The main advantages of the XPAD are its high dynamic range and highly programmable interface (Fertey et al. 2013), which can be programmed to work with automatic attenuators (Dawiec et al. 2016), crucial in SXRD when navigating between bulk and surface scattered signals.

2.8 Computer programs

With the upgrade of synchrotrons to more brilliant sources, BCDI beamlines (ID01 - ESRF, P10 - PETRA III, SixS and CRISTAL - SOLEIL, NanoMAX - MAX IV, 34-ID-C - APS) have received increasing attention from the scientific community. Imaging experiments yield larger and more complex data that far exceed the basic diffraction pattern (a reconstructed BCDI measurement consists of a complex array in 3 dimensions). In a general frame, the increase in flux at synchrotrons leads to quicker experiments, which in turn leads to an increased amount of data stored on the beamlines, often in different formats.

Data produced at synchrotron has reached a volume and complexity that can nowadays be considered as part of *big data* (Alizada et al. 2017; C. Wang, Steiner et al. 2018), referring to vast volumes, generated at high velocities, and from various sources. Big data becomes too complex or large to be processed and analysed using traditional tools or methods, originally written to simulate or fit reduced amounts of data. In the specific case of Bragg coherent diffraction imaging, new tools have been developed during this thesis (sec. 2.8.1, Carnis, Atlan et al. 2021; Simonne, Carnis et al. 2022) to help create a fast and reproducible workflow. Nevertheless, it is a more general way of working that must be adopted in synchrotrons to adapt and profit from the transition to big data (C. Wang, Steiner et al. 2018). This does not

only concern scientific analysis, but also the complexity of operating synchrotron beamlines, that could benefit from this transition to upgrade their performances (Agence Nationale de la Recherche 2023).

First, synchrotron data must be stored in a comprehensive format (e.g. *NeXuS* format, Könnecke et al 2015). The stored files must not only contain detector images, but routinely include all of the important metadata (informational data) to provide a more comprehensive and detailed view of the experiments.

Secondly, synchrotrons must offer high performance computing (HPC) clusters (C. Wang, Yu et al. 2021), and make the data available to their users through an interface compatible with the most common integrated development environment (IDE).

Finally, synchrotrons must either have an internal data analysis strategy, or trust their users to be able to upgrade and develop tools that, in a first stage, are able to handle large volumes of data. In a second stage, those tools can take advantage from that volume to uncover valuable insights (Boyu et al. 2016; Khaleghi et al. 2019). These insights can lead to new discoveries and enhance our understanding of complex phenomena, driving scientific progress.

Result reproducibility

At synchrotrons, where experimental techniques become ever more complicated, the first step of result reproducibility consists in the capacity for scientists to replicate experiments while obtaining consistent data. The data that stems from the experiment is also sometimes called *raw data*, which is then *reduced* (ordered and simplified, *e.g.* by phase retrieval in BCDI or integration in SXRD) and *analysed* to derive scientific *results*. The second step refers to the ability to replicate or re-run the data reduction and analysis processes from the raw data to obtain similar results. A *dataset* is then defined as a collection of data, *e.g.* in BCDI a dataset is constituted by the raw data, the detector mask, the measurement metadata, the retrieved Bragg electronic density, the displacement and strain arrays, and the data reduction parameters.

Achieving reproducibility with big data can be challenging due to the massive volume, velocity, variety and complexity of the data involved. However, linking reproducibility and big data is crucial for ensuring the credibility and reliability of the insights derived from large and complex datasets.

For example, it is possible to measure a single rocking curve in less than a minute at specialised BCDI beamlines, such as ID01 at the upgraded European synchrotron (S. J. Leake et al. 2019). The high complexity of the data reduction and analysis process in BCDI makes the replication of result complex for external scientists, that often do not have access to the same data reduction softwares, or to the value of the parameters used during the process.

Discussions about defining a set of rules that regulate research practice (Kretser et al. 2019), and reduce the grey zone that includes scientific misconduct at all levels of academia (Kornfeld et al. 2016) are growing, raising awareness on reproducibility in the scientific community.

Staggering numbers (Baker 2016) show that about 65 % of scientists in the field of physics and engineering struggle to reproduce others' results, and about 50 % fail to reproduce their own results. These numbers can sometimes be linked to very precise environments and techniques, with experimental conditions and processes difficult to replicate between different laboratories, or to knowledge transfer from academia to industry (Sarwitz 2015). However, according to the same study (Baker 2016), code availability, insufficient peer reviewing, and access to raw data contribute together to this issue. Moreover, it is largely accepted that the publishing industry has its own role to play by facilitating peer-reviewing to promote reproducibility (C. J. Lee et al. 2017).

Therefore, code-availability, access to raw data combined with metadata, and well-defined workflows are goals of utmost importance for experimental science (Munafò et al. 2017). Reproducible results lead to a global improvement of confidence in new techniques, such as BCDI, which could subsequently result in growth of interest and community. Key problems are for example the difficulty to reconstruct highly strained objects, or the determination of a metric that would allow scientists to *blindly* trust reconstructed data, permitting a fully automatised data reduction workflow. Reproducibility is first permitted by the use of a common data reduction and analysis environment.

Python in the *Jupyter* environment

The *Jupyter Notebook* environment (Perez et al. 2007; Kluyver et al. 2016) was chosen for the development of data reduction and analysis tools during this thesis for its versatile, user-friendly and browser-based interface. Notebooks can be used to take notes during experiments, shared in the *.ipynb* format or as *.pdf* documents. They allow the use of *Python*, an accessible programming language that has gradually become one of the most popular, versatile (Perez et al. 2007; Behnel et al. 2011; Newville et al. 2016; Ronaghi et al. 2017), and widely-taught (Ayer et al. 2014; Scopatz et al. 2015; McKinney 2017; Boulle et al. 2019) programming languages in science.

Moreover, *Jupyter Notebook* has proven to be an effective tool for the reduction and analysis of synchrotron data in terms of graphical user interface (GUI) (Martini et al. 2019; Simonne, Martini et al. 2020), but also in terms of supporting scientific communities looking for high-performance frameworks (Yin et al. 2017; Glick et al. 2018; Milligan 2018; Stubbs et al. 2020).

Large scale facilities and institutions seek ways to provide remote-access to high performance computing services for their users, which combine existing solutions in an interactive and user-friendly environment. To simplify the data reduction and analysis pipelines in fourth-generation synchrotrons, it is of critical importance to offer the possibility for external users to analyse raw data remotely, with access to computational environments. *Jupyter* (`https://jupyter.org/`) is particularly advantageous and was chosen by several institutions for such purposes, *e.g.* Google (Google Colab), the EGI federation, or the European Synchrotron.

Remote access to high performance computational environments, interfaced with *Jupyter Notebook* or *JupyterLab*, is provided by *JupyterHub*. For example, specific hardware such as graphical processing units (GPUs), mandatory for accelerated phase retrieval with *PyNX*, can be managed with *JupyterHub*. Researchers can create their own work-spaces, with direct access to tailored computational environments, while relying on system administrators that can efficiently manage complex environments accessible for all users. Remotely accessing data avoids storage issues, which can quickly become problematic with current experiments. Note that in the latest version (*Jupyter Notebook 7* 2023), real-time collaboration (RTC) will be supported, which also pushes *Jupyter Notebook* forward as a tool for laboratory notebooks.

2.8.1 *Gwaihir*

BCDI relies on iterative algorithms to solve the phase lost during the measurement (I. Robinson et al. 2009). A 3D intensity distribution in the vicinity of a Bragg peak (stack of diffraction patterns forming a 3D reciprocal space map with the proper sampling) is collected from a sample illuminated with coherent light (I. K. Robinson, Da et al. 2005), and serves as input for phase retrieval.

There are three main steps to compute the strain, detailed in fig. 2.31. The raw data must first be pre-processed. It can then be inverted *via* phase retrieval, the phase containing structural information about the sample that are lost during the measurement. Finally, it is

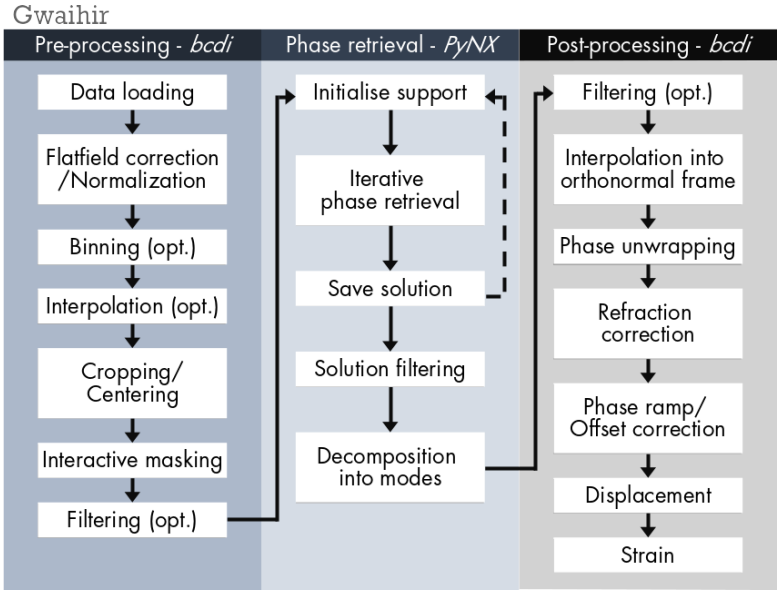

Figure 2.31: Flow chart illustrating the main steps in the BCDI data reduction workflow. Gwaihir links the bcdi and PyNX packages via its graphical user interface and command line scripts, resulting in a complete and understandable workflow. Opt. stands for optional.

possible to extract information on the physical state of the particle such as its shape or internal strain from the images after post-processing. Several software packages were developed to solve these steps but none bring a comprehensive pipeline from start to finish.

For example, *PyNX* (Favre-Nicolin, Coraux et al. 2011) focuses on the phase retrieval step, *bcdi* (Carnis, Atlan et al. 2021) on data pre-processing and post-processing, while *Cohere* (Frosik B. 2021) focuses on pre-processing and phase retrieval. A few graphical user interfaces also exist, such as *Cohere* (Frosik B. 2021), *Phasor* (Dzhigaev 2021), and *Bonsu* (Newton, Nishino et al. 2012). Providing a workflow will reduce the time spent on data reduction for newcomers, and improve results reproducibility by facilitating sharing while keeping track of parameters and metadata.

Gwaihir is a tool developed during this thesis, which brings together the *PyNX* and *bcdi* packages, binding them in a graphical user interface built for the *Jupyter* framework (Kluyver et al. 2016). It provides an interface to the bleeding edge of data reduction in BCDI, and can be used both locally or remotely, offering an interactive and user-friendly interface with complex functionality satisfying both beginners and experts.

Gwaihir works with *Python* 3.9 and is licensed under the GNU General Public License v3.0. The source code as well as the latest developments are available on GitHub, while each stable version is released on the *Python* Package Index (PyPi), along with its documentation.

Workflow for Bragg coherent diffraction imaging

Gwaihir offers an interactive workflow meant to be reproducible, and resulting in the phase and amplitude of the probed object (fig. 2.32). To illustrate this, the results of the following procedure on a dataset collected at the P10 beamline in at PETRA III are shown in fig. 2.33 (CXI dataset ID 195).

Pre-processing

Data pre-processing aims at improving the quality of phase retrieval by optimising the size and content of the 3D array used as input (Oztürk et al. 2017). The minimal processing consists in loading the raw data and stacking it together as an input for the phase retrieval.

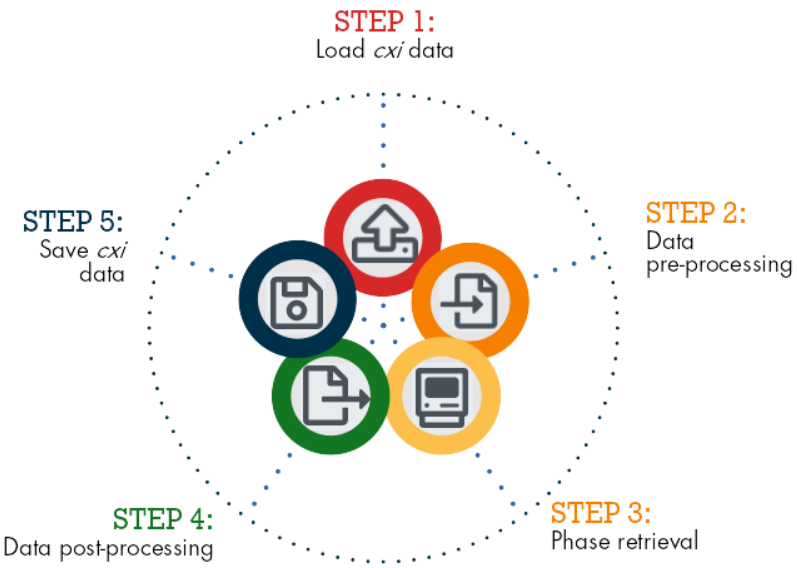

Figure 2.32: Workflow steps taken in Gwaihir; the circular workflow illustrates result reproducibility, a key concept, facilitated by using the cxi architecture.

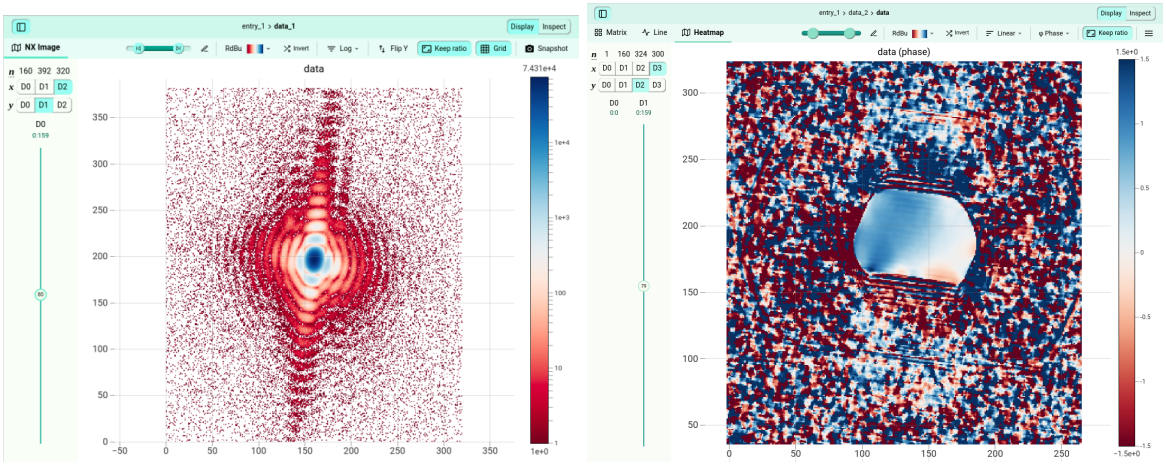

Figure 2.33: A 2D slice of a 3D coherent diffraction pattern is shown (left). The phase of the Bragg electronic density (rad) *of the reconstructed object is shown (right), the facets are clearly visible. Image displayed via JupyterHub. The particle is* 300 nm *wide.*

Intermediate optional steps can be added *via* a YAML (YAML Ain't Markup Language) configuration file.

Once the raw data is collected, different pre-processing parameters can be modified to optimise the 3D diffraction intensity. For example, the array must be centred for the Fourier transforms, the centre is either fixed manually as the centre of the Bragg peak if known, or determined as the centre of mass of the 3D array during the reduction process. The array can also be cropped to reduce its size and decrease the computing time during phase retrieval by removing the points furthest from the Bragg peak where the signal-to-noise ratio is low (fig. 2.33).

It is important to create a detector mask prior to the experiment to correct the raw data for hypothetical hot-pixels and uneven background. Moreover, it is also possible to correct the raw data image by image for spurious data which taints the diffraction pattern. For example, it is possible, while recording the 3D diffracted intensity of a given reflection, to have signal coming either from the substrate or from neighbouring objects that will be summed to the probed object's intensity.

Finally, it is possible to normalise the raw data by an intensity monitor, or compute the

scattering vector $\vec{q}$ of the measurement, from the instrumental geometry and parameters.

Aside from the specific details of the experimental setup (diffractometer and setup geometry, detector type, file system), the majority of the data reduction process is beamline-independent (D. Yang et al. 2019). Based on this observation, *bcdi* leverages inheritance and transforms the raw data to a common data format used for phase-retrieval (fig. 2.31). It frees the user from having to learn or remember the technical details for each beamline and sets a common strategy across beamlines.

Phase retrieval

To retrieve the phase from the diffracted intensity, *PyNX* functions with different iterative algorithms (Gerchberg et al. 1972; Fienup 1982; Fienup 1978; Marchesini 2007; Favre-Nicolin, Girard et al. 2020). *PyNX*'s recent update includes mathematical operators (Favre-Nicolin, Girard et al. 2020) which represent most of the reconstruction operations traditionally used in phase retrieval, and is at the foundation of quick and interactive phase retrieval in *Gwaihir*. Indeed, state-of-the-art GPUs available onsite where data collection occurs enable almost real time data reduction. This results in quick visualisation of the probed object's amplitude and phase, offering the possibility to optimise data acquisition during the experiment. Such live feedback is critical to the success of an experiment, and provides broader opportunities in the type of experiments that can be carried on.

The different parameters such as e.g. the support threshold, the number of iterations for each algorithm, the object initialisation procedure (square, sphere, auto-correlation, ...) can be modified in the GUI (fig. 2.34). Initial guesses are given for each parameter but must be refined by the user to optimise the results. The impact of each parameter can be viewed directly in the GUI after phase retrieval. This allows to refine the phase retrieval input parameters before submitting a *batch job*, that will spawn a sub-process on the computing cluster for phase retrieval. This highly optimised procedure can yield dozens of solutions in a few minutes.

With well-tuned parameters and high quality datasets, phase retrieval converges towards the same solution, but with minor differences between each reconstructed object, related to the phase retrieval process. The most important limiting factors for the convergence of the reconstruction algorithms are the quality of the measurement, and the amount of strain going through the particle. In the case of highly strained object, part of the intensity will be scattered in a direction that does not fit the area collected by the detector, resulting in void areas inside the reconstructed electronic density. Moreover, the support becomes very difficult to determine since the diffraction intensity does not correspond to the lattice factor anymore.

Gwaihir provides a wide range of selection criteria to find the best solution. Each reconstructed object has a list of final attributes that can be used as a criterion for selection, such as the free log-likelihood (Favre-Nicolin, S. Leake et al. 2020) or the standard deviation of the modulus of the reconstructed object. In the case of crystallographic defects, specific metrics (Chi, Sharp, Max volume, ...) were derived that perform best depending on the type of defect in the object (Ulvestad, Y. Nashed et al. 2017). Following the selection criterion, it is possible to quickly identify the solutions of poor quality that must be ignored to create a set of best solutions. *PyNX* then offers a method that merges this set into a single solution by computing eigen-vectors for the selected solutions (Favre-Nicolin, Girard et al. 2020). An alternative approach also available in *Gwaihir* is to take the average of the best solutions (Ulvestad, Cho et al. 2014).

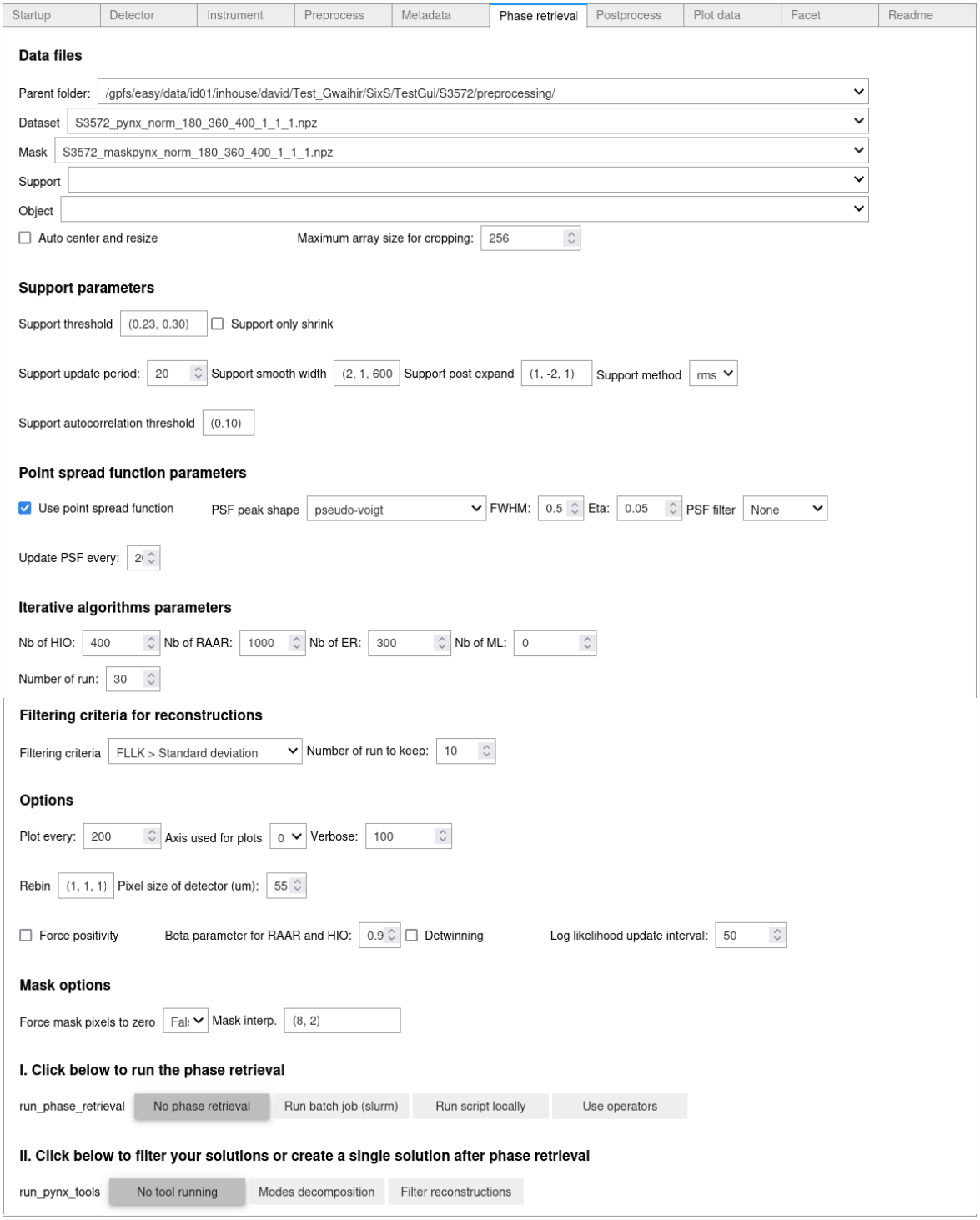

Figure 2.34: Phase retrieval tab in Gwaihir. Parameters are separated into groups (files, support, point-spread function, algorithms, ...) and detailed in the Readme tab. The object can be reconstructed through a batch job, submitted to the computing cluster in the backend, or with operators, that will plot the evolution of the reconstruction object in the Notebook.

Post-processing

Post-processing regroups methods applied to the complex output of the phase retrieval. Once the solution with the best figure of merit is selected, it is possible to use the *bcdi* scripts to process the object. If the data is still in the detector frame (geometric transformation not applied during pre-processing), the data can be interpolated in the orthogonal laboratory

frame ($\vec{z}$ downstream, $\vec{y}$ vertical up, $\vec{x}$ outboard) or in the sample frame ($\vec{z}$ out-of-plane, $\vec{y}$ perpendicular to the beam, $\vec{x}$ parallel to the beam) using a transformation matrix. This allows an easier comparison between the object's evolution when probing different Bragg reflections (Lauraux, Labat et al. 2021). The correct beamline and instrumental parameters must be selected (*e.g.* sample-detector distance, probing energy, detector pixel size, *etc*...), usually constant throughout the experiment. The geometric transformation can be realised using either the transformation matrix (M. Pfeifer 2005) or the *xrayutilities* package (Kriegner et al. 2013), depending on which reference basis is needed.

After phase unwrapping, a refraction and absorption correction are optionally applied, and possible phase ramp and phase offset are removed. At this point the displacement and the strain component are calculated from the phase. The phase origin can first have an impact when comparing the lattice displacement between different reconstructions (Atlan et al. 2023). In the case of weak strain, it can be sufficient to consider the centre of mass of the object as the origin of phase. However, this can become quite complex in the case of defects or defaults in the object. Special methods are defined to target this issue in *bcdi*. For example, Guizar-Sicairos et al. (2011) and Hofmann et al. (2020) proposed a convenient method for the numerical calculation of phase gradients in the presence of phase jumps.

Graphical interface

Gwaihir links in a unique user-friendly and interactive GUI the aforementioned packages, whilst offering 2D/3D browser-based data visualisation tools. Therefore, the main purpose of *Gwaihir*, is to offer a possibility for the user to work solely in the *Jupyter* environment. The graphical user interface is divided into 10 tabs, aiming to achieve a comprehensible but fluid workflow, whilst still separating each step. A final *Readme* tab contains information about the different methods and parameters used in the workflow, as well as a tutorial on the GUI.

Jupyter natively offers multiple options for interactive data plotting. Most of the figures displayed in the GUI are based on the *matplotlib* package (Hunter 2007). For example, it is possible to select a list of 3D complex data arrays, and to visualise 2D slices in each dimension of their amplitude or phase, with different colour-maps (diverging, sequential, cyclic) and scale (linear, logarithmic).

Moreover, an interactive 3D visualisation tool is provided that relies on the *ipyvolume* library (Breddeld 2021), itself built on top of *ipywidgets*, and specifically designed to quickly render large 3D data arrays. In the specific case of single volume rendering for the reconstructed object, the object's surface is defined by a threshold of its maximum density (fig. 2.35). The object surface can be colour-mapped with the values of the displacement and strain retrieved during the data reduction.

More complex interaction with figures and images (*e.g.* zoom, set the colorbar range) is implemented with *Bokeh* (Bokeh Development Team 2018), a *Python* library that transforms figures in interactive web-pages (fig. 2.36), that can also be displayed in *Jupyter Notebook*.

Command line scripts

The complete workflow for data processing can also be launched from the command-line using *Python* scripts, whereas the link between each package is based on *BASH* scripts. This approach is both fast and versatile, designed to quickly iterate on several datasets to test parameters values, but less intuitive compared to the interactive GUI.

A set of default parameters stored in a configuration file is used, that can also be overwritten by directly providing keywords directly in the command line. For example, the same file can be used for different measurements by just changing the scan number in the command. The configuration files are written in *YAML* (fig. 2.37).

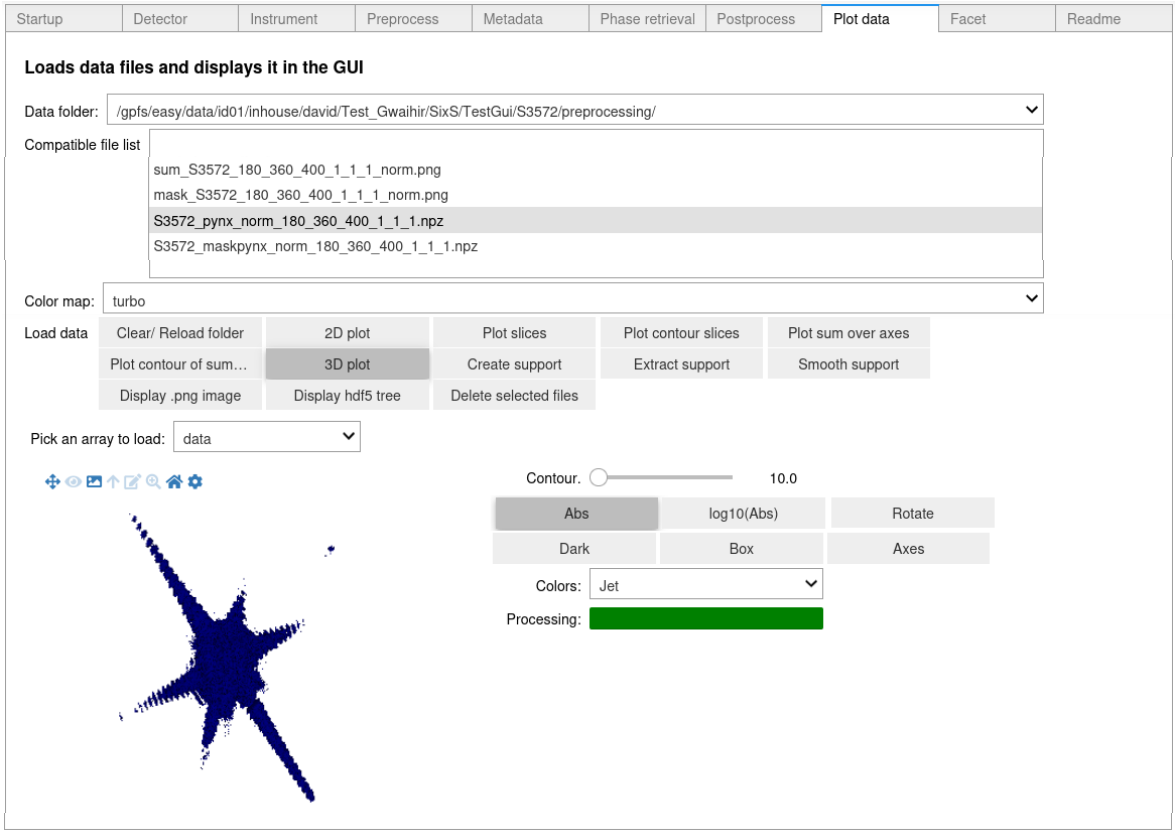

Figure 2.35: Visualisation tab in Gwaihir. The selection of the data array, the colormap, and the contour of the resulting 3D object are performed through different widgets.

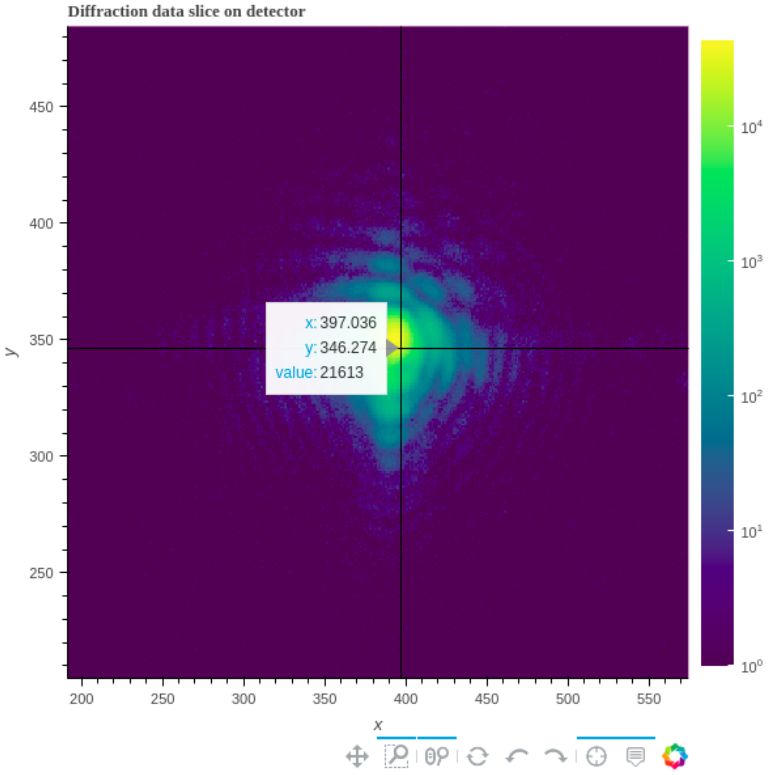

Figure 2.36: Detector images can be viewed interactively with Bokeh, to zoom on the data, and visualise, for example, the intensity collected on each pixel.

```yaml
scan: 1968
reconstruction_file: "result_1.cxi"
phasing_binning: [3, 1, 1]
preprocessing_binning: [1, 1, 1]
data_frame: "detector"
ref_axis_q: "y"
save_frame: "lab_flat_sample"
simulation: False
invert_phase: True
flip_reconstruction: False
setup:
    beamline: "P10"
    rocking_angle: "inplane"
    sdd: 1.818
    energy: 11294
    beam_direction: [1, 0, 0]
    sample_offsets: [0, 0, 0, 0]
    tilt_angle: 0.003
    direct_beam: [1340, 876]
    dirbeam_detector_angles: [0, 0]
    outofplane_angle: 40.0
    inplane_angle: 5.0
saving:
    save_rawdata: False
    save_support: False
detector:
    detector: "Eiger4M"
    roi_detector: [626, 1126, 1125, 1625]
phase_processing:
    phase_ramp_removal: "gradient"
    threshold_gradient: 1.0
    phase_offset: 0.0
    offset_method: "mean"
    isosurface_strain: 0.3
    strain_method: "default"
data_visualization:
    strain_range: 0.002
    phase_range: 3.142
    grey_background: True
    tick_spacing: 100
    tick_direction: "inout"
    tick_length: 3
    tick_width: 1
apodization:
    half_width_avg_phase: 1
    apodize: True
    apodization_window: "blackman"
    apodization_mu: [0.0, 0.0, 0.0]
    apodization_sigma: [0.3, 0.3, 0.3]
    apodization_alpha: [1.0, 1.0, 1.0]
```

Figure 2.37: Configuration file in YAML, a human-readable data-serialisation language with a minimalist syntax. A configuration file is generated for the pre-processing and post-processing scripts, as well as for the phase retrieval.

The CXI database

Raw and processed data can both be accessed for the BCDI technique through the *.cxi* database (https://cxidb.org/, Maia 2012), which aims at creating a single data-storing architecture/format for coherent X-ray imaging experiments. The data input/output follows Nexus definitions (Könnecke et al. 2015). Both clarity and consistency in data formatting encourages the reproducibility of the science produced (https://www.panosc.eu/) and guarantees the workflow.

Since not all beamlines provide self-explaining NeXuS datasets, it is the *bcdi* package together with *xrayutilities* (Kriegner et al. 2013) that allows the support of most of the coherent imaging beamlines: ID01 (ESRF), P10 (PETRA III), SixS and CRISTAL (SOLEIL), NanoMAX (MAX IV) and 34-ID-C (APS). Data pre-processing will generate two files stored as NumPy arrays (Van der Walt et al. 2011), corresponding to the diffraction intensity and mask. These two files are then used for phase retrieval, for which the final object is saved in a *cxi* file, later used for data post-processing. In the case of simulation, the simulated diffraction intensity can be stored as a NumPy array to start the workflow from phase retrieval.

In *Gwaihir*, results sharing across teams and team members is facilitated by the creation of a single output file, respecting the *CXI* (Maia 2012), and thus the NeXuS (Könnecke et al. 2015) architecture (fig. 2.38), which pushes towards results reproducibility.

Key parameters are the transformation matrix used for the interpolation in the final frame, the voxel size of the resulting 3D array, the probed reciprocal space range after data pre-processing ($\delta q_x, \delta q_y, \delta q_z$), the iso-surface threshold, *etc.* Comments or metadata, such as the horizontal and vertical coherence lengths, or beam size, if determined prior to the experiment, can also be saved. The aim is first to have a comprehensible architecture, and secondly to be able to reproduce anyone result from a *single file*. On a small scale, results are easier to share between collaborators and more understandable, while on a larger scale peer-review is facilitated.

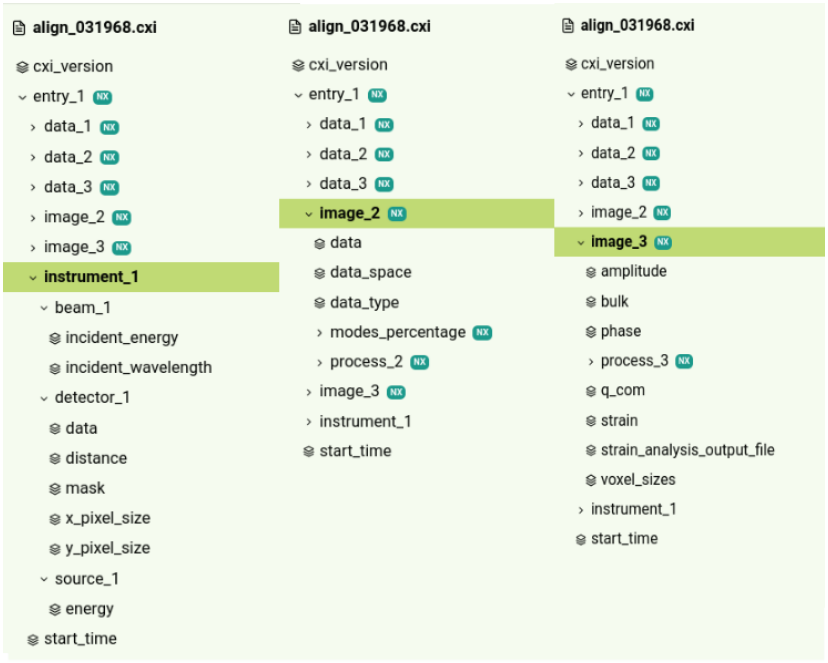

Figure 2.38: Each parameter value used during the workflow is stored in the same .cxi file, along with the results, in a nested architecture, displayed via JupyterHub. instrument_1 regroups parameters associated with the instrumental setup. data_1 is the collected diffraction pattern. image_2 regroups the parameters associated with phase retrieval. data_2 is the reconstructed Bragg electronic density chosen for post-processing. image_3 regroups parameters linked to data processing, as well as the processed amplitude, phase and resulting strain. data_3 is a link to the processed phase of the object.

2.8.2 BINoculars

BINoculars (Roobol et al. 2015) is a data reduction software used to concatenate the scattering intensity from successive angular scans. It can also be used to optionally change the data's reference frame (e.g. from angular space to q space). Those two steps can be performed simultaneously by assigning to each voxel of the 3D scattered intensity a position in the new frame. From subsequent scans, it is possible that each position in the new frame was scanned multiple times, meaning that there were multiple contributions (possibly with different intensity attenuation correction) to the total scattered intensity at that position. The correct intensity is therefore the division of the total scattering intensity in each voxel by the number of contribution to that voxel (eq. 2.63). If there are no contributions, the intensity is set to NaN (Not a Number).

$$Intensity = \begin{cases} counts\,/\,contributions & \text{if contributions} \neq 0 \\ NaN & \text{if contributions} = 0 \end{cases} \tag{2.63}$$

Different orthonormal frames can be of interest when analysing the data, the q-space (q_x, q_y, q_z) is useful to index Bragg peaks and to access the related inter-reticular spacing d_{hkl}. Different lattices can be used to highlight the difference of geometry between the bulk structure and the surface structure (fig. 2.39).

The reciprocal space in-plane maps collected during surface x-ray diffraction experiments are usually projected perpendicular to l (or q_z), to show possible Bragg peaks from surface reconstruction (fig. 2.39). They contain the sum of the scattering intensity in a small out-of-plane layer δl (or δq_z). It is of utmost importance to select a thin layer to not drown the surface signal with the background or bulk signal.

BINoculars also contains a sub-module (*fitaid*) that allows the integration of the scattered intensity in the reciprocal space as a function of one axis. Usually, to study the evolution of

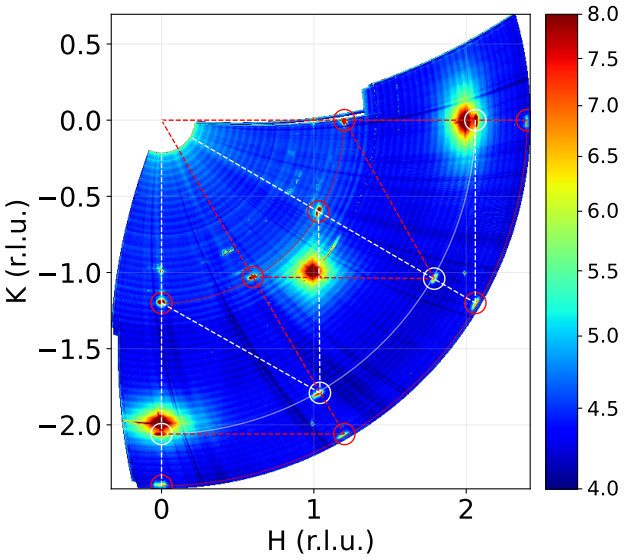

Figure 2.39: Reciprocal space in-plane maps. The large high intensity peaks are Bragg peaks from the bulk structure, the low intensity peaks are from surface structures. The map is computed using a cubic unit cell, two hexagonal unit cells corresponding to the surface structures are drawn as diamonds.

crystal truncation rods, the data is projected either in the (h, k, l) or (q_x, q_y, q_z) frame and then integrated in a square area around the CTR signal as a function of l or q_z (fig. 2.40).

The voxel size in each direction is set through a parameter, which raises a compromise between array size, resolution, and an interpolation process. Moreover, to compare different maps, it is better to use the same resolution so that the intensities of the different signals are on the same scale.

When in the (q_x, q_y, q_z) space, it is possible to go as low as $0.005\,\text{Å}^{-1}$ in each direction, the limit being set by instrumental parameters such as the detector pixel size, the amount of angular scans performed, the counting time, or the number of iteration per scans (and by the computer memory when computing or visualising the final space).

If the number of iteration is too low for the desired resolution, the process will yield an image with empty areas corresponding to voxels where no data could be recorded. This is often the case during the collection of crystal truncation rods, at high values of l, since the region probed by the detector becomes thinner in l with every iteration (sec. 2.5.3 - Drnec et al. 2014). To avoid having to rely on an interpolation to fill these voxels, it is better to use a larger resolution when concatenating the images, and then to use the same step when integrating the data.

To quantitatively compare the integrated intensity with simulated structure factors, it is mandatory to subtract the background intensity from the total intensity. The background is calculated by taking the sum of all the values of selected background regions (fig. 2.40), around the CTR, corrected by the number of voxels in those area. The average background value per voxel is then subtracted to each voxel in the CTR region of interest (ROI), the structure factor F can then be computed as follows:

$$|F|^2 \propto I_{roi} - \frac{N_{roi}}{N_{bkg}} \times I_{bkg} \tag{2.64}$$

I_{roi} is the integrated intensity in the ROI, N_{roi} the number of voxels in the ROI, I_{bkg} the integrated background intensity, and N_{bkg} the number of voxels in the background.

A very fine resolution (e.g. $0.005 \times 0.005 \times 0.05$) will result in extremely large arrays that can be difficult to manipulate on low resources computer. For example, the maps shown in

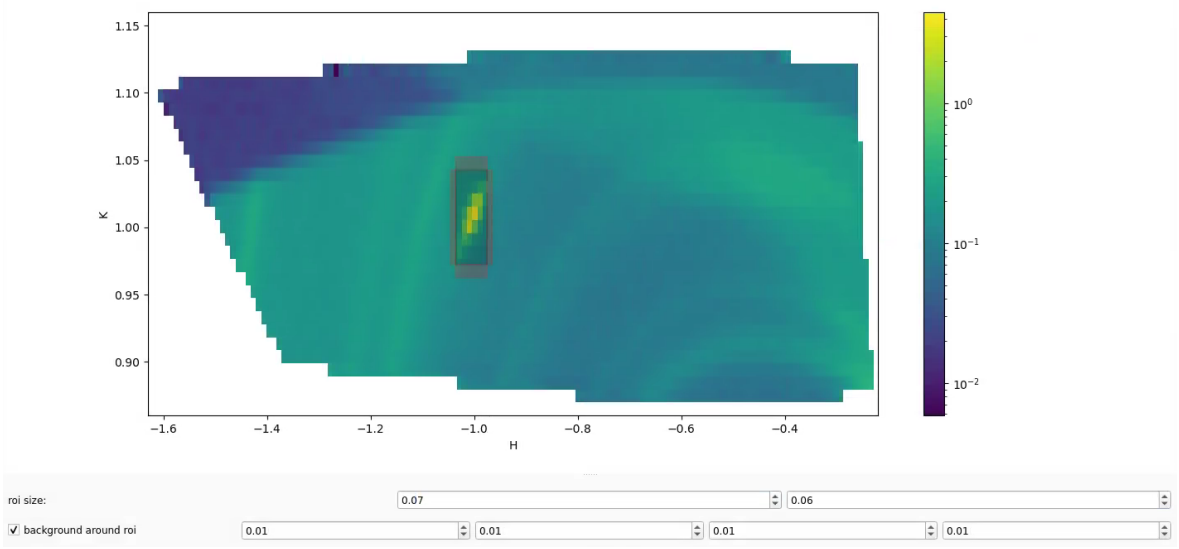

Figure 2.40: Graphical user interface for the fitaid module of BINoculars. The CTR structure factor is computed using eq. 2.64 in a rectangular region of interest around the CTR signal. Four rectangular regions of interests around the signal are used to compute the background.

fig. 2.39 have a three dimensional shape equal to $(560 \times 953 \times 39)$ which results in 2.1×10^7 voxels in the array. Originally, this corresponds to the concatenation of 40 angular scans, each with 1010 steps, *i.e.* containing 1010 2D detector images that have a shape equal to (240×560). This represents 5.5×10^9 pixels to process together to create such in-plane maps. High performance computing clusters are therefore needed for the reduction of surface x-ray diffraction data with BINoculars, the data analysis is performed in a second step with programs such as *ROD* (Vlieg 2000).

2.8.3 *ROD*

Part of the aim of SXRD data analysis can be to comprehend the 3D structure of potential surface layers on top of the sample surface, as well as the magnitude of surface relaxations on its topmost layers. Such information can be extracted by combining in-plane reciprocal space maps and crystal truncation rods, *i.e.* by comparing the position and intensity of the scattered intensity (and structure factor) in reciprocal space with simulated data.

The primary challenge associated with surface x-ray diffraction lies in the complexity of data analysis, as researchers are limited to a small portion of the reciprocal space due to the extended data acquisition time (Gustafson et al. 2014). On one hand, a fine sampling of the reciprocal space will take hours which is hardly compatible with time-resolved experiments. On the other hand, skipping areas of the reciprocal space could result in missing critical information if the symmetry of the surface structure is not known prior to the experiment. For high symmetry structures, a small portion of the reciprocal space can sometimes be sufficient to have a final solution. The typical approach for time-resolved experiments is to follow the intensity of a surface signal as a function of time.

ROD is a computer program written by Vlieg et al. (2000), that can be used qualitatively to simulate structure factors from a given structure, and quantitatively to refine the atomic positions within the structure by fitting the structure factors with the experimental data. Since *ROD* is written in *C* and does not come with a graphical user interface, alternatives have been developed such as GenX (Björck et al. 2007; Glavic et al. 2022) written in *Python* which mostly focuses on reflectivity. In the frame of this thesis, *ROD* was chosen for the analysis of SXRD data.

The structure of our crystal must be understood as follows when working with surfaces,

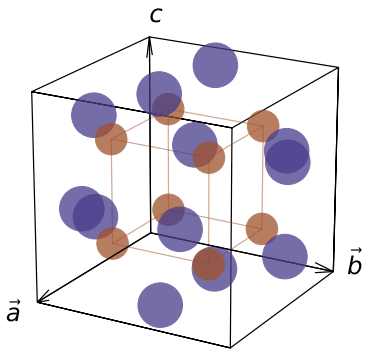

Figure 2.41: Pt_3O_4 bulk unit cell. Platinum atoms are situated on the faces on the cubic unit cell (e.g. $(0, 1/2, 1/4)$, $(0, 1/2, 3/4)$), while the eight oxygen atoms are inside the unit cell at the positions $(1/4, 1/4, z)$, $(1/4, 2/4, z)$, $(2/4, 1/4, z)$, $(2/4, 2/4, z)$ for $z = 1/4$ and $z = 3/4$.

infinite in both in-plane dimensions, finite in the out-of-plane dimension. The origin of the out-of-plane axis, commonly denoted $\vec{z}$, is situated at the surface of the crystal. When z is negative the *bulk* structure of the crystal is described, whereas when z is positive, the *surface* structure of the crystal is described, usually only a few atomic layers thick where e.g. surface relaxation and reorganisation effects can be detected.

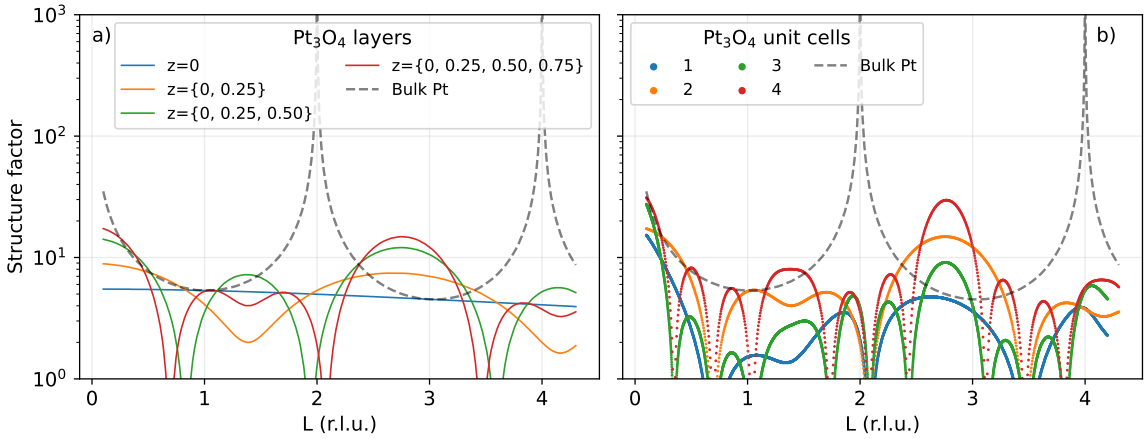

Figure 2.42: Simulation of out-of-plane structure factors computed with ROD. Different layers within a single unit cell of Pt_3O_4 are used in (a), while a different amount of the same Pt_3O_4 unit cell is used in (b). Contribution from Pt_3O_4 are most important in the anti-Bragg region.

Additional surface layers can be present on top of the main crystal structure, the example of a Pt_3O_4 platinum oxide is presented in fig. 2.42. At least two layers in $\vec{c}$ are necessary to see a modulation of the out-of-plane signal, the Bragg peaks linked to the presence of a bulk oxide start to be clearly visible after 4 unit cells of Pt_3O_4 are present on the platinum surface. The unit cell of Pt_3O_4 is presented in fig. 2.41.

In a second step, it is possible to refine the position of each atom in the unit cell to take into account possible strain along $\vec{c}$, that will have a significant effect in the shape of the crystal truncation rods as shown previously in fig. 2.13. The structure along $\vec{c}$ is refined by computing the shape of crystal truncation rods, and comparing them with experimental data. The more rods measured, and the higher the extent of each rod in L, the more accurate the final structure.

Chapter 3

Pt nanoparticles during ammonia oxidation

3.1 Introduction

During the catalytic oxidation of ammonia, Pt catalysts were first used when aiming at the production of nitrogen oxide for the Ostwald process, Pt-Rh catalysts have then proven to be more effective since the 1920s (Handforth et al. 1934; Heck, Bonacci et al. 1982). Recently, the ammonia oxidation reaction over a $Pt_{25}Rh_{75}(001)$ single crystal was studied with a surface science approach, by combining *operando* techniques such as near-ambient pressure X-ray photoemission spectroscopy (NAP-XPS) and surface x-ray diffraction (SXRD) with mass spectrometry (Resta et al. 2020). It was shown that NO production coincides with significant changes of the surface structure, and the formation of a RhO_2 surface oxide. Moreover, changes in the surface relaxation related to the catalyst selectivity were reported.

Using single crystals as model catalysts to understand *in situ* and *operando* the structure-activity relationship offers some advantages. For example, the large surface area increases the surface signal. It is also possible to isolate specific facets to progressively build up the understanding of the role of the sample surface on the catalytic activity (Hejral, Mu et al. 2016; Resta et al. 2020). However, single crystals fall short when aiming at closing the material gap since they only exhibit a single crystallographic orientation on their surface, and are much larger (almost a cm large) than the width of Pt-Rh gauzes used for the oxidation of ammonia (few 10s of µm large, Kaiser 1909).

To reduce the material gap in heterogeneous catalysis, nanoparticles can be used, approaching the size of individual grains on the industrial catalysts, and exhibiting many different types of facets on their surface. Therefore, the catalytic structure-activity relationships of Pt nanoparticles will be investigated during the oxidation of ammonia, as a stepping stone to the study of Pt-Rh nanoparticles. Pt-Rh nanoparticles have recently been successfully studied with BCDI during the CO oxidation (Y. Y. Kim et al. 2021), but the presence of compositional strain in bi-metallic catalysts makes the study of surface strain increasingly complex (Kawaguchi, Keller et al. 2019).

It is first intended to measure the signal scattered from α-Al_2O_3 (sapphire) supported platinum particles by taking advantage of the possibility to carry out grazing-incidence diffraction measurements at the SixS beamline. At grazing incidence, the beam footprint occupies a large ratio of the sample surface, covered by nanoparticles. The scattered beam is then proportional to their average behaviour (Nolte et al. 2008; Hejral, Vlad et al. 2013; Hejral, Mu et al. 2016).

As seen in the previous chapter, surfaces give rise to crystal truncation rods (CTR) in the reciprocal space, the intensity of which is related to the facet size, roughness and atomic structure. The average nanoparticle shape and structure will be probed by studying the

intensity of crystal truncation rods in directions perpendicular to the expected facets on the nanoparticle surface. Prior experiments with similar samples (Dupraz, Beutier et al. 2017; N. Li et al. 2020; B. Lim et al. 2021; Dupraz, N. Li et al. 2022) have shown that the particles exhibit a Winterbottom shape (Winterbottom 1967; Boukouvala et al. 2021), typical of nanoparticles epitaxied on a substrate, with mainly {111}, {110}, and {100} facets, and a [111] orientation perpendicular to the substrate.

By having the incident beam illuminating multiple particles, the CTR signals in e.g. the [111] direction is the sum of the contribution from the (111) facet of every illuminated nanoparticle (as well as their $(\bar{1}\bar{1}\bar{1})$ facets). Therefore, phenomena inducing structural change such as particle re-faceting/reshaping at a given condition are expected to be visible by an evolution of the different CTR.

With Bragg coherent diffraction imaging (BCDI), the individual three-dimensional (3D) structural response of *isolated* nanoparticles to changes in the gas mixtures will be measured under reacting conditions. The same reaction conditions will be used in both experiments. *Operando* analysis of the nanoparticles properties (size, shape, strain, re-faceting, support interaction, oxide formation, *etc.*) are essential to better understand their behaviour during the catalytic reaction.

However, it must first be ensured that the nanoparticles do not move, or change their epitaxial relationship with the substrate during the oxidation reaction. Indeed, in a BCDI experiment, the beam is reduced to micrometric size, and nanoparticles movements will prevent good quality measurements. Thus, the SXRD experiment will also aim at resolving the evolution of the epitaxial relationship between the Pt nanoparticles and the Al_2O_3 substrate.

3.1.1 α-Al_2O_3 supported Pt nanoparticles synthesis

The platinum nanoparticles were grown by the Israel Institute of Technology (Technion, collaboration with Dr. Eugene Rabkin). A first use is showcased in the work by Dupraz et al. (2017).

Two different samples are used in this thesis. To obtain a more important scattered intensity with SXRD, the first sample's surface is homogeneously covered with Pt particles, 100 nm to 1000 nm large. For the second sample, a mask is applied during the lithographic process route to ensure that the platinum layer transforms to isolated nanoparticles (fig. 3.1), thereby avoiding alien signal coming from neighbouring nanoparticles with BCDI. The second sample is also called *patterned* sample. Dewetting is obtained by annealing at 1100 °C for 24 h, that also guarantees a good re-crystallisation of the particle.

In the patterned sample, single nanoparticles are located in the middle of squares (fig. 3.1). The position of the squares is designated with Arabic numbers (row), letters (column) and Roman numbers (large rectangle). All of the position indicators are constituted of platinum nanoparticle as well, which allows the mapping of the sample's surface in Bragg condition to find the nanoparticles' positions (fig. 2.27).

The epitaxial relationship between the platinum nanoparticles and the α-Al_2O_3 substrate has been shown to consist of Pt {111} planes on top of the α-Al_2O_3 (0001) surface (fig. 3.2 - Farrow et al. 1993). This arrangement can be described with the following matrix, α-$Al_2O_3(0001)$-$\begin{pmatrix} \sqrt{3} & 0 \\ 0 & \sqrt{3} \end{pmatrix}$-R30°.

Lattice strain in diffraction is usually defined as the difference between the reference and experimental lattice parameter values, respectively a_{ref} and a (eq. 3.1).

$$\epsilon = \frac{a - a_{ref}}{a_{ref}} \tag{3.1}$$

In this case, when computing the misfit strain, *i.e.* the strain induced in the Pt nanoparticles by the substrate due to slightly different hexagonal lattices, the reference lattice

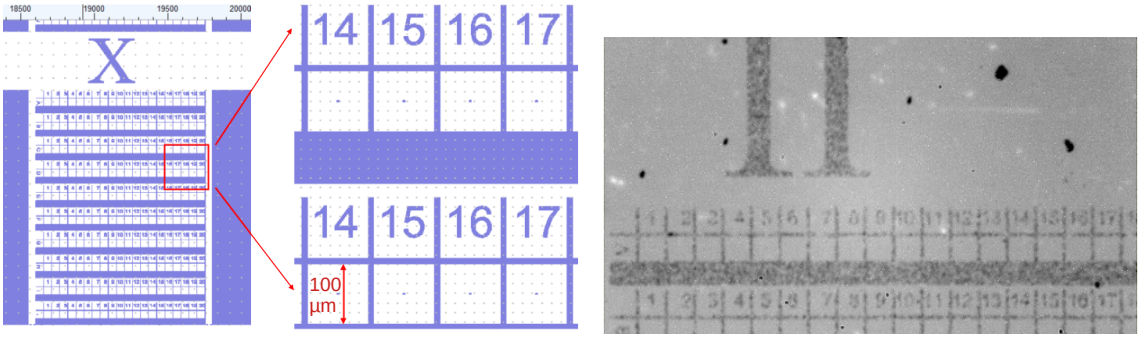

Figure 3.1: Mask applied during sample preparation (left) and resulting pattern on the sample surface observed with an optical microscope (right).

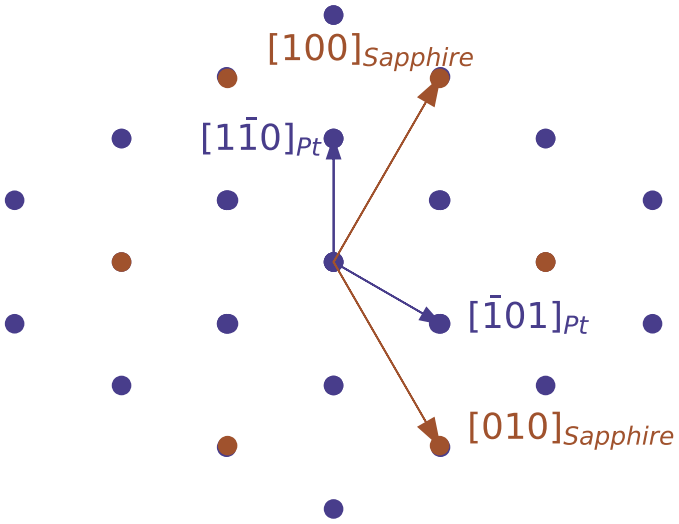

Figure 3.2: Epitaxial relationship between {111} Pt planes and [0001]-oriented sapphire substrate.

parameter is equalled to the in-plane lattice parameter of sapphire, $a_{Sapphire} = 4.76\,\text{Å}$. The lattice parameter of the larger hexagonal arrangement of the platinum atoms on the (111) surface is equal to $\sqrt{3}a_{Pt}/\sqrt{2}$. At room temperature, the misfit strain computed from literature values, $a_{Pt} = 3.92\,\text{Å}$ (Waseda et al. 1975), is equal to $\epsilon = 0.86\,\%$. To fit on the (0001) sapphire surface, the platinum atoms at the interface are expected to suffer compressive in-plane strain.

3.1.2 Catalysis reactor for near-ambient pressure *operando* studies

The catalytic activity of the platinum nanoparticles was first studied as a function of the temperature to (i) be certain that the sample is sufficiently catalytically active for the reaction products to be detected by the mass spectrometer, (ii) identify the catalyst light-off temperature and (iii) observe an evolution of the product selectivity as a function of the temperature. Similar measurements were also performed on the empty reactor/sample holder to ensure the absence of activity towards the ammonia oxidation.

The heater was calibrated by measuring the sample temperature at different argon pressures, with a type K thermocouple fixed on the sample, as a function of the current intensity (fig. 3.3 - a). 10 min separate consecutive datapoints to ensure the heater stability. The thermal conductivity of the gases involved in the ammonia oxidation are in the similar order of magnitude (tab. 3.1). Moreover, the same inert gas used to set the reactor pressure -

Argon - is used as a carrier gas during the experiments, constituting at least 80 % of the gas flow, and allowing us to assume that the temperature in the reaction chamber is well approximated.

	Ar	NH_3	O_2	NO	N_2O	N_2	H_2O
300 K	17.7	25.1	26.5	25.9	17.4	26.0	18.6
400 K	22.4	37.2	34.0	33.1	26.0	32.8	26.1
500 K	26.5	53.1	41.0	39.6	34.1	39.0	35.6
600 K	30.3	68.6	47.7	46.2	41.8	44.8	46.2

Table 3.1: Thermal conductivity in $\mathrm{mW\,m^{-1}\,K^{-1}}$ *of gases (Huber et al. 2023).*

A temperature ramp at a reactor pressure of 0.3 bar (fig. 3.3 - b) was carried out to probe the evolution of the reaction products as a function of the temperature under reacting conditions. The patterned sample was used. A constant gas flow is used that consists of 41 mL/min of Ar, 8 mL/min of O_2, and 1 mL/min of NH_3. In the frame of this thesis, the same ratio between incoming gas flows in assumed to be respected between the different gas partial pressures, in this case the partial pressure of oxygen is then equal to 80 mbar, the partial pressure of ammonia to 10 mbar, and the partial pressure of argon to 410 mbar.

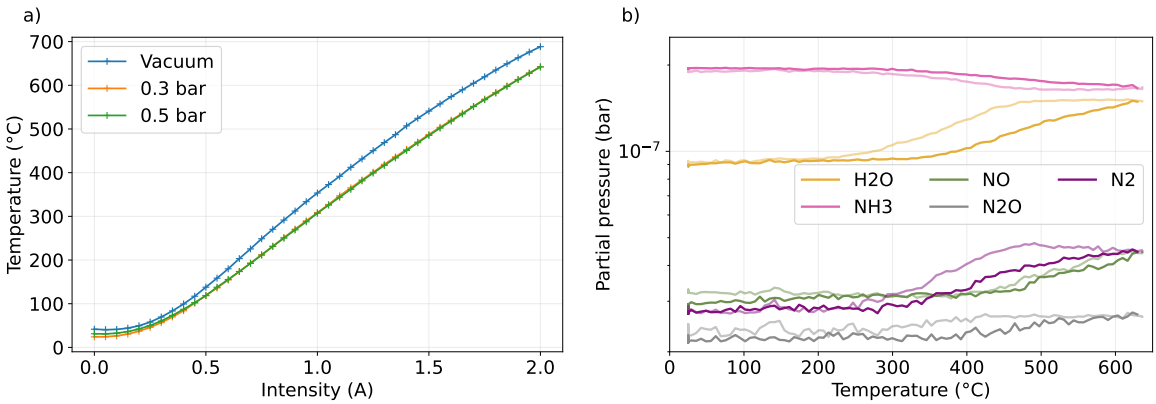

Figure 3.3: a) Sample temperature measured with a type K thermocouple under vacuum and different Ar pressures. b) Evolution of the partial pressures in the RGA chamber under a constant gas flow (41 mL/min of Ar, 8 mL/min of O_2, 1 mL/min of NH_3). Reactor pressure of 0.3 bar, and increasing and decreasing (low transparency) temperature ramp to 650 °C. The ramp is performed with 100 steps, each lasting 10 s. The partial pressure of oxygen and argon are omitted for simplicity.

The catalyst light off temperatures for the production of N_2, NO and N_2O are 300 °C, 450 °C, and 550 °C (fig. 3.3). The production of NO increases at high temperatures, with a partial pressure similar to the partial pressure of nitrogen at 650 °C. An exponential decrease as a function of increasing temperature in reported in literature for the production of N_2, with industrial catalysts, and at industrial conditions (Hatscher et al. 2008). This decrease starts at 200 °C, only a few percent of N_2 are produced at 900 °C. This behaviour is not observed during the temperature ramps in fig. 3.3. The production of nitrous oxide stays at low values during the temperature ramp, almost imperceptible from the background pressure.

According to these primary results, the study of the oxidation of ammonia was first carried out at 300 °C, a temperature before the catalyst light off. The measurements were then performed at 500 °C and 600 °C to measure the importance of the temperature after catalyst light off on the reaction selectivity. To probe the importance of the O_2/NH_3 ratio between partial pressures on the reaction selectivity, and its link with the catalyst structure, ammonia is first introduced in the reactor, followed by a step by step increase of the oxygen pressure. The different gas conditions used at each temperature are resumed in tab. 3.2.

Order	Gas Flow (mL/min)			Total pressure (mbar)	Partial pressures (mbar)			Targeted information
	Ar	O_2	NH_3		Ar	O_2	NH_3	
1	50	0	0	300	300	0	0	Catalyst state without reactants (unactive)
2	49	0	1	300	294	0	6	Ammonia adsorption
3	48.5	0.5	1	300	291	3	6	
4	48	1	1	300	288	6	6	Influence of (NH_3/O_2) ratio on the
5	47	2	1	300	282	12	6	catalyst selectivity and structure
6	41	8	1	300	276	48	6	
7	50	0	0	300	300	0	0	Returning to pristine state

Table 3.2: Different atmospheres used to probe the ammonia oxidation on Pt nanoparticles.

3.2 Collective behaviour of Pt nanoparticles: SXRD

3.2.1 Experimental setup for SXRD experiments in the vertical geometry

The MED diffractometer was used in a vertical geometry (fig. 2.15). The incident angle μ was fixed to 0.3°, to illuminate a larger portion of the sample surface. The incoming energy was set to 18.44 keV. In the vertical configuration, the sample surface must be parallel to the plane defined by the incoming beam and the vertical axis, so that sample rotations do not change the orientation of the sample atomic planes. The alignment of the sample was performed in two consecutive steps, first the out-of-plane sample position was adjusted by using the direct beam, secondly any possible tilt of the sample surface was corrected by recording the intensity of the *reflected* beam as a function of the u (when $\omega = 0°$) or v (when $\omega = 90°$) angles of the hexapod (fig. 2.15).

3.2.2 Epitaxial relationship under different atmospheres and temperature

To ensure that the Al_2O_3 supported particles have the expected epitaxial relationship with the substrate, the scattering intensity in the plane parallel to the sample surface was measured.

Room temperature study under inert atmosphere

The unit cell used to index the different Bragg peaks of platinum in this section is the FCC unit cell presented in sec. 2.4. This first map of the reciprocal space was recorded under inert argon atmosphere at room temperature (fig. 3.4), and shows the six expected (220)-type in-plane peaks for [111] oriented nanoparticles (fig. 3.2). The h, k, l Miller indices must have the same parity for the Bragg reflection to be allowed for face-centred cubic crystals, leading to the extinctions of (110)-type Bragg peaks. From the average position of these peaks in q-space is computed the average in-plane lattice parameter of the platinum nanoparticles $a_{Pt} = 3.91$ Å, from which the scattering vectors $\vec{q}$ of the (200) and (111) Bragg peaks are computed (tab. 3.3).

Three arcs are drawn in fig. 3.4 to underline the value of the (111), (200) and (220) scattering vectors. If no (200) and (111) Bragg peaks are observed, powder signals are visible for each reflection, which shows that some of the nanoparticles have a random orientation. Six $(2\bar{1}0)$-type Bragg peaks coming from the Al_2O_3 substrate are also observed at the lowest magnitude of the scattering vector ($q = 2.64\,\text{Å}^{-1}$, tab. 3.3). From the average position of these peaks in q-space is also computed the in-plane lattice parameter of the substrate, $a_{Sapphire} = 4.77$ Å. A first approximation of the in-plane misfit strain at the interface of the nanoparticles with the substrate is given following eq. 3.1: $\epsilon = 0.45\,\%$. This value must be considered with caution since the Pt in-plane lattice parameter is averaged over the volume of all the nanoparticles present on the sample, and is not representative of the platinum-sapphire interface. $(3\bar{3}00)$-type Bragg peaks from the substrate are also visible, next to (220)-type platinum Bragg peaks. Not all six peaks can be seen which may be due

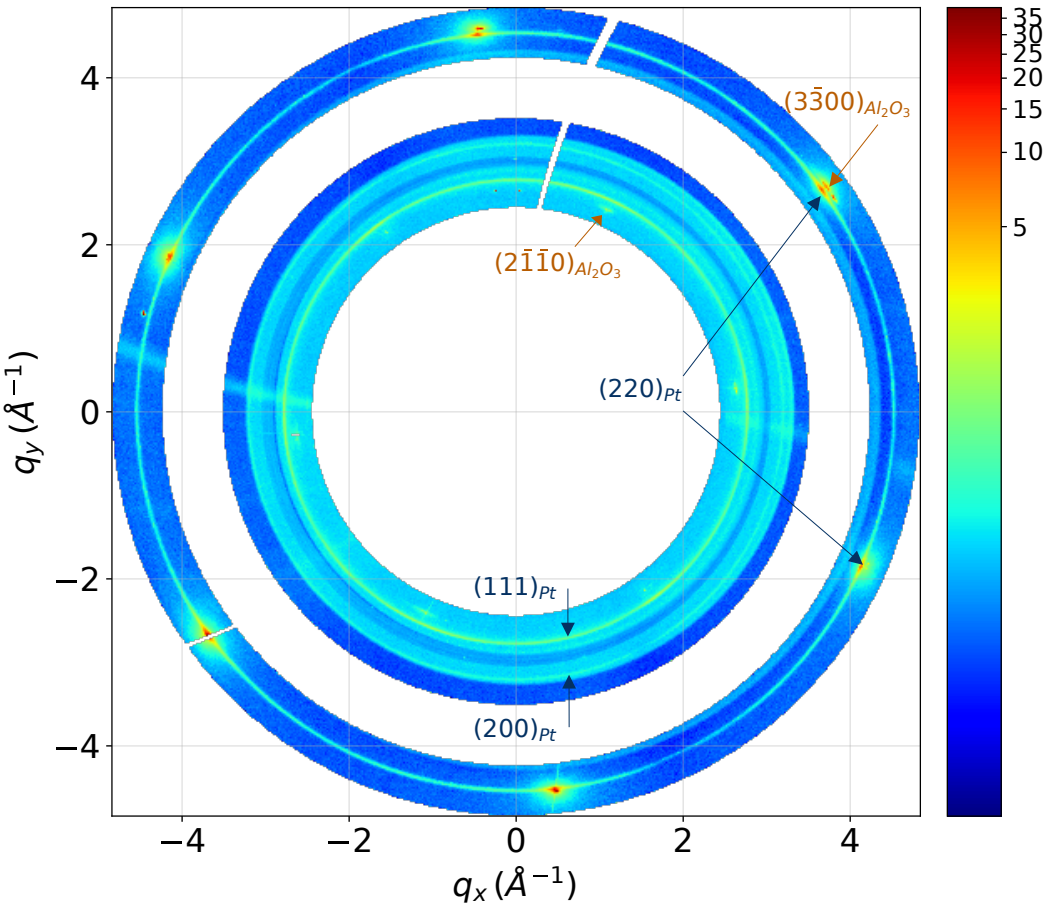

Figure 3.4: In-plane reciprocal space map at room temperature. Starting from the centre of the map are (i) six $(2\bar{1}\bar{1}0)$*-type Bragg peak from the substrate. (ii) thin circular powder signals for the* (111)*,* (200) *and* (220) *platinum Bragg peaks. (iii) six isolated* (220)*-type platinum Bragg peaks. (iv)* $(3\bar{3}00)$*-type Bragg peaks from the substrate next to the* (220)*-type platinum Bragg peaks.*

to the sample alignment, or to the sample coverage by platinum nanoparticles, important for the patterned sample.

Platinum Bragg peaks				
(h k l)	2θ	q	Int	Int (%)
(1 1 1)	17.13°	2.78 $\AA^{-1}$	6362.52	100.0
(2 0 0)	19.80°	3.21 $\AA^{-1}$	3251.30	51.10
(2 2 0)	28.14°	4.55 $\AA^{-1}$	2399.87	37.72

Al_2O_3 Bragg peaks				
(h k i l)	2θ	q	Int	Int (%)
(2 $\bar{1}$ $\bar{1}$ 0)	16.21°	2.64 $\AA^{-1}$	16.81	38.73
(3 $\bar{3}$ 0 0)	28.27°	4.57 $\AA^{-1}$	28.40	65.43
(2 $\bar{1}$ 1 3)	18.52°	3.01 $\AA^{-1}$	38.90	89.60

Table 3.3: Scattering angle, scattering vector magnitude, and intensity of the scattered waves for selected Pt and Al_2O_3 *Bragg peaks, computed for an energy of* 18.44 keV *using eq. 2.29 and eq. 2.24.*

Study during ammonia oxidation before and after catalyst light off temperature

In-plane maps were recorded on a smaller angular range (shown by the extent of black arcs in fig. 3.4) due to the long experimental time needed to collect large maps. The intensity was then integrated in a 0.1° wide region around the (111), (200) and (220) scattering angles. The region around the (220) Bragg peak was carefully selected to avoid the Bragg peaks of the substrate. These measurements are presented respectively in fig. A.2, fig. A.1 and fig. 3.5.

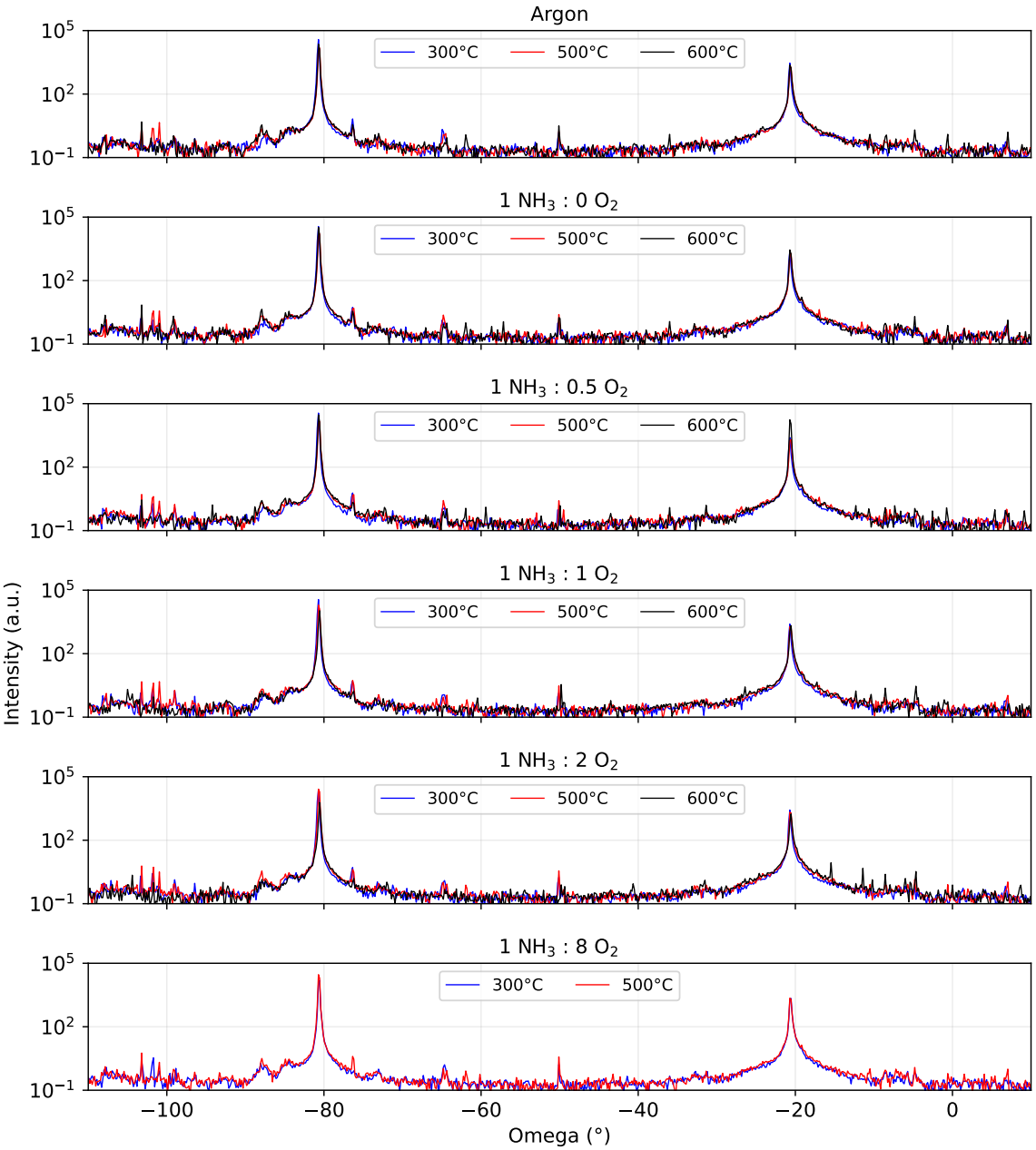

Figure 3.5: Integrated intensity in a 0.1° *range around the value of the (220) platinum scattering angle, as a function of the in-plane sample angle* ω*, presented for different atmospheres.*

Two (220)-type Bragg peaks are measured in each condition, with a stable position, shape, and intensity (fig. 3.5), which shows that the crystals do not rotate around their [111] axis on the surface, and that they all share the same out-of-plane [111] orientation. No (200) or (111)-type Bragg peaks appear during the different measurements (figures visible in the appendix A.1, and A.2). There is no variation of the powder signal for the (200) Bragg peak, but a slight decrease of the powder signal for the (111) Bragg peak when increasing the temperature from 300 °C to 500 °C. Most importantly, these measurements confirm that the nanoparticles are still epitaxied on the substrate even at high temperature under highly aggressive environments, proving a strong epitaxial relationship of the nanoparticles with the substrate

$(\bar{1}\bar{1}\bar{1})$ and (111) facets are expected to be present on all nanoparticles, respectively at the interface with the substrate and at the top of the nanoparticles. For that reason, we followed

the signal of those facets by measuring the CTR intensity as a function of q_z (fig. 3.6).

The $(\bar{1}11)$ and (200) Bragg peaks can be identified respectively at $q_z{\approx}0.92\,\text{Å}^{-1}$ and $q_z{\approx}1.85\,\text{Å}^{-1}$. Both peaks being visible along the same CTR shows that all nanoparticles do not share the same in plane orientation, due to different stacking of the (111) layers along the [111] axis, e.g. ABC or ACB stacking, rotated by 180° (Jones et al. 2019). Low intensity CTRs in other directions due to other facets present on the nanoparticles can be seen around both Bragg peaks. The peak at $q_z{\approx}1.46\,\text{Å}^{-1}$ corresponds to a $\{2\bar{1}13\}$ Bragg peak from the Al_2O_3 substrate ($q = 3.01\,\text{Å}^{-1}$, tab. 3.3). The substrate is also at the origin of its own CTR in the [111] direction, parallel to the more intense Pt CTR (fig. 3.6).

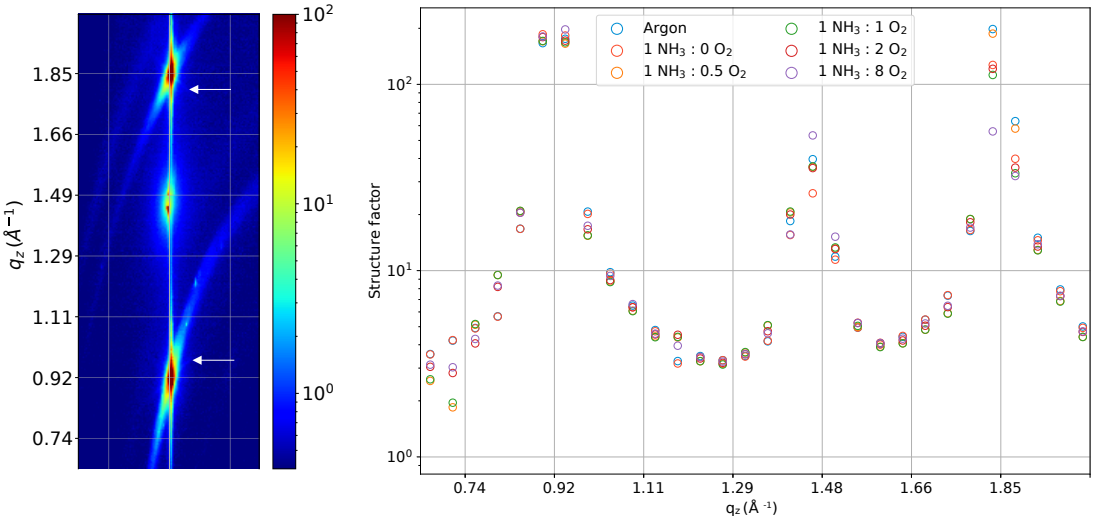

Figure 3.6: Left: Large out-of-plane reciprocal space map in which a CTR signal in the [111] direction can be identified, as well as weaker CTRs passing through the Bragg peaks. The $(\vec{q}_x, \vec{q}_y)$ plane was rotated around $\vec{q}_z$ to highlight the presence of signals from facets on the particles other than the (111) facet, indicated by white arrows. Right: Crystal truncation rod signals in the [111] *direction as a function of q_z, presented for different atmospheres, at* 300 °C.

The CTR intensity as a function of q_z is presented in fig. 3.6 (right). There is no visible evolution of the CTR shape, the anti-Bragg region where the relaxation effects are the most visible near $q_z{\approx}1.46\,\text{Å}^{-1}$ being masked by the Bragg peak of the substrate. Efforts were then focused on resolving the CTR signal around the Bragg peaks coming from different facets present on the nanoparticles surfaces.

3.2.3 Particle reshaping during the oxidation of ammonia

A volume of the reciprocal space was collected around the $(\bar{1}11)$ Bragg peak to find the direction of the observed facet signals, and to quantify their evolution as a function of the different conditions. Similar experiments have shown the oxygen-induced shape transformation of rhodium (Nolte et al. 2008), or platinum nanoparticles (Hejral, Vlad et al. 2013), which was also linked to the presence of surface oxides. The data was computed in q-space with different in-plane offsets, so that each rod observed in fig. 3.7 (a) becomes parallel to the $\vec{q}_x$ direction for a certain in-plane offset, thereby facilitating the data analysis. A figure without patches is available in app. A.6, where the rods are more visible.

Beside the crystal truncation rods, there are two different parasitic signals going through the Bragg peak. First, a curved signal almost parallel to $\vec{q}_y$ extends from $q_y = -2.80\,\text{Å}^{-1}$ to $-2.40\,\text{Å}^{-1}$ in the $(\vec{q}_x, \vec{q}_y)$ plane (near the white dashed line in fig. 3.7 - a). This signal comes from scattered x-rays diffusing towards the detector in position near the Bragg peak, and increasing the background signal. Secondly, a very intense powder ring ($\approx 1 \times 10^2$) can be

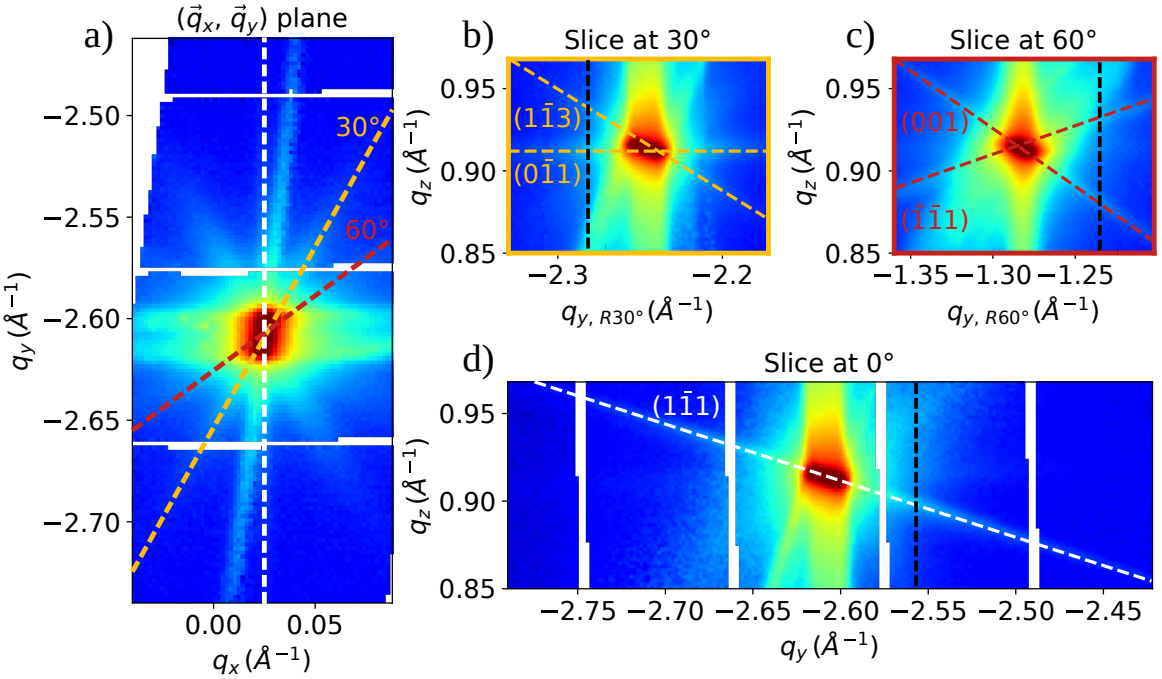

Figure 3.7: Reciprocal space volume around the $(\bar{1}11)$ Bragg peak, collected at 300 °C, under argon atmosphere. a) Projection perpendicular to $\vec{q}_z$. The three dashed line are respectively a projection in the $(\vec{q}_x, \vec{q}_y)$ plane of the $[\bar{1}11]$, $[\bar{1}10]$ and $[010]$ directions. b-c) Slices in the $(\vec{q}_y, \vec{q}_z)$ plane after rotation of the $\vec{q}_x$ and $\vec{q}_y$ axis around the $\vec{q}_z$ axis by 30° and 60° to highlight the presence of crystal truncation rods in different directions. d) Slice in the $(\vec{q}_y, \vec{q}_z)$ plane to highlight the presence of a crystal truncation rod in the $[1\bar{1}1]$ direction. The interval delimited by the vertical black dashed lines in (b-c-d) is used for the qualitative analysis of the CTRs intensities.

seen around the crystal truncation rod perpendicular to $\vec{q}_z$, especially in fig. 3.7 (c).

The identification of the crystallographic direction of each CTR present around the Bragg peak was performed thanks to the [111] stereographic projection. This stereographic projection is presented in fig. 3.8, which in the current experiment is parallel to $\vec{q}_z$. Each dot represents a crystallographic direction, *e.g.* [100], [110], etc. The distance between the dots and the centre of the figure is a function of the angle with the [111] direction, whereas their angular distribution corresponds to the planar angle of the component perpendicular to the [111] direction. Therefore, a signal that is for example at an angle of 30° with the [111] direction and 30° with the $[\bar{1}01]$ direction can be identified to be in the [113] direction thanks to fig. 3.8.

A CTR parallel to $\vec{q}_y$ is visible in fig. 3.7 - (a), with an angle of 72° with the [111] direction (fig. 3.7 - (d)), thus corresponding to a signal in the $[1\bar{1}1]$ direction. After having first identified the [111] and $[1\bar{1}1]$ directions, the identification of the direction of the other CTRs becomes straightforward.

Two CTRs in the $[1\bar{1}3]$ and $[0\bar{1}1]$ directions are identified, both have an angle of 30° with the $[1\bar{1}1]$ direction (visible in fig. 3.7 - a), and an angle of respectively 30° and 90° with the $[\bar{1}\bar{1}\bar{1}]$ direction in the $(\vec{q}_x, \vec{q}_{y,30})$ plane visible in fig. 3.7 - (b).

A [001] oriented CTR visible at 60° from the $[1\bar{1}1]$ direction (fig. 3.7 - a), has an angle of 60° with the $[\bar{1}\bar{1}\bar{1}]$ direction in the $(\vec{q}_x, \vec{q}_{y,60})$ plane visible in fig. 3.7 - (c).

Two $[11\bar{1}]$ and $[\bar{1}11]$-oriented CTRs are expected at 120° in the $(\vec{q}_x, \vec{q}_y)$ plane with the $[1\bar{1}1]$-oriented CTR. Each $[1\bar{1}1]$-oriented CTR is also linked to a $[\bar{1}1\bar{1}]$-oriented CTR in the opposite direction, which is why there is a $[1\bar{1}1]$-oriented rod at 60° from the $[1\bar{1}1]$ direction (fig. 3.7 - a), with an angle of 108° with the $[\bar{1}\bar{1}\bar{1}]$ direction in the $(\vec{q}_x, \vec{q}_{y,60})$ plane visible in fig. 3.7 - (c).

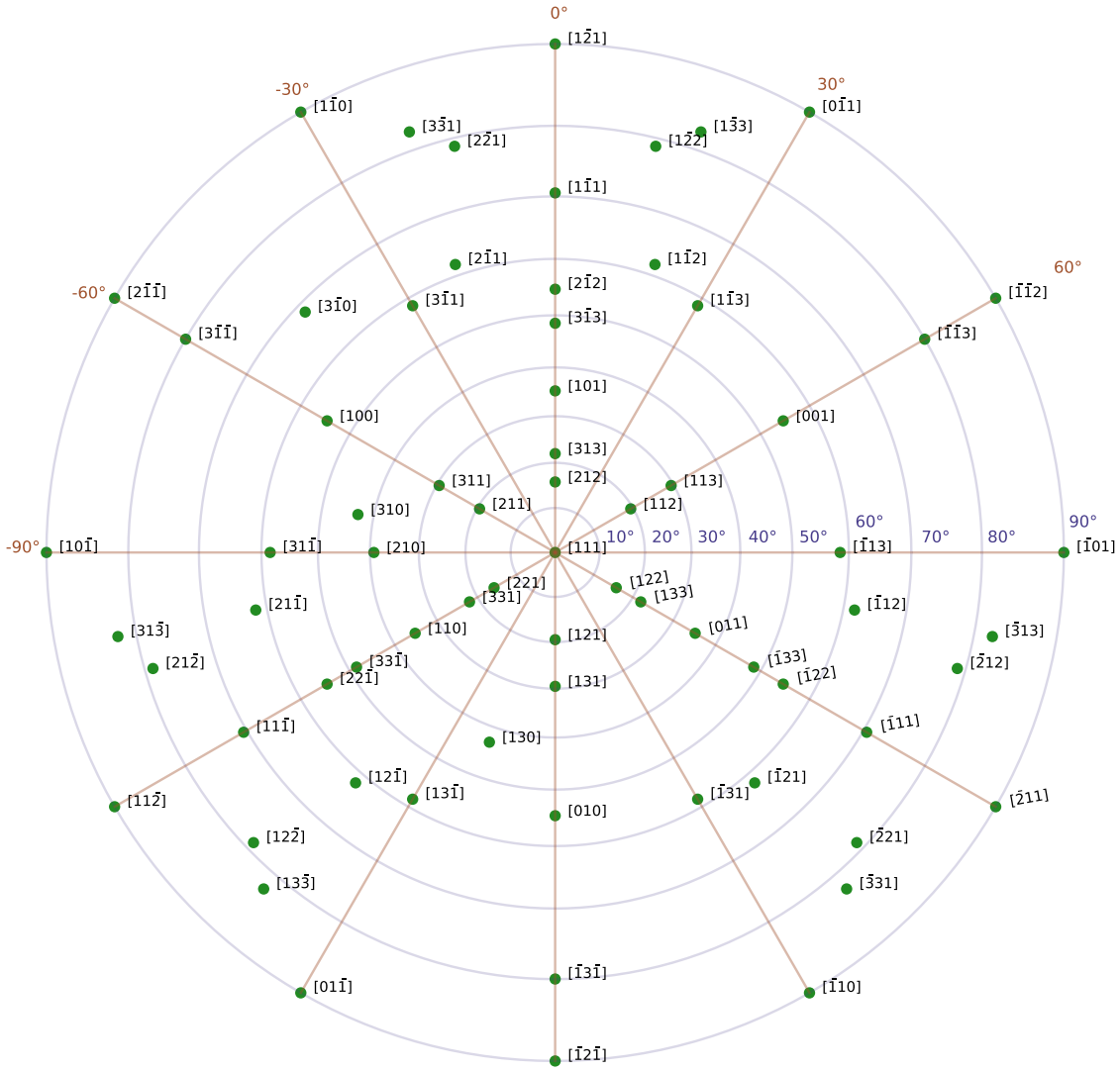

Figure 3.8: [111] *stereographic projection (for a face-centred cubic lattice). The circles describe the angle with the* [111] *direction from* 0° *(centre) to* 90° *(outer-ring).*

Despite the high intensity parasitic signal, it was possible to determine the orientation of 5 crystal truncation rods. From these results, the average shape of the particles on the sample is expected to be highly faceted, with not only small ({100}, {110}, {111}) but also high indices facets ({113}) present on their surface.

The intensity of the crystal truncation rods listed above was studied by measuring the scattered intensity as a function of q_z in a square area in the $(\vec{q}_x, \vec{q}_y)$ plane. The same width was used for each study, the region of integration is detailed in fig. 3.7 - (b-c-d) with black dashed lines. The evolution of the integrated scattered intensity as a function of q_z is presented if fig. 3.9 for different atmospheres and temperatures.

The scattered intensity does not evolve at 300 °C and 500 °C as a function of the atmosphere in the reactor cell. However, there is a transition between 300 °C and 500 °C when looking at the signal from the $(0\bar{1}1)$ facets, that evolves from a double to a single peak when increasing the reactor temperature. This can be due to defects present in the nanoparticles at lower temperature despite the high temperature annealing, that are removed when heating the sample (sec. 3.3.2).

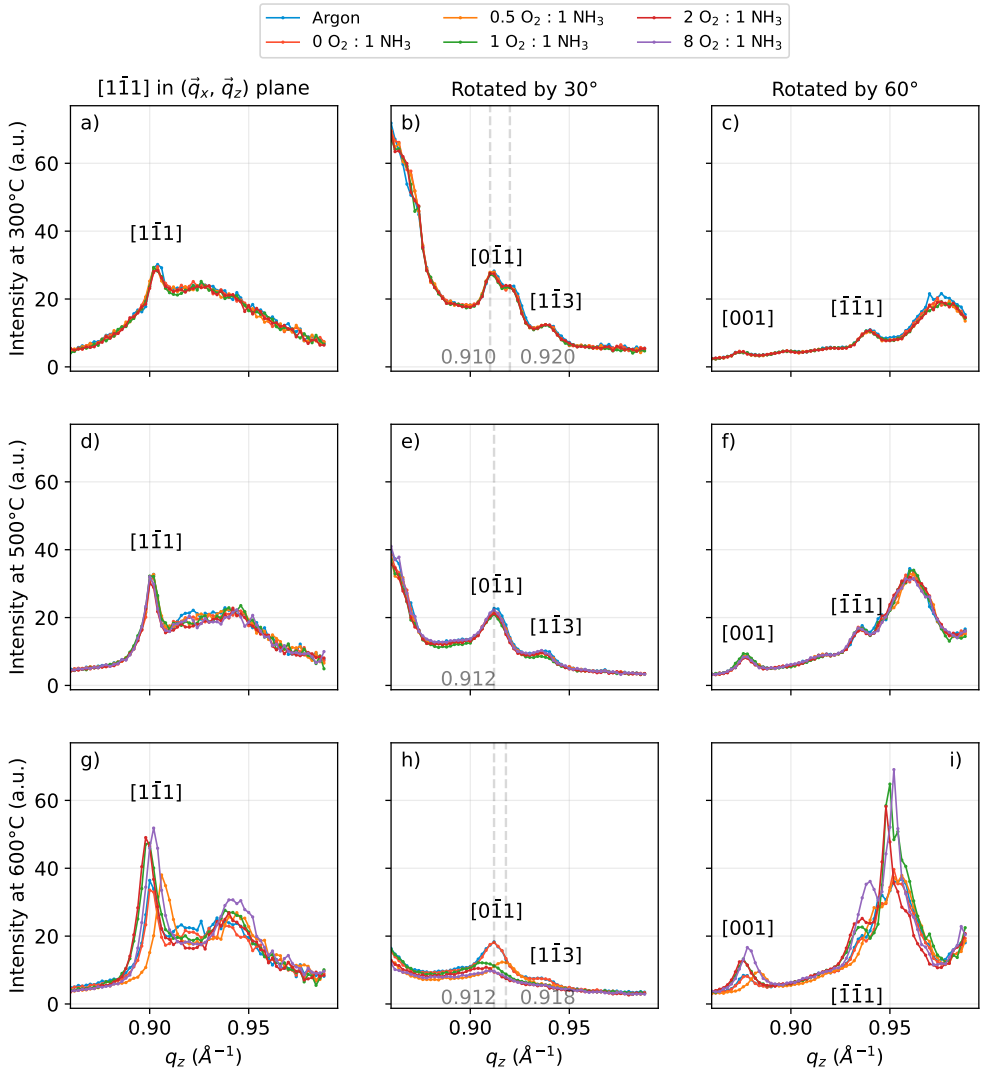

Figure 3.9: Evolution of the scattered intensity taken along a square area perpendicular to the [111] direction at three different positions in the ($\vec{q}_x, \vec{q}_z$) plane to probe the intensity evolution of crystal truncation rods.

At 600 °C, a progressive increase of the intensity is observed for the [1$\bar{1}$1], [$\bar{1}\bar{1}$1] and [001]-oriented rods, whereas a progressive decrease of the intensity is observed for the [0$\bar{1}$1] and [1$\bar{1}$3]-oriented rods, starting after the introduction of oxygen in the reactor. There is an increase of scattered intensity in fig. 3.9 (i) at $q_z \approx 0.95$ Å^{-1} which could be from (110) facets at 35° with the [111] direction (fig. 3.8). The low signal-to-background ratio in that region due to the powder ring makes it challenging to be certain of the existence of this CTR.

Moreover, the introduction of oxygen induces a global shift of the facet signals towards higher q_z values which can be linked to a homogeneous compressive lattice strain in the [111] direction, shifting the position of the Bragg peak. The position of the [0$\bar{1}$1]-oriented CTR, whose direction is perpendicular to the [111] direction, follows that shift in q_z, but its intensity vanishes after having more than 1 mL/min of oxygen in the reactor cell. A qualitative evolution of the strain in the [111] direction can be obtained by looking at the remaining CTR position in q_z (fig. 3.9 - g&i). The gradual increase of the oxygen partial pressure in the cell is accompanied by two additional changes of strain (i) from compressive to tensile strain

when increasing the oxygen partial pressure from 5 mbar to 10 mbar in the reactor and (ii) from tensile to compressive strain when increasing the oxygen partial pressure from 20 mbar to 80 mbar, the reference position being taken under argon and ammonia atmosphere.

These result indicate a progressive reshaping of the nano-catalysts towards particles exhibiting mostly {111} and {100} facets, together with the increase of the O_2/NH_3 ratio. A roughening of the particles could explain the loss of intensity from the $[0\bar{1}1]$-oriented CTR but not the increased intensity of the $[1\bar{1}1]$, $[\bar{1}\bar{1}1]$, and [001]-oriented CTRs.

The catalytic activity of the particles was recorded *via* the use of a mass spectrometer and shows the production of nitrogen, nitrous oxide and nitrogen oxide (fig. 3.10), proving the activity of the catalyst. At 600 °C, the production of N_2 is favoured at lower oxygen partial pressures in comparison with N_2O and NO. The opposite effects takes place at high oxygen partial pressures, with a clear transition between the main products from N_2 towards NO when the oxygen to ammonia ratio is equal to 8. The original mass spectrometer signal as a function of time can be seen in the appendix A.3, A.4, and A.5.

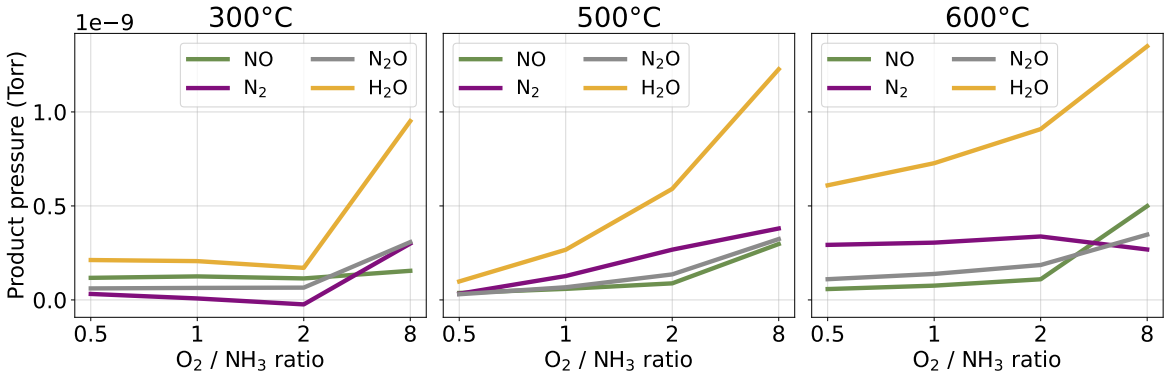

Figure 3.10: Evolution of reaction product partial pressures during the SXRD experiment on the non-patterned sample containing Pt nanoparticles, at 300 °C, 500 °C, *and* 600 °C. *Mean partial pressures during* 1 min *at the end of each condition, recorded from a leak in the reactor output by a residual gas analyser (RGA). The background pressure in the absence of reaction has been subtracted.*

The same measurements at 600 °C were not repeated at a fixed atmosphere which prevents us from knowing whether or not the observed phenomena would have occurred as a function of time under a fixed atmosphere. Moreover, the reversibility of this effect and the formation of possible platinum oxides on the nanoparticles (*via* large in-plane maps) could not be investigated from the lack of available experimental time.

Similar experiments on Pt nanoparticles (average size about 50 nm) have been carried at 6.5×10^{-6} bar and 0.5 bar of oxygen by Hejral, Vlad et al. 2013 which show the formation of Pt_3O_4 and $\alpha-PtO_2$ bulk oxides, the formation of high indices facets, a decrease of {111} facet signals and an increase of {100} facet signals. Different effects have been observed in this study with an increase in intensity of {111} and {100} facets, and the decrease in intensity of {110} facets during the oxidation of ammonia, highlighting the impact of the reaction on the particles' surface.

A study of the structure/activity relationship of each facet must be undertaken during the ammonia oxidation to better understand the role of the surface structure, and of potential surface oxides in the catalytic reaction, which is the subject of chapter 4.

3.3 Single Pt nanoparticles: BCDI

3.3.1 Experimental setup for BCDI experiments

The BCDI experiment was performed at the SixS beamline, in a vertical theta-two theta geometry, and at a beam energy of 8.5 keV (1.46 Å). The alignment of the sample was

performed with the same procedure as for SXRD detailed in sec. 3.2.1.

Each rocking curve consisted of 201 steps, counting between 5 s to 40 s, resulting in an angular step of 0.005°. The measurement of a rocking curve took approximately 22 min. Each particle was measured multiple times under each condition to ensure result reproducibility.

The diffracted beam was recorded with a 2D MAXIPIX photon-counting detector (515×515 square pixels, $55\,\mu m \times 55\,\mu m$ wide) positioned on the detector arm at a distance of 1.22 m. The out-of-plane angles of the sample (μ) and detector (γ) are set respectively to 18.6° and 37.2° when measuring at room temperature.

Gwaihir was used to process the data using the workflow detailed in sec. 2.8.1, each dataset was saved as a *cxi* file containing all of the data and metadata related to the reduction process. The use of iterative algorithm for phase retrieval is detailed in tab. 3.4. After 50 successful reconstructions, the 10 best solutions were chosen based on the homogeneity of the Bragg electronic density amplitude, and free log-likelihood value (Favre-Nicolin, S. Leake et al. 2020). A unique solution was then computed by performing a mode decomposition to find the most reproducible solution, thus reducing noise in the data, following an algorithm first derived by Schmid et al. (2010).

Iteration	Algorithm	PSF	Description
0-199	HIO	False	Work on the gross identification of the support/shape
200-599	RAAR	False	Refining the support
600	RAAR	True	Activate the use of a point-spread function (PSF) to take into account the partial coherence of the beam.
601-999	RAAR	True	Refine the PSF shape, the support must be already well defined to avoid diverging from the best solution.
1000-1200	ER	True	Further refine the support by reducing the algorithm flexibility.

Table 3.4: Example of algorithm chain used in BCDI for the phase retrieval. The support corresponds to the volume of the particle in real space.

3.3.2 Effects of temperature under inert atmosphere from 25 °C to 600 °C

To be able to de-correlate the effect of temperature from the effect of the catalytic reaction on the particle structure, the sapphire-supported nanoparticles were gradually heated from 25 °C to 600 °C under a constant argon-based gas flow (50 mL/min), and at a pressure of 0.5 bar.

The same particle (so-forth called particle A) was tracked during the heating process, rocking-curves around the (111) Bragg peak were measured at different temperatures to probe its structural evolution.

Shape evolution

The surface of the Pt particle coloured by the voxel strain values is presented in fig. 3.11 from 150 °C to 350 °C, to show the evolution of the particle shape under an inert gas flow as a function of the temperature. The $(\vec{x}, \vec{y}, \vec{z})$ frame in the figure corresponds to the sample frame, with $\vec{z}$ out-of-plane. At 150 °C, a dislocation is observed at the particle interface with the substrate from its strain signature and missing pipe of Bragg electronic density (Dupraz 2015). After a flash annealing at 800 °C for a few minutes, the dislocation was removed indicating the mobility of dislocations at high temperature.

The recovered phase spanning from $-\pi$ to π could not be perfectly unwrapped near the interface of the particle with the substrate at 150 °C (fig. 3.11) and 600 °C (fig. 3.14), resulting in saturated strain regions on the $(\bar{1}\bar{1}\bar{1})$ facet visible in the bottom view of the particle.

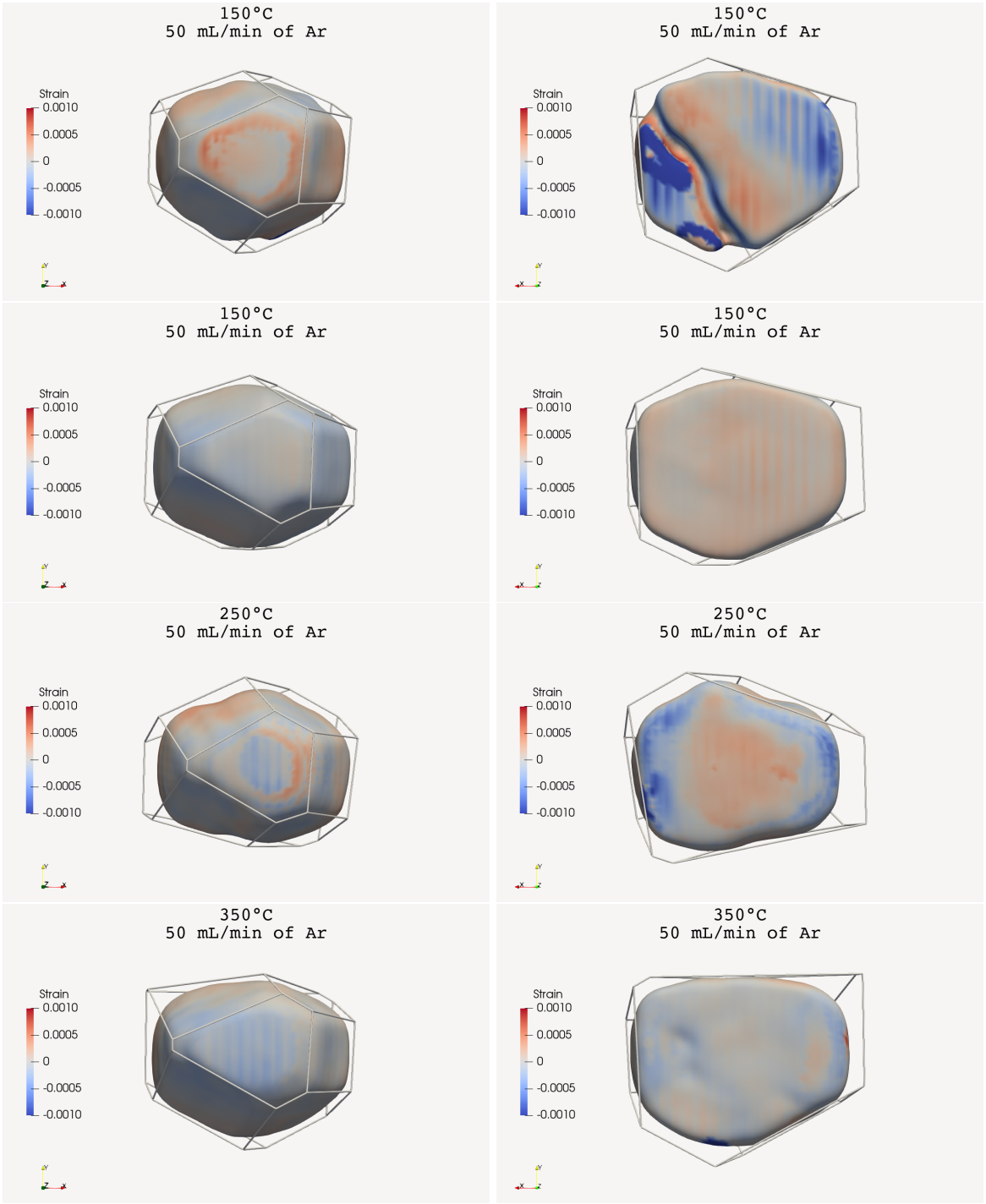

Figure 3.11: Surface of the reconstructed particle A at 150 °C *(before and after the flash annealing),* 250 °C*, and* 350 °C*. The surface is coloured by the values of the heterogeneous out-of-plane strain as described in eq. 3.5 at each surface voxel, the limit of each facet is delimited by thick white lines.*

A first approximation of the spatial resolution of the experiments was computed by fitting the derivative of the Bragg electronic density amplitude, following the procedure detailed by Hofmann et al. (2020). A minimum value of 30 nm was found in the [111] direction throughout the experiment, with otherwise values going up to 60 nm in other directions.

The average voxel size is equal to $10\,\mathrm{nm}^3$, which shows that the signal to noise ratio is not sufficient in all of the collected volume in reciprocal space to assume for the voxel size to be a good resolution estimate. The low resolution of the experiment makes the identification of the smallest facets on the nanoparticles, as well as their orientation complicated for two

reasons.

First, crystal truncation rods perpendicular to small facets are less intense in comparison to large facets, which is at the origin of the direction-dependent spatial resolution in BCDI (Cherukara, Cha et al. 2018). The spatial resolution in the direction perpendicular to small facets is thus smaller than e.g. in the [111] direction since the (111) and $(\bar{1}\bar{1}\bar{1})$ facet are some of the largest.

Secondly, the small amount of voxels belonging to those facets increases the error when computing the facets orientation in real space by the means of *FacetAnalyser* (sec. 2.6.4). The crystallographic orientation of each facet was determined by (i) comparing the angles between their normals and the [111] direction, which is known to be along the $\vec{z}$ axis of the sample frame. (ii) comparing the angles between the component of their normals *perpendicular* to the [111] direction and the normal to one $(1\bar{1}0)$-type facet, easily identified since they are at 90° with the [111] direction. If no $(1\bar{1}0)$-type facet is present on the particle, the $\vec{x}$ or $\vec{y}$ axis is used instead. The value of both angles then allows us to situate the normal of each facet in the circular frame drawn using a stereographic projection perpendicular to the [111] crystallographic direction (fig. 3.8), and thus to find their corresponding Miller planes.

To be more precise, the angular value in the first step is computed as the average of the angle between the facet normal and the [111] direction plus the angle between the facet normal and the $[\bar{1}\bar{1}\bar{1}]$ direction minus 180°, *i.e.* $(\angle([111], \vec{n}) + (\angle([\bar{1}\bar{1}\bar{1}], \vec{n}) - 180))/2$.

An equivalent procedure is to use the direction of the crystal truncation rods in reciprocal space (M. I. Richard et al. 2018), similarly to the procedure performed in the previous section.

The particle shape stayed roughly the same during the beginning of the temperature ramp, and after the introduction of ammonia. The triangular (111) facet at the top of the particle can be recognised, with the same agency of the surrounding facets, *i.e.* (111) facet surrounded by the (100), (010), (001), $(1\bar{1}1)$, $(11\bar{1})$, $(\bar{1}11)$ facets. The bottom facet, in contact with the substrate, has a $[\bar{1}\bar{1}\bar{1}]$ orientation.

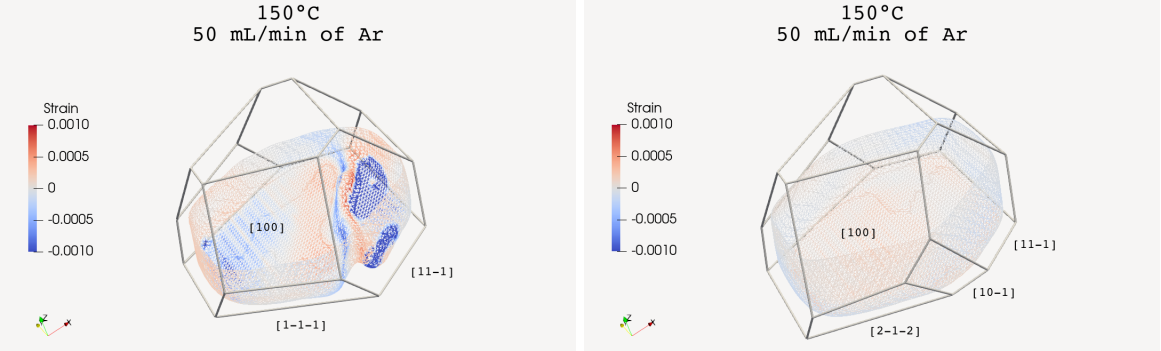

Figure 3.12: Surface of the reconstructed particle A at 150 °C before (left) and after the removal of the dislocation (right). A wire-frame representation of the lower half of the particle facilitates the visualisation of the dislocation loop at the interface. The surface is coloured by the values of the heterogeneous out-of-plane strain as described in eq. 3.5 at each surface voxel, the limit of each facet is delimited by thick white lines.

After the flash annealing, the particle shape near the interface has become less round and more faceted from the disappearance of the dislocation (fig. 3.12), the surface strain on the $(\bar{1}\bar{1}\bar{1})$ facet at the interface has decreased.

The evolution of the different type of facets present on the particle surface, as well as their relative surface area is presented in fig. 3.13.

A $(10\bar{1})$ facet appeared after the flash annealing on the side of the particle near a $(2\bar{1}\bar{2})$ facet that replaced a $(1\bar{1}\bar{1})$ facet (fig. 3.12). The large cylindrical surface area spanned by the dislocation loop (also visible in fig. 3.11) results in a large volume (pipe) of the particle not visible in the selected contour of the reconstructed Bragg electronic density. This is due to

low amplitude in the Bragg electronic density regions around dislocation loops, demonstrated *via* atomic simulations by Clark et al. (2015), and Dupraz et al. (2017).

Removing the dislocation also removed this effect, which lead to an increase of the area recognised as belonging to the surrounding facets, especially for the $(\bar{1}\bar{1}\bar{1})$ facet, at the interface with the substrate. Almost 10 % more of the sample surface was recognised as part of the different facets by the algorithm, which is displayed in fig. 3.13 (b).

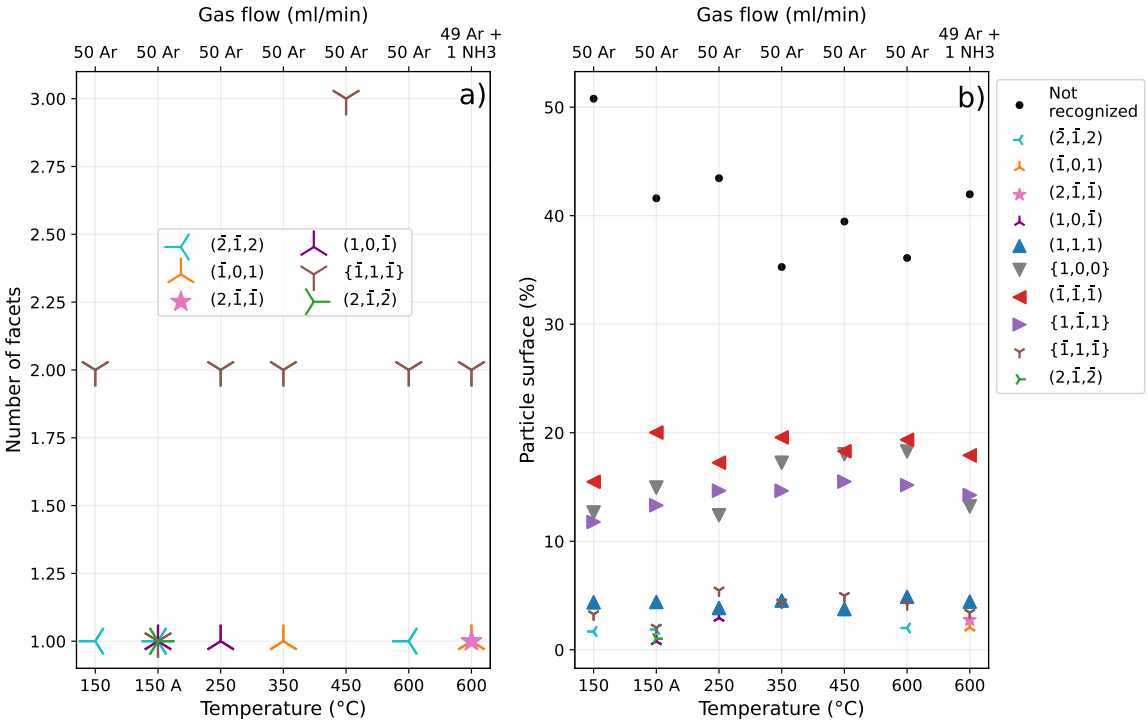

Figure 3.13: a) Evolution of the number of facets in contact with the $(\bar{1}\bar{1}\bar{1})$ facet at the interface with the substrate. b) Evolution of the particle surface area occupied by specific facets (indicated with parenthesis) or facet families (indicated with {}). The surface not recognised as part of a facet by the algorithm is taken into account and shown in black. "150 °C A" designates the measurement performed after annealing.

When heating from 150 °C to 250 °C , the $(\bar{2}\bar{1}2)$ facet present before the dislocation removal is transformed towards a $(\bar{1}\bar{1}1)$ facet (fig. 3.13 - a). The $(10\bar{1})$ facet disappeared after heating to 350 °C, and a $(\bar{1}01)$ facet appeared on the opposite side of the particle (fig. 3.13 - a), this transformation is visible in fig. 3.11.

The surface of the Pt particle coloured by the voxel strain values from 450 °C to 600 °C is presented in fig. 3.14. If one expects a certain degree of symmetry from the equilibrium Winterbottom shape of a particle on a substrate (Winterbottom 1967; Boukouvala et al. 2021), this symmetry seems to only be reached at 450 °C (fig. 3.14). Three $(\bar{1}\bar{1}\bar{1})$, $(1\bar{1}\bar{1})$, and $(\bar{1}\bar{1}1)$ facets are indexed close to the substrate for a total of 11 facets (8 {111} facets and 3 {100} facets). 450 °C is also the temperature at which the particle does not exhibit any $(\bar{2}\bar{1}2)$, $(\bar{1}01)$ and $(2\bar{1}\bar{1})$-type facets (fig. 3.13 - a).

Overall, the surface occupied by the facets around the top of the particle increases during heating, while the surface area not recognised as faceted by the algorithm decreases, which could mean that smaller facets (not resolved by the algorithm) are absorbed by large low index facets when the temperature increases, the particle thus becoming gradually less round. The respective number of $(1\bar{1}1)$-type and (100)-type facet does not change during the experiment. The facets that are around the bottom of the particle are the most subject to change during this temperature ramp, while the facets at the top of particle are more stable (fig. 3.13).

Interestingly, after the reshaping of the particle at 450 °C that shows the disappearance

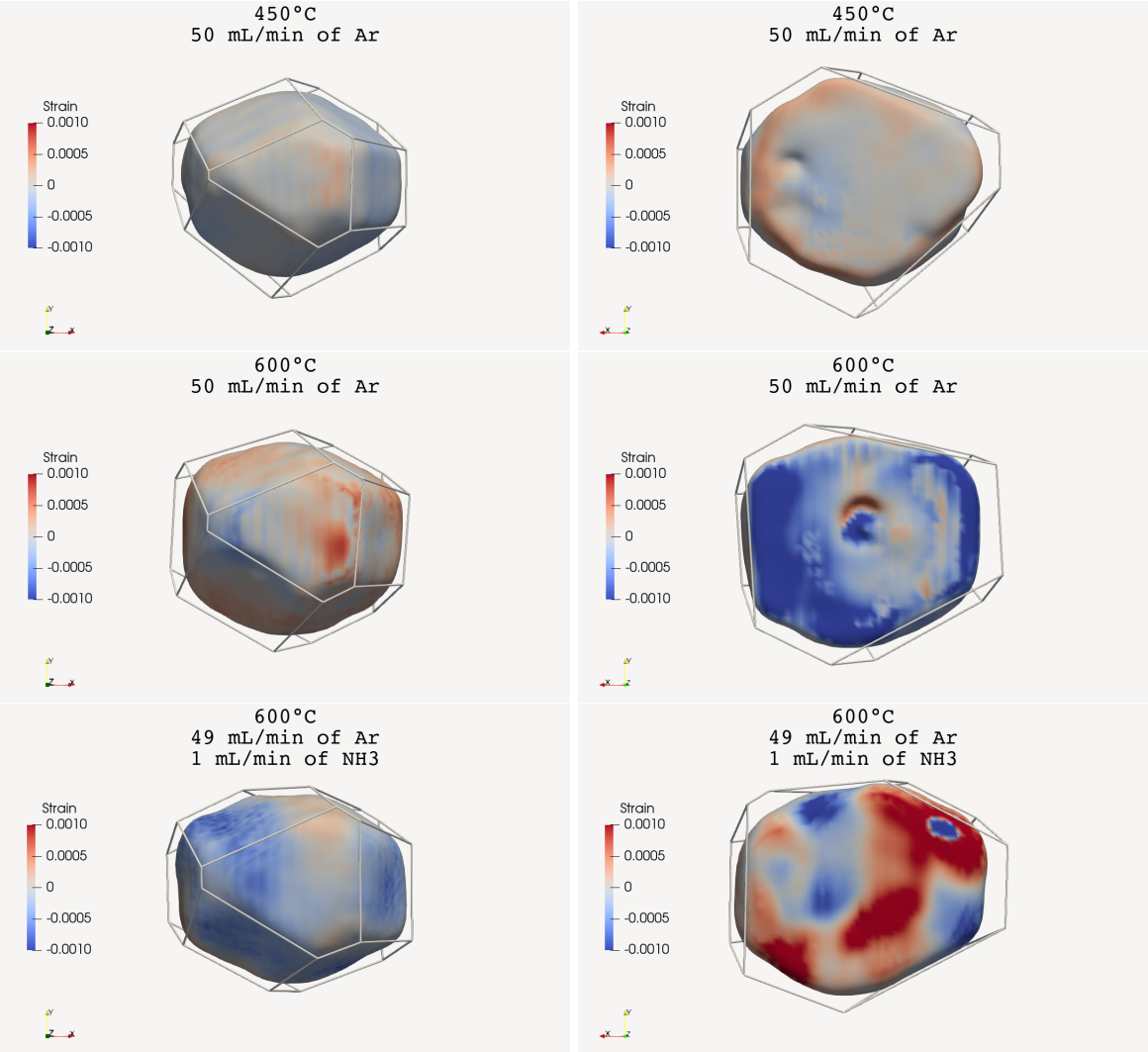

Figure 3.14: Surface of the reconstructed particle A at 450 °C and 600 °C under both inert argon atmosphere and 60 min after the introduction of NH_3 in the reactor. The surface is coloured by the values of the heterogeneous out-of-plane strain as described in eq. 3.5 at each surface voxel, the limit of each facet is delimited by thick white lines.

of the higher Miller indices facets (fig. 3.13 - a), the following rocking curves at 550 °C did not reconstruct.

A reconstruction at 600 °C under inert atmosphere shows the appearance of a hole at the interface with the substrate (fig. 3.14), and of the same $(\bar{2}\bar{1}2)$ facet that was present on the particle at 150 °C (fig. 3.13 - a), replacing the $(\bar{1}\bar{1}1)$ facet.

After the introduction of NH_3 at 600 °C, the reconstructed particle exhibits a $(2\bar{1}\bar{1})$ facet for the first time, replacing a $(1\bar{1}\bar{1})$ facet (fig. 3.13 - a). The $(\bar{2}\bar{1}2)$ facet is replaced by a $(\bar{1}01)$ (previously observed at 350 °C), and a $(\bar{1}\bar{1}1)$ facet (fig. 3.13 - a, 3.15). Similar changes occurred between 150 °C and 350 °C after the removal of the dislocation (fig. 3.15). Overall, the $\{\bar{1}\bar{1}1\}$-type facets seem to be the most unstable, shifting towards $\{\bar{1}01\}$-type, $\{\bar{2}\bar{1}1\}$-type and $\{\bar{2}\bar{1}2\}$-type facets as a function of temperature (fig. 3.15). The change is also visible in fig. 3.13 (b), for example the relative surface occupied by the (100), (010) and (001) facets decreases, occupied by the $(\bar{1}01)$ and $(1\bar{1}\bar{1})$ facets. The alternating highly positive and negative strain regions in the middle of the $(\bar{1}\bar{1}\bar{1})$ facet (fig. 3.14) is the signature of a dislocation network forming at the interface with the substrate (Dupraz 2015).

When introducing O_2 at 600 °C to study the oxidation of ammonia, the particle was definitely lost during the measurement, not to be found again, which underlines the difficulty

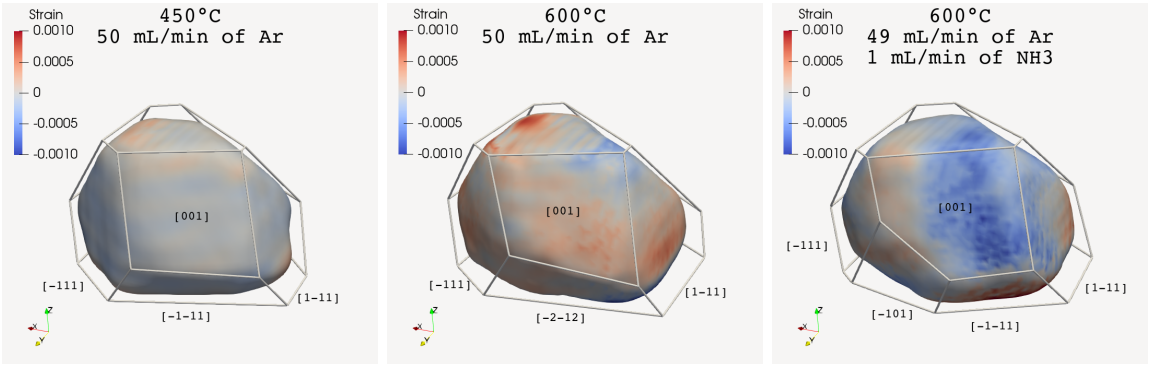

Figure 3.15: Surface of the reconstructed particle A at 450 °C *under Argon and at* 600 °C*, before and* 60 min *after the introduction of* NH_3*. The surface is coloured by the values of the heterogeneous strain at each surface voxel, the limit of each facet is delimited by thick white lines.*

to study a highly exothermic reaction with BCDI (Pérez-Ramírez, E. Kondratenko et al. 2004; Hatscher et al. 2008). The reaction can heat the catalyst to very high temperatures which in our case could have been the trigger for the loss of the particle during the measurement, especially since the particle had so far resisted to the beam during the temperature ramp to 600 °C.

Determination of strain

The average value of the out-of-plane lattice parameter can be extracted from the position $\vec{G}$ of the Bragg peaks in reciprocal space *via* eq. 2.34 and eq. 2.30. This value can then be used to compute the average out-of-plane lattice strain *via* eq. 3.1, by comparing with a reference value, e.g. room temperature values under inert atmosphere (Fernàndez et al. 2019).

However, the information extracted from the retrieved phase in BCDI is more complex since, by measuring three non-coplanar Bragg peaks, one may retrieve the full strain tensor (eq. 3.3) from the reconstructed displacement field $\vec{u}_{\hat{q_x},\hat{q_y},\hat{q_z}}$ (eq. 3.2), $\hat{q_x}, \hat{q_y}, \hat{q_z}$ being three orthonormal basis vectors in the reciprocal space (Karpov et al. 2019).

$$\vec{u}_{\hat{q_x},\hat{q_y},\hat{q_z}} = \begin{pmatrix} u_{q_x} \\ u_{q_y} \\ u_{q_z} \end{pmatrix} \tag{3.2}$$

$$\epsilon = \begin{bmatrix} \epsilon_{xx} & \epsilon_{yx} & \epsilon_{zx} \\ \epsilon_{xy} & \epsilon_{yy} & \epsilon_{zy} \\ \epsilon_{xz} & \epsilon_{yz} & \epsilon_{zz} \end{bmatrix} \tag{3.3}$$

$$\epsilon_{ij} = \frac{1}{2}\left(\frac{\partial u_{q_i}}{\partial q_j} + \frac{\partial u_{q_j}}{\partial q_i}\right) \tag{3.4}$$

$$\epsilon_{ii} = \left(\frac{\partial u_{q_i}}{\partial q_i}\right) \tag{3.5}$$

The idea behind using the strain tensor is to identify shear components in the displacement field, *i.e.* see if components in one direction depend on other directions, which can also help to identify defects present in nanoparticles (Lauraux, Labat et al. 2021). Using a single Bragg peak, only one component of the displacement field can be retrieved, obtained from the division of the retrieved phase Φ of the scattered x-rays by the modulus of the scattering vector at the position of the Bragg peak (*i.e.* $\vec{q} = \vec{G}$), following the assumptions for phase retrieval detailed in sec. 2.6.1, eq. 2.54 - 2.58.

In our case, the direction of the (111) scattering vector, $\vec{G}_{111}$, is perpendicular to the sample, along the $\vec{z}$ axis of the sample frame. Therefore, $\vec{G}_{111}$ is so forth described as $\vec{q}_z$, of magnitude $|\vec{q}_z|$, with the direction described by the unit vector $\hat{q}_z$, to be consistent with the equations detailed above. Our approach to the strain is considerably simplified since only one component of the strain tensor can be correctly derived, here the out-of-plane strain ϵ_{zz} (eq. 3.5) as detailed below in eq. 3.6 - 3.8.

$$\Phi = \vec{q}_z.\vec{u} \tag{3.6}$$

$$\frac{\Phi}{|\vec{q}_z|} = \frac{\vec{q}_z}{|\vec{q}_z|}.\vec{u} = \hat{q}_z.\vec{u} = \vec{u}_{q_z} \tag{3.7}$$

$$\vec{\nabla}\vec{u}_{\hat{q}_z} = \frac{\partial u_{q_z}}{\partial q_x} + \frac{\partial u_{q_z}}{\partial q_y} + \frac{\partial u_{q_z}}{\partial q_z} = \epsilon_{zz} \tag{3.8}$$

Homogeneous strain evolution

The deviation of the interplanar spacing from the room temperature value due to the thermal expansion of the crystal is expected to be homogeneous within the particle. This isotropic *homogeneous* strain (ϵ_{hmg}) in the particle is removed by centring the Bragg peak before phase retrieval, otherwise resulting in a linear phase ramp after the Fourier transform operation.

It is of utmost importance to first study the evolution of the material under an inert atmosphere to differ evolution of the homogeneous strain due to the thermal expansion of the crystal from for example the adsorption of molecules involved in the catalytic reaction. The average interplanar spacing between {111} crystallographic planes (d_{111}) in the particle is computed from the Bragg peak position in q-space *via* eq. 2.34, presented in fig. 3.16. Repeated measurements at fixed condition yield additional data points in the figure.

The interplanar spacing follows approximately two distinct linear increases, first from 25 °C to 150 °C before the dislocation removal, and secondly from 150 °C to 600 °C after the dislocation removal (fig. 3.16 - c). Qualitative lines are drawn from linear fits in fig. 3.16 (c) to indicate those linear behaviours. The temperature dependant increase of interplanar spacing is 2.5 more important before the defect removal, which shows that interfacial defects have an impact on the thermal relaxation of nanoparticles.

Utilising the (111) Bragg peak in the current specular geometry can only bring information about out-of-plane distortions. Homogeneous in-plane lattice distortions in $\vec{x}$ and $\vec{y}$ (*i.e.* $[\bar{1}01]$ and $[1\bar{2}1]$, fig. 3.8) are invisible in this study. The rocking curves presented in fig. 3.16 (a) were fitted with a Lorentzian model (fig. 3.16 - b) to retrieve the peak full width at half maximum in the $\vec{z}$ direction (FWHM_z). The flash annealing and removal of the dislocation at 150 °C had the effect of increasing the average interplanar spacing d_{111}, and decreasing FWHM_z, which can be linked to a decrease of heterogeneous out-of-plane strain inside the particle (Warren 1990). In this discussion, variations in the FWHM are qualitatively attributed to the particle heterogeneous strain. Other effects may contribute such as changes of particle size, but the 3D reconstructions show that the particle has a stable size.

The particle was realigned after the removal of the dislocation to be sure of the absence of any angular offset, the flash heating process possibly moving the sample positions from thermal expansion.

The measurement at 550 °C shows a very large FWHM_z, reaching similar magnitude as when the interfacial dislocation was present at lower temperatures. This increase can be attributed to an increase of strain in the particle, possibly behind the failure of the phase retrieval process to successfully converge at that temperature.

One one hand, the two values of the average interplanar spacing under inert atmosphere at 600 °C are similar to the value at 550 °C, and decrease slightly after the introduction of ammonia. On the other hand, FWHM_z decreases importantly (divided by 1.4) after having

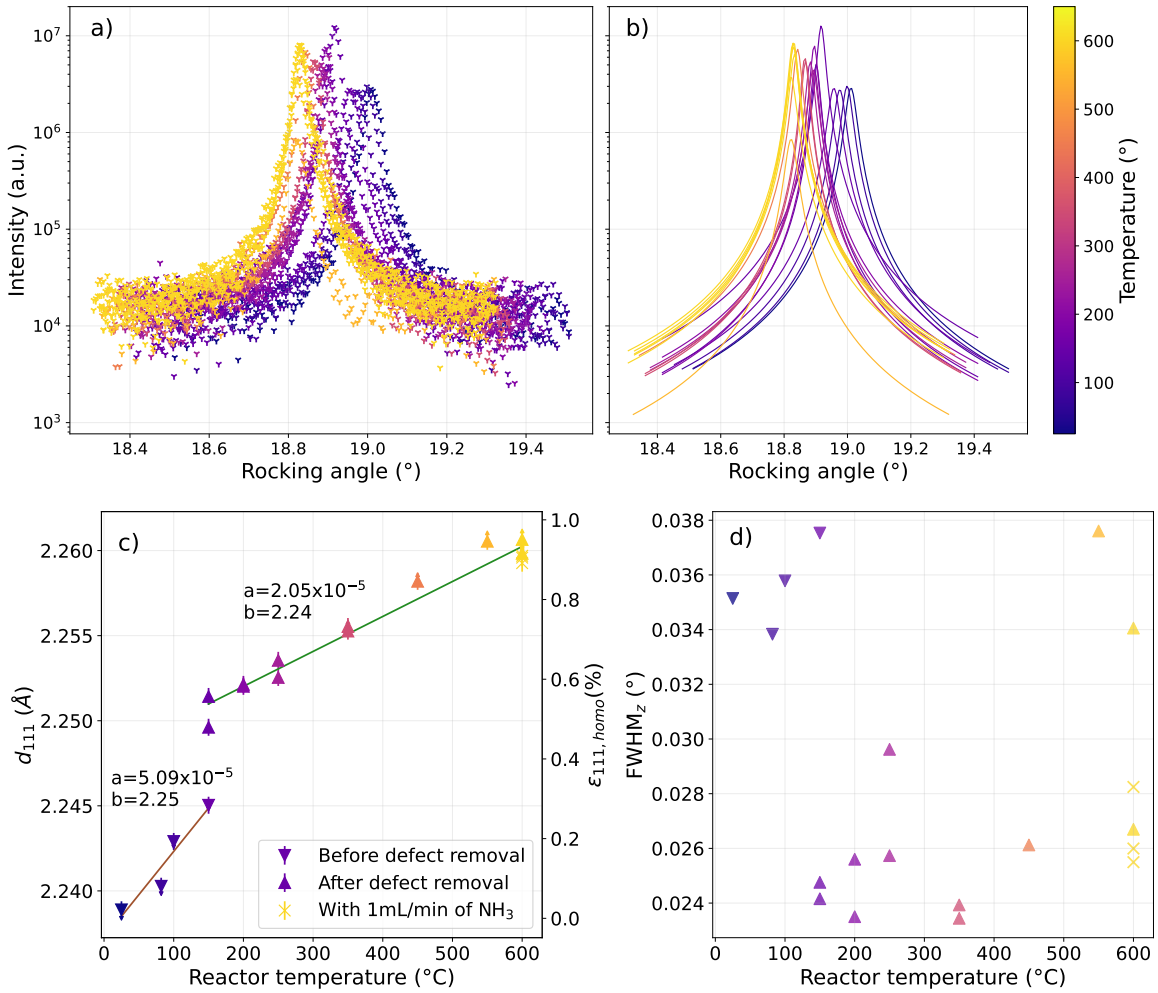

Figure 3.16: a) Evolution of the integrated scattered intensity in the detector as a function of the scattering angle during the rocking scans, fitted (b) with a Lorentzian profile to retrieve the peak positions and full width at half maximum (FWHM). Evolution of the d_{111} interplanar spacing (c), and associated homogeneous strain values as a function of the temperature. The reference for the computation of homogeneous strain is taken at 25 °C. Evolution of the Bragg peak FWHM$_z$ in $\vec{z}$ as a function of the temperature (d). The slope (a) and y-intercept (b) parameters of interplanar spacing linear fits before and after the defect removal is also indicated.

reached 600 °C, returning to the previous values observed between 150 °C and 450 °C. The introduction of ammonia has no visible effect on FWHM$_z$. The decrease of the interplanar spacing between 550 °C and 600 °C occurs together with the decrease of FWHM$_z$, ultimately resulting in the formation of a dislocation network at the interface imaged with BCDI (fig. 3.14). The presence of the dislocation network is not clear from the values of FWHM$_z$, a future characterisation of the peak FWHM in other directions will yield additional information.

Computing the misfit strain resulting from the epitaxial relationship of the Pt nanoparticles with the substrate could have revealed if an absolute minimum is reached at 450 °C, possibly explaining the low interfacial strain and equilibrium shape observed in fig. 3.11. However, no in-plane Bragg peak corresponding to the sapphire substrate, or to platinum, was measured during the temperature ramp, preventing us from performing this analysis.

Heterogeneous strain evolution

The remaining strain after phase retrieval is called the *heterogeneous* strain (ϵ_{htg}) (Grédiac 1996; Favier et al. 2007; Atlan et al. 2023), the total out-of-plane strain observed during this

experiment being equal to $\epsilon_{tot} = \epsilon_{111,hmg} + \epsilon_{zz,htg}$ when considering the changes relative to a reference state (usually room temperature data).

In BCDI, it is the displacement of small unit blocks making up the crystal lattice that is observed. Depending on the instrumental parameters, these small unit blocks, or *voxels*, have a more or less large size. In this study, they are approximately $10\,\mathrm{nm}^3$ large. The strain is thus not directly related to the deviation between the interreticular planes, but to the gradient of the displacement field of these unit blocks from their equilibrium position. The outermost layers of the crystal only constitute a low percentage within the surface voxels ($\approx$11 % if 5 atomic layers separated by the value of the interplanar spacing d_{111} are considered). This effectively lowers the contribution of the surface strain to the total strain contained in the surface voxels, reducing the ability to properly resolve e.g. surface relaxation effects. The use of padding during the reconstruction algorithm decreases the voxel size, but without relying on the sampling of high-frequency components of the scattering amplitude, and therefore does not increase the strain resolution.

It is important to realise that the displacement observed is *only* in the [111] direction (as only the (111) Bragg peak is measured), sensitive to deviations of the crystal structure perpendicular to the (111) and $(\bar{1}\bar{1}\bar{1})$ facets, but parallel to $(\bar{1}10)$-type facets, themselves perpendicular to the [111] direction (fig. 3.8). On one hand, if there existed an out-of-plane displacement of the atoms on $(\bar{1}10)$-type facets, *i.e.* in the direction perpendicular to the $(\bar{1}10)$ planes, its contribution to the displacement field observed in this experiment would not be directly visible. On the other hand, the in-plane displacement of the atoms on $(\bar{1}10)$-type facets is visible, whereas the in-plane displacement on the (111) and $(\bar{1}\bar{1}\bar{1})$ facets is not visible.

The ϵ_{zz} component of the strain tensor on the (111) and $(\bar{1}\bar{1}\bar{1})$ facets is easily assimilated to variation of the interplanar spacing d_{111} (positive strain is tensile strain, negative strain is compressive). However, the physical meaning of the strain becomes more complex when observing facets that are neither parallel nor perpendicular to the [111] direction, such as $\{1\bar{1}1\}$ or {100} facets. For this reason, the following analysis of the heterogeneous strain is meant to be qualitative, by comparing the strain evolution of the same facets at different conditions but not between different facets, a quantitative analysis could only be performed with the full strain tensor, and not only one of its components.

If equivalent orientation translates into equal surface atomic structures (e.g. (111) and $(\bar{1}\bar{1}\bar{1})$ facets), the environment of equivalent facets is not always the same. For example, it is important to differ between $(1\bar{1}1)$-type and $(\bar{1}1\bar{1})$-type facets, the higher the value of the *interplanar angle*, defined as the angle between the facets normals and the [111] direction, the closer the facet is to the interface with the substrate, and thus the more its influence in prominent. Moreover, if the (111) facet is at the top of the crystal and the furthest away from the substrate, the $(\bar{1}\bar{1}\bar{1})$ facet is expected to be fully in contact with the substrate.

Therefore, the mean value and standard deviation of the heterogeneous strain distribution on each facet is presented in fig. 3.17, as a function of the interplanar angle, to highlight this difference. $(\bar{1}\bar{1}1)$-type facets near the substrate are also smaller than their $(11\bar{1})$-type equivalent, which can have an effect on the facet strain.

The values of the strain are in general quite low, always below 0.1 %, while the highest value of the displacement field on the particle facets is of about 1 Å (app. A.7). To see how the current experiment situates itself regarding the low-strain hypothesis necessary for phase retrieval detailed in sec. 2.6, the example of the particle at 600 °C under Argon flow is taken. The magnitude of the scattering vector at the position of the Bragg peak is $|\vec{G}|\approx 2.772\,\mathrm{Å}^{-1}$, while the magnitude of the scattering vector probed furthest from the Bragg peak during the measurement is along the [111] direction, $|\vec{q}|\approx 2.742\,\mathrm{Å}^{-1}$. $\delta q = 0.03\,\mathrm{Å}^{-1}$ gives $(\vec{q} - \vec{G}).\vec{u} = 0.03 << 1$, which places the experiment far away from the BCDI limit.

The very large strain standard deviations seen in fig. 3.17 at 150 °C for the $(\bar{1}\bar{1}\bar{1})$, $(\bar{1}1\bar{1})$, $(1\bar{1}\bar{1})$ and $(11\bar{1})$ facets can be explained by the presence of the dislocation, around which the

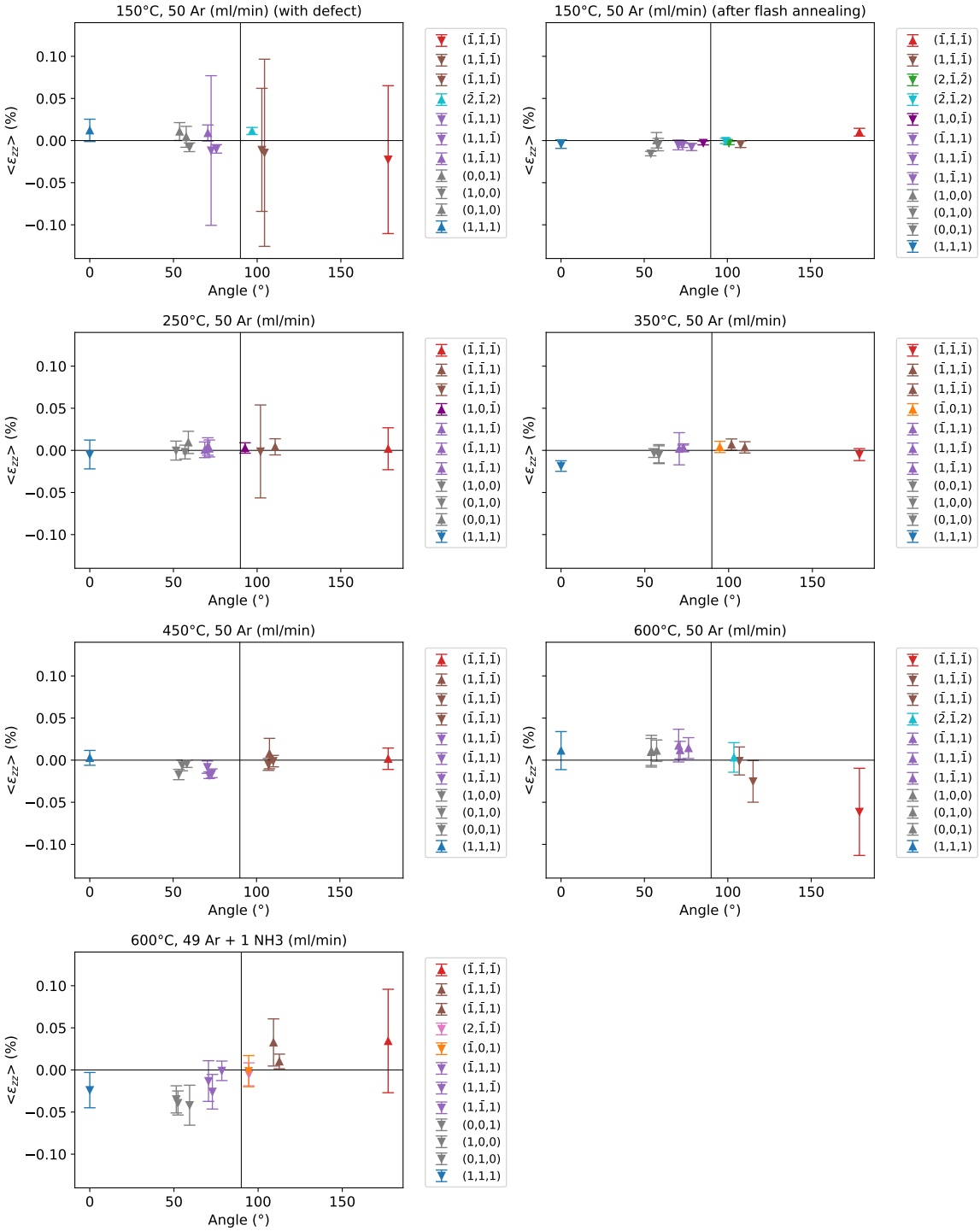

Figure 3.17: Mean value and standard deviation of the heterogeneous strain ($\epsilon_{zz,htg}$) distribution for each facet as a function of the angle between the normal of each facet on the particle surface and the [111] *direction. Upwards and downwards arrows are represented for respectively positive and negative strain.*

phase was not unwrapped as seen in fig. 3.12 (due to a 2π phase jump, Clark et al. 2015). Dislocations are also expected to be at the origin of regions with large strain deviations from this impact on the displacement field, as observed for example in the middle of the $(\bar{1}\bar{1}\bar{1})$ facet in fig. 3.14 at 600 °C. At 150 °C, after removal of the dislocation, all of the facets show low strain values as well as low strain standard deviation, which is also the case at 250 °C, 350 °C, and 450 °C (fig. 3.17).

The most interesting changes in the facet strain occur at 600 °C. The appearance of a hole at the interface with the substrate has the effect of *splitting* the particle in two states, characterised by negative strain near the sapphire-particle interface and positive strain at the top of the particle.

This effect is reflected into respectively tensile and compressive strain on the (111) and $(\bar{1}\bar{1}\bar{1})$ facets, and is reversed by the introduction of ammonia at 600 °C, visible also in fig. 3.14 and 3.15, when the hole is replaced by a dislocation network.

It is also during the presence of ammonia in the reactor that a $(2\bar{1}\bar{1})$ facet appears for the first time, perpendicular to the [111] direction (fig. 3.8). Both facets perpendicular to the [111] direction, *i.e* $(2\bar{1}\bar{1})$ and $(\bar{1}01)$, show low ϵ_{zz} values, corresponding to the absence of in-plane lattice strain in their cases. In fig. 3.18, the three (100)-type facets exhibit the same strain values, none of which have the same surrounding facets, while the areas between the (111) and {100} facets show a slightly positive strain.

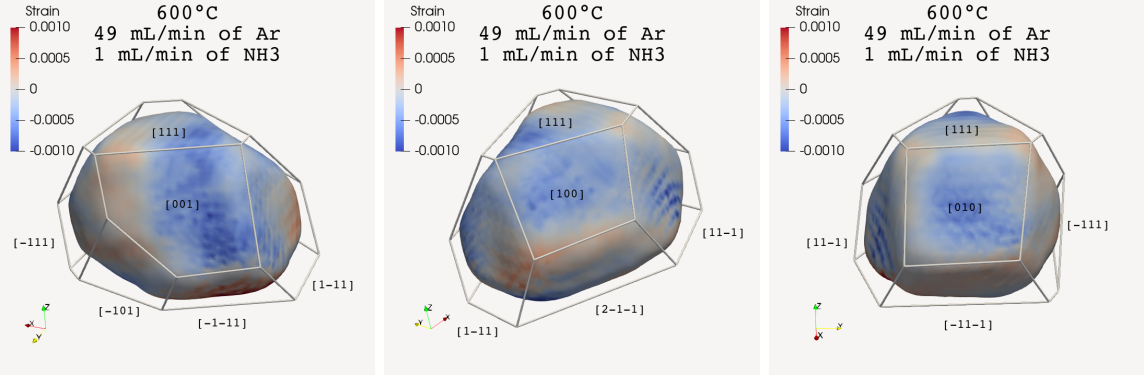

Figure 3.18: View of the particle A at 600 °C after the introduction of ammonia. The three {100} facets are surrounded by either 4 {111} facets and one {110} facets (left), by 3 {111} facets and one {110} facets (middle) or by 4 {111} facets (right).

All facets that have a similar environment regarding the substrate and structure show a similar strain (e.g. the three {100}, and three $(1\bar{1}1)$-type facets) in fig. 3.17 and 3.18. When considering all the {111} facets, different strain states are observed. The {111} facets close to the substrate do not show the same strain than those closer to the top of the particle (fig. 3.17). The strain being in the [111] direction with the origin of the displacement field in the centre of the particle, if all of these facets had experienced the same compressive (tensile) strain perpendicular to their surface *via* e.g. the adsorption of ammonia, they would all show a negative (positive) strain.

This behaviour could be linked to a strong effect of the support, which has the dual effect of first preventing the $(\bar{1}\bar{1}\bar{1})$ facet from being exposed to the gases in the reactor and secondly forcing them to accommodate the strain linked to epitaxial relationship with the substrate. The $(\bar{1}\bar{1}1)$-type facets near the substrate have also a significantly smaller size than the $(11\bar{1})$-type facets near the top of the particle, which can influence their initial strain state, and thus adsorption properties. There are three possibilities, first ammonia is effectively adsorbed on all these facets but the influence of the substrate/facet size hides a possible common signature in the strain. Secondly ammonia is not adsorbed and the strain difference is due to the influence of the substrate/facet size. Thirdly, ammonia is adsorbed but only on the three top facets or only on the 2 bottom facets due to the influence of the substrate/facet size that either limits or facilitates the adsorption process.

Overall, it is difficult to conclude on any potential effect of the absorption of ammonia on the particle due to the presence of the dislocation network at the interface, whose origin related to the adsorption of ammonia or from interfacial strain is unclear. It is also possible that the observed effect is linked to the reduction of the particle surface, since the particle has only been exposed to air and argon prior to ammonia. The fact that only one component of

the strain tensor is available makes it difficult to quantify any relaxation effect on the facets that are not perpendicular to the [111] direction.

To summarise, the structure of the facets in contact with the $(\bar{1}\bar{1}\bar{1})$ facet at the interface with the substrate evolve during the heating process, with a perfectly symmetric particle only measured at 450 °C, exhibiting only {111}, and {100} facets. Annealing the particle to 800 °C for a few minutes effectively removed the dislocation present at the particle substrate.

It was observed that the d_{111} interplanar spacing follows two different linear trends as a function of the temperature, depending on the presence of a dislocation at the particle interface with the substrate. The removal of the dislocation resulted in a large increase of the interplanar spacing. Different ϵ_{zz} strain values were observed on facets sharing the same structure and equivalent orientation with the direction of the scattering vector, but different local environments because of the presence of a substrate, as well as different sizes. A similar influence of the epitaxied substrate on the facet strain has been observed for a 100 nm large Pt-Rh particle by Kim et al. (2021).

The introduction of ammonia in the reactor was related to an inversion of the ϵ_{zz} strain, and also to the appearance of a dislocation network at the interface of the particle with the substrate.

From this first set of results, the measurement of Pt nanoparticles with BCDI during the oxidation of ammonia was decided to be carried out at lower temperatures, e.g. 300 °C and 400 °C.

3.3.3 Particle structure evolution during ammonia oxidation at 300 °C and 400 °C

Particle *A* being unstable on the substrate during the oxidation of ammonia at 600 °C, the reaction was measured at lower temperatures before and after the catalyst light off, respectively 300 °C, and 400 °C. Two particles, namely *B* and *C*, were identified on the substrate, first measured at room temperature under inert argon atmosphere.

The support of particle *B* (fig. 3.19) was well determined at room temperature, exhibiting a round shape with a total of 30 facets. Approximately 76 % of the particle surface voxels were recognised to belong to facets.

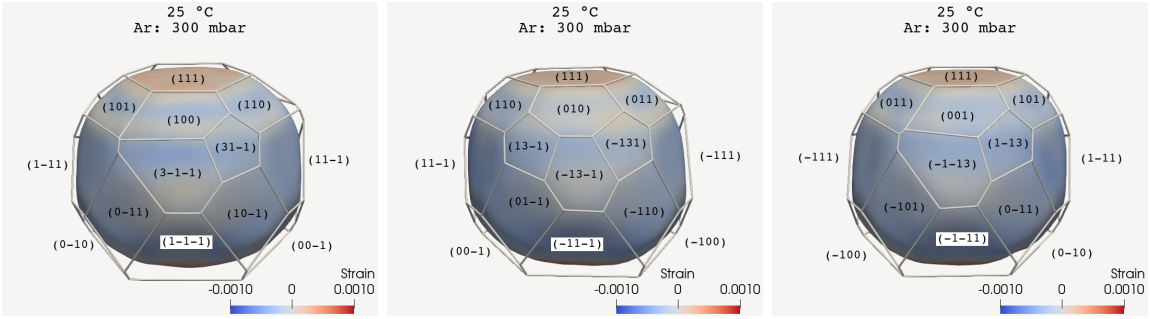

Figure 3.19: Surface of the reconstructed particle B at 25 °C under inert argon atmosphere. The surface is coloured by the values of the heterogeneous out-of-plane strain as described in eq. 3.5 at each surface voxel, the limit of each facet is delimited by thick white lines.

About 10.5 % of the particle surface is covered by {100} facets, 23.1 % by {110} facets, 35.2 % by {111} facets, and 7.3 % by {113} facets. The particle has a round shape, with a diameter of 300 nm.

From the 3D representation of the particle in fig. 3.19, the existence of the $(3\bar{1}1)$ and $(\bar{1}13)$ facets seem to be highly probable when considering the symmetry and shape of the particle. Those facets could not be detected by the recognition algorithm, probably due to a lack of spatial resolution, necessary to detect the smallest facets on the particle.

In contrast with particle *B*, the support of particle *C* could not be determined at room temperature, parts of the particle systematically missing from the reconstructions. No dislocation could be identified at the interface with the substrate but rather a lack of convergence of the support. Heating the sample to 300 °C under Argon did not improve the quality of the reconstruction. Interestingly, the introduction of ammonia in the reactor at the beginning of the oxidation cycle had the effect of lowering the average strain inside the particle (discussed further), and allowed the convergence of the support. The particle *C*, shown in fig. 3.20, was thus first reconstructed at 300 °C under 294 mbar of argon and 6 mbar of ammonia in the reactor.

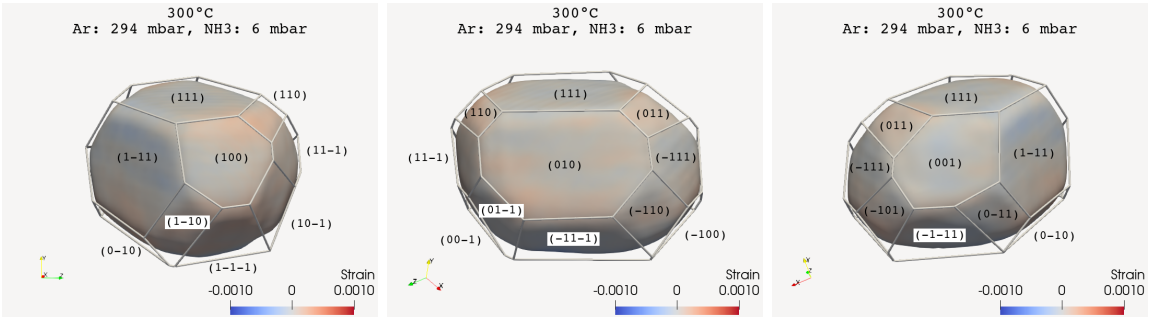

Figure 3.20: Surface of the reconstructed particle C at 300 °C under a partial pressure of ammonia equal to 10 mbar. The surface is coloured by the values of the heterogeneous out-of-plane strain as described in eq. 3.5 at each surface voxel, the limit of each facet is delimited by thick white lines.

Particle *C* exhibits a more rectangular shape without any {113} facets, 10.8 % of its surface is covered by six {100} facets, 6.4 % by {110} facets, and 36.3 % by {111} facets. The particle is at the largest 800 nm wide. Only 53.4 % of the surface voxels were determined to belong to facets, there is for example a large area between the (111) and (1$\bar{1}$1) facets (fig 3.20 - left) that could correspond to the missing (101) facet. Compared to particle *B*, the area between the (100)-type facets and ($\bar{1}1\bar{1}$)-type facets is clearly determined, and not expected to contains higher index facets.

The two nanoparticles have a very different shape and facet coverage, resumed in tab. 3.5. The percentage of the total surface area covered by {100} and {111} facets is similar (respectively about 10 % and 36 %). The largest difference in the {110} facet coverage can be partially explained by the non-detection of the (101) facet. Most importantly, the large particle does not exhibit high Miller index facets.

	{100}	{110}	{111}	{113}	Undefined
Particle B (300 nm wide)	10.5 % (6)	23.1 % (9)	35.2 % (8)	7.3 % (7)	23.9 %
Particle C (800 nm wide)	10.8 % (6)	6.4 % (8)	36.3 % (8)	0 %	46.5 %

Table 3.5: Particle surface area covered by facet type, the number in parenthesis designates the amount of each facet identified on the surface.

Together with particle *A*, this results shows that the sample used during this experiment is covered with many different nanoparticles that all together contribute to the catalytic activity, and probably show an even greater variance of shape and size. The current analysis using BCDI aim to reveal the structure variation during a catalytic reaction of a few selected nanoparticles. Statistically representing the population on the sample is impossible, the measurement process being currently too time consuming to probe more than a few nanoparticles.

The ammonia oxidation cycle was started at 300 °C, with the introduction of ammonia. The different atmospheres used to probe the relation between particle structure and selectivity have been introduced in tab. 3.2. A maximum of three scans were recorded under each

condition (tab. 3.2) at 300 °C and 400 °C for each particle to probe for any evolution of the particles surface structure during a fixed atmosphere as a function of time, and to otherwise demonstrate the reproducibility of the measurements.

A 3D view of the reconstructed nanoparticles at 300 °C and 400 °C during the ammonia oxidation cycle is presented in appendix A. The surface is coloured by the values of the heterogeneous out-of-plane strain as described previously in eq. 3.5 at each surface voxel. The view perpendicular to the three axes of the laboratory frame is represented, the particles are tilted due to the incoming angle θ for the measurement of the (111) Bragg peak. Both the retrieved displacement and strain fields are represented with their respective colour-bars, the ammonia to oxygen ratio is represented on the right part of the figure.

Particle B

A different behaviour during the oxidation of ammonia was observed on both nanoparticles. Particle *B*, which is smaller and thus scatters less than particle *C*, was difficult to reconstruct once the temperature increased to 300 °C.

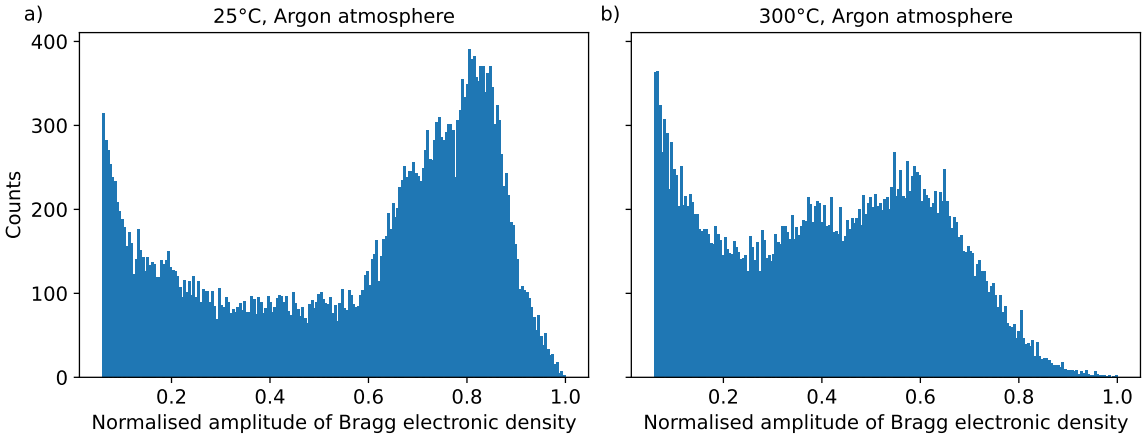

Figure 3.21: Histograms of normalised Bragg electronic density amplitude, for particle B. Values below 0.05 are ignored since they typically belong to voxels located far away from particle support. The difference between bulk, surface, and voxels outside the support is smeared out in b).

Normalised histograms of the particle reconstructed Bragg electronic density showed no more clear distinctions between regions inside and outside the support (fig. 3.21), and choosing a threshold value to draw the particle iso-surface no longer became evident.

Choosing a low threshold for the particle iso-surface could still be done, but resulted in a round object without clear facets. The small volume of the particle also probably impacts the quality of the measurements, increasing the spatial resolution and leading to this *rounding* of the particle. Some reconstructions showed a good quality at 300 °C, but in a larger sense recovering the facets on the particle surface in a reproducible way became impossible.

To be able to quantify the strain inside the particle, the 3D diffraction patterns were orthogonalised in q-space (fig. 3.22). Increasing the temperature to 400 °C under inert atmosphere was at the origin of the appearance of a defect in the particle, visible directly in reciprocal space by the shape of the 3D diffraction patterns, split in two parts (fig. 3.22, transition from a to b), which did not improve the phase retrieval quality.

A signal parallel to the crystal truncation rod in the [111] direction is observed slightly shifted in $\vec{q}_y$, interfringes in the [111] direction are also visible with a slightly lower interval than on the original CTR. The distance between the [111] oriented rod and the second signal increases in q_y during the ammonia oxidation cycle, at the end of which a third signal parallel to the two others can be observed (fig. 3.22 - c). The maximum of both signals seems to be

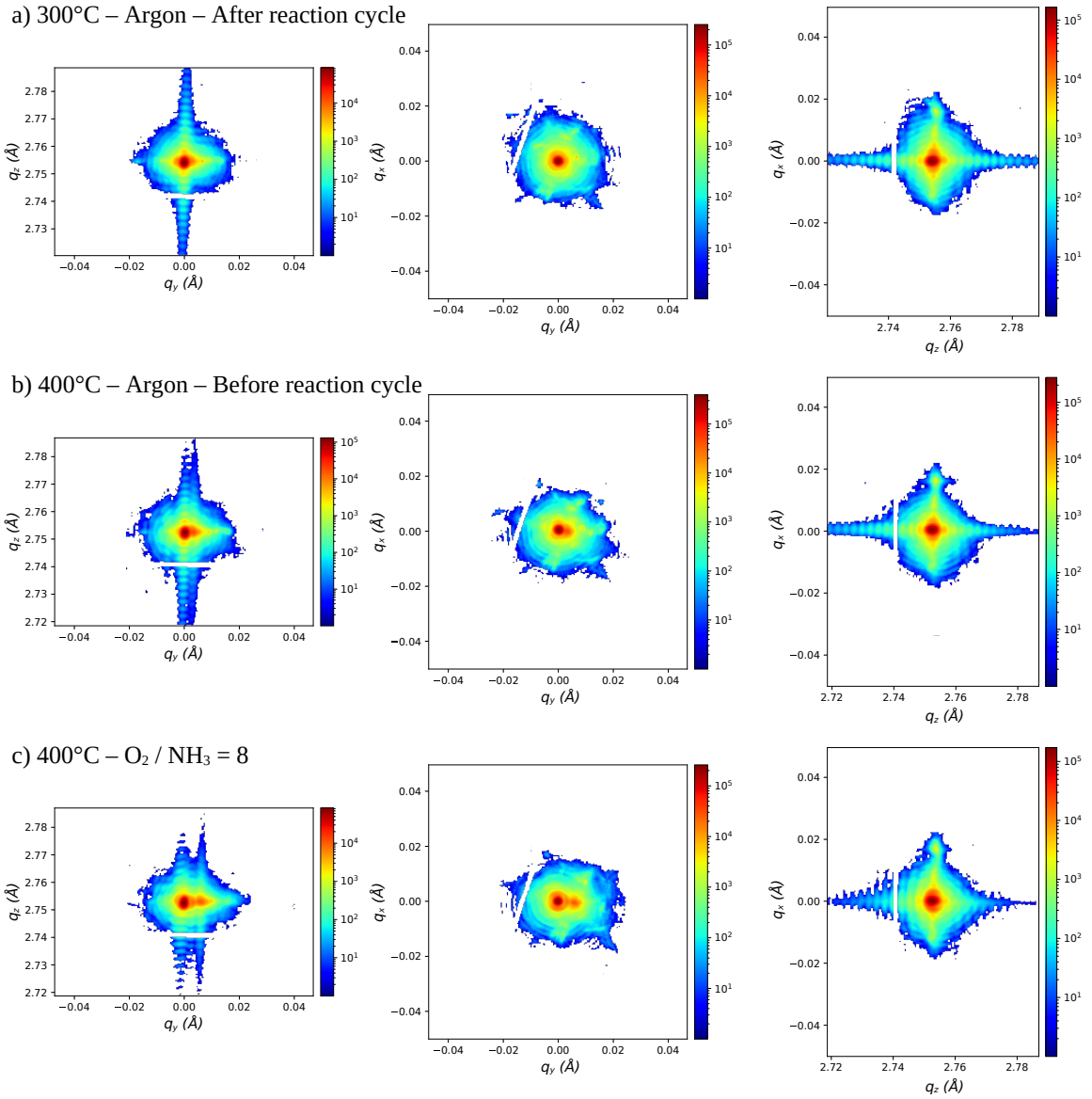

Figure 3.22: Sum of the intensity scattered from particle B around the (111) platinum Bragg peak in the $\vec{q}_x$, $\vec{q}_z$ and $\vec{q}_y$ directions after orthogonalisation of the diffraction pattern. The [111]-oriented crystal truncation rod is visible parallel to the $\vec{q}_z$ axis. Detector gaps lead to rectangular areas of missing intensity.

at the same value in q_z, which can be related to the average out-of-plane lattice parameter inside the particle.

The defects are also visible perpendicularly to the particle substrate and through the particle in 3D in appendix A, ultimately resulting in holes in the Bragg electronic density (Clark, Ihli et al. 2015; Dupraz 2015).

The intensity scattered from particle B around the (111) platinum Bragg peak was summed along the ($\vec{q}_x$, $\vec{q}_y$), ($\vec{q}_y$, $\vec{q}_z$) and ($\vec{q}_z$, $\vec{q}_x$) planes, and respectively fitted in the $\vec{q}_z$, $\vec{q}_x$ and $\vec{q}_y$ directions. ($\vec{x}$, $\vec{y}$, $\vec{z}$) designates the sample frame, where the $\vec{z}$ direction is parallel to the [111] direction from the epitaxy relationship of the particle on the substrate. The sum in the planes perpendicular to the $\vec{q}_x$ and $\vec{q}_y$ directions carry information about the in-plane particle shape and strain, whereas the sum perpendicular to the $\vec{q}_z$ direction carries information about the out-of-plane particle shape and strain.

The summed intensities were then fitted in each direction by a Lorentzian shape function

to extract the Bragg peak full width at half maximum (FWHM) in each direction: FWHM_x, FWHM_y, FWHM_z. The average interplanar spacing was also computed from the peak position in q-space. Once the second signal appeared in $\vec{q}_y$, two Lorentzian profiles were used to fit both peaks, FWHM_y in fig. 3.23 is equal to the sum of FWHM_y from each peak.

A typical fit is shown in appendix A.9, the retrieved FWHM are shown in fig. 3.23, the average interplanar spacing and homogeneous strain are shown in fig. 3.24.

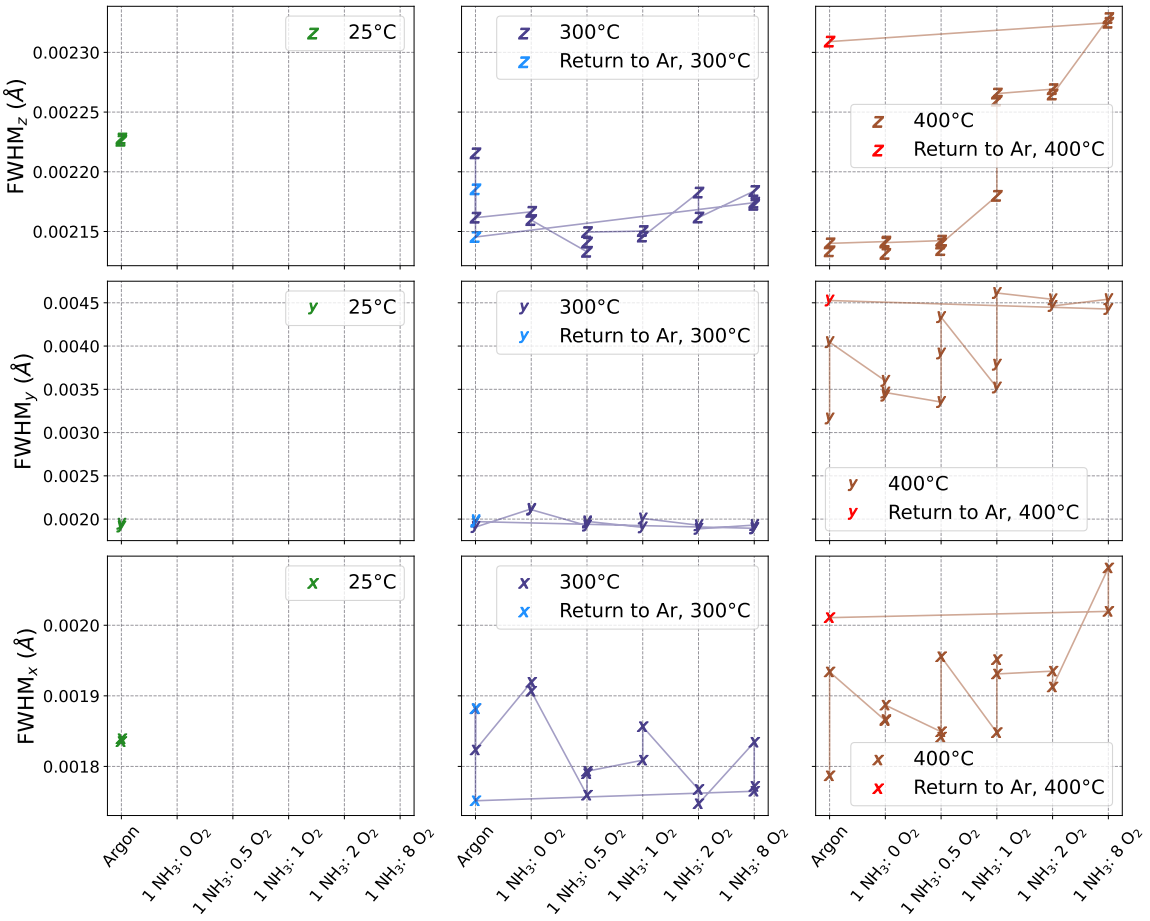

Figure 3.23: Evolution of the full width at half maximum (FWHM) for particle B in the $\vec{q}_x$, $\vec{q}_y$ and $\vec{q}_z$ directions at 25 °C, 300 °C and 400 °C as a function of the ammonia to oxygen ratio. The reproduction of measurements at fixed conditions yields multiple data points, lines at 300 °C and 400 °C link the data points in the order of the measurements.

A decrease of FWHM_z can be observed between successive measurements under argon after heating the sample to 300 °C, whereas the values of FWHM_x and FWHM_y are stable, which could be due to the stabilisation of the particle after the temperature increase. Introducing ammonia in the reactor has the effect of increasing FWHM_x and FWHM_y without increasing FWHM_z, thus probably related to an increase of the in-plane strain in the particle. A decrease of the FWHM can be seen in all three directions when oxygen is introduced in the reactor, which may be associated to a global decrease of the particle strain. The range of values in FWHM_z is very low and if a slight increase is observed as a function of the ammonia to oxygen ratio, it is only for very small values. No clear evolution can be observed in FWHM_x or FWHM_y.

On one hand, the values of FWHM_z at 400 °C are stable until the ammonia to oxygen ratio becomes equal to one, which can be linked to an increase of the out-of-plane strain in the particle. Higher amounts of oxygen further continue this increase.

A large jump is observed for FWHM_y after the increase of temperature under inert at-

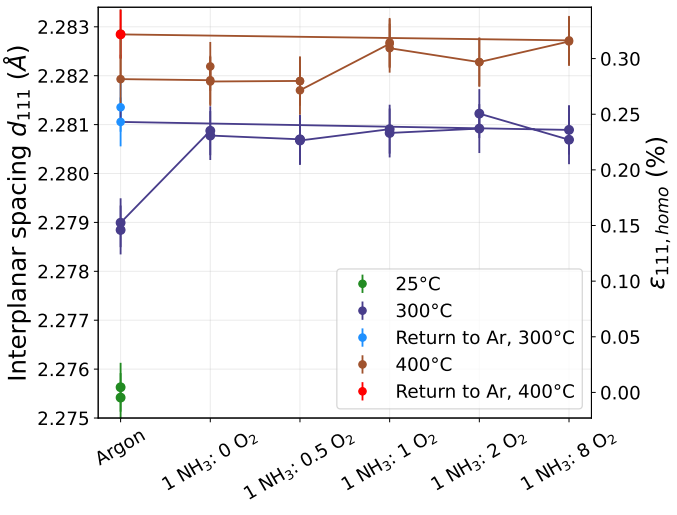

Figure 3.24: Evolution of the interplanar spacing d_{111} and homogeneous strain $\epsilon_{111,homo}$ for particle B as a function of the ammonia to oxygen ratio. The reference for the computation of $\epsilon_{111,homo}$ was taken as the mean value at 25 °C. The reproduction of measurements at fixed conditions yields multiple data points, lines at 300 °C and 400 °C link the data points in the order of the measurements.

mosphere, being multiplied by 50 % and 100 % in the first and second measurements. No jump is observed for FWHM$_x$ in the first measurement, an increase is observed in the second measurement, but not as important as for FWHM$_y$. This coincides with the appearance of a new signal observed in fig. 3.22 perpendicular to $\vec{q}_z$, *i.e.* in the $(\vec{q}_x, \vec{q}_y)$ plane, mostly shifted in q_y in comparison to the centre of the Bragg peak. This signal is linked to the appearance of a defect in the particle.

The introduction of ammonia does not have a visible effect in $\vec{q}_z$, but decreases the FWHM in both $\vec{q}_x$ and $\vec{q}_y$ in comparison to the second measurement under argon. Both FWHM$_x$ and FWHM$_y$ increase together with the ammonia to oxygen ratio, FWHM$_y$ plateaus when the ratio is equal to 1, whereas FWHM$_x$ largely increases when the ratio becomes equal to 8.

The FWHM under argon after and before the oxidation cycle are similar at 300 °C but not at 400 °C, a temperature at which the oxidation cycle completely changed the shape and strain state of the particle, visible in app. A. The particle shape is not reversible at 400 °C after the oxidation cycle.

Two main phenomena of interest must be kept in mind from the evolution of the interplanar spacing in fig. 3.24, besides the expected increase with temperature, verified in the previous section. First there is a 0.08 % increase of the homogeneous strain following the introduction of ammonia at 300 °C. The interplanar spacing stays approximately equal to the same value afterwards during the ammonia oxidation cycle. Secondly, there is an increase of about 0.02 % of the homogeneous strain at 400 °C when the ammonia to oxygen ratio reaches the value of one. Both of these phenomena are observed at conditions for which changes in the FWHM are also seen.

Finally, to be able to give a first estimation of the amount of strain inside the particle, the strain field energy defined as the sum of the product of stress and strain integrated over the particle (Cahn 2004) was computed following the work performed by Ulvestad et al (2015) and by Kim et al. (2019).

Assuming cubic symmetry and isotropic shear-free conditions within the unit cell, the strain field energy is simplified to eq. 3.9. Here, G and L represent the material's Lame constants, which can be estimated from Young's modulus E and Poisson ratio ν, as described in eq. 3.10 (Mavko et al. 2020).

$$E_s = \frac{2G + 3L}{2} \int \epsilon_{zz}^2 dV \tag{3.9}$$

$$G = \frac{E}{2(1+\nu)} \qquad L = \frac{E\nu}{(1+\nu)(1-2\nu)} \tag{3.10}$$

The evolution of the strain field energy as a function of each scan to be able to compare with the 3D reconstructions of the particle shown in app. A is presented in fig. 3.25. For a qualitative approximation of the strain field energy, the Young's modulus was taken equal to 153.3 GPa and the Poisson ratio to 0.401 based on literature values at 400 °C (*High Temperature Mechanical Properties of the Platinum Group Metals* 2022).

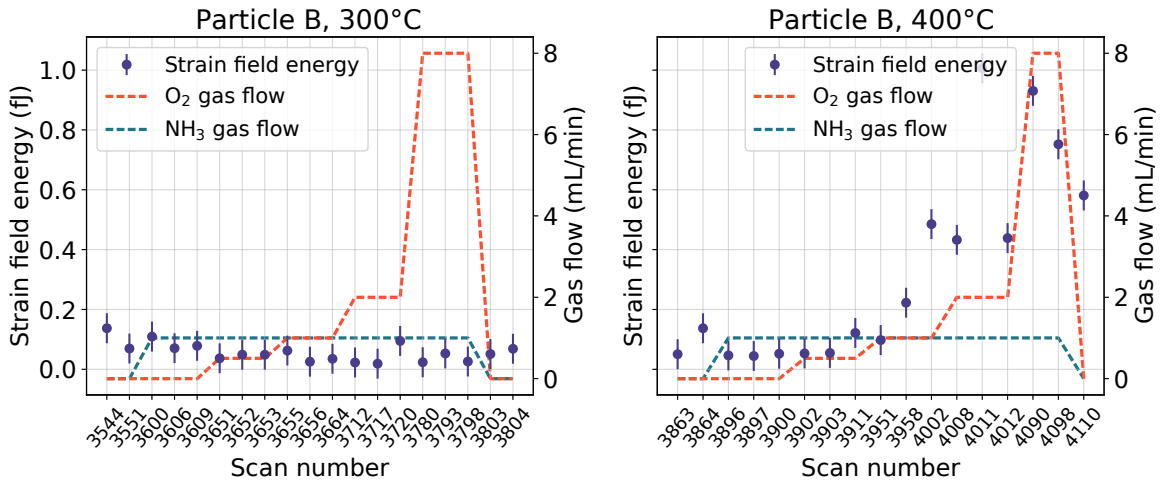

Figure 3.25: Evolution of the strain field energy for particle B as a function of the scan number. The evolution of the NH_3 and O_2 gas flows in the reactor are also plotted to highlight the effect of the simultaneous presence of ammonia and oxygen and of the increasing amount of oxygen on the values of the strain field energy.

The strain field energy shows very little evolution at 300 °C, decreasing a little under the presence of ammonia and further under reacting conditions. However, the values of the strain field energy are observed to increase under reacting conditions at 400 °C, multiplied approximately by 3 when the O_2/NH_3 ratio is equal to 1, and by 9 when equal to 8. This result is consistent with the evolution of the different FWHM in fig. 3.23 and with the 3D shape of the particle.

To summarise, the introduction of ammonia at 300 °C has resulted in (i) a slight increase of the in-plane strain, observed from the evolution of the peak FWHM in the $\vec{q}_x$ and $\vec{q}_y$ directions in fig. 3.23; in (ii) a large increase of the homogeneous strain, observed from the value of the d_{111} interplanar spacing in fig. 3.24, which was not reversed after the removal of ammonia following the end of the oxidation cycle. These changes can be linked to the first reduction of the particle, previously only exposed to air and argon, since such changes are not observed at 400 °C. No changes in the particle strain and structure as a function of the ammonia to oxygen ratio could be detected at 300 °C.

The most important changes in the particle structure occur at 400 °C. Heating the sample under inert atmosphere has resulted in the appearance of a defect visible directly in reciprocal space (fig. 3.22), and by the evolution of $FWHM_y$ (fig. 3.23). The increase of strain inside the particle is also visible in 3D by the progressive importance of holes in the reconstructed volume (app. A), and by the evolution of the strain field energy (fig. 3.25). Interestingly, a transition is observed during the simultaneous presence of both ammonia and oxygen in the reactor, when $O_2/NH_3 = 1$ (scans 3951, 3958 and 4002). This transition is also visible in $FWHM_z$ (fig. 3.23), which can be related to an increase of the out-of-plane strain inside the particle.

Particle C

As mentioned earlier, particle *C* could only be reconstructed under the presence of ammonia in the reactor. Interestingly, no changes in the particle shape or surface strain values have

been observed during the exposition to the reactants (appendix A).

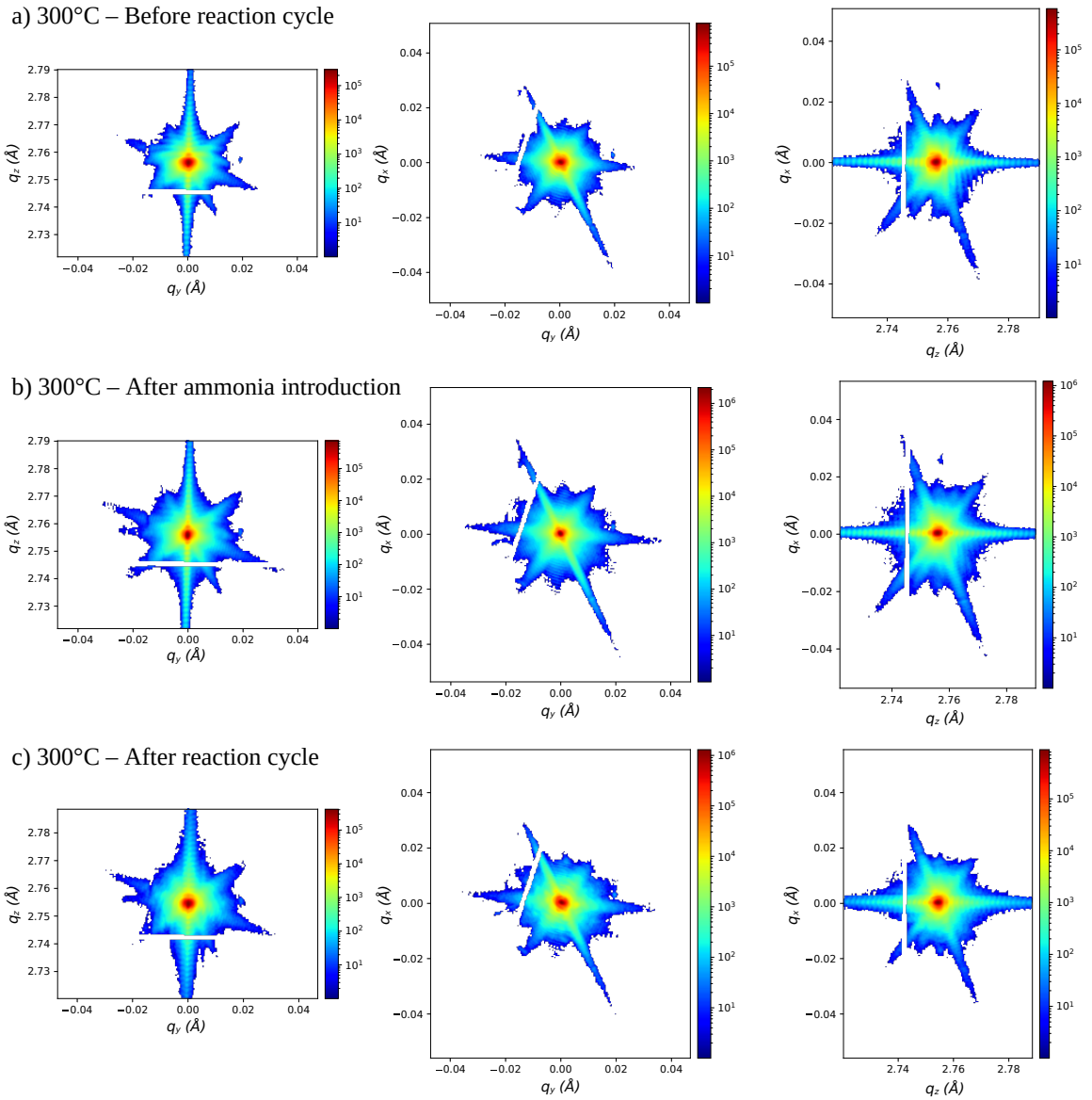

Figure 3.26: Sum of the intensity scattered from particle C around the (111) platinum Bragg peak in the $\vec{q}_x$, $\vec{q}_z$ and $\vec{q}_y$ directions after orthogonalisation of the diffraction pattern. The [111]-oriented crystal truncation rod is visible parallel to the $\vec{q}_z$ axis. Detector gaps lead to rectangular areas of missing intensity.

When removing ammonia and oxygen at 300 °C, the particle could not be reconstructed anymore, reproducing the same behaviour as before the introduction of ammonia. Increasing the temperature to 400 °C did not improve the reconstruction quality as the support did not converge during phase retrieval. Using the support of the particle reconstructed at 300 °C under ammonia as a starting guess for the algorithms did not suffice to reach a good final solution. The reconstructions under inert atmosphere before introducing ammonia or after removing both reactants from the cell presented in appendix A have been performed by limiting the support update to every 200 iteration (for a total of 1100 algorithm iteration during phase retrieval, meaning that the support is only changed 5 times), and still present a highly heterogeneous Bragg electronic density.

To understand why it was impossible to successfully carry out the phase retrieval process, the diffraction pattern around the (111) Bragg peak under the presence of both reacting gases

and after their removal was orthogonalised in q-space, presented in fig. 3.26.

The diffraction pattern before the introduction of ammonia (fig. 3.26 - a) exhibits a slightly distorted shape along $\vec{q}_z$, which can be related to the presence of heterogeneous strain in the particle, typically at the interface with the substrate. The introduction of ammonia in the reactor has removed this distortion (fig. 3.26 - b), which generally improves the quality of phase retrieval.

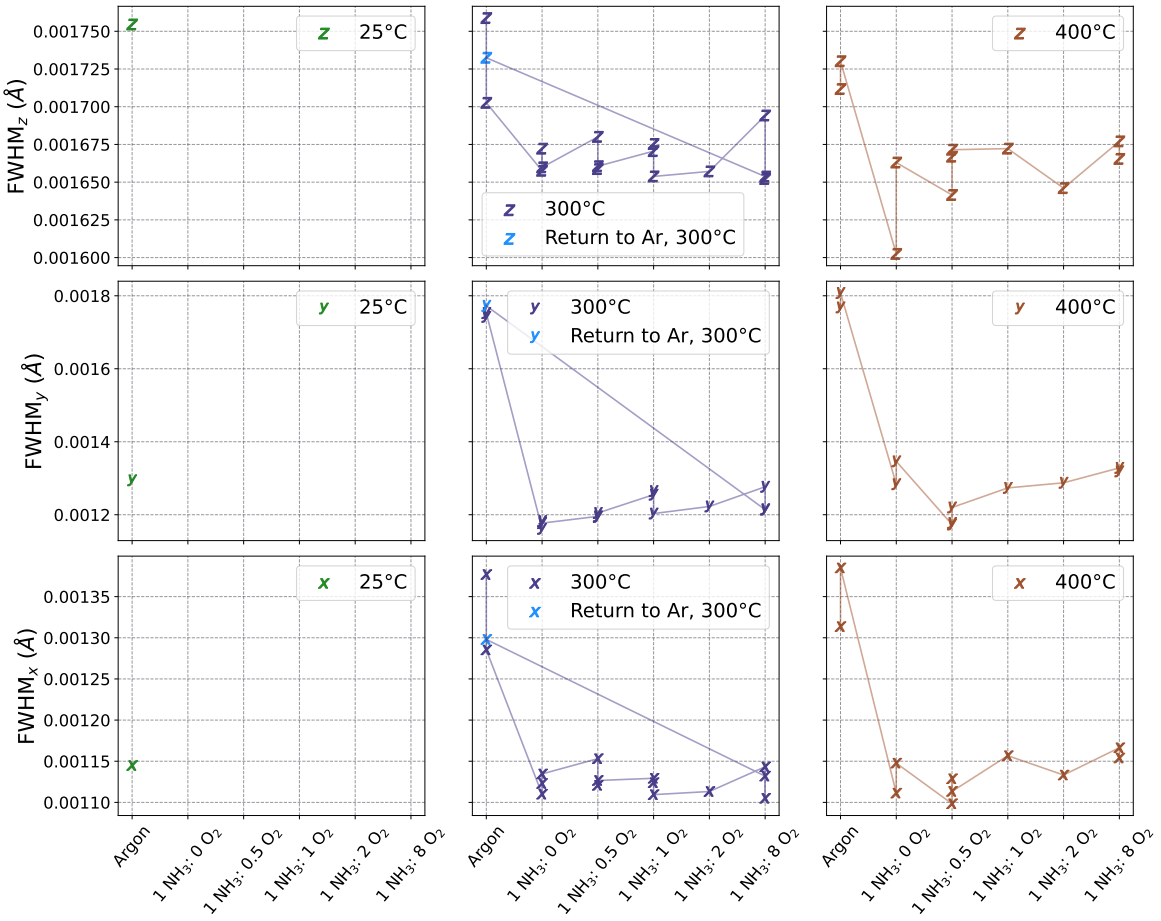

Figure 3.27: Evolution of the full width at half maximum (FWHM) for particle C in the $\vec{q}_x$, $\vec{q}_y$ and $\vec{q}_z$ directions at 25 °C, 300 °C and 400 °C as a function of the ammonia to oxygen ratio. The reproduction of measurements at fixed conditions yields multiple data points, lines at 300 °C and 400 °C link the data points in the order of the measurements. No scans were performed at 400 °C under Argon after the oxidation cycle.

Interestingly, the diffraction pattern after the removal of both gases in the reactor (fig. 3.26 - c) is not similar to the measurement before the oxidation cycle (fig. 3.26 - b), both diffraction patterns are collected under argon. In general, the fringes are less visible in all direction, especially in the ($\vec{q}_x$, $\vec{q}_y$) plane, areas of higher intensity also appeared around the Bragg peak. Most importantly, the coherence fringes situated in the [111] direction, *i.e.* along $\vec{q}_z$ show a completely different pattern, as if two CTRs were on top of each other, one with larger rectangular fringes, while the other one has smaller round fringes. The particle clearly suffered a change of shape after the removal of the reacting gases, meaning that different phenomena before and after the oxidation cycle impinge on the reconstruction quality. It is possible that the first exposition to ammonia has the effect of reducing the particle that was beforehand only exposed to air and argon. Thus, removing ammonia and oxygen at the end of the cycle can yield a different state than before the oxidation cycle.

The same kind of diffraction patterns are observed at 400 °C after heating under argon

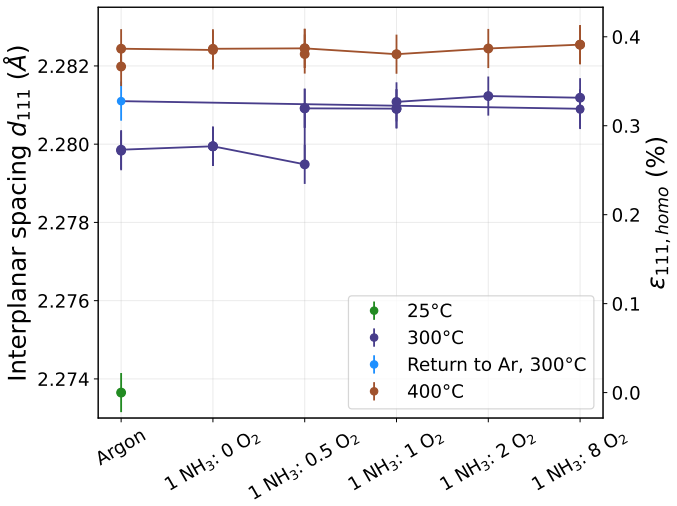

Figure 3.28: Evolution of the interplanar spacing d_{111} and homogeneous strain ϵ_{111} for particle C as a function of the ammonia to oxygen ratio. The reference for the computation of ϵ_{111} was taken at 25 °C. The reproduction of measurements at fixed conditions yields multiple data points, lines at 300 °C and 400 °C link the data points in the order of the measurements. No scans were performed at 400 °C under Argon after the oxidation cycle.

as in fig. 3.26 (c), and after the introduction of ammonia as in fig. 3.26 (b), meaning that the presence of NH_3 in the reactor lowers the strain in the particle, which can then easily be reconstructed.

The particle FWHM in all three directions follows the same evolution as a function of the different atmospheres, meaning that the same phenomena occurs in all direction of the particle. The FWHM decreases following the introduction of ammonia both at 300 °C and 400 °C, and only slightly increases during the exposition to oxygen. Returning to argon atmosphere, *i.e.* removing ammonia and oxygen yields FWHM values similar to those measured after heating to 300 °C under argon.

The evolution of the d_{111} interplanar spacing (fig. 3.28) is not the same as a function of different temperatures. The interplanar spacing of the particle under the sole presence of ammonia at 300 °C is remarkably reproducible with all three measurements yielding approximately the same value as under argon atmosphere. A large increase of the interplanar spacing is observed when oxygen is introduced in the reactor, at a ratio of 0.5 with ammonia, which gives a homogeneous strain evolution of approximately 0.07 % in reference to the value measured at room temperature. The strain at the interface with the substrate also becomes more homogeneous at this condition, slightly negative (appendix A). The interplanar spacing then stays approximately the same at 300 °C during the oxidation cycle. This transition is not observed at 400 °C, a temperature for which an increase of the interplanar spacing can be observed under argon, without any large deviations during the oxidation cycle.

The strain field energy was also computed for particle *C*, transitions between large and low magnitudes can be linked to the presence of ammonia in the reactor (fig. 3.29). No measurement was performed at 400 °C at the end of the oxidation cycle which prevents us from being certain that the decrease in the strain field energy observed at 300 °C could be reproduced, similar as for the evolution of the FWHM in fig. 3.27.

To summarise, particle *C* seems to have suffered a transition at 300 °C following the introduction of ammonia in the reactor, which helped improved the quality of phase retrieval, probably from a decrease of strain. The diffraction pattern was shown to not be exactly reproducible when returning to inert atmosphere, but still showing a decrease of sharpness regarding the position and intensity of the interfringes.

The transition can be observed in both the strain field energy (fig. 3.29), and in the FWHM of the three-dimensional Bragg peak (fig. 3.27). The interplanar spacing computed from the position of the Bragg peak in *q*-space shows an additional transition when first introducing oxygen in the cell, not visible in the strain field energy or in the FWHMs, which can tentatively be linked to a change of strain at the interface with the substrate.

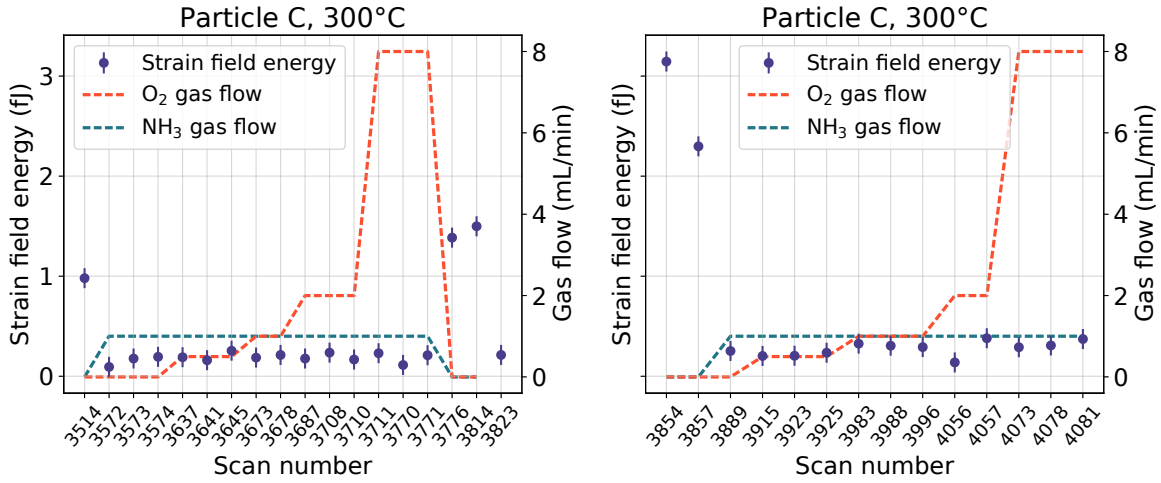

Figure 3.29: Evolution of the strain field energy for particle C as a function of the scan number. The evolution of the NH_3 and O_2 gas flows in the reactor are also plotted to highlight the effect of the presence of ammonia on the values of the strain field energy.

Mass spectrometry results

The catalytic activity of the particles was recorded *via* the use of a mass spectrometer and shows the production of nitrogen, nitrous oxide and nitrogen oxide (fig. 3.30), proving the activity of the catalyst. The original mass spectrometer signal as a function of time is available in the appendix A.10, and A.11.

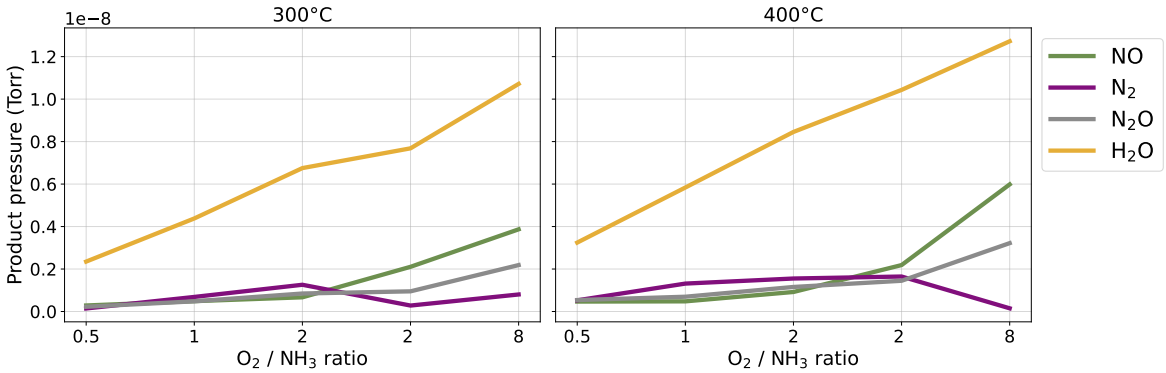

Figure 3.30: Evolution of reaction products partial pressures during the BCDI experiment on the patterned sample containing Pt nanoparticles, at 300 °C *and* 400 °C*. Mean partial pressures during* 1 min *at the end of each condition, recorded from a leak in the reactor output. The pressure under* 49 mL/min *of argon and* 1 mL/min *of ammonia has been subtracted.*

Interestingly, a transition was recorded at both 300 °C, and 400 °C approximately 4 h after the increase of the oxygen partial pressure from 10 mbar to 20 mbar, leading to a NH_3/O_2 ratio equal to 2. The partial pressure of N_2 is approximately divided by two while the partial pressure of NO is inversely multiplied by two.

In a general sense, the production of N_2 is favoured at lower oxygen partial pressures in comparison with N_2O and NO. The opposite effects takes place at high oxygen partial pressures, with a clear transition between the main products from N_2 towards NO when the oxygen to ammonia ratio is equal to 8, this transition happens at a lower NH_3/O_2 ratio at 300 °C.

3.4 Discussion

The reshaping of a Pt particle (particle *A*) during heating from 125 °C to 600 °C under an inert gas flow was put into evidence. An important evolution in the type of facets present near the particle interface with the substrate was reported as a function of the sample temperature (fig. 3.13). An interfacial dislocation was successfully removed by temperature treatment (fig. 3.11), yielding a defect free interface until the introduction of ammonia at 600 °C, which induced the appearance of a dislocation network (fig. 3.14). The importance of the metal-support interactions for catalysis was demonstrated for smaller nanoparticles (below 4 nm) in a general study by van Deelen et al. (2019). In the current study, the importance of taking into account the presence of interfacial strain was also highlighted with particle *A* (fig. 3.17), similarly to other BCDI studies of catalytic reactions. For example, Kim et al. (2021) have measured different strain evolution for {111} facets depending on their orientation with the $SrTiO_3$ substrate (CO oxidation, Pt-Rh nanoparticles, 100 nm large). Similar conclusions have been reached by Dupraz et al. (2022), also during the oxidation of CO with Pt nanoparticles (300 nm large particle). The relative facet size can also have an impact on the facet strain. Both effects could not be de-correlated in this study since facets of same structure but different orientation, *i.e.* $(1\bar{1}1)$ and $(\bar{1}1\bar{1})$, have different sizes, whereas facets of same orientation have similar sizes (e.g. $(1\bar{1}1)$-type facets in fig. 3.18). Particle *A* exhibited a symmetric shape only at 450 °C (fig. 3.13), isolated {110}, {221} and {211} facets were otherwise detected. A reconstruction at a higher temperature (600 °C) showed a hole in the Bragg electronic density near the particle substrate (fig. 3.14). The evolution of the interplanar spacing as a function of the temperature (fig. 3.16) shows that nanoparticles do not follow the same thermal relaxation curves when in the presence of interfacial defects, having an impact on the strain field.

The oxidation of ammonia has been extensively studied by the means of surface techniques in the previous and current century as detailed in sec. 1.4. Since BCDI is still a recent technique, first applied to catalysis less than 10 years ago (Ulvestad, Sasikumar et al. 2016), no comparative measurements could be found during the presence of ammonia or nitrogen based species.

The introduction of ammonia in the reactor at 600 °C was linked to an inversion of the average facet strain for particle *A* (fig. 3.17), together with the appearance of a dislocation network at the interface with the substrate (fig. 3.14). Facets of the same structure, size, and distance from the substrate showed similar strain state (fig. 3.17). It is possible that a strong adsorption of nitrogen species induced such a modification of the strain field that the appearance of a dislocation network was provoked. Indeed, no other variation of particle shape, or appearance of dislocation was observed without a change of temperature. Time-resolved measurements of the dynamics of the dislocation network as well as adsorption/desorption cycles could bring additional information supporting this hypothesis. The influence of the introduction of oxygen at 600 °C could not be probed due to the loss of particle *A*. The high temperature reached by the nano catalyst during the exothermic oxidation of ammonia (Hatscher et al. 2008) could have resulted in a loss of quality of the epitaxial relationship with the substrate.

Two additional particles, namely *B* and *C*, were measured at both 300 °C and 400 °C, respectively before and after the activation temperature expected from the characterisation of the catalyst shown in fig. 3.3. The two particles have different shape, facet coverage, and initial strain state. They show different structural evolution during ammonia oxidation.

The introduction of ammonia at 300 °C can be linked to a global decrease of the heterogeneous strain in particle *C*, whose surface consists exclusively of {111}, {110} and {100} facets (tab. 3.5). This effect is visible from the decrease of the strain field energy in fig. 3.29, the return to a symmetrical diffraction pattern in fig. 3.26, and the decrease of the FWHM in all three directions in fig. 3.27. The opposite (same) effect was observed after

removing (introducing) ammonia from the reactor at 300 °C and 400 °C, supporting the hypothesis of a nitrogen species (NH_x, N) adsorption/desorption induced cycle on the particle surface. The mechanism of such a cycle could correspond to a decrease of the surface strain by adsorption, propagating into the particle bulk. Such a scenario implies changes in the surface strain when introducing ammonia, which are not visible since the reconstruction of the measurements performed under inert atmosphere do not converge towards a well defined support. The introduction of ammonia at 600 °C when measuring particle *A* has had the opposite effect, *i.e.* the creation of a dislocation network. The absence of change in the facet strain following the introduction of oxygen and during the oxidation of ammonia can be due to different reasons. First, the change in the facet strain is too small to be detected with the low spatial resolution of the experiment, meaning that it is damped by being averaged with *bulk* layers. For example, oxygen adsorption induced strain on the Pt terminated {100} and {111} facets has been simulated to be zero 8 nm away from the surface in the bulk (Y. Y. Kim et al. 2021). However, Dupraz et al (2022) have shown in a higher resolution experiment that reaction-induced changes in the facet strain can propagate over the bulk of the particle. Changes in surface strain are thus expected to be possible to measure even with a lower resolution. Secondly, there is no change of facet strain following the introduction of oxygen, which could be interpreted by nitrogen species being so strongly adsorbed on the particle surface that they do not participate in the catalytic reaction. If this was indeed the case, it would mean that all three types of facets are poisoned at a NH_3 pressure equal to 6 mbar, showing a remarkably strong adsorption on many different atomic sites, and preventing catalytic activity on this nanoparticle. A strong evolution of particle *A* was also observed under the sole presence of ammonia at 600 °C, with the main structural differences being the absence of {110} facets (fig. 3.13), and a dislocation network at the interface (fig. 3.14). Thirdly, the oxidation of ammonia at ambient pressure does not involve the adsorption of oxygen on the catalyst surface, functioning *via* an Eley-Rideal mechanism (Rideal 1939), the production of NO and N_2O happening by the reaction of gas-phase oxygen with nitrogen adsorbed species. The surface strain would then not be expected to evolve during change of atmospheres. However, this would be in contradiction with literature findings that have proved the importance of prior atomic O and OH coverage for the de-hydrogenation process of NH_3, during a largely accepted Langmuir-Hinshelwood reaction mechanism (J. M. Bradley et al. 1995; Mieher et al. 1995; van den Broek et al. 1999; M. Kim et al. 2000). The pre-exposition of the particle to ammonia would prevent this mechanism, and thus the production of N_2, NO and NO_2. XPS results detailed in the next chapter have also highlighted the importance of adsorbed oxygen in the reaction mechanism. Moreover, a transition was observed in the homogeneous strain for particle *C* at 300 °C when first achieving reacting condition (fig. 3.28, up by 0.07 %, not reproduced at 400 °C).

Particle *B*, which exhibits {113} facets on its surface at room temperature in addition to {111}, {110} and {100} facets (tab. 3.5), follows a different structural evolution during the experiment. The surface coverage of {110} facets is also four times higher than for particle *C*. Heating the sample to 300 °C has decreased the visible presence of facets on the particle surface. While particle *C* observes a large decrease of heterogeneous strain during the introduction of ammonia, particle *B* suffers both a large increase of homogeneous strain with respect to the room temperature interplanar spacing (fig. 3.24, up by 0.09 %), together with an increase of the in-plane heterogeneous strain (fig. 3.23). This effect is not reversible when removing ammonia from the reactor at 300 °C, nor it is observed again when introducing ammonia at 400 °C. It is possible to link this phenomenon to the particle first exposition to reducing atmosphere after argon and air. The absence of strain evolution in the same condition for particle *C* (fig. 3.28) can be attributed to different surface states under argon from contaminants/oxides, linked to different facet coverage. The introduction of oxygen slightly decreases the heterogeneous strain in the particle (fig. 3.23), the in-plane heterogeneous

strain is stable during the oxidation of ammonia while the out-of-plane heterogeneous strain increases slightly. Thus, small changes are already visible at 300 °C for particle *B* during the oxidation of ammonia. The most impressive evolution for particle *B* occurs at 400 °C, with the appearance of a defect, characterised by a second peak in the 3D scattered intensity, shifted in $\vec{q}_y$ with respect to the Bragg peak (fig. 3.22). The influence of the defect in both the heterogeneous (fig. 3.23, fig. 3.25) and homogeneous strain (fig. 3.24) is clear once the O_2/NH_3 ratio is equal to one. A non reversible increase of homogeneous and heterogeneous strain is observed. Indeed, if the defect appeared during the increase of temperature to 400 °C, the particle shape and strain state seems to be stable until specific reaction conditions are achieved. To safely link defect dynamics and catalytic activity, several oxidation cycles would have to be measured, as well as an exposition of the particle to progressive amount of oxygen. Nevertheless, it can safely be said that the evolution of particle *B* seems to follow the reported activation and reconstruction process of industrial catalyst by defects reported by Hannevold et al. (2005b).

The exposition of platinum nanoparticles epitaxied on glassy carbon to oxygen at 200 °C has been probed by Fernandez et al. (2019), shown to be linked with an 0.09 % homogeneous tensile expansion of the particle in the [111] direction, attributed to the formation of platinum surface oxides. The nanoparticles were not exposed to oxygen without ammonia during this experiment. Nevertheless, a similar expansion was observed on particle *C* but during reacting conditions, and only at 300 °C (fig. 3.28, up by 0.07 %). Further increasing the oxygen pressure at 300 °C did not have a significant effect on the homogeneous strain. The increase of strain on particle *B* under reacting conditions in not reversible when removing the reactants, and not observed at 400 °C. This means that if oxides have grown under reacting conditions at 300 °C, they are stable throughout the experiment, and not removed by the sole presence of ammonia at 400 °C. Questions on Pt nanoparticles remain, do platinum oxides grow on the sample surface, and are they stable under reacting conditions? Experiments on single crystals will yield completing information to answer this question (chapter 4). Moreover, a different behaviour is observed for particle *B*, for which the homogeneous strain does not evolve with oxygen at 300 °C (fig. 3.24), which would necessarily link the growth of surface oxides to the particle shape, facet coverage, and initial strain state. Kim et al. (2018) have also shown that the introduction of oxygen was followed by its adsorption on edge sites, visible by magnitude changes in the neighbouring displacement field. Their hypothesis could be at the origin of different nano catalyst reshaping phenomena measured during the oxidation of CO *via* SXRD (Nolte et al. 2008; Hejral, Mu et al. 2016), TEM (Vendelbo et al. 2014) and also other BCDI studies (Abuin et al. 2019). No reshaping of the particles *B* or *C* was observed during the study of the ammonia oxidation with BCDI. However, a global reshaping of the nanoparticles was revealed by SXRD at 600 °C under reacting conditions favouring oxygen rich products, {113} and {110} facets being replaced by {100} and {111} facets for which the CTR intensity increased. This reshaping was not detected at lower temperatures, no decrease of the $[1\bar{1}3]$ oriented CTR could be identified at 300 °C or 500 °C, meaning that the {113} facets present at room temperature on particle *B* may yet still exist at 300 °C and 400 °C. A particle with a similar shape to that of particle *B* was measured by Dupraz et al. (2022), {113} facets are still visible during the presence of oxygen in the cell. The spatial resolution of the experiment is much higher than in the present study, due to the very high brilliance of Petra III in comparison with other 3^{rd} generation synchrotrons (Bilderback et al. 2005). A relaxation of the out-of-plane heterogeneous strain ϵ_{zz} was observed on all facets (besides $(\bar{1}10)$-type facets) during the presence of oxygen in the cell. No such relaxation was observed during this experiment, which supports that the adsorption/desorption of species linked to the catalytic reaction is measured, and not the effect of the oxidation of the particle surface.

The presence of steps/surface defects on Pt(111) facets has been shown to increase the catalytic activity of Pt nanoparticles (Segner et al. 1984; Q.-S. Chen et al. 2012). Indeed,

defects have an impact of the local strain field, which can in turn influence the adsorption properties of molecules taking part in the reaction. Similarly to our results on particle *B*, Kim et al. (2019) have measured the defect dynamics on a Pt particle during the catalytic methane oxidation. They have shown a reversible transition of the particle shape induced by the adsorption of oxygen at 425 °C , no such transition was observed at 325 °C. A second peak has been observed in the diffraction pattern in the $\vec{q}_z$ direction, 10 min after the introduction of oxygen, which is accompanied by an increase of the strain field energy, and the presence of defects in the particle. Two main differences are noted in the current study, first a defect seems to appear on particle *B* when *heating* the sample up to 400 °C, and not during reacting conditions. Secondly, the transformation of the particle shape is not reversible upon removal of the reactants. The reaction product partial pressures can be seen to drop in the minutes following the return to inert atmosphere at 400 °C (fig. A.11). From the evolution of the strain field energy, the interplanar spacing, and the FWHM, it is likely that the magnitude of the defect appearing at 400 °C under inert atmosphere has been increased from the reaction, which irreversibly transformed the particle shape. Defect dynamics have also been reported during the catalytic oxidation of CO on Pt nanoparticles (Carnis, L. Gao, Fernández et al. 2021) using BCDI. These results tend to support the importance of defects in the catalytic activity of nanoparticles during the oxidation of ammonia. The defect introduced by heating at 400 °C has probably altered the adsorption properties of particle *B*, possibly creating e.g. steps on top of the particle surface. Interestingly the change in the particle strain field is only visible after a certain O_2/NH_3 ratio is reached (fig. 3.25, 3.23), which can be linked to a transition to the adsorption of oxygen rich species (e.g. O, OH, NO, N_2O) on the catalyst surface. The reproducibility of the result at 300 °C and 400 °C for particle *C* for the same exposition time allow us to safely rule out the possibility of beam induced structural changes in particle *C*.

Reaction products were detected at 300 °C and 400 °C (fig. 3.30), overall an oxygen favoured O_2/NH_3 ratio resulted in a higher proportion of NO and N_2O, which enabled us to probe the relationship between strain and catalyst selectivity. Interestingly, an *activation* of the sample was observed at both 300 °C (fig. A.10) and 400 °C (fig. A.11) when $O_2/NH_3 = 2$. No such effect was observed at 300 °C in the previous experiment when using the non-patterned sample during surface x-ray diffraction (fig. 3.10). The only difference in the history of both samples being that the patterned sample was exposed to reacting conditions at 600 °C for approximately 1 h before this experiment. This transition in the product partial pressures when $O_2/NH_3 = 2$ does not correspond to the condition at which particle *B* showed a transition in terms of strain field energy or FWHM at 400 °C, which occurred under an equal amount of ammonia and oxygen in the reactor ($O_2/NH_3 = 1$). This structural transition could be a precursor to the *activation* process, keeping in mind that, as underlined by this experiment, the large difference in shape of the nanoparticles on the sample implies different structural evolution under various atmospheres.

Summary

SXRD measurements have unveiled the α-$Al_2O_3(0001)$-$\begin{pmatrix}\sqrt{3} & 0\\ 0 & \sqrt{3}\end{pmatrix}$-R30° epitaxial relationship between the Pt nanoparticles and the substrate. The Pt nanoparticles exhibit distinct in-plane orientations, with their c-axis aligning along the [111] direction. Notably, during ammonia oxidation, no change of the epitaxial relationship between the particles and the substrate has been observed.

During the SXRD experiment on the Pt particle assembly, we have demonstrated that the particles are highly faceted, showing both low and high-index facets: {100}, {110}, {111} and {113}. Interestingly, reshaping of the particles occurs at 600 °C, and depends on the gas conditions. A high O_2 / NH_3 ratio favours {111} and {001} facets over {110} and {113}

facets. The catalyst light-off temperatures for the production of N_2, NO and N_2O are 300 °C, 450 °C and 550 °C, respectively. Selectivity analysis in the temperature range of 300 °C to 600 °C reveals a preference for N_2 over NO and N_2O, except at 600 °C and high oxygen partial pressures.

Bragg coherent diffraction imaging was employed on individual Pt nanoparticles to investigate the role of single particles and the structure/activity of each facet during the ammonia oxidation. The structure, including morphology, out-of-plane displacement and strain fields of three single particles (*A*, *B* and *C*) have been imaged.

Particle *A* has been used to follow the effect of thermo-elasticity between the particle and its substrate. A flash annealing of the particle at 800 °C allowed to remove the initial dislocation located at the particle-substrate interface. During thermal annealing under inert atmosphere (Ar), an important reshaping of the particle has been observed between 250 °C and 350 °C, demonstrating the mobility of the Pt atoms at a rather low temperature. At 600 °C, facets of same structure (e.g. {111}) but at different distances with the interface experience opposite strain variation, suggesting an influence of support strain on the particle. Interestingly, flowing NH_3 at 600 °C induced an inversion of the out-of-plane strain at each facet, and the formation of a dislocation network at substrate interface. As the particle was not stable during the oxidation of ammonia at 600 °C (possibly linked to the existence of the dislocation network), two other particles have been measured at lower temperatures: 300 °C and 400 °C, before and after the catalyst light off.

The two other particles, *B* and *C*, show a different morphology (size, aspect ratio and types of facets), particle *C* is for example not covered by {113} facets. They show as well different behaviours during the oxidation of ammonia. Defects arise in particle *B* while increasing the temperature to 400 °C under inert atmosphere. Strong changes in strain heterogeneity and strain energy are observed for the small particle during the oxidation reaction at 400°C, while very weak changes occur for the large particle. These results tend to support the importance of defects in the catalytic activity of nanoparticles during the oxidation of ammonia, and warrants for monitoring multiple particles during reaction to obtain meaningful statistics. It is possible that the transformation of particle *B* corresponds to the onset of activation and reconstruction observed in industrial samples, driven by the appearance of defects. Moreover, this behaviour could be connected to a more global behaviour of the nanoparticles present on the sample from the visible transition in terms on product pressure visible in the RGA.

Particle *C* has a completely different behaviour, showing no strain evolution during the catalytic reaction, possibly from an initial strain state that leads to strongly adsorbed species not participating in the catalytic activity.

To conclude, it is of utmost importance to probe different nanoparticles before drawing a conclusion regarding their global behaviour during a heterogeneous catalytic reaction. The importance of the particle shape, *i.e.* facet size, coverage as well as initial strain state was put into perspective by the study of the oxidation of ammonia at 300 °C and 400 °C, as a function of the ratio between O_2 and NH_3.

This experiment has confirmed the importance of initial strain states for heterogeneous catalysis and will push forward particle strain engineering. The possibility of having different phenomena occurring under the same reacting conditions was revealed.

Finally, this experiment has both demonstrated the value and limits of Bragg coherent diffraction imaging when studying heterogeneous catalytic reactions. The recent improvement of the instrumental setup (rocking curves performed in fly mode instead of step-by-step mode, sample scanning in Bragg conditions to find the nanoparticles, sapphire window in the dome) tend in the right direction. The planned upgrade of SOLEIL to a 4^{th} generation synchrotron will also play a key role in the hierarchy of SixS in the very competitive list of coherent imaging beamlines, the current resolution of the experiment being too low to properly resolve the smallest facets present of the particles, to distinguish between facets

with similar orientations, to observe the growth of surface oxides or the strain in the topmost atomic layers.

In order to have a better understanding of surface dependent effects on the catalyst selectivity, and to probe for the possible growth of surface oxide during similar oxygen pressures, specific facets have been measured by SXRD, presented in the next chapter.

Chapter 4

Pt single crystals during ammonia oxidation

4.1 Introduction

Past ammonia oxidation experiments on $Pt_{25}Rh_{75}$ (100) (Resta et al. 2020) single-crystals gave significant new insights on the relaxation dynamics when the system crosses the catalyst activation barrier. The experiment focused on measuring the catalyst selectivity before and above the light off temperature (at 175 °C and 375 °C). The transition from a nitrogen-rich to oxygen-rich input mixture coincides with a relaxation change in the topmost metallic layer: moving from outward to inward. The existence of a rhodium surface oxide during reacting conditions favouring NO is revealed.

Thanks to near-ambient pressure x-ray photoelectron spectroscopy (NAP-XPS) experiments, nitrogen rich species (such as N_2) were associated to out-of-plane expansion of the topmost layer; while oxidative species (such as NO and atomic oxygen) were linked to out-of-plane contraction. This change in relaxation has an impact on the band structure, and therefore on the catalytic properties as proposed in the *d*-band model (Mavrikakis et al. 1998). Therefore, our intention is to investigate whether this modification in relaxation is specific to the Pt-Rh alloy, or if it holds a broader applicability to the constituent elements of the alloy, such as different relaxation states, transient structures, and surface moieties are expected to exist as a function of the ammonia to oxygen partial pressure ratio.

The previous chapter has highlighted our results on Pt nanoparticles during ammonia oxidation. The average shape of multi-faceted Pt nanoparticles was measured at the SixS beamline under the reaction using surface x-ray diffraction. A global reshaping of the nanoparticles at 600 °C and under reacting conditions was put under evidence, favouring {111} and {100} facets over {110} and {113} facets. This could be the signature of surface oxides playing an important role in the reaction, predicted to be the most stable on the {111} and {100} facets by Seriani et al. (2008). The evolution of two single nanoparticles exhibiting different types of facets on their surfaces was also probed with Bragg coherent diffraction imaging. The importance of the initial particle shape and facet coverage on its structural evolution during the ammonia oxidation cycle was highlighted.

To fully understand the impact of the Pt surface structure on the catalyst selectivity, two different single crystals, Pt(111) and Pt(100) will here be measured by SXRD. In-plane reciprocal space maps were first carried out to search for new structures, and surface reconstructions induced by the reaction environment, as well as to assess the potential growth of surface and bulk oxides on the catalyst surface. Crystal truncation rods were measured to probe surface relaxation effects, and to assert the average roughness of the catalyst surface. Additional super-structure rods were performed at HK coordinates of the newly discovered features to investigate the potential corresponding out-of-plane structures. Reflectivity meas-

urements were conducted to gather further insights into the various layers existing on the catalyst surface, along with their respective roughness.

Lastly, core-level XPS offers distinct signatures for moieties adsorbed on the surface during reactions. To link internal surface relaxation effects obtained from specific crystalline structures with the chemistry on its surfaces, the same Pt(111) and Pt(100) single crystals are used for both SXRD and NAP-XPS. For each combination of temperature and ammonia to oxygen ratio, the O 1s, N 1s, and Pt 4f core levels were measured, carrying information on the surface state. This approach aimed to establish a connection between selectivity, surface moieties, and internal stress. The Fermi edge is also measured after each core level to be able to find the zero binding energy.

The oxidation of ammonia on single crystals was measured at 450 °C, a temperature above the catalyst light-off. Higher temperatures were avoided in favour of the setup life expectancy in the aggressive reaction environment, and the long time required to perform all the measurements. The different conditions are resumed in tab. 4.1 and 4.2. The sample was characterised under argon before (1) and after (6) the oxidation cycle to assess the reversibility of the catalyst surface. To ensure that any surface relaxation effects are attributed to the simultaneous presence of ammonia and oxygen in the reactor, the sample initially underwent exposure to a high-oxygen atmosphere (2), monitoring potential surface oxide growth. Subsequent introduction of ammonia (3) facilitated the examination of existing surface oxides' impact on catalyst selectivity during the reaction, as well as their stability under reaction conditions. Two different partial pressures of oxygen were employed alongside the same partial pressure of ammonia (3, 4), to investigate the influence of the O_2/NH_3 ratio on the catalyst structure, surface species, and selectivity. Maintaining only ammonia in the reactor (5) enabled the separation of the effect of ammonia's presence from the combined presence of ammonia and oxygen. Lastly, the sample surface was exposed to a reduced pressure of oxygen, to make certain that the phenomena observed when lowering the O_2/NH_3 ratio by reducing the oxygen pressure are effectively due to the combined presence of the reactants.

Order	Gas Flow (mL/min)			Total pressure (mbar)	Partial pressures (mbar)			Targeted information
	Ar	O_2	NH_3		Ar	O_2	NH_3	
1	50	0	0	500	500	0	0	Catalyst state without reactants (unactive)
2	42	8	0	500	420	80	0	Growth of surface oxides
3	41	8	1	500	410	80	10	Influence of (NH_3/O_2) ratio and impact
4	48.5	0.5	1	500	485	5	10	on/of potential surface oxides
5	49	0	1	500	490	0	10	Ammonia adsorption
6	50	0	0	500	500	0	0	Returning to pristine state
7	49.5	0.5	0	500	495	5	0	Growth of surface oxides

Table 4.1: Different atmospheres used to probe the ammonia oxidation on Pt(100) and Pt(111) single crystals with SXRD. The duration of each condition was at least 8 h.

Due to important electron absorption in high atmospheres, the same atmospheres used for *in situ* and *operando* SXRD cannot be reproduced for NAP-XPS, and the total pressure had to be lowered. The total atmosphere is not anymore kept constant by the use of Argon between each condition, while the reactant partial pressure is approximately 10 % of the partial pressures used in BCDI and SXRD, with an equivalent (O_2 / NH_3) ratio.

The use of a residual gas analyser during *in situ* and *operando* XPS and SXRD experiments allowed us to monitor the sample's catalytic activity.

Order	Total pressure mbar)	Partial pressures (mbar)			Targeted information
		Ar	O_2	NH_3	
1	1	1	0	0	Catalyst state without reactants (unactive)
2	8.8	0	8.8	0	Growth of surface oxides
3	9.9	0	8.8	1.1	Influence of (NH_3/O_2) ratio and impact
4	1.65	0	0.55	1.1	on/of potential surface oxides
5	1.1	0	0	1.1	Ammonia adsorption
6	1	1	0	0	Return to pristine state
7	0.55	0	0.55	0	Growth of surface oxides

Table 4.2: Different atmospheres used to probe the ammonia oxidation on Pt(100) and Pt(111) single crystals with NAP-XPS. The duration of each condition was approximately 5 h.

4.1.1 Experimental setup for SXRD experiments in the horizontal geometry

The surface x-ray diffraction experiment was performed at the SixS beamline. The diffractometer was used in a horizontal geometry (fig. 2.15), accommodating the large XCAT reactor. This enables the cleaning of the sample surface by sputtering (bombardment with argon ions) and annealing directly in the reactor chamber, under UHV, before exposing the sample to different atmospheres. Two successive sputtering and annealing cycles have been carried out before the start of the SXRD experiment.

To do so, the reactor cell was brought to low pressure by respectively closing and opening the entrance and exit valves, while pumping the reactor volume. The volume inside the XCAT reactor (fig. 4.1 - a) was increased by *opening* the chamber while the height of the sample was changed so that the ion gun situated on the side of the XCAT reactor is aligned with the sample surface. The sputtering current resulting from the impact of ions on the sample surface was measured by a circuit directly connected to the sample. The sample height was tuned to maximise the sputtering current and surface cleaning, the Pt surface was then cleaned by sputtering for 30 min at room temperature. The sample was then heated up to 800 °C for 15 min for annealing. The sputtering and annealing efficiency could be observed directly by a quick increase of the reactor pressure in the first minutes, linked to the removal of surface impurities, and followed by a progressive decrease of the reactor pressure from pumping. The same procedure was applied to both Pt(111) and Pt(100) surfaces.

The experiment was performed at an energy of 18.44 keV. The alignment of the beam was performed with the direct beam using the same procedure detailed previously in sec. 3.2.1. In the horizontal configuration, the incident angle is β, set to grazing incidence (0.3°) so that the beam recovers the entire sample surface. The beam footprint is larger than the sample surface, which presents a round shape (diameter ≈8 mm - fig. 4.1). This allows us to consider that the beam is always covering the entire sample surface, thereby ignoring illumination effects. Crystal truncation rods were performed in the out-of-plane direction, perpendicular to the sample plane, *i.e.* in the vertical plane $(\vec{x}, \vec{z})$ to maximise the intensity of the scattered field and to ignore polarisation effects in the evolution of the CTR intensity (fig. 2.5). The sample alignment was verified at the beginning of each condition to ensure that the beam consistently impinges on the sample surface. The orientation matrix U of the crystal (Schlepütz, Mariager et al. 2011) was also recomputed by measuring two different Bragg peaks to be able to quickly navigate in the reciprocal space.

4.1.2 Experimental setup for x-ray photoelectron spectroscopy

The NAP-XPS experiment was performed at the B07 end station at Diamond Light Source (Held et al. 2020). The electron analyser axis is at an angle of 60.1° with respect to the beam

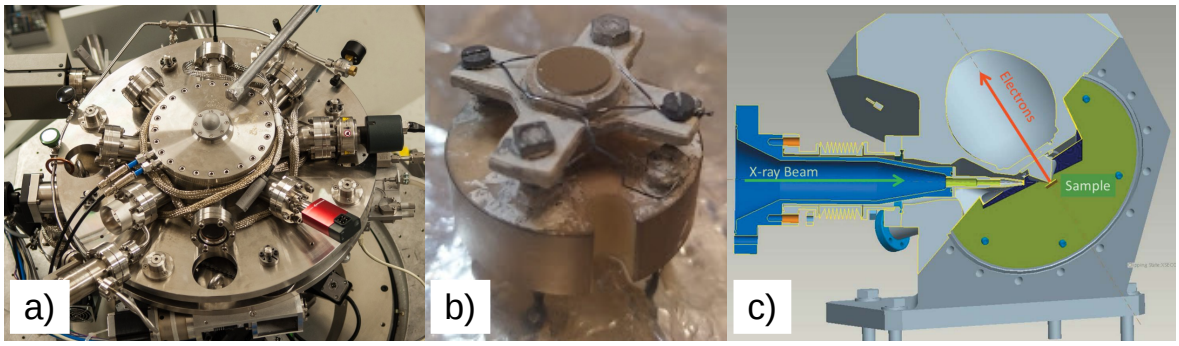

Figure 4.1: a) Large XCAT reactor. b) Round single crystal set on sample holder, the crystal presents here a (111) top surface. The surface area of the single crystal is ≈50 mm², the Pt(100) sample has the same shape. c) Detailed drawing of the XPS chamber at the B07 beamline at the Diamond Light Source (right), taken from Held et al. (2020).

and tilted at 30° with respect to the horizontal plane. The cone aperture of the analyser has a diameter equal to 0.3 mm. Four different pumping stages protect the vacuum in the UHV section of the analyser from the endstation, that can reach a working pressure of 100 mbar. The first two differential pumping stages contain each a quadrupole mass spectrometer used for the analysis of the sample environment, depending on the total pressure in the reactor cell. The increased attenuation through high pressures is compensated by limiting the photoelectron path length to sub-millimetre range, from the sample surface to the analyser. The typical working distance between cone aperture and sample is between 0.2 mm and 0.3 mm.

The energy or the incident photons was chosen to optimise the photoelectron signal, as a compromise between electron transmission and excitation cross-sections, which respectively increase and decrease as a function of the photon energy. Guidelines on how to choose the best instrumental settings are detailed in Held et al. (2020). The combined energy resolution of the beamline and analyser, while working in NAP conditions, ranged between 0.8 eV and 1.2 eV.

4.2 Pt(111) single crystal studied at 450 °C

Platinum crystallises in a face-centred cubic structure with a lattice parameter a_{Pt} equal to 3.92 Å at room temperature (Waseda et al. 1975). Its structure was first presented in sec. 2.4 to introduce the notions of crystals. The arrangement of the Pt atoms on the (111) surface is hexagonal, which leads to the definition of the surface unit cell shown in fig. 4.2 to better represent the surface arrangement of the Pt atoms. The in-plane vectors $\vec{a}_{(111)}$ and $\vec{b}_{(111)}$ are of equal magnitude ($a_{Pt}/\sqrt{2} = 2.77$ Å), separated by 120°. The out-of-plane vector $\vec{c}_{(111)}$ is perpendicular to the (111) plane, and of magnitude $a_{Pt}\sqrt{3} = 6.79$ Å. The stacking of the Pt layers perpendicular to the $\vec{c}$ axis follows a ABCA arrangement, *i.e.* Pt atoms occupy the same positions in the $\vec{a}, \vec{b}$ plane every three layers.

4.2.1 Oxide growth under 80 mbar of oxygen

To identify the presence of surface reconstructions and/or surface oxides, in-plane reciprocal space maps were collected at the atmospheres detailed in tab. 4.1. This was done by rotating the in-plane sample and detector angles (μ and γ) from 0° to 120° to collect a third of the reciprocal space in the ($\vec{q}_x$, $\vec{q}_y$) plane, while keeping the out-of-plane detector angle δ at a constant value. The incident angle β was kept at 0.3°.

The reciprocal space in-plane maps and rods were computed in (hkl)-space (fig. 4.3 and 4.8) to visualise the arrangement of surface structures or surface relaxations in comparison with the hexagonal surface unit cell described in fig. 4.2.

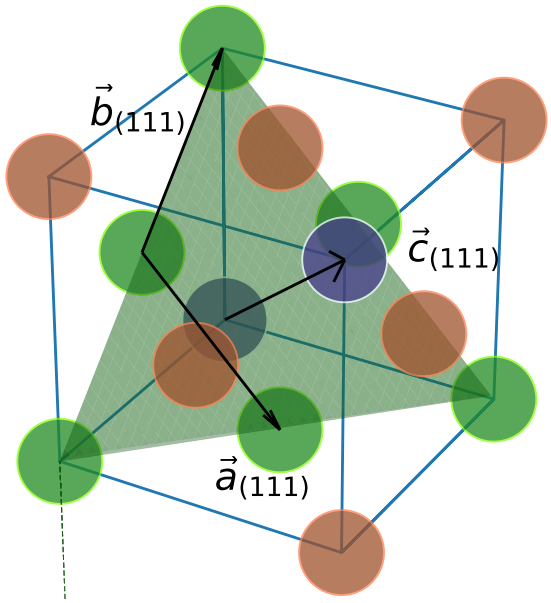

Figure 4.2: Face-centred cubic unit cell of Pt with (111) crystallographic plane drawn in green. $\vec{a}_{(111)}$, $\vec{b}_{(111)}$ and $\vec{c}_{(111)}$ are the (111) surface unit cell vectors. There are three {111} planes spanned by the magnitude of $\vec{c}_{(111)}$ (blue, red and green on the figure).

The first map was collected at low pressure ($<1 \times 10^{-7}$ mbar) after the cleaning of the sample by sputtering and annealing (fig. 4.3 - a). The (110) and (2$\bar{1}$0) Bragg peaks can be observed, together with the intersection of the [0, 1, L], [0, 2, L], [1, $\bar{1}$, L], [1, 0, L], and [2, 0, L] CTRs with the [H, K, 0] plane (circled in white). No additional signal can be observed when introducing 500 mbar of argon in the reactor (fig. 4.3 - b).

New peaks can first be observed under 80 mbar of oxygen, identified by different colour circles in fig. 4.3 (c), the corresponding interplanar spacings are given in app. B.1. The angle between the peaks circled in grey and white, and the peaks circled in red and purple is approximately equal to 60°. This could be the signature of the existence of two hexagonal surface structures, each one rotated by ±8.8° with respect to the Pt(111) surface unit cell and with a larger in-plane lattice parameter (drawn in green and grey in fig. 4.3 - c, d). However, no apparent second order peak can be linked to those rotated hexagonal structures, the related intensity is possibly too low at high scattering vector to be detected.

The matrix notation describing one of those rotated structures is Pt(111)-p$\begin{pmatrix} 1.20 & 0.00 \\ 0.00 & 1.20 \end{pmatrix}$-R±8.8°. The closest rotated superstructure is Pt(111)-(6 × 6)-R±8.8°. This means that in real space, the node closest to the origin where the Pt(111) and Pt(111)-p$\begin{pmatrix} 1.20 & 0.00 \\ 0.00 & 1.20 \end{pmatrix}$-R±8.8° lattices meet is at ($6a_{Pt_{111}}$, $6b_{Pt_{111}}$), after rotation by ±8.8°. This notation does not describe a surface reconstruction in this case, a sketch describing the real space unit cell can be found in app. B.1.

Interestingly, summing the two vectors going from the centre of the reciprocal space to the white and purple circled peaks yields the position of the black circled peak in fig. 4.3 (c). The angle between both vectors is then equal to 42.6°, equivalent to 137.4° in real space. No other peak linked to this unit cell can be identified in this in-plane map.

The measurement of the entire reciprocal space in-plane map took about 3 h35 min, the entire map being a concatenation of multiple μ scans during which the plane of the sample is rotated around its normal, the first scan starting near the centre of the reciprocal space. The contribution of each scan during the measurement is visible from their different background. There is approximately 1 h between the measurement of the peaks circled in red, grey, purple and white, and the peak circled in black.

A second map was measured in a smaller region of the reciprocal space 9 h30 min after the introduction of oxygen in the cell, to see if the intensity and position of the newly found

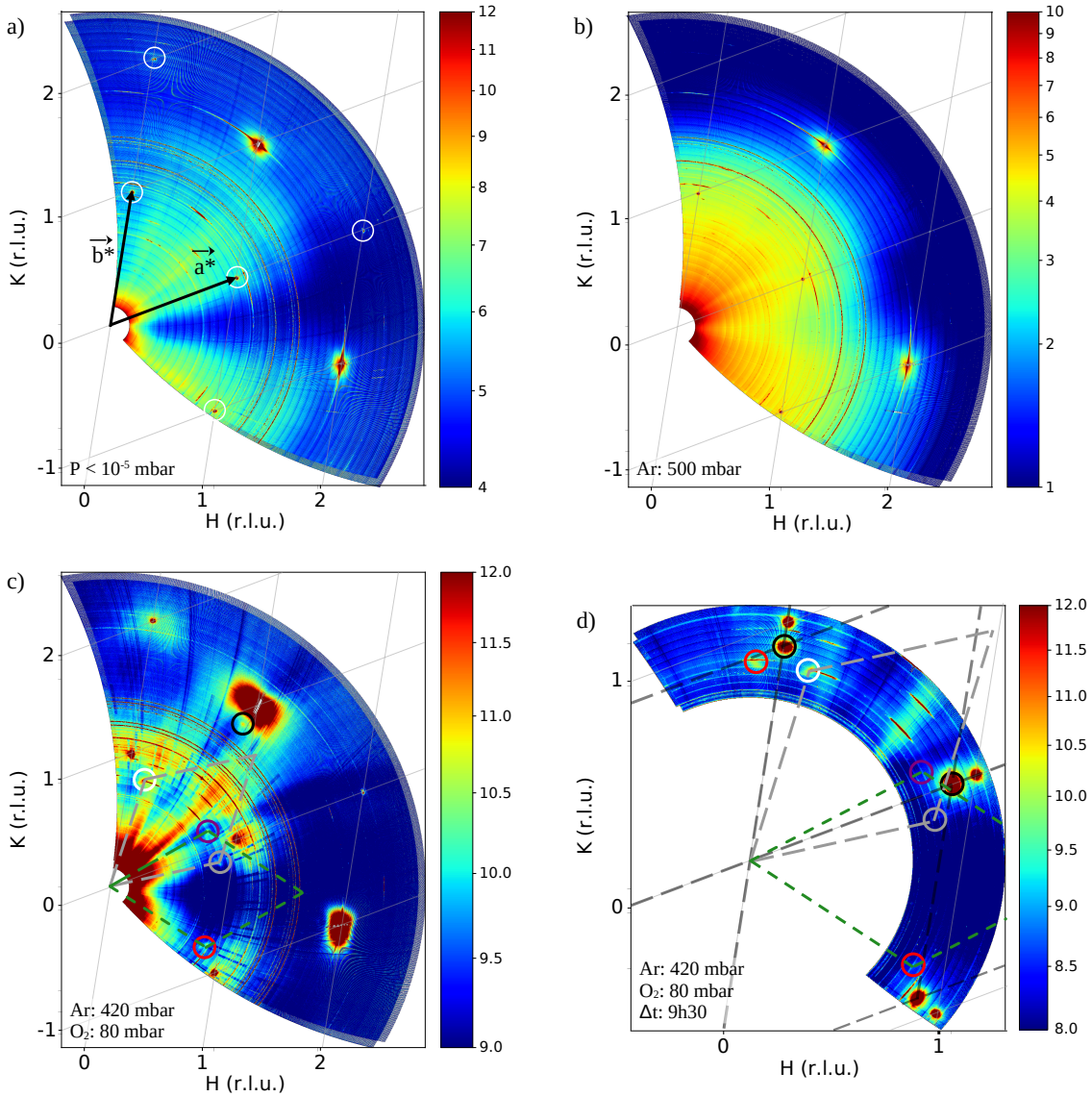

Figure 4.3: Reciprocal space in-plane maps collected under different atmospheres at 450 °C, *computed using the hexagonal lattice of Pt(111).*

peaks changed (fig. 4.3 - d). The measurement of this map took about 1 h15 min. Three additional peaks (circled in black in fig. 4.3 - d) appeared describing an epitaxied hexagonal lattice of parameter equal to $|\vec{a_{hex}}| = 3.10$ Å (drawn in black dashed lines in fig. 4.3 - d). This relation can also be described as follows : Pt(111)-p$\begin{pmatrix} 1.116 & 0 \\ 0 & 1.116 \end{pmatrix}$. The average position of the three peaks with respect to the reciprocal space lattice nodes was used to determine the matrix. The closest commensurate superstructure is Pt(111)-(26 × 26), a sketch describing the real space unit cell can be found in app. B.2.

The grey and purple circled peaks seem to have disappeared from the reciprocal map (fig. 4.3, c, d), but an additional peak circled in red is revealed at 120° from the other peak circled in red, and at 60° from the peak circled in purple, at the same distance from the centre (fig. 4.3 - d). From these measurements, a first hypothesis to explain the observed peaks position is given. First, two rotated hexagonal structures Pt(111)-(6 × 6)-R±8.8° appear (fig. 4.3 - c). Secondly, a Pt(111)-(26 × 26) structure is observed, its second order peaks already detected while measuring the large reciprocal space in-plane map (black peak in fig. 4.3 - c), while the first order peaks can only be identified in the second reciprocal space map (fig. 4.3 - d).

It is possible that the disappearance of the grey and purple circled peaks is linked to some alignment problems, visible from the large low intensity region in fig. 4.3 (d). Otherwise, those peaks may disappear after the growth of the Pt(111)-(26 × 26) structure. It is not clear however why the remaining peaks are at 120° of each other, in contradiction with the hypothesis of different hexagonal structures on the Pt(111) surface.

Super-structure rods (SSRs) were collected on the peaks belonging to the Pt(111)-(26×26) structure, [H, K] = [0.89, 0] (fig. 4.4 - a), and to the rotated hexagonal structures, [H, K] = [0.15, 0.74] (fig. 4.4 - b), to probe their out-of-plane structures. A second SSR was performed at [H, K] = [1.78, 0] to probe the intensity of a potential second-order peak associated to the Pt(111)-(26 × 26) structure (fig. 4.4 - c), approximately 10 h after the measurement at [H, K] = [0.89, 0].

Interestingly, the position of the two peaks in [H, K] (visible in fig. 4.4, a-c) leads to a new definition of the structure since the closest commensurate superstructure is now Pt(111)-(8 × 8), with a lattice parameter equal to 3.12 Å. It is possible that the elapsed time under oxidising atmosphere has had an effect of the 2D structure, that has become more relaxed. The background-subtracted scattered intensity was integrated as a function of L using the *fitaid* module of *BINoculars* (fig. 4.4).

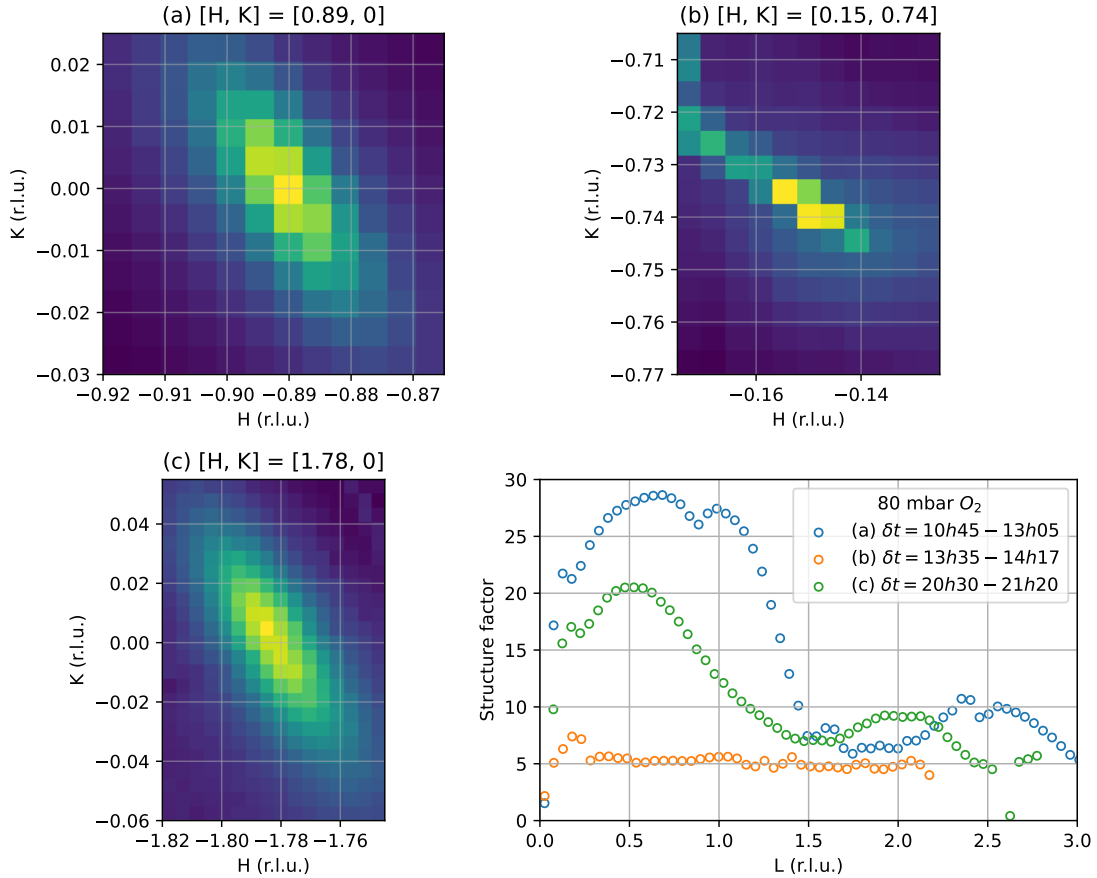

Figure 4.4: 2D detector slices at $L = 0$ during super-structure rods (SSRs) measurements for three different [H, K] positions under 80 mbar of O_2 (a-b-c). Images have the same colour scale. The integrated intensity is presented in (d) as a function of L for each signal. δt designates the elapsed time since the introduction of oxygen.

The integrated intensity for [H, K] = [-0.15, -0.74] shows a small peak at $L \approx 0.2$ followed by a constant intensity, characteristic of flat monolayers (fig. 2.42, Robinson et al. 1991).

Mainly four different bulk platinum oxides have been reported to exist in literature, α-PtO_2, β-PtO_2, Pt_3O_4 and PtO. The corresponding experimental structures are described

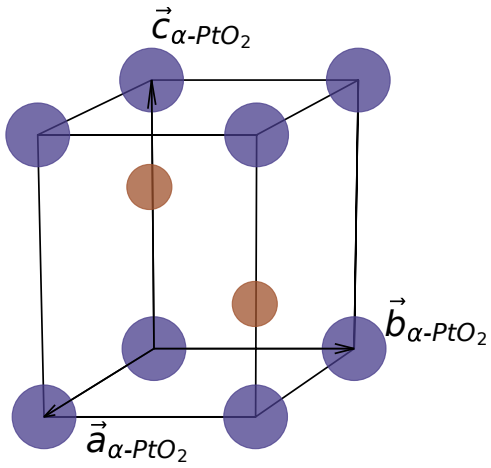

Figure 4.5: α-PtO_2 bulk unit cell. Platinum atoms are situated on the unit cell corners (blue) while the two oxygen atoms are at the positions $(1/3, 2/3, 1/4)$ and $(2/3, 1/3, 3/4)$ (orange).

in tab. 4.3, together with the expected equilibrium structure found by Seriani et al (2006; 2008) using first-principles atomistic thermodynamics calculations, and molecular dynamics simulations based on density functional theory.

	PtO	Pt_3O_4	β-PtO_2	α-PtO_2
Bravais lattice	Tetragonal	Cubic	Orthorhombic	Hexagonal
a (Å)	3.10 (3.08)	5.65 (5.59)	4.49 (4.48)	3.14 (3.10)
b (Å)	3.10 (3.08)	5.65 (5.59)	4.71 (4.52)	3.14 (3.10)
c (Å)	5.41 (5.34)	5.65 (5.59)	3.14 (3.14)	5.81 (4.28-4.40)
α	90°	90°	90°	90°
β	90°	90°	90°	90°
γ	90°	90°	90°	120°

Table 4.3: Experimental values taken from McBride et al. 1991 for PtO, from Muller et al. 1968 for Pt_3O_4 and α-PtO_2, and from McBride et al. 1991 for β-PtO_2. Theoretical values (in parenthesis) and table adapted from Seriani et al. (2006). Similar values have been reported by Nomiyama et al. (2011) from DFT calculations.

The intensity distribution along L for Pt(111)-(8×8) (fig. 4.4) suggests the presence of a multi-layer structure, possibly not even reaching the full unit cell (see simulated oxides structure in fig. 2.42 - a). Seriani et al. (2006) have determined that the most stable surface oxide on the Pt(111) surface is hexagonal α-PtO_2. A high uncertainty regarding the lattice parameter in the $\vec{c}$ direction is reported in experimental and theoretically studies due to a poor crystallisation of the bulk oxide (Muller et al. 1968), and to underestimation of weak interlayer Van der Waals forces in theoretical studies (W. Li et al. 2005).

The formation of hexagonal on hexagonal surface α-PtO_2 on Pt(111) is expected to induce a high amount of in-plane compressive strain in the oxide layer, from the large difference between the Pt-Pt distance on the (111) surface (2.77 Å) and the in-plane lattice parameter of α-PtO_2 (3.14 Å). A rotation of 30° is expected to reduce the in-plane strain, resulting in a (2×2) arrangement, no such structure was observed in this experiment on Pt(111). The presence of α-PtO_2 on the Pt(111) surface was also shown to provide favourable special sites that could contribute to the catalytic activity (W. Li et al. 2005). The unit cell of α-PtO_2 is presented in fig. 4.5.

Ellinger et al. (2008) reported the existence of surface α-PtO_2 on Pt(111) using SXRD at 500 mbar of oxygen, and at a temperature between 245 °C and 635 °C. The in-plane lattice parameter is equal to 3.15 Å, close to the reported bulk value of α-PtO_2 (tab. 4.3, 3.14 Å). Similarly to the current experiment, a Pt(111)-(8×8) superstructure is reported, linked

to surface α-PtO_2, also previously reported by Ackermann (2007). Ellinger et al. (2008) proposed a model for surface α-PtO_2 consisting of a full unit cell, with an out-of-plane lattice parameter reduced by 15 % in comparison with the bulk structure (3.62 Å). They introduced a displacement of ≈33 % of the platinum atoms on the top layers with respect to those of the bottom layer, in the $(\vec{a}_{\alpha-PtO_2} + \vec{b}_{\alpha-PtO_2})$ direction (fig. 4.5) . A super-structure rod collected at [H, K] = [0, 0.88] present a peak at $L = 0.65$ (L computed using the distorted α-PtO_2 unit cell).

The two SSRs performed in the current study were fitted using two Gaussian peaks sharing the same full width at half maximum (FWHM), and a constant background (fig. 4.6). The second peak near $L = 1$ in the SSR at [H, K] = [0.89, 0] comes from a Pt powder signal, while the peak at $L = 2.4$ is from alien signal.

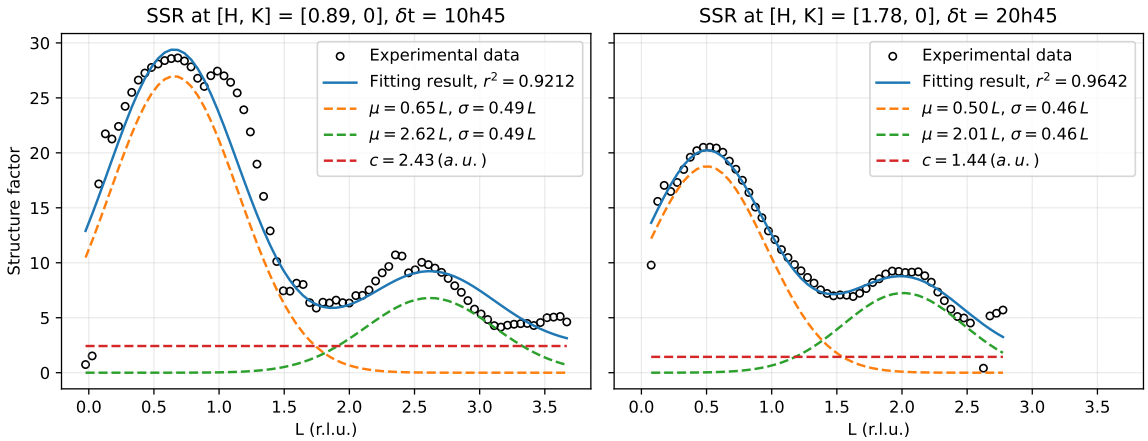

Figure 4.6: SSRs and fit results under 80 mbar *of O_2. μ, and σ are the peak positions and standard deviations in L.*

A peak at [0.89, 0, 0.65] is visible, but using the Pt(111) surface unit cell, with an out-of-plane lattice parameter of 6.79 Å. This is incompatible with the results presented in Ellinger et al (2008) since they used the lattice parameter of the refined α-PtO_2 structure, $|\vec{c}| = 4.16$ Å. It seems that a different out-of-plane structure is present in the current work.

XPS studies have also reported α-PtO_2 above 6.66 mbar of O_2 at 450 °C (D. J. Miller et al. 2011; D. Miller et al. 2014). As mentioned by Fantauzzi et al (2017), the extended exposure to oxygen necessary to grow the oxide structure makes its characterisation difficult, the structure possibly evolving with time.

Additional simulations are needed to fully understand the structures in this study using the proposed distorted α-PtO_2 structure, but also different surface models including the *spoked-wheel* superstructure identified *via* scanning tunnelling microscopy (STM) by Van Spronsen et al (2017) and Boden et al. (2022). This structure, identified above 1 bar of oxygen, and at approximately 200 °C, also exhibits a (8×8) coincidence with the Pt(111) lattice.

Reflectivity curves measured in a specular geometry and fitted using *GenX* (Björck et al. 2007; Glavic et al. 2022) are presented in fig. 4.7. The specular X-ray reflectivity simulations are conducted using the Parratt algorithm (Parratt 1954). The classical way of implementing roughness is based on a Gaussian distribution, introducing corrective factors to the electric field amplitudes at the interfaces in accordance with the Nevot-Croce model (Névot, L. et al. 1980). For the computation of material refractive indices, the Henke tables (Henke et al. 1993) are employed.

A simple model was used consisting of a semi-infinite slab of platinum, on top of which is present a homogeneous layer of platinum oxide. The density of the layer (ρ_{ox}) was set free during the minimisation process, between zero and 21.2×10^{-3} FU/Å^3 (formula unit

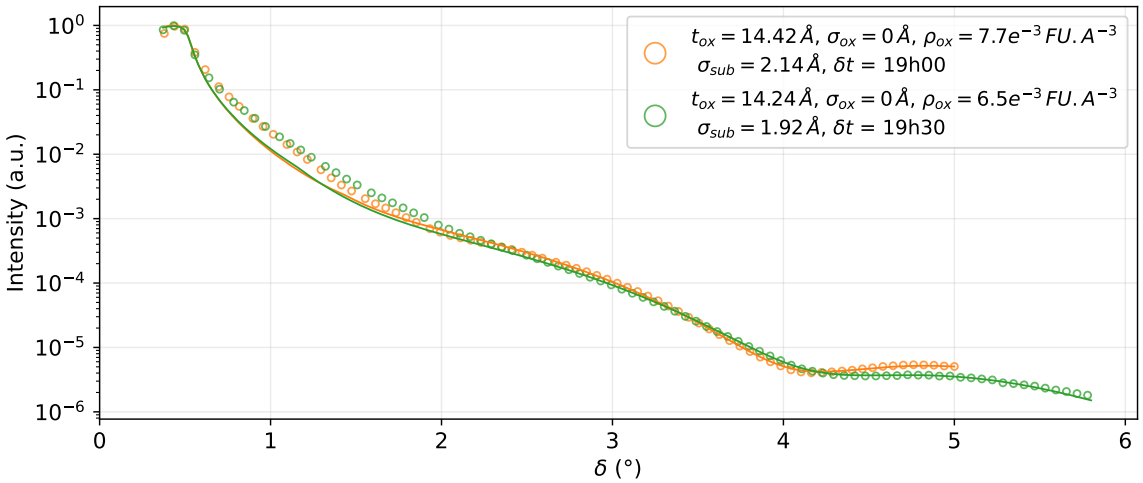

Figure 4.7: X-ray reflectivity curves measured in a specular geometry (circles) under 80 mbar *of oxygen. Curves fitted using GenX are shown as lines. δt designates the elapsed time since the introduction of oxygen. ρ_{ox}, t_{ox}, and σ_{ox} are the oxide density, thickness, and root mean square roughness. σ_{sub} is the substrate root mean square roughness.*

per cubic Angström, computed from unit cell elements and volume), the value for α-PtO_2. The initial intensity is fixed to obtain the best match at low incident angles, the intensity drop after the critical angle is difficult to fit, but the period of the oscillations, as well as the intensity at high angles are in general well represented. The oscillation magnitude can be linked to the density of the oxide layer on top of the Pt(111) surface. The fitted values ($7 \times 10^{-3}\,\mathrm{FU/Å}^3$ and $6.5 \times 10^{-3}\,\mathrm{FU/Å}^3$) are an order of magnitude below the expected value for a homogeneous layer of α-PtO_2. The root mean square roughness of the oxide layer σ_{ox} is always zero, whereas the roughness of the Pt(111) surface (σ_{sub}) is of the same order of magnitude for both measurements.

The position of the oscillations visible in fig. 4.7 can be linked to the thickness of the oxide layer (t_{ox}). The layer is 14.42 Å and 14.24 Å thick in the first and second reflectivity curves, stable between both measurements. The lateral information is lost during reflectivity measurements, meaning that different structures covering the Pt(111) surface cannot be distinguished with a simple model.

By combining the information obtained from in-plane, SSRs and reflectivity measurements, it is probable that the platinum surface is first covered by two types of domains corresponding to two rotated hexagonal structures. Secondly, a Pt(111)-(8×8) structure is identified on the surface. The layer thickness retrieved with reflectivity can indicate that a thin film is present on the surface, but no corresponding structure was yet identified with SXRD, which rather supports the existence of hexagonal monolayers, with a multi-layer thick epitaxied structure. Future work will help identify the out-of-plane catalyst structure.

4.2.2 Near ambient pressure ammonia oxidation cycle

Ammonia was subsequently introduced in the reactor cell to investigate the evolution of the platinum oxide structures, as well as the presence of additional surface structures or surface reconstructions during ammonia oxidation (fig. 4.8, a-b). The presence of α-PtO_2 on Pt(111) has been shown to not hinder the oxidation of CO by Ackermann et al. (2007), that would then occur *via* a Mars-Van Krevelen mechanism (Mars et al. 1954), inducing a progressive roughening of the platinum surface.

During ammonia oxidation, none of the previously observed peaks could be discerned, while no additional peaks emerged. When the oxygen pressure within the cell was reduced

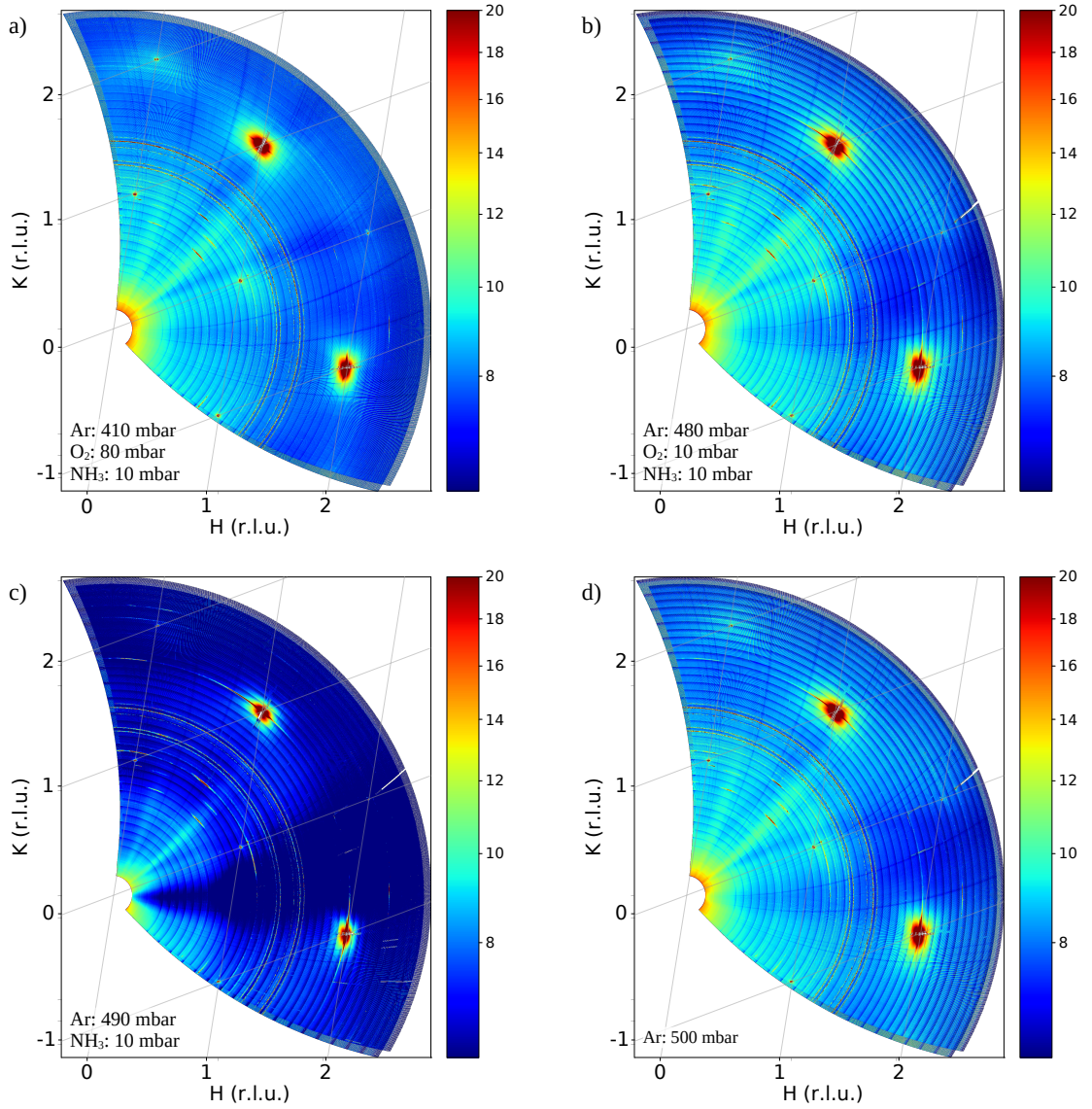

Figure 4.8: Reciprocal space in-plane maps collected under different atmospheres at 450 °C*, computed using the hexagonal lattice of Pt(111).*

to 5 mbar (favouring alternate products) or eliminated at 0 mbar, there was no formation of surface reconstructions or surface structures. This result shows that the reaction removes the oxide layer present of the surface until the structure disappears.

No transition between the reaction products is observed in the first hours following the introduction of ammonia in the reactor (fig. B.5), the presence of the surface oxide at the beginning of the condition seemingly not influencing the product selectivity. All reciprocal space in-plane maps following the introduction of ammonia to a final atmosphere of 500 mbar of Argon showed a bulk-terminated surface (fig. 4.8 - a, b, c, d), proving that the oxidation cycle is reproducible, and that ammonia effectively removed the different surface oxides that grew under 80 mbar of oxygen.

Reflectivity curves were also measured and fitted with *GenX* under pure Argon atmosphere (before and after the oxidation cycle), under different reacting conditions, and with only ammonia and argon in the reactor, presented in fig. 4.9. In accordance with the results of the in-plane reciprocal space maps in fig. 4.8, no oxide layer was used in the surface model. Interestingly, the roughness of the [111]-oriented platinum crystal increased to 2.80 Å following the introduction of ammonia (fig. 4.9 - b), after having reached 2.14 Å when previously

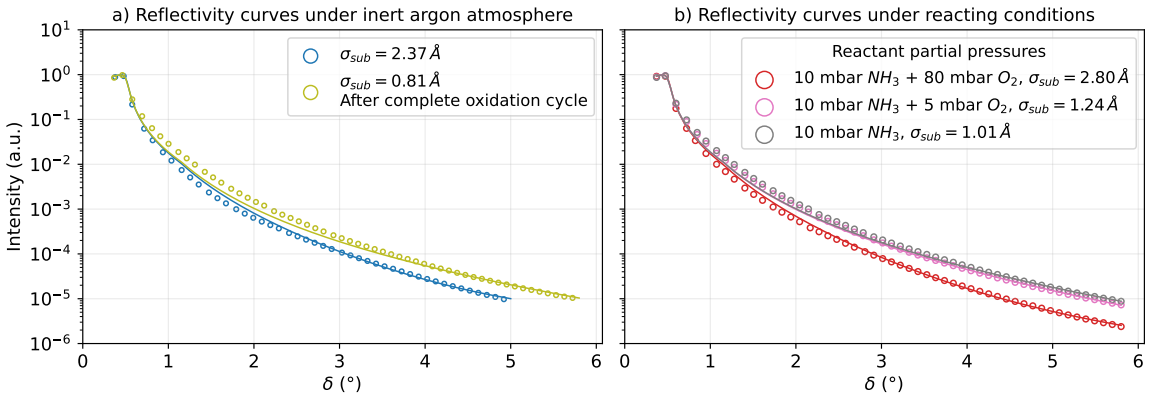

Figure 4.9: X-ray reflectivity curves measured in a specular geometry (circles) under different atmospheres during ammonia oxidation. Curves fitted using GenX are shown as lines. σ_{sub} is the substrate root mean square roughness.

exposed to 80 mbar of oxygen (fig. 4.7). Since the reflectivity curves are measured at the start of each condition, it is possible that this high roughness is linked to the removal of the surface oxides. Lowering the amount of oxygen is globally linked to a decrease of roughness (fig. 4.9 - b). The largest decrease is observed when switching the O_2/NH_3 partial pressure ratio from 8 to 0.5, *i.e.* during reacting conditions. The low roughness and removal of SXRD signals during ammonia oxidation is in contradiction with a possible Mars-Van Krevelen mechanism involving surface oxides at the current conditions, consistent with the reported Langmuir-Hinshelwood literature mechanism (sec. 1.2.2).

4.2.3 Oxide growth under 5 mbar of oxygen

At the end of the complete ammonia oxidation cycle, the sample was put under 5 mbar of oxygen to see if the surface structures detected under high oxygen pressure can exist under lower oxygen pressure. The aim being also to de-correlate the effect of the simultaneous presence of ammonia and oxygen in the cell on the surface when the O_2/NH_3 ratio is equal to 0.5. The sample was cleaned with two sputtering and annealing cycles before the introduction of oxygen. Large and small reciprocal space in-plane maps were measured to have the best compromise between a higher temporal resolution of the oxide growth, and the possibility to detect other peaks from corresponding surface unit cells. The larger reciprocal space in-plane maps are shown in fig. 4.10.

In the first map that started directly after the stabilisation of the oxygen pressure at 5 mbar in the reactor cell, low intensity signals can be detected (fig. 4.10 - a). The detected peaks correspond to those detected previously shortly after having a pressure of 80 mbar in the cell (fig. 4.3 - c). The same coloured circles are used to indicate peaks at similar positions, the related interplanar spacing is also recapitulated in app. B.1. Some peaks start to split in a similar pattern, exhibiting three distinct signals around a more diffuse region (clearly visible for the red circled peak in fig. 4.10 - d). The grey circled peak becomes fully visible after 4 h of measurement.

This splitting of the peaks can be interpreted as the signature of a Pt(111) surface covered by different domains exhibiting similar hexagonal structures. These domains are rotated by ±8.8° with respect to the Pt(111) surface unit cell, with a higher magnitude of the in-plane lattice parameter, following the same Pt(111)-(6 × 6)-±8.8° structures observed under an oxygen pressure of 80 mbar (fig. 4.3 - c). No second order peak corresponding to these structures was observed.

A peak can be observed at [H, K] = [0.89, 0.89] in the large reciprocal space in-plane map collected between 41 min and 4 h3 min after the start of the condition (circled in black in fig.

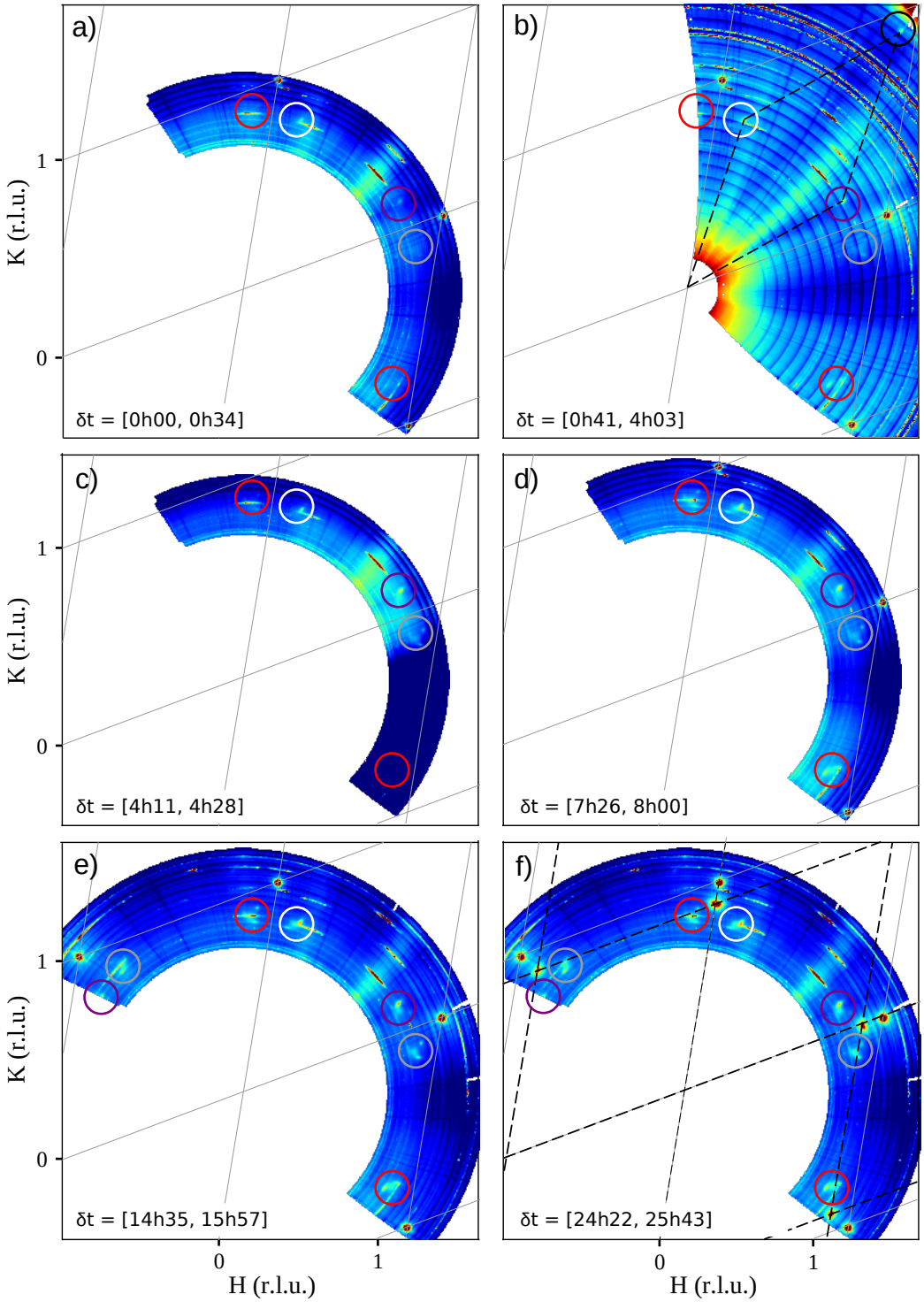

Figure 4.10: Reciprocal space in-plane maps collected under 495 mbar *of argon and* 5 mbar *of oxygen at* 450 °C*, for different exposure times.*

4.10 - b). The peak position is the same as in the first large reciprocal space in-plane map measured under 80 mbar of oxygen (fig. 4.3 - c, tab. B.1). The position of this signal also corresponds to the Pt(111)-(8×8) superstructure on Pt(111). However, no peaks at [0.89, 0, 0] and [0, 0.89, 0] can yet be detected, before (fig. 4.3 - b), and after (fig. 4.3 - c) measuring this signal. Such peaks are only detected in the large maps after ≈24 h of measurements, (described by the hexagonal lattice drawn with black dashed lines in fig. 4.3 - f).

As mentioned before, it is possible to draw a surface unit cell in fig. 4.3 (b) that includes

the peak at [0.89, 0.89] together with the white and purple circled peaks, but with an in-plane angle γ^* equal in this case to 42.2°.

The area sampled during the measurement was extended in the last two maps to observe more signals around the $(\bar{1}10)$ region (fig. 4.10 - e, f). For each map, the purple and red circled peaks around the Pt(111)-(8×8) peaks are separated by 60°, likewise for the grey and white circled peaks. In the last two map, four doublet of peaks are visible, all peaks are split in a similar pattern.

During this set of measurement, the grey circled peak did not disappear in contrast with the measurements carried out under 80 mbar of oxygen, which furthermore supports the existence of two rotated hexagonal structures. One linked to the red and purple peaks, while the other one is linked to the grey and white peaks. Overall, it seems that both structures appear after introducing oxygen and the cell, and coexist with the Pt(111)-(8×8) structure.

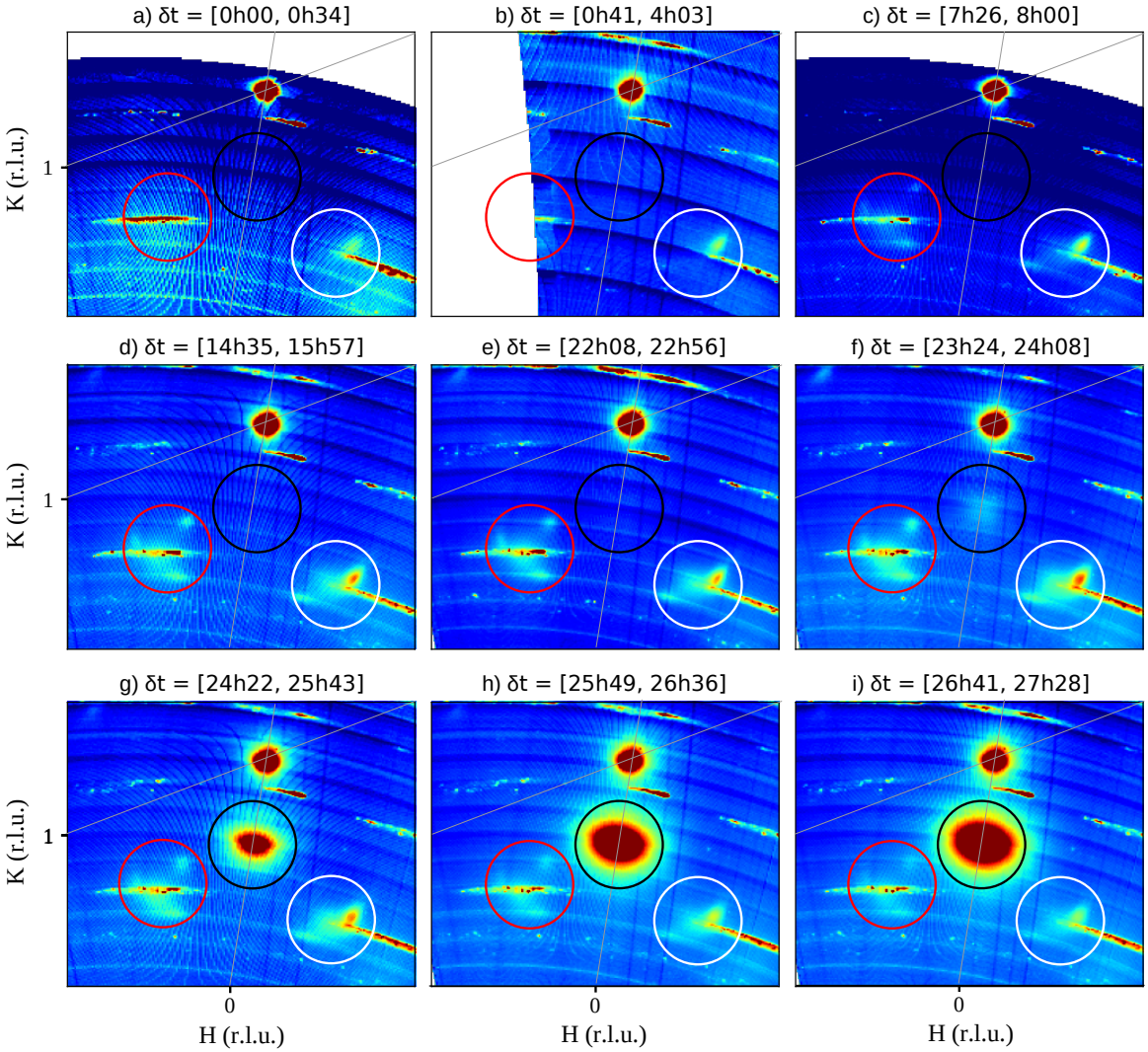

Figure 4.11: Reciprocal space in-plane maps collected under 495 mbar *of argon and* 5 mbar *of oxygen at* 450 °C*, for different exposure times.*

Smaller maps taken with a shorter time interval are presented in fig. 4.11, in which a Pt(111)-(8×8) peak is detected after ≈23 h of measurements (circled in black). The same peak was already detected after 13 hour under 80 mbar of oxygen (fig. 4.3 - d), highlighting the importance of the oxygen pressure in the surface oxidation.

A more quantitative analysis of the different structures appearing during the exposition to oxygen was performed by integrating the scattered intensity around the Pt(111)-(8×8)

and two Pt(111)-(6 × 6)-R±8.8° signals present in the (100) region (respectively circled in black, red and white in fig. 4.11). The average background was subtracted to each reciprocal space voxel before integration. The starting time of each reciprocal space in-plane map is used as estimate for the time since the introduction of oxygen, the evolution of each peak is presented in fig. 4.12. The growth of the Pt(111)-(8 × 8) peak at [H, K] = [0, 0.89] follows an exponential increase after 23 h of exposition.

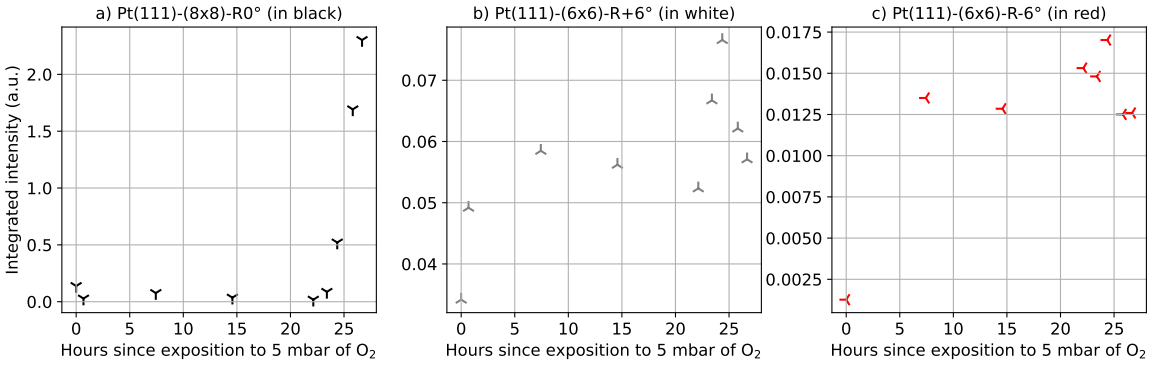

Figure 4.12: Intensity evolution as a function of time since introduction of 5 mbar *of oxygen for peaks corresponding to the Pt(111)-(6 × 6)-R±8.8° and Pt(111)-(8 × 8) structures.*

The white Pt(111)-(6×6)-R±8.8° peak is visible from the start of the exposition to oxygen (fig. 4.11 - a), whereas the red Pt(111)-(6 × 6)-R±8.8° peak is only clearly visible after 7 h (fig. 4.11 - c), with a lower intensity. Both peaks intensity quickly increases in the first hours of oxygen exposure, and then reach a steady state between 8 h and 23 h, increasing again together with the appearance of the Pt(111)-(8×8) signal. The Pt(111)-(6×6)-R±8.8° peak intensity then starts to decreases after ≈25 h.

Several SSRs have been measured at the positions of the Pt(111)-(6 × 6)-R±8.8° peaks, presented in app. B.3. The intensity is constant as a function of L, similarly to the SSRs presented in fig. 4.4, which shows that the rotated hexagonal structures are flat monolayers on the Pt(111) surface. No SSR was measured at the position of the Pt(111)-(8 × 8) peak.

Lowering the oxygen partial pressure in the reactor cell from 80 mbar to 5 mbar has demonstrated that similar in-plane structures appear, but with a slower growth rate. All peaks are absent in the simultaneous presence of oxygen and ammonia in the reactor. Additional studies are needed to understand if whether or not the rotated hexagonal structures act only as precursors for the Pt(111)-(8×8) superstructure, or if those peaks are still present after an extended exposure to oxygen. This structure could correspond to the oxide stripe hypothesised to be a precursor for surface α-PtO_2 oxide on Pt(111) by Hawkins et al. (2009).

Finally, reflectivity curves were measured just before the introduction of oxygen (in blue), 14 h (orange) and 23 h (green) after the introduction of oxygen, shown in fig. 4.13. The last reflectivity curve was measured just before the detection of the Pt(111)-(8×8) structure with SXRD (fig. 4.11 - f). The curves were fitted with *GenX*. Following the information gathered by SXRD, a homogeneous layer on top of Pt(111) was introduced in the model for the orange and green measurements, to represent the rotated structures visible in fig. 4.11. The oxide layer was necessary for the green curve to achieve a good fit, but only slightly improved the result for the orange curve. The layer thickness and density are difficult to estimate since no oscillations are visible, which shows that those measured under 80 mbar or oxygen in fig. 4.7 are linked to the Pt(111)-(8×8) structure. This also further confirms that the red and white peaks are linked to thin layers, as observed in the SSRs in app. B.3. A transition in terms of oxide roughness and density is observed between the orange and green curves. Interestingly, the final density is equal to that retrieved under 80 mbar of oxygen (fig. 4.7), but without the same layer thickness, and roughness. This effect is clearly visible in the reflectivity curve

with a decrease of intensity starting at low δ angles. The substrate roughness increases with the elapsed time since the introduction of oxygen, coherent with the creation of a surface oxide.

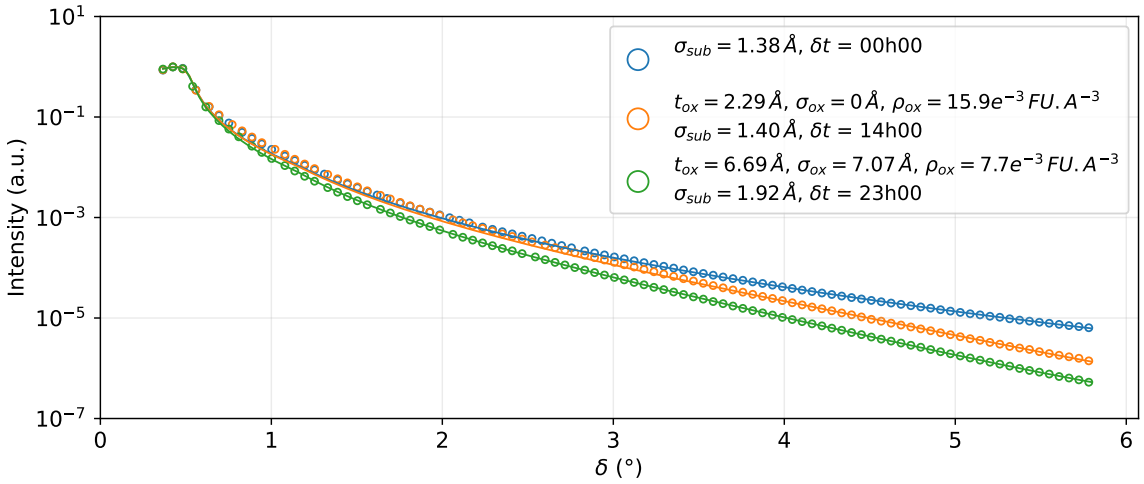

Figure 4.13: X-ray reflectivity curves measured in a specular geometry (full lines) under 5 mbar *of oxygen. Curves fitted using GenX are shown as lines. δt designates the elapsed time since the introduction of oxygen. ρ_{ox}, t_{ox}, and σ_{ox} are the oxide density, thickness, and root mean square roughness. σ_{sub} is the substrate root mean square roughness.*

4.2.4 Surface roughness and surface relaxation effects

The $(2\bar{1}L)$, (10L) and (11L) crystal truncation rods have been measured 6 h after the start of each condition, each measurement took 2 h. The CTRs background-subtracted intensity was integrated using the *fitaid* module of *BINoculars* (sec. 2.8.2), as a function of L, and with the same integration width in H and K.

The CTRs intensities are presented in fig. 4.14, they display only the expected features for the Pt(111) surface. At first sight, mostly the surface roughness seems to evolve when changing condition, visible from the variation of intensity minimum near $L = 1.5$ (or $L = 2.5$ for the (10L) CTR). Only the $(2\bar{1}L)$ CTR measured under 500 mbar of argon before the oxidation cycle is available.

To investigate potential surface relaxation effects, the three CTRs were fitted together with *ROD*. A simple model was used, consisting of three stacked layers of {111} platinum planes (fig. 4.15). These three layers, in which relaxation effects can be detected, constitute the *surface* of the crystal, on top of the *bulk*. A is the layer closest to the bulk, whereas C is the outermost layer.

Each atomic layer is treated rigidly, allowing only vertical displacement, to see if surface relaxations effect can be detected at different atmospheres. Four different models have been tested to fit the CTR intensity as a function of L. In the first, second, and third models, the one (C), two (C & B), and three (C & B & A) topmost layers have their own out of plane displacement parameter. In the fourth model, the two topmost layers (C & B) share the same out-of-plane atomic displacement.

During the fitting process, in-plane atomic displacements were excluded as one of the parameters to be adjusted. The presence of too many parameters posed challenges in achieving a successful convergence of the fitting routine. The roughness parameter β was set free.

The best fit is with the first model, the C layer was allowed to have an out-of-plane atomic displacement $\delta_{z,C}$ between -0.05 Å and 0.05 Å. The position of the Pt atoms on the A and B layers were fixed, following the positions of the Pt atoms in the bulk.

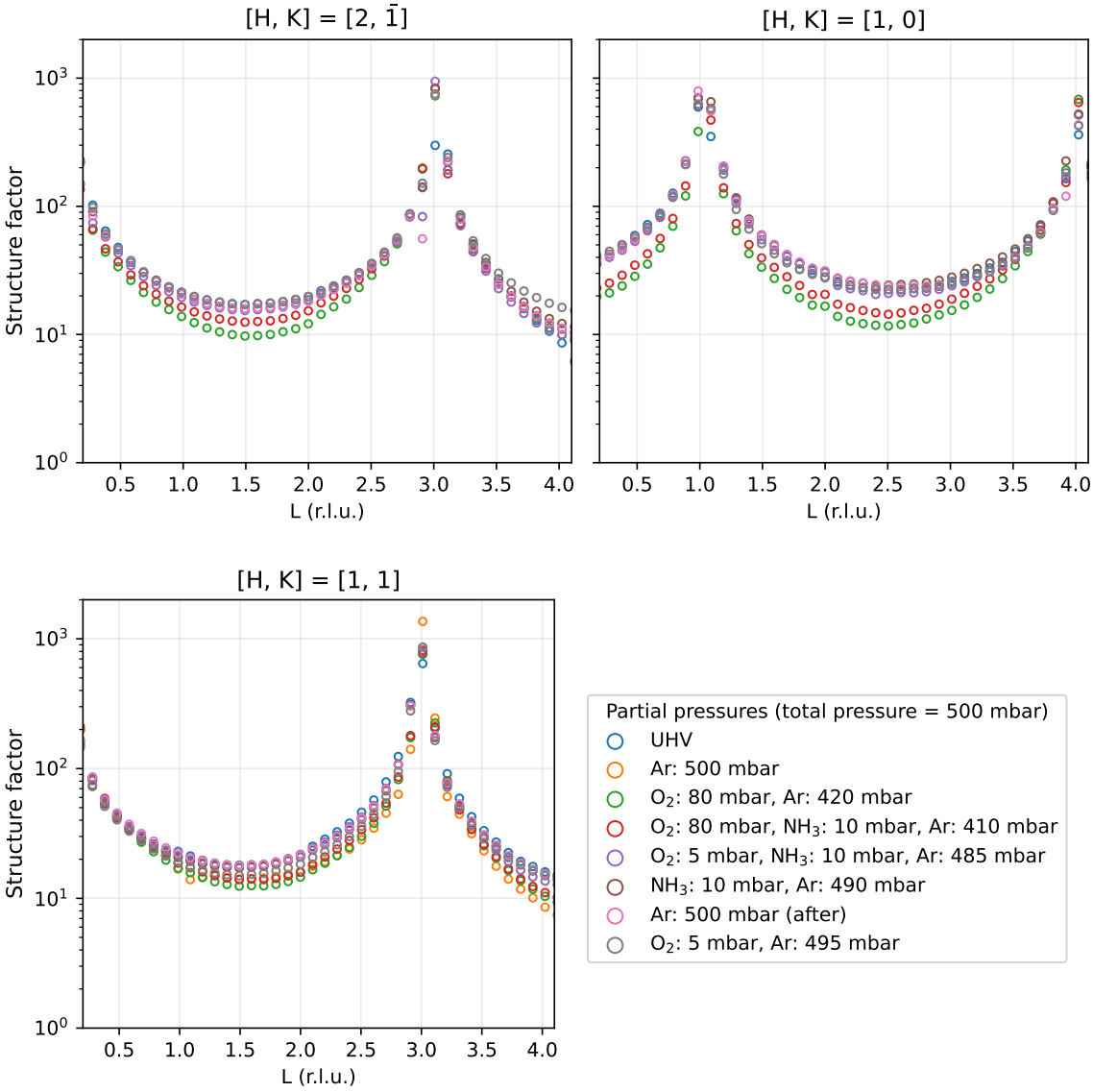

Figure 4.14: Evolution of crystal truncation rods under different atmospheres.

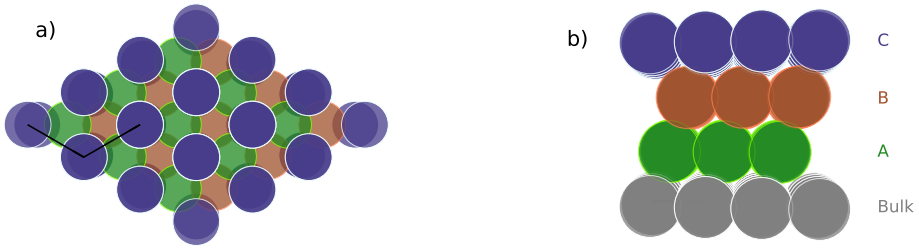

Figure 4.15: View from above (a) and from the side (b) of the Pt(111) surface with the atoms belonging to the A, B and C layers respectively coloured in green, red and blue. The size of the Pt atoms has been tuned from (a) to (b) to visualise the arrangement of the A, B and C layers.

The strain with respect to the bulk was computed according to eq. 3.1, the reference was set to the Pt(111) surface unit cell, *i.e.* $|\vec{c}_{(111)}| = 6.79\,\text{Å}$. The evolution of the surface roughness and out-of-plane strain is shown in fig. 4.16.

The Pt(111) surface roughness increases with the introduction of Argon in the cell at 450 °C (fig. 4.16 - a), probably due to the presence of impurities contained in the argon gas flow. The introduction of oxygen in the cell further increases the surface roughness, as

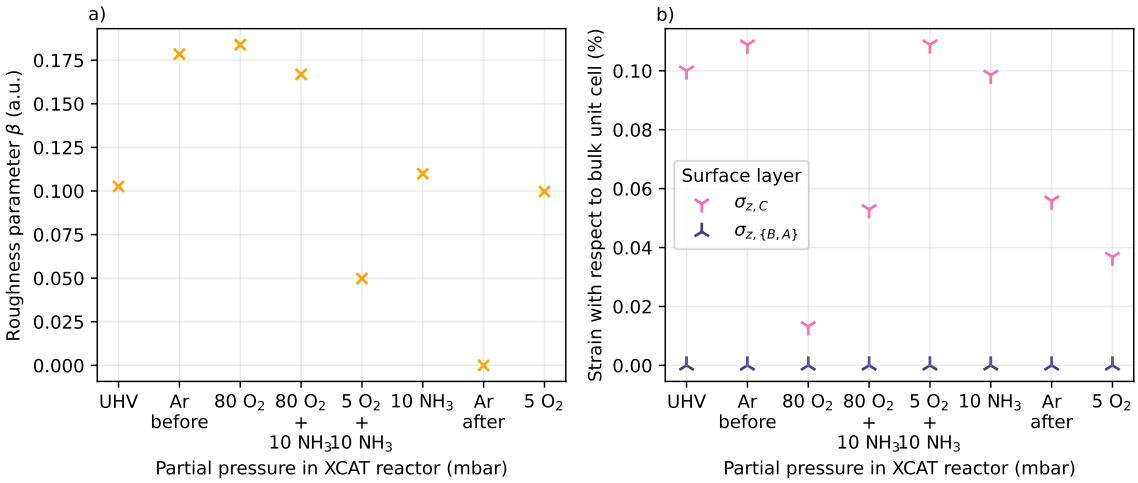

Figure 4.16: Fitting results for roughness parameter β (a) and out-of-plane strain σ_z (b) as a function of the experimental conditions.

expected from the formation of the different surface oxides visible in the in-plane reciprocal space maps (fig. 4.3, CTR recorded between c and d). Adding ammonia in the reactor cell, which was shown to remove the different surface oxides, has also the effect of decreasing the surface roughness. The β parameter increases slightly again when oxygen is removed (fig. 4.16 - a). This result is probably more linked to a low quality fitting result, the corresponding curve (brown in fig. 4.14) is similar with the curve recorded previously under reacting conditions (purple in fig. 4.14), and with the following curve recorded under inert atmosphere (pink in fig. 4.14). Moreover, the reflectivity results (fig. 4.9) have shown a decreasing roughness at this condition. It seems that the ammonia oxidation cycle has effectively *smoothed* the surface, possible by removing the presence of impurities and/or surface oxides. Finally, the re-introduction of 5 mbar of oxygen increases the surface roughness again (fig. 4.16 - a), in accordance with the formation of surface oxides detected during in-plane reciprocal space maps (fig. 4.10).

Overall, a very low amount of strain is detected on the surface, almost imperceptible when observing the CTR minimum position in fig. 4.14. From the fitting results, the topmost layer is already under tensile strain at UHV, further increased by the presence of Argon and possible impurities from the opening of the gas valves.

The largest evolution in the strain values comes from the high oxygen atmosphere, which has the effect of decreasing the surface strain, with an out-of-plane lattice parameter almost equal to the bulk value. The formation of surface oxides observed under this atmosphere does not seem to have a very important effect on the surface relaxation state (with respect to the bulk lattice parameter). It is possible that the oxide is preventing the metallic surface from directly interacting with oxygen, therefore allowing it to assume a lattice parameter similar to the bulk. The introduction of ammonia increases again the surface strain, higher ammonia to oxygen ratio coincides with higher tensile strain.

Therefore, reacting conditions and the sole presence of ammonia had the effect of removing the surface oxides, and decreasing the surface roughness. It is possible that the tensile strain in the last layer under Argon after the oxidation cycle corresponds to the equilibrium state of a clean Pt(111) surface.

Finally, the re-introduction of 5 mbar of oxygen decreases slightly the tensile strain on the topmost layer, a weaker but similar effect to the presence of 80 mbar of oxygen. To conclude, no changes from tensile to compressive strain are observed during the reaction with respect to the bulk parameters. The presence of oxygen alone has the effect of lowering the surface

strain, while the presence of ammonia has the opposite effect. Different reacting conditions are related to the same direction of displacement but with a higher magnitude when lowering the partial pressure of oxygen.

4.2.5 Surface species

To link surface structure, surface moieties and reaction products, the Pt 4f, N 1s and O 1s XPS spectra were recorded at near ambient pressure at the B07 beamline (Diamond Light Source), at 450 °C. The same sequence of conditions in the ammonia oxidation cycle was repeated as for the SXRD experiment, with the same ratio between reactants.

To keep the total pressure in a range compatible with the setup, all the measurements were performed without carrier gas and with a reactant pressure one order of magnitude lower than the SXRD experiments. The conditions have been resumed in tab. 4.2. Thanks to the geometry of the B07 beamline, the mass spectrometer allows us to monitor the presence of the reactants and products close to the sample surface (fig. 4.1 - c). The gas composition in the vicinity of the sample surface is reported in fig. 4.17.

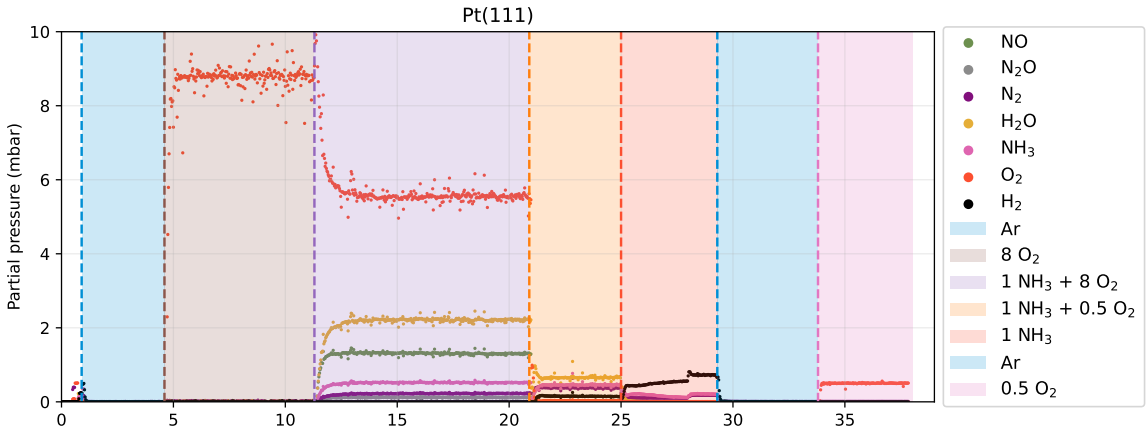

Figure 4.17: Evolution of reaction product partial pressures as a function of time during the XPS experiment on the Pt(111) single crystals at 450 °C. Transition between conditions are indicated with dashed vertical lines.

After setting an inert atmosphere in the chamber, the oxidation cycle starts by the introduction of 8.8 mbar of oxygen, as detected in the RGA. 1.1 mbar of NH_3 is then introduced in the reactor so that the O_2/NH_3 partial pressure ratio becomes equal to 8. This favours the production of NO as expected, accompanied by a high amount of water, small amounts of N_2 and N_2O can also be detected. Despite the high pressure of oxygen in the reactor, approximately half of the pressure of ammonia is still detected. The complete oxidation of ammonia may be limited by the availability of active sites, the transportation of reactants towards the catalyst surface or the relatively low temperature compared to industrial conditions (>700 °C) which can for example impact the active sites turnover frequency.

Reducing the O_2/NH_3 ratio to 0.5 by lowering the oxygen pressure has the remarkable effect of shifting the reaction selectivity *entirely* towards N_2, water is still the main product (fig. 4.17). H_2 coming from the simultaneous dissociation of NH_3 can be measured, not observed under a higher pressure of oxygen, which means that this reaction is not favoured when oxygen is present in the reactor. Oxygen is undetected by the mass spectrometer when the O_2/NH_3 ratio is equal to 0.5. All of the oxygen available near the catalyst surface participates in the production of N_2 and H_2O *via* the oxidation reaction. Ammonia can be thus considered to be in excess, and partly decomposing towards N_2.

The following condition is pure ammonia. Only the dissociation of ammonia happens on

the catalyst surface, put into evidence by the presence of hydrogen and absence of water. The glitch in the partial pressure at 28.5 h is due to a re-setting of the total pressure to 1.1 mbar.

N 1s and O 1s levels

N 1s and O 1s levels were measured to probe for the existence of specific surface species, allowing us to obtain more information about the reaction mechanism, and thus to link surface state and selectivity. The evolution of the N 1s and O 1s XPS spectra for different atmospheres is presented in fig. 4.18. Binding energies are obtained by aligning the Fermi level to 0 eV, all the reported peaks and corresponding species are detailed in tab. 4.4.

The oxidation cycle is started by introducing 8.8 mbar of oxygen in the reactor. The presence of gas phase oxygen ($O_{2,g}$) can be confirmed in the O 1s spectra by a characteristic peak doublet around 538 eV. The positions are shifted by 2.2 eV in binding energy with respect to literature (539.3 eV, 540.4 eV, Avval et al. 2022). This is explained by a change in the work function of the sample-analyser setup, impacting gas species exclusively since not in electrical contact with the system (Starr 2021). This signal is also present when the O_2/NH_3 ratio is equal to 8, but not when equal to 0.5, suggesting that all the oxygen is used in the surface vicinity, in accordance with the RGA signals (fig. 4.17). $O_{2,g}$ is also detected when only 0.55 mbar of oxygen is in the cell.

The broad signal extending from 528.5 eV to 533 eV is hiding various peaks, linked to the presence of oxygen species. Fisher et al (1980) report the signal for adsorbed oxygen (O_a) and adsorbed hydroxyl groups (OH_a) at respectively 529.8 eV and 531 eV when exposing the Pt(111) surface to water. Peuckert et al. (1984) have studied various oxidised Pt surfaces and indexed a peak at 530.2 eV for O_a on Pt(111), and at 531.5 eV for OH_a on polycristalline Pt. Derry et al. (1984) report 530.8 eV for O_a on Pt(111) during its exposition to oxygen, while Zhu et al. (2003) report O_a at 529.9 eV when probing the dissociation of NO on the Pt(111) surface. Fantauzzi et al. (2017) report oxygen surface species at 529.7 eV during the oxidation of Pt(111) at 225 °C, similarly to Miller et al. (2014).

During a recent study of the oxidation of ammonia at different pressures and O_2/NH_3 ratio on Pt(111), (2×2) chemisorbed oxygen and hydroxyl groups were reported respectively at 529.7 eV and 531.4 eV in 1 mbar of oxygen at 325 °C (Ivashenko et al. 2021).

In the current XPS study, the signal to noise ratio does not allow to clearly discern and locate peaks between 528.5 eV and 533 eV. It is probable however that hydroxyl groups as well as atomic oxygen are adsorbed on the surface around 529.7 eV and 531.4 eV respectively. Such O 1s features can be seen when the oxygen pressure is equal to 0.55 mbar, but with a higher apparent amount of atomic oxygen species in comparison to hydroxyl groups.

From the previous SXRD measurements, it was seen that a Pt(111)-(8×8) superstructure grows under the presence of 5 mbar of oxygen, but only after at least 22 h. Similar structures have been linked to a surface α-PtO_2 oxide (Ackermann 2007; Ellinger et al. 2008). Two Pt(111)-(6×6)-R$\pm$8.8° structures, possibly precursors of the Pt(111)-(8×8) structure, have been measured in the minutes following the introduction of oxygen. Therefore, if the Pt(111)-(8×8) structure is not expected here since the duration of each condition is below 5 h, the precursor structure may yield some signals between 528.5 eV and 533 eV in the O 1s level. For example, a large peak at 530.7 eV attributed to Pt surface oxides has been observed at an oxygen pressure of 1 bar by Van Spronsen et al. (Van Spronsen et al. 2017).

For the $O_2/NH_3 = 8$ condition, only a weak signal at 402.6 eV can be detected in the N 1s spectrum. At those reaction condition, and with 40 min acquisition time, most of the signals can still be below detection limits. Gas phase nitric oxide (NO_g), ammonia ($NH_{3,g}$), nitrogen ($N_{2,g}$), and nitrous oxide ($NO_{2,g}$) are visible in the RGA signals (fig. 4.17).

The main product, NO_g, is expected between 404.5 eV and 406.7 eV in the N 1s level, observed during reacting conditions with an equal amount of oxygen and ammonia, a total pressure of 1 mbar, and temperature of 325 °C (Ivashenko et al. 2021). Since not observed in

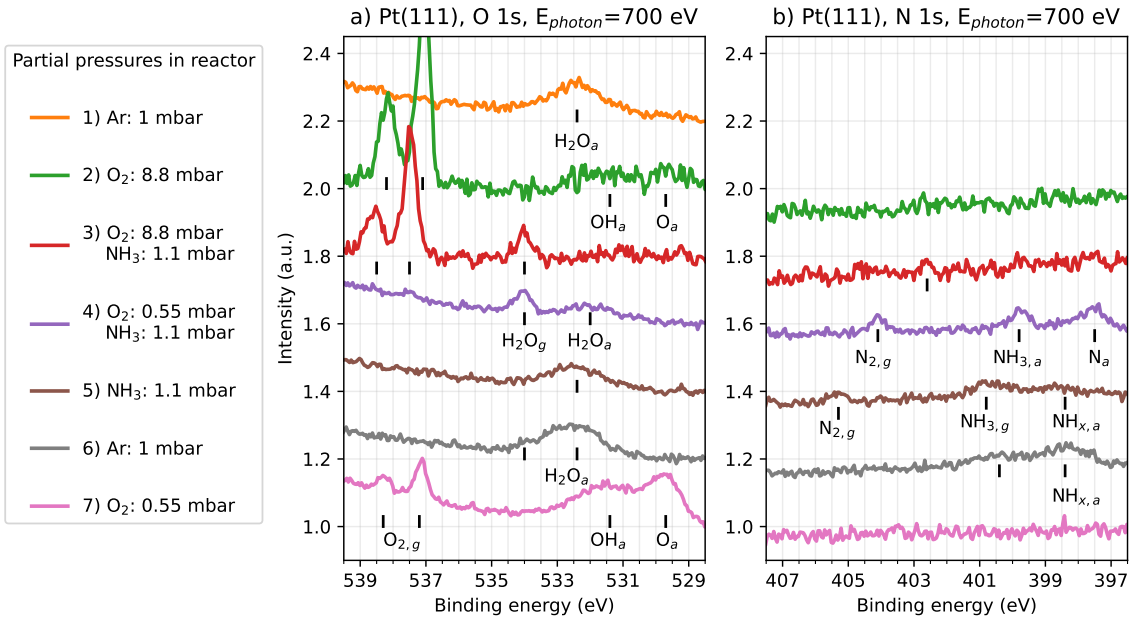

Figure 4.18: XPS spectra collected at the O 1s (a) and N1 s (b) levels under different atmospheres at 450 °C with an incoming photon energy of 700 eV. The spectra are normalised and shifted in intensity to highlight the presence of different peaks.

Partial pressures (mbar)	Ar	1	0	0	0	0	1	0
	NH_3	0	0	1.1	1.1	1.1	0	0
	O_2	0	8.8	8.8	0.55	0	0	0.55
Gas signals (decreasing pressure order)		Ar	O_2	O_2, H_2O, NO NH_3, N_2, N_2O	H_2O, NH_3 N_2, H_2	H_2, NH_3 N_2	Ar	O_2
N 1s: peak positions		No data	No peak	402.6 eV	404.1 eV 399.8 eV 397.5 eV	405.3 eV 400.8 eV 398.4 eV	400.4 eV 398.4 eV	No peak
Attributed surface species				Not indexed	$N_{2,g}$ $NH_{3,a}$ N_a	$N_{2,g}$ $NH_{3,g}$ $NH_{x,a}$	$NH_{3,a}$ $NH_{x,a}$	
O 1s: peak positions		532.4 eV	538.2 eV 537.1 eV 531.4 eV 529.7 eV	538.5 eV 537.5 eV 534.0 eV	534.0 eV 532.0 eV	532.4 eV	534.0 eV 532.4 eV	538.3 eV 537.2 eV 531.4 eV 529.7 eV
Attributed surface species		H_2O_a	$O_{2,g}$ $O_{2,g}$ OH_a O_a	$O_{2,g}$ $O_{2,g}$ H_2O_g	H_2O_g H_2O_a	H_2O_a	H_2O_g H_2O_a	$O_{2,g}$ $O_{2,g}$ OH_a O_a

Table 4.4: Indexing of peaks measured during ammonia oxidation of the Pt(111) surface.

the O 1s level, the authors have proposed that the related signal is hidden by the important gas phase oxygen features. The same study reports $N_{2,g}$ between 403.9 eV and 404.8 eV, and $NH_{3,g}$ at 400.4 eV. $NH_{3,g}$ was also measured shifted to 400.7 eV under 1 mbar of ammonia, without oxygen present in the cell.

Adsorbed nitrogen oxide (NO_a) is absent, expected to yield peaks between 530 eV and 532 eV in the O 1s level, and between 400.4 eV and 401.3 eV in the N 1s level (Kiskinova et al. 1984; Zhu et al. 2003; Günther et al. 2008). It is worth noticing that this region is also populated by water and OH_a signals. Since NO is one of the main products at this condition, the absence of NO_a can be explained by short desorbing time from the Pt(111) surface after formation (Ivashenko et al. 2021).

The peak at 402.6 eV in this study could not be safely indexed, since situated far away in binding energy from any of the reported gas phase peaks, and of adsorbed nitrogen and NH_x type features. Gas phase water (H_2O_g) is visible in the O 1s spectra by a peak at 534 eV, as reported during ammonia oxidation by Weststrate et al. (2006), probably generated by the oxidation reaction. The energy difference between the low energy peak of $O_{2,g}$ and H_2O_g, 3.5 eV, is close to the difference reported in literature for pure gas phases, equal to 3.3 eV (Linford et al. 2019; Avval et al. 2022).

By lowering the oxygen pressure to 0.55 mbar so that $O_2/NH_3 = 0.5$, nitrogen production is favoured (fig. 4.17), three peaks can be detected in the N 1s level. 397.5 eV is characteristic of adsorbed atomic nitrogen (N_a) on Pt(111) (van den Broek et al. 1999; Zhu et al. 2003). The energy difference between N_a, NH_a, and $NH_{2,a}$ is reported to be approximately 0.95 eV, 1.9 eV in total on Pt(111) (Ivashenko et al. 2021), which is too few to link the peak at 399.8 eV to NH_a or $NH_{2,a}$ with respect to the N_a peak. Since there is a peak at 400.8 eV in the following spectrum that can be linked to gas phase ammonia from similar reported binding energies, the peak at 399.8 eV is attributed to adsorbed ammonia ($NH_{3,a}$). The peak at 404.1 eV is attributed to $N_{2,g}$, which is the only measured nitrogen product, and also in accordance with reported binding energies.

No oxygen is anymore detected in the reactor, as observed with the mass spectrometer (fig. 4.17). Moreover, no OH_a and O_a peaks can be detected in the O 1s level (fig. 4.18), even though the total pressure was divided by 6, increasing the detection of photo-electrons. Adsorbed water groups (H_2O_a) are reported between 532.2 and 532.9 eV on Pt(111) depending on the surface coverage (Fisher et al. 1980; Kiskinova et al. 1985), to which is attributed the peak at 532 eV.

The presence of adsorbed water supports a Langmuir-Hinshelwood mechanism with quick stripping of hydrogen from $NH_{x,a}$ species by OH_a and O_a, eventually forming adsorbed water. The de-hydrogenation process must be limiting the catalytic activity due to the lack of available adsorbed oxygen species near adsorbed ammonia, which could be why $NH_{3,a}$ is observed, but not $NH_{x,a}$. The key importance of available atomic oxygen for the production of NO is supported by the simultaneous absence of O_a in the O 1s level, and the absence of NO in the RGA signals (fig. 4.17). The presence of adsorbed nitrogen could be due to long residual times on the catalyst before recombination and desorption of N_2. This hypothesis is in accordance with the commonly accepted reaction mechanism detailed in sec. 1.2.2.

Once oxygen is removed, gas phase water disappears from the O 1s level, suggesting that water in gas phase is mostly present from the oxidation reaction rather than as UHV/gas contaminant. Adsorbed water is still visible, possibly from long desorption time before producing water, or from contaminants. The energy level differs by 0.5 eV from adsorbed water during reacting conditions, signifying different chemical environments. As observed in the mass spectrometer, the dissociation of ammonia towards nitrogen still occurs, a slightly shifted $N_{2,g}$ peak is reported at 405.3 eV. There is a clear effect of the presence of oxygen on the position of gas phase signals. The large peak linked to atomic nitrogen has disappeared, a peak linked to $NH_{3,g}$ is reported as well as a large and weak peak probably linked to NH_x groups. The dissociation of ammonia is reported to be slower without the help of oxygen species on Pt(111) (Offermans, Jansen and van Santen 2006; Offermans, Jansen, Van Santen et al. 2007; Imbihl et al. 2007; Novell-Leruth, Ricart et al. 2008). This could explain why such a large peak is observed for $NH_{x,a}$, and why $NH_{3,g}$ is observed rather than $NH_{3,a}$, since most of the adsorption sites are probably occupied by $NH_{x,a}$ species. The difficulty to fully dissociate ammonia is also correlated to the production of hydrogen, it is possible that the combination of two hydrogen atoms removed from ammonia to produce H_2 is slow, and thus occupies part of the adsorption sites.

The introduction of argon and removal of ammonia increases the H_2O_g signal, possibly from contaminants. Some nitrogen rich species are still visible. Just like water, ammonia has

the tendency to adsorb well on the inner walls of the chamber resulting in a slow pumping speed. Removing argon and introducing 0.55 mbar of oxygen has removed all the N 1s peaks by the oxidation of the leftover NH_x species. As previously discussed, comparable peaks are observed in the O 1s level as under 8.8 mbar of oxygen, linked to hydroxyl groups, O_a, and $O_{2,g}$.

Pt 4f level

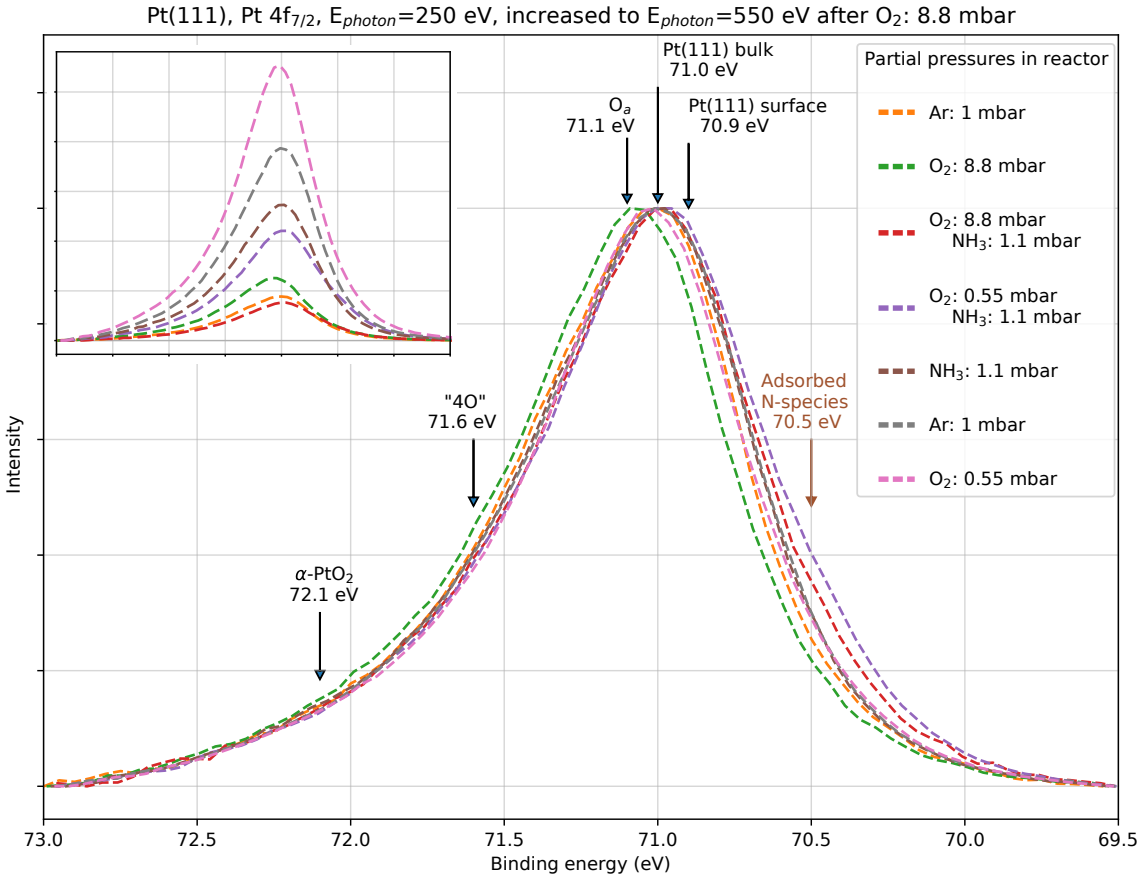

Figure 4.19: XPS spectra collected at the Pt 4f level under different atmospheres at 450 °C with an incoming photon energy of 550 eV. A Shirley-type background has been subtracted from all XPS spectra. Normalisation performed first by the background intensity and secondly by the maximum intensity to allow a qualitative comparison between different total pressures. Spectra before normalisation by maximum intensity are shown on the top left.

The Pt 4f level was also measured to report possible differences in the chemical environment of surface platinum atoms (fig.4.19). Miller et al. (2011) have measured two peaks at 72.1 eV and 73.5 eV under 6.66 mbar of oxygen at 450 °C. The 72.1 eV peak is assigned to (i) oxygen between the metallic surface and surface α-PtO_2 oxide as reported by Ellinger et al. (2008). The 73.5 eV peak is attributed to (ii) Pt atoms within the trilayer oxide structure.

However, both peaks are absent at 0.66 mbar of oxygen at 350 °C, for which the presence of (iii) (2×2) chemisorbed oxygen and (iv) "4O" oxide surface stripes are linked to two other peaks, respectively 71.1 eV, and 71.6-71.7 eV.

In a following study under 13.33 mbar of oxygen, slightly shifted high intensity peaks at 72.2 eV and 73.6 eV are linked to the presence of surface α-PtO_2 oxide, fully covering a Pt(111) crystal (D. Miller et al. 2014). The photon energy for both experiments is equal to 275 eV, whereas the photon energy is here equal to 550 eV. Thus, both studies by the Miller group

are more sensitive to the surface structure since the emitted photo-electrons have increased inelastic mean free paths. Interestingly the crystal preparation to grow surface α-PtO_2 oxide is not too far from this study. The Pt(111) crystal was exposed to 13.33 mbar of oxygen for 10 min while cycling the temperature from 25 °C to 525 °C four times.

A small peak can be identified near 71.6 eV in the current experiment under 8.88 mbar of oxygen that could correspond to the oxide stripe structure. Its presence is not certain since the intensity is very low, corresponding potential peaks in the O 1s level cannot be resolved either. No clear peak could be detected near 73.5 eV in the Pt $4f_{7/2}$ level, but a very small peak can be seen at 72.1 eV. Since the presence of surface α-PtO_2 oxide was linked to very high intensity peaks by Miller et al. (2014), this structure can safely be ruled out in this study. It seems that the temperature cycling is crucial to grow α-PtO_2 on Pt(111). The peak maxima is shifted by 0.09 eV when introducing 8.88 mbar of oxygen in the cell after pure argon atmosphere. Overall, the lack of clear peak corresponding to the "4O" oxide stripe and α-PtO_2 phases suggests that the oxygen on the Pt(111) surface is mostly chemisorbed, which could also be why the peak is slightly shifted towards 71.1 eV.

When introducing 1 mbar of ammonia in the reactor, the maximum of the Pt $4f_{7/2}$ peak is measured back at the position under inert atmosphere, while a new component is measured at 70.5 eV. Reducing the pressure of oxygen to 0.55 mbar further increases the intensity of the latter component compared to the maximum peak intensity. Removing oxygen but keeping ammonia in the reactor removes this peak. Since the intensity of this peak increases when the O_2/NH_3 ratio decreases, *i.e.* when all the oxygen is consumed, it is probably linked to the presence of adsorbed nitrogen species on the platinum surface. The absence of this peak under the presence of ammonia in the cell, for which adsorbed nitrogen can not be detected, supports a link with N_a or $NH_{3,\,a}$ (fig. 4.18).

Only a smaller shift is repeated when 0.55 mbar of oxygen is introduced after 1 mbar or argon, approximately equal to 0.2 eV. Both spectra collected under argon before and after the oxidation cycle are very similar, some nitrogen species possibly left on the surface are probably removed by oxygen, which explains the increased intensity after the oxidation cycle near 70.5 eV.

4.3 Pt(100) single crystal studied at 450 °C

A similar experiment was carried out on a Pt(100) sample. The arrangement of the Pt atoms on this surface is square, the distance between in-plane neighbouring Pt atoms is smaller than between out-of-plane atoms. A surface unit cell must be derived, shown in fig. 4.20, to represent the surface arrangement of the Pt atoms with the smallest unit vectors possible. The in-plane vectors $\vec{a}_{(100)}$ and $\vec{b}_{(100)}$ are of equal magnitude ($a_{Pt}/\sqrt{2} = 2.77$ Å), separated by 90°. The out-of-plane vector $\vec{c}_{(100)}$ is perpendicular to the (100) plane, and of magnitude $a_{Pt} = 3.92$ Å.

Reciprocal space in-plane maps were collected to probe the structural evolution of the sample during ammonia oxidation, using the same experimental setup and atmospheres as for Pt(111) (tab. 4.1). Considering the square symmetry in the position of the Bragg peaks, the in-plane reciprocal space maps were collected by rotating the in-plane sample and detector angles (μ and γ) from 0° to 90° to collect a quarter of the reciprocal space in the ($\vec{q}_x$, $\vec{q}_y$) plane

The reciprocal space in-plane maps were computed in (hkl)-space (fig. 4.21) to visualise the arrangement of surface structures or surface relaxations in comparison with the hexagonal surface unit cell described in fig. 4.20.

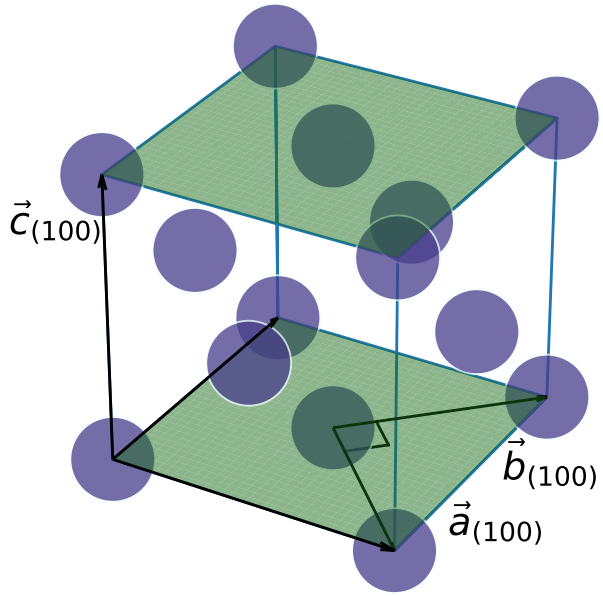

Figure 4.20: Face-entered cubic unit cell of Pt with (100) crystallographic plane drawn in green. $\vec{a}_{(100)}$, $\vec{b}_{(100)}$ and $\vec{c}_{(100)}$ are the (100) surface unit cell vectors.

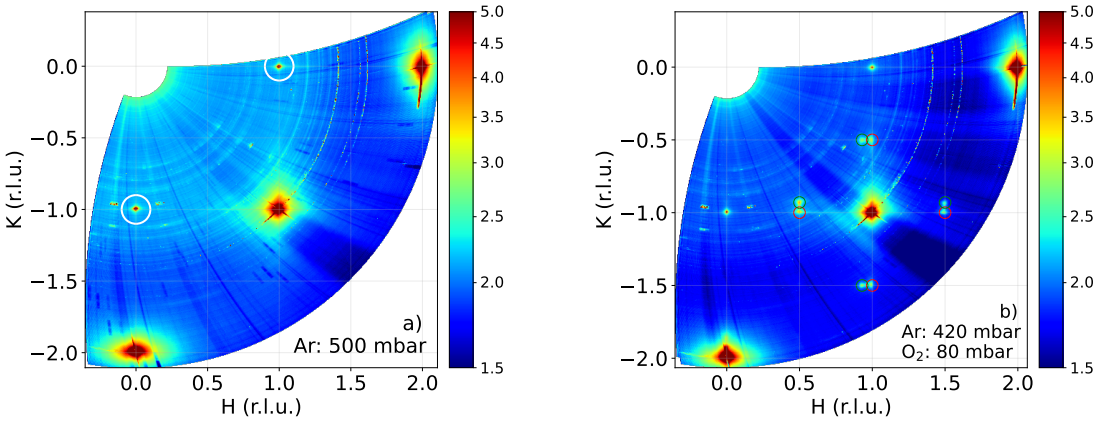

Figure 4.21: Reciprocal space in-plane maps collected under different atmospheres at 450 °C, computed using the surface lattice of Pt(100).

4.3.1 Oxide growth under 80 mbar of oxygen

The first map was collected under 500 mbar of Ar, after the cleaning of the sample by sputtering and annealing (fig. 4.21 - a). The (200), (1$\bar{1}$0) and (0$\bar{2}$0) Bragg peaks can be observed, together with the intersection of the [1, 0, L] and [0, $\bar{1}$, L] CTRs with the [H, K, 0] plane (circled in white).

The sample was then first exposed to 80 mbar of oxygen, while keeping the total pressure to 500 mbar by compensation with argon (fig. 4.21 - b). The signals generated by the rich oxygen condition can be divided into two groups, identified by red and green circles. The red peaks are situated approximately at [H, K] = [1, -0.5], [H, K] = [1, -1.5], [H, K] = [0.5, $\bar{1}$] and [H, K] = [0.5, -1.5]. These signal follow a Pt(100)-(2 × 2) reconstruction, keeping in mind that it is related to surface unit cell of Pt(100). A (2 × 2) reconstruction of the Pt(100) surface has been reported for nanoparticles measured under 1×10^{-3} mbar of oxygen, by the use of environmental TEM (H. Li et al. 2016).

The green peaks are slightly shifted from the red peaks by the same amount $\delta = 0.07$ in either H or K. No simple surface unit cell could be derived from their in-plane positions.

Two super structure rods (SSRs) were performed on each group of signal, up to $L = 3.5$, to probe the related out-of-plane structure. The background-subtracted intensity was integrated as a function of L using the *fitaid* module of *BINoculars* (fig. 4.22), following the same kind

of procedure performed on Pt(111).

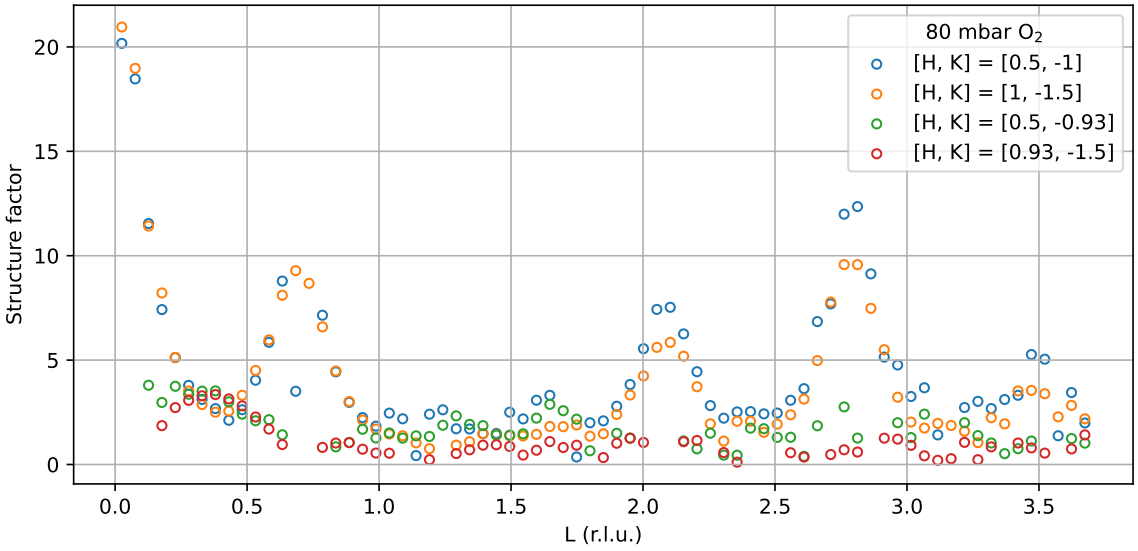

Figure 4.22: SSRs for four different positions in [H, K] under 80 mbar *of O_2, and* 420 mbar *of Ar.*

The intensity distribution as a function of L for the shifted peaks quickly decreases down to zero, which shows they correspond to flat monolayers (simulation example in fig. 2.42, Robinson et al. 1991). However, four peaks at different L values are visible on both SSRs measured on the Pt(100)-(2 × 2) reconstruction in fig. 4.22, including at $L = 0$, which is characteristic of a bulk structure, *i.e.* more than a few unit cells thick (simulation example also in fig. 2.42, Robinson et al. 1991). The peaks were fitted using a model with four Gaussian peaks and a constant background, the same full width at half maxima was used for all four peaks since they are assumed to be linked to the same structure (fig. 4.23). A r^2 value of 0.86 and 0.98 was reached for the SSRs at [H, K] = [0.5, $\bar{1}$], and [H, K] = [0.5, -1.5], respectively. In the second fit, the maximum value of each peak is better represented which explains the difference in the r^2 values.

Corresponding interplanar spacings were computed from the position of the peaks, corresponding to a slightly distorted cubic unit cell with an in-plane lattice parameter equal to 5.60 Å, and an out-of-plane lattice parameter equal to 5.64 Å. This unit cell was used to index each Bragg peak in fig. 4.23.

Pt_3O_4 has a cubic structure (space group $P_{m\bar{3}n}$) with a lattice parameter equal to 5.65 Å (Galloni and Roffo 2004; Galloni and Busch 1952; Muller et al. 1968), presented in fig. 4.24. Recent theoretical studies have proposed a lattice parameter equal to 5.59 Å, (tab. 4.3, Seriani et al. 2006), which is also close to the values reported in this study. Moreover, the (212) and (232) reflections are not allowed for the proposed due to the symmetry of the Pt_3O_4 structure. Those reflections are indeed absent from fig. 4.23.

The lattice parameter of Pt_3O_4 is approximately twice that of the Pt(100) surface lattice parameter, which allows the formation of a cubic on cubic coherent interface. The nature of the atoms at the interface is addressed later in this chapter. To match perfectly with the Pt(100) surface, the in-plane lattice parameter of Pt_3O_4 would need to reach the value of $2 \times a_{100} = 5.55$ Å, which is lower than the reported literature values for the cubic unit cell. This interfacial strain can be the reason for the distorted structure observed in this study. The possibility to perform out-of-plane measurements with SXRD allows us to link the Pt(100)-(2 × 2) reconstruction with certainty to bulk Pt_3O_4, which exhibits a slightly distorted lattice.

A first estimate of the oxide layer thickness can be obtained with the full-width at half maxima of the Bragg peaks in q_z: $FWHM_{q_z}$, and using the equation $2\pi/FWHM_{q_z}$ (Pat-

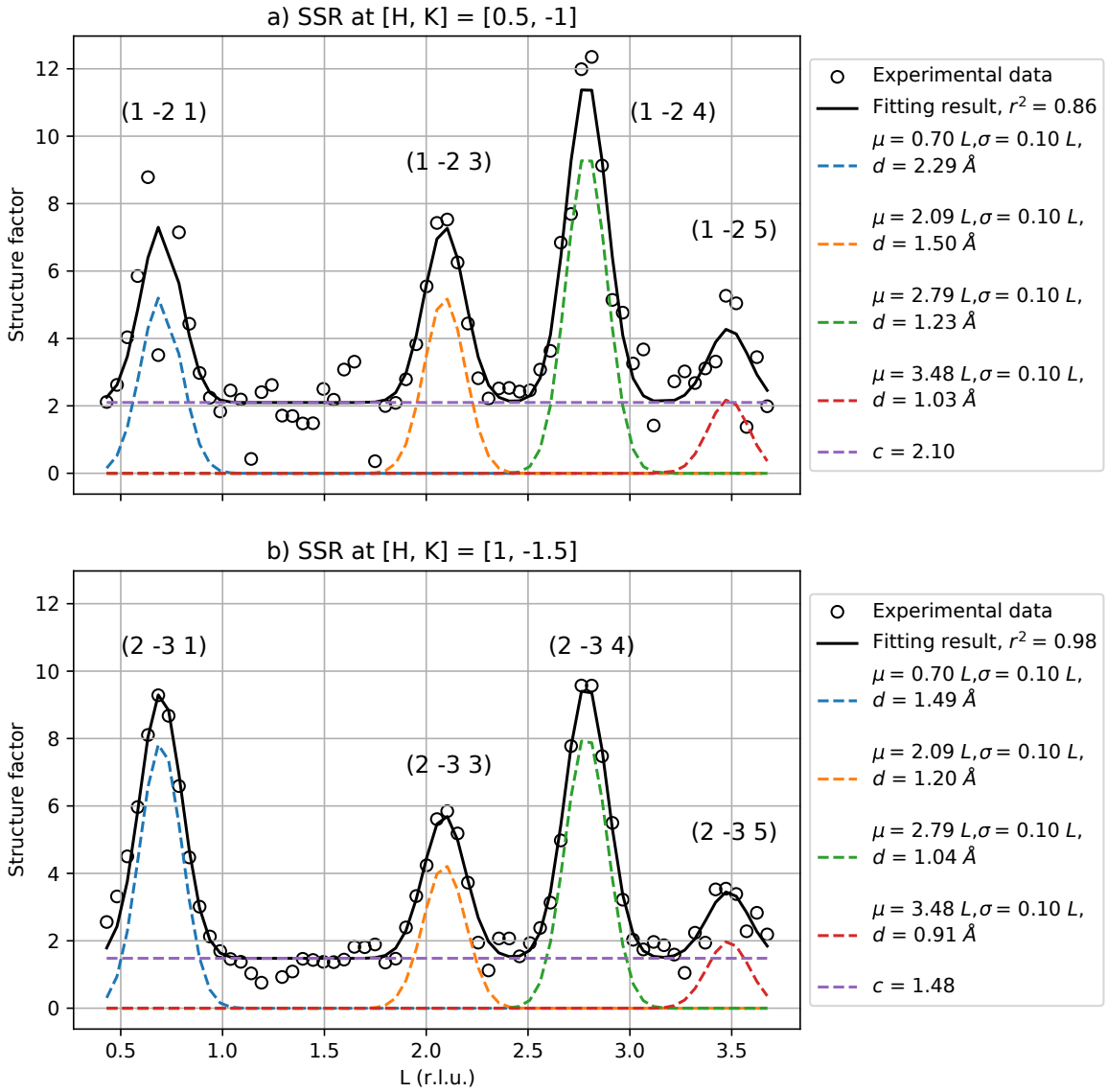

Figure 4.23: Fit results for the two SSRs performed at $[H, K] = [0.5, -1]$ and $[H, K] = [1, -1.5]$. μ, and σ are the Bragg peak positions and standard deviations in L. The different peaks were indexed using a distorted cubic structure, corresponding to bulk Pt_3O_4, d are the corresponding interplanar spacings.

terson 1939; Warren 1990). This yields a thickness of ≈16.3 Å, which for bulk Pt_3O_4 would correspond to approximately 3 unit cells.

4.3.2 Near ambient pressure ammonia oxidation cycle

The combination of high temperature, oxygen and ammonia define a very harsh environment, that can result in the oxidation of the screws responsible for the contact on the sample holder. Fig 4.25 (a) shows a map in which the heating system failed after the introduction of ammonia in the reactor, reaching reacting conditions. Nevertheless, half of the large reciprocal space in-plane maps could be measured, the red circled peaks corresponding to Pt_3O_4 are still visible, showing that Pt_3O_4 is not immediately removed during reacting condition. The two other peaks at [0.93, -0.5] and [0.5, -0.93] have disappeared, the related structure is not stable during the reaction.

After repair of the sample heater, the sample was cleaned by sputtering and annealing

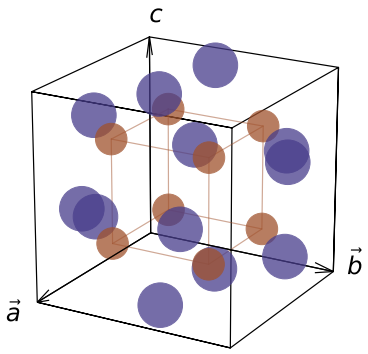

Figure 4.24: Pt_3O_4 bulk unit cell. Platinum atoms are situated on the faces on the cubic unit cell (e.g. $(0, 1/2, 1/4)$, $(0, 1/2, 3/4)$), while the eight oxygen atoms are inside the unit cell at the positions $(1/4, 1/4, z)$, $(1/4, 2/4, z)$, $(2/4, 1/4, z)$, $(2/4, 2/4, z)$ for $z = 1/4$ and $z = 3/4$.

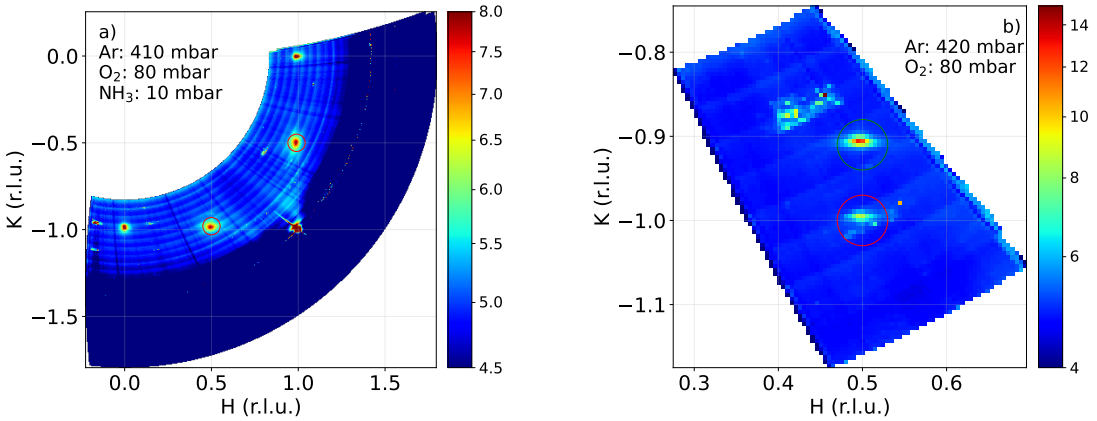

Figure 4.25: Reciprocal space in-plane maps collected under different atmospheres at 450 °C, computed using the surface lattice of Pt(100). The heater has failed during the reacting conditions (a), the sample was then cleaned and put again under oxygen atmosphere (b).

cycles, and replaced in the reactor. In order to probe for the reproducibility of the Pt_3O_4 growth on the surface, the partial pressure of oxygen was set to 80 mbar, while measuring a small area of the reciprocal space to detect the same peaks (fig. 4.21 - b). Such peaks could indeed be detected, but with a shift between the green and red groups of peaks equal to 0.09, more important than the previously measured value of 0.07. The second structure is possibly linked to the exposure to oxygen atmosphere, the smaller in-plane map was collected faster, and directly after the introduction of oxygen in the reactor.

Ammonia was subsequently introduced in the cell to probe the relation between surface structure and selectivity during ammonia oxidation.

Signals separated by 0.1 in H or in K were observed around the platinum Bragg peaks in a square arrangement, compatible with a Pt(100)-(10×10) surface reconstruction. Most of the peaks are observed at $H = 0, 1, 2$ or $K = 0, -1$ (fig. 4.26 - a). The other features are observed in rows or columns *shifted* by 0.09 with respect to the (1, $\bar{1}$, 0) Bragg peak, following the shift of the green circled peaks observed while only oxygen is present in the cell (fig. 4.25 - b).

SSRs at [H, K] = [1.9, 0], [H, K] = [0.5, $\bar{1}$], and [H, K] = [0, -1.2] are performed on the Pt(100)-(10×10) reconstructions (fig. 4.26 - b). The peaks measured earlier at [H, K] = [0.5, $\bar{1}$] at $L = 0.7$, $L = 1.4$, and $L = 2.1$ corresponding to bulk Pt_3O_4 are no longer visible. For [H, K] = [1.9, 0], two peaks are visible near $L = 0.15$ and $L = 2.15$. The reconstructed signal effectively disappears near $L = 1.9$, but reappears with a strong intensity at $L = 2$, following the same decrease as a function of L as from $L = 0$. For [H, K] = [0, -1.2], large oscillations are visible with a minimum at $L = 1.2$, which could be the signature of a multi-layer structure (e.g. simulated Pt_3O_4 in fig. 2.42 - a). Large oscillations are also visible for [H, K] = [0.5, -1], with a minimum between $L = 1$ and $L = 1.7$, and local maxima at $L = 0.4$, and $L = 2.5$.

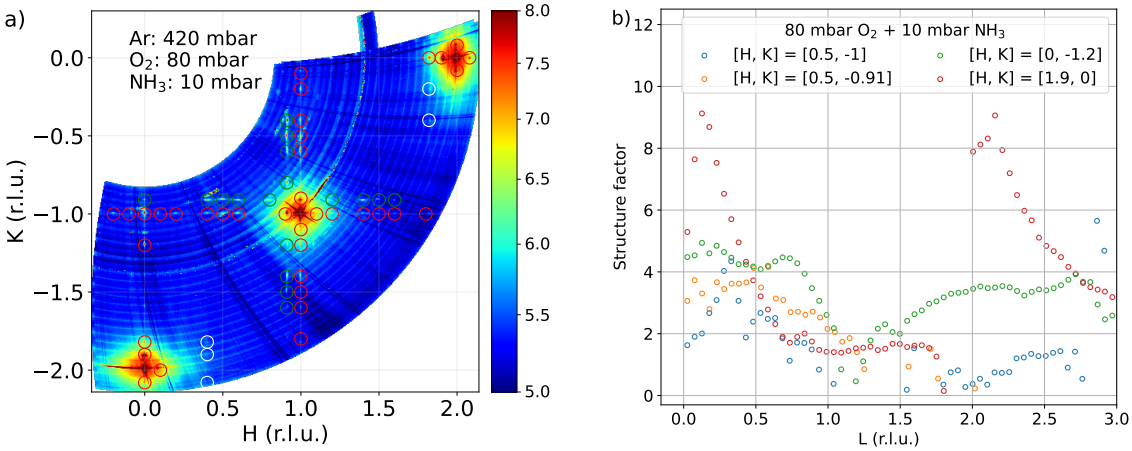

Figure 4.26: (a) Reciprocal space in-plane maps collected under different atmospheres at 450 °C, *computed using the surface lattice of Pt(100). (b) SSR for four different positions in [H, K] under* 80 mbar *of* O_2, 10 mbar *of* NH_3, *and* 410 mbar *of Ar.*

The SSR at [H, K] = [0.5, -0.91] (fig. 4.26 - b) is performed on the shifted Pt(100)-(10 × 10) reconstruction. The intensity decreases gradually with increasing L, characteristic of a monolayer, no signal can be detected above $L = 2$. Note that such an intensity decrease was also observed for the shifted peak at [H, K] = [0.5, -0.93] in the previous condition (fig. 4.23).

It is not certain that the same thickness of Pt_3O_4 was present on the catalyst surface at the beginning of the reacting conditions. Indeed, the sample was exposed to 80 mbar of oxygen for 6 h before SSRs could be measured. The second exposition only lasted for 1 h, during which the same in-plane peaks could effectively be measured, but without out-of-plane information. The thickness of Pt_3O_4 is very likely to be related to the time spent under 80 mbar of O_2. However, it is clear that i) new signals appear during reacting conditions, related to structures that themselves differ depending on the thickness of Pt_3O_4, and ii) the bulk oxide cannot grow under reacting conditions. Therefore, different types of structures coexist on the Pt(100) surface when the O_2/NH_3 ratio is equal to 8, possibly linked to different adsorbed species participating in the catalytic reaction.

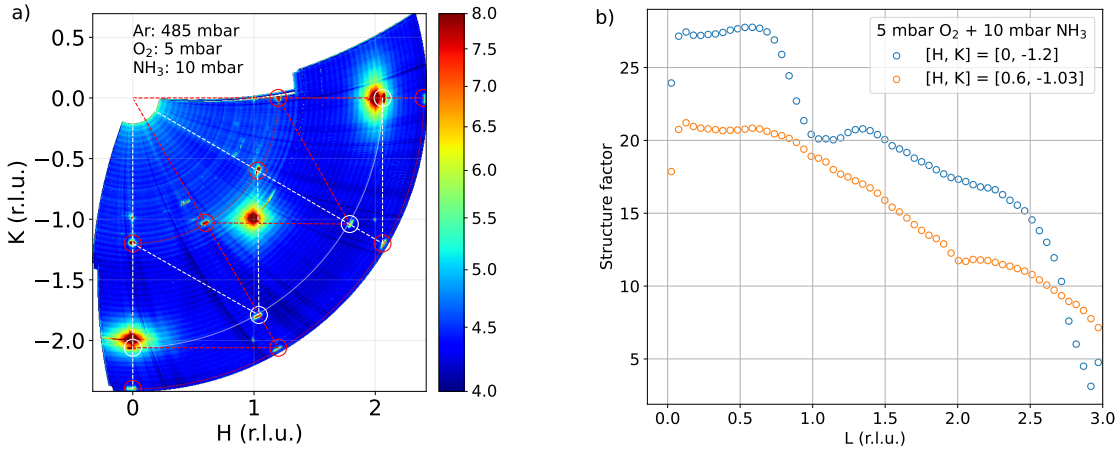

Figure 4.27: (a) Reciprocal space in-plane maps collected under different atmospheres at 450 °C, *computed using the surface lattice of Pt(100). (b) SSRs under* 5 mbar *of* O_2, 10 mbar *of* NH_3, *and* 485 mbar *of Ar.*

Lowering the partial pressure of oxygen from 80 mbar to 5 mbar in the reactor has completely removed the Pt(100)-(10 × 10) reconstruction (fig. 4.27 - a).

Co-existing domains with the same hexagonal lattice on top on the Pt(100) surface are revealed, with an in-plane lattice parameter equal to 2.68 Å, ≈3.36 % lower than the distance between neighbouring Pt atoms on the Pt(100) surface (2.77 Å). Second order peaks can also be seen at the borders of the reciprocal space in-plane map, each domain has one axis parallel to either $\vec{a}_{(100)}$ or $\vec{b}_{(100)}$. The hexagonal reconstructions can be described as follows: Pt(100)-p$\begin{pmatrix} 0.96 & 0.00 \\ -0.48 & 0.83 \end{pmatrix}$. For simplicity, this structure will be named Pt(100)-Hex in the rest of this thesis.

Different hexagonal reconstructions on the Pt(100) surface have been reported in literature, in the same directions, and under ultra-high vacuum. This has been summarised by Hammer et al. (2016), based on an important body of work (Heilmann et al. 1979; Van Hove et al. 1981; Heinz et al. 1982; Mase et al. 1992; Kuhnke et al. 1992; Borg et al. 1994; Van Beurden et al. 2004; Havu et al. 2010). Hexagonal reconstructions have been measured to evolve to rotated hexagonal reconstructions with angles between 0.77° and 0.94° depending on the sample temperature, and the previous temperature treatment. The unit cell describing those reconstructions with respect to the Pt(100) surface varies, if first contained to (5XN) where N = 20–30, the latest study reports a c(26x118) superstructure. Exposition to oxygen at 450 °C studied by low energy electron diffraction (LEED) removes the hexagonal reconstructions, and precipitate the growth of surface oxides *via* different phases (Bradley Shumbera et al. 2007b; Bradley Shumbera et al. 2007a). A similar conclusion was reached by Deskins et al. 2005 by DFT studies. Exposition to NO has been reported to stabilise the clean Pt(100) phase (Heinz et al. 1982), while exposition to CO removes the hexagonal reconstruction. An oscillatory behaviour between a clean Pt(100)-(1x1) surface and the rotated hexagonal reconstruction was reported by Cox et al. (1983) during CO oxidation.

Subsurface oxygen has also been predicted to exist on Pt(100) (Gu et al. 2007), reported at a pressure of 0.133 mbar (McMillan et al. 2005), and participating in the catalytic oxidation of CO. It was identified as a precursor to a stable surface oxide during the catalytic oxidation of CO by Dicke et al. (2000), at an oxygen pressure of 0.09 mbar. The appearance of subsurface oxygen was linked to the lifting of surface reconstructions on the clean Pt(100) surface from the adsorption of CO, which then allowed oxygen atoms to penetrate under the topmost layer of platinum (Rotermund et al. 1993; Lauterbach et al. 1994).

Overall, few works at ambient pressure have been found to exist, even less during the catalytic oxidation of ammonia. SSRs were collected at the position of the two peaks (fig. 4.27 - b), no bulk structure could be detected. A different behaviour is measured when lowering the O_2/NH_3 ratio from 8 to 0.5, which also has an impact on the product selectivity. The partial pressure of NO and N_2O decreases quickly after the change of condition (fig. B.9), whereas the partial pressure of N_2 is more stable.

After removing oxygen from the reactor, only the first order reflections corresponding to the hexagonal reconstruction could be detected during the measurement of the reciprocal space in-plane map (fig. 4.28 - a), the following measurement under Argon showed a clean Pt(100) surface (fig. 4.28 - b).

4.3.3 Oxide growth under 5 mbar of oxygen

To make sure that the hexagonal reconstruction are related to the reaction conditions, and not only to a lower pressure of oxygen in the reactor, a partial pressure of 5 mbar of oxygen was set. The following measurement showed the presence of many peaks that appeared in the first hour of the measurement (fig. 4.29 - a). A second map was measured directly after the end of the first map, in which none of the newly detected peaks could be observed (fig. 4.29 - b).

These two measurements showed first that the hexagonal reconstructions observed under reacting conditions when the O_2/NH_3 ratio is equal to 0.5 are linked to the *simultaneous*

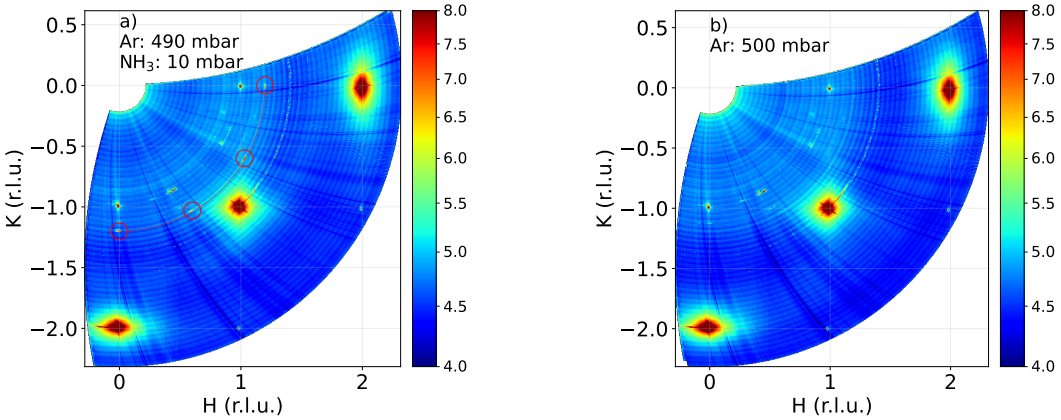

Figure 4.28: Reciprocal space in-plane maps collected under different atmospheres at 450 °C, computed using the surface lattice of Pt(100).

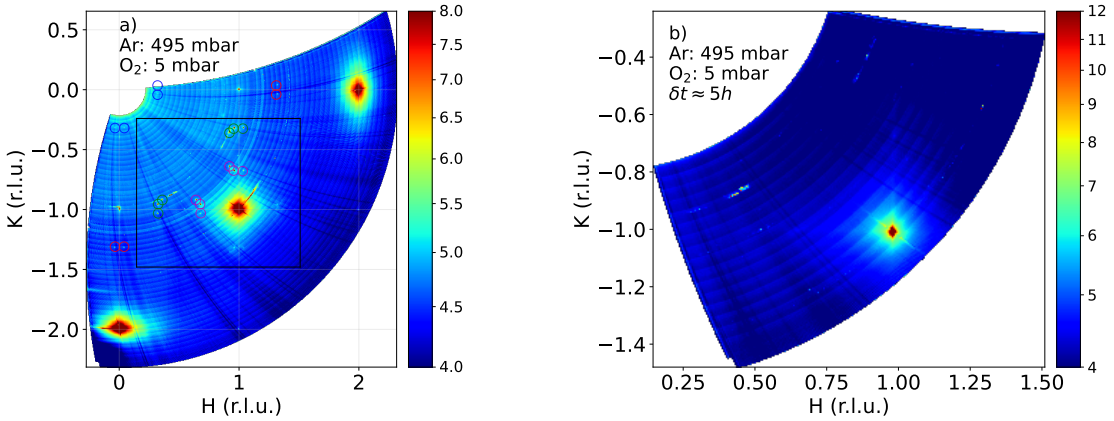

Figure 4.29: Reciprocal space in-plane maps collected under different atmospheres at 450 °C, computed using the surface lattice of Pt(100). The area covered in (b) is drawn by a black rectangle in (a).

presence of ammonia and oxygen in the reactor. Secondly, the dynamics of some of the observed phenomena under 5 mbar of oxygen are too short to be effectively measured with the current time-resolution of in-plane reciprocal space maps. Weak signals in the H and K directions can be seen in the second map, starting from the (1, $\bar{1}$, 0) Bragg peak (fig. 4.29 - b).

4.3.4 Surface roughness and surface relaxation effects

The (20L), (1$\bar{1}L$) and (0$\bar{1}L$) crystal truncation rods have been measured 6 h after the start of each condition, each measurement lasted for 2 h. The background-subtracted intensity of the CTR was integrated using the *fitaid* module of *BINoculars* as a function of L with the same integration range. The CTR intensity is displayed in fig. 4.30, additional peaks are detected under exposition to 80 mbar of O_2, confirming that bulk Pt_3O_4 is epitaxied on the Pt(100) surface following a Pt(100)-(2×2) arrangement.

Those peaks prevent us from resolving the minimal position of the CTR intensity, highly sensitive to surface relaxation effects. The absence of oscillations in the evolution of the CTR intensity as a function of L also shows that Pt_3O_4 is not homogeneously covering the Pt(100) substrate (such signal is presented in fig. 2.42 - b). This phenomena is here explained by Pt_3O_4 islands of different thickness covering the substrate, the fringes linked to islands of same thickness being smeared out from the contribution of others.

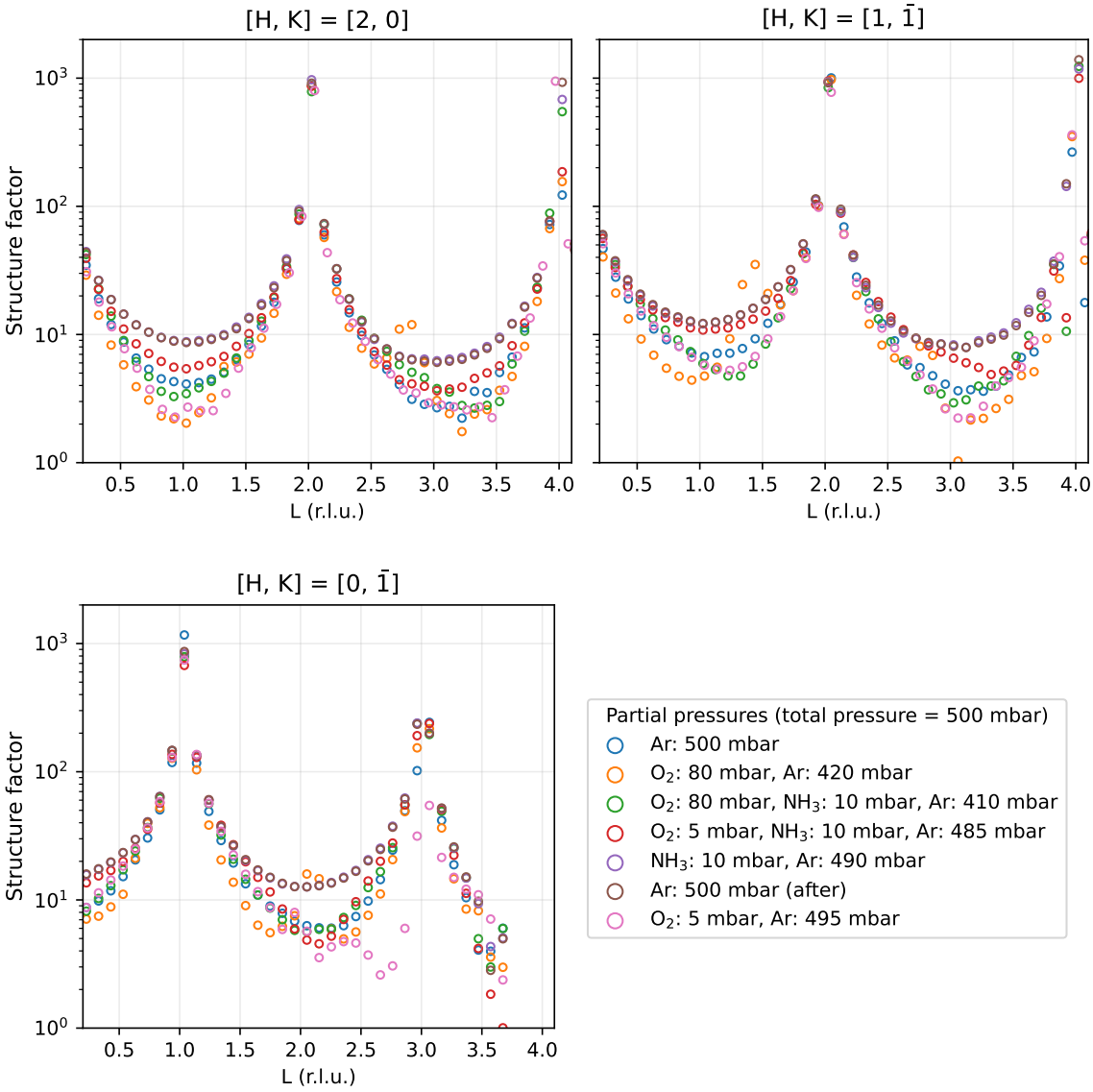

Figure 4.30: Evolution of crystal truncation rods under different atmospheres.

The catalyst surface can be divided in three different components as a function of $\vec{z}$. First, bulk Pt(100). Secondly, the interface between bulk platinum and the different islands of Pt_3O_4, in which the platinum atoms are expected to be displaced from their equilibrium positions due to the interaction with the oxide layer. Thirdly, the Pt_3O_4 islands, on top of the previous layers, with different thickness. A first approach to approximate the catalyst surface is discussed below.

The structure factors F_i resulting from the presence of one to nine unit cells of Pt_3O_4 on the Pt(100) surface was simulated with *ROD*, the same interface with the substrate is used in each simulation. The fitting routine consists in minimising the square root difference between the CTR structure factors F_{obs}, and the square root of the squared simulated structure factors sum by adjusting the weight W_i of each signal in the total signal F_{calc} (eq. 4.1).

$$F_{calc} = \sqrt{\sum_{i=1}^{9} W_i F_i^2} \tag{4.1}$$

In this first hypothesis, the topmost Pt(100) layers were assumed to be strain free. Different β roughness parameters (explained in fig. 2.13) were used, the best fit is with $\beta = 0.6$.

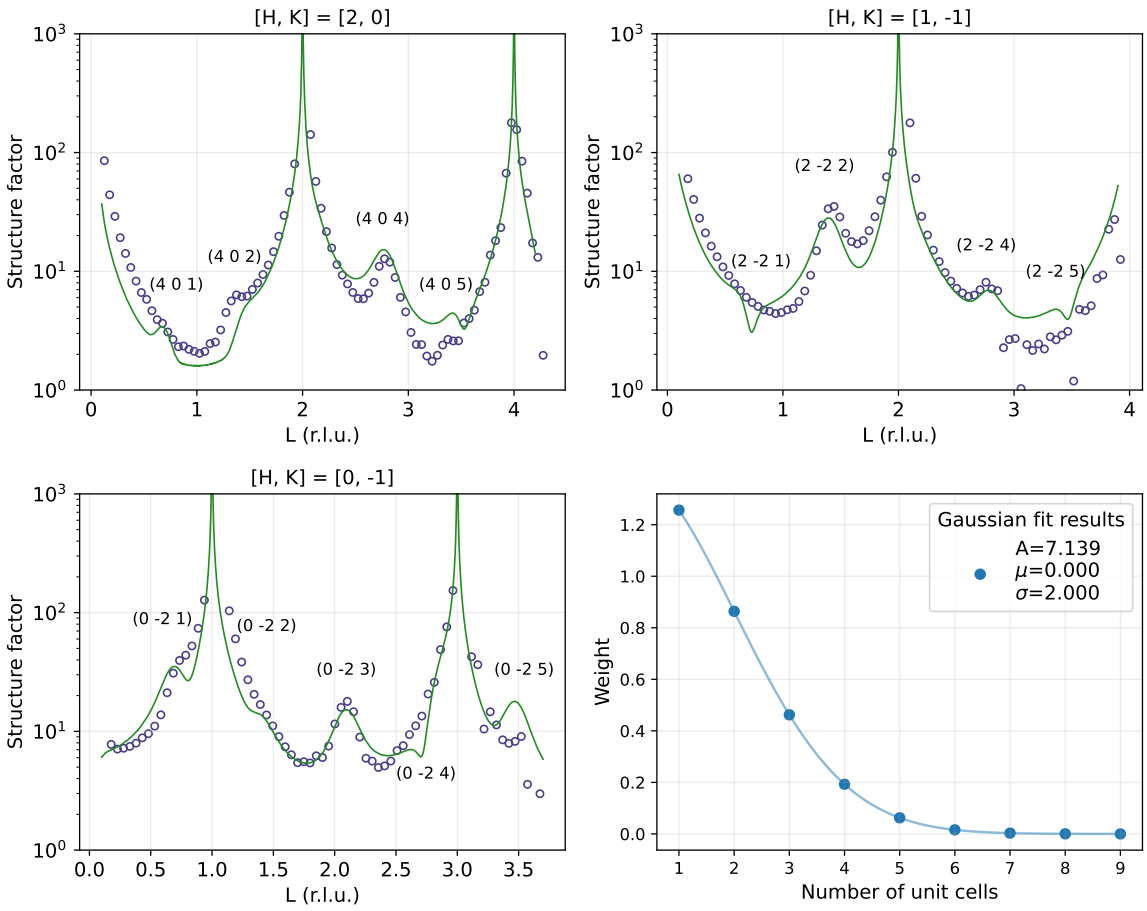

Figure 4.31: Fitting results for crystal truncation rods collected under a 80 mbar *of* O_2. Pt_3O_4 *Bragg peaks are indicated on the figure.*

The β roughness parameter only lowers the intensity of the bulk signal and not that of the surface layers. Moreover, it is assumed that Pt_3O_4 islands have the same out-of-plane and in-plane lattice parameter in each layer, independently of the island thickness. For example, the 7^{th} unit cell in a 8 unit cell thick island has the same lattice parameters than the second unit cell in a 4 unit cell thick island.

The relation between each weight was adjusted by following a Gaussian distribution, expecting the different islands to not differ too much in thickness. The result of the fitting routine is shown in fig. 4.31, with a Gaussian distribution centred around 0 unit cells, and with a standard deviation σ equal to 2 unit cells. The presence and width of the Pt_3O_4 peaks is well adjusted, see for example the presence of the (405) Pt_3O_4 Bragg peak in the [2, 0, L] CTR. The intensity shape near the platinum Bragg peak is also quite accurate, but tends to fall too quickly. This can be adjusted by lowering the β roughness, but low intensity regions then become impossible to represent. Indeed, the simulation struggles to accurately reproduce the intensity when below a certain threshold. The position of some peaks is very well reproduced, but some peaks are a little shifted, such as the (402) and $(2\bar{2}2)$ Pt_3O_4 Bragg peaks in the [2, 0, L], and [1, $\bar{1}$, L] CTRs. The ratio of intensity between the Pt_3O_4 peaks is also not perfect, and could possibly be further adjusted by changing the type of atoms present at the interface, as well as the distance between the oxide and surface. The positions of the Pt atoms at the interface are explained by a sketch in fig. 4.32.

The distance between the Pt atoms in the Pt(100) bulk and Pt_3O_4 was chosen equal to 0.5 unit cell lattice length, following the spacing between Pt atoms in {100} planes. The fitting result may be further improved by adjusting this parameter, as well as the interfacial

strain. Overall, the existence of bulk Pt_3O_4 islands is confirmed to remove the oscillations visible when a homogeneous layer is present of the sample surface (fig. 2.42). Moreover, the average thickness retrieved by fitting the SSRs in fig. 4.22, ≈16.3 Å, *i.e.* 3 unit cells, is in good agreement with the mean value and standard deviation of the Gaussian distribution returned here.

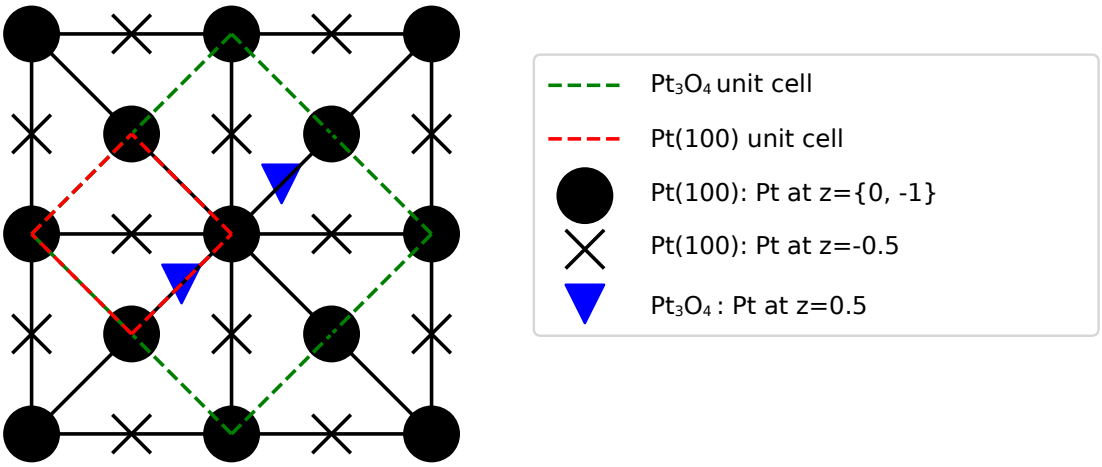

Figure 4.32: Epitaxy relationship used when simulating structure factors for Pt_3O_4 on Pt(100) in a Pt(100)-(2×2) arrangement.

When observing the CTR intensity under other atmospheres, a clear evolution in the position of the minimum intensity between both reacting conditions (in red and green in fig. 4.30) is visible. The CTR recorded after exposition to reacting conditions under ammonia or under argon have similar intensities and are almost indistinguishable.

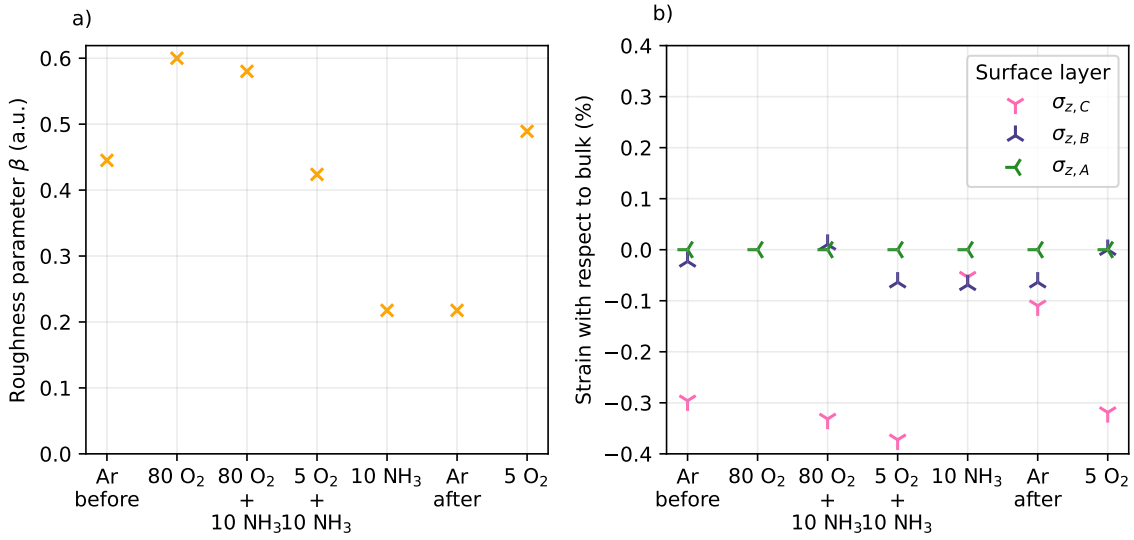

Figure 4.33: Fitting results for roughness parameter β (a) and out-of-plane strain σ_z (b) as a function of the experimental conditions. The innermost layer is named A, which has the same lattice parameter as in the bulk. The second and first topmost layers of the Pt(100) single crystal are respectively named B and C.

All three CTRs were fitted together using *ROD*, at each condition besides the oxygen rich atmosphere. Different models were tested, adding the possibility of in-plane lattice

displacement did not show any improvement of the fit quality, and a simple surface model was kept consisting of two Pt(100) layers, each sharing an out-of-plane lattice displacement parameter, on top of bulk Pt(100). The evolution of the surface roughness and out-of-plane strain is shown in fig. 4.33, the C layer is the topmost layer, the A layer is in the bulk.

The surface roughness evaluated *via* the β parameter in fig. 4.33 (a) is consistent with the evolution of the CTR intensity in fig. 4.30. The initial value for the surface roughness is equal to 0.44 when exposed to a total pressure of argon equal to 500 mbar. The average roughness after introducing a partial pressure of 80 mbar of oxygen was estimated to increase to 0.6, coherent with the creation of a bulk oxide layer on the sample surface. The minimal intensity can be seen to decrease after introduction of oxygen, see for example at $L = 1$ for the [$\bar{1}$, $\bar{1}$, L] CTR in fig. 4.30.

The following crystal truncation rods having been measured after the second introduction of ammonia in the cell, *i.e.* after sample cleaning and short exposition to high oxygen atmosphere. The roughness under reacting conditions, when observing the Pt(100)-(10×10) reconstructions (fig. 4.26), decreases only slightly in comparison to having only oxygen in the cell, and is still more important than under inert atmosphere. Lowering the amount of oxygen in the cell decreases the surface roughness, coming back to the initial value. In this condition, the hexagonal reconstructions are observed (fig. 4.27).

The lowest roughness value is reached when only ammonia is present in the reactor, without oxygen. The hexagonal reconstructions slowly disappear (fig. 4.28), their presence linked to increased roughness on the sample surface. Removing ammonia does not change the surface roughness, which shows that oxygen plays a key role in the increased surface roughness.

Finally, the presence of 5 mbar of oxygen after the ammonia oxidation cycle increases the surface roughness to higher values, almost equal to the maximum value reached under the presence of 80 mbar of oxygen. Bulk Pt_3O_4 was not observed in this condition, small peaks were visible linked to transient structures (fig. 4.29).

The strain of the second topmost layer, (B in fig. 4.33 - b) is always very close to 0 %. The strain of the topmost layer (C in fig. 4.33 - b) is always compressive with respect to bulk parameters, and seen to increase during reacting conditions in comparison with the initial values under argon atmosphere. A slight increase is reported when changing the O_2/NH_3 ratio from 8 to 0.5. Keeping only ammonia in the reactor after the oxidation reaction brings the lowest strain observed, both layers almost exhibit the bulk lattice parameters.

The presence of ammonia can be associated with reduced roughness and strain, whereas the presence of oxygen is associated with increased roughness and strain. Different reacting conditions, which can be linked to a different selectivity in the product, show a larger difference in the surface roughness than in the surface strain. For example, when observing the [2, 0, L] CTR in fig. 4.33, the local minima positions do not show a significant change. However, the change in intensity indicates different surface roughness. The shape of the [0, $\bar{1}$, L] CTR when the O_2/NH_3 ratio is equal to 0.5 is interesting (fig. 4.30). The intensity minimum at $L = 2.1$ is very low, whereas the decrease of intensity around the Bragg peaks is not very strong, in comparison with the same CTR but when the O_2/NH_3 ratio is equal to 8. It is possible that low intensity peaks are present near $L = 1.8$ or $L = 2.5$ that would explain this shape, linked to the hexagonal reconstructions observed in fig. 4.27.

4.3.5 Surface species

As for the Pt(111), the Pt(100) crystal was measured with NAP-XPS at B07 beamline. The conditions have been resumed in tab. 4.2. The RGA signals are presented in fig. 4.34.

The high O_2/NH_3 ratio favours the production of NO as expected, accompanied by water. With the gas probe near the sample surface, it is possible to detect a different selectivity

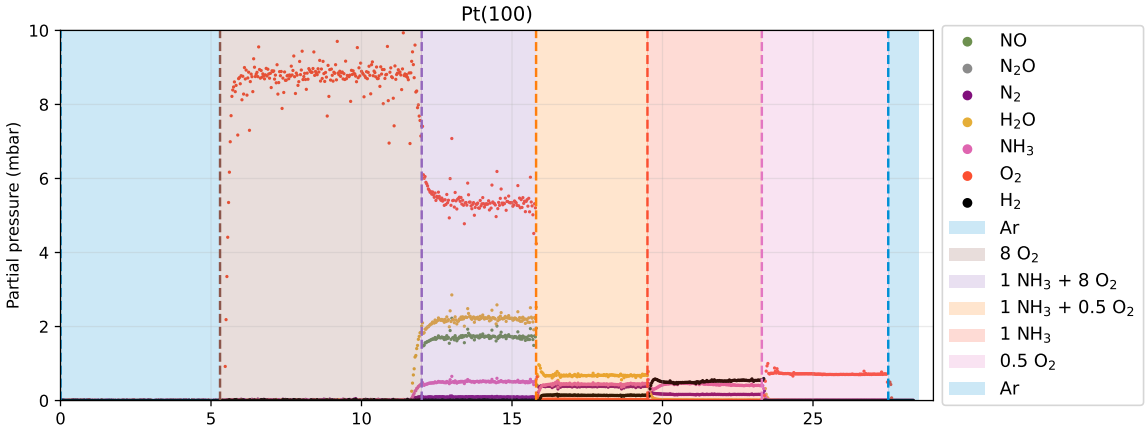

Figure 4.34: Evolution of reaction product partial pressures as a function of time during the XPS experiment on the Pt(100) single crystals at 450 °C. Transition between conditions are indicated with dashed vertical lines.

between the two surfaces: for the high oxygen condition Pt(100) produces mostly NO, whereas N_2 was still detected for Pt(111) (fig. 4.17).

Lowering the amount of oxygen by reducing the O_2/NH_3 ratio to 0.5 has the remarkable effect of shifting the reaction selectivity entirely towards N_2, just like for the Pt(111) surface. Oxygen being undetected by the mass spectrometer, all of the available oxygen at the surface dissociates on the catalyst surface and participates in the production of N_2 and H_2O *via* the oxidation reaction. H_2 coming from the simultaneous dissociation of NH_3 can also be measured, not observed under a higher pressure of oxygen. Thus, the more oxygen is present in the reactor, the less the dissociation of NH_3 is favoured. Ammonia can be considered to be in excess, and partly decomposing towards N_2.

Under pure ammonia there is still production of N_2, with an increase in H_2 production and essentially no H_2O yield.

N 1s and O 1s levels

The evolution of the N 1s and O 1s XPS spectra for different atmospheres is presented in fig. 4.35. Binding energy are given with reference to the Fermi level, all the reported peaks and corresponding species are detailed in tab. 4.5.

During the study of the Pt(100) oxidation by Derry et al. (1984), O 1s peaks between 530.4 eV and 530.5 eV are reported as a function of the oxygen surface coverage. Sugai et al (1993) report a low intensity peak at 531.5 eV during the dissociation of NO at 400 °C, which they cannot specifically assign to either NO_a or O_a. Different types of adsorbed oxygen species are observed during the dissociation of NO by Rienks et al. (2003) at 527.7 eV and 529.7 eV, the latter only shortly distant from NO_a reported at 529.8 eV. Kondratenko et al. (2006) report O_a and OH_a at 529.7 eV and 532 eV respectively during the decomposition of N_2O after exposition to H_2, based on previous works by Wild et al. (2000).

The Pt(100) surface was exposed to 8.8 mbar of oxygen after argon. The peaks at 538.3 eV and 537.2 eV can be attributed to $O_{2,g}$. As observed for Pt(111), the positions are shifted in energy with respect to literature (Avval et al. 2022). Oxide signals were measured after 1 h under 80 mbar of oxygen with SXRD (fig. 4.25), but no stable surface of bulk oxide was observed at an oxygen pressure of 5 mbar. Some transient peaks were measured but disappeared after a few hours of measurements (fig. 4.29). By comparing with the previously reported literature values, the large peak at 529.7 eV is attributed to adsorbed oxygen. It is possible that the oxygen atoms linked to the transient surface structure yield some intensity

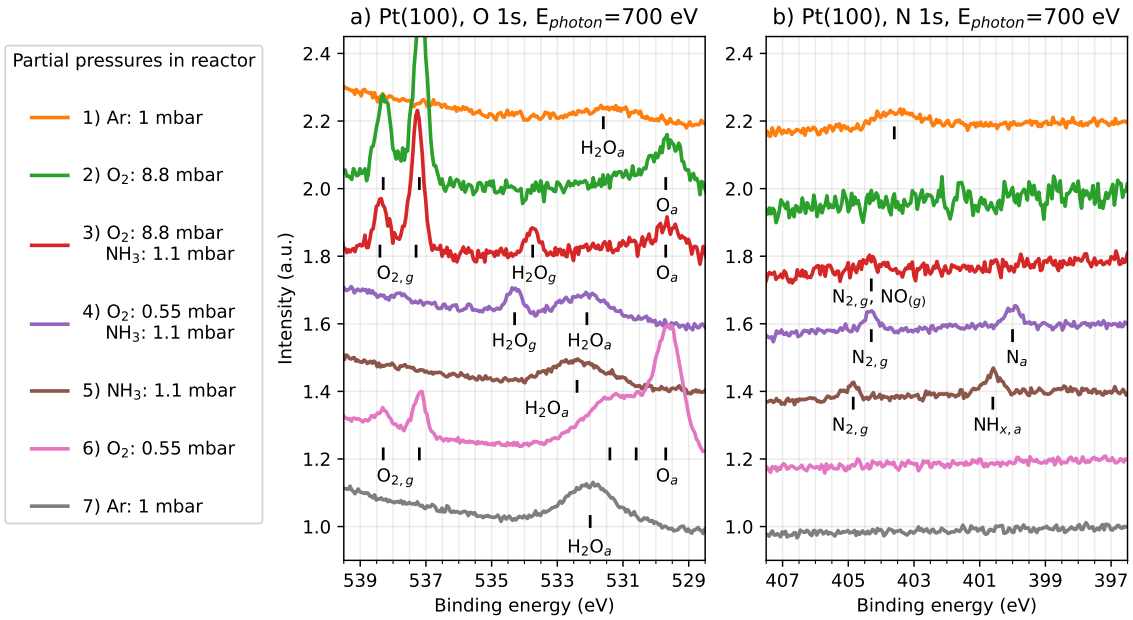

Figure 4.35: XPS spectra collected at the O 1s (a) and N1 s (b) levels under different atmospheres at 450 °C with an incoming photon energy of 700 eV. The spectra are normalised by the pre-edge intensity and shifted to highlight the presence of different peaks.

Partial pressures (mbar)	Ar	1	0	0	0	0	0	1
	NH_3	0	0	1.1	1.1	1.1	0	0
	O_2	0	8.8	8.8	0.55	0	0.55	0
Gas presence (decreasing pressure order)		Ar	O_2	O_2, H_2O, NO NH_3, N_2, N_2O	H_2O, NH_3 N_2, H_2	H_2, NH_3 N_2	O_2	Ar
N 1s: peak positions		403.6 eV	No peak	404.3 eV	404.3 eV 400.0 eV	404.9 eV 400.6 eV	No peak	No peak
Attributed surface species		Not assigned		$N_{2,g}$ & NO_g	$N_{2,g}$ N_a	$N_{2,g}$ $NH_{x,a}$		
O 1s: peak positions		531.6 eV	538.3 eV 537.2 eV 529.7 eV	538.4 eV 537.3 eV 533.7 eV 529.7 eV	534.3 eV 532.1 eV	532.4 eV	538.3 eV 537.2 eV 531.4 eV 530.6 eV 529.7 eV	532 eV
Attributed surface species		H_2O_a	$O_{2,g}$ $O_{2,g}$ O_a	$O_{2,g}$ $O_{2,g}$ H_2O_g O_a	H_2O_g H_2O_a	H_2O_a	$O_{2,g}$ $O_{2,g}$ O_a O_a O_a	H_2O_a

Table 4.5: Indexing of peaks measured during ammonia oxidation of the Pt(100) surface.

around 530.5 eV, where a small region of higher intensity is observed. No peak near 527.7 eV was observed throughout the experiment.

Adding ammonia in the cell brings us to reacting conditions with $O_2/NH_3 = 8$. Interestingly, this does not remove the O_a peak in the O 1s level, but introduces a gas phase water (H_2O_g) peak at 533.7 eV (Weststrate et al. 2006; Linford et al. 2019), probably generated by the oxidation reaction. The O_a peak has a lower intensity, which can be linked to the oxidation reaction utilising oxygen to produce water and nitric oxide. A 1 eV wide peak at 404.3 eV is reported in the N 1s level, linked to NO_g and possibly to $N_{2,\,g}$. NO_g is expected between 404.5 eV and 406.7 eV, while $N_{2,g}$ between 403.9 eV and 404.8 eV (Ivashenko et al. 2021), which could explain the broad peak shape. Since gas phase peaks are shifting when changing the partial pressure of oxygen, it is difficult to be certain of the peak nature. Most

importantly, the presence of the peak at 529.7 eV shows that oxygen is adsorbed on Pt(100), even during reacting conditions, which was not as clear for Pt(111) (fig. 4.18). Novell-Leruth et al. (2008) have reported that the de-hydrogenation process of ammonia is favoured to occur *via* O_a rather than OH_a on Pt(100) in comparison with Pt(111). No peak could be linked to OH_a, reported at 532 eV on Pt(100). It is possible that a second peak exist near 530.5 eV, linked also to adsorbed oxygen as reported by Derry et al. (1984), possibly on different sites. This differs from the Pt(111) surface for which both O_a and OH_a could be clearly identified, and with similar intensity. This difference in chemisorbed oxygen presence could explain the Pt(100) surface higher selectivity towards the production of NO. All the NH_x species are probably quickly oxidised towards atomic nitrogen, which then reacts with a neighbouring oxygen to form NO_a. Adsorbed NO at 401.3 eV was not observed during the dissociation of NO on Pt(100) above room temperature by XPS (Rienks et al. 2003). NO desorbs too quickly from the catalyst surface to be here detected, as reported by Ivashenko et al. (2021).

Reducing the partial pressure of oxygen to obtain $O_2/NH_3 = 0.5$ induces a remarkable change in the O 1s spectrum, removing the O_a peak, introducing a H_2O_a peak at 532.1 eV, and shifting the H_2O_g peak by 0.6 eV. It is difficult to differ between OH_a and H_2O_a. OH_a is reported at 532.0 eV, but such a peak also exists under argon atmosphere, characteristic of water contamination in the reactor. A binding energy of 400.0 eV in the N 1s spectrum is linked to adsorbed atomic nitrogen on Pt(100) (Sugai et al. 1993; van den Broek et al. 1999). Since the only product of the ammonia oxidation is now nitrogen, the peak at 404.3 eV can safely be assigned to $N_{2,g}$, similar to reported values (Ivashenko et al. 2021). Ammonia being in excess in the surface vicinity, all of the oxygen is used during ammonia oxidation yielding H_2O, since NO or N_2O can not be detected. This can be explained by the lack of available atomic oxygen adsorbed on the surface to form NO_a, which is also the first step in the production of N_2O. H_2 is also produced from the dissociation of NH_3 on the catalyst. It seems that in this condition, the oxygen atoms are preferably used for the de-hydrogenation process rather than the formation of NO by reacting with adsorbed nitrogen. The recombination of two nitrogen atoms on the catalyst surface is probably energetically preferred to the reaction of adsorbed nitrogen with adsorbed oxygen at low O_2/NH_3 ratios. $NH_{3,g}$ reported between 400.4 eV and 400.7 eV (Ivashenko et al. 2021) was not clearly detected. Nevertheless, it is possible that it also gives a contribution to the peak at 400.0 eV.

The next condition is pure ammonia. Removing oxygen from the reactor removes the gas phase water peak from the O 1s level, adsorbed water is still present but shifted in energy, with the same peak shape, maybe from a lower presence of OH_a groups since no more oxygen is present. The dissociation of ammonia towards N_2 and H_2 is measured with the mass spectrometer. $N_{2,g}$ is measured, shifted by 0.6 eV. The peak at 400.6 eV can tentatively be linked to a superposition of gas phase ammonia and adsorbed $NH_{x,a}$ species. No N_a peak can be observed which supports a slow dissociation process of ammonia of the Pt(100) surface.

Removing ammonia and adding 0.55 mbar of oxygen in the reactor shows at least five peaks in the O 1s level. Both peaks at 538.3 eV and 537.2 eV are from gas phase oxygen. At least three different oxygen species are present on the catalyst. The peak at 529.7 eV exhibits a high intensity and low width, attributed to the presence of chemisorbed oxygen on Pt(100). At least two other peaks can be detected at higher energy, around 530.6 eV and 531.4 eV. If only one peak was present at 531.4 eV the intensity would drop between at 530.6 eV which is not the case here. OH_a reported at 532 eV (E. V. Kondratenko et al. 2006) is too far from the energies indexed here to be linked to the peak at 531.4 eV. Thus, various oxygen species, adsorbed on different sites (e.g. hollow, on-top, bridge) may be linked to the peaks at 530.6 eV, and 531.4 eV. The peak at 530.6 eV may also correspond to the transient structure measured with SXRD under 5 mbar of oxygen, also measured near 530.4 eV with XPS under 8.8 mbar of oxygen partial pressure. The oxygen specie at 529.7 eV is predominant compared

to the other species.

Pt 4f level

The Pt 4f level was also measured, presented in fig. 4.36. No bulk oxide could be detected during reacting conditions, or under the presence of 5 mbar of oxygen with SXRD. However, many different surface structures were identified under reacting conditions, changing as a function of the O_2/NH_3 ratio (fig. 4.26 - 4.27).

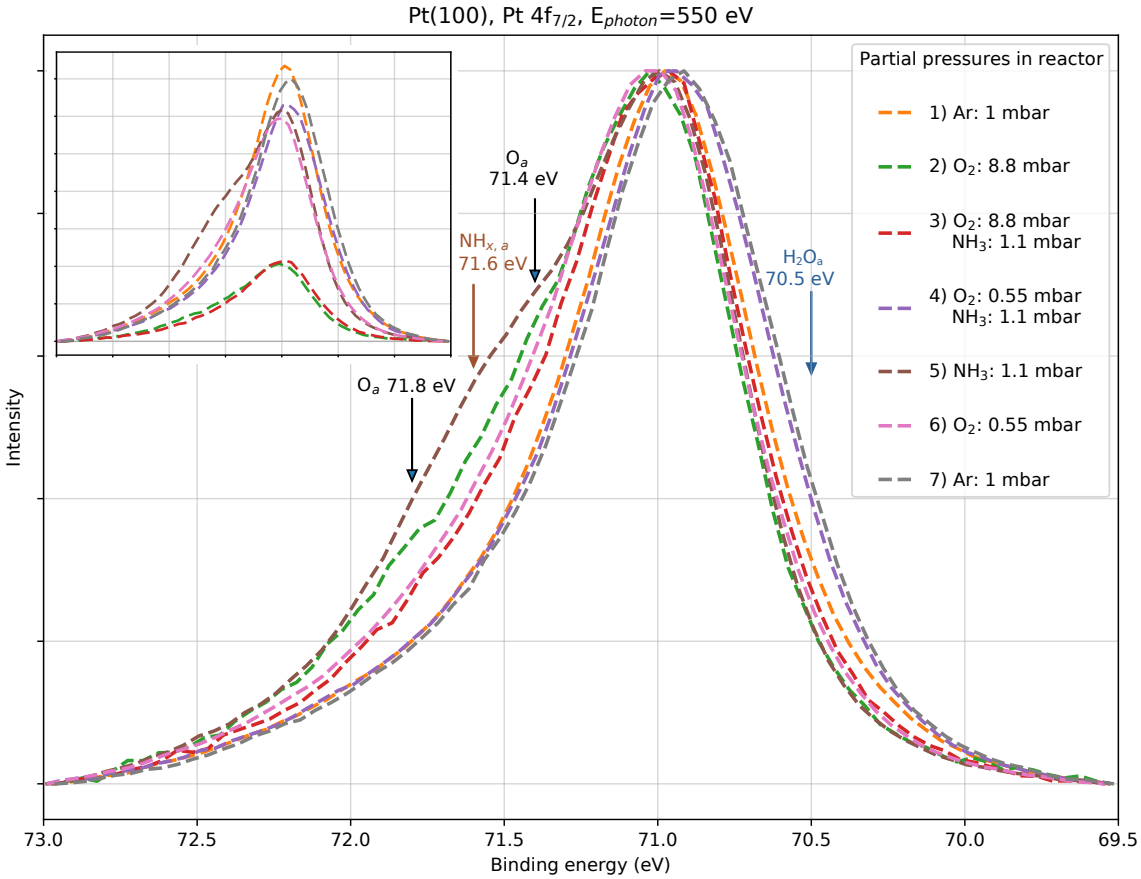

Figure 4.36: XPS spectra collected at the Pt 4f level under different atmospheres at 450 °C with an incoming photon energy of 550 eV. A Shirley-type background has been subtracted from all XPS spectra. Normalisation performed first by the background intensity and secondly by the maximum intensity to allow a qualitative comparison between different total pressures. Spectra before normalisation by maximum intensity are shown on the top left.

The introduction of 8.8 mbar of oxygen in the reactor induces a shift of 0.1 eV in the main peak position compared to pure argon atmosphere. Two new features can be detected, at 71.8 eV and 71.4 eV, linked to the presence of oxygen atoms on top of the catalyst surface. One new peak was clearly identified to appear in the O 1s level during this condition at 529.7 eV (fig. 4.35), attributed to chemisorbed oxygen based on reported literature values (Rienks et al. 2003; E. V. Kondratenko et al. 2006). One of the two peaks at 71.8 eV and 71.4 eV is probably from the same specie. The other may be linked to the moieties yielding peaks near 530.5 eV in the O 1s level.

The next condition is $O_2/NH_3 = 8$. The main peak is shifted towards lower binding energy, possibly from the appearance of a new peak linked to adsorbed water as discussed below. Both peaks identified under oxygen do not disappear but have a decreased intensity, similarly to what has been observed in the O 1s level, as a result of the participation of

oxygen species in the catalytic reaction.

Reducing the partial pressure of oxygen to 0.55 mbar so that $O_2/NH_3 = 0.5$ has the effect of removing the oxygen induced features at high binding energy. The peak region near 71.5 eV closely resembles that observed under argon atmosphere. The O_a peaks in the O 1s level also disappeared during this condition. Interestingly, the peak shape is broader and extended towards lower binding energy. Adsorbed water is detected in the O 1s level at this condition. H_2O_a could not be detected in the O 1s level when $O_2/NH_3 = 8$. However, it is not possible to rule out its presence due to the low intensity of the XPS spectrum. Thus, the shift towards lower energy in the Pt 4f level may be due to adsorbed water for both reacting conditions, more important when $O_2/NH_3 = 0.5$. The same reasoning can be applied to adsorbed nitrogen.

The following condition is pure ammonia atmosphere, the broadening effect at low binding energy is reverted. Removing oxygen from the reactor removed the N_a peak from the N 1s level, adsorbed water does not disappear. However, the related energy position in the O 1s level is slightly shifted, from 532.1 eV to 532.4 eV, which underlines different chemical environments. A new signal near 71.6 eV can safely be attributed to the presence of adsorbed $NH_{x,a}$ species, also identified in the N 1s level. The peak intensity with respect to the maximum intensity is the highest measured, translating a large coverage of the platinum surface by $NH_{x,a}$.

Changing the reactor atmosphere to 0.55 mbar of oxygen removes this $NH_{x,a}$ signal at 71.6 eV. Overall the peak shape is similar to that under 8.8 mbar of oxygen. The weaker intensity at higher binding energy is probably linked to a lower presence of the species measured under 8.8 mbar of oxygen.

Finally, reverting to argon atmosphere removed the peaks linked to O_a. However, the peak has not completely reverted to its shape before the oxidation cycle, and is very similar to the shape under a O_2/NH_3 ratio equal to 0.5. The adsorbed nitrogen is absent from the Pt surface, only adsorbed water is present at both conditions, which was also present before the oxidation cycle but in a lower amount. Therefore, adsorbed water is linked to the peak at lower binding energy, rather than N_a.

4.4 Discussion

In this chapter was presented the structural and chemical evolution of Pt(111) and Pt(100) single crystals during ammonia oxidation. The pre-oxidation of the platinum surfaces under 80 mbar of oxygen has allowed the identification of different surface structures and reconstructions. For Pt(111), a Pt(111)-(8×8) superstructure was measured (fig. 4.3 - d), preceded by two Pt(111)-(6×6)-R$\pm$8.8° superstructures (no visible second order peak, fig. 4.3 - c). Out-of-plane measurements have revealed a multi-layer thick structure (fig. 4.4), possibly corresponding to a α-PtO_2 surface oxide. The Pt(111)-(6×6)-R$\pm$8.8° structures have been linked to monolayers (fig. 4.4 - app. B.3). The complete understanding of the out-of-plane structures will be the subject of additional work. A precursor relation was hypothesised between the Pt(111)-(6×6)-R$\pm$8.8° and Pt(111)-(8×8) structures by time-resolved diffraction studies, under a lowered oxygen atmosphere (fig. 4.12). The importance of the partial pressure of oxygen in the growth kinetics has also been highlighted.

On Pt(100), a bulk Pt_3O_4 oxide was identified during exposure to 80 mbar of oxygen (fig. 4.21 - b, fig. 4.23), but not under 5 mbar (fig. 4.29), which shows the importance of the total pressure on the growth of Pt_3O_4. Pt_3O_4 follows a Pt(100)-(2×2) epitaxial relationship with the Pt(100) surface (fig. 4.32). A second family of peaks was measured under high oxygen pressure (fig. 4.21 - b), slightly shifted in H or K with respect to the Pt_3O_4 peaks measured at $L = 0$. The shift was determined to depend on the elapsed time under oxygen atmosphere, two values were measured, $\delta_{H,K} = 0.07$ and $\delta_{H,K} = 0.09$, respectively after 3 h (fig. 4.21 - b)

and 1 h (fig. 4.25 - b) of measurement. No clear unit cell could be associated to the shifted peaks, the related out-of-plane signal is compatible with the existence of a monolayer on the Pt(100) surface (fig. 4.22). Transient structures were observed at low oxygen pressure, which disappeared in the second measurement after 5 h of elapsed time (fig. 4.29).

The measurement of crystal truncation rods revealed more important intensity changes on the Pt(100) surface (fig. 4.30) in comparison with the Pt(111) surface during the oxidation cycle (fig. 4.14). For both surfaces (fig. 4.16 - a, 4.33 - a), the maximal roughness value is reached during exposition to high oxygen atmosphere, consistent with the formation of oxides under oxygen pressure. An important surface roughness can result in the formation of a large variety of surface sites, affecting the catalytic properties of the surface atoms due to the important change of local environments (Hendriksen et al. 2010; Calle-Vallejo, Martínez et al. 2014; Calle-Vallejo and Bandarenka 2018). Out-of-plane surface strain on Pt(111) was estimated to be contained on the topmost atomic layer, the presence of surface oxide structures was associated with compressive strain with respect to the initial values under argon atmosphere (fig. 4.16 - b). The influence of bulk Pt_3O_4 grown on Pt(100) under high oxygen atmosphere on the surface strain was not yet estimated, a lower oxygen atmosphere was related to compressive out-of-plane strain. Pt_3O_4 was shown to not grow in a homogeneous layer, but rather in terms of islands with different thickness (fig. 4.31).

The XPS experiment was conducted at similar oxygen to ammonia partial pressure ratio, but with a decreased total pressure. The highest oxygen pressure reached during the XPS experiment is 8.8 mbar, in the same order of magnitude as the low oxygen pressure condition for SXRD (5 mbar). Adsorbed oxygen was identified by XPS on both surfaces during this condition (fig. 4.18, 4.35), as well as under reduced oxygen pressure (0.55 mbar). The normalised intensity of the related peaks is approximately three times higher on the Pt(100) surface compared to the Pt(111) surface, which shows that the Pt(100) surface is more easily oxidised than the Pt(111) surface. The duration of the high oxygen condition of Pt(111) was not long enough to enable the growth of the Pt(111)-(8×8) structure if dynamics at 8.8 mbar can be translated to 5 mbar (23 h vs. 5 h). Therefore, only the Pt(111)-(6×6)-R$\pm$8.8° structure is expected to yield an additional peak in the O 1s and Pt 4f levels. A signal was effectively identified in the Pt 4f level at 71.6 eV, but with low intensity (fig. 4.19). Interestingly, two more peaks are identified in the O 1s level on Pt(100) at low oxygen pressure (0.55 mbar) in addition to the O_a signal, which could be linked to the transient structures measured with SXRD under 5 mbar of oxygen (fig. 4.29).

None of the aforementioned structures were measured under reacting conditions on Pt(111), for both O_2/NH_3 ratios (8 and 0.5, fig. 4.8 - a & b), which underlines that platinum oxides are not stable during the catalytic oxidation of ammonia on Pt(111) under those conditions. Adsorbed nitrogen species (N_a, NH_3) were observed in the Pt4f (fig. 4.19) and N 1s (fig. 4.18) levels, but without related surface reconstructions observable by SXRD on Pt(111) (fig. 4.8 - c). Only adsorbed water was measured during the oxidation of ammonia in the O 1s level.

In contrast with Pt(111), reacting conditions were found to be linked with the appearance of surface reconstructions on Pt(100), depending on the oxygen exposure time. After oxygen exposure for approximately 17 h, the introduction of ammonia was linked to the removal of the shifted peaks near Pt_3O_4 signals (fig. 4.25 - a). Both Pt_3O_4 and shifted signals could again be measured during a second exposure of the cleaned sample to oxygen for approximately 1 h (fig. 4.25 - b). The following introduction of ammonia was seen to induce signals compatible with Pt(100)-(10×10) surface reconstructions (fig. 4.26 - a). Some periodicity can be observed in the related out-of-plane signals at [H, K] = [0, -1.2] and [H, K] = [0.5, -1], high intensity peaks are observed at $L = 1$ and $L = 2$ for the measurement at [H, K] = [1.9, 0] (fig. 4.26 - b), which can link the Pt(100)-(10×10) surface reconstructions with the presence of multilayers. Additional in-plane signals are observed in fig. 4.26 (a), shifted by the same

amount $\delta_{H,K} = 0.09$ as the signals present under high oxygen atmosphere (fig. 4.25 - b). The intensity of this signal as a function of L was measured at [H, K] = [0.5, -0.91] (fig. 4.26 - b), decreasing with L, and thus showing no out-of-plane periodicity.

Lowering the O_2/NH_3 ratio to 0.5 has removed the Pt(100)-(10 × 10) surface reconstructions, and induced the appearance of a hexagonal Pt(100)-Hex reconstruction, with an out-of-plane signal consistent with that of monolayers (fig. 4.27). Removing oxygen from the reactor resulted in the progressive removal of the hexagonal reconstruction (fig. 4.28), clearly linked to the simultaneous presence of both reactants. Another key difference with Pt(111) is reported in the XPS spectra for Pt(100), with the visible presence of oxygen species in the O 1s level during reacting condition when the O_2/NH_3 ratio is equal to 8 (fig. 4.35), but not when this ratio is reduced to 0.5 by lowering the oxygen pressure. No adsorbed nitrogen specie was identified when the O_2/NH_3 ratio is equal to 8 in the N 1s level (fig. 4.35). Therefore, the Pt(100)-(10 × 10) surface reconstruction can be linked to the presence of a surface oxide on the Pt(100) surface, which is only permitted by the simultaneous presence of ammonia, *i.e.* linked to the reaction mechanism. Additionally, the selectivity towards NO in comparison with N_2 is three times more important than for Pt(111) (fig. 4.37), which highlights the importance of oxygen adsorbed on the catalyst surface to facilitate the production of NO.

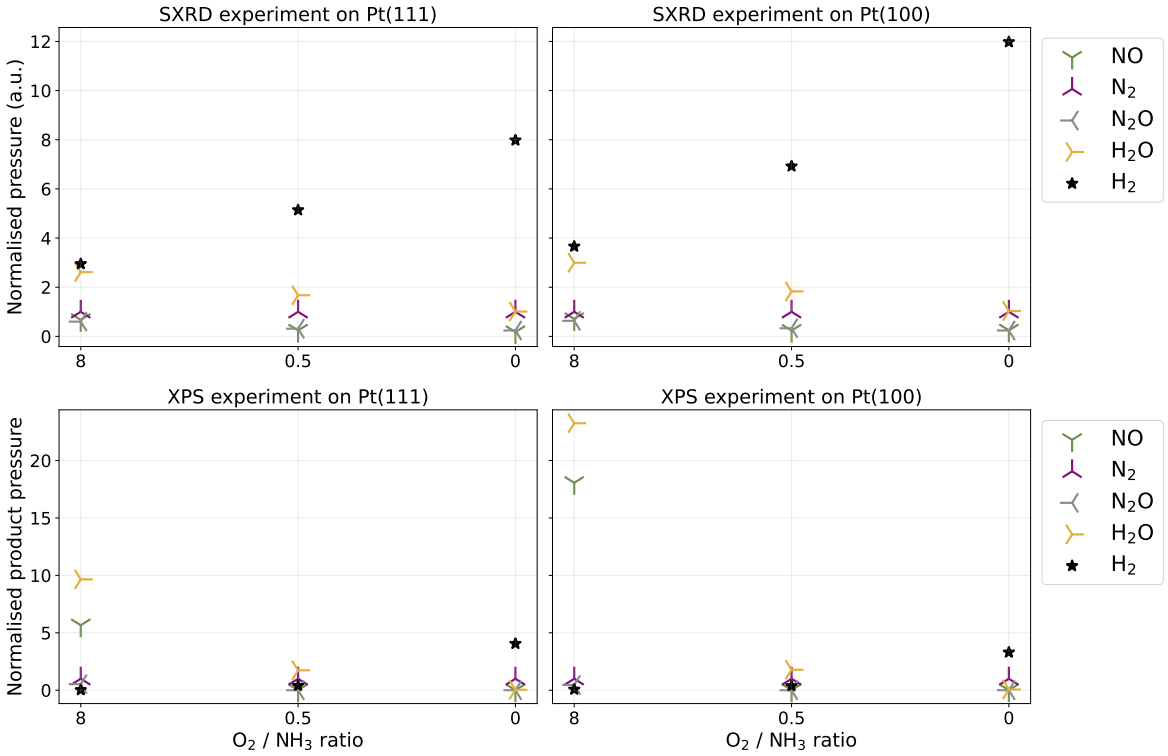

Figure 4.37: Evolution of reaction product partial pressures during the SXRD (top) and XPS (bottom) experiment on the Pt(111) and Pt(100) single crystals at 450 °C*. Mean partial pressures during* 1 min *at the end of each condition, recorded from a leak in the reactor output by a residual gas analyser (RGA). The partial pressures have been normalised by the partial pressure of nitrogen.*

This difference in selectivity is not observed during the SXRD experiments, this can be related to the position of the gas outlet far away from the sample (fig. 2.28), in contrast with the XPS experiment where the analyser nose is situated a few millimetres away from the sample surface (fig. 4.1 - c). The contribution of the sample edges (fig. 4.1 - b), as well as the presence of steps on the single crystal surface may lower the specific contribution of the sample facet (*i.e* (111) or (100)).

The persisting presence of oxygen on the Pt(100) surface can also be linked to different

evolution of the catalysts surface roughness. The roughness on the Pt(111) surface decreases during ammonia oxidation (fig. 4.16 - a), consistent with the removal of surface oxides following the introduction of ammonia. Indeed, low roughness is already achieved when the O_2/NH_3 ratio is equal to 0.5 (fig. 4.16 - a). For Pt(100), reacting conditions can also be associated to a decreasing roughness following pure oxygen atmosphere (fig. 4.33 - a). However, the minimal roughness is only reached once oxygen is completely removed from the reactor, *i.e.* after the oxidation cycle. The Pt(100)-(10×10) and Pt(100)-Hex reconstructions present on the Pt(100) surface during reacting conditions (fig. 4.26 - a, 4.27 - a), can be linked to the remaining high roughness, whereas Pt(111) exhibits a bulk terminated surface (fig. 4.8 - a & b).

A similar behaviour is observed for the out-of-plane lattice strain. The introduction of ammonia on Pt(111) was accompanied by a progressive reversal of the strain state, returning to the initial values measured under inert atmosphere when the O_2/NH_3 ratio is equal to 0.5 (fig. 4.16 - b). For Pt(100), both reacting conditions show a strain state similar to the initial state under inert atmosphere (fig. 4.33 - b). The difference in out-of-plane strain compared to $O_2/NH_3 = 8$ is in the same order of magnitude for both surfaces, but of different nature, $\approx$0.06 % tensile / compressive strain on Pt(100) / Pt(111). Overall, the strain measured in this experiment is more important on Pt(100) than Pt(111).

Stopping the oxidation reaction by removing oxygen has finally resulted in the removal of surface structure on the Pt(100) surface (fig. 4.28 - a). If the oxygen pressure is seen to decrease directly after the change of condition in the RGA signal (fig. B.9), the hexagonal reconstructions are still measured during the first hours of measurement. It is possible that this progressive removal of the hexagonal reconstructions is due to a slow transition between adsorbed nitrogen (N_a) measured during the reaction, and adsorbed de-hydrogenated species observed only in the absence of oxygen (fig. 4.35 & 4.36). The largest transition in terms of surface strain is also during this change of condition for Pt(100), as the topmost layer goes from important compressive strain to almost bulk atomic positions for the Pt atoms (fig. 4.33 - b, difference of $\approx$0.33 %). Atomic nitrogen is also observed in the N 1s level of Pt(111), but together with other nitrogen species (fig. 4.18 - 4.19), possibly impinging on its long-range ordering. No important change is measured in strain while removing oxygen on Pt(111) (fig. 4.16 - b), supporting the link between the Pt(111)-(8×8) surface structure, and changes in the out-of-plane strain.

The return to inert atmosphere after the oxidation cycle has shown that the final catalyst surface is more smooth from the roughness evolution (fig. 4.16 - b, 4.33 - b), without any adsorbed nitrogen or oxygen species (fig. 4.18, 4.35), and overall weaker strain values than during the reacting conditions. For both surfaces, the surface roughness and strain are lower than measured at first under argon, before the reaction cycle.

The different structures observed during this experiment are resumed in tab. 4.6. There is no apparent role of surface and bulk oxides on the Pt(111) surface, as the structures growing under high oxygen pressure have been removed directly during the reaction. Pt(111)-(8×8) and Pt(111)-(6×6)-R$\pm$8.8° cannot be linked to an increase or decrease of the catalytic activity, and thus do not seem to take part in the reaction mechanism.

Pt_3O_4, observed here in the Pt(100)-(2×2) arrangement, has proven to be a source of oxygen atoms sustaining the catalytic oxygenation of CO *via* a Mars Van Krevelen mechanism (Seriani, Pompe et al. 2006; Seriani and Mittendorfer 2008). In the current experiment, a second structure possibly related to Pt_3O_4 was measured. When under reacting conditions favouring NO, which is the desired product for the Ostwald process, the in-plane peaks related to both structures were still measured, but being part of a Pt(100)-(10×10) reconstruction. The presence of bulk Pt_3O_4 is clearly ruled out. Nevertheless, it is possible that the reconstruction is due to the interaction of surface Pt_3O_4 with ammonia, resulting in an increased selectivity towards NO. Reducing the oxygen to ammonia ratio is linked to the re-

O_2 (mbar)	NH_3 (mbar)	Pt(111)	Pt(100)
0	0	No oxide layer / no reconstruction	No oxide layer / no reconstruction
80	0	Two hexagonal rotated Pt(111)-(6×6)-R$\pm$8.8° superstructures (monolayer) After 9 h30 min: Pt(111)-(8×8) superstructure (multilayer)	Epitaxial Pt(100)-(2×2) structure (bulk Pt_3O_4), and signals shifted in H or K (monolayer)
80	10	No oxide layer / no reconstruction Weak signals in O 1s	Pt(100)-(10×10) reconstruction (multilayer) and signals shifted in H or K (monolayer) Higher NO selectivity, and High signal in O 1s in comparison with Pt(111)
10	10	No oxide layer / no reconstruction No signal in O 1s level N_a and $NH_{3,a}$ in N 1s	Pt(100)-Hex structure (monolayer) No signal in O 1s level Only N_a in N 1s
0	10	No oxide layer / no reconstruction	Progressive removal of Pt(001)-Hex structure
0	0	No oxide layer / no reconstruction	No oxide layer / no reconstruction
5	0	Back to the same structures as at 80 mbar of O_2, but with decreased kinetics	Transient structures, different from signals observed at 80 mbar of O_2

Table 4.6: Brief summary of surface structures identified with SXRD, and relevant changes in XPS or RGA signals.

construction removal, the stopping of NO production, as well as the removal of the adsorbed oxygen peak in the O 1s level.

The formation of RhO_2 was observed on a Pt-Rh(100) single crystal by Resta et al. (2020) at similar reactant partial pressures (total pressure of 300 mbar, 3.5 mbar of ammonia, and from 0 mbar to 20 mbar of oxygen). The rhodium surface oxide signal is only clearly measured when $O_2/NH_3 > 2$, and escalates when the temperature is increased from 175 °C to 375 °C. Both change of conditions are also linked to higher selectivity towards NO. The presence of this rhodium surface oxide is possibly impinging on the formation of Pt_3O_4 on Pt(100), observed in the current experiment, but at an oxygen partial pressure 4 times higher. This would explain the role of rhodium in stabilising the catalyst surface (Fierro et al. 1990; Fierro et al. 1992; Bergene et al. 1996), since platinum oxides have been reported to be more volatile at higher temperature (Alcock et al. 1960). Rh_2O_3 has been observed at elevated oxygen pressure on the same Pt-Rh(100) model crystal (Westerström et al. 2008). It is of key importance to increase the reactant partial pressure in future studies to be able to understand the role of platinum and rhodium oxides in the ammonia oxidation, facilitated now that in-plane signals have been detected. This can help in the comprehension of the mechanisms driving the selectivity towards NO.

Chapter 5

Conclusion

5.1 Research aim and results

This thesis was aimed at understanding, *operando*, the evolution of catalysts surfaces during ammonia oxidation. To do so, mainly three techniques have been used, Bragg coherent diffraction imaging, surface x-ray diffraction, and x-ray photoelectron spectroscopy, combined with mass spectrometry measurements. These techniques are compatible with near-ambient pressure conditions, allowing to reduce the pressure gap in heterogeneous catalysis. To bridge the material gap, large Pt nanoparticles and single crystals were used. Throughout this work, low O_2/NH_3 partial pressure ratios and temperatures were linked with selectivity towards N_2, whereas high O_2/NH_3 ratios and temperatures were linked to an increased selectivity towards NO and N_2O. This is consistent with the reaction selectivity reported for industrial catalysts, which supports the use of nanoparticles and single crystals as model catalysts to improve the system understanding.

Pt nanoparticles epitaxied on sapphire were first measured at 300 °C, 500 °C and 600 °C with SXRD during ammonia oxidation, starting with the introduction of ammonia in the reactor, and followed by a progressive increase of the oxygen pressure (O_2/NH_3 = {0, 0.5, 1, 2, 8}). The average shape of the Pt nanoparticles is mainly constituted of {111}, {110}, {100} and {113} facets. A progressive reshaping of the nanoparticles was revealed at 600 °C during reacting conditions. Once $O_2/NH_3 = 1$, and for increasing oxygen to ammonia ratios, the {110} and {113} facets surface coverage decreases, replaced by {111}, and {100} facets.

A single nanoparticle was then imaged with BCDI under inert atmosphere, at temperatures between 25 °C and 600 °C. A dislocation present at the interface from room temperature to 125 °C was successfully removed by flash annealing above 800 °C. This dislocation was shown to have an impact of the thermal relaxation of the particle. The {111} facets close to the interface evolve between {211}, {221} and {110} facets as a function of the sample temperature, and interfacial strain. The introduction of ammonia in the reactor at 600 °C resulted in a reversal of the facet strain, likely at the origin of the creation of an interfacial dislocation network, highlighting the link between facet and interfacial strain in nanoparticles.

Two additional nanoparticles were measured at 300 °C and 400 °C during ammonia oxidation. Different behaviours were revealed on the two nanoparticles, that exhibit a different size, shape, facet coverage, and initial strain state. The surface of the larger nanoparticle (particle *C*, 800 nm wide) is constituted by {111}, {110}, and {100} facets. Particle *C* showed a reversible decrease/increase of homogeneous strain when ammonia was introduced/removed from the reactor, and could not be reconstructed without it. A non-reversible increase in heterogeneous strain was measured at 300 °C when first exposing the sample to reacting condition ($O_2/NH_3 = 0.5$), no such increase was reproduced at the same conditions at 400 °C.

The increase of homogeneous strain linked to the presence/absence of ammonia was not reproduced on the second nanoparticle (particle *B*, 300 nm wide), and with {113} facets also

present on its surface. A non-reversible increase of heterogeneous strain was also measured at 300 °C, but induced by the presence of ammonia, without oxygen. The possibility of having an oxidised sample can explain this evolution under a reducing atmosphere, but is not observed for particle *C*. The appearance of a defect at 400 °C was linked to a non-reversible and important increase of homogeneous strain during the oxidation of ammonia, which further increased as a function of the O_2/NH_3 ratio. This structural evolution is clearly visible in 3D, with volumes of missing Bragg electronic density. The presence of defects could have a prominent role in the catalyst strain field and thus catalytic properties. A global activation of the catalyst at 300 °C and 400 °C was reported while the O_2/NH_3 ratio was kept equal to 2, with an increased production of NO, and in a lesser extent N_2O, at the detriment of N_2.

To better understand the role of each facet in the behaviour of the Pt nanoparticles, SXRD and XPS experiments were carried out at 450 °C on Pt(111) and Pt(100) single crystals. The samples were first exposed to high oxygen atmosphere (80 mbar) to oxidise the Pt surfaces (total pressure always kept to 500 mbar by the use of argon for SXRD). Two different oxygen to ammonia ratios are used after surface oxidation, by first introducing 10 mbar of ammonia ($O_2/NH_3 = 8$), and then reducing the oxygen pressure to 5 mbar ($O_2/NH_3 = 0.5$). The XPS experiment was performed with the same ammonia to oxygen ratios, but at lower partial pressures (approximately 10 % regarding the SXRD experiment).

The oxidation of both surfaces is first discussed. Bulk Pt_3O_4 was identified on Pt(100), in a Pt(100)-(2×2) arrangement of mean thickness equal to 16 Å (*i.e.* 3 unit cells thick). Signals shifted in reciprocal space in comparison to the Pt_3O_4 peaks are also measured. Both the Pt_3O_4 and shifted peaks were measured 1 h after the introduction of oxygen, but could not be detected under a reduced oxygen atmosphere (5 mbar), even after several hours. Transient signals are measured instead, underlying the importance of the oxygen pressure in the surface oxidation. Bulk Pt_3O_4 was not observed on Pt(111). Nevertheless, a Pt(111)-(8×8) commensurate superstructure was clearly identified after 9 h30 min of elapsed time under high oxygen atmosphere, and after 23 h30 min under reduced oxygen atmosphere. From the intensity distribution of the related out-of-plane signals, this structure was determined to be a few layers thick. Additional in-plane signals are also detected as soon as oxygen is introduced in the reactor, at both pressures, linked to a Pt(111)-(6×6)-R±8.8° structure. The intensity of those signals decreases once the Pt(111)-(8×8) structure is present, which supports a precursor link between both structures. Signals measured in the XPS O 1s level at reduced oxygen atmosphere and attributed to surface oxygen species are more important for Pt(100) than Pt(111), showing that Pt(100) surface is more readily oxidised than Pt(111). Oxidation of Pt(111) and Pt(100) was linked to increased surface roughness, and to compressive out-of-plane strain with respect to inert atmosphere for Pt(111).

Different behaviours were measured on both surfaces during reacting conditions. Under high O_2/NH_3 ratio, which favours the production of NO, surface oxides are directly removed from Pt(111), but reconstruct with a (10x10) arrangement on Pt(100). Oxygen species signals in the O 1s level are weak for Pt(111), difficult to dissociate from the background, whereas peaks are clearly detected for Pt(100). The difference in surface oxygen presence is already observed during previous surface oxidation. The reconstruction of the Pt(100) surface is linked to the persisting presence of surface oxygen species during ammonia oxidation, thereby differing from the Pt(111) surface. Moreover, the selectivity towards NO is increased for Pt(100), also linked to the more importance presence of surface oxygen, which is crucial in the production of NO during the reaction mechanism (Novell-Leruth, Valcárcel et al. 2005; Offermans, Jansen and van Santen 2006; Offermans, Jansen, Van Santen et al. 2007; Imbihl et al. 2007; Novell-Leruth, Ricart et al. 2008). Increased roughness is also observed during this condition for both surfaces.

Pt(111) and Pt(100) show a similar selectivity towards N_2 when lowering the O_2/NH_3 ratio to 0.5. The magnitude of the out-of-plane strain (surface relaxation), and the surface

roughness, are already reduced in this condition for Pt(111), but stay at similar values for Pt(100). On both surfaces, oxygen species are absent from the O 1s level, and adsorbed atomic nitrogen is measured, linked to the Pt(100)-Hex surface superstructure for Pt(100). Adsorbed ammonia is also observed on Pt(111).

The difference in out-of-plane strain (surface relaxation) when lowering the O_2/NH_3 ratio from 8 to 0.5 is in the same order of magnitude, but of different nature. ≈0.06 % tensile / compressive strain on Pt(100) / Pt(111). Most importantly, the strain is contained on the topmost layers of the platinum catalysts. If one considers a Pt(100) surface voxel 10 nm thick, the corresponding averaged voxel strain would be equal to 0.002 % with respect to the bulk lattice. Therefore, the change of strain between reacting conditions becomes difficult to resolve, which can explain why no differences are observed on particle *C* during ammonia oxidation. Another factor to take into account is the increased surface roughness linked to high oxygen pressure, which has the effect of decreasing the intensity of the scattered photons far from the Bragg peak, and will thus reduce the experimental resolution. Additional high-resolution studies could contribute to understanding the effect of adsorbates on surface relaxation.

The thesis demonstrates the importance of combining structural measurements at both the individual particle and particle assembly levels. With Bragg coherent diffraction imaging (BCDI), we have demonstrated that depending on the morphology (shape, size, facet type and coverage, *etc.*) and initial strain state of the Pt particles, different structural evolution are observed (in terms of strain, morphology, and defects) during the ammonia oxidation. A better representation of the different behaviours followed by Pt particles during reaction, by measuring multiple individual particles, appears mandatory for a comprehensive understanding of the structure-activity relationship. It is noteworthy that the strain at the particle/support interface seems to exert a pronounced influence on the particle behaviour. Nanoparticles serve as a platform to explore the simultaneous structural evolution of diverse crystallographic facets at once. Single crystal studies allow to better isolate the behaviours of single facets on nanoparticles.

5.2 Perspectives

This thesis has underlined the importance of bridging the material gap, by combining model catalysts with samples approaching the shape of industrial samples. The structure evolution of Pt nanoparticles was shown to strongly depend on their size, shape, facet coverage and initial strain state. The ammonia oxidation, which posses at least four different products, and a selectivity dependant on the reactant ratio, working temperature, and total pressure, draws a multi-dimensional parameter space only correctly addressed with information of different nature.

BCDI has proven to be powerful, but limited by the reconstruction process, as well as the time needed to find and image isolated nanoparticles. Significant progress has already been made at the European synchrotron at the ID01 beamline, where rocking curves can be acquired under a minute. *Operando* measurements have proven to be challenging, Pt nanoparticles moving on the substrate at 600 °C under reacting conditions, and sample environments failing during SXRD measurements. Closing the pressure gap can be achieved for SXRD and BCDI by designing reactors resistant to highly oxidising atmosphere, and in this case, compatible with the ammonia/nitrogen oxide gas family, often banned due to their corrosive and toxic nature. Future experiments must move towards industrial condition to be relevant, the importance of total pressure was demonstrated in this thesis with e.g. oxide formation on Pt(100) at 80 mbar and not at 5 mbar. Simpler reaction cycles (e.g. by reducing the amount of O_2/NH_3 ratios) will also help reduce the complexity of the data analysis. A future reaction cycle is proposed. First exposing the sample to increased oxygen pressure

will reduce the time needed to detect potentially relevant oxides, as showcased here with the detection time of the Pt(111)-(8×8) structure, divided by 2.5 under 80 mbar of oxygen compared to 5 mbar. A significant thickness of those platinum oxides could also be sufficient to be detected during BCDI experiments, especially now that the corresponding interplanar spacings are clearly determined. Their impact of the facet strain in BCDI could then be determined by reconstructing the 3D strain tensor. Higher oxygen pressure may reveal a role of platinum oxides during ammonia oxidation, invisible at lower pressure. This will also remove the unknown regarding initial oxidised/contaminated states when introducing ammonia, and set a more systematic starting point for chemical cycles. Ending the reaction cycle by having only ammonia in the reactor is also at the origin of large strain variations measured with SXRD, that could be more easily detected with BCDI. In the future, surface x-ray experiments on Pt(110) and Pt(113) samples will add to our knowledge, and help better understand the structural behaviour of Pt nanoparticles.

Nevertheless, experimentally resolving the role of interfacial strain *operando* could be performed by e.g. (i) exposing a nanoparticle that possesses an interfacial defect to reacting atmosphere, (ii) subsequently removing this defect by annealing, and (iii) repeating the exposition to reacting condition to observe a potential difference in the facet strain. However, a certain control of the initial particle strain is needed. The development of efficient simulation workflows to understand and de-correlate the effect of interfacial strain from adsorbant strain is also part of the solution. The development of x-ray techniques that can bring higher statistics in the study of individual nanoparticles must be pushed forward. In this perspective, x-ray Bragg ptychography is a technique that should receive increased interest since the measurement process can provide a unique solution.

The upgrade of synchrotrons is of key importance to efficiently navigate between different temperatures/pressures/reactant ratios. For SXRD and BCDI, a reduced counting time will help catch transient structures, while increased photon count will increase the possibility to detect weak second and third order signals. Moreover, BCDI gains from the increased coherent flux, while NAP-XPS also benefits from the increased photon flux. Reaction cycles could also be repeated to increase the results significance, while changing the steps order. Furthermore, a software upgrade is also needed, the surface x-ray diffraction community lacks an efficient and complete software combining data reduction and analysis. For BCDI, the development of *Gwaihir* was undertaken to respond to such needs from the community. Additional work may address the data reduction automatisation by developing error-metrics for phase retrieval, methods to find the best solution, automatic facet detection in Python, *etc.* This would largely reduce the data reduction time, facilitating the analysis of multiple particles at various conditions. A detailed study of the impact of trying to improve the image resolution by increasing the distance from the centre of the Bragg peak by combining simulations and experimental reconstructions would be of great interest to the community.

Bibliography

Abuin, M. et al. (2019). 'Coherent X-ray Imaging of CO-Adsorption-Induced Structural Changes in Pt Nanoparticles: Implications for Catalysis'. In: *ACS Applied Nano Materials* 2.8. DOI: 10.1021/acsanm.9b00764.

Ackermann, M. (2007). 'Operando SXRD: A New View on Catalysis'. PhD thesis.

Afif, A. et al. (2016). 'Ammonia-fed fuel cells: a comprehensive review'. In: *Renewable and Sustainable Energy Reviews* 60. DOI: doi.org/10.1016/j.rser.2016.01.120.

Agence Nationale de la Recherche (2023). *Dispositifs Intégrés pour l'Accélération du DEploiement de Matériaux Emergents*. URL: anr.fr/fr/france-2030/france2030/call/pepr-diadem-appel-a-projets-dispositifs-integres-pour-lacceleration-du-deploiement-de-materiaux/ (visited on 17/08/2023).

Ahmad, H. et al. (2015). 'Hydrogen from photo-catalytic water splitting process: A review'. In: *Renewable and Sustainable Energy Reviews* 43. DOI: doi.org/10.1016/j.rser.2014.10.101.

Ahrens, J. et al. (2001). 'Large-scale data visualization using parallel data streaming'. In: *IEEE Computer Graphics and Applications* 21.4. DOI: 10.1109/38.933522.

AirParif (2023). *État de la qualité de l'air à Paris*. URL: www.paris.fr/pages/etat-des-lieux-de-la-qualite-de-l-air-a-paris-7101 (visited on 09/02/2023).

Alcock, C. B. : G. W. : Hooper and R. S. Nyholm (1960). 'Thermodynamics of the gaseous oxides of the platinum-group metals'. In: *Proceedings of the Royal Society of London. Series A. Mathematical and Physical Sciences* 254.1279. DOI: 10.1098/rspa.1960.0040.

Alizada, S. and A. Khaleghi (2017). 'The Study of Big Data Tools Usages in Synchrotrons'. In: *Int. Conf. on Accelerator and Large Experimental Control Systems*. DOI: 10.18429/JACoW-ICALEPCS2017-THPHA034.

Altantzis, T. et al. (2019). 'Three-Dimensional Quantification of the Facet Evolution of Pt Nanoparticles in a Variable Gaseous Environment'. In: *Nano Letters* 19.1. DOI: 10.1021/acs.nanolett.8b04303.

An, K. and G. A. Somorjai (2012). 'Size and Shape Control of Metal Nanoparticles for Reaction Selectivity in Catalysis'. In: *ChemCatChem* 4.10. DOI: doi.org/10.1002/cctc.201200229.

Andrews, S. R. and R. A. Cowley (1985). 'Scattering of X-rays from crystal surfaces'. In: *Journal of Physics C: Solid State Physics* 18.35. DOI: 10.1088/0022-3719/18/35/008.

Anstine, D. M. and O. Isayev (2023). 'Machine Learning Interatomic Potentials and Long-Range Physics'. In: *The Journal of Physical Chemistry A* 127.11. DOI: 10.1021/acs.jpca.2c06778.

Aricò, A. S. et al. (2005). 'Nanostructured materials for advanced energy conversion and storage devices'. In: *Nature Materials* 4.5. DOI: 10.1038/nmat1368.

Ashcroft, N. W. and N. D. Mermin (1976). *Solid State Physics*. Saunders College Publishing.

Asscher, M. et al. (1984). 'A molecular beam surface scattering study of ammonia oxidation on the platinum(111) crystal face'. In: *The Journal of Physical Chemistry* 88.15. DOI: 10.1021/j150659a020.

Astruc, D., F. Lu and J. R. Aranzaes (2005). 'Nanoparticles as Recyclable Catalysts: The Frontier between Homogeneous and Heterogeneous Catalysis'. In: *Angewandte Chemie International Edition* 44.48. DOI: doi.org/10.1002/anie.200500766.

Astruc, D. (2020). 'Introduction: Nanoparticles in Catalysis'. In: *Chemical Reviews* 120.2. DOI: 10.1021/acs.chemrev.8b00696.

Atlan, C. et al. (2023). 'Imaging the strain evolution of a platinum nanoparticle under electrochemical control'. In: *Nature Materials* 22.6. DOI: 10.1038/s41563-023-01528-x.

Avval, T. G. et al. (2022). 'Oxygen gas, O_2(g), by near-ambient pressure XPS'. In: *Surface Science Spectra* 2. DOI: 10.1116/1.5100962.

Ayer, V. M., S. Miguez and B. H. Toby (2014). 'Why scientists should learn to program in Python'. In: *Powder Diffraction* 29.S2. DOI: 10.1017/S0885715614000931.

Baerns, M. et al. (2005). 'Bridging the pressure and material gap in the catalytic ammonia oxidation: Structural and catalytic properties of different platinum catalysts'. In: *Journal of Catalysis* 232.1. DOI: 10.1016/j.jcat.2005.03.002.

Baker, M. (2016). '1,500 scientists lift the lid on reproducibility'. In: *Nature* 533.454. DOI: doi.org/10.1038/533452a.

Barringer, Z. et al. (2021). 'Imaging defects in vanadium(iii) oxide nanocrystals using Bragg coherent diffractive imaging'. In: *CrystEngComm* 23 (36). DOI: 10.1039/D1CE00736J.

Basolo, S. et al. (2005). 'XPAD: pixel detector for material sciences'. In: *IEEE Transactions on Nuclear Science* 52.5. DOI: 10.1109/TNS.2005.856818.

Baxter, R. J. and P. Hu (2002). 'Insight into why the Langmuir–Hinshelwood mechanism is generally preferred'. In: *The Journal of Chemical Physics* 116.11. DOI: 10.1063/1.1458938.

Behnel, S. et al. (2011). 'Cython: The Best of Both Worlds'. In: *Computing in Science & Engineering* 13.2. DOI: 10.1109/MCSE.2010.118.

Bergene, E., O. Tronstad and A. Holmen (1996). 'Surface Areas of Pt–Rh Catalyst Gauzes Used for Ammonia Oxidation'. In: *Journal of Catalysis* 160.2. DOI: doi.org/10.1006/jcat.1996.0133.

Berger, M. et al. (2010). *NIST Standard Reference Database 8 (XGAM)*. DOI: dx.doi.org/10.18434/T48G6X. URL: www.nist.gov/pml/xcom-photon-cross-sections-database (visited on 15/06/2023).

Bewley, R. et al. (2006). 'MERLIN, a new high count rate spectrometer at ISIS'. In: *Physica B: Condensed Matter* 385-386. DOI: doi.org/10.1016/j.physb.2006.05.328.

Bikondoa, O. and D. Carbone (2021). 'On Compton scattering as a source of background in coherent diffraction imaging experiments'. In: *Journal of Synchrotron Radiation* 28.2. DOI: 10.1107/S1600577521000722.

Bilderback, D. H., P. Elleaume and E. Weckert (2005). 'Review of third and next generation synchrotron light sources'. In: *Journal of Physics B: Atomic, Molecular and Optical Physics* 38.9. DOI: 10.1088/0953-4075/38/9/022.

Björck, M. and G. Andersson (2007). '*GenX*: an extensible X-ray reflectivity refinement program utilizing differential evolution'. In: *Journal of Applied Crystallography* 40.6. DOI: 10.1107/S0021889807045086.

Björling, A. et al. (2019). 'Coherent Bragg imaging of 60 nm Au nanoparticles under electrochemical control at the NanoMAX beamline'. In: *Journal of Synchrotron Radiation* 26. DOI: 10.1107/S1600577519010385.

Boden, D., I. M. N. Groot and J. Meyer (2022). 'Elucidating the Initial Oxidation of Pt(111) Using Large-Scale Atomistic Thermodynamics: A ReaxFF Study'. In: *The Journal of Physical Chemistry C* 126.47. DOI: 10.1021/acs.jpcc.2c05769.

Bokeh Development Team (2018). *Bokeh: Python library for interactive visualization*. URL: bokeh.pydata.org/.

Borg, A., A. M. Hilmen and E. Bergene (1994). 'STM studies of clean, CO- and O_2-exposed Pt(100)-hex-R0.7°'. In: *Surface Science* 306.1-2. DOI: 10.1016/0039-6028(94)91179-7.

Borodin, D. et al. (2021). 'Kinetics of NH_3 Desorption and Diffusion on Pt: Implications for the Ostwald Process'. In: *Journal of the American Chemical Society* 143.43. DOI: 10.1021/jacs.1c09269.

Boudart, M. (1995). 'Turnover Rates in Heterogeneous Catalysis'. In: *Chemical Reviews* 95.3. DOI: 10.1021/cr00035a009.

Boukouvala, C., J. Daniel and E. Ringe (2021). 'Approaches to modelling the shape of nanocrystals'. In: *Nano Convergence* 8 (1). DOI: 10.1186/s40580-021-00275-6.

Boulle, A. and J. Kieffer (2019). 'High-performance Python for crystallographic computing'. In: *Journal of Applied Crystallography* 52. DOI: 10.1107/S1600576719008471.

Boyu, W. et al. (2016). 'Deep learning for analysing synchrotron data streams'. In: *IEEE*. DOI: 10.1109/NYSDS.2016.7747813.

Bradley, J. M., A. Hopkinson and D. A. King (1995). 'Control of a Biphasic Surface Reaction by Oxygen Coverage: The Catalytic Oxidation of Ammonia over Pt{100}'. In: *The Journal of Physical Chemistry* 99.46. DOI: 10.1021/j100046a032.

— (1997). 'A molecular beam study of ammonia adsorption on Pt100'. In: *Surface Science* 371.2. DOI: doi.org/10.1016/S0039-6028(96)01018-7.

Bradley Shumbera, R., H. H. Kan and J. F. Weaver (2007a). 'Oxidation of Pt(1 0 0)-hex-R0.7° by gas-phase oxygen atoms'. In: *Surface Science* 601.1. DOI: 10.1016/j.susc.2006.09.040.

— (2007b). 'The transition from surface to bulk oxide growth on Pt(1 0 0): Precursor-mediated kinetics'. In: *Surface Science* 601.21. DOI: 10.1016/j.susc.2007.07.027.

Bratan, V. et al. (2022). 'Insights into the Redox and Structural Properties of CoOx and MnOx: Fundamental Factors Affecting the Catalytic Performance in the Oxidation Process of VOCs'. In: *Catalysts* 12.10. DOI: 10.3390/catal12101134.

Bratlie, K. M. et al. (2007). 'Platinum Nanoparticle Shape Effects on Benzene Hydrogenation Selectivity'. In: *Nano Letters* 7.10. DOI: 10.1021/nl0716000.

Breddeld, M. (2021). *ipyvolume, 0.6.0*. URL: github.com/maartenbreddels/ipyvolume.

Brown, P. J. et al. (2006). *International Tables for Crystallography*. Vol. C. Chap. 6.1. DOI: 10.1107/97809553602060000600.

Cahn, J. W. (2004). 'Free Energy of a Nonuniform System. II. Thermodynamic Basis'. In: *The Journal of Chemical Physics* 30.5. DOI: 10.1063/1.1730145.

Calle-Vallejo, F. (2023). 'The ABC of Generalized Coordination Numbers and Their Use as a Descriptor in Electrocatalysis'. In: *Advanced Science* 10.20. DOI: doi.org/10.1002/advs.202207644.

Calle-Vallejo, F. and A. S. Bandarenka (2018). 'Enabling Generalized Coordination Numbers to Describe Strain Effects'. In: *ChemSusChem* 11.11. DOI: doi.org/10.1002/cssc.201800569.

Calle-Vallejo, F., J. I. Martínez et al. (2014). 'Fast Prediction of Adsorption Properties for Platinum Nanocatalysts with Generalized Coordination Numbers'. In: *Angewandte Chemie International Edition* 53.32. DOI: doi.org/10.1002/anie.201402958.

Calle-Vallejo, F., M. D. Pohl et al. (2017). 'Why conclusions from platinum model surfaces do not necessarily lead to enhanced nanoparticle catalysts for the oxygen reduction reaction'. In: *Chem. Sci.* 8 (3). DOI: 10.1039/C6SC04788B.

Calle-Vallejo, F., J. Tymoczko et al. (2015). 'Finding optimal surface sites on heterogeneous catalysts by counting nearest neighbors'. In: *Science* 350.6257. DOI: 10.1126/science.aab3501.

Carnis, J., C. Atlan et al. (2021). *carnisj/bcdi: v0.2.1*. Version v0.2.1. DOI: 10.5281/zenodo.5741935.

Carnis, J., L. Gao, S. Fernández et al. (2021). 'Facet-Dependent Strain Determination in Electrochemically Synthetized Platinum Model Catalytic Nanoparticles'. In: *Small* 2007702. DOI: 10.1002/smll.202007702.

Carnis, J., L. Gao, S. Labat et al. (2019). 'Towards a quantitative determination of strain in Bragg Coherent X-ray Diffraction Imaging: artefacts and sign convention in reconstructions'. In: *Scientific Reports* 9.1. DOI: 10.1038/s41598-019-53774-2.

Carnis, J., F. Kirner et al. (2021). 'Exploring the 3D structure and defects of a self-assembled gold mesocrystal by coherent X-ray diffraction imaging'. In: *Nanoscale* 13.23. DOI: 10.1039/d1nr01806j.

Carnis, J., A. R. Kshirsagar et al. (2021). 'Twin boundary migration in an individual platinum nanocrystal during catalytic CO oxidation'. In: *Nature Communications* 12.1. DOI: 10.1038/s41467-021-25625-0.

Castán-Guerrero, C. et al. (2018). 'A reaction cell for ambient pressure soft x-ray absorption spectroscopy'. In: *Review of Scientific Instruments* 89.5. DOI: 10.1063/1.5019333.

Chahine, G. A. et al. (2014). 'Imaging of strain and lattice orientation by quick scanning X-ray microscopy combined with three-dimensional reciprocal space mapping'. In: *Journal of Applied Crystallography* 47.2. DOI: 10.1107/S1600576714004506.

Chamard, V. et al. (2010). 'Strain analysis by inversion of coherent Bragg X-ray diffraction intensity: the illumination problem'. In: *Journal of Modern Optics* 57.9. DOI: 10.1080/09500341003746645.

Chan, H. et al. (2021). 'Rapid 3D nanoscale coherent imaging via physics-aware deep learning'. In: *Applied Physics Reviews* 8.2. DOI: 10.1063/5.0031486.

Chapman, H. N. et al. (2006). 'High-resolution ab initio three-dimensional x-ray diffraction microscopy'. In: *J. Opt. Soc. Am. A* 23.5. DOI: 10.1364/JOSAA.23.001179.

Chatelier, C. (2020). 'On the surface structures and catalytic properties of Al-based intermetallics'. PhD thesis.

Che, M. (2013). 'Nobel Prize in chemistry 1912 to Sabatier: Organic chemistry or catalysis?' In: *Catalysis Today* 218-219. DOI: doi.org/10.1016/j.cattod.2013.07.006.

Che, M. and C. O. Bennett (1989). 'The Influence of Particle Size on the Catalytic Properties of Supported Metals'. In: *Advances in Catalysis* 36. DOI: doi.org/10.1016/S0360-0564(08)60017-6.

Chen, B. et al. (2012). 'Diffraction imaging: The limits of partial coherence'. In: *Phys. Rev. B* 86 (23). DOI: 10.1103/PhysRevB.86.235401.

Chen, J. G. et al. (2018). 'Beyond fossil fuel–driven nitrogen transformations'. In: *Science* 360.6391. DOI: 10.1126/science.aar6611.

Chen, Q.-S. et al. (2012). 'Role of surface defect sites: from Pt model surfaces to shape-controlled nanoparticles'. In: *Chem. Sci.* 3 (1). DOI: 10.1039/C1SC00503K.

Cherukara, M. J., W. Cha and R. J. Harder (2018). 'Anisotropic nano-scale resolution in 3D Bragg coherent diffraction imaging'. In: *Applied Physics Letters* 113.20. DOI: 10.1063/1.5055235.

Cherukara, M. J., Y. S. Nashed and R. J. Harder (2018). 'Real-time coherent diffraction inversion using deep generative networks'. In: *Scientific Reports* 8.1. DOI: 10.1038/s41598-018-34525-1.

Choi, S. et al. (2020). 'In Situ Strain Evolution on Pt Nanoparticles during Hydrogen Peroxide Decomposition'. In: *Nano Letters* 20.12. DOI: 10.1021/acs.nanolett.0c03005.

Clark, J. N., L. Beitra et al. (2013). 'Ultrafast Three-Dimensional Imaging of Lattice Dynamics in Individual Gold Nanocrystals'. In: *Science* 341.6141. DOI: 10.1126/science.1236034.

Clark, J. N., X. Huang et al. (2012). 'High-resolution three-dimensional partially coherent diffraction imaging'. In: *Nature Communications* 3. DOI: 10.1038/ncomms1994.

Clark, J. N., J. Ihli et al. (2015). 'Three-dimensional imaging of dislocation propagation during crystal growth and dissolution'. In: *Nature Materials* 14.8. DOI: 10.1038/nmat4320.

Cochran, W. et al. (1967). 'What is the fast Fourier transform?' In: *Proceedings of the IEEE* 55.10. DOI: 10.1109/PROC.1967.5957.

Cooley, J. W. and J. W. Tukey (1965). 'An algorithm for the machine calculation of complex Fourier series'. In: *Mathematics of computation* 19.90.

Cornelius, T. W. et al. (2011). 'Three-dimensional diffraction mapping by tuning the X-ray energy'. In: *Journal of Synchrotron Radiation* 18.3. DOI: 10.1107/S0909049511003190.

Cox, M. P. et al. (1983). 'Non-equilibrium surface phase transitions during the catalytic oxidation of CO on Pt(100)'. In: *Surface Science* 134.2. DOI: 10.1016/0039-6028(83)90423-5.

Croset, B. (2017). 'Form factor of any polyhedron: A general compact formula and its singularities'. In: *Journal of Applied Crystallography* 50.5. DOI: 10.1107/S1600576717010147.

Dann, E. K. (2019). 'Improving Synchrotron Methods for Advanced Characterisation of Heterogeneous Catalysts'. PhD thesis.

Davidson, E. A. (2009). 'The contribution of manure and fertilizer nitrogen to atmospheric nitrous oxide since 1860'. In: *Nature Geoscience* 2.9. DOI: 10.1038/ngeo608.

Dawiec, A. et al. (2016). 'Real-time control of the beam attenuation with XPAD hybrid pixel detector'. In: *Journal of Instrumentation* 11.12. DOI: 10.1088/1748-0221/11/12/P12018.

Deelen, T. W. van, C. Hernández Mejía and K. P. de Jong (2019). 'Control of metal-support interactions in heterogeneous catalysts to enhance activity and selectivity'. In: *Nature Catalysis* 2.11. DOI: 10.1038/s41929-019-0364-x.

Derry, G. and P. Ross (1984). 'High coverage states of oxygen adsorbed on Pt(100) and Pt(111) surfaces'. In: *Surface Science* 140.1. DOI: doi.org/10.1016/0039-6028(84)90389-3.

Desjonquères, M. and F. Cyrot-Lackmann (1975). 'Electronic surface states in cleaved transition metals'. In: *Surface Science* 53.1. DOI: doi.org/10.1016/0039-6028(75)90142-9.

Deskins, N. A., J. Lauterbach and K. T. Thomson (2005). 'Lifting the Pt100 surface reconstruction through oxygen adsorption: A density functional theory analysis'. In: *Journal of Chemical Physics* 122.18. DOI: 10.1063/1.1893718.

Diaz, A. et al. (2009). 'Coherent diffraction imaging of a single epitaxial InAs nanowire using a focused x-ray beam'. In: *Physical Review B* 79.12. DOI: 10.1103/PhysRevB.79.125324.

Dicke, J., H. H. Rotermund and J. Lauterbach (2000). 'Formation of surface oxides on Pt(100) during CO oxidation in the millibar pressure range'. In: *Surface Science* 454.1. DOI: 10.1016/S0039-6028(00)00189-8.

Doornkamp, C. and V. Ponec (2000). 'The universal character of the Mars and Van Krevelen mechanism'. In: *Journal of Molecular Catalysis A: Chemical* 162.1. DOI: doi.org/10.1016/S1381-1169(00)00319-8.

Drnec, J. et al. (2014). 'Integration techniques for surface X-ray diffraction data obtained with a two-dimensional detector research papers'. In: *Journal of Applied Crystallography* 47. DOI: 10.1107/S1600576713032342.

Dupraz, M., G. Beutier et al. (2017). '3D Imaging of a Dislocation Loop at the Onset of Plasticity in an Indented Nanocrystal'. In: *Nano Letters* 17.11. DOI: 10.1021/acs.nanolett.7b02680.

Dupraz, M. (2015). 'Coherent X-ray diffraction applied to metal physics'. PhD thesis.

Dupraz, M., N. Li et al. (2022). 'Imaging the facet surface strain state of supported multifaceted Pt nanoparticles during reaction'. In: *Nature Communications*. DOI: 10.1038/s41467-022-30592-1.

Dzhigaev, D. (2021). *DzhigaevD/phasor*. (Visited on 16/12/2021).

Egelhoff, W. (1987). 'Core-level binding-energy shifts at surfaces and in solids'. In: *Surface Science Reports* 6.6. DOI: doi.org/10.1016/0167-5729(87)90007-0.

Einstein, A. (1905). 'Über einen die Erzeugung und Verwandlung des Lichtes betreffenden heuristischen Gesichtspunkt'. In: *Annalen der Physik* 322.6. DOI: 10.1002/andp.19053220607.

Ellinger, C. et al. (2008). 'Atmospheric pressure oxidation of Pt(111)'. In: *Journal of Physics Condensed Matter* 20.18. DOI: 10.1088/0953-8984/20/18/184013.

EPA (2023). *Greenhouse gases overview*. URL: www.epa.gov/ghgemissions/overview-greenhouse-gases (visited on 20/06/2023).

Erisman, J. et al. (2007). 'Reduced nitrogen in ecology and the environment'. In: *Environmental Pollution* 150.1. DOI: doi.org/10.1016/j.envpol.2007.06.033.

Erisman, J. W. et al. (2008). 'How a century of ammonia synthesis changed the world'. In: *Nature Geoscience* 1.10. DOI: 10.1038/ngeo325.

Fadenberger, K. et al. (2010). 'In situ observation of rapid reactions in nanoscale Ni-Al multilayer foils using synchrotron radiation'. In: *Applied Physics Letters* 97.

Fang, H. et al. (2022). 'Challenges and Opportunities of Ru-Based Catalysts toward the Synthesis and Utilization of Ammonia'. In: *ACS Catalysis* 12.7. DOI: 10.1021/acscatal.2c00090.

Fantauzzi, D. et al. (2017). 'Growth of Stable Surface Oxides on Pt(111) at Near-Ambient Pressures'. In: *Angewandte Chemie - International Edition* 56.10. DOI: 10.1002/anie.201609317.

Farrow, R. F. C. et al. (1993). 'Epitaxial growth of Pt on basal-plane sapphire: a seed film for artificially layered magnetic metal structures'. In: *Journal of Crystal Growth* 133. DOI: doi.org/10.1016/0022-0248(93)90102-3.

Favier, D. et al. (2007). 'Homogeneous and heterogeneous deformation mechanisms in an austenitic polycrystalline Ti-50.8at.% Ni thin tube under tension. Investigation via temperature and strain fields measurements'. In: *Acta Materialia* 55.16. DOI: doi.org/10.1016/j.actamat.2007.05.027.

Favre-Nicolin, V. (2011). 'Semiconductor nano-structures in the light of synchrotron radiation'. HDR.

Favre-Nicolin, V., J. Coraux et al. (2011). 'Fast computation of scattering maps of nanostructures using graphical processing units'. In: *Journal of Applied Crystallography* 44.3. DOI: 10.1107/S0021889811009009.

Favre-Nicolin, V., G. Girard et al. (2020). '*PyNX*: high-performance computing toolkit for coherent X-ray imaging based on operators'. In: *Journal of Applied Crystallography* 53.5. DOI: 10.1107/S1600576720010985.

Favre-Nicolin, V., S. Leake and Y. Chushkin (2020). 'Free log-likelihood as an unbiased metric for coherent diffraction imaging'. In: *Scientific Reports* 10.1. DOI: 10.1038/s41598-020-57561-2.

Fechete, I., Y. Wang and J. C. Védrine (2012). 'The past, present and future of heterogeneous catalysis'. In: *Catalysis Today* 189.1. DOI: doi.org/10.1016/j.cattod.2012.04.003.

Feidenhans'l, R. (1989). 'Surface structure determination by X-ray diffraction'. In: *Surface Science Reports* 10.3. DOI: doi.org/10.1016/0167-5729(89)90002-2.

Fernàndez, S. et al. (2019). 'In situ structural evolution of single particle model catalysts under ambient pressure reaction conditions'. In: *Nanoscale* 11.1. DOI: 10.1039/c8nr08414a.

Fertey, P. et al. (2013). 'Diffraction studies under in situ electric field using a large-area hybrid pixel XPAD detector'. In: *Journal of Applied Crystallography* 46.4. DOI: 10.1107/S0021889813013903.

Fienup, J. R. (1978). 'Reconstruction of an object from the modulus of its Fourier transform'. In: *Optics Letters* 3.1. DOI: 10.1364/OL.3.000027.

— (1982). 'Phase retrieval algorithms: a comparison'. In: *Applied Optics* 21.15. DOI: 10.1364/ao.21.002758.

Fienup, J. R. and C. C. Wackerman (1986). 'Phase-retrieval stagnation problems and solutions'. In: *Journal of the Optical Society of America A* 3.11. DOI: 10.1364/josaa.3.001897.

Fierro, J. L. G., J. M. Palacios and F. Tomas (1990). 'Redistribution of Platinum Metals within an Ammonia Oxidation Plant'. In: *Platinum Metals Review* 34.2.

— (1992). 'Characterization of catalyst and catchment gauzes used in medium- and low-pressure ammonia oxidation plants'. In: *Journal of Materials Science* 27.3. DOI: 10.1007/BF02403880.

Fish, D. A. et al. (1995). 'Blind deconvolution by means of the Richardson–Lucy algorithm'. In: *J. Opt. Soc. Am. A* 12.1. DOI: 10.1364/JOSAA.12.000058.

Fisher, G. B. and J. L. Gland (1980). 'The interaction of water with the Pt(111) surface'. In: *Surface Science* 94.2. DOI: doi.org/10.1016/0039-6028(80)90018-7.

Flytzani-Stephanopoulos, M. and L. Schmidt (1979). 'Morphology and etching processes on macroscopic metal catalysts'. In: *Progress in Surface Science* 9.3. DOI: doi.org/10.1016/0079-6816(79)90001-7.

Frosik B., H. R. (2021). *Cohere*. URL: github.com/AdvancedPhotonSource/cohere (visited on 17/12/2021).

Gaggioli, C. A. et al. (2019). 'Beyond Density Functional Theory: The Multiconfigurational Approach To Model Heterogeneous Catalysis'. In: *ACS Catalysis* 9.9. DOI: 10.1021/acscatal.9b01775.

Galloni, E. E. and R. H. Busch (1952). 'The structure of platinum oxides'. In: *The Journal of Chemical Physics* 20. DOI: 10.1063/1.1700179.

Galloni, E. E. and J. Roffo Angel E. (2004). 'The Crystalline Structure of Pt_3O_4'. In: *The Journal of Chemical Physics* 9.12. DOI: 10.1063/1.1750860.

Galloway, J. N. and G. E. Likens (1981). 'Acid precipitation: The importance of nitric acid'. In: *Atmospheric Environment (1967)* 15.6. DOI: doi.org/10.1016/0004-6981(81)90109-8.

Gandhi, H., G. Graham and R. McCabe (2003). 'Automotive exhaust catalysis'. In: *Journal of Catalysis* 216.1. DOI: doi.org/10.1016/S0021-9517(02)00067-2.

Gao, Y. et al. (2022). 'Modeling and experimental validation of dynamical effects in Bragg coherent x-ray diffractive imaging of finite crystals'. In: *Physical Review B* 106 (18). DOI: 10.1103/PhysRevB.106.184111.

Gerchberg, R. and O. Saxton (1972). 'A practical algorithm for the determination of the phase from image and diffraction plane pictures'. In: *Optik* 35.

Girard, G. (2020). 'Development of Bragg coherent X-ray diffraction and Ptychography methods, application to the study of semiconductor nanostructures'. PhD thesis.

Gland, J. and V. Korchak (1978a). 'Ammonia oxidation on a stepped platinum single-crystal surface'. In: *Journal of Catalysis* 53.1. DOI: doi.org/10.1016/0021-9517(78)90003-9.

— (1978b). 'The catalytic reduction of nitric oxide with ammonia over a stepped platinum single crystal surface'. In: *Journal of Catalysis* 55.3. DOI: doi.org/10.1016/0021-9517(78)90220-8.

Gland, J., G. Woodard and V. Korchak (1980). 'Ammonia oxidation on the Pt(111) and Pt(S)-12(111) × (111) surfaces'. In: *Journal of Catalysis* 61.2. DOI: doi.org/10.1016/0021-9517(80)90405-4.

Glavic, A. and M. Björck (2022). '*GenX 3*: the latest generation of an established tool'. In: *Journal of Applied Crystallography* 55.4. DOI: 10.1107/S1600576722006653.

Glick, B. and J. Mache (2018). 'Using Jupyter Notebooks to Learn High-Performance Computing'. In: *J. Comput. Sci. Coll.* 34.1. DOI: 10.5555/3280489.3280518.

Godard, P. (2021). 'On the use of the scattering amplitude in coherent X-ray Bragg diffraction imaging'. In: *Journal of Applied Crystallography* 54.3. DOI: 10.1107/S1600576721003113.

Goncharova, L. V. (2018). 'Surface structure in real and reciprocal space'. In: *Basic Surfaces and their Analysis*. 2053-2571. Morgan & Claypool Publishers. DOI: 10.1088/978-1-6817-4954-9ch3.

Goodman, D. (1994). 'Catalysis: from single crystals to the "real world"'. In: *Surface Science* 299-300. DOI: doi.org/10.1016/0039-6028(94)90701-3.

Grédiac, M. (1996). 'The use of heterogeneous strain fields for the characterization of composite materials'. In: *Composites Science and Technology* 56.7. DOI: doi.org/10.1016/0266-3538(96)00030-9.

Grothausmann, R. and R. Beare (2015). 'Facet Analyser: ParaView plugin for automated facet detection and measurement of interplanar angles of tomographic objects'. In: *The MIDAS Journal*.

Grothausmann, R., S. Fiechter et al. (2012). 'Automated quantitative 3D analysis of faceting of particles in tomographic datasets'. In: *Ultramicroscopy* 122.August. DOI: 10.1016/j.ultramic.2012.07.024.

Gsell, M., P. Jakob and D. Menzel (1998). 'Effect of Substrate Strain on Adsorption'. In: *Science* 280.5364. DOI: 10.1126/science.280.5364.717.

Gu, Z. and P. B. Balbuena (2007). 'Absorption of atomic oxygen into subsurfaces of Pt(100) and Pt(111): Density functional theory study'. In: *Journal of Physical Chemistry C* 111.27. DOI: 10.1021/jp0711693.

Guizar-Sicairos, M. et al. (2011). 'Phase tomography from x-ray coherent diffractive imaging projections'. In: *Optics Express* 19.22. DOI: 10.1364/OE.19.021345.

Günay, M. E. and R. Yıldırım (2021). 'Recent advances in knowledge discovery for heterogeneous catalysis using machine learning'. In: *Catalysis Reviews* 63.1. DOI: 10.1080/01614940.2020.1770402.

Günther, S. et al. (2008). 'In Situ X-ray Photoelectron Spectroscopy of Catalytic Ammonia Oxidation over a Pt(533) Surface'. In: *The Journal of Physical Chemistry C* 112.39. DOI: 10.1021/jp803264v.

Gustafson, J. et al. (2014). 'High-energy surface x-ray diffraction for fast surface structure determination'. In: *Science* 343 (6172). DOI: 10.1126/science.1246834.

Hagen, J. (2016). *Industrial Catalysis: A Practical Approach*. John Wiley & Sons, Ltd. DOI: 10.1002/3527607684.

Hammer, B. (2006). 'Special Sites at Noble and Late Transition Metal Catalysts'. In: *Topics in Catalysis* 37.1. DOI: 10.1007/s11244-006-0004-y.

Hammer, B. and J. K. Nørskov (1995). 'Why gold is the noblest of all the metals'. In: *Nature* 376.6537. DOI: 10.1038/376238a0.

— (2000). 'Theoretical surface science and catalysis—calculations and concepts'. In: *Advances in Catalysis* 45.C. DOI: 10.1016/S0360-0564(02)45013-4.

Hammer, R. et al. (2016). 'Surface reconstruction of Pt(001) quantitatively revisited'. In: *Physical Review B* 94.19. DOI: 10.1103/PhysRevB.94.195406.

Handforth, S. L. and J. N. Tilley (1934). 'Catalysts for Oxidation of Ammonia to Oxides of Nitrogen'. In: *Industrial & Engineering Chemistry* 26.12. DOI: 10.1021/ie50300a016.

Hannevold, L. et al. (2005a). 'Chemical vapor transport of platinum and rhodium with oxygen as transport agent'. In: *Journal of Crystal Growth* 279.1. DOI: doi.org/10.1016/j.jcrysgro.2005.02.024.

— (2005b). 'Reconstruction of platinum–rhodium catalysts during oxidation of ammonia'. In: *Applied Catalysis A: General* 284.1. DOI: doi.org/10.1016/j.apcata.2005.01.033.

Harder, R. et al. (2007). 'Orientation variation of surface strain'. In: *Physical Review B* 76 (11). DOI: 10.1103/physrevb.76.115425.

Harlow, G. S., E. Lundgren and M. Escudero-Escribano (2020). 'Recent advances in surface x-ray diffraction and the potential for determining structure-sensitivity relations in single-

crystal electrocatalysis'. In: *Current Opinion in Electrochemistry* 23. DOI: 10.1016/j.coelec.2020.08.005.

Harrison, R. and J. Webb (2001). 'A review of the effect of N fertilizer type on gaseous emissions'. In: vol. 73. Advances in Agronomy. Academic Press. DOI: doi.org/10.1016/S0065-2113(01)73005-2.

Hatscher, S. T. et al. (2008). 'Ammonia Oxidation'. In: *Handbook of Heterogeneous Catalysis*. John Wiley & Sons, Ltd. Chap. 12.2. DOI: doi.org/10.1002/9783527610044.hetcat0130.

Havu, P. et al. (2010). 'Large-scale surface reconstruction energetics of Pt(100) and Au(100) by all-electron density functional theory'. In: *Physical Review B - Condensed Matter and Materials Physics* 82.16. DOI: 10.1103/PhysRevB.82.161418.

Hawkins, J. M., J. F. Weaver and A. Asthagiri (2009). 'Density functional theory study of the initial oxidation of the Pt(111) surface'. In: *Phys. Rev. B* 79 (12). DOI: 10.1103/PhysRevB.79.125434.

Haydock, R. et al. (1972). 'Electronic Density of States at Transition-Metal Surfaces'. In: *Phys. Rev. Lett.* 29 (13). DOI: 10.1103/PhysRevLett.29.868.

Heck, R. M., J. C. Bonacci et al. (1982). 'A new research pilot plant unit for ammonia oxidation processes and some gauze data comparisons for nitric acid process'. In: *Industrial & Engineering Chemistry Process Design and Development* 21.1. DOI: 10.1021/i200016a014.

Heck, R. M. and R. J. Farrauto (2001). 'Automobile exhaust catalysts'. In: *Applied Catalysis A: General* 221.1. DOI: doi.org/10.1016/S0926-860X(01)00818-3.

Heilmann, P., K. Heinz and K. Müller (1979). 'The superstructures of the clean Pt(100) and Ir(100) surfaces'. In: *Surface Science* 83.2. DOI: 10.1016/0039-6028(79)90058-X.

Heinz, K. et al. (1982). 'Observation of the structural transition Pt(100) $1 \times 1 \rightarrow$ hex by LEED intensities'. In: *Applications of Surface Science* 11-12.C. DOI: 10.1016/0378-5963(82)90106-4.

Hejral, U., D. Franz et al. (2018). 'Identification of a Catalytically Highly Active Surface Phase for CO Oxidation over PtRh Nanoparticles under Operando Reaction Conditions'. In: *Phys. Rev. Lett.* 120 (12). DOI: 10.1103/PhysRevLett.120.126101.

Hejral, U., P. Mu et al. (2016). 'Tracking the shape-dependent sintering of platinum–rhodium model catalysts under operando conditions'. In: *Nature Communications*. DOI: 10.1038/ncomms10964.

Hejral, U., M. Shipilin et al. (2021). 'High energy surface x-ray diffraction applied to model catalyst surfaces at work'. In: *Journal of Physics Condensed Matter* 33 (7). DOI: 10.1088/1361-648X/abb17c.

Hejral, U., A. Vlad et al. (2013). 'In Situ Oxidation Study of Pt Nanoparticles on MgO(001)'. In: *Journal of Physical Chemistry C* 117. DOI: 10.1039/c4cp01271b.

Held, G. et al. (2020). 'Ambient-pressure endstation of the Versatile Soft X-ray (VerSoX) beamline at Diamond Light Source'. In: *Journal of Synchrotron Radiation* 27.5. DOI: 10.1107/S1600577520009157.

Hendriksen, B. L. M. et al. (2010). 'The role of steps in surface catalysis and reaction oscillations'. In: *Nature Chemistry* 2.9. DOI: 10.1038/nchem.728.

Henke, B., E. Gullikson and J. Davis (1993). 'X-Ray Interactions: Photoabsorption, Scattering, Transmission, and Reflection at E = 50-30,000 eV, Z = 1-92'. In: *Atomic Data and Nuclear Data Tables* 54.2. DOI: doi.org/10.1006/adnd.1993.1013.

High Temperature Mechanical Properties of the Platinum Group Metals (2022). URL: technology.matthey.com/article/45/2/74-82/ (visited on 10/09/2022).

Hofmann, F. et al. (2020). 'Nanoscale imaging of the full strain tensor of specific dislocations extracted from a bulk sample'. In: *Physical Review Materials* 4.1. DOI: 10.1103/PhysRevMaterials.4.013801.

Hosmer, H. R. (1917). 'Literature Of The Nitrogen Industries, 1912-1916'. In: *Journal of Industrial & Engineering Chemistry* 9.4. DOI: 10.1021/ie50088a035.

Hu, W., X. Huang and H. Yan (2018). 'Dynamic diffraction artefacts in Bragg coherent diffractive imaging'. In: *Journal of Applied Crystallography* 51 (1). DOI: 10.1107/S1600576718000274.

Huang, W. J. et al. (2008). 'Coordination-dependent surface atomic contraction in nanocrystals revealed by coherent diffraction'. In: *Nature Materials* 7.4. DOI: 10.1038/nmat2132.

Huber, M. L. and H. Harvey (2023). *Thermal conductivity of gases*. URL: tsapps.nist.gov/publication/get_pdf.cfm?pub_id=907540 (visited on 20/08/2023).

Hughes, E. D., C. K. Ingold and R. I. Reed (1950). '493. Kinetics and mechanism of aromatic nitration. Part II. Nitration by the nitronium ion, NO_2^+, derived from nitric acid'. In: *J. Chem. Soc.* (0). DOI: 10.1039/JR9500002400.

Hunter, J. D. (2007). 'Matplotlib: A 2D graphics environment'. In: *Computing in science & engineering* 9.3.

Imbihl, R. et al. (2007). 'Catalytic ammonia oxidation on platinum: Mechanism and catalyst restructuring at high and low pressure'. In: *Physical Chemistry Chemical Physics* 9.27. DOI: 10.1039/b700866j.

Ivashenko, O. et al. (2021). 'How Surface Species Drive Product Distribution during Ammonia Oxidation: An STM and Operando APXPS Study'. In: *ACS Catalysis*. DOI: 10.1021/acscatal.1c00956.

Jacques, V. (2010). 'Application de la diffraction cohérente des rayons X à l'étude de défauts topologiques dans les structures atomiques et électroniques'. PhD thesis.

Jakob, P., M. Gsell and D. Menzel (2001). 'Interactions of adsorbates with locally strained substrate lattices'. In: *The Journal of Chemical Physics* 114.22. DOI: 10.1063/1.1369161.

Jeerh, G., M. Zhang and S. Tao (2021). 'Recent progress in ammonia fuel cells and their potential applications'. In: *J. Mater. Chem. A* 9 (2). DOI: 10.1039/D0TA08810B.

Jens Als-Nielsen, D. M. (2011). *Elements of Modern X-ray Physics*. John Wiley & Sons, Ltd. DOI: 10.1002/9781119998365.

Jerome, A. (1920). 'The Award of the Nobel Prize to Professor Haber'. In: *Science* 51.1318. DOI: 10.1126/science.51.1318.348.a.

Jiang, T. et al. (2009). 'Trends in CO Oxidation Rates for Metal Nanoparticles and Close-Packed, Stepped, and Kinked Surfaces'. In: *The Journal of Physical Chemistry C* 113.24. DOI: 10.1021/jp811185g.

Jones, D. R. and M. F. Ashby (2019). 'Chapter 5 - Packing of Atoms in Solids'. In: *Engineering Materials 1 (Fifth Edition)*. Ed. by D. R. Jones and M. F. Ashby. Fifth Edition. Butterworth-Heinemann. DOI: doi.org/10.1016/B978-0-08-102051-7.00005-1.

Jupyter Notebook 7 (2023). URL: blog.jupyter.org/announcing-jupyter-notebook-7-8d6d66126dcf (visited on 17/08/2023).

Kaganer, V. M. (2007). 'Crystal truncation rods in kinematical and dynamical x-ray diffraction theories'. In: *Physical Review B* 75 (February). DOI: 10.1103/PhysRevB.75.245425.

Kaiser, K. (1909). 271517.

Karpov, D. and E. Fohtung (2019). 'Bragg coherent diffractive imaging of strain at the nanoscale'. In: *Journal of Applied Physics* 125.12. DOI: 10.1063/1.5054294.

Kawaguchi, T., T. F. Keller et al. (2019). 'Gas-Induced Segregation in Pt-Rh Alloy Nanoparticles Observed by in Situ Bragg Coherent Diffraction Imaging'. In: *Physical Review Letters* 123.24. DOI: 10.1103/PhysRevLett.123.246001.

Kawaguchi, T., V. Komanicky et al. (2021). 'Electrochemically Induced Strain Evolution in Pt-Ni Alloy Nanoparticles Observed by Bragg Coherent Diffraction Imaging'. In: *Nano Letters* 21.14. DOI: 10.1021/acs.nanolett.1c00778.

Khaleghi, A., K. Mahmoudi and S. Mozaffari (2019). 'Design of a vertical search engine for synchrotron data: a big data approach using Hadoop ecosystem'. In: *SN Applied Sciences* 1 (12). DOI: 10.1007/s42452-019-1582-1.

Khorshidi, A. et al. (2018). 'How strain can break the scaling relations of catalysis'. In: *Nature Catalysis* 1.4. DOI: 10.1038/s41929-018-0054-0.

Kibler, L. A. et al. (2005). 'Tuning Reaction Rates by Lateral Strain in a Palladium Monolayer'. In: *Angewandte Chemie International Edition* 44.14. DOI: doi.org/10.1002/anie.200462127.

Kiessig, H. (1931). 'Interferenz von Röntgenstrahlen an dünnen Schichten'. In: *Annalen der Physik* 402.7. DOI: doi.org/10.1002/andp.19314020702.

Kim, D., M. Chung, J. Carnis et al. (2018). 'Active site localization of methane oxidation on Pt nanocrystals'. In: *Nature Communications* 9.1. DOI: 10.1038/s41467-018-05464-2.

Kim, D., M. Chung, S. Kim et al. (2019). 'Defect Dynamics at a Single Pt Nanoparticle during Catalytic Oxidation'. In: *Nano Letters* 19.8. DOI: 10.1021/acs.nanolett.9b01332.

Kim, J. W. et al. (2021). 'Inversion of coherent surface scattering images via deep learning network'. In: *Applied Physics Letters* 119.19. DOI: 10.1063/5.0063903.

Kim, M., S. J. Pratt and D. A. King (2000). 'In Situ Characterization of the Surface Reaction between Chemisorbed Ammonia and Oxygen on Pt{100}'. In: *Journal of the American Chemical Society* 122.10. DOI: 10.1021/ja994124r.

Kim, Y. Y. et al. (2021). 'Single alloy nanoparticle x-ray imaging during a catalytic reaction'. In: *Science Advances* 7.40. DOI: 10.1126/sciadv.abh0757.

Kiskinova, M., G. Pirug and H. Bonzel (1984). 'NO adsorption on Pt(111)'. In: *Surface Science* 136.2. DOI: doi.org/10.1016/0039-6028(84)90612-5.

— (1985). 'Adsorption and decomposition of H_2O on a K-covered Pt(111) surface'. In: *Surface Science* 150.2. DOI: doi.org/10.1016/0039-6028(85)90649-1.

Kitchin, J. R. et al. (2004). 'Role of strain and ligand effects in the modification of the electronic and chemical Properties of bimetallic surfaces'. In: *Physical Review Letters* 93.15. DOI: 10.1103/PhysRevLett.93.156801.

Kitchin, J. R. (2018). 'Machine learning in catalysis'. In: *Nature Catalysis* 1.4. DOI: 10.1038/s41929-018-0056-y.

Kluyver, T. et al. (2016). 'Jupyter Notebooks – a publishing format for reproducible computational workflows'. In: *Positioning and Power in Academic Publishing: Players, Agents and Agendas*. Ed. by F. Loizides and B. Schmidt. IOS Press.

Kondratenko, E. V. et al. (2006). 'Distinct activity and time-on-stream behavior of pure Pt and Rh metals and Pt–Rh alloys in the high-temperature N_2O decomposition'. In: *Applied Catalysis A: General* 298. DOI: doi.org/10.1016/j.apcata.2005.09.022.

Kondratenko, V. A. and M. Baerns (2007). 'Mechanistic insights into the formation of N_2O and N_2 in NO reduction by NH_3 over a polycrystalline platinum catalyst'. In: *Applied Catalysis B: Environmental* 70.1. DOI: doi.org/10.1016/j.apcatb.2005.11.037.

Könnecke, M. et al. (2015). 'The NeXus data format'. In: *Journal of Applied Crystallography* 48 (1). DOI: 10.1107/S1600576714027575.

Kornfeld, D. S. and S. L. Titus (2016). 'Stop ignoring misconduct'. In: *Nature* 537. DOI: doi.org/10.1038/537029a.

Kraehnert, R. and M. Baerns (2008). 'Kinetics of ammonia oxidation over Pt foil studied in a micro-structured quartz-reactor'. In: *Chemical Engineering Journal* 137.2. DOI: doi.org/10.1016/j.cej.2007.05.005.

Kretser, A. et al. (2019). 'Scientific Integrity Principles and Best Practices: Recommendations from a Scientific Integrity Consortium'. In: *Science and Engineering Ethics* 25.2. DOI: 10.1007/s11948-019-00094-3.

Kriegner, D., E. Wintersberger and J. Stangl (2013). '*xrayutilities*: a versatile tool for reciprocal space conversion of scattering data recorded with linear and area detectors'. In: *Journal of Applied Crystallography* 46.4. DOI: 10.1107/S0021889813017214.

Kuhnke, K. et al. (1992). 'Top-layer superstructures of the reconstructed Pt(100) surface'. In: *Phys. Rev. B* 45 (24). DOI: 10.1103/PhysRevB.45.14388.

Labat, S., V. Chamard and O. Thomas (2007). 'Local strain in a 3D nano-crystal revealed by 2D coherent X-ray diffraction imaging'. In: *Thin Solid Films* 515.14. DOI: 10.1016/j.tsf.2006.12.031.

Labat, S., M.-I. Richard et al. (2015). 'Inversion Domain Boundaries in GaN Wires Revealed by Coherent Bragg Imaging'. In: *ACS Nano* 9.9. DOI: 10.1021/acsnano.5b03857.

Lange, J.-P. (2021). 'Performance metrics for sustainable catalysis in industry'. In: *Nature Catalysis* 4.3. DOI: 10.1038/s41929-021-00585-2.

Langmuir, I. (1922). 'Part II.—"Heterogeneous reactions". Chemical reactions on surfaces'. In: *Trans. Faraday Soc.* 17 (0). DOI: 10.1039/TF9221700607.

Latychevskaia, T. (2018). 'Iterative phase retrieval in coherent diffractive imaging: practical issues'. In: *Applied Optics* 57.25. DOI: 10.1364/ao.57.007187.

Lauraux, F., T. W. Cornelius et al. (2020). 'Multi-wavelength Bragg coherent X-ray diffraction imaging of Au particles Multi-wavelength BCDI imaging of Au particles'. In: *Journal of Applied Crystallography* 53.2011. DOI: 10.1107/S1600576719017163.

Lauraux, F., S. Labat et al. (2021). 'Simultaneous Multi-Bragg Peak Coherent X-ray Diffraction Imaging'. In: *Crystals* 11.3. DOI: 10.3390/cryst11030312.

Lauterbach, J., K. Asakura and H. Rotermund (1994). 'Subsurface oxygen on Pt(100): kinetics of the transition from chemisorbed to subsurface state and its reaction with CO, H_2 and O_2'. In: *Surface Science* 313.1. DOI: doi.org/10.1016/0039-6028(94)91156-8.

Leake, S. J. et al. (2019). 'The Nanodiffraction beamline ID01/ESRF: a microscope for imaging strain and structure'. In: *Journal of Synchrotron Radiation* 26.2. DOI: 10.1107/S160057751900078X.

Lee, C. J. and D. Moher (2017). 'Promote scientific integrity via journal peer review data'. In: *Science* 357.6348. DOI: 10.1126/science.aan4141.

Lee, F. (2005). '11 - Process Design'. In: *Lees' Loss Prevention in the Process Industries (Third Edition)*. Ed. by S. Mannan. Third Edition. Burlington: Butterworth-Heinemann. DOI: doi.org/10.1016/B978-075067555-0.50099-2.

Lee, H. et al. (2006). 'Morphological Control of Catalytically Active Platinum Nanocrystals'. In: *Angewandte Chemie International Edition* 45.46. DOI: doi.org/10.1002/anie.200603068.

Lee, I. et al. (2009). 'Tuning selectivity in catalysis by controlling particle shape'. In: *Nature Materials* 8.2. DOI: 10.1038/nmat2371.

Li, H. et al. (2016). 'Observation of Pt-{100}-p(2×2)-O reconstruction by an environmental TEM'. In: *Progress in Natural Science: Materials International* 26 (3). DOI: 10.1016/j.pnsc.2016.05.009.

Li, N. et al. (2020). 'Continuous scanning for Bragg coherent X-ray imaging'. In: *Scientific Reports* 10.1. DOI: 10.1038/s41598-020-69678-5.

Li, W. and B. Hammer (2005). 'Reactivity of a gas/metal/metal-oxide three-phase boundary: CO oxidation at the Pt(111)–c(4×2)-2CO/α-PtO_2 phase boundary'. In: *Chemical Physics Letters* 409.1. DOI: doi.org/10.1016/j.cplett.2005.04.064.

Li, Y., S. H. Chan and Q. Sun (2015). 'Heterogeneous catalytic conversion of CO_2: a comprehensive theoretical review'. In: *Nanoscale* 7 (19). DOI: 10.1039/C5NR00092K.

Li, Y. and J. N. Armor (1997). 'Selective NH_3 oxidation to N_2 in a wet stream'. In: *Applied Catalysis B: Environmental* 13.2. DOI: doi.org/10.1016/S0926-3373(96)00098-7.

Lim, B. et al. (2021). 'A convolutional neural network for defect classification in Bragg coherent X-ray diffraction'. In: *npj Computational Materials* 7.1. DOI: 10.1038/s41524-021-00583-9.

Lim, J. et al. (2021). 'Ammonia and Nitric Acid Demands for Fertilizer Use in 2050'. In: *ACS Energy Letters* 6.10. DOI: 10.1021/acsenergylett.1c01614.

Linford, M. R. et al. (2019). 'Water vapor, by near-ambient pressure XPS'. In: *Surface Science Spectra*. DOI: 10.1116/1.5111634.

Lo, Y. H. et al. (2018). 'In situ coherent diffractive imaging'. In: *Nature Communications* 9.1. DOI: 10.1038/s41467-018-04259-9.

Lorensen, W. E. and H. E. Cline (1987). 'Marching Cubes: A High Resolution 3D Surface Construction Algorithm'. In: *SIGGRAPH Comput. Graph.* 21.4. DOI: 10.1145/37402.37422.

Lucy, L. (1974). 'An iterative technique for the rectification of observed distributions'. In: *Astronomical Journal* 79. DOI: 10.1086/111605.

Ludwig, J. R. and C. S. Schindler (2017). 'Catalyst: Sustainable Catalysis'. In: *Chem* 2.3. DOI: doi.org/10.1016/j.chempr.2017.02.014.

Luke, D. R. (2005). 'Relaxed averaged alternating reflections for diffraction imaging'. In: *Inverse Problems* 21.1. DOI: 10.1088/0266-5611/21/1/004.

Ma, H. and W. F. Schneider (2019). 'Structure- and Temperature-Dependence of Pt-Catalyzed Ammonia Oxidation Rates and Selectivities'. In: *ACS Catalysis* 9.3. DOI: 10.1021/acscatal.8b04251.

Maia, F. R. (2012). 'The coherent X-ray imaging data bank'. In: *Nature Methods* 9.9. DOI: 10.1038/nmeth.2110.

Marchesini, S. (2007). 'A unified evaluation of iterative projection algorithms for phase retrieval'. In: *Review of Scientific Instruments* 78.1. DOI: 10.1063/1.2403783.

Marchesini, S., H. N. Chapman et al. (2003). *Coherent X-ray diffractive imaging: applications and limitations*.

Marchesini, S., H. He et al. (2003). 'X-ray image reconstruction from a diffraction pattern alone'. In: *Physical Review B - Condensed Matter and Materials Physics* 68.14. DOI: 10.1103/PhysRevB.68.140101.

Mars, P. and D. van Krevelen (1954). 'Oxidations carried out by means of vanadium oxide catalysts'. In: *Chemical Engineering Science* 3. DOI: doi.org/10.1016/S0009-2509(54)80005-4.

Martini, A. et al. (2019). 'PyFitit: The software for quantitative analysis of XANES spectra using machine-learning algorithms'. In: *Computer Physics Communications*. DOI: 10.1016/j.cpc.2019.107064.

Mase, K. and Y. Murata (1992). 'LEED study of NO adsorption-induced restructuring of a single-domain Pt(001)-(20 × 5) surface at 80–410 K'. In: *Surface Science* 277.1. DOI: doi.org/10.1016/0039-6028(92)90615-D.

Mason, D. M. (1956). 'Properties of Fuming Nitric Acid Affecting Its Storage and Use as a Rocket Propellant'. In: *Journal of Jet Propulsion* 26.9. DOI: 10.2514/8.7130.

Mastropietro, F. et al. (2011). 'Coherent x-ray wavefront reconstruction of a partially illuminated Fresnel zone plate'. In: *Optics Express* 19 (20). DOI: 10.1364/oe.19.019223.

Mavko, G., T. Mukerji and J. Dvorkin (2020). In: *The Rock Physics Handbook*. 3rd ed. Cambridge University Press.

Mavrikakis, M., B. Hammer and J. Nørskov (1998). 'Effect of Strain on the Reactivity of Metal Surfaces'. In: *Physical Review Letters* 81.13. DOI: 10.1016/j.jcat.2020.07.030.

McAlister, H. A. (2003). 'Speckle Interferometry'. In: *Encyclopedia of Physical Science and Technology (Third Edition)*. Ed. by R. A. Meyers. Third Edition. New York: Academic Press. DOI: doi.org/10.1016/B0-12-227410-5/00719-5.

McBride, J. R. et al. (1991). 'Growth and characterization of reactively sputtered thin-film platinum oxides'. In: *Journal of Applied Physics* 69.3. DOI: 10.1063/1.347255.

McCabe, A. R., G. D. W. Smith and A. S. Pratt (1986). 'The Mechanism of Reconstruction of Rhodium-Platinum Catalyst Gauzes'. In: *Platinum Metals Review* 30.2.

McCabe, R., T. Pignet and L. Schmidt (1974). 'Catalytic etching of platinum in NH_3 oxidation'. In: *Journal of Catalysis* 32.1. DOI: doi.org/10.1016/0021-9517(74)90165-1.

McGreevy, R. L. (2001). 'Reverse Monte Carlo modelling'. In: *Journal of Physics: Condensed Matter* 13.46. DOI: 10.1088/0953-8984/13/46/201.

McKinney, W. (2017). *Python for Data Analysis: Data Wrangling with Pandas, NumPy, and IPython*. Vol. 15. O Reilly.

McMillan, N. et al. (2005). 'Subsurface oxygen formation on Pt(1 0 0): Experiments and modeling'. In: *Catalysis Today* 105.2. DOI: 10.1016/j.cattod.2005.02.042.

Meirer, F. and B. M. Weckhuysen (2018). 'Spatial and temporal exploration of heterogeneous catalysts with synchrotron radiation'. In: *Nature Reviews Materials* 3.9. DOI: 10.1038/s41578-018-0044-5.

Miao, J., J. Kirz and D. Sayre (2000). 'The oversampling phasing method'. In: *Acta Crystallographica Section D: Biological Crystallography* 56.10. DOI: 10.1107/S0907444900008970.

Miao, J. and D. Sayre (2000). 'On possible extensions of X-ray crystallography through diffraction-pattern oversampling'. In: *Acta Crystallographica Section A Foundations of Crystallography* 56.6. DOI: 10.1107/S010876730001031X.

Miao, J., D. Sayre and H. N. Chapman (1998). 'Phase retrieval from the magnitude of the Fourier transforms of nonperiodic objects'. In: *Journal of the Optical Society of America A* 15.6. DOI: 10.1364/josaa.15.001662.

Miao, J., P. Charalambous et al. (1999). 'Extending the methodology of X-ray crystallography to non-crystalline specimens'. In: *Nature* 400. DOI: 10.1063/1.1291749.

Miao, J., T. Ishikawa et al. (2015). 'Beyond crystallography: Diffractive imaging using coherent X-ray light sources'. In: *Science* 348.6234. DOI: 10.1126/science.aaa1394.

Mieher, W. and W. Ho (1995). 'Thermally activated oxidation of NHs on Pt(111): intermediate species and reaction mechanisms'. In: *Surface Science* 322.1. DOI: doi.org/10.1016/0039-6028(95)90026-8.

Miller, D. et al. (2014). 'Different reactivity of the various platinum oxides and chemisorbed oxygen in CO oxidation on Pt(111)'. In: *Journal of the American Chemical Society* 136 (17). DOI: 10.1021/ja413125q.

Miller, D. J. et al. (2011). 'Oxidation of Pt(111) under Near-Ambient Conditions'. In: *Phys. Rev. Lett.* 107 (19). DOI: 10.1103/PhysRevLett.107.195502.

Milligan, M. B. (2018). 'Jupyter as Common Technology Platform for Interactive HPC Services'. In: *Proceedings of the Practice and Experience on Advanced Research Computing*. PEARC '18. Pittsburgh, PA, USA: Association for Computing Machinery. DOI: 10.1145/3219104.3219162.

'Mind the gap' (2018). In: *Nature Catalysis* 1. DOI: 10.1038/s41929-018-0188-0.

Minkevich, A. A. et al. (2007). 'Inversion of the diffraction pattern from an inhomogeneously strained crystal using an iterative algorithm'. In: *Physical Review B - Condensed Matter and Materials Physics* 76 (10). DOI: 10.1103/PhysRevB.76.104106.

MIT (2023). *Greenhouse gases*. URL: climate.mit.edu/explainers/greenhouse-gases (visited on 20/04/2023).

Mitsubishi (2023). *Selective Catalytic Reduction System*. URL: power.mhi.com/products/aqcs/lineup/flue-gas-denitration/ (visited on 06/08/2023).

Molenbroek, A. M. et al. (2009). 'Nano-particles in heterogeneous catalysis'. In: *Topics in Catalysis* 52 (10). DOI: 10.1007/s11244-009-9314-1.

Moritz, W. and M. A. Van Hove (2022). 'Surface X-ray Diffraction'. In: *Surface Structure Determination by LEED and X-rays*. Cambridge University Press. DOI: 10.1017/9781108284578.009.

Muller, O. and R. Roy (1968). 'Formation and stability of the platinum and rhodium oxides at high oxygen pressures and the structures of Pt_3O_4, β-PtO_2 and RhO_2'. In: *Journal of the Less Common Metals* 16.2. DOI: doi.org/10.1016/0022-5088(68)90070-2.

Munafò, M. R. et al. (2017). 'A manifesto for reproducible science'. In: *Nature Human Behaviour* 1.1. DOI: 10.1038/s41562-016-0021.

Musket, R. et al. (1982). 'Preparation of atomically clean surfaces of selected elements: A review'. In: *Applications of Surface Science* 10.2. DOI: doi.org/10.1016/0378-5963(82)90142-8.

Ndolomingo, M. J., N. Bingwa and R. Meijboom (2020). 'Review of supported metal nanoparticles: synthesis methodologies, advantages and application as catalysts'. In: *Journal of Materials Science* 55.15. DOI: 10.1007/s10853-020-04415-x.

Névot, L. and Croce, P. (1980). 'Caractérisation des surfaces par réflexion rasante de rayons X. Application à l'étude du polissage de quelques verres silicates'. In: *Rev. Phys. Appl. (Paris)* 15.3. DOI: 10.1051/rphysap:01980001503076100.

Newton, M. C., S. J. Leake et al. (2010). 'Three-dimensional imaging of strain in a single ZnO nanorod'. In: *Nature Materials* 9.2. DOI: 10.1038/nmat2607.

Newton, M. C., Y. Nishino and I. K. Robinson (2012). 'Bonsu: The interactive phase retrieval suite'. In: *Journal of Applied Crystallography* 45.4. DOI: 10.1107/S0021889812026751.

Newville, M. et al. (2016). *Lmfit: Non-Linear Least-Square Minimization and Curve-Fitting for Python*. URL: lmfit.github.io/lmfit-py/.

Nilsen, O., A. Kjekshus and H. Fjellvåg (2001). 'Reconstruction and loss of platinum catalyst during oxidation of ammonia'. In: *Applied Catalysis A: General* 207.1. DOI: doi.org/10.1016/S0926-860X(00)00615-3.

Nilsson, A. et al. (2005). 'The electronic structure effect in heterogeneous catalysis'. In: *Catalysis Letters* 100.3. DOI: 10.1007/s10562-004-3434-9.

Nilsson Pingel, T. et al. (2018). 'Influence of atomic site-specific strain on catalytic activity of supported nanoparticles'. In: *Nature Communications* 9.1. DOI: 10.1038/s41467-018-05055-1.

Nolte, P. et al. (2008). 'Shape Changes of Supported Rh Nanoparticles During Oxidation and Reduction Cycles'. In: *Science* 321.5896. DOI: 10.1126/science.1160845.

Nomiyama, R. K., M. J. Piotrowski and J. L. F. Da Silva (2011). 'Bulk structures of PtO and PtO_2 from density functional calculations'. In: *Phys. Rev. B* 84 (10). DOI: 10.1103/PhysRevB.84.100101.

Nørskov, J. K. et al. (2009). 'Towards the computational design of solid catalysts'. In: *Nature Chemistry* 1.1. DOI: 10.1038/nchem.121.

Novell-Leruth, G., A. Valcárcel et al. (2005). 'DFT Characterization of Adsorbed NH_x Species on Pt(100) and Pt(111) Surfaces'. In: *The Journal of Physical Chemistry B* 109.38. DOI: 10.1021/jp0516821.

Novell-Leruth, G., J. M. Ricart and J. Pérez-Ramírez (2008). 'Pt(100)-catalyzed ammonia oxidation studied by DFT: Mechanism and microkinetics'. In: *Journal of Physical Chemistry C* 112.35. DOI: 10.1021/jp802489y.

Nugent, K. A. (2010). 'Coherent methods in the X-ray sciences'. In: *Advances in Physics* 59.1. DOI: 10.1080/00018730903270926.

Nutt, C. W. and S. Kapur (1968). 'Mechanism of Oxidation of Ammonia on Platinum'. In: *Nature* 220.5168. DOI: 10.1038/220697a0.

— (1969). 'Oxidation of Ammonia on Platinum'. In: *Nature* 224.5215. DOI: 10.1038/224169a0.

Offermans, W. K., A. P. J. Jansen and R. A. van Santen (2006). 'Ammonia activation on Pt(111): A density functional theory study'. In: *Surface Science* 600.9. DOI: 10.1016/j.susc.2006.01.031.

Offermans, W. K., A. P. J. Jansen, R. A. Van Santen et al. (2007). 'Ammonia dissociation on Pt(100), Pt(111), and Pt(211): A comparative density functional theory study'. In: *Journal of Physical Chemistry C* 111.47. DOI: 10.1021/jp073083f.

Ontaneda, J., R. A. Bennett and R. Grau-Crespo (2015). 'Electronic Structure of Pd Multilayers on Re(0001): The Role of Charge Transfer'. In: *The Journal of Physical Chemistry C* 119.41. DOI: 10.1021/acs.jpcc.5b06070.

Oommen, C. and S. Jain (1999). 'Ammonium nitrate: a promising rocket propellant oxidizer'. In: *Journal of Hazardous Materials* 67.3. DOI: doi.org/10.1016/S0304-3894(99)00039-4.

Ostermaier, J., J. Katzer and W. Manogue (1974). 'Crystallite size effects in the low-temperature oxidation of ammonia over supported platinum'. In: *Journal of Catalysis* 33.3. DOI: doi.org/10.1016/0021-9517(74)90292-9.

— (1976). 'Platinum catalyst deactivation in low-temperature ammonia oxidation reactions. I. Oxidation of ammonia by molecular oxygen'. In: *Journal of Catalysis* 41.2. DOI: 10.1016/0021-9517(76)90343-2.

Ostwald, W. (1902a). GB190200698A.

— (1902b). GB190208300A.

Ouellette, R. J. and J. D. Rawn (2014). '13 - Electrophilic Aromatic Substitution'. In: *Organic Chemistry*. Ed. by R. J. Ouellette and J. D. Rawn. Boston: Elsevier. DOI: doi.org/10.1016/B978-0-12-800780-8.00013-9.

OWID (2023). *Fertilizers*. URL: ourworldindata.org/fertilizers (visited on 15/02/2023).

Oztürk, H. et al. (2017). 'Performance evaluation of Bragg coherent diffraction imaging'. In: *New Journal of Physics* 19.10. DOI: 10.1088/1367-2630/aa83a9.

Paganin, D. (2006). *Coherent X-Ray Optics*. Oxford University Press.

Parratt, L. G. (1954). 'Surface Studies of Solids by Total Reflection of X-Rays'. In: *Phys. Rev.* 95 (2). DOI: 10.1103/PhysRev.95.359.

Parsons, C. L. (1919). 'Commercial Oxidation of Ammonia to Nitric Acid.' In: *Journal of Industrial & Engineering Chemistry* 11.6. DOI: 10.1021/ie50114a012.

Passos, A. R. et al. (2020). 'Three-dimensional strain dynamics govern the hysteresis in heterogeneous catalysis'. In: *Nature Communications* 11.1. DOI: 10.1038/s41467-020-18622-2.

Patterson, A. L. (1939). 'The Scherrer Formula for X-Ray Particle Size Determination'. In: *Phys. Rev.* 56 (10). DOI: 10.1103/PhysRev.56.978.

Perez, F. and B. E. Granger (2007). 'IPython: A System for Interactive Scientific Computing'. In: *Computing in Science Engineering* 9 (3). DOI: 10.1109/MCSE.2007.53.

Pérez-Ramírez, J., F. Kapteijn et al. (2003). 'Formation and control of N_2O in nitric acid production: Where do we stand today?' In: *Applied Catalysis B: Environmental* 44.2. DOI: doi.org/10.1016/S0926-3373(03)00026-2.

Pérez-Ramírez, J., E. Kondratenko et al. (2004). 'Selectivity-directing factors of ammonia oxidation over PGM gauzes in the Temporal Analysis of Products reactor: Primary interactions of NH_3 and O_2'. In: *Journal of Catalysis* 227.1. DOI: doi.org/10.1016/j.jcat.2004.06.023.

Pérez-Ramírez, J., E. V. Kondratenko et al. (2009). 'Mechanism of ammonia oxidation over PGM (Pt, Pd, Rh) wires by temporal analysis of products and density functional theory'. In: *Journal of Catalysis* 261.2. DOI: doi.org/10.1016/j.jcat.2008.11.018.

Peuckert, M. and H. Bonzel (1984). 'Characterization of oxidized platinum surfaces by X-ray photoelectron spectroscopy'. In: *Surface Science* 145.1. DOI: doi.org/10.1016/0039-6028(84)90778-7.

Pfeifer, M. (2005). 'Structural studies of lead nanocrystals using coherent X-ray diffraction'. PhD thesis.

Pfeifer, M. A. et al. (2006). 'Three-dimensional mapping of a deformation field inside a nanocrystal'. In: *Nature* 442 (7098). DOI: 10.1038/nature04867.

Pignet, T. and L. Schmidt (1974). 'Selectivity of NH_3 oxidation on platinum'. In: *Chemical Engineering Science* 29.5. DOI: doi.org/10.1016/0009-2509(74)80111-9.

— (1975). 'Kinetics of NH_3 oxidation on Pt, Rh, and Pd'. In: *Journal of Catalysis* 40.2. DOI: doi.org/10.1016/0021-9517(75)90249-3.

Platinum / Rhodium Catalyst Gauzes (2023). URL: http://www.ravindraheraeus.com/platinum_rhodium.html (visited on 10/09/2023).

Ponchut, C. et al. (2011). 'MAXIPIX, a fast readout photon-counting X-ray area detector for synchrotron applications'. In: *Journal of Instrumentation* 6.01. DOI: 10.1088/1748-0221/6/01/C01069.

Pottbacker, J. et al. (2022). 'Resolving gradients in an ammonia oxidation reactor under industrial conditions : A combined experimental and simulation study'. In: *Chemical Engineering Journal* 439 (March). DOI: doi.org/10.1016/j.cej.2022.135350.

Prins, R. (2018). 'Eley–Rideal, the Other Mechanism'. In: *Topics in Catalysis* 61.9. DOI: 10.1007/s11244-018-0948-8.

Rafiqul, I. et al. (2005). 'Energy efficiency improvements in ammonia production—perspectives and uncertainties'. In: *Energy* 30.13. DOI: doi.org/10.1016/j.energy.2004.12.004.

Rafti, M. et al. (2007). 'Homogeneous and front-induced surface transformations during catalytic oxidation of ammonia over Pt(100)'. In: *Chemical Physics Letters* 446.4-6. DOI: 10.1016/j.cplett.2007.08.054.

Raimondi, F. et al. (2005). 'Nanoparticles in Energy Technology: Examples from Electrochemistry and Catalysis'. In: *Angewandte Chemie International Edition* 44.15. DOI: doi.org/10.1002/anie.200460466.

Raschka, S. and V. Mirjalili (2019). *Python Machine Learning, 3rd Ed.* 3rd ed. Birmingham, UK: Packt Publishing.

Rebrov, E. V., M. H. De Croon and J. C. Schouten (2002). 'Development of the kinetic model of platinum catalyzed ammonia oxidation in a microreactor'. In: *Chemical Engineering Journal* 90.1-2. DOI: 10.1016/S1385-8947(02)00068-2.

Resta, A. et al. (2020). 'Ammonia Oxidation over a Pt25Rh75(001) Model Catalyst Surface: An Operando Study'. In: *Journal of Physical Chemistry C* 124.40. DOI: 10.1021/acs.jpcc.0c07128.

Reuter, K., D. Frenkel and M. Scheffler (2004). 'The Steady State of Heterogeneous Catalysis, Studied by First-Principles Statistical Mechanics'. In: *Phys. Rev. Lett.* 93 (11). DOI: 10.1103/PhysRevLett.93.116105.

Richard, M.-I. et al. (2017). 'Reactor for nano-focused x-ray diffraction and imaging under catalytic in situ conditions'. In: *Review of Scientific Instruments* 88.9. DOI: 10.1063/1.5000015.

Richard, M. I. et al. (2018). 'Crystallographic orientation of facets and planar defects in functional nanostructures elucidated by nano-focused coherent diffractive X-ray imaging'. In: *Nanoscale* 10.10. DOI: 10.1039/c7nr07990g.

Richardson, W. H. (1972). 'Bayesian-Based Iterative Method of Image Restoration'. In: *J. Opt. Soc. Am.* 62.1. DOI: 10.1364/JOSA.62.000055.

Rideal, E. K. (1939). 'A note on a simple molecular mechanism for heterogeneous catalytic reactions'. In: *Mathematical Proceedings of the Cambridge Philosophical Society* 35.1. DOI: 10.1017/S030500410002082X.

Rienks, E. D. L. et al. (2003). 'The reduction of NO on Pt(100) by H_2 and CO studied with synchrotron x-ray photoelectron spectroscopy'. In: *The Journal of Chemical Physics* 119.12. DOI: 10.1063/1.1602059.

Rijn, R. V. et al. (2010). 'Ultrahigh vacuum/high-pressure flow reactor for surface x-ray diffraction and grazing incidence small angle x-ray scattering studies close to conditions for industrial catalysis'. In: *Review of Scientific Instruments* 81 (1). DOI: 10.1063/1.3290420.

Robach, O. et al. (2000). 'Corrections for surface X-ray diffraction measurements using the *Z*-axis geometry: finite size effects in direct and reciprocal space'. In: *Journal of Applied Crystallography* 33.4. DOI: 10.1107/S0021889800004696.

Robinson, I. K. (1983). 'Direct Determination of the Au(110) Reconstructed Surface by X-Ray Diffraction'. In: *Phys. Rev. Lett.* 50 (15). DOI: 10.1103/PhysRevLett.50.1145.

Robinson, I. K. (1986). 'Crystal truncation rods and surface roughness'. In: *Phys. Rev. B* 33.6. DOI: doi.org/10.1103/PhysRevB.33.3830.

Robinson, I. K., Y. Da et al. (2005). 'Coherent diffraction patterns of individual dislocation strain fields'. In: *Journal of Physics D: Applied Physics* 38.10A. DOI: 10.1088/0022-3727/38/10A/002.

Robinson, I. K. and D. J. Tweet (1991). 'Surface X-ray diffraction'. In: *Rep. Prog. Phys.* Vol. 55. DOI: 10.1088/0034-4885/55/5/002.

Robinson, I. K., I. A. Vartanyants et al. (2001). 'Reconstruction of the Shapes of Gold Nanocrystals Using Coherent X-Ray Diffraction'. In: *Phys. Rev. Lett.* 87.19. DOI: 10.1103/PhysRevLett.87.195505.

Robinson, I. and R. Harder (2009). 'Coherent X-ray diffraction imaging of strain at the nanoscale'. In: *Nature Materials* 8.4. DOI: 10.1038/nmat2400.

Roldan Cuenya, B. (2010). 'Synthesis and catalytic properties of metal nanoparticles: Size, shape, support, composition, and oxidation state effects'. In: *Thin Solid Films* 518.12. DOI: doi.org/10.1016/j.tsf.2010.01.018.

Ronaghi, Z. et al. (2017). 'Python in the NERSC Exascale Science Applications Program for Data'. In: *Proceedings of the 7th Workshop on Python for High-Performance and Scientific Computing*. PyHPC'17. Denver, CO, USA: Association for Computing Machinery.

Roobol, S. et al. (2015). 'BINoculars: Data reduction and analysis software for two-dimensional detectors in surface X-ray diffraction'. In: *Journal of Applied Crystallography* 48. DOI: 10.1107/S1600576715009607.

Ross, J. R. (2019). 'Chapter 7 - The Kinetics and Mechanisms of Catalytic Reactions'. In: *Contemporary Catalysis*. Ed. by J. R. Ross. Amsterdam: Elsevier. DOI: doi.org/10.1016/B978-0-444-63474-0.00007-2.

Rotermund, H. H., J. Lauterbach and G. Haas (1993). 'The formation of subsurface oxygen on Pt(100)'. In: *Applied Physics A* 57.6. DOI: 10.1007/BF00331749.

Ruan, C. et al. (2022). 'Selective catalytic oxidation of ammonia to nitric oxide via chemical looping'. In: *Nature Communications* 13.1. DOI: 10.1038/s41467-022-28370-0.

Santen, R. A. van, M. Neurock and S. G. Shetty (2010). 'Reactivity Theory of Transition-Metal Surfaces: A Brønsted-Evans-Polanyi Linear Activation Energy-Free-Energy Analysis'. In: *Chemical Reviews* 110.4. DOI: 10.1021/cr9001808.

Sarwitz, D. (2015). 'Reproducibility will not cure what ails science'. In: *Nature* 525.159. DOI: doi.org/10.1038/525159a.

Satio, T. (1969). 'A dynamical theory of diffraction for a Distorted Crystal'. In: *Journal of the Physical Societey of Japan* 26 (5). DOI: doi.org/10.1143/JPSJ.26.1239.

Sayre, D. (1952). 'Some implications of a theorem due to Shannon'. In: *Acta Crystallographica* 5.6. DOI: 10.1107/S0365110X52002276.

Schäffer, J. et al. (2013). 'Highly selective ammonia oxidation to nitric oxide over supported Pt nanoparticles'. In: *Journal of Catalysis* 301. DOI: doi.org/10.1016/j.jcat.2013.02.010.

Schauermann, S. et al. (2013). 'Nanoparticles for Heterogeneous Catalysis: New Mechanistic Insights'. In: *Accounts of Chemical Research* 46.8. DOI: 10.1021/ar300225s.

Schavkan, A. et al. (2013). 'Using the MAXIPIX detector for coherent X-ray scattering applications'. In: *Journal of Physics: Conference Series* 425. DOI: 10.1088/1742-6596/425/20/202004.

Scheibe, A., U. Lins and R. Imbihl (2005). 'Kinetics of ammonia oxidation on stepped platinum surfaces. I. Experimental results'. In: *Surface Science* 577.1. DOI: doi.org/10.1016/j.susc.2004.12.027.

Schlepütz, C. M., R. Herger et al. (2005). 'Improved data acquisition in grazing-incidence X-ray scattering experiments using a pixel detector'. In: *Acta Crystallographica Section A: Foundations of Crystallography* 61 (4). DOI: 10.1107/S0108767305014790.

Schlepütz, C. M., S. O. Mariager et al. (2011). 'Angle calculations for a (2+3)-type diffractometer: focus on area detectors'. In: *Journal of Applied Crystallography* 44.1. DOI: 10.1107/S0021889810048922.

Schlexer Lamoureux, P. et al. (2019). 'Machine Learning for Computational Heterogeneous Catalysis'. In: *ChemCatChem* 11.16. DOI: doi.org/10.1002/cctc.201900595.

Schlögl, R. (2015). 'Heterogeneous Catalysis'. In: *Angewandte Chemie International Edition* 54.11. DOI: doi.org/10.1002/anie.201410738.

Schmid, P. J. (2010). 'Dynamic mode decomposition of numerical and experimental data'. In: *Journal of Fluid Mechanics* 656. DOI: 10.1017/S0022112010001217.

Schroer, C. G. et al. (2008). 'Coherent X-Ray Diffraction Imaging with Nanofocused Illumination'. In: *Phys. Rev. Lett.* 101 (9). DOI: 10.1103/PhysRevLett.101.090801.

Scopatz, A. and K. D. Huff (2015). *Effective computation in physics*. O'Reilly.

Segner, J. et al. (1984). 'Catalytic oxidation of CO on Pt(111): The influence of surface defects and composition on the reaction dynamics'. In: *Surface Science* 138.2. DOI: doi.org/10.1016/0039-6028(84)90262-0.

Seriani, N. and F. Mittendorfer (2008). 'Platinum-group and noble metals under oxidizing conditions'. In: *Journal of Physics: Condensed Matter* 20.18. DOI: 10.1088/0953-8984/20/18/184023.

Seriani, N., W. Pompe and L. C. Ciacchi (2006). 'Catalytic oxidation activity of Pt_3O_4 surfaces and thin films'. In: *Journal of Physical Chemistry B* 110 (30). DOI: 10.1021/jp063281r.

Shabalin, A. G. et al. (2017). 'Dynamical effects in Bragg coherent x-ray diffraction imaging of finite crystals'. In: *Phys. Rev. B* 96 (6). DOI: 10.1103/PhysRevB.96.064111.

Shannon, C. (1949). 'Communication in the Presence of Noise'. In: *Proceedings of the IRE* 37.1. DOI: 10.1109/JRPROC.1949.232969.

Shen, W., Y. Jia and Y. Wu (2019). '3D shape reconstruction from images in the frequency domain'. In: *Proceedings of the IEEE Computer Society Conference on Computer Vision and Pattern Recognition* 2019-June. DOI: 10.1109/CVPR.2019.00460.

Simonne, D., J. Carnis et al. (2022). '*Gwaihir*: *Jupyter Notebook* graphical user interface for Bragg coherent diffraction imaging'. In: *Journal of Applied Crystallography* 55.4. DOI: 10.1107/S1600576722005854.

Simonne, D., A. Martini et al. (2020). 'Thorondor: software for fast treatment and analysis of low-energy XAS data'. In: *Journal of Synchrotron Radiation* 7 (6). DOI: doi.org/10.1107/S1600577520011388.

Sinha, S. K., M. Tolan and A. Gibaud (1998). 'Effects of partial coherence on the scattering of x rays by matter'. In: *Phys. Rev. B* 57 (5). DOI: 10.1103/PhysRevB.57.2740.

Sneed, B. T., A. P. Young and C. K. Tsung (2015). 'Building up strain in colloidal metal nanoparticle catalysts'. In: *Nanoscale* 7.29. DOI: 10.1039/c5nr02529j.

Sobczyk, D. et al. (2004). 'Low-temperature ammonia oxidation on platinum sponge studied with positron emission profiling'. In: *Journal of Catalysis* 225.2. DOI: doi.org/10.1016/j.jcat.2004.04.035.

Solomon, S. (2007). *Climate change 2007-the physical science basis: Working group I contribution to the fourth assessment report of the IPCC*. Vol. 4. Cambridge university press.

Somorjai, G. A. (1991). 'Directions of theoretical and experimental investigations into the mechanisms of heterogeneous catalysis'. In: *Catalysis Letters* 9.3. DOI: 10.1007/BF00773188.

Somorjai, G. A. et al. (2007). 'The evolution of model catalytic systems; studies of structure, bonding and dynamics from single crystal metal surfaces to nanoparticles, and from low pressure (<10-3 Torr) to high pressure (>10-3 Torr) to liquid interfaces'. In: *Phys. Chem. Chem. Phys.* 9 (27). DOI: 10.1039/B618805B.

Starr, D. E. (2021). 'A Brief Overview of the Principles of Ambient Pressure X-ray Spectroscopies'. In: vol. 1396. ACS Symposium Series. American Chemical Society. DOI: 10.1021/bk-2021-1396.ch001.

Stubbs, J. et al. (2020). 'Integrating Jupyter into Research Computing Ecosystems: Challenges and Successes in Architecting JupyterHub for Collaborative Research Computing Ecosystems'. In: *Practice and Experience in Advanced Research Computing*. PEARC '20. Portland, OR, USA: Association for Computing Machinery. DOI: 10.1145/3311790.3396648.

Sugai, S. et al. (1993). 'Adsorption and dissociation of NO on Pt(100) and (310) studied by AES, UPS and XPS'. In: *Surface Science* 282.1. DOI: doi.org/10.1016/0039-6028(93)90610-V.

Suzana, A. F. et al. (2019). 'In situ three-dimensional imaging of strain in gold nanocrystals during catalytic oxidation'. In: *Nanoscale Advances* 1.8. DOI: 10.1039/c9na00231f.

Suzuki, K. et al. (2019). 'Statistical Analysis and Discovery of Heterogeneous Catalysts Based on Machine Learning from Diverse Published Data'. In: *ChemCatChem* 11.18. DOI: doi.org/10.1002/cctc.201900971.

Svintsitskiy, D. A. et al. (2020). 'Insight into the Nature of Active Species of Pt/Al_2O_3 Catalysts for low Temperature NH_3 Oxidation'. In: *ChemCatChem* 12.3. DOI: doi.org/10.1002/cctc.201901719.

Taglauer, E. (1990). 'Surface cleaning using sputtering'. In: *Applied Physics A* 51.3. DOI: 10.1007/BF00324008.

Takagi, S. (1962). *Dynamical theory of diffraction applicable to crystals with any kind of small distortion.* DOI: doi.org/10.1107/S0365110X62003473.

Taylor, H. S. and E. F. Armstrong (1925). 'A theory of the catalytic surface'. In: *Proceedings of the Royal Society of London. Series A, Containing Papers of a Mathematical and Physical Character* 108.745. DOI: 10.1098/rspa.1925.0061.

Thermofischer (2023). *Reducing ammonia slip in selective catalytic reduction.* URL: www.thermofisher.com/blog/identifying-threats/reducing-NH$_3$-slip-in-selective-catalytic-reduction-scr/ (visited on 06/08/2023).

Thiemann, M., E. Scheibler and K. W. Wiegand (2000). 'Nitric Acid, Nitrous Acid, and Nitrogen Oxides'. In: *Ullmann's Encyclopedia of Industrial Chemistry*. John Wiley & Sons, Ltd. DOI: doi.org/10.1002/14356007.a17_293.

Tian, N. et al. (2007). 'Synthesis of Tetrahexahedral Platinum Nanocrystals with High-Index Facets and High Electro-Oxidation Activity'. In: *Science* 316.5825. DOI: 10.1126/science.1140484.

Ulvestad, A., H. M. Cho et al. (2014). 'Nanoscale strain mapping in battery nanostructures'. In: *Applied Physics Letters* 104.7. DOI: 10.1063/1.4866030.

Ulvestad, A., Y. Nashed et al. (2017). 'Identifying Defects with Guided Algorithms in Bragg Coherent Diffractive Imaging'. In: *Scientific Reports* 7.1. DOI: 10.1038/s41598-017-09582-7.

Ulvestad, A., A. Singer et al. (2015). 'Topological defect dynamics in operando battery nanoparticles'. In: *Science* 348.6241. DOI: 10.1126/science.aaa1313.

Ulvestad, A., J. N. Clark et al. (2015). 'In situ strain evolution during a disconnection event in a battery nanoparticle'. In: *Physical Chemistry Chemical Physics* 17.16. DOI: 10.1039/c5cp00372e.

Ulvestad, A., K. Sasikumar et al. (2016). 'In Situ 3D Imaging of Catalysis Induced Strain in Gold Nanoparticles'. In: *Journal of Physical Chemistry Letters* 7.15. DOI: 10.1021/acs.jpclett.6b01038.

Unertl, W. (1996). 'Chapter 1 - Surface Crystallography'. In: *Physical Structure*. Ed. by W. Unertl. Vol. 1. Handbook of Surface Science. North-Holland. DOI: doi.org/10.1016/S1573-4331(96)80006-0.

Van Beurden, P. and G. J. Kramer (2004). 'Atomistic mechanisms for the (1×1) - hex surface phase transformations of Pt(100)'. In: *Journal of Chemical Physics* 121.5. DOI: 10.1063/1.1763834.

van den Broek, A., J. van Grondelle and R. van Santen (1999). 'Determination of Surface Coverage of Catalysts: Temperature Programmed Experiments on Platinum and Iridium Sponge Catalysts after Low Temperature Ammonia Oxidation'. In: *Journal of Catalysis* 185.2. DOI: doi.org/10.1006/jcat.1999.2506.

Van der Walt, S., S. C. Colbert and G. Varoquaux (2011). 'The NumPy Array: A Structure for Efficient Numerical Computation'. In: *Computing in Science Engineering* 13.2. DOI: 10.1109/MCSE.2011.37.

Van Heel, M. and M. Schatz (2005). 'Fourier shell correlation threshold criteria'. In: *Journal of Structural Biology* 151.3. DOI: 10.1016/j.jsb.2005.05.009.

Van Hove, M. et al. (1981). 'The surface reconstructions of the (100) crystal faces of iridium, platinum and gold: I. Experimental observations and possible structural models'. In: *Surface Science* 103.1. DOI: doi.org/10.1016/0039-6028(81)90107-2.

Van Spronsen, M. A., J. W. Frenken and I. M. Groot (2017). 'Observing the oxidation of platinum'. In: *Nature Communications* 8.1. DOI: 10.1038/s41467-017-00643-z.

Vartanyants, I. A. and I. K. Robinson (2001). 'Partial coherence effects on the imaging of small crystals using coherent x-ray diffraction'. In: *Journal of Physics: Condensed Matter* 13.47. DOI: 10.1088/0953-8984/13/47/305.

Vaxelaire, N. et al. (2010). '3D strain imaging in sub-micrometer crystals using cross-reciprocal space measurements: Numerical feasibility and experimental methodology'. In: *Nuclear Instruments and Methods in Physics Research Section B: Beam Interactions with Materials and Atoms* 268.3–4. DOI: 10.1016/j.nimb.2009.09.010.

Vendelbo, S. B. et al. (2014). 'Visualization of oscillatory behaviour of Pt nanoparticles catalysing CO oxidation'. In: *Nature Materials* 13.9. DOI: 10.1038/nmat4033.

Vicente, R. A. et al. (2021). 'Bragg Coherent Diffraction Imaging for In Situ Studies in Electrocatalysis'. In: *ACS Nano*. DOI: 10.1021/acsnano.1c01080.

Vlieg, E. (1997). 'Integrated Intensities Using a Six-Circle Surface X-ray Diffractometer'. In: *Journal of Applied Crystallography* 30 (5). DOI: 10.1107/S0021889897002537.

— (2000). 'ROD: a program for surface X-ray crystallography'. In: *Journal of Applied Crystallography* 33.2. DOI: doi.org/10.1107/S0021889899013655.

Vogt, C. and B. M. Weckhuysen (2022). 'The concept of active site in heterogeneous catalysis'. In: *Nature Reviews Chemistry* 6.2. DOI: 10.1038/s41570-021-00340-y.

Vries, J. G. de and S. D. Jackson (2012). 'Homogeneous and heterogeneous catalysis in industry'. In: *Catal. Sci. Technol.* 2 (10). DOI: 10.1039/C2CY90039D.

Wachs, I. E. (2022). 'Number of surface sites and turnover frequencies for oxide catalysts'. In: *Journal of Catalysis* 405. DOI: doi.org/10.1016/j.jcat.2021.12.032.

Wang, C., U. Steiner and A. Sepe (2018). 'Synchrotron Big Data Science'. In: *Small* 14 (46). DOI: 10.1002/smll.201802291.

Wang, C., F. Yu et al. (2021). 'Deploying the Big Data Science Center at the Shanghai Synchrotron Radiation Facility: The first superfacility platform in China'. In: *Machine Learning: Science and Technology* 2 (3). DOI: 10.1088/2632-2153/abe193.

Wang, H. et al. (2016). 'Direct and continuous strain control of catalysts with tunable battery electrode materials'. In: *Science* 354.6315. DOI: 10.1126/science.aaf7680.

Wang, Z., O. Gorobtsov and A. Singer (2020). 'An algorithm for Bragg coherent x-ray diffractive imaging of highly strained nanocrystals'. In: *New Journal of Physics* 22.1. DOI: 10.1088/1367-2630/ab61db.

Warren, B. (1990). *X-Ray Diffraction*. Dover Publications. Chap. 3.

Waseda, Y., K. Hirata and M. Ohtani (1975). 'High-temperature thermal expansion of platinum, tantalum, molybdenum, and tungsten measured by X-ray diffraction'. In: *High Temperatures-High Pressures* 7.2.

Wei, T.-C. and J. Phillips (1996). 'Thermal and Catalytic Etching: Mechanisms of Metal Catalyst Reconstruction'. In: Advances in Catalysis 41. Ed. by D. Eley, W. O. Haag and B. Gates. DOI: doi.org/10.1016/S0360-0564(08)60044-9.

Weinberg, W. H. (1996). 'Eley-Rideal Surface Chemistry: Direct Reactivity of Gas Phase Atomic Hydrogen with Adsorbed Species'. In: *Accounts of Chemical Research* 29.10. DOI: 10.1021/ar9500980.

Weiner, S. C. (1998). 'Technology vision 2020: The U.S. chemical industry'. In: *Air pollution in the 21st century*. Ed. by T. Schneider. Vol. 72. Studies in Environmental Science. Elsevier. DOI: doi.org/10.1016/S0166-1116(98)80054-X.

Weissmüller, J. (2019). 'Adsorption–strain coupling at solid surfaces'. In: *Current Opinion in Chemical Engineering* 24. DOI: doi.org/10.1016/j.coche.2018.12.012.

Westerström, R. et al. (2008). 'Structure and reactivity of a model catalyst alloy under realistic conditions'. In: *Journal of Physics: Condensed Matter* 20.18. DOI: 10.1088/0953-8984/20/18/184018.

Weststrate, C. et al. (2006). 'Ammonia oxidation on Pt(410)'. In: *Journal of Catalysis* 242.1. DOI: doi.org/10.1016/j.jcat.2006.06.011.

Whitehead, L. W. et al. (2009). 'Diffractive Imaging Using Partially Coherent X Rays'. In: *Phys. Rev. Lett.* 103 (24). DOI: 10.1103/PhysRevLett.103.243902.

WHO (2023). *Air pollution*. URL: www.who.int/health-topics/air-pollution (visited on 25/07/2023).

Wild, U. et al. (2000). 'Surface composition and possible rearrangement of disperse Pt and Rh catalysts: does the presence of carbon and oxygen contribute to different catalytic properties?' In: *Catalysis Letters* 67.2. DOI: 10.1023/A:1019061420659.

Williams, G. J. et al. (2007). 'Coherent diffractive imaging and partial coherence'. In: *Phys. Rev. B* 75 (10). DOI: 10.1103/PhysRevB.75.104102.

Willmott, P. (2009). *An Introduction to Synchrotron Radiation: Techniques and Applications*. John Wiley & Sons, Ltd. DOI: 10.1002/9781119280453.

Winterbottom, W. (1967). 'Equilibrium shape of a small particle in contact with a foreign substrate'. In: *Acta Metallurgica* 15.2. DOI: doi.org/10.1016/0001-6160(67)90206-4.

Wood, E. A. (1964). 'Vocabulary of Surface Crystallography'. In: *Journal of Applied Physics* 35.4. DOI: 10.1063/1.1713610.

Wu, C.-Y. et al. (2017). 'High-spatial-resolution mapping of catalytic reactions on single particles'. In: *Nature* 541.7638. DOI: 10.1038/nature20795.

Wu, L. et al. (2021). 'Three-dimensional coherent X-ray diffraction imaging via deep convolutional neural networks'. In: *npj Computational Materials* 7.1. DOI: 10.1038/s41524-021-00644-z.

Wu, T., M. Sun and B. Huang (2021). 'Atomic-Strain Mapping of High-Index Facets in Late-Transition-Metal Nanoparticles for Electrocatalysis'. In: *Angewandte Chemie International Edition* 60.42. DOI: doi.org/10.1002/anie.202110636.

Wulff, G. (1901). 'XXV. Zur Frage der Geschwindigkeit des Wachsthums und der Auflösung der Krystallflächen'. In: *Zeitschrift für Kristallographie - Crystalline Materials* 34.1-6. DOI: doi:10.1524/zkri.1901.34.1.449.

Xiong, G. et al. (2014). 'Coherent X-ray diffraction imaging and characterization of strain in silicon-on-insulator nanostructures'. In: *Advanced Materials* 26.46. DOI: 10.1002/adma.201304511.

Yan, H. and L. Li (2014). 'X-ray dynamical diffraction from single crystals with arbitrary shape and strain field: A universal approach to modeling'. In: *Physical Review B - Condensed Matter and Materials Physics* 89 (1). DOI: 10.1103/PhysRevB.89.014104.

Yang, D., N. W. Phillips and F. Hofmann (2019). 'Mapping data between sample and detector conjugated spaces in Bragg coherent diffraction imaging'. In: *Journal of Synchrotron Radiation* 26.6. DOI: 10.1107/S160057751901302X.

Yang, W. et al. (2013). 'Coherent diffraction imaging of nanoscale strain evolution in a single crystal under high pressure'. In: *Nature Communications* 4. DOI: 10.1038/ncomms2661.

Yau, A. et al. (2017). 'Imaging the Hydrogen Absorption Dynamics of Individual Grains in Polycrystalline Palladium Thin Films in 3D'. In: *ACS Nano* 11.11. DOI: 10.1021/acsnano.7b04735.

Yin, D. et al. (2017). 'A CyberGIS-Jupyter Framework for Geospatial Analytics at Scale'. In: *Proceedings of the Practice and Experience in Advanced Research Computing 2017 on Sustainability, Success and Impact*. PEARC17. New Orleans, LA, USA: Association for Computing Machinery. DOI: 10.1145/3093338.3093378.

Zakharchenko, N. I. (2001). 'Catalytic properties of platinum(II, III) oxide in ammonia oxidation'. In: *Russian Journal of Applied Chemistry* 74.10. DOI: 10.1023/A:1014861303777.

Zambelli, T. et al. (1996). 'Identification of the "Active Sites" of a Surface-Catalyzed Reaction'. In: *Science* 273.5282. DOI: 10.1126/science.273.5282.1688.

Zeng, Y. F. (2008). 'Surface Structure and Reactivity of Platinum in the Oxidation of Ammonia'. PhD thesis.

Zeng, Y. F. and R. Imbihl (2009). 'Structure sensitivity of ammonia oxidation over platinum'. In: *Journal of Catalysis* 261.2. DOI: doi.org/10.1016/j.jcat.2008.05.032.

Zhang, M. et al. (2019). 'How to Measure the Reaction Performance of Heterogeneous Catalytic Reactions Reliably'. In: *Joule* 3.12. DOI: doi.org/10.1016/j.joule.2019.11.005.

Zhang, S. et al. (2014). 'Tuning Nanoparticle Structure and Surface Strain for Catalysis Optimization'. In: *Journal of the American Chemical Society* 136.21. DOI: 10.1021/ja5030172.

Zhdanov, V. P. and B. Kasemo (1997). 'Effect of adsorption on surface roughening'. In: *Phys. Rev. B* 56 (16). DOI: 10.1103/PhysRevB.56.R10067.

— (1998). 'Surface roughening: Kinetics, adsorbate-induced effects, and manifestation in catalytic reactions'. In: *The Journal of Chemical Physics* 108.11. DOI: 10.1063/1.476504.

Zhong, L. et al. (2021). 'Effect of manganese promotion on the activity and selectivity of cobalt catalysts for CO preferential oxidation'. In: *Applied Catalysis B: Environmental* 297 (June). DOI: 10.1016/j.apcatb.2021.120397.

Zhou, K. and Y. Li (2012). 'Catalysis Based on Nanocrystals with Well-Defined Facets'. In: *Angewandte Chemie International Edition* 51.3. DOI: doi.org/10.1002/anie.201102619.

Zhu, J. F. et al. (2003). 'In situ high-resolution XPS studies on adsorption of NO on Pt(111)'. In: *Surface Science* 529.3. DOI: 10.1016/S0039-6028(03)00298-X.

Appendices

Appendix A

Nanoparticles study

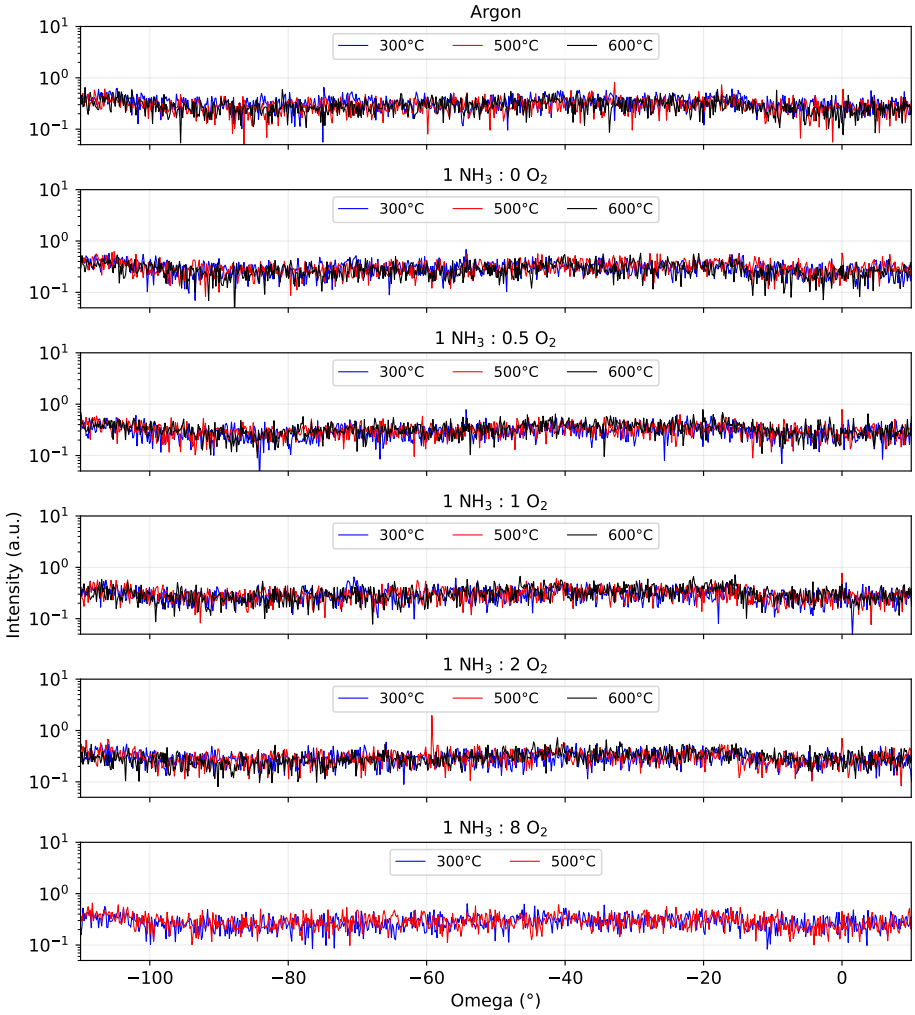

Figure A.1: Integrated intensity in a 0.1° range around the value of the (200) scattering angle, as a function of the in-plane sample angle ω.

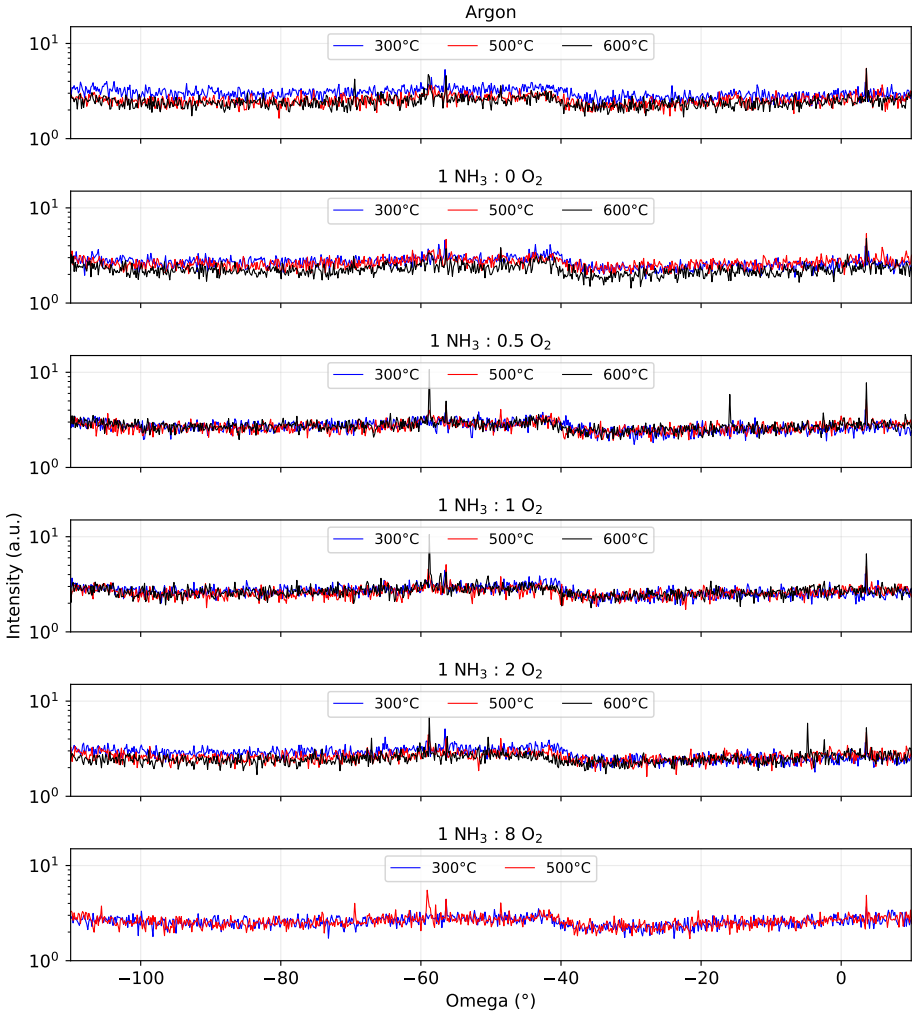

Figure A.2: Integrated intensity in a $0.1°$ *range around the value of the (111) scattering angle, as a function of the in-plane sample angle* ω*.*

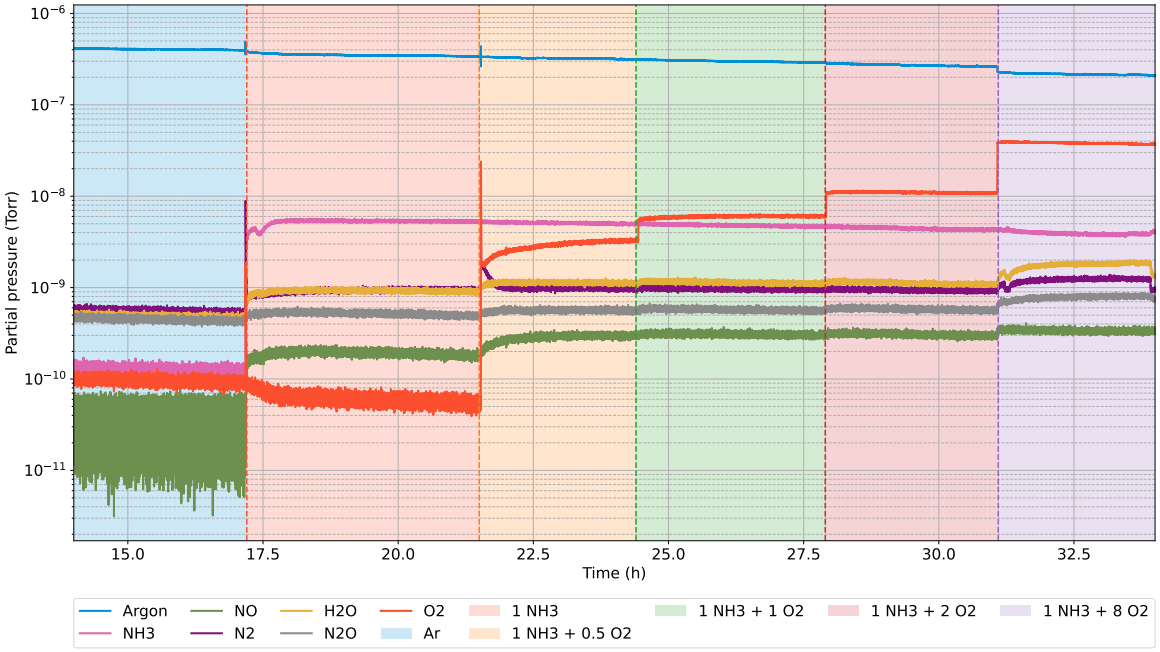

Figure A.3: Time dependent partial pressures recorded from a leak in the reactor output by a residual gas analyser (RGA) during the SXRD experiment on the non-patterned sample containing Pt nanoparticles at 300 °C. *Vertical dotted lines indicate transitions between two conditions for which the NH_3 and O_2 flow is indicated in the legend.*

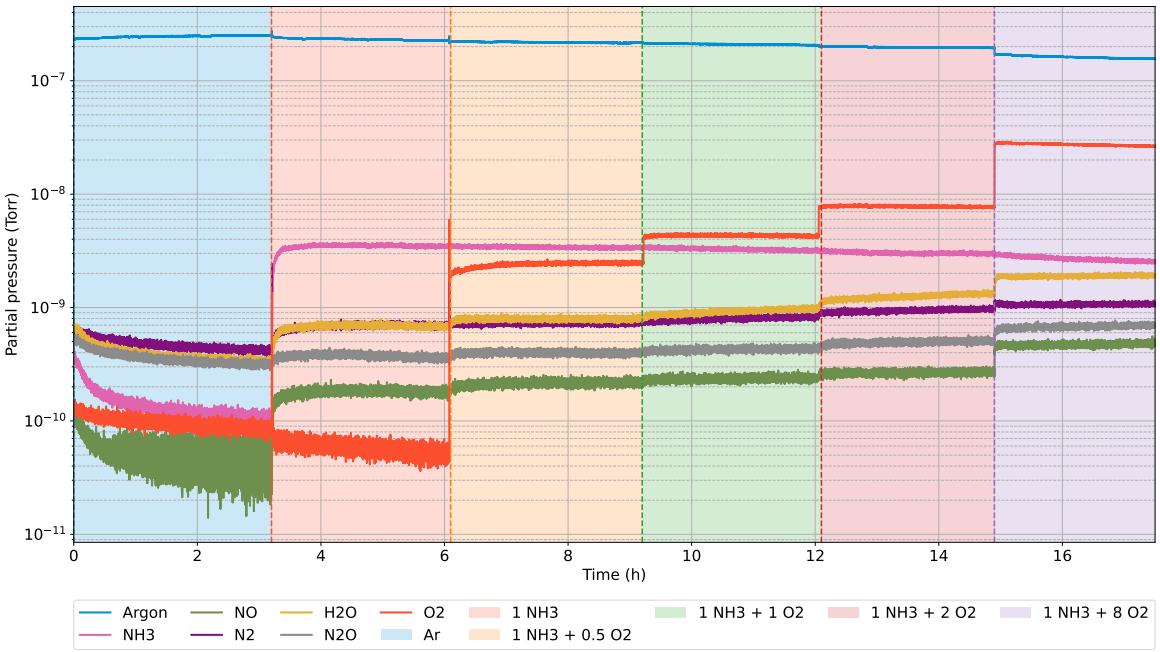

Figure A.4: Time dependent partial pressures recorded from a leak in the reactor output by a residual gas analyser (RGA) during the SXRD experiment on the non-patterned sample containing Pt nanoparticles at 500 °C. *Vertical dotted lines indicate transitions between two conditions for which the NH_3 and O_2 flow is indicated in the legend.*

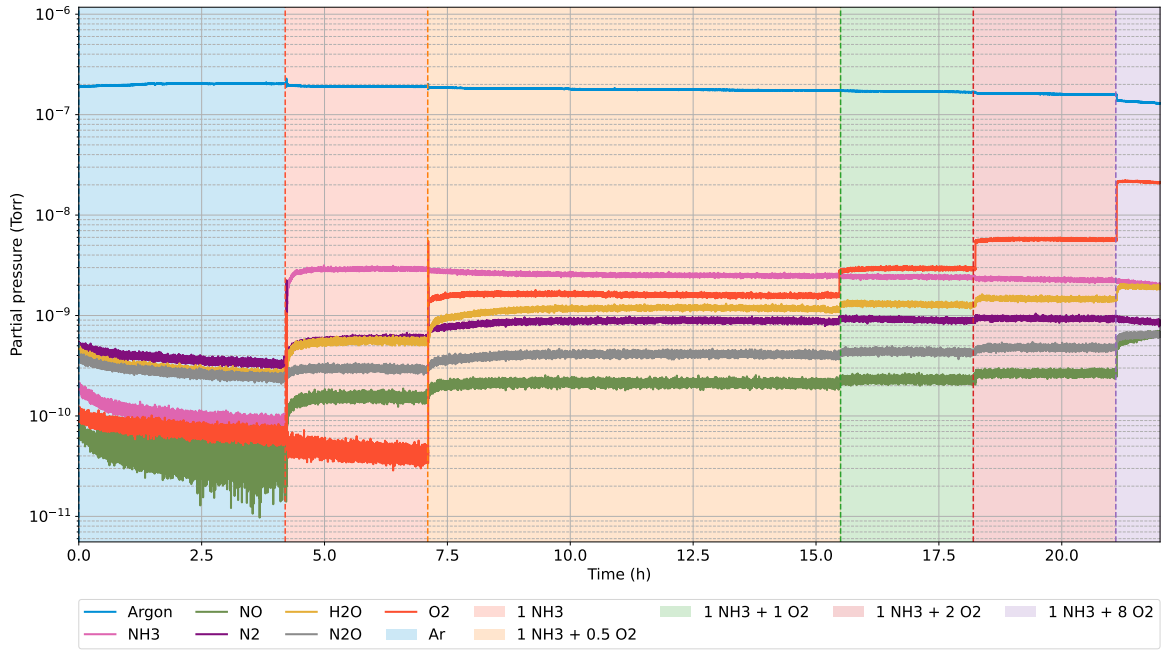

Figure A.5: Time dependent partial pressures recorded from a leak in the reactor output by a residual gas analyser (RGA) during the SXRD experiment on the non-patterned sample containing Pt nanoparticles at 600 °C. Vertical dotted lines indicate transitions between two conditions for which the NH_3 and O_2 flow is indicated in the legend.

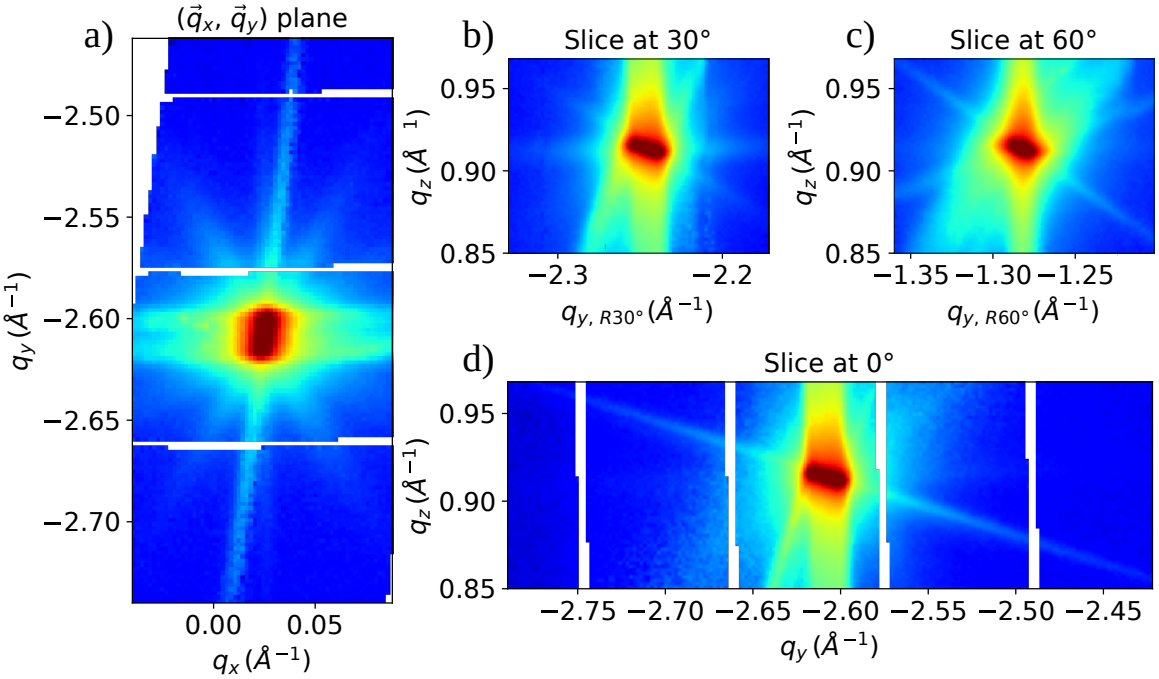

Figure A.6: Reciprocal space volume around the $(\bar{1}11)$ Bragg peak, collected at 300 °C, under argon atmosphere. a) Projection perpendicular to $\vec{q}_z$. b-c) Slices in the $(\vec{q}_y, \vec{q}_z)$ plane after rotation of the $\vec{q}_x$ and $\vec{q}_y$ axis around the $\vec{q}_z$ axis by 30° and 60° to highlight the presence of crystal truncation rods in different directions. d) Slice in the $(\vec{q}_y, \vec{q}_z)$ plane to highlight the presence of a crystal truncation rod in the $[1\bar{1}1]$ direction.

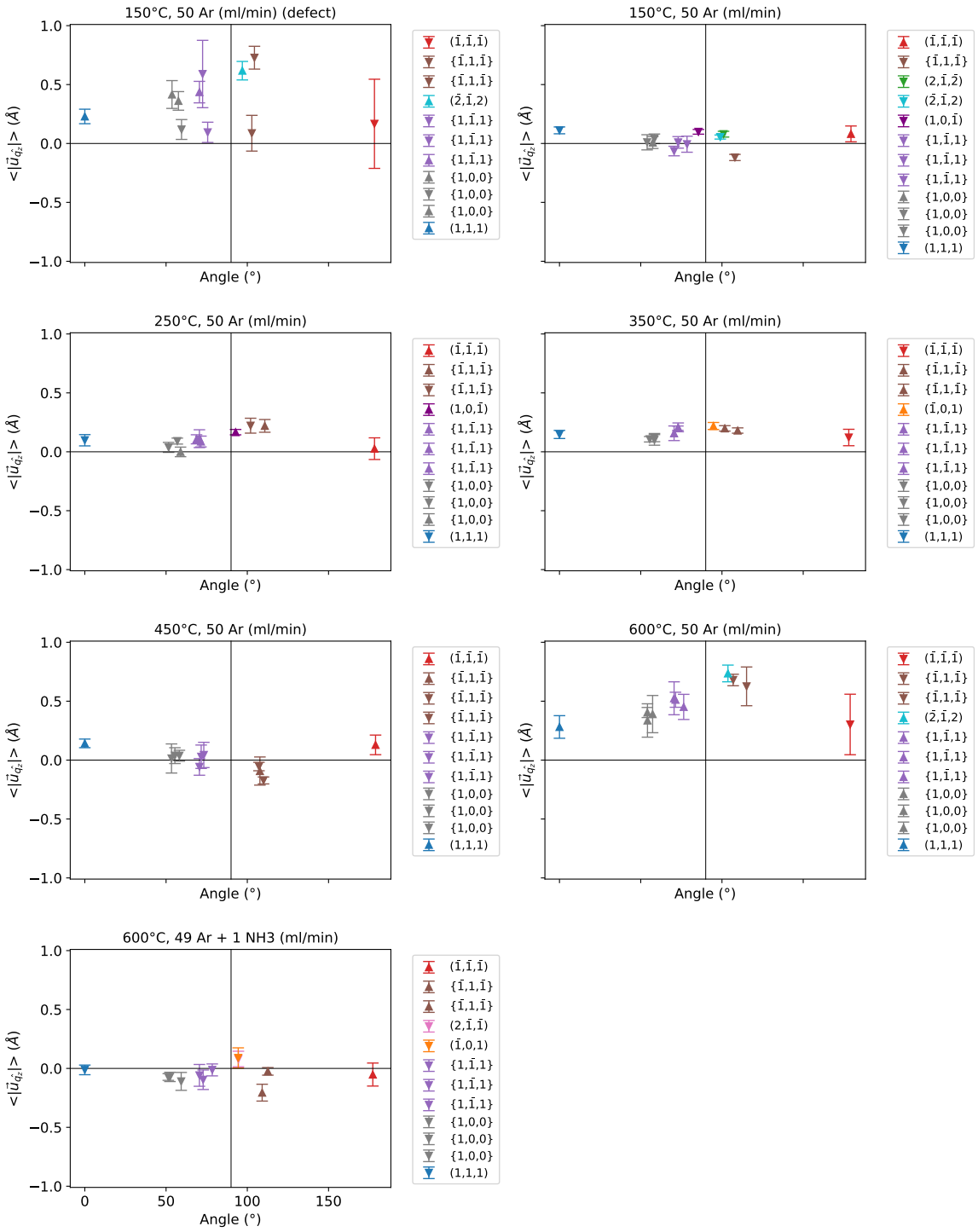

Figure A.7: Mean value and standard deviation of the displacement ($\vec{u}_{\hat{q}_z}$) distribution as a function of the angle between the normal of each facet on the particle surface and the [111] direction. Upwards and downwards arrow are represented for respectively positive and negative displacement.

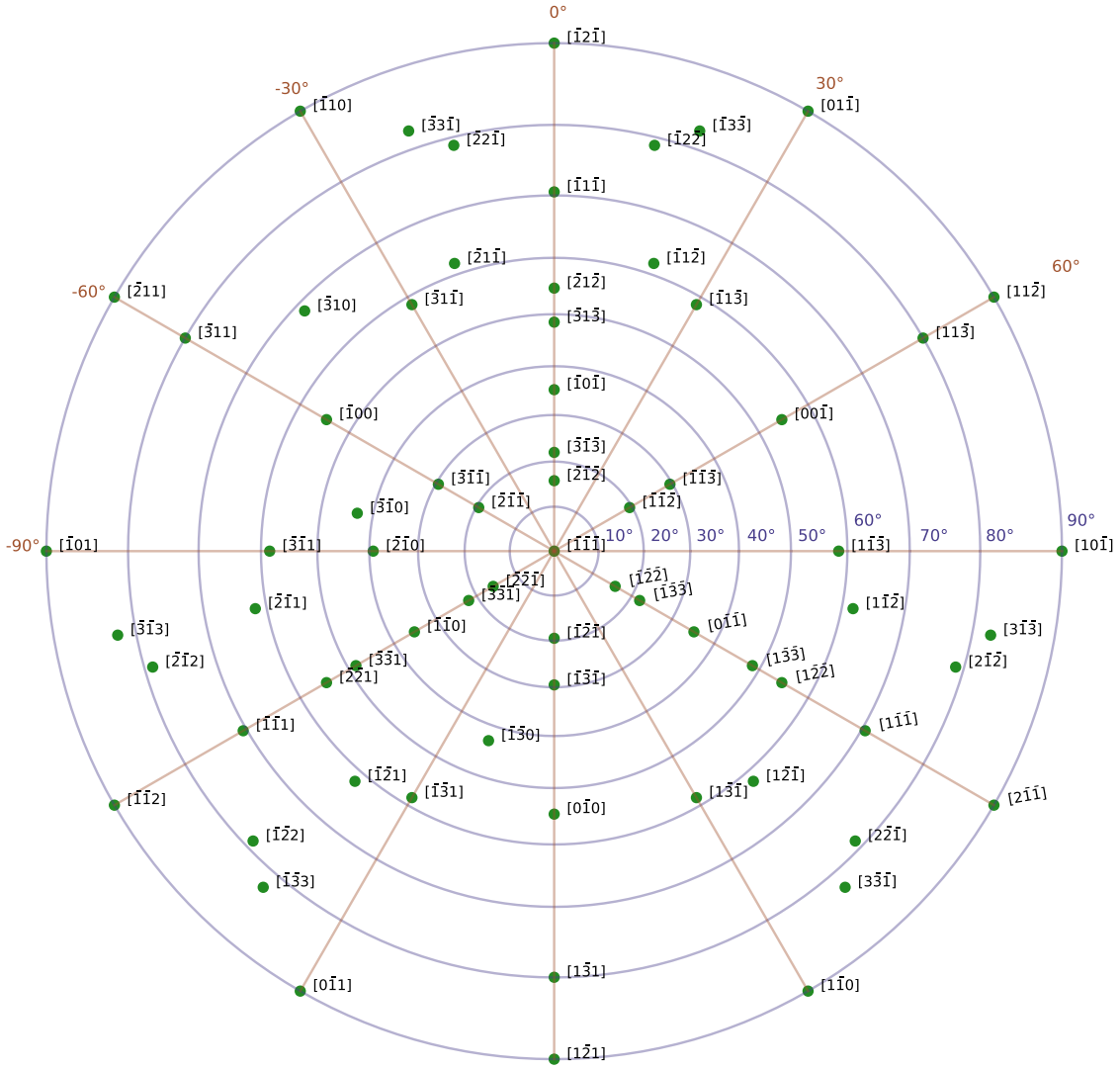

Figure A.8: Stereographic projection perpendicular to $[\bar{1}\bar{1}\bar{1}]$ crystallographic orientation. The circles describe the angle with the $[\bar{1}\bar{1}\bar{1}]$ direction from 0° (centre) to 90° (outer-ring).

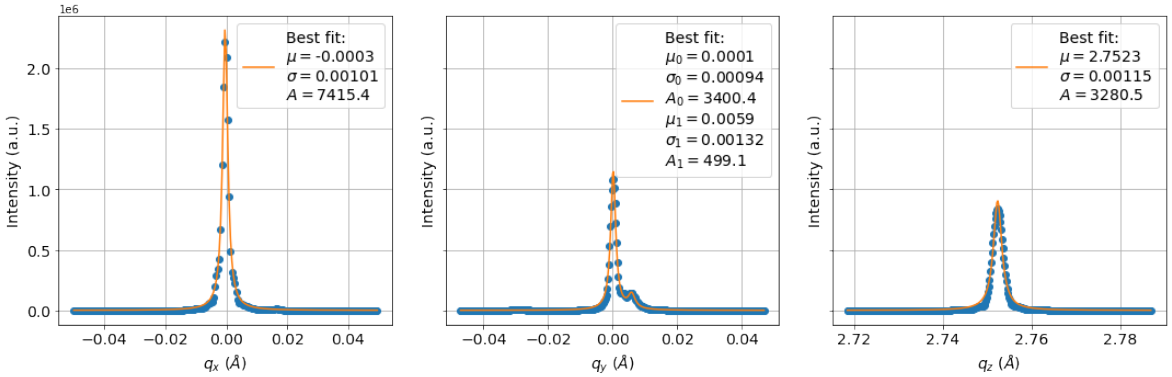

Figure A.9: Sum of Bragg peak intensity perpendicular to $\vec{q}_x$ and $\vec{q}_y$ and $\vec{q}_z$, fitted by Lorentzian profiles.

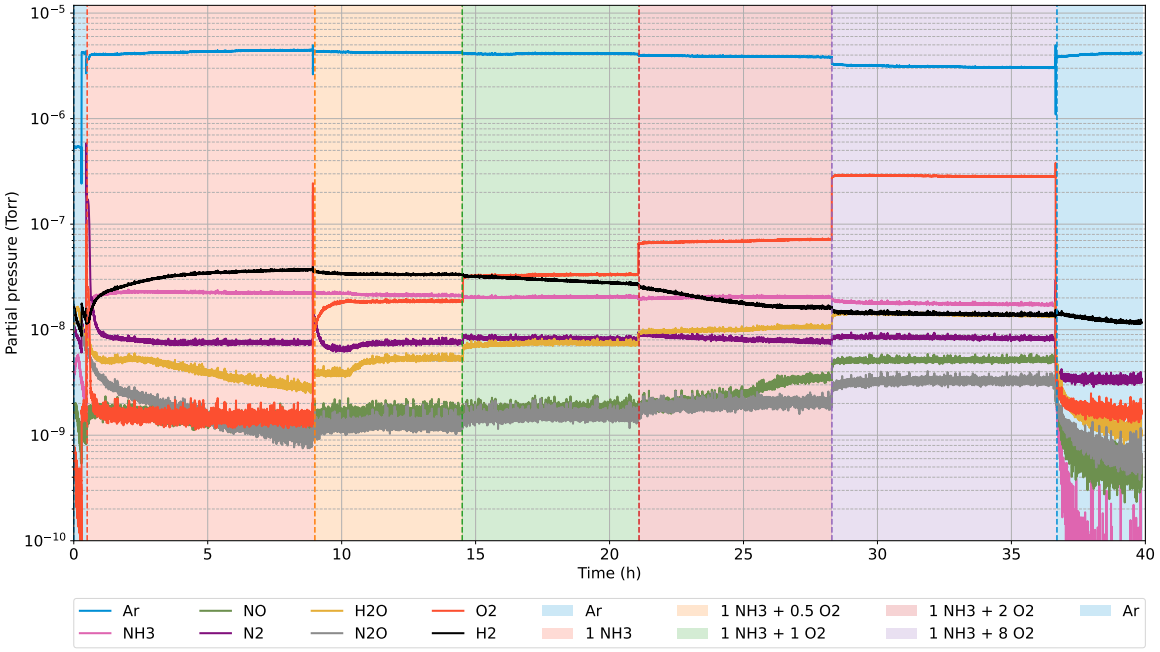

Figure A.10: Time dependent partial pressures recorded from a leak in the reactor output by a residual gas analyser (RGA) during the BCDI experiment on the patterned sample containing Pt nanoparticles at 300 °C. *Vertical dotted lines indicate transitions between two conditions for which the NH_3 and O_2 flow is indicated in the legend.*

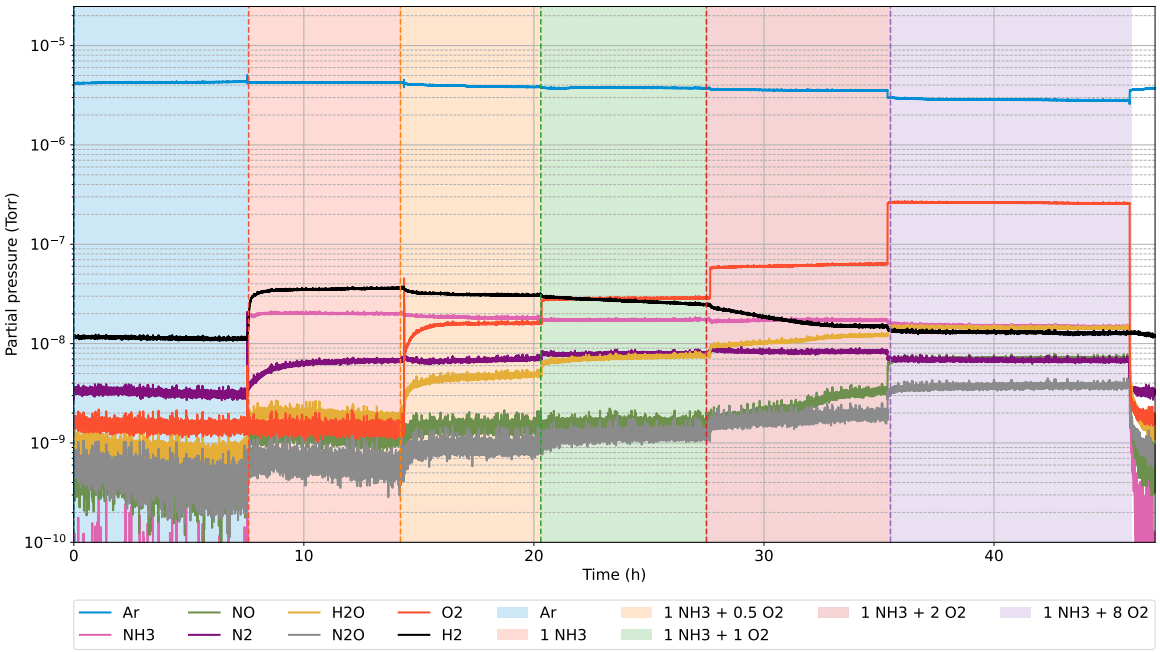

Figure A.11: Time dependent partial pressures recorded from a leak in the reactor output by a residual gas analyser (RGA) during the BCDI experiment on the patterned sample containing Pt nanoparticles at 400 °C. *Vertical dotted lines indicate transitions between two conditions for which the NH_3 and O_2 flow is indicated in the legend.*

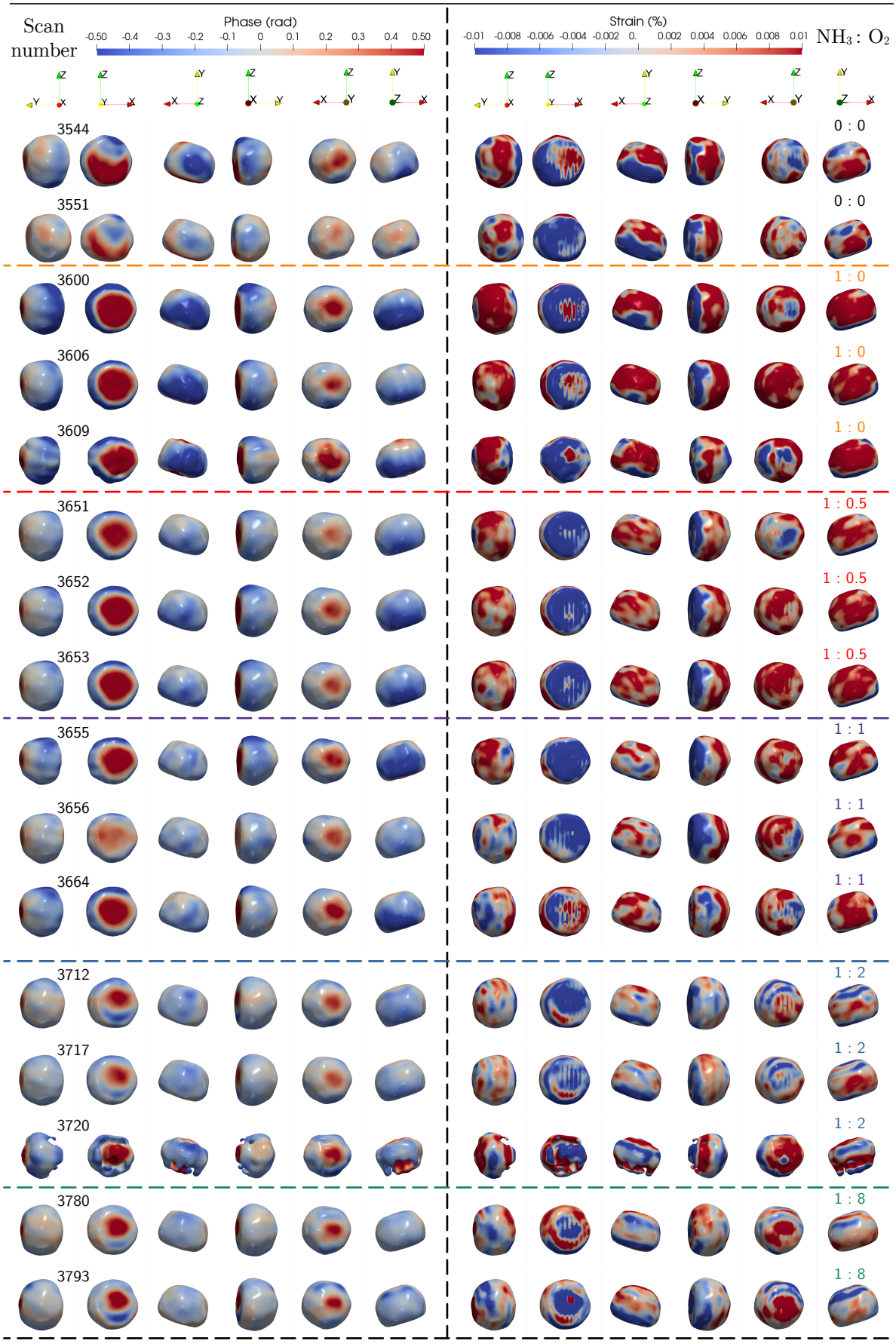

Figure A.12: Operando reconstructions of particle B during ammonia oxidation at 300°C. The ammonia to oxygen ratio is indicated in the top right part of the image, the scan number in the top left.

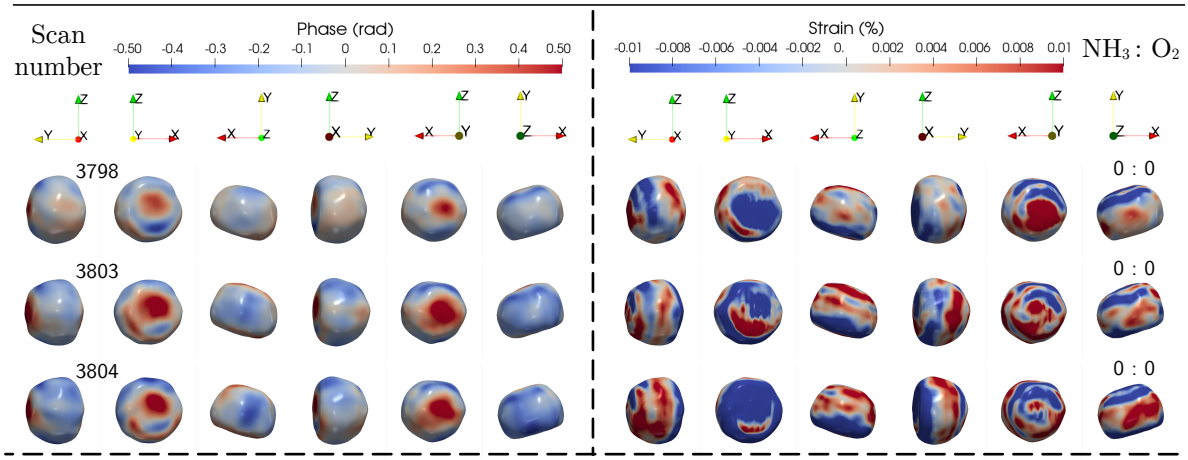

Figure A.13: Operando reconstructions of particle B during ammonia oxidation at 300°C. The ammonia to oxygen ratio is indicated in the top right part of the image, the scan number in the top left.

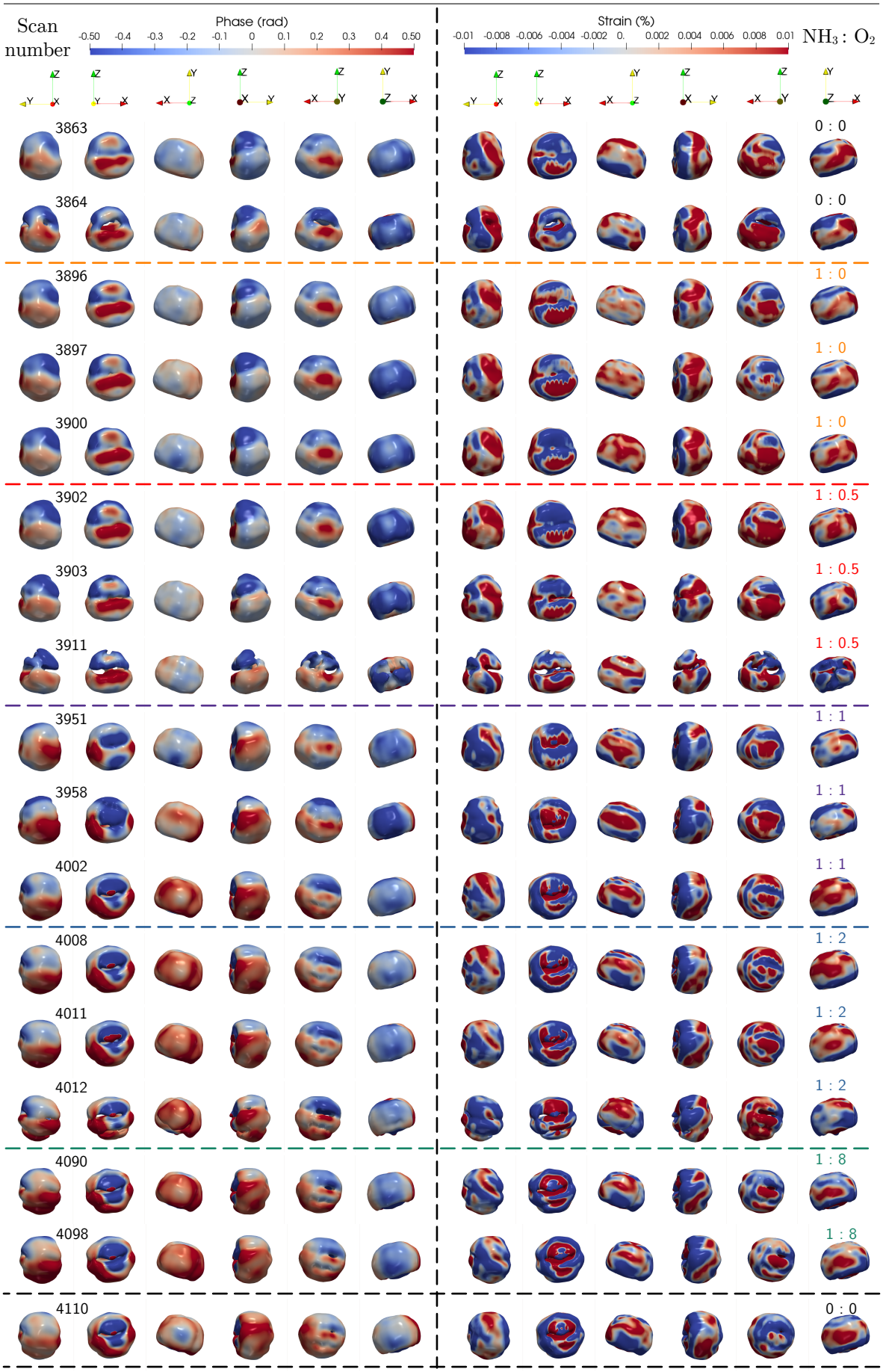

Figure A.14: Operando reconstructions of particle B during ammonia oxidation at 400°C. The ammonia to oxygen ratio is indicated in the top right part of the image, the scan number in the top left.

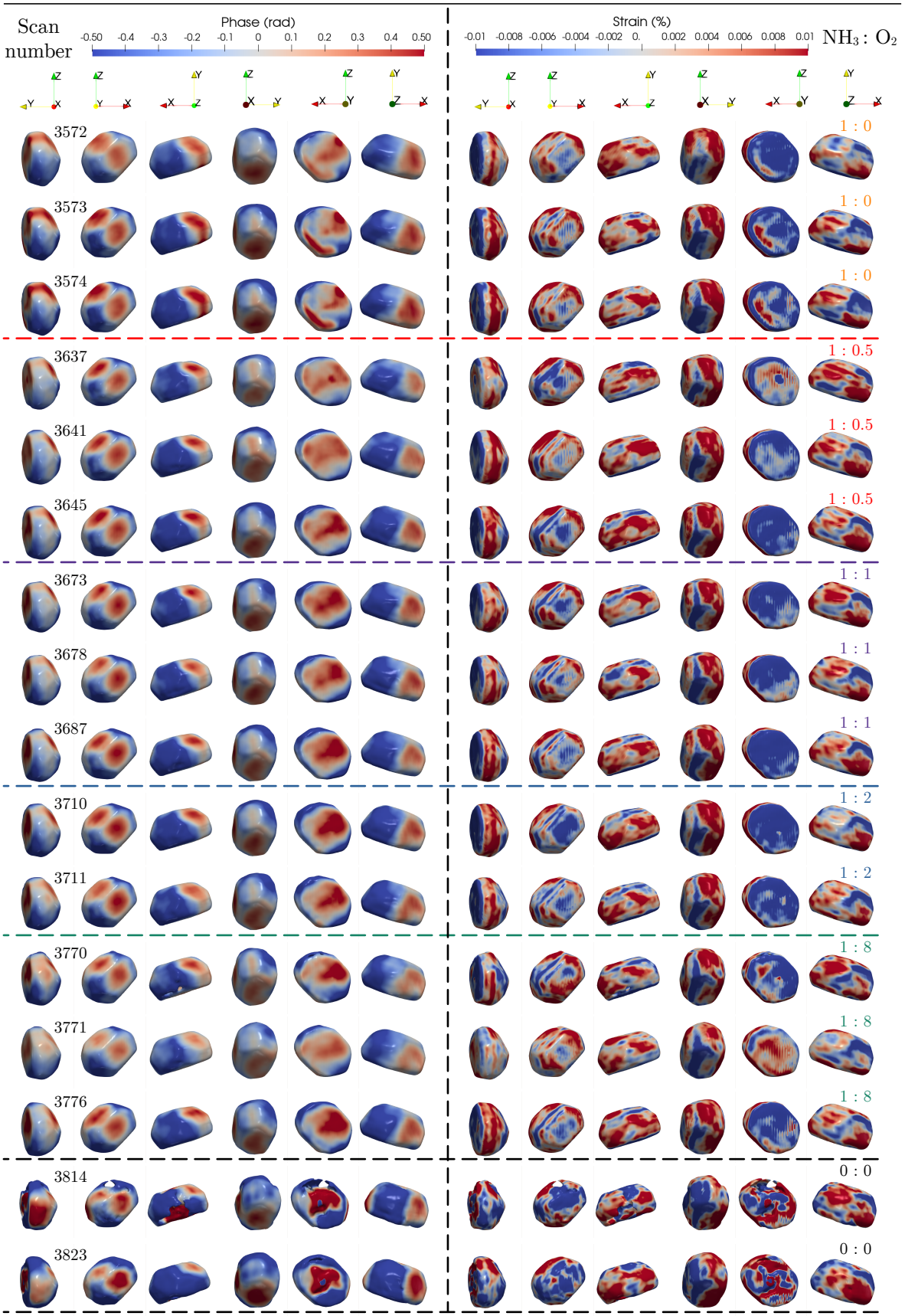

Figure A.15: Operando reconstructions of particle C during ammonia oxidation at 300°C. The ammonia to oxygen ratio is indicated in the top right part of the image, the scan number in the top left.

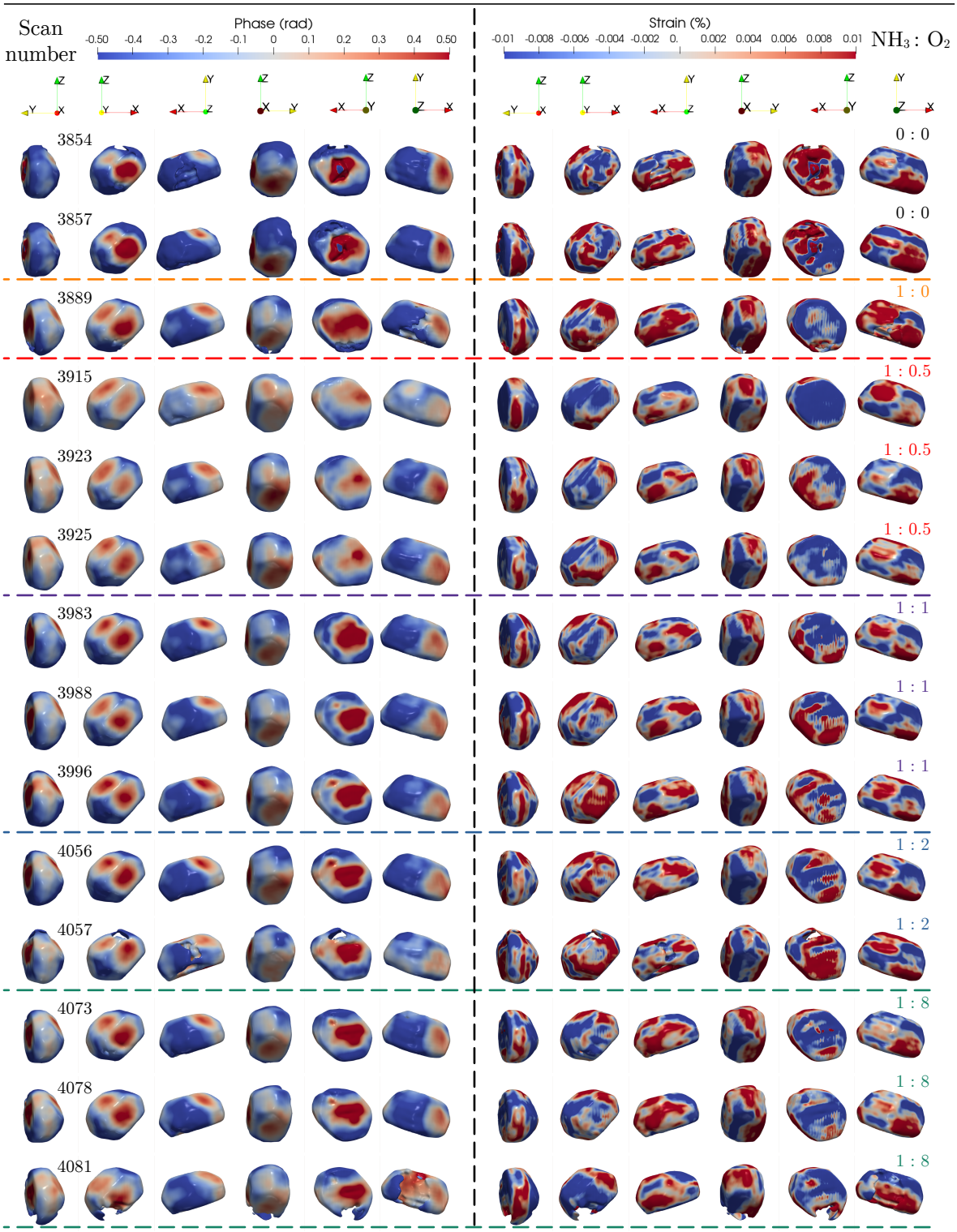

Figure A.16: Operando reconstructions of particle C during ammonia oxidation at 400°C. The ammonia to oxygen ratio is indicated in the top right part of the image, the scan number in the top left.

Appendix B

Single crystals study

Structure	Interplanar	Oxygen pressure										
	spacing (Å)	80 mbar		5 mbar								
		Time since gas introduction (end of measurement)										
		03h23	09h53	00h34	04h03	08h00	15h57	22h56	24h08	25h43	26h36	27h28
Pt(111)-(6 × 6)-R±8.8°	3.01 ± 0.01	0	0	0	0	0	0	0	0	0	0	0
Pt(111)-(6 × 6)-R±8.8°	2.92 ± 0.03	0	0	x	x	x	x	x	x	0	x	x
Pt(111)-(6 × 6)-R±8.8°	2.87 ± 0.02	x	x	0	0	0	0	0	0	0	0	0
Pt(111)-(6 × 6)-R±8.8°	2.79 ± 0.07	x	x	x	x	0	0	0	0	0	0	0
Pt(111)-(8 × 8)	2.69 ± 0.02	x	0	x	x	x	x	x	0	0	0	0
Pt(111)-(8 × 8)	1.53 ± 0.00	0	nv	nv	0	nv	nv	nv	nv	nv	nv	nv

Table B.1: Interplanar spacings computed from signals observed during in-plane reciprocal maps, for different oxygen pressure and exposition times for Pt(111). The three markers (0, x, nv) correspond to observed, non-observed, and non visible signals (i.e. not in the area spanned by the map). The errors on the interplanar spacings are computed by considering the positions of similar peaks in q-space.

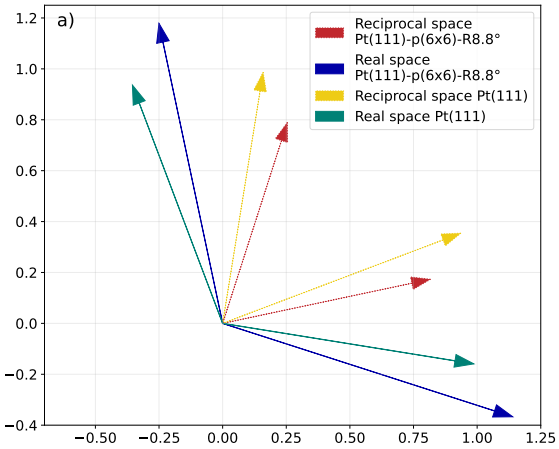

Figure B.1: Sketch of Pt(111) surface and Pt(111)-(6 × 6) structure unit cell vectors, in real and reciprocal space (a).

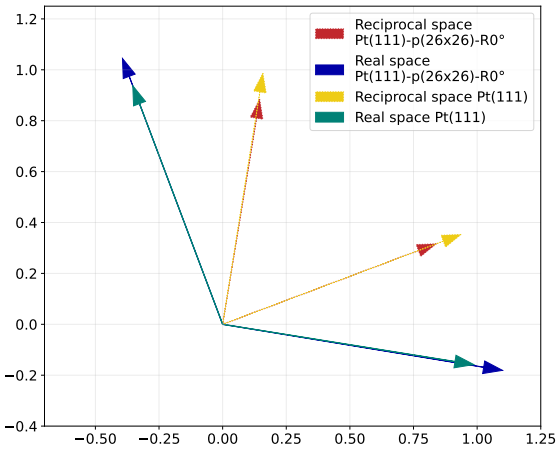

Figure B.2: Sketch of Pt(111) surface and Pt(111)-(8×8) structure unit cell vectors, in real and reciprocal space (a).

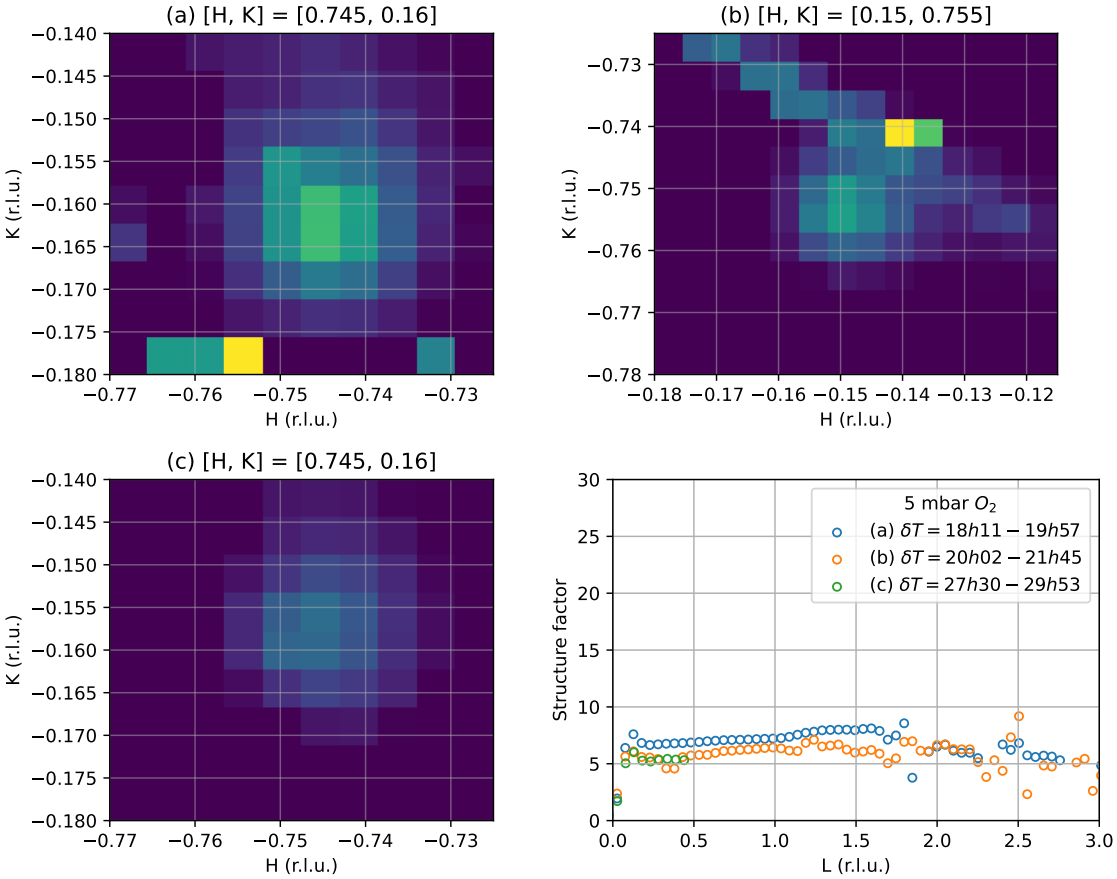

Figure B.3: SSR observed under 5 mbar *of* O_2.

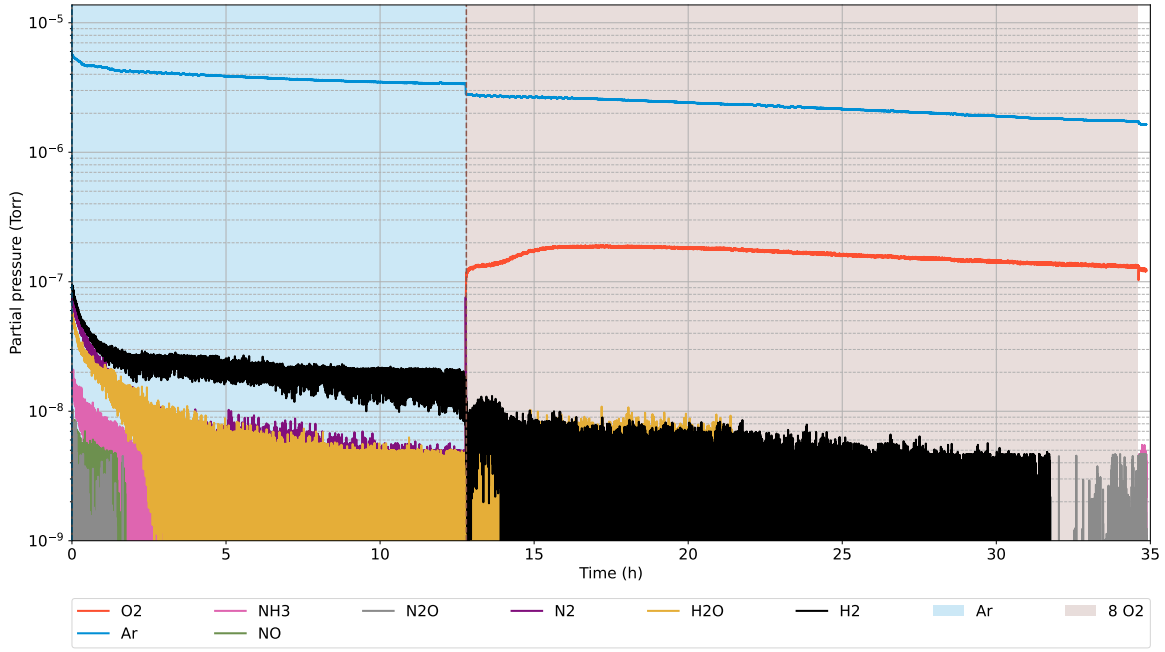

Figure B.4: Time dependent partial pressures recorded from a leak in the reactor output by a residual gas analyser (RGA) during the SXRD experiment on the Pt(111) single crystal at 450 °C. Vertical dotted lines indicate transitions between two conditions for which the NH_3 and O_2 flow is indicated in the legend. The RGA electron multiplier is off for all the masses.

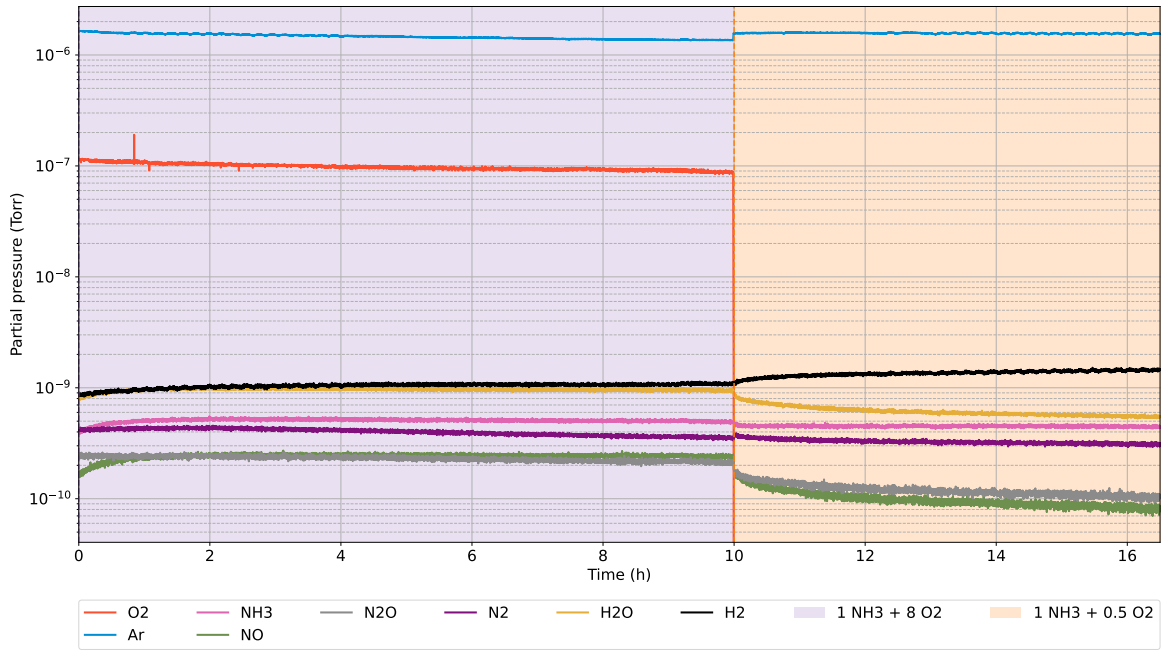

Figure B.5: Time dependent partial pressures recorded from a leak in the reactor output by a residual gas analyser (RGA) during the SXRD experiment on the Pt(111) single crystal at 450 °C. Vertical dotted lines indicate transitions between two conditions for which the NH_3 and O_2 flow is indicated in the legend. The RGA electron multiplier is on for all the masses besides oxygen and argon.

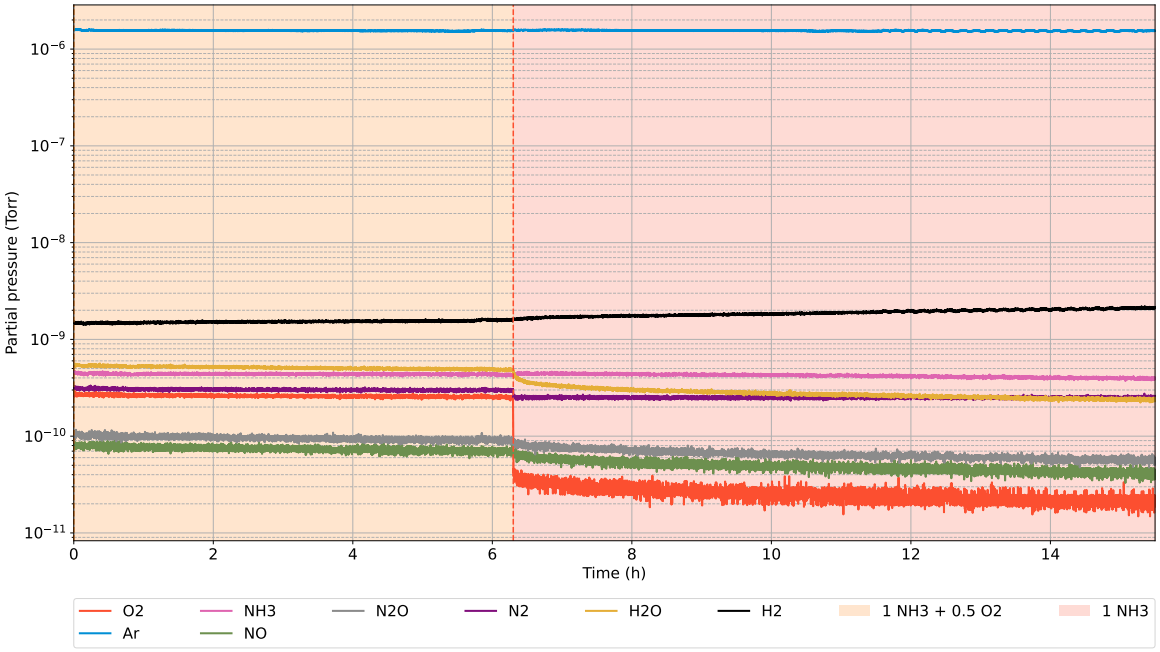

Figure B.6: Time dependent partial pressures recorded from a leak in the reactor output by a residual gas analyser (RGA) during the SXRD experiment on the Pt(111) single crystal at 450 °C. Vertical dotted lines indicate transitions between two conditions for which the NH_3 and O_2 flow is indicated in the legend. The RGA electron multiplier is on for all the masses besides argon.

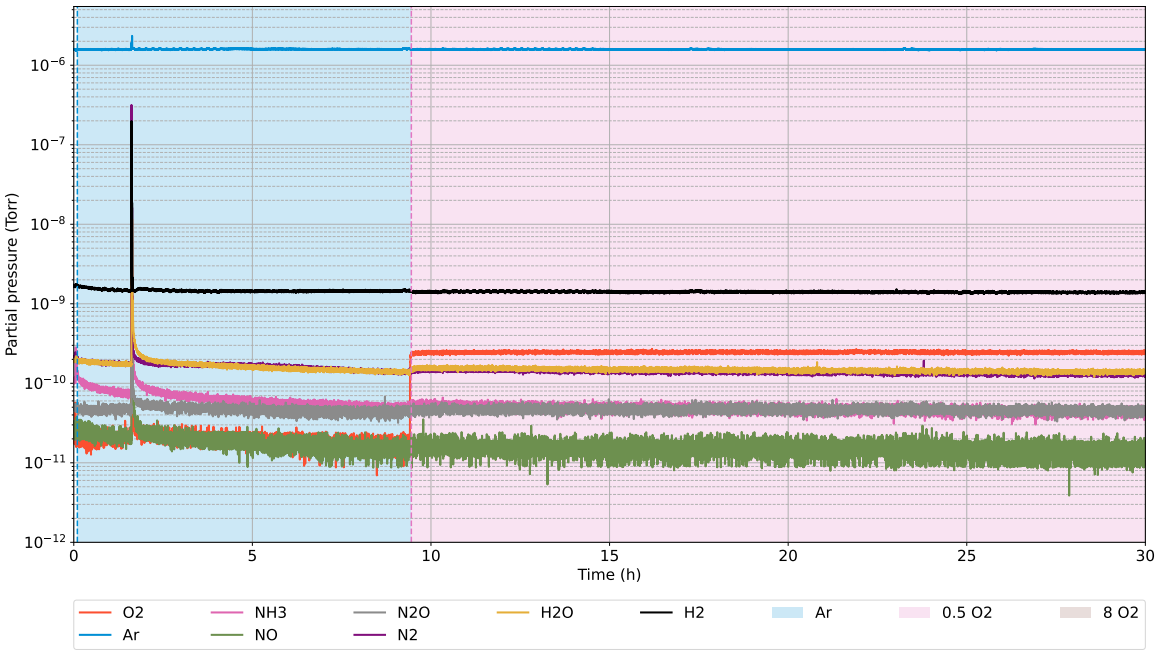

Figure B.7: Time dependent partial pressures recorded from a leak in the reactor output by a residual gas analyser (RGA) during the SXRD experiment on the Pt(111) single crystal at 450 °C. Vertical dotted lines indicate transitions between two conditions for which the NH_3 and O_2 flow is indicated in the legend. The RGA electron multiplier is on for all the masses besides argon.

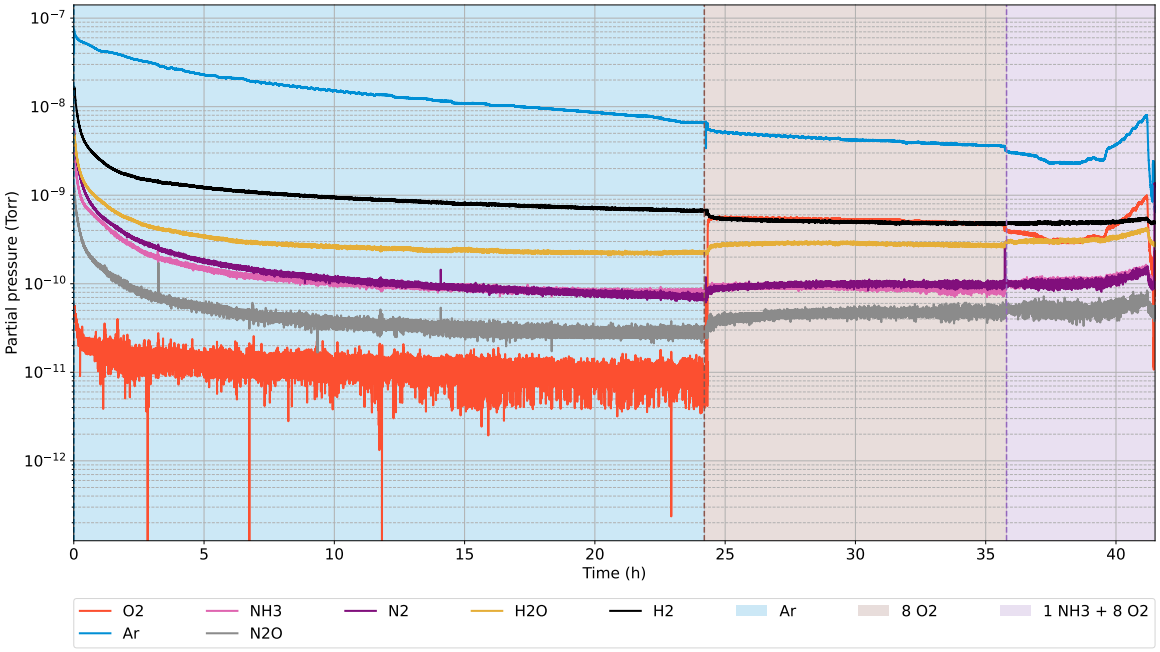

Figure B.8: Time dependent partial pressures recorded from a leak in the reactor output by a residual gas analyser (RGA) during the SXRD experiment on the Pt(100) single crystal at 450 °C, before the change of heater. Vertical dotted lines indicate transitions between two conditions for which the NH_3 and O_2 flow is indicated in the legend.

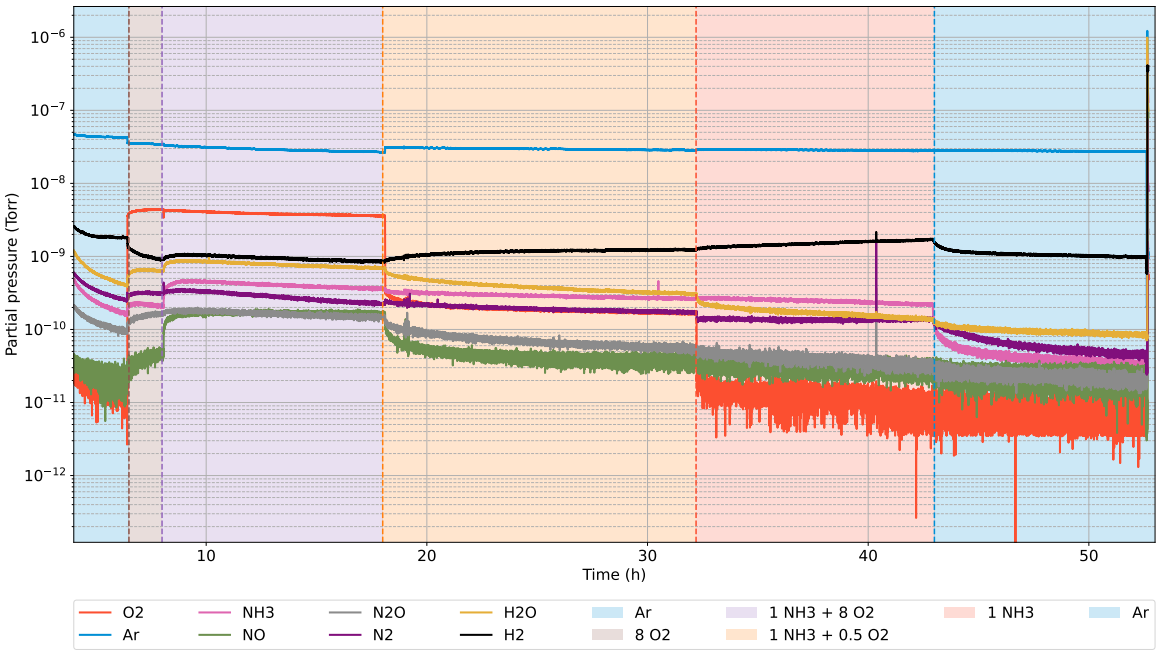

Figure B.9: Time dependent partial pressures recorded from a leak in the reactor output by a residual gas analyser (RGA) during the SXRD experiment on the Pt(100) single crystal at 450 °C, after the change of heater. Vertical dotted lines indicate transitions between two conditions for which the NH_3 and O_2 flow is indicated in the legend.

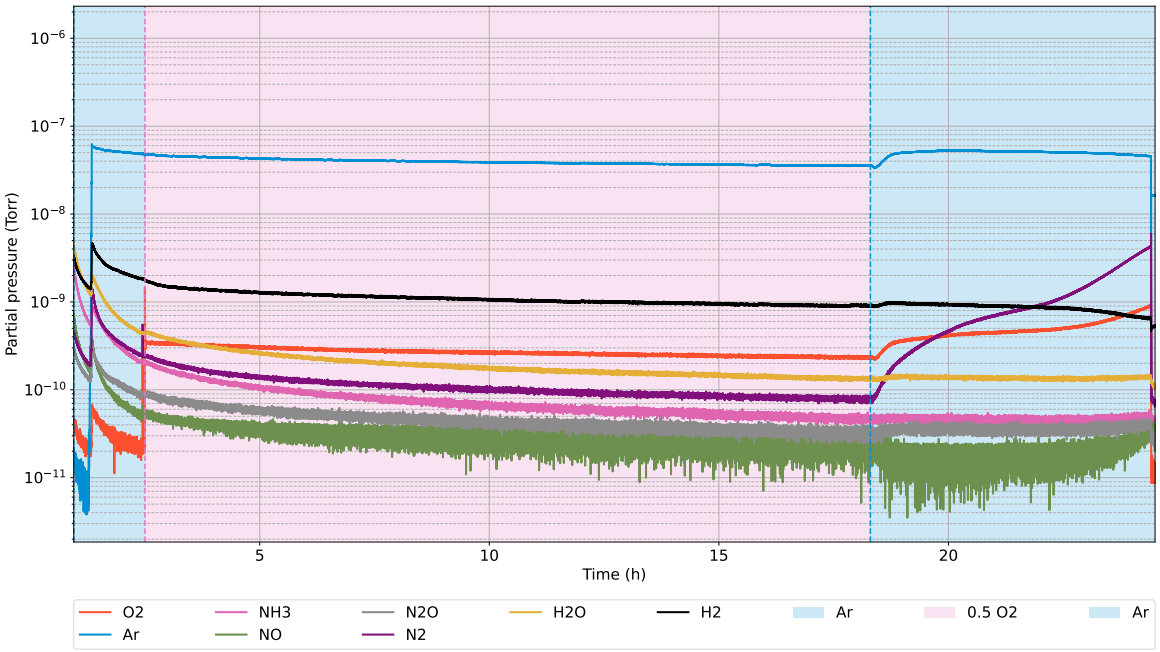

Figure B.10: Time dependent partial pressures recorded from a leak in the reactor output by a residual gas analyser (RGA) during the SXRD experiment on the Pt(100) single crystal at 450 °C*, after ammonia oxidation cycle. Vertical dotted lines indicate transitions between two conditions for which the NH_3 and O_2 flow is indicated in the legend.*

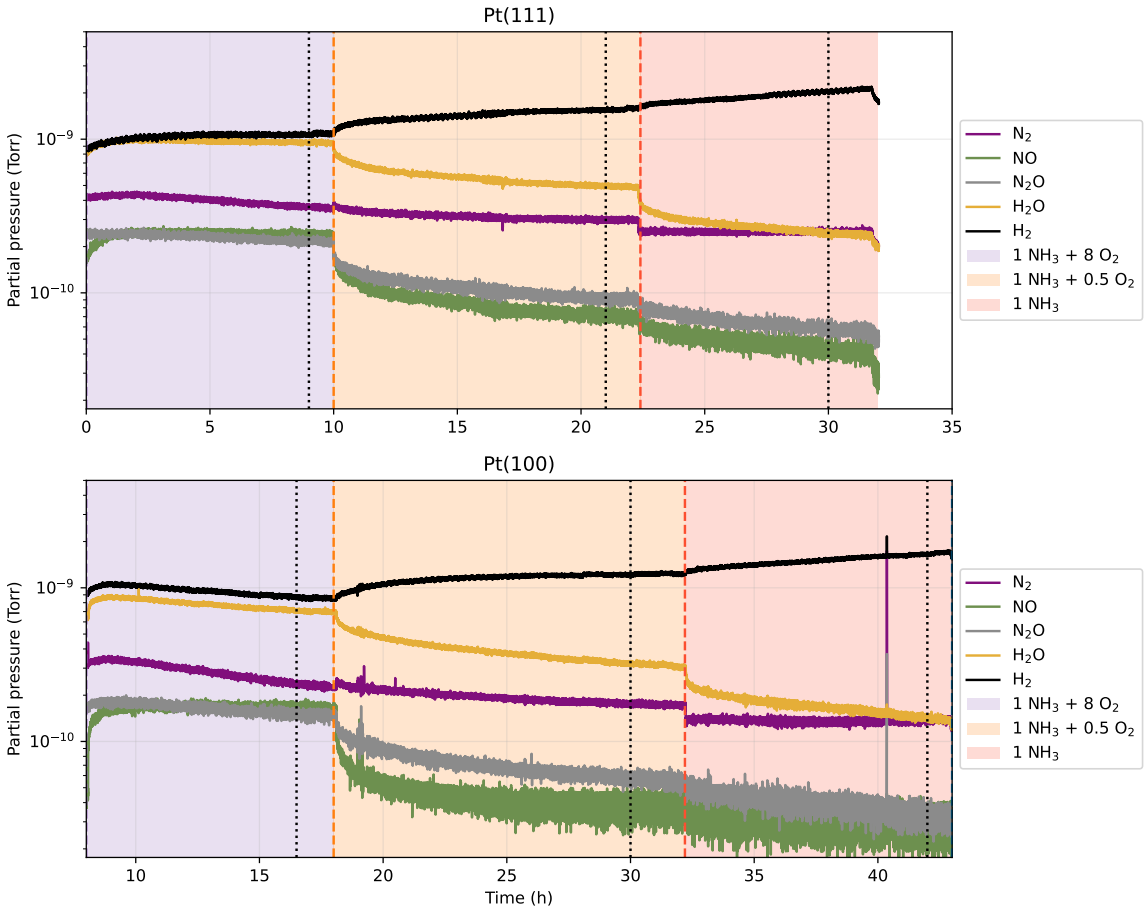

Figure B.11: Evolution of reaction product partial pressures as a function of time during the SXRD experiment on the Pt(111) and Pt(100) single crystals at 450 °C. *Mean partial pressures during* 1 min *at the end of each condition, recorded from a leak in the reactor output by a residual gas analyser (RGA) as detailed in sec. 2.7.3.*

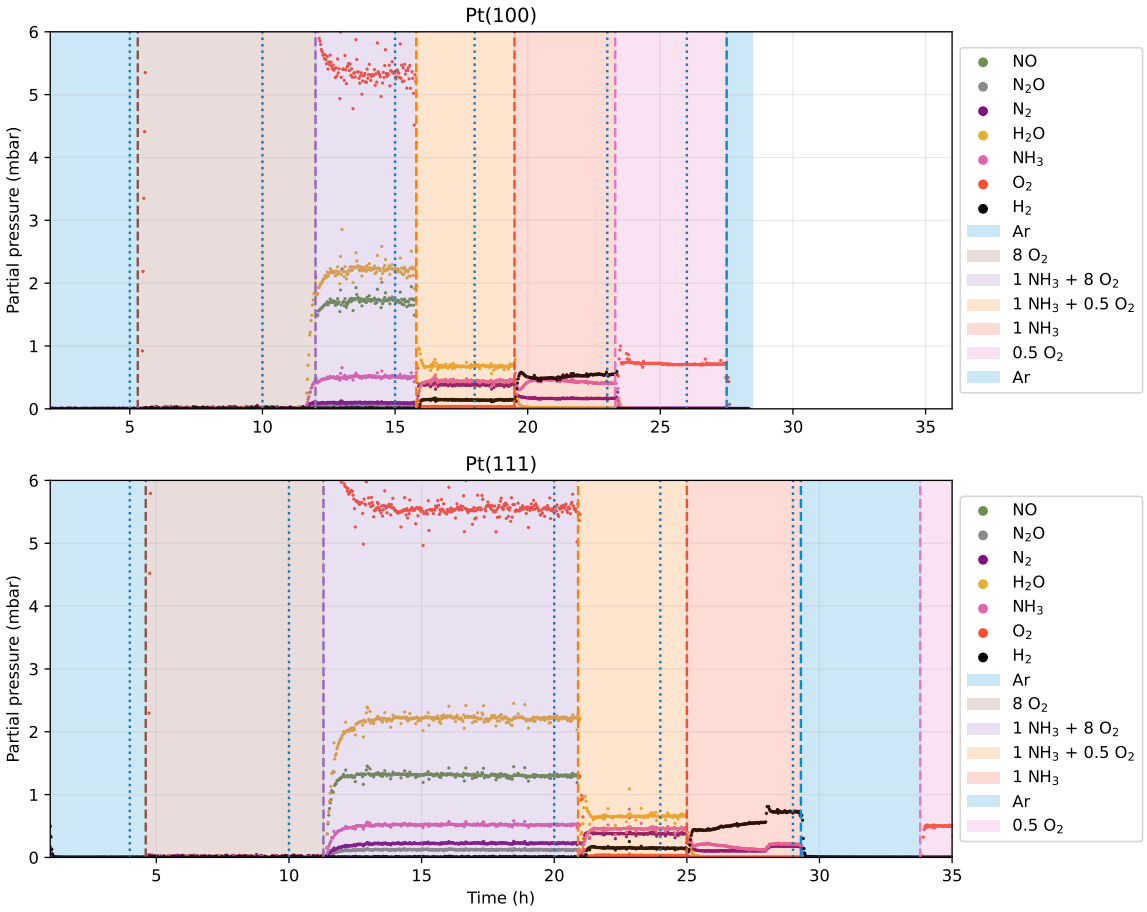

Figure B.12: Evolution of reaction product partial pressures as a function of time during the XPS experiment on the Pt(111) and Pt(100) single crystals at 450 °C. *Mean partial pressures during* 1 min *at the end of each condition, recorded from a leak in the reactor output by a residual gas analyser (RGA) as detailed in sec. 2.7.3.*